



Institut für Erd- und Umweltwissenschaften
Mathematisch-Naturwissenschaftliche Fakultät
Universität Potsdam



The orogenic evolution of the Central Kyrgyz Tien Shan

Dissertation
zur Erlangung des akademischen Grades
"doctor rerum naturalium"
(Dr. rer. nat.)
in der Wissenschaftsdisziplin Geologie

eingereicht an der
Mathematisch-Naturwissenschaftlichen Fakultät
der Universität Potsdam

von

Euan Angus Macaulay
geboren am 17.10.1986 in Aberdeen, Schottland.

Potsdam, den 02.12.2013

This work is licensed under a Creative Commons License:
Attribution - Noncommercial - Share Alike 3.0 Germany
To view a copy of this license visit
<http://creativecommons.org/licenses/by-nc-sa/3.0/de/>

Published online at the
Institutional Repository of the University of Potsdam:
URL <http://opus.kobv.de/ubp/volltexte/2014/6898/>
URN [urn:nbn:de:kobv:517-opus-68985](http://nbn-resolving.org/urn:nbn:de:kobv:517-opus-68985)
<http://nbn-resolving.de/urn:nbn:de:kobv:517-opus-68985>

Abstract

Intra-continental mountain belts typically form as a result of tectonic forces associated with distant plate collisions. In general, each mountain belt has a distinctive morphology and orogenic evolution that is highly dependent on the unique distribution and geometries of inherited structures and other crustal weaknesses. In this thesis, I have investigated the complex and irregular Cenozoic orogenic evolution of the Central Kyrgyz Tien Shan in Central Asia, which is presently one of the most active intra-continental mountain belts in the world. This work involved combining a broad array of datasets, including thermochronologic, magnetostratigraphic, sediment provenance and stable isotope data, to identify and date various changes in tectonic deformation, climate and surface processes. Many of these changes are linked and can ultimately be related to regional-scale processes that altered the orogenic evolution of the Central Kyrgyz Tien Shan.

The Central Kyrgyz Tien Shan contains a sub-parallel series of structures that were reactivated in the late Cenozoic in response to the tectonic forces associated with the distant India-Eurasia collision. Over time, slip on the various reactivated structures created the succession of mountain ranges and intermontane basins which characterises the modern morphology of the region. In this thesis, new quantitative constraints on the exhumation histories of several mountain ranges have been obtained by using low temperature thermochronological data from 95 samples (zircon (U-Th)/He, apatite fission track and (U-Th)/He). Time-temperature histories derived by modelling the thermochronologic data of individual samples identify at least two stages of Cenozoic cooling in most of the region's mountain ranges: (1) initially low cooling rates ($<1^{\circ}\text{C}/\text{Myr}$) during the tectonic quiescent period and (2) increased cooling in the late Cenozoic, which occurred diachronously and with variable magnitude in different ranges. This second cooling stage is interpreted to represent increased erosion caused by active deformation, and in many of the sampled mountain ranges, provides the first available constraints on the timing of late Cenozoic deformation. New constraints on the timing of deformation have also been derived from the sedimentary record of intermontane basins. In the intermontane Issyk Kul basin, new magnetostratigraphic data from two sedimentary sections suggests that deposition of the first Cenozoic syn-tectonic sediments commenced at ~ 26 Ma. Zircon U-Pb provenance data, paleocurrent and conglomerate clast analysis reveals that these sediments were sourced from the Terskey Range to the south of the basin, suggesting that the onset of the late Cenozoic deformation occurred >26 Ma in that particular range. Elsewhere, growth strata relationships are used to identify syn-tectonic deposition and constrain the timing of nearby deformation. Collectively, these new constraints obtained from thermochronologic and sedimentary data have allowed me to infer the spatiotemporal distribution of deformation in a transect through the Central Kyrgyz Tien Shan, and determine the order in which mountain ranges started deforming.

These data suggest that deformation began in a few widely-spaced mountain ranges in the late Oligocene and early Miocene. Typically, these earlier mountain ranges are bounded on at least one side by a reactivated structure, which probably corresponds to the frictionally weakest and most suitably orientated inherited structures for accommodating the roughly north-south directed horizontal crustal shortening of the late Cenozoic. Moreover, tectonically-induced rock uplift in the Terskey Range, following the reactivation of the bounding structure before 26 Ma, likely caused significant surface uplift across the range, which in turn lead to enhanced orographic precipitation. These wetter conditions have been inferred from stable isotope data collected in the two magnetostratigraphically-dated sections in the Issyk Kul basin.

Subsequently, in the late Miocene ($\sim 12\text{--}5$ Ma), more mountain ranges and inherited structures appear to have started actively deforming. Importantly, the onset of deformation at these locations in the late Miocene coincides with an increase in exhumation of ranges that had started deforming earlier in the late Oligocene–early Miocene. Based on this observation, I have suggested that there must have

been an overall increase in the rate of horizontal crustal shortening across the Central Kyrgyz Tien Shan, which likely relates to regional tectonic changes that affected much of Central Asia. Many of the mountain ranges that started deforming in the late Miocene were associated with out-of-sequence tectonic reactivation and initiation, which lead to the partitioning of larger intermontane basins. Moreover, within most of the intermontane basins in the Central Kyrgyz Tien Shan, this inferred late Miocene increase in horizontal crustal shortening occurs roughly at the same time as an increase in sedimentation rates and a significant change sediment composition. Therefore, I have suggested that the overall magnitude of deformational processes increased in the late Miocene, promoting more flexural subsidence in the intermontane basins of the Central Kyrgyz Tien Shan.

Zusammenfassung

Intrakontinentale Gebirge sind typischerweise das Ergebnis tektonischer Kräfte, die auf entfernte Plattenkollisionen beruhen. Im Allgemeinen hat jedes Gebirge sein charakteristisches morphologisches Erscheinungsbild und seine eigene und einzigartige Entstehungsgeschichte, die zum Großteil von der Verteilung und der Geometrie vorgeprägter Strukturen und anderer Schwächzonen innerhalb der Erdkruste abhängt. In der vorliegenden Arbeit habe ich die komplexe känozoische Gebirgsbildung des zentral-kirgisischen Tian Shan Gebirges, eines der weltweit aktivsten intrakontinentalen Gebirge, untersucht. Diese Arbeit kombiniert verschiedenste Datensätze, darunter thermochronologische und magnetostratigraphische Daten, Sedimentprovenienzen und stabile Isotopenzusammensetzungen, um Änderungen der tektonischen Deformationsprozesse sowie Klima- und Oberflächenveränderungen zu erkennen und gegebenenfalls zu datieren. Viele dieser Veränderungen sind eng miteinander verknüpft und können letztendlich auf regionale Prozesse zurückgeführt werden, die die Entwicklung des zentral-kirgisischen Tian Shan beeinflussen.

Das Tian Shan Gebirge besteht aus einer subparallelen Folge einzelner Gebirgsrücken und deren Strukturen, welche im späten Känozoikum als Reaktion auf die entfernt stattfindende Indo-Eurasische Kollision reaktiviert wurden. Im Laufe der Zeit haben Deformation und Versatz entlang dieser reaktivierten Strukturen eine Abfolge von individuellen Gebirgszügen und dazwischen liegenden Sedimentbecken geschaffen deren Morphologie prägend für die heutige Region ist. In dieser Arbeit wurden neue quantitative Altersbestimmungen zur Exhumationsgeschichte mehrerer Gebirgszüge durch thermochronologische Auswertungen an 95 Gesteinsproben durchgeführt (ZHe, AFT und AHe). Die aus Modellierungen einzelner thermochronologischer Datensätze gewonnenen Temperaturgeschichten lassen für die meisten untersuchten Gebirgszüge mindestens zwei Abschnitte känozoischer Abkühlung erkennen: (1) anfänglich niedrige Abkühlungsraten ($<1^{\circ}\text{C}/\text{Myr}$) während einer tektonische Ruhephase und (2) stärkere Abkühlung im späten Känozoikum, die in den verschiedenen Gebirgsketten diachron und mit unterschiedlicher Intensität einsetzt. Diese zweite Abkühlungsphase kann durch einen Anstieg der Erosionsraten durch aktive Deformation interpretiert werden und stellt für viele der untersuchten Gebirgszüge die erste verfügbare Alterabschätzung spätkänozoischer Deformation dar.

Neue Deformationsalter wurden weiterhin aus den Sedimenten intermontaner Becken gewonnen. Im intermontanen Issyk Kul Becken lassen neue magnetostratigraphische Daten zweier Sedimentabschnitte vermuten, dass die Ablagerung der ersten syntektonischen Sedimente im Känozoikum um ca. 26 Ma begann. Weiterhin zeigen Zirkon-Provenienzen, Paläoströmungsrichtungen sowie Klastenanalysen konglomeratischer Sedimente, dass diese Sedimente aus der *Terskey Range* südlich des Beckens stammen, was vermuten lässt, dass der Beginn der spätkänozoischen Deformation in diesem Teil des Gebirgszuges älter als 26 Ma ist. In anderen Bereichen wurden sedimentäre Wachstumsstrukturen zur Identifikation syntektonischer Ablagerung herangezogen, um somit den Zeitpunkt nahe gelegener Deformation zu bestimmen.

Zusammengenommen haben meine Beobachtungen und Auswertungen ermöglicht, die räumlichen und zeitlichen Deformationsmuster quer durch das zentral-kirgisischen Tian Shan Gebirge zu erschließen um eine zeitliche Abfolge in der Entstehung und Entwicklung einzelner Gebirgszüge zu entwickeln. Meine Daten lassen vermuten, dass die Deformation in einigen wenigen, weit auseinander liegenden Bergketten im Spätoligozän bis Frühmiozän begann. Typischerweise sind diese frühen Gebirgsketten auf mindestens einer Seite an eine reaktivierte Struktur gebunden. Diese sind die wahrscheinlich schwächsten oder am besten orientierten Strukturen, um die annähernd Nord-Süd gerichtete Einengung im späten Känozoikum aufzunehmen. Darüber hinaus ist es sehr wahrscheinlich, dass die tektonische Gesteinshebung innerhalb der *Terskey Range*, entlang reaktivierter Störungen vor 26 Ma, eine signifikante Topographiezunahme zur Folge hatte. Dies führte höchstwahrscheinlich zur Ausbildung einer orographischen Barriere und der damit verbundenen Verstärkung der Regenfälle im Becken nördlich des Rückens. Diese Bedingungen konnten mithilfe stabiler Isotopenzusammensetzungen entlang der zwei magnetostratigraphisch datierten Sedimentprofile im Issyk Kul Becken nachgewiesen werden.

Während des späten Miozäns (~12–5 Ma) begann zeitnah die aktive Deformation und Heraushebung mehrerer neuer Gebirgsrücken. Wichtig dabei erscheint, dass der Zeitpunkt dieser spätmiozänen Deformation mit einem Exhumationsschub derer Gebirgszüge zusammenfällt, die schon

viel früher (Spätoligozän bis Frühmiozän) mit der Deformation begannen. Aufgrund dieser Beobachtungen habe ich vorgeschlagen, dass es einen generellen Anstieg der Einengungsraten im Tian Shan gegeben haben muss, welcher auf regionale tektonische Veränderungen zurückzuführen ist die große Teile Zentralasiens betrafen. Viele der Gebirgrücken, die initial im späten Miozän herausgehoben wurden, sind durch unsystematische, tektonische Prozesse der Reaktivierung und Initialisierung von Strukturen (*out-of-sequence*) entstanden, die zur Teilung vormals großer, zusammenhängender Sedimentbecken führte. Darüber hinaus weisen die meisten intermontanen Becken im zentral-kirgisischen Tian Shan, in etwa zur Zeit der beobachteten, verstärkten Einengung im Spätmiozän, ebenfalls erhöhte Sedimentationsraten und eine signifikante Änderung der Sedimentzusammensetzung. Daher vermute ich, dass die allgemeine Intensität der Deformation im Spätmiozän zunahm, was eine tektonische Absenkung (*flexural subsidence*) in den intermontane Becken des zentral-kirgisischen Tian Shan Gebirges zur Folge hatte.

Allgemeine Zusammenfassung

Die meisten der Hochgebirge weltweit wurden entlang konvergenter Plattengrenzen durch Überschiebung und Stapelung kontinentaler Kruste gebildet. Es gibt jedoch auch Gebirgszonen die tausende Kilometer von Plattengrenzen entfernt entstanden sind. Typischerweise werden diese intrakontinentalen Gebirge an krustalen Schwächezonen gebildet, deren Reaktivierung durch Transfer der entlang entfernter Plattenränder generierten Spannungen resultiert.

Das zentralasiatische Tian-Shan-Gebirge ist das derzeit größte und aktivste intrakontinentale Gebirge der Welt. Gelegen zwischen dem rigiden Krustenblock des Tarim-Beckens im Süden und dem kasachischen Schild im Norden, erfolgte seine Reaktivierung im späten Känozoikum infolge der Indo-Eurasischen Kollision, deren Deformation sich zunehmend nach Norden ausbreitete und dabei Krustenverkürzungen innerhalb der Eurasischen Platte verursachte. Im Tian Shan gibt es keine dominanten Großstrukturen. Stattdessen wird die Einengung auf mehrere, weit verteilte Überschiebungs-Systeme verteilt. Diese führten zur Entstehung einer Abfolge von annähernd Ost-West streichenden Gebirgsketten und dazwischen liegenden Sedimentbecken die den heutigen Tian Shan prägen. Da die meisten Überschiebungen an prä-känozoischen Schwächezonen gebildet wurden stellt es sich oft als schwierig heraus die jüngeren Deformationsphasen von der jeweiligen Vorgeschichte zu isolieren. Folglich bleibt der Zeitpunkt tektonischer Aktivität für weite Teile des Gebirges unbekannt und zentrale Fragen zur Entwicklung und zum Wachstum der Gebirgskette bleiben unbeantwortet.

Diese Arbeit liefert neue Daten, die sich mit fundamentalen und bisher offenen Fragen zur Bildung des Tian Shan beschäftigen. Daten aus thermochronologischen Untersuchungen wurden unter anderem verwendet um strukturelle Markerhorizonte aufzuzeigen, die ausschließlich spät-känozoische Deformation anzeigen und es erlauben, Störungsversätze und interne Strukturen der Gebirgszüge (*Terskey Range*) zu erfassen, die ansonsten ausschließlich aus kristallinem Grundgebirge aufgebaut sind. Gemeinsam mit neuen Daten und Altersbeziehungen intramontaner Beckensedimente, wurden diese Daten außerdem genutzt den Zeitpunkt verstärkter Erosionsereignisse zu dokumentieren, die im Zusammenhang mit spät-känozoischer Deformation stehen. Dadurch lassen sich Deformationsphasen für die meisten Gebirgszüge des zentralkirgisischen Tian Shan (~76.0–79.5°E) zeitlich bestimmen. In Übereinstimmung mit früheren Studien zeigen meine Ergebnisse, dass das Einsetzen der Deformation innerhalb der verschiedenen Gebirgszüge keiner gleichmäßigen Abfolge entspricht, sondern unsystematisch vonstatten ging (*out-of-sequence*). In dieser Studie kann erstmals die Reihenfolge der Gebirgsentwicklung im Tian Shan dokumentiert werden, wodurch wesentliche Informationen über deformation-auslösende Prozesse bestimmter Strukturen zu einem gewissen Zeitpunkt zur Verfügung stehen. Der Schlüssel zur Beantwortung dieser Frage liegt in der Beobachtung, dass Deformation und Hebung der frühen Gebirgszüge nicht vermindert wurde als die Deformation in anderen Abschnitten begann. Dies lässt vermuten, dass der Tian Shan nicht durch voranschreitende Deformation gewachsen ist, sondern Hebungen das Resultat diskreter Phasen erhöhter Krustenverkürzung innerhalb der Region reflektiert.

In Kombination mit anderen Daten werfen diese Erkenntnisse ein neues Licht auf die Entwicklung des zentralkirgisischen Tian Shan. Zum Beispiel zeigen Sauerstoff-Isotopendaten datierter Sedimente des Issyk Kul Beckens, dass die Region nach einsetzender Deformation des südlichen Gebirgszuges (*Terskey Range*) feuchter wurde. Eine Erklärung dafür könnten verstärkte Niederschläge entlang neu gebildeter Topographie sein (orographische Barriere). Diese Kombination aus tektonischen und klimatischen Daten gewährt einen einzigartigen Blick auf die Entstehung des Tian Shan und stellt einen bedeutenden Schritt auf dem Weg zum besseren Verständnis der Mechanik und Interaktion tektonischer Deformation, Klima und Oberflächenprozessen wie Exhumation und Sedimentation dar.

Acknowledgements

I arrived in Germany in the summer of 2008 having just graduated. If I am being honest, I had a naive or even poor understanding of how people do science and soon realised that everyone else was much more experienced and knowledgeable than me. Hopefully since then I have improved a bit, and now I have a slightly better understanding of geosciences and how to work in them. The vast majority of this improvement can be attributed to my supervisor, Ed Sobel. Throughout my time in Germany, Ed has provided valuable insights into my work and geosciences in general, and has helped me immeasurably with the numerous problems I encountered along the way, ranging from my troubles with punctuation especially commas, and semi-colons; to the key scientific questions of my work. As with all good teachers and supervisors, he would typically phrase his pointers and suggestions as questions, prompting me to think in the right direction and gain a better understanding of my work – for this I am very grateful. In general, there are so many big and small things that I need to thank Ed for that it is difficult to know where to begin. Probably the logical place to start is at the beginning and say thanks for writing the proposal to work in Kyrgyzstan, and allowing me to be involved in the project. Since the *very* long walk on the fifth day of our first field season together, Ed has become a kind and considerate friend.

Someone else who has helped me a great deal since arriving in Germany and become a fantastic friend along the way is graphics expert extraordinaire, computer-problem trouble-shooter and occasionally drinking partner Heiko Pingel. When I first arrived in Germany, Heiko helped me adapt; he taught me some of the most fundamental, and often, especially for a naive Scottish *loon*, some of the most surprising aspects of life in Germany. For example, he explained that it was possible in Germany to eat doner kebabs sober, and what's more enjoy them!

There are many more people in the institute that have helped me who deserve enormous thanks. Special thanks go to Alejandro Bande, Paolo Ballato, Rasmus Thiede and Taylor Schildgen, who have provided important assistance and many suggestions for improving my papers. In fact, all of my colleagues in the SMURF group, both past and present, have provided me with so many great ideas over the years, for which I am very grateful. I would also like to thank these SMURF colleagues for providing the perfect environment to learn about different and often very diverse aspects of geosciences, as well as the many fun and exciting discussions that have arisen. The person most to blame for fostering this atmosphere is Manfred Strecker, who's extensive knowledge and keen interest in a large variety of geoscience disciplines has infected the entire group and made it a joy to be involved with.

Outside of the institute, I would like to thank the various co-workers who have been involved in this project through the years. Fin Stuart and Barry Kohn in East Kilbride and Melbourne, respectively, are thanked for their assistance and suggestions related to the thermochronology data. Michael Wack and Stuart Gilder, the paleo-mag guys, are thanked for their vast contribution and companionship in the field. Andreas Mulch and Scott Hynek are thanked for performing the stable isotope analysis and assisting with the interpretation. Angela Landgraf is doubly thanked for being a key member of the SMURF group and for being a co-author who provided vital assistance in the field and whilst preparing this thesis. Alexander Mikolaichuk is thanked for being a fount of knowledge about the Tien Shan and Kyrgyz geology, as well as organising lots of important things for our field visits. In particular, his selection of Vasyl Hyshchyn as a field assistant and two excellent drivers in Ivan Andreev and Yuri Sergeev. Without these three people, much of the work presented in this thesis could not have been accomplished and I am very grateful to have had them as companions in the field. The positive attitude of the drivers was especially important during the field trips in Kyrgyzstan. No obstacle was too much for their vehicles, Blondie and the Vaz, even if it resulted in being stranded in

the waist-high water of the incorrectly named *Kichi* Naryn river (*Kichi* means small in Kyrgyz – and believe me it did not seem small at the time).

Finally, this work would not have been possible without the financial support of the Deutsche Forschungsgemeinschaft (DFG) (grant SO 436/4-1), the Universität Potsdam and the Mathematisch-Naturwissenschaftliche Fakultät. Or without the emotional support of my family, which increased in number during my time in Germany. I would like to end by thanking my partner Pia, who has been regularly kept awake at nights by me worrying and thinking about my work, but who fortunately continues to put up with me.

Contents

List of figures	13
List of tables	15
Chapter 1 – Introduction	16
Chapter 2 – Thermochronological insight into late Cenozoic deformation in the basement-cored Terskey Range, Kyrgyz Tien Shan	20
2.1. Introduction	20
2.2. Geological setting	23
2.3. Methodology and results	24
2.3.1. Thermochronological data	24
2.3.2. Thermochronological results	24
2.3.2.1. Thermochronological ages	24
2.3.2.2. Age-elevation relationships (AERs)	25
2.3.2.3. Thermal modelling	28
2.3.3. Structural data	28
2.3.3.1. Fault kinematic data	29
2.3.3.2. Thermochronologically-derived structural data	30
2.4. Discussion	32
2.4.1. Isochron and late Mesozoic–Tertiary basement unconformity	32
2.4.2. Cenozoic structural interpretation	32
2.4.3. Exhumation and deformation history	34
2.5. Conclusions	35
Chapter 3 – Cenozoic deformation and exhumation history of the Central Kyrgyz Tien Shan	37
3.1. Introduction	37
3.2. Geological setting	38
3.3. Methodology and results	41
3.3.1. Sample locations	41
3.3.2. Thermochronological systems	41
3.3.2.1. Apatite fission track (AFT)	41
3.3.2.2. Apatite and Zircon (U-Th-Sm)/He analysis (AHe and ZHe)	42
3.3.3. Thermal modelling	42
3.4. Data interpretation	48
3.4.1. Data evaluation	48
3.4.2. Spatial distribution of thermochronological ages	50
3.4.3. Age-elevation relationships (AERs)	52
3.5. Discussion	54
3.5.1. Mesozoic and Cenozoic exhumation history	54
3.5.2. Onset of late Cenozoic deformation	56
3.5.3. Geological history	58
3.6. Conclusions	62

Chapter 4 – Cenozoic magnetostratigraphy and rock magnetism of the southern Issyk Kul basin, Kyrgyzstan	64
4.1. Introduction	64
4.2. Geology, Sampling and Methodology	65
4.3. Results	67
4.3.1. Magnetic Mineralogy	67
4.3.2. Anisotropy of Anhyseretic Remanence	71
4.3.3. Magnetic Remanence	75
4.3.4. Magnetostratigraphy	77
4.4. Discussion and Conclusions	81
Chapter 5 – The sedimentary record of the Issyk Kul basin, Kyrgyzstan: climatic and tectonic inferences	83
5.1. Introduction	83
5.2. Setting	85
5.2.1. Tectonic history of the Central Kyrgyz Tien Shan	85
5.2.2. Issyk Kul basin stratigraphy	86
5.2.3. Pollen data	90
5.3. Methodology and results	90
5.3.1. Sedimentological analysis	90
5.3.2. Zircon U-Pb provenance analysis	92
5.3.3. Oxygen and carbon isotopes	92
5.4. Discussion	98
5.4.1. Sediment provenance	98
5.4.2. Stable isotopes	99
5.4.2.1. Isotopic signal from over-bank deposits	99
5.4.2.2. Potential contamination of initial authigenic isotopic signal	100
5.4.2.3. Vegetation inferences	101
5.4.2.4. Stable isotope values through time	101
5.4.2.5. Decreasing $\delta^{13}\text{C}$ values between 0 and 250 m in the Chon Kyzylsu section.	101
5.4.2.6. Increased $\delta^{18}\text{O}$ scatter after ~420 m in the Chon Kyzylsu section	102
5.5. Conclusions	103
Chapter 6 – Discussion and conclusions	105
6.1. Late Cenozoic orogenic evolution of the Central Kyrgyz Tien Shan	105
6.2. Structural architecture of the Central Kyrgyz Tien Shan	107
6.3. Remaining research questions and future directions	108
References	111
Appendix 1 – Thermochronological data from the Barskoon transect (Supplementary material for Chapter 2)	119
A1.1. Thermochronological methodology	119
A1.1.1. Apatite fission track (AFT) methodology	119
A1.1.2. Apatite (U-Th-Sm)/He (AHe) methodology	119
A1.1.3. Thermal modelling	119
A1.2. Apatite (U-Th-Sm)/He (AHe) variability	120

Appendix 2 – Thermochronological data from the Central Kyrgyz Tien Shan (Supplementary material for Chapter 3)	130
A2.1. Apatite fission track (AFT) data	130
A2.2. Apatite (U-Th-Sm)/He (AHe) data	130
A2.3. Zircon (U-Th-Sm)/He (ZHe) data	130
 Appendix 3 – Magnetostratigraphy data (Supplementary material for Chapter 4)	 158
 Appendix 4 – Zircon U-Pb data (Supplementary material for Chapter 5)	 162

List of figures

Chapter 1 – Introduction

Figure 1.1. Elevation map of Central Asia and map of Kyrgyzstan	19
---	----

Chapter 2 – Thermochronological insight into late Cenozoic deformation in the basement-cored Terskey Range, Kyrgyz Tien Shan

Figure 2.1. Elevation map of Tien Shan and geological map of central Terskey Range	21
Figure 2.2. Thermochronological age transect and age-elevation relationships (AERs)	26
Figure 2.3. Selected time-temperature histories and paleo-temperature estimates	29
Figure 2.4. Structural constraints from transect through Terskey Range	31
Figure 2.5. Interpretation of structural constraints	34
Figure 2.6. Exhumation through time	36

Chapter 3 – Cenozoic deformation and exhumation history of the Central Kyrgyz Tien Shan

Figure 3.1. Map of Tien Shan and simplified geological map of Central Kyrgyz Tien Shan . . .	39
Figure 3.2. Representative time-temperature histories from thermal modelling	47
Figure 3.3. Thermochronological data evaluation	49
Figure 3.4. Swath profiles through Central Kyrgyz Tien Shan	51
Figure 3.5. Thermochronological age-elevation relationships (AERs)	53
Figure 3.6. Compilation of exhumation and cooling rates from the Terskey Range	55
Figure 3.7. Map showing the onset of deformation in the Central Kyrgyz Tien Shan	57
Figure 3.8. Conceptual model for the geological history of the Central Kyrgyz Tien Shan . . .	60

Chapter 4 – Cenozoic magnetostratigraphy and rock magnetism of the southern Issyk Kul basin, Kyrgyzstan

Figure 4.1. Topographic map of Tien Shan and geological map of study area	66
Figure 4.2. Stratigraphic columns of the Issyk Kul basin	68
Figure 4.3. Magnetic moments of stepwise demagnetization	69
Figure 4.4. Representative field magnetization measurements	70
Figure 4.5. Variations in magnetic properties in sampled sections	72
Figure 4.6. Partial anhysteretic remanent magnetization (pARM) spectra	73
Figure 4.7. Principal directions of magnetic anisotropy	74
Figure 4.8. Representative thermal demagnetization	76
Figure 4.9. High temperature magnetization directions	77
Figure 4.10. Polarity chrons for age model A	78
Figure 4.11. Polarity chrons for age model B	79
Figure 4.12. Sedimentation rates through time	80

Chapter 5 – The sedimentary record of the Issyk Kul basin, Kyrgyzstan: climatic and tectonic inferences

Figure 5.1. Maps of Tien Shan and eastern Kyrgyzstan	84
Figure 5.2. Geological map of the southern-eastern Issyk Kul basin	87
Figure 5.3. Simplified stratigraphic column of Issyk Kul basin and pollen data	89
Figure 5.4. Sedimentological data from sampled sections	91
Figure 5.5. Zircon U-Pb provenance data	97
Figure 5.6. Plots of stable isotope data	98

Figure 5.7. Compilation of climate data from Central Asia and Tien Shan	103
Chapter 6 – Discussion and conclusions	
Figure 6.1. Summary of key events	110
Appendix 1	
Figure A1.1. Plots of AFT data	123
Figure A1.2. Time-temperature histories for all samples	125
Figure A1.3. eU-AHe age and grain size-AHe age plots	129
Appendix 2	
Figure A2.1. Plots of AFT data	134
Figure A2.2. eU-AHe age and grain size-AHe age plots	148
Figure A2.3. Well constrained time-temperature histories from thermal modelling	152
Figure A2.4. Conglomerate clast count data and interpretation from Naryn basin	156
Appendix 3	
Figure A3.1. Stratigraphic variations in selected magnetic parameters	159
Figure A3.2. Flinn diagrams for sampled sections	160
Figure A3.3. Fisher mean directions for all sampled sites	160
Figure A3.4. Computered correlations (age model B)	161

List of tables

Chapter 2 – Thermochronological insight into late Cenozoic deformation in the basement-cored Terskey Range, Kyrgyz Tien Shan

Table 2.1. Summary of new thermochronological data from Terskey Range transect	27
--	----

Chapter 3 – Cenozoic deformation and exhumation history of the Central Kyrgyz Tien Shan

Table 3.1. Summary of thermochronological data	43
--	----

Chapter 5 – The sedimentary record of the Issyk Kul basin, Kyrgyzstan: climatic and tectonic inferences

Table 5.1. Summary of zircon U-Pb provenance data	93
---	----

Table 5.2. Stable isotope data from sediments	93
---	----

Appendix 1

Table A1.1. Apatite fission track (AFT) data	122
--	-----

Table A1.2. Apatite (U-Th-Sm)/He (AHe) data	126
---	-----

Table A1.3. Summary of thermal modelling results	128
--	-----

Appendix 2

Table A2.1. Apatite fission track (AFT) data	131
--	-----

Table A2.2. Apatite (U-Th-Sm)/He (AHe) data	144
---	-----

Table A2.3. Zircon (U-Th-Sm)/He (ZHe) data	151
--	-----

Appendix 3

Table A3.1. Magnetostratigraphic sample detail	158
--	-----

Table A3.2. Properties of normalized average tensors	158
--	-----

Table A3.3. Fisher and bipolar Watson directions of high temperature magnetization	158
--	-----

Appendix 4

Table A4.1. Zircon U-Pb data	162
--	-----

Table A4.2. Compilation of basement zircon U-Pb ages	184
--	-----

Chapter 1.

Introduction

In the last thirty years, an increasing body of evidence has suggested that the spatiotemporal evolution of mountain belts is governed by interactions between tectonic deformation, climate and surface processes [e.g. *Davis et al.*, 1983; *Koons*, 1987; 1990; *Molnar and England*, 1990; *Burbank*, 1992; *Willett et al.*, 1993; *Avouac and Burov*, 1996; *Willett*, 1999; *Thiede et al.*, 2004; *Simpson*, 2006; *Whipple and Meade*, 2006; *Whipple*, 2009]. Initially, most of this evidence came from analogue and numerical modelling of critical Coulomb wedges, where links between deformation and erosion allow the maintenance of a critical taper [*Davis et al.*, 1983; *Dahlen et al.*, 1984; *Dahlen*, 1990]. More recently, the predictions of these models have been verified by empirical evidence from real-world mountain belts [e.g. *Berger et al.*, 2008]. However, in some orogens, where tectonic forces act upon a mosaic of inherited structures and other pre-existing crustal weaknesses, these models often fail to predict the spatiotemporal distribution of deformation [e.g. *Hilley et al.*, 2005]. This type of orogen is commonly found within intra-continental settings, where tectonic forces associated with distant collisions exploit numerous pre-existing weaknesses, causing active deformation and mountain building [e.g. *Molnar and Tapponnier*, 1975; *Windley et al.*, 1990; *Allen and Vincent*, 1997]. Typically, within these settings, deformation will become focussed around pre-existing weaknesses, reactivating structures that are frictionally weak and suitably orientated with respect to the maximum horizontal stress [*Holdsworth et al.*, 1997; *Kley et al.*, 2005]. If these reactivated structures are widely distributed, they will drive rock uplift in a series of fault-bounded blocks and eventually build a succession of mountain ranges and intermontane basins [*Jordan and Allmendinger*, 1986; *Sobel et al.*, 2003; *Strecker et al.*, 2011]. In other words, the morphology and spatiotemporal evolution of these intra-continental mountain belts depends on a unique distribution and geometry of reactivated structures [e.g. *Mortimer et al.*, 2007; *Neely and Erslev*, 2009]. Therefore, in order to understand orogenic development of a particular intra-continental mountain belt, it is first necessary to constrain the timing and effects of tectonic deformation, climate changes and surface processes, such as erosion and sedimentation, in every mountain range and intermontane basin.

The world's largest active intra-continental mountain belt is the Tien Shan of Central Asia (Figure 1.1a+b). Tectonic deformation related to the India-Eurasia collision first reached the Tien Shan in the late Oligocene–early Miocene [*Windley et al.*, 1990; *Hendrix et al.*, 1994; *Métivier and Gaudemer*, 1997; *Yin et al.*, 1998; *Sobel and Dumitru*, 1997; *Dumitru et al.*, 2001; *Sobel et al.*, 2006a; *Heermance et al.*, 2007, 2008; *Glorie et al.*, 2011; *De Grave et al.*, 2011a, 2013; *Macaulay et al.*, 2013]. Since then, a series of sub-parallel mountain ranges and intervening basins have developed (e.g. Figure 1.1d), forming a deformational zone that stretches ~2500 km east-west along strike and in places exceeds 400 km in width (Figure 1.1b). Deformation in different mountain ranges appears to have occurred diachronously and often involved the out-of-sequence tectonic reactivation of inherited structures (e.g. Figure 1.1d). However, to date, the sequence of deformation has not been well-constrained across multiple mountain ranges, and many fundamental questions about the spatial distribution of deformation through time and what triggers rock uplift at a particular location remain unanswered. Today, deformation is widely distributed throughout the Tien Shan, with slip on numerous structures accommodating up to 20 mm/a of horizontal crustal shortening (Figure 1.1c+d). This maximum amount of shortening across the Tien Shan is achieved between longitudes of 76 and 78°E, where it corresponds to nearly two-thirds of the total India-Eurasian convergence [*Zubovich et al.*, 2010]. At these longitudes, most of this shortening is accommodated in the series of mountain ranges and intermontane basins east of the Talas-Ferghana Fault (TFF) that form the Central Kyrgyz Tien Shan (Figure 1.1c).

In the Central Kyrgyz Tien Shan, most mountain ranges are bounded on at least one side by high angle reverse faults, which often correspond to reactivated Paleozoic structures, particularly Permian strike-slip faults [Bazhenov and Mikolaichuk, 2004; Selander et al., 2012]. Most of these mountain ranges have been sufficiently eroded to remove younger lithologies, leading to the exhumation of basement rocks (Figure 1.1d). Structural marker beds, fault kinematic and other geological data from within these basement-cored ranges typically record the cumulative effects of multiple deformational phases that cannot easily be differentiated. Consequently, in most of the basement-cored ranges in the Central Kyrgyz Tien Shan, the underlying structural architecture as well as the timing and magnitude of the late Cenozoic deformation therein remains largely unquantified. Such information is essential for understanding the construction and development of individual mountain ranges and the tectonic evolution of the entire Central Kyrgyz Tien Shan.

Two possible ways to address this deficiency and tackle this problem are by using low-temperature thermochronological data from basement-cored ranges and through the sedimentary record of the various intermontane basins. The onset of contractile deformation in a mountain range will usually lead to an increase in exhumation, which can often be detected and dated using thermochronological age-elevation relationships [e.g. Fitzgerald et al., 1995], thereby constraining the timing of deformation. Furthermore, within intermontane basins, the onset of deformation in a nearby mountain range will typically affect the amount and composition of sediment delivered to the basin, while surface uplift will increase the topographic load and therefore the amount of flexurally-driven accommodation space in the adjacent basin [e.g. Allen et al., 2013]. As a result, dating increases in sedimentation rates or changes in sediment composition are well-established methods for inferring the timing of nearby deformation, and constraining the erosion history of the sources areas, providing vital insights into interactions between tectonic and surface processes that have controlled the development of nearby mountain ranges and the intermontane basin [e.g. Charreau et al., 2005]. Similar insights into tectonic and surface processes can also be obtained by using thermochronological data to quantify the exhumation of basement-cored ranges through time, either by exploiting age-elevation relationships or through modelled cooling histories of individual samples [Ketcham, 2005]. Moreover, the modelled cooling histories of a collection of samples taken across a basement-cored ranges can also be used to determine which samples were hotter and therefore structurally deeper prior to the onset of deformation. Provided samples from similar elevations and modern structural positions are compared, this approach can be used to differentiate recent and older deformation, ultimately to infer the underlying structural architecture and identify which inherited structures have been reactivated.

In this thesis, I have studied the spatiotemporal evolution of a ~47000 km² portion of the Central Kyrgyz Tien Shan in the south-east corner of Kyrgyzstan (Figure 1.1d). Using a broad array of techniques, I have helped address the shortage of data on the timing and magnitude of deformation and erosion in the Central Kyrgyz Tien Shan. This new information is primarily obtained by using the low-temperature thermochronologic systems of apatite fission track (AFT), apatite (U-Th)/He (AHe) and zircon (U-Th)/He (ZHe) to constrain the exhumation history of various mountain ranges, which in turn can be used to infer the onset of deformation. These thermochronology-based inferences about the timing of deformation are supplemented and in places independently verified by new data, particularly the magnetostratigraphically-derived age controls on the stratigraphy of the Issyk Kul basin (Figure 1.1d). Together with paleoclimate proxy data obtained from stable isotope analysis of sediments, this combination of thermochronologic and geologic data allows me to identify and date many of the key changes in tectonic deformation, climate and surface processes that have affected the Central Kyrgyz Tien Shan's orogenic evolution. Moreover, this new data allows the causes and feedbacks associated with changes in tectonic deformation, surface uplift, climate, erosion and sedimentation to be investigated. In particular, the combination of thermochronologic, sedimentologic and climate proxy data from the well-studied Terskey Range and southern Issyk Kul basin suggests that significant surface uplift occurred shortly after the onset of late Cenozoic deformation, which

resulted in orographically enhanced precipitation. These different datasets are explained and interpreted in four manuscripts, each of which is presented here as a chapter.

In chapter two, I have used thermochronological data to constrain exhumation in part of the basement-cored Terskey Range, located to the south of the Issyk Kul basin (Figure 1.1d). More significantly, together with geological observations, this dataset is used to construct new thermochronologically-derived structural markers, which have only experienced the most recent, late Cenozoic deformational phase. These structural markers provide unique insights into the underlying structural architecture of the basement-cored range and can be used to quantify the amount of deformation. This chapter has been published in *Tectonics*, vol. 32, 487–500, 2013, doi: 10.1002/tect.20040 by Euan A. Macaulay, Edward R. Sobel, Alexander Mikolaichuk, Angela Landgraf, Barry Kohn and Finlay Stuart.

In chapter three, new thermochronological data from 80 samples is presented and used to infer the onset of deformation in many mountain ranges of the Central Kyrgyz Tien Shan. Based on this data and geological evidence from adjacent intermontane basins, I have been able to unravel the timing of deformation across a series of mountain ranges and establish the likely sequence in which they were constructed. I link the new constraints on the timing of deformation and structural observations with previously published sedimentary data [Abdrakhmatov *et al.*, 2001] in order to develop a new evolutionary model for the Central Kyrgyz Tien Shan, which highlights the importance of the region's numerous inherited structures in controlling the spatiotemporal distribution of late Cenozoic deformation. This chapter was submitted in May 2013 to *Tectonics* by Euan A. Macaulay, Edward R. Sobel, Alexander Mikolaichuk, Barry Kohn and Finlay M. Stuart.

In chapter four, paleomagnetic data are used to date the first syn-tectonic sedimentary unit (Shamsi group) deposited in the Issyk Kul basin. Importantly, the basal age of this unit provides independent constraints on the timing of deformation inferred from thermochronological data in the Terskey Range, which was presented in the previous two chapters. Work for this chapter was primarily conducted by colleagues in Munich, in particular as part of Michael Wack's doctoral thesis. I was responsible for field measurements of bedding and sedimentary thicknesses, and was involved in sample collection, interpreting the regional significance of derived age constraints and correcting the manuscript. In May 2013, it was submitted by Michael R. Wack, Stuart A. Gilder, Euan A. Macaulay, Edward R. Sobel, Julien Charreau and Alexander Mikolaichuk to a special issue of *Tectonophysics* in tribute to Graham Borradaile. This chapter has been included to provide details about the magnetostratigraphically-derived age constraints for the first syn-tectonic sediments, which are used and discussed further in the following chapter.

Chapter five uses stable isotope, zircon U-Pb provenance, paleocurrent and conglomerate clast count data from the two magnetostratigraphically-dated sections (chapter 4) to investigate the climatic and tectonic evolution of the Issyk Kul basin and the surrounding mountain ranges (Figure 1.1d). This is the first time climate variations have been identified from a stable isotope record of an intermontane basin within the Tien Shan. In particular, the new data supplies valuable insights into the surface uplift history of the Terskey Range and potential feedbacks between tectonic deformation, climate and sedimentation (Figure 1.1d). Moreover, comparing the stable isotope data from the two sections provides additional constraints on the timing of deposition and allows the magnetostratigraphically-derived age models presented in chapter 4 to be improved. This chapter was submitted in the November 2013 to *Basin Research* by Euan A. Macaulay, Edward R. Sobel, Alexander Mikolaichuk, Michael Wack, Stuart Gilder, Andreas Mulch, Alla B. Fortuna, Scott A. Hynek and Farid Apayarov.

In chapter six, the key conclusions of the previous four chapter are summarized and their significance in terms of understanding the overall spatiotemporal evolution of the Central Kyrgyz Tien Shan are discussed. Finally, I summarize several significant unresolved research questions and suggest possible ways in which these could be addressed in the future.

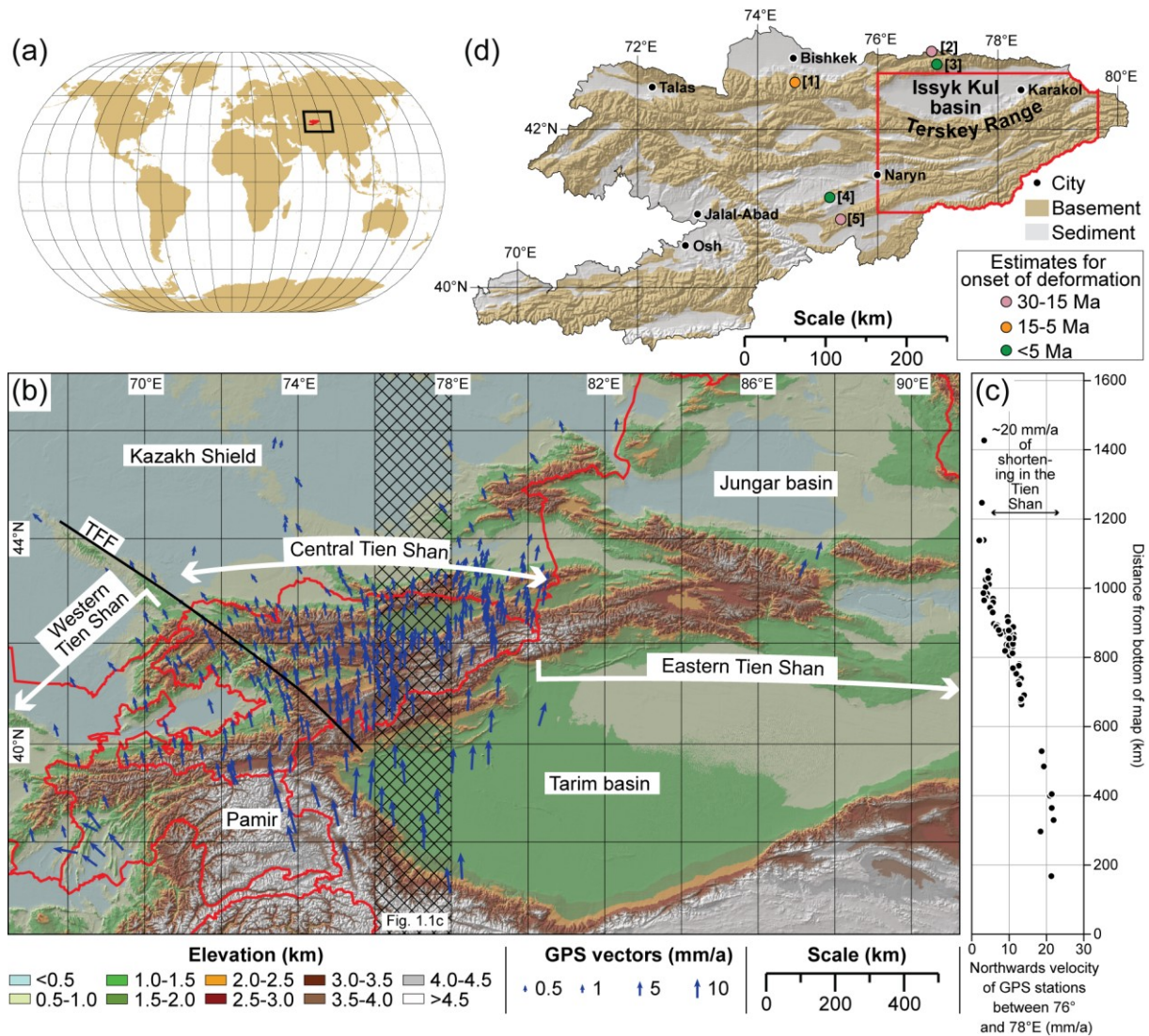


Figure 1.1. (a) Location of Kyrgyzstan (highlighted in red) and Figure 1.1b (black outline). Land shown in light brown from the Kaartlagen van de Wereld dataset (<http://www.geodan.nl>). Grid lines have 20° intervals. Map in World Winkel II projection. (b) Digital elevation model (DEM) of the Tien Shan based on GTOPO90 data. Blue arrows denote the velocity of Global Positioning System (GPS) stations with respect to stable Eurasia [Zubovich *et al.*, 2010]. Political borders shown by red lines. TFF= Talas Ferghana Fault. Hatching shows location of transect used to construct Figure 1.1c. Map in Mercator projection. (c) Plot of northwards velocity of all GPS stations located in hatched area of Figure 1.1b, shows ~20 mm/a of shortening is accommodated by deformation throughout the Central Tien Shan. (d) Map of Kyrgyzstan showing the distribution of Precambrian and Paleozoic basement (brown) and Mesozoic–Cenozoic sediments (grey). Study area is outlined by red line. Locations of major cities are shown. Corresponding references for selected estimates for the onset of deformation. 1: Bullen *et al.* [2001, 2003], Sobel *et al.* [2006b]; 2: De Grave *et al.* [2013]; 3: Selander *et al.* [2012]; 4: Makarov *et al.* [2010]; 5: Glorie *et al.* [2011]. Map in Mercator projection.

Chapter 2.

Thermochronologic insight into late Cenozoic deformation in the basement-cored Terskey Range, Kyrgyz Tien Shan

Published by Euan A. Macaulay, Edward R. Sobel, Alexander Mikolaichuk, Angela Landgraf, Barry Kohn and Finlay Stuart (2013) in *Tectonics*, vol. 32, 487–500, doi: 10.1002/tect.20040, 2013

Abstract

Basement-cored ranges formed by reverse faulting within intra-continental mountain belts are often composed of poly-deformed lithologies. Geological data capable of constraining the timing, magnitude and distribution of the most recent deformational phase is usually missing in such ranges. In this chapter, we present new low temperature thermochronological and geological data from a transect through the basement-cored Terskey Range, located in the Kyrgyz Tien Shan. Using this data, we are able to investigate the range's late Cenozoic deformation for the first time. Displacements on reactivated faults are constrained and deformation of thermochronologically-derived structural markers is assessed. These structural markers post-date the earlier deformational phases, providing the only record of Cenozoic deformation and of the reactivation of structures within the Terskey Range. Overall, these structural markers have a southern inclination, interpreted to reflect the decreasing inclination of the reverse fault bounding the Terskey Range. Our thermochronological data is also used to investigate spatial and temporal variations in the exhumation of the Terskey Range, identifying a three stage Cenozoic exhumation history: (1) virtually no exhumation in the Paleogene, (2) increase to slightly higher exhumation rates at ~26–20 Ma, and (3) significant increase in exhumation starting at ~10 Ma.

2.1. Introduction

Contractional intra-continental mountain belts are usually composed of numerous sub-parallel ranges and intermontane basins [e.g. *Tapponnier and Molnar, 1979; Jordan and Allmendinger, 1986*]. Structurally, every range is different with deformation significantly influenced by the distribution of pre-existing weaknesses and other crustal heterogeneities [*Hilley et al., 2005*]. Most ranges are bound on at least one side by high angle reverse faults (dips $>30^\circ$); typically, these are mechanically unsuitable for accommodating slip and require pre-existing weaknesses that can be reactivated [*Sibson, 1985*], or assist in their initiation [*Selander et al., 2012*]. Other ranges consist of broad arch anticlines that developed at upper crustal temperatures by slip on numerous pre-existing fractures and discontinuities [*Schmidt et al., 1993; Garcia and Davis, 2004*]; these are often interpreted to correspond to blind reverse faults at depth [e.g. *Jordan and Allmendinger, 1986*]. Frequently structures have been reactivated or initiated out-of-sequence, with deformation not simply propagating into adjacent basins. Instead the migration of deformation is controlled by rock uplift and erosional processes that respectively build and reduce topography, and the suitability of variably-orientated inherited weaknesses to reactivation [*Hilley et al., 2005*]. Constraining the timing, magnitude and distribution of deformation and exhumation is therefore essential for understanding the construction and development of these ranges. Unfortunately, appropriate geological data, such as marker beds, is absent in many ranges. Typically, these are basement-cored ranges that have been sufficiently eroded to completely remove younger lithologies that have only experienced the most recent deformational phase, when the range was constructed. Geological data from the remaining basement rocks tends to record the cumulative effects of multiple deformational phases that cannot be easily differentiated to isolate and quantify the recent deformation. This deficiency poses a significant challenge for understanding the underlying structural architecture of these basement-cored ranges, and often prevents the spatiotemporal evolution of many ranges from being constrained.

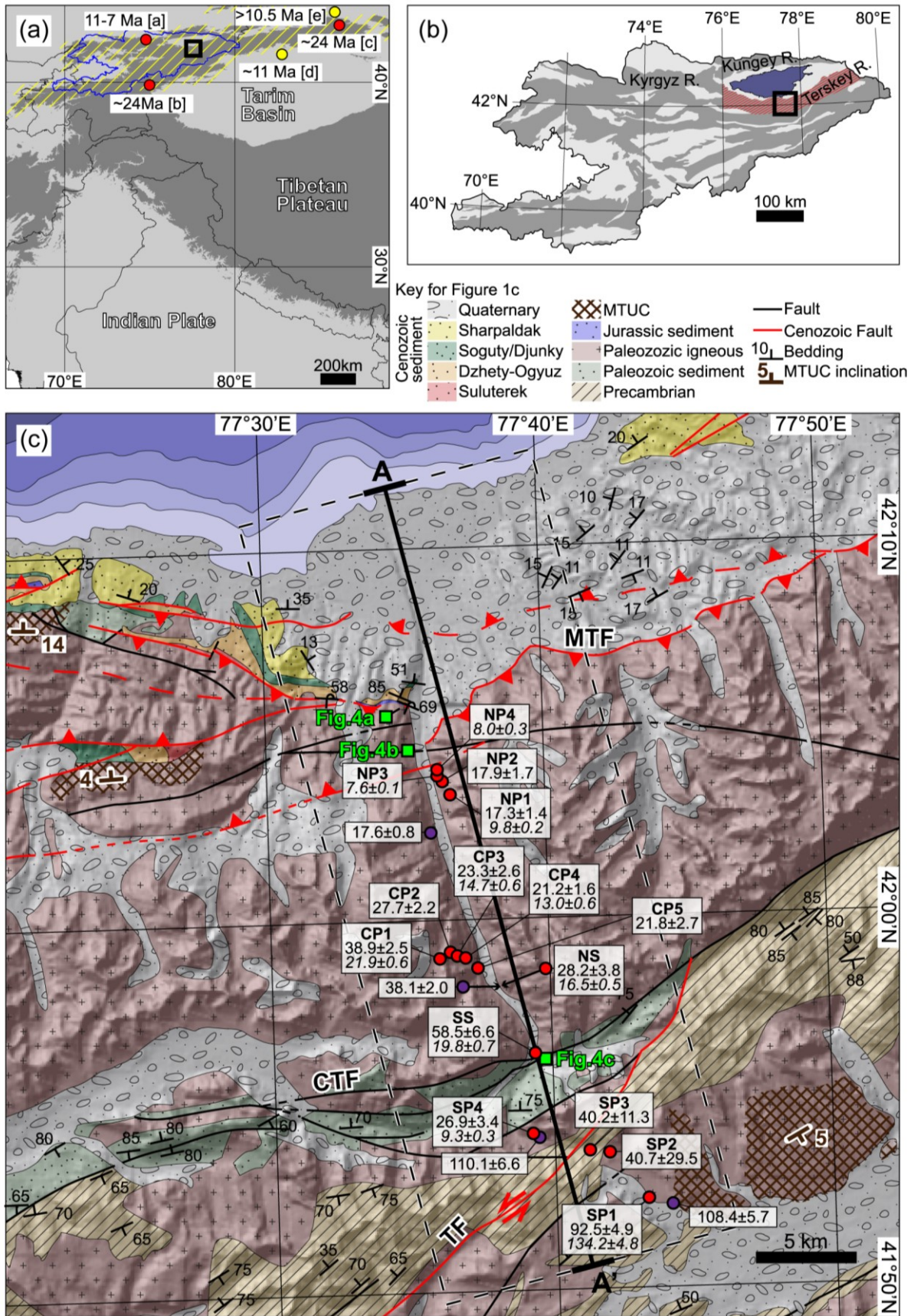


Figure 2.1. (a) Elevation map of Central Asia constructed using GTOPO data. Light grey <2000 m; dark grey >2000 m. Tien Shan highlighted with yellow diagonal lines. Kyrgyzstan outlined in blue (shown in Figure 2.1b). Black box denotes location of Figure 2.1c. Localities of selected estimates for the onset of Cenozoic deformation in the Tien Shan are shown with dots: red identifies thermochronology based estimates and yellow

Figure 2.1. *continued.* shows sedimentation based estimates. a: Kyrgyz Range [Bullen *et al.*, 2001, 2003; Sobel *et al.*, 2006b]; b: Sobel *et al.* [2006a]; c: Hendrix *et al.* [1994]; d: Charreau *et al.* [2006]; e: Charreau *et al.* [2005]. Map in Behrmann projection. (b) Map showing the distribution of basement-cored ranges (dark grey) and intermontane basins (light grey) in Kyrgyzstan. Terskey Range is highlighted by red diagonal lines. Lake Issyk Kul shown by blue. Black box denotes location of Figure 2.1c. Map in UTM43N projection. (c) Geological map of central Terskey Range, adapted from Zhukov [1969], Turchinskiy [1970], and Burgette [2008]. Studied transect outlined by dashed black box. MTF: Main Terskey Fault; CTF: Central Terskey Fault; TF: Tyulek Fault. Red circles show sample locations. Purple circles shows AFT data from De Grave *et al.* [2013]. Sample names shown in bold. AFT and AHe ages stated underneath; AHe ages in italics. Green squares show locations of fault kinematic analysis. Triangular fault tags denote reverse faults and point to dip direction. Arrows around faults show inferred strike-slip displacement from Bazhenov and Mikolaichuk [2004]. MTUC = Late Mesozoic–Tertiary basement unconformity.

One possible solution to this problem involves using thermochronological data to determine the internal structure of basement-cored ranges. Relative structural depths of different samples prior to the onset of recent deformation can be quantitatively assessed by comparing thermochronological ages and paleo-temperature estimates derived from thermal modelling. Samples with similar thermochronological ages are assumed to have cooled approximately simultaneously through the relevant closure temperature isotherm, forming an isochron [Brandon *et al.*, 1998; Thomson *et al.*, 2010]. Lateral extrapolation allows the position of this isochron to be mapped. Although not visible in the landscape, this isochron has the potential to provide a record of deformation comparable to traditional geological structural markers, such as sedimentary bedding.

In this study, we employ this approach to investigate late Cenozoic deformation in the basement-cored Terskey (Ala-Too) Range in the Kyrgyz Tien Shan (Figure 2.1a+b). In total, fifteen samples were collected at regular intervals along a transect perpendicular to the strike of the range and the major structures (Figure 2.1c); these were analysed with apatite fission track (AFT) and (U-Th)/He (AHe). New fault kinematic data are also presented and used to determine whether three structures have a pre-Cenozoic deformational history. Our thermochronological data identifies a significant cooling increase at ~26–20 Ma, which we relate to the onset of late Cenozoic deformation in the Terskey Range. A second cooling increase at ~10 Ma likely dates an intensification of deformation in the Terskey Range, when it appears that deformation stepped back into the range, reactivating two inherited strike-slip faults.

Based on our relatively densely sampled transect, it is clear there are significant spatial variations in the exhumation of the Terskey Range that we relate to the differences in tectonic rock uplift caused by the underlying structure of the range. Comparing differences in the magnitude of exhumation provides an insight into structures that have been active in the Cenozoic and the likely deformation of the Terskey Range. To constrain this deformation, we construct an AFT isochron at 28 Ma that slightly pre-dates the onset of late Cenozoic deformation at ~26–20 Ma. The present position of the isochron reflects its initial geometry and the subsequent deformation of the surrounding rocks. The initial geometry can be assumed to be horizontal, making it the ideal post-reactivation structural marker. Additionally, our thermochronological data suggests that a low relief surface preserved in the south of the Terskey Range is part of a pre-reactivation basement unconformity; this is used as another structural marker to measure late Cenozoic fault displacements within the Terskey Range.

Our new thermochronologically-derived structural data provides the first constraints on late Cenozoic deformation within the Terskey Range, and identifies reactivated basement structures within the range. The techniques used here to constrain late Cenozoic deformation could easily be adapted and applied to other basement-cored ranges to identify and quantify previously unconstrained deformation.

2.2. Geological setting

The 2500 km long Tien Shan, situated between the Tarim basin and the Kazakh Platform (Figure 2.1a) is presently the world's largest intra-continental mountain belt. Most of the present topography is related to late Cenozoic intra-continental deformation, the most recent orogenic episode in the Tien Shan, which is driven by the India-Eurasia collision [Tapponnier and Molnar, 1979]. Multiple deformational phases occurred in the Paleozoic, associated with the assembly of numerous terranes [e.g. Burtman, 1975; Bazhenov et al., 2003] and the subsequent development of a series of large strike-slip faults in the Permian [e.g. Bazhenov and Mikolaichuk, 2004]. Throughout the Mesozoic and early Cenozoic, the Tien Shan has also been periodically reactivated in response to distal collisions [Hendrix et al., 1992].

Estimates for the precise timing of late Cenozoic deformation vary across the Tien Shan. Thermochronologic data from the southern and eastern Tien Shan suggest deformation started at ~24 Ma [Hendrix et al., 1994; Sobel et al., 2006a; Heermance et al. 2008]; later, at ~11 Ma, deformation initiated in the Kyrgyz Range to the north-west (Figure 2.1a+b). The latter period in particular has been shown to be coincident with sedimentation increases on both sides of the Tien Shan [Charreau et al., 2005, 2006]. Selected estimates for the onset of deformation are shown in Figure 2.1a. Our study area in the Terskey Range occupies a relatively central location within the Tien Shan (Figure 2.1a) and provides an important marker for understanding the late Cenozoic development of the mountain belt.

The Terskey Range is a ~350 km long basement-cored range, located south of the Issyk Kul basin in eastern Kyrgyzstan (Figure 2.1b). Our study area is located approximately in the center of the Terskey Range (Figure 2.1b) around the ~N-S trending Barskoon valley (Figure 2.1c). Within the study area, Precambrian and Paleozoic basement lithologies are separated from 4–5 km thick Cenozoic sediments stored in the Issyk Kul basin by the Main Terskey Fault zone (MTF) [Turchinskiy, 1970]. The MTF is composed of multiple fault strands that have collectively generated at least 4–5 km of structural relief between the basement-cored Terskey Range and the Issyk Kul basin. The other principle structures of the Terskey Range are the Central Terskey Fault (CTF) and the Tyulek Fault (TF). These faults run approximately through the middle of the Terskey Range and exclusively offset basement lithologies (Figure 2.1c). To the west, the TF has been shown to be a reactivated Paleozoic fault that has accommodated 8 km of sinistral strike-slip displacement during the Cenozoic [Bazhenov and Mikolaichuk, 2004].

Prior to the late Cenozoic deformational phase, the study area and much of the Kyrgyz Tien Shan experienced a protracted period of tectonic quiescence starting in the late Mesozoic. Bedding orientations are approximately consistent between Jurassic and early Cenozoic sediments, suggesting that no tectonically driven tilting occurred during this period. Where preserved, Jurassic sediment overlie a low relief basement unconformity; late Cretaceous–Eocene sediments (Suluterek Formation) [Fortuna et al., 1994; Sobel and Arnaud, 2000] disconformably overlie these Jurassic sediments or lie directly above a low relief erosional unconformity with Precambrian and Paleozoic basement [Vakhrameev, 1964; Zhukov, 1969; Turchinskiy, 1970; Pomazkov, 1972; Cobbold et al., 1996]. From this stratigraphy it is clear that two significant time gaps exist in Issyk Kul; one between Paleozoic basement and Jurassic sediments, and a second between Jurassic and the overlying late Cretaceous–Eocene Suluterek Formation. Therefore we suggest that two unconformities exist, spanning the early–mid Mesozoic and late Mesozoic–Tertiary. The latter unconformity corresponds to a well documented period of tectonic quiescence [Afonichev and Vlasov, 1984; Bullen et al., 2001; 2003; Sobel et al., 2006b; De Grave et al., 2007a; 2011]. Many low relief surfaces cut into basement rocks are often interpreted as being part of the late Mesozoic–Tertiary basement unconformity [Cobbold et al., 1996]. There is one such low relief surface to the south of the TF in the study area (Figure 2.1c); whether this surface is part of the same late Mesozoic–Tertiary basement unconformity is discussed in Section 2.4.1.

2.3. Methodology and results

2.3.1. Thermochronological data

Fifteen samples were collected from a transect running NNW-SSE through the Terskey Range (A–A'; Figure 2.1c). The transect consists of 3 topographic profiles, and an additional 2 spot samples (Figure 2.1c). Samples are labelled according to their location. Northern topographic profile samples are NP1–4, central profile samples are CP1–5 and southern profile samples are SP1–4; the 2 spot samples are called the northern and southern spot samples (NS and SS). Within topographic profiles, samples are numbered from highest to lowest elevations. Samples were analysed using apatite fission track (AFT) and (U-Th)/He (AHe); details of analytical procedures are provided in the supplementary material.

Both thermochronological systems are based on temperature dependent retention of radiogenically-produced daughter products (fission tracks for AFT and ^4He for AHe). Over geological timescales, daughter products are not preserved above a particular temperature. For AFT the temperature corresponds to the bottom of the partial annealing zone (PAZ) [Ketcham *et al.*, 1999]; for AHe the temperature is the base of the partial retention zone (PRZ) [Wolf *et al.*, 1998]. Above these temperatures daughter products are only partially retained within the PAZ and PRZ: fission tracks are shortened and eventually removed through annealing, while ^4He is lost through diffusion. Temperatures of the PAZ and PRZ depend on crystal kinetic characteristics and cooling rates [Brandon *et al.*, 1998; Ehlers and Farley, 2003; Donelick *et al.*, 2005]; typically, the PAZ extends from ~140–120 to 60°C [Ketcham *et al.*, 1999], and the PRZ from ~85 to 40°C [Wolf *et al.*, 1998]. Resistance to AFT annealing can be assessed by measuring the diameter of fission tracks parallel to the crystallographic axis (D_{par}) [Ketcham *et al.*, 1999]. Measuring AFT length distributions allows the amount of annealing to be assessed, since fission tracks form at a constant rate over time and initially have the same length [Green *et al.*, 1989]. AHe diffusivity can be comparatively assessed by measuring the effective uranium concentration, grain size and number of crystal terminations (see supplementary material for more details about both methods).

For rapidly cooled samples, thermochronological ages correspond to cooling through a particular closure temperature within the PAZ or PRZ [Ehlers and Farley, 2003; Donelick *et al.*, 2005]. Rocks hotter than the PAZ or PRZ have thermochronological ages reset to zero. Prior to an increase in exhumation, rocks that had cooled sufficiently to retain fission tracks or ^4He have ages recording earlier exhumation and subsequent modification whilst residing in the AFT PAZ or AHe PRZ. As rocks are exhumed, deeper structural levels begin to cool below these temperatures, recording progressively younger ages. Comparing ages of samples collected at different elevations can be used to infer the exhumation history of a mountain range, thereby dating exhumational increases [e.g. Fitzgerald *et al.*, 1995]. The relationship between thermochronological age and present-day elevation of reset samples is the apparent exhumation rate (km/Myr), provided samples have followed vertical exhumation pathways and cooled through horizontal isotherms [Huntington *et al.*, 2007]. Violating these assumptions will lead to inaccuracies in the derived apparent exhumation rates.

2.3.2. Thermochronological results

2.3.2.1. Thermochronological ages

Our ages range from 17.3 ± 1.4 to 92.5 ± 5.3 Ma for apatite fission track (AFT), and from 6.8 ± 0.2 to 143.1 ± 8.9 Ma for apatite (U-Th)/He (AHe) (Table 2.1). Some samples have a high degree of AHe age variability in different aliquots; these samples and the reasons for the variability are discussed in the supplementary material. Crucially, many of these aliquots are reliable and can be interpreted (Table 2.1). In addition to our ages, De Grave *et al.* [2013] report 4 AFT ages from within this transect. Two of these ages are in close proximity to our samples and yield discordant results (Figure 2.1c). Our AFT ages for samples NS and SP4 are 28.2 ± 3.8 and 26.9 ± 3.4 Ma, respectively; significantly younger than the AFT ages of 38.1 ± 2.0 and 110.1 ± 6.6 Ma obtained by De Grave *et al.* [2013] from adjacent samples. NS has a relatively small mean D_{par} value of $1.78 \mu\text{m}$, suggesting it

may anneal quickly and have a relatively low closure temperature [Donelick *et al.*, 2005]. Unfortunately, no kinetic parameters were reported by *De Grave et al.* [2013] to test whether the ~10 Myr age difference might relate to the annealing properties of these 2 samples. The ~83 Myr age difference between SP4 and the proximal sample is more difficult to explain. However, sample SP4 has a relatively young AHe age of 9.3 ± 0.3 Ma, which is more consistent with our younger AFT age than the nearby 110.1 ± 6.6 Ma AFT age reported by *De Grave et al.* [2013]. The older ages of both discordant samples can be matched with observed or expected ages from higher elevations. Therefore, we suspect that one or both of the older samples may not have been collected in-situ.

Samples from similar elevations along the transect reveal that thermochronological ages are youngest near the Main Terskey Fault zone (MTF) and increase towards the south (Figure 2.2a). This trend is interrupted by sample SP4, which despite being collected from a higher elevation is younger than sample SS (Table 2.1).

2.3.2.2. Age-elevation relationships (AERs)

Although 3 topographic profiles were sampled, the southern profile is offset by the Tyulek Fault (TF) and possibly a second fault; therefore, its AER should not be interpreted. Before interpreting the remaining 2 topographic profiles, we first discuss potential complications and inaccuracies in apparent exhumation rates due to non-vertical exhumation and isothermal deflection caused by topography, faulting and advection [Stüwe *et al.*, 1994; Mancktelow and Grasemann, 1997; Ehlers and Farley, 2003]. The magnitude of these effects depends on the orientation of the sampled profile with respect to the geometry of non-planar isotherms and the horizontal component of exhumation [Huntington *et al.*, 2007]. The greatest inaccuracies are expected when the sampled topographic profile is sub-parallel to inclined isotherms and the lateral transport direction. Our samples have a north-directed horizontal component of transport imposed by the Main Terskey Fault zone (MTF).

The northern profile (NP) was collected between elevations of 2.2 and 2.7 km, covering a horizontal distance of ~1.5 km. The profile increases in elevation towards the SSE and runs sub-parallel to the dominant northward lateral transport direction and the N-S orientated long wavelength topography (>100 km) of the Terskey Range. This topographic relief has undoubtedly increased during the Cenozoic. Both lateral transport and topographic growth could result in apparent exhumation rates under-estimating true rates [Braun, 2002; Huntington *et al.*, 2007]. Faulting and advection near the MTF could have deflected isotherms, potentially leading to an under- or over-estimation of true rates. However, the apparent exhumation rates of >0.07 km/Myr around 19–16 Ma and >0.2 km/Myr between ~8 and 6 Ma (Figure 2.2b) are likely to be too small to represent a significant over-estimation caused by thermal advection. Instead, it is more likely that the rates will be influenced by lateral transport and topographic growth, both of which may lead to an under-estimation of the true rates; our apparent exhumation rates are therefore taken as minimum estimates.

The central profile (CP) was sampled at elevations between 2.6 and 3.5 km over a horizontal distance of ~1.9 km. The profile is aligned approximately E-W and therefore is unlikely to have been significantly affected by the growth of N-S long wavelength topography, northward lateral transport or advection caused by the MTF [Huntington *et al.*, 2007]. Furthermore, E-W orientated short wavelength topography (~12 km) relating to the U-shaped Barskoon valley is probably too small to cause significant errors in derived rates [Braun, 2002]. Generally, thermochronological ages increase with elevation, except for apatite (U-Th)/He (AHe) ages of sample CP2, where all three aliquots are anomalously old (25.2–36.4 Ma) with respect to the apatite fission track (AFT) age (27.2 ± 2 Ma) and the AER trend established by the youngest aliquots of the other samples (Figure 2.2c). Since no analytical or geological reason exists to account for this age difference, we assume the CP2 AHe ages are incorrect and they have been discarded. The youngest aliquots of the remaining AHe ages (CP1,3 and 4) suggest an apparent exhumation rate of <0.12 km/Myr between ~20 and 10 Ma (Figure 2.2c).

The AFT age of sample CP1 (38.9 ± 2.6 Ma) does not fit on a linear AER trend defined by the lower elevation samples (Figure 2.2c). The inflection point produced in the AER plot defines the base

of an exhumed partial annealing zone (PAZ) which developed prior to an increase in exhumation. Although the base of the exhumed PAZ is poorly constrained on the AER plot, an inflection point can be placed between 33 and 20 Ma, suggesting that exhumation increased during this interval (Figure 2.2c). The imprecision of this estimate relates to the low apparent exhumation rate of <0.12 km/Myr derived from the Central Profile's AHe Age-elevation relationship following this increase. If exhumation rates had been higher, rocks would have cooled more quickly through the PAZ, resulting in a more distinctive break-in-slope on the age-elevation plot.

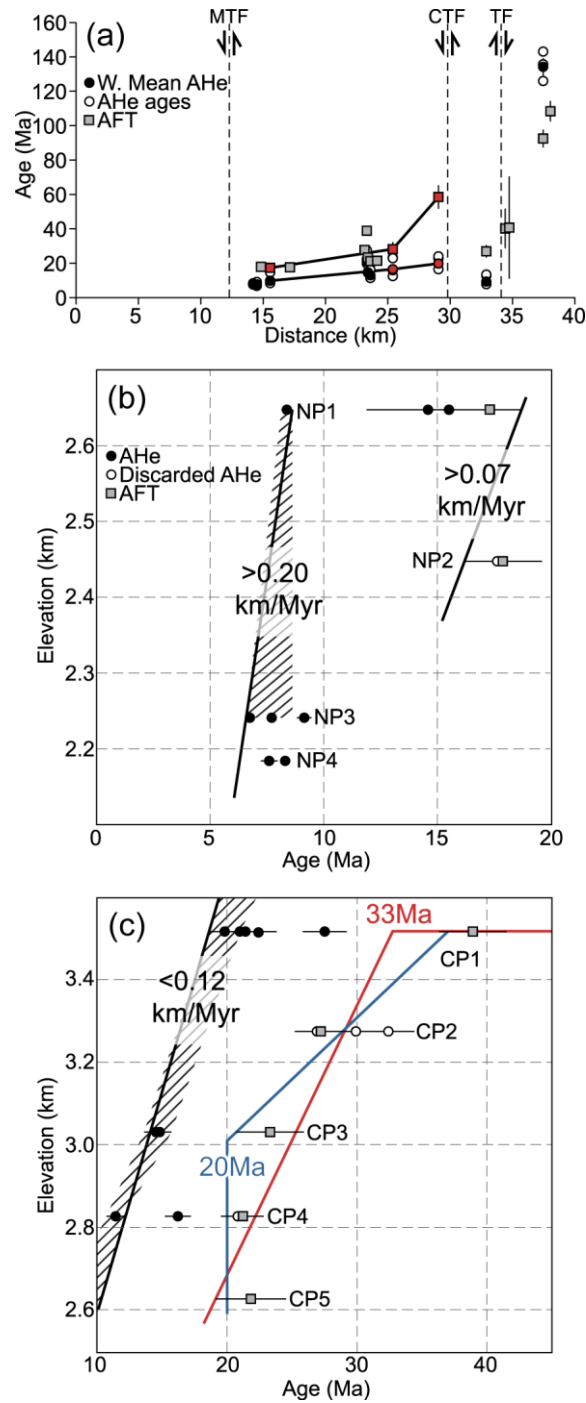


Figure 2.2. (a) Thermochronological ages of samples through transect. (b+c) Age-elevation relationships (AERs) for the northern (b) and central (c) profiles. Hatching denotes swath around possible linear AER, the gradient of which equates to the apparent exhumation rate. In the central profile (c) an increase in exhumation is observed by a kink in the AFT AER interpreted to represent an exhumed PAZ and an increase in apparent exhumation between 33 (red) and 20 Ma (blue).

Table 2.1. Summary of new thermochronological data from Terskey Range transect

Sample ^a	Code	Age/ Lithology	Latitude	Longitude e	Altitude, m ^b	AFT Age, ±1σ Ma	Dpar ^c , μm	SD, μm	Corrected AHe age ^d , Ma	AHe error	AHe std.	AHe Note
<i>Northern profile (NP)</i>												
NP1	9TS492	S/granite	42.0563	77.6100	2645	17.3	1.4	1.92	0.11	9.8	0.2	3.9
NP2	9TS493	S/granite	42.0624	77.6056	2447	17.9	1.7	2.00	0.13	-	-	All AHe aliquots discarded
NP3	9TS494	S/granite	42.0650	77.6024	2243	-	-	-	-	7.6	0.1	1.2
NP4	9TS495	S/granite	42.0677	77.6026	2184	-	-	-	-	8.0	0.3	0.5
<i>Central profile (CP)</i>												
CP1	TS177	O3/granite	41.9831	77.6009	3520	38.9	2.5	1.36	0.06	21.9	0.6	3.0
CP2	TS176	O3/granite	41.9859	77.6074	3282	27.7	2.2	1.24	0.08	-	-	All AHe aliquots discarded
CP3	TS178	O3/granite	41.9842	77.6113	3040	23.3	2.6	1.71	0.19	14.7	0.6	0.2
CP4	TS179	O3/granite	41.9832	77.6163	2839	21.2	1.6	1.76	0.19	13.0	0.6	3.4
CP5	8TS386	O3/granite	41.9766	77.6229	2626	21.8	2.7	1.81	0.18	-	-	1 AHe aliquot discarded
<i>Spot samples</i>												
NS	mav105	O3/granite	41.9703	77.6377	2605	28.2	3.8	1.78	0.16	16.5	0.5	5.3
SS	mav104	O3/granite	41.9397	77.6564	2721	58.5	6.6	1.89	0.14	19.8	0.7	4.0
<i>Southern profile (SP)</i>												
SP1	TS183	O3/granite	41.8735	77.7219	3780	92.5	4.9	1.40	0.09	134.2	4.8	8.6
SP2	TS171	PreC /phyllite	41.8945	77.6993	3821	40.7	29.5	1.85	0.39	-	-	No AHe analysis
SP3	TS172	PreC /phyllite	41.8956	77.6874	3641	40.2	11.3	1.48	0.09	-	-	No AHe analysis
SP4	TS173	O3/granite	41.9038	77.6537	3430	26.9	3.4	1.80	0.12	9.3	0.3	3.1

^a Sample names used in text.

^b Altitude (meters) taken from Shuttle Radar Topography Mission (STRM) dataset.

^c Mean of at least four Dpar measurements. The correction factor [Sobel and Seward, 2010] was found to 1 with respect to the Durango apatite standard

[Donelick et al., 1999].

^d Weighted mean aliquots that have been utilised.

2.3.2.3. Thermal modelling

Time-temperature histories for 12 samples were modelled using the HeFTy program [Ketcham, 2005]. The goal of this modelling was to test the feasibility of previously observed late Cenozoic cooling increases (at ~26–20 Ma, 15–5 Ma and < 5 Ma), and to constrain the paleo-temperature range of each sample prior to the onset of late Cenozoic deformation. Details of the modelling strategy and time-temperature histories obtained from each sample can be found in the supplementary material.

Acceptable-fitting thermal models of sample CP1 are relatively tightly constrained and suggest that the first late Cenozoic cooling increase occurred at ~26–20 Ma (CP1; Figure 2.3a). Subsequently, cooling rates generally remained low (<6°C/Myr), in keeping with a low apparent exhumation rate of <0.12 km/Myr derived from the Central Profile (CP) age-elevation relationship (AER) at this time. As a result, the ~26–20 Ma increase is not detected in thermal models of some samples, which instead identify a pronounced cooling increase at ~10 Ma (e.g. CP4; Figure 2.3a). Prior to the ~26–20 Ma increase, cooling rates were universally low. Higher elevation samples (e.g. SP1; Figure 2.3a) suggest relatively monotonic cooling of <1.5°C/Myr since at least 110 Ma. Low cooling rates between ~110 and 20 Ma would have allowed a steady state thermal field to develop. As a result, paleo-temperatures at 28 Ma, before the late Cenozoic cooling increase, can be assumed to directly correlate with a sample's structural depth.

Plotting paleo-temperature estimates from thermal modelling of individual samples along the transect reveal significant spatial variations in exhumation since 28 Ma (Figure 2.3b). Paleo-temperatures at 28 Ma were specifically selected to pre-date the onset of late Cenozoic deformation, as inferred from our AERs and thermal models, and independently from an increase in clastic sedimentation in the adjacent Issyk Kul basin at ~26 Ma (Chapter 4). Comparing samples from a similar elevation (NP1, NS, SS; ~2.6–2.7 km) suggests paleo-temperatures at 28 Ma decreased away from the Main Terskey Fault zone (MTF), meaning that exhumation is greatest near the MTF. If this trend continues south of the Central Terskey Fault (CTF), sample SP4 ought to have had lower temperature than SS at 28 Ma. Furthermore, if the present-day elevation of these samples reflects structural depths at 28 Ma, SP4 should have a lower paleo-temperature than SS, since it has a higher elevation (Table 2.1). For a reasonable geothermal gradient of 25°C/km, SP4 ought to have been at least 18°C colder than SS. However, thermal models suggest that SP4 resided at temperatures >71°C at 28 Ma, compared to 41–84°C for SS. The simplest interpretation of this difference in paleo-temperature and therefore in structural depth is that the CTF has been reactivated in the late Cenozoic, causing its southern side to be up thrown and more deeply exhumed than its northern side. Paleo-temperature estimates also vary across the Tyulek Fault (TF): SP1 has a relatively well constrained 28 Ma paleo-temperature of 3–37°C. The elevation difference between SP1 and SP4 is 0.35 km and the minimum temperature difference at 28 Ma inferred from thermal models is 34°C. If the TF has been inactive since 28 Ma and the present-day elevation were to reflect structural depth, this would require the geothermal gradient to be >97°C/km, which is unrealistic. Some of this variation may relate to a continuation of the southward decreasing exhumational trend observed in northern block of the Terskey Range. However, the magnitude of the difference suggests the TF must have also been reactivated after 28 Ma, causing its northern side to be exhumed more than the southern side.

2.3.3. Structural data

Existing structural data from the Terskey Range is mostly unhelpful for assessing and quantifying Cenozoic deformation. For example, present bedding geometries of Precambrian and Paleozoic lithologies (Figure 2.1c) record multiple deformational phases and cannot be used to constrain Cenozoic deformation. In this section we present results from fault kinematic analysis, and use our thermochronological data to provide the first constraints on Cenozoic deformation within the Terskey Range.

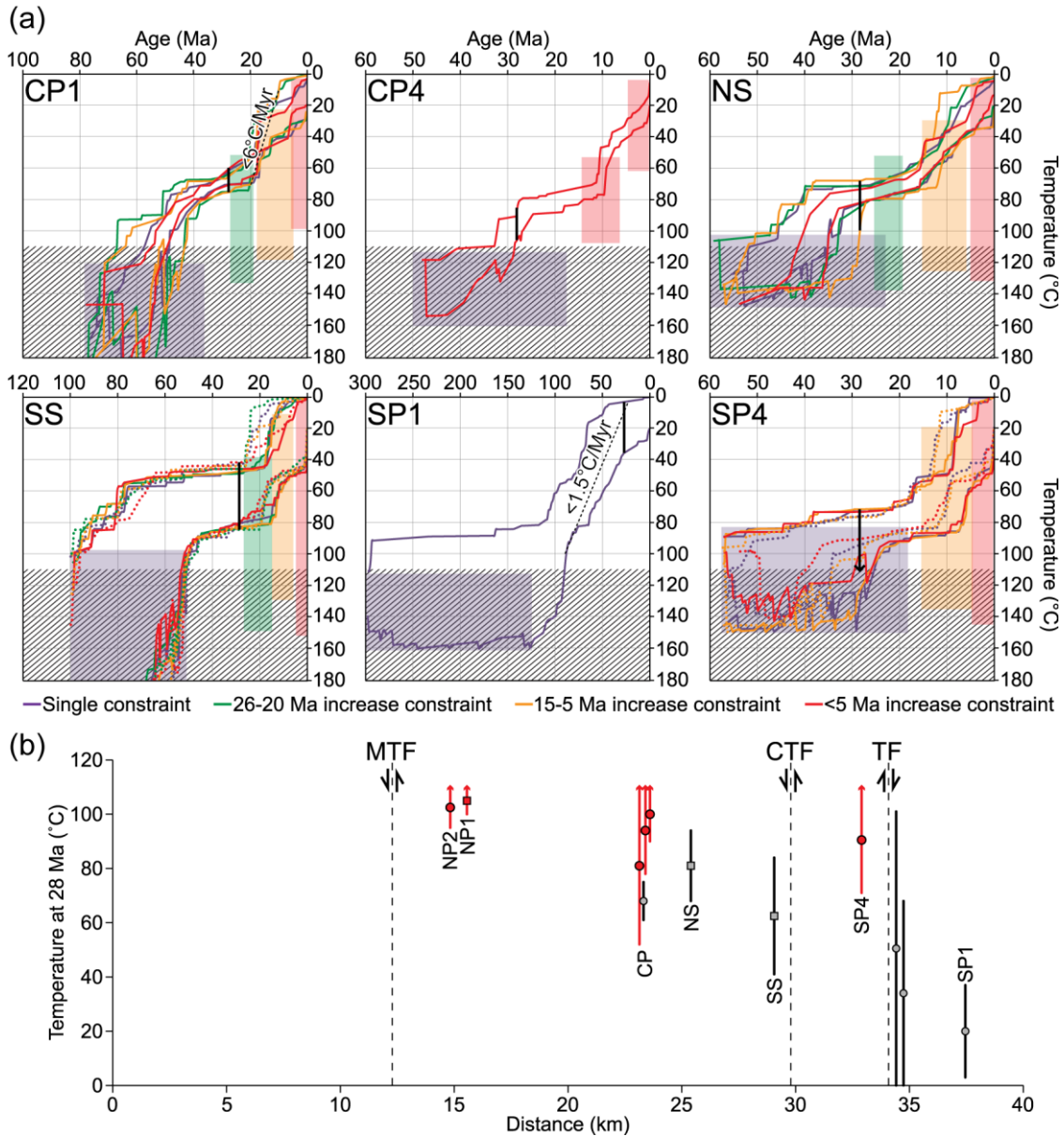


Figure 2.3. (a) Selected time-temperature histories derived from thermal modelling of individual samples using HeFTy software [Ketcham, 2005]. AFT and AHe input data for thermal models is included in the supplementary material. Acceptable time-temperature pathway envelopes are colour coded to match the input constraints (faded boxes), see key at bottom for list. Dotted lines = thermal models including old AHe aliquot component; Solid lines = remaining AHe component. Diagonal lines = portion of time-temperature histories above the assumed total AFT annealing temperature ($\sim 110^{\circ}\text{C}$); not constrained by thermochronological data. Vertical black lines indicate possible temperature range at 28 Ma. Note that SP1 was only modelled with the basic constraint, since it was cooler than model sensitivity by 28 Ma. (b) Paleo-temperature estimates at 28 Ma derived from thermal modelling. Plotted for individual samples through the transect. Square points denote samples from similar elevations (2.6–2.7 km); all other samples have circular points. Red denotes samples that have an upper paleo-temperature estimate hotter than the assumed total AFT annealing temperature ($\sim 110^{\circ}\text{C}$); the upper limit is unconstrained. Arrows show the throw of the main faults (MTF, CTF and TF) required to account for differences in exhumation across them.

2.3.3.1. Fault kinematic data

Fault kinematic analysis was carried out at three locations near two separate strands of the Main Terskey Fault zone (MTF), and along the Central Terskey Fault (CTF) (Figure 2.1c). Measurements were made on slickensides at each location. Striations on these surfaces were measured when reliable indicators to infer the sense of slip could be identified; these included subsidiary fractures (P-, T- and

Riedel fractures) and ridge-in-groove lineations [Petit, 1987]. The primary objective of this analysis was to determine whether the nearby faults have a pre-Cenozoic deformational history. Faults that were initiated in the Cenozoic are more likely to yield consistent kinematic solutions, with tightly clustering P-axes. On the other hand, faults that were reactivated in the Cenozoic have experienced multiple deformational phases with different strain orientations, leading to a highly scattered distribution of P-axes. Based on this criterion, the CTF is an inherited structure (Figure 2.4c). At the other locations near the two strands of the MTF (Figure 2.1c), fewer measureable striations were identified and it is unclear whether these faults have an earlier deformational history. However, based on the degree of variability observed in fault plane orientations, it seems likely that the southern strand corresponds to a pre-existing structure (Figure 2.4b), whereas the northern strand has a younger, possibly exclusively Cenozoic deformation history (Figure 2.4a).

2.3.3.2. Thermochronologically-derived structural data

As discussed above, thermochronologically-derived structural data provides the only means of quantifying Cenozoic deformation in the Terskey Range. A thermochronologic structural marker is constructed by connecting samples of equal thermochronologic age, forming an isochron that records the simultaneous cooling below an equal closure temperature. The position can also be determined by interpolating ages from an age-elevation profile. The present position of an isochron records the initial geometry of the closure temperature isotherm, shifted by subsequent deformation [Brandon *et al.*, 1998; Thomson *et al.*, 2010].

We have constrained an isochron with an apatite fission track (AFT) age of 28 Ma by projecting our samples onto a 2-dimensional cross section through the range (Figure 2.4d). The 28 Ma age for the isochron was specifically selected to pre-date the onset of late Cenozoic deformation. The isochron is constrained at the Central Profile (CP) by sandwiching it between samples CP1 at ~ 3.5 km (38.9 ± 2.5 Ma) and CP3 at ~ 3.0 km (23.3 ± 2.6 Ma). CP1 has a lower mean D_{par} value than CP3 (1.36 compared to $1.71 \mu\text{m}$; Table 2.1), suggesting faster annealing and a lower closure temperature for CP1 [Donelick *et al.*, 2005]. If CP1 had the same annealing characteristics as CP3, we would expect it to have an even older AFT age; therefore, the isochron must lie below CP1. Comparing sample NS with an AFT age of 28.2 ± 3.7 Ma to the CP AER, we find that the isochron must lie between the AFT ages of CP1 and CP3. NS and CP3 have similar mean D_{par} value (1.71 – $1.78 \mu\text{m}$; Table 2.1), suggesting that they have similar closure temperatures and annealing properties. We apply an ~ 0.5 km elevation uncertainty to the isochron's position around NS, corresponding to the uncertainty on the CP AER. These constraints around CP1–3 and NS are primarily used to determine the position of the isochron. However, the remaining samples can also constrain the relative position of the isochron: samples with AFT ages >28 Ma are likely to be above the isochron, while those with younger ages are below (Figure 2.4d). Furthermore, the 28 Ma isochron formed towards the end of the long tectonic quiescence period, when the late Mesozoic–Tertiary basement unconformity developed; at this time the isochron would have been parallel to the unconformity surface. If the low relief surface exposed south of the Tyulek Fault (TF) is part of the late Mesozoic–Tertiary basement unconformity, the isochron should also dip $\sim 5^\circ\text{S}$ in that part of the transect.

Assuming the isochron is planar allows us to project it across the transect; between the CP and NS constraints, a planar isochron is required to dip 5 – 29°S (Figure 2.4e). Extrapolating these inclinations across the entire transect fits with the AFT ages of the other samples, provided that the plane is displaced by the Central Terskey Fault (CTF) (Figure 2.4f). Furthermore, the minimum inclination ($\sim 5^\circ\text{S}$) also matches the low relief surface south of the TF (Figure 2.4f). However, if the Terskey Range basement has been folded, the isochron could be non-planar. Folding within the basement is a real possibility, with compelling evidence from similar ranges suggesting that movement along numerous pre-existing fractures and discontinuities at low temperatures could facilitate deformation that is perceived as folding on the macro-scale [Schmidt *et al.*, 1993; Garcia and Davis, 2004]. Although folding is possible, it is unlikely that multiple, tight folds developed in the

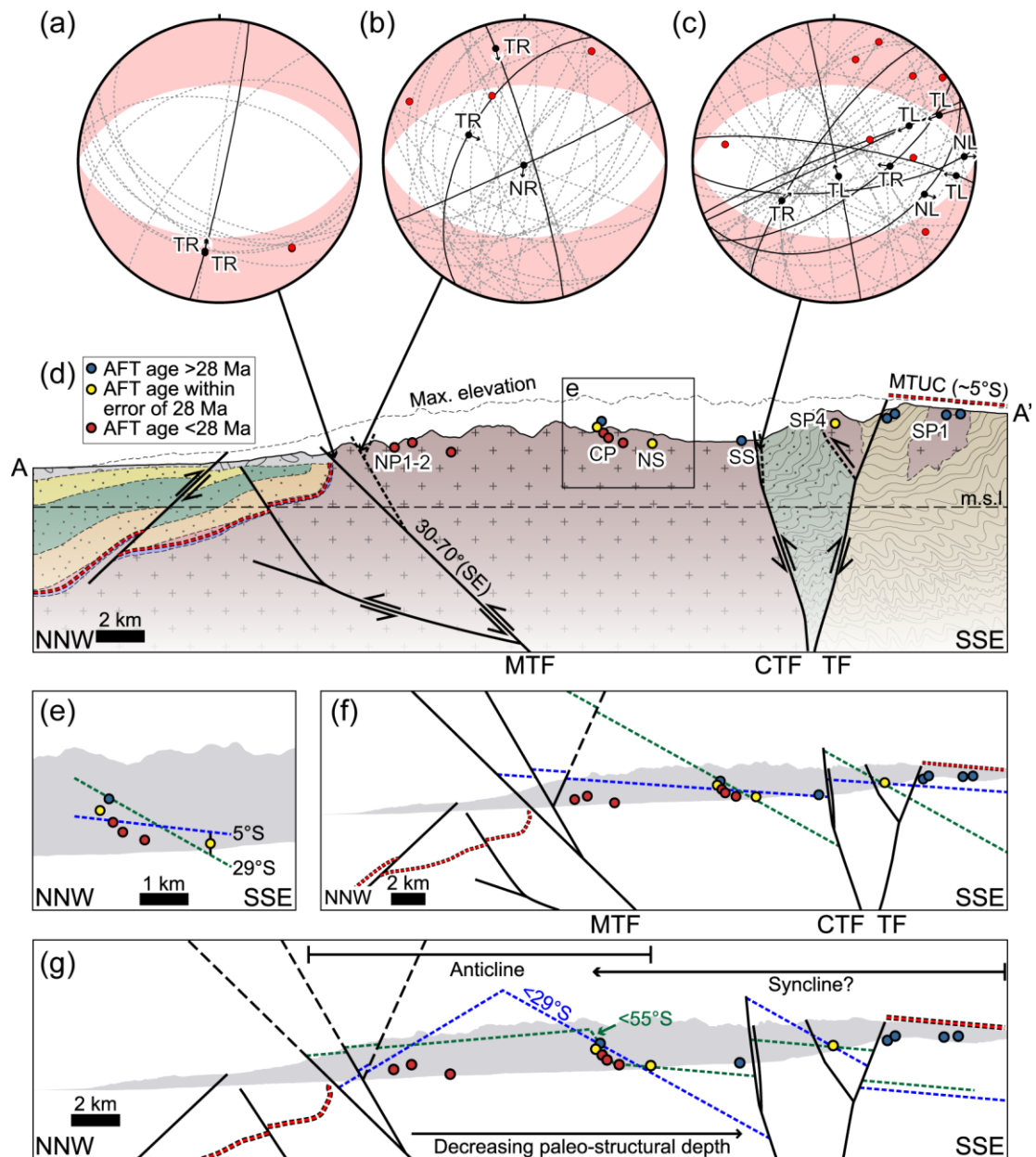


Figure 2.4. (a–c) Fault kinematic data from three faults; locations shown in Figure 2.1c. Solid black lines denote great circles of slickensides where striations were measured. Black points and arrows show the hanging wall motion of the measured lineation. Abbreviations correspond to sense of slip on fault planes; N: Normal; T: Reverse; L: Left-lateral; R: Right-lateral. Red points show calculated P-axes for individual measurements. Approximate area of P-axes expected from N–S Cenozoic shortening is shown by faded red colour. Note that P-axes outside these zones are likely to be inherited from an earlier deformational phase. Dashed grey lines show fracture planes without lineation measurements. Plots created using FaultKin 5.1 [Marrett and Allmendinger, 1990; Allmendinger et al., 2012]. (d) Cross section along A–A' (Figure 2.1c), summarizing new structural constraints. Red dots show samples with AFT ages <28 Ma; yellow dots are those within error of 28 Ma, and blue dots are samples >28 Ma. SP2 and SP3 are shifted south to fit with their locations with respect to TF, which strikes slightly oblique to the transect. Colours of lithologies matches those used in Figure 2.1c. Faults that are active in Cenozoic are solid black lines. Other faults are dashed lines. MTF orientation from Abdrachmatov et al. [2002]. MTUC (red dashed lines) = Late Mesozoic–Tertiary basement unconformity.

predominantly crystalline basement of the Terskey Range below the AFT closure temperature (<110 °C). For this reason, we limit the number of potential folds within the Terskey Range to two, and suggest any major Cenozoic fold must strike ~E–W with limbs dipping north or south, since the maximum horizontal stress has been aligned N–S during the Cenozoic. The decreasing paleo-

structural depth inferred from the thermochronological ages and paleo-temperatures at 28 Ma for similar elevation samples (NP1, NS and SS) suggests that an anticline could exist over the northern part of the transect; its axis could be located anywhere between the Main Terskey Fault zone (MTF) and the NS sample (Figure 2.4g). Therefore, the most likely two fold combination is a northern anticline and a southern syncline (Figure 2.4g).

2.4. Discussion

2.4.1. Isochron and late Mesozoic–Tertiary basement unconformity

As discussed above, the low relief surface exposed to the south of the Tyulek Fault (TF) could correspond to the late Mesozoic–Tertiary basement unconformity. Our thermal modelling of sample SP1 (Figure 2.3a), which was collected ~250 m below this low relief surface (Figure 2.4d), suggests that near surface temperatures (<40°C) were maintained for much of the period of tectonic quiescence, when this unconformity developed; only minor thicknesses of rock could have existed between SP1 and the surface at this time. Therefore, although low relief surfaces can be created by other mechanisms [e.g. *Nielsen et al.*, 2009], it seems likely that the low relief surface is part of late Mesozoic–Tertiary basement unconformity.

The occurrence of the low relief late Mesozoic–Tertiary basement unconformity in both the Terskey Range and beneath Cenozoic strata in the Issyk Kul basin suggests that the region was relatively flat during the period of tectonic quiescence. The inference of low topographic relief is supported by the late Cretaceous–Eocene sediments of the Suluterek Formation, which have been interpreted as representing frequently reworked sediments and soils deposited in a low energy, distal depositional setting [*Chediya*, 1986; *Fortuna et al.*, 1994]. Furthermore, the Suluterek Formation is universally thin (<60 m), suggesting that limited accommodation space existed and erosion rates were low across the transect. Our thermal modelling results agree with the latter point, documenting low cooling rates for >80 Myr during the period of tectonic quiescence between the mid–Cretaceous and the Oligo–Miocene (e.g. SP1; Figure 2.3a). Since the 28 Ma isochron formed towards the end of this period, it is unlikely to record a thermal field significantly warped by topography or advection. We therefore assume that the isochron and the late Mesozoic–Tertiary basement unconformity were horizontal at 28 Ma and that their present inclinations record the subsequent deformation of the Terskey Range. If this assumption is incorrect and some residual topography existed, it is more likely that the isochron and unconformity would dip north, since the Terskey Range and other basement-cored ranges to the south would probably have been higher than Issyk Kul, which was a Jurassic depocenter. Therefore, the southern inclinations of the isochron and unconformity inferred from our structural data still records late Cenozoic deformation.

2.4.2. Cenozoic structural interpretation

Our new fault kinematic data suggests that the Central Terskey Fault (CTF) was reactivated as an inherited structure (Figure 2.4c). Many P-axes are consistent with sinistral strike-slip faulting, suggesting that it could have originated during the Permian transpressional phase, as did the Tyulek Fault (TF) [*Bazhenov and Mikolaichuk*, 2004]. In the field, both structures are steeply dipping (>60°), in keeping with their likely strike-slip origins. During the Cenozoic both structures were reactivated as oblique slip faults with significant dip-slip components, causing the intervening block containing sample SP4 to be preferentially exhumed (Figures 2a + 3b). We assume this dip-slip component has a reverse displacement, since these faults strike approximately perpendicular to the ~N-S maximum horizontal stress axis. The CTF and TF therefore have a north and south sense of vergence respectively (Figure 2.4d).

Despite the existence of some south-vergent branches that likely correspond to back-thrusts, the Main Terskey Fault zone (MTF) must have an overall north vergence that up-throws the Terskey Range (Figure 2.4d). Based on our fault kinematic data, it appears that the southern branch is a pre-existing structure (Figure 2.4b), whilst the more northern branch has more uniform faults planes and

P-axes solutions (Figure 2.4a), suggesting that it only initiated in the Cenozoic. Interestingly it seems that the MTF has propagated northwards into the Issyk Kul basin, as the branch presently separating basement lithologies from Cenozoic sediments has remained inactive throughout the Holocene and deformation has migrated into the Issyk Kul basin [Abdrachmatov *et al.*, 2002]. If a south to north propagation has occurred throughout the late Cenozoic, it is likely that the MTF initially reactivated a pre-existing weakness, before propagating into the Issyk Kul basin along a series of newly initiated foot wall short-cuts.

The MTF undoubtedly exerts a significant control on the Terskey Range's exhumation; the most deeply exhumed samples (NP1–2) are those nearest the MTF and exhumation generally decreases towards the south (Figure 2.3b). Non-structural explanations for this exhumational decrease, such as differences in erosional efficiency, can be ruled out as they are unlikely to account for the variability in exhumation between such closely spaced samples (<15 km) taken from similar elevations and rock types (e.g. NP1, CP4 and SS; Figure 2.3b). This exhumational decrease suggests that paleo-structural depths increase towards the MTF (Figure 2.4g); this is incompatible with having a broad arch anticline centered in the Terskey Range, which would require paleo-structural depth to decrease away from the middle of the range. Instead, we interpret the decreasing exhumation to reflect differences in tectonic rock uplift caused by the MTF's sub-surface geometry. How these differences in tectonic rock uplift are accommodated in the Terskey Range depends on the rigidity of the basement rocks; if strong enough, the entire Terskey Range could have behaved as a rigid block that only deforms by faulting. On the other hand, if the numerous fractures and discontinuities present in the basement that were inherited from earlier deformational phases have been reactivated and accommodated Cenozoic slip, individual fault-bounded blocks would be able to deform internally. Based on the available structural data, both options are possible.

If the Terskey Range has behaved as a rigid block, arguably the simplest interpretation of the available Cenozoic structural data involves block rotation around a concave upward MTF that has caused the entire Terskey Range to be inclined $\sim 5^\circ$ S (Figure 2.5a) [Erslev, 1986]. If correct, this would allow the isochron and the late Mesozoic–Tertiary basement unconformity to be reconstructed across the entire transect as parallel planar features dipping at $\sim 5^\circ$ S. Calculating the distance between them therefore allows one to be reconstructed from the other. The minimum distance between the isochron and basement unconformity is defined by the maximum thickness of preserved basement overlying the isochron around the NS sample (1.9 km; Figure 2.5a); the maximum distance cannot be precisely constrained, but is unlikely to exceed 4.3 km based on a likely paleo-geothermal gradient $>20^\circ\text{C}/\text{km}$ (Figure 2.5b). However, between the CTF and TF, neither the isochron or the late Mesozoic–Tertiary basement unconformity is preserved and they can only be reconstructed by converting the paleo-temperature of SP4 into a structural depth with respect to the isochron, based on the paleo-geothermal gradient defined by the other samples (Figure 2.5b). The minimum calculated vertical displacements of the CTF and TF are 0.8 and 0.3 km. The minimum structural relief between Issyk Kul and the Terskey Range created by the MTF in the block rotation model is 8.6 km. In this structural model, horizontal shortening within the range is 0.7 km; 0.6 km is accommodated by the CTF and TF dipping at 60° and 0.1 km is accommodated by block rotation. This is relatively modest in comparison with the >3.1 km of shortening accommodated by the MTF. This value corresponds to the minimum shortening accommodated by a single fault dipping at 70° ; however, it is likely that multiple faults with shallower inclinations have accommodated significantly more horizontal shortening.

Internal deformation between faults could also allow significantly more deformation to be accommodated within the Terskey Range through folding and greater displacements along the CTF and TF. Unfortunately, from the available data, the positions of a non-planar isochron and late Mesozoic–Tertiary basement unconformity cannot be sufficiently constrained to calculate fault displacement or fold geometry. However, as discussed in Section 2.3.3.2, the most likely fold

geometry involves a northern anticline and a southern syncline (Figure 2.4g). We interpret this as reflecting a single fault-bend syncline (Figure 2.5c), where structural markers became inclined as they passed through a kink band above a fault bend in the MTF from a relatively flat segment to a steeper ramp [Suppe, 1983; Narr and Suppe, 1994]. In this model, vertical displacements of the CTF and TF cannot be smaller than those calculated for the block rotation model (Figure 2.5c), so the minimum constraints of 0.8 and 0.3 km still apply. Uncertainty in the position of the isochron in the forelimb of the northern anticline means the same is not true for displacement across the MTF, which could be slightly less than the minimum constraint calculated for the block rotation model.

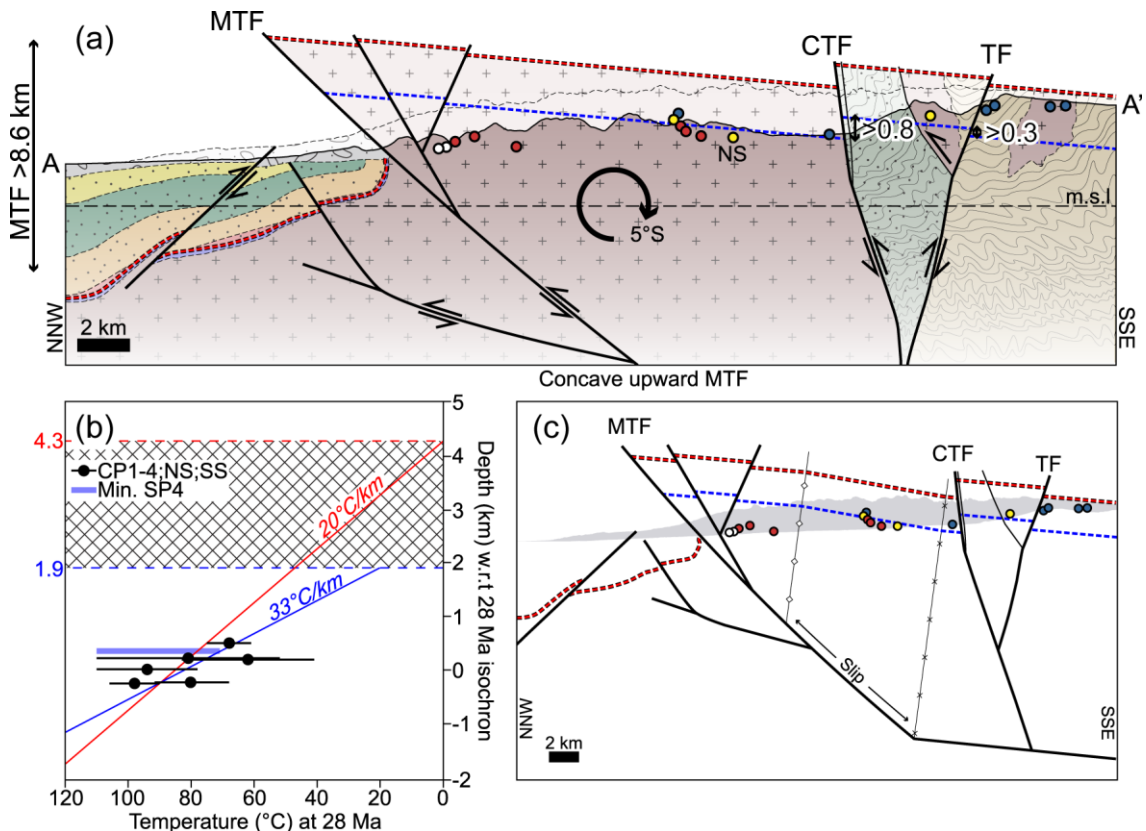


Figure 2.5. (a) Block rotation model to explain structural constraints. The MTF has a slight concave upward curvature that causes 5° rotation of hanging wall. Faded colouring indicates eroded area. (b) Geothermal gradient plot for the block rotation model. Hatched area denotes possible position of Late Mesozoic–Tertiary basement unconformity. (c) Schematic illustration showing fault-bend syncline interpretation of structural data.

2.4.3. Exhumation and deformation history

Exhumation in the Terskey Range varied considerably through time. Thermal modelling suggests that erosion rates were low for >80 Myr during the period of tectonic quiescence; cooling rates of <1.5°C/Myr, defined by sample SP1, are converted into exhumation rates by assuming a geothermal gradient of >20°C/km, giving rates of <0.08 km/Myr (Figure 2.6). Based on our new results, we can sub-divide the subsequent exhumation of the Terskey Range into two stages (Figure 2.6): (1) low exhumation rates in the Oligo–Miocene (starting at ~26–20 Ma), and (2) significantly increased exhumation starting at ~10 Ma. Assigning representative exhumation rates to these two stages is difficult given the degree of spatial variation in exhumation (Figure 2.3b). Furthermore, deformation within the Terskey Range means that present-day elevation is unlikely to be a true representation of a sample's initial structural position, therefore violating a key assumption for deriving apparent exhumation rates from age-elevation relationships (AERs). We suggest that future thermochronologic studies consider spatial variations in exhumation and the effect of the underlying structure on AER-

derived rates; employing a sampling strategy of multiple topographic profiles through a range would allow these effects to be investigated and potentially constrained.

The first stage of the Terskey Range's exhumation history is dated by an increase between 33 and 20 Ma to <0.12 km/Myr in the Central Profile (CP) AER (Figure 2.2c). The southern inclination of the isochron around the CP (Figure 2.4e+g) means the 681 m elevation difference used to calculate this apparent exhumation rate over-estimates the true structural difference, particularly if the southern inclination is greater. Thermal modelling of sample CP1 refines the timing of this exhumation increase estimate to ~ 26 – 20 Ma (Figure 2.3a). We interpret this ~ 26 – 20 Ma exhumation increase as reflecting the onset of deformation in the Terskey Range, when the Main Terskey Fault zone (MTF) became active. Our estimate is in good agreement with the 26 – 25 Ma onset of deposition proposed on the basis of magnetostratigraphic dating of syntectonic sediments deposited in the Issyk Kul basin ~ 50 km along strike to the east (Chapter 5) [Wack *et al.*, in review] and other late Oligocene–early Miocene estimates for the initiation of Cenozoic deformation in the southern and western Tien Shan [Hendrix *et al.*, 1994; Sobel *et al.*, 2006a].

A second exhumation increase at ~ 10 Ma is required by some well constrained thermal models (CP4 and SP4; Figure 2.3a). Thermal models for CP4 suggest a cooling rate since 10 Ma of ~ 5 – $8^\circ\text{C}/\text{Myr}$, which converts to an exhumation rate of ~ 0.1 – 0.4 km/Myr when the geothermal gradient is between 20 – $40^\circ\text{C}/\text{km}$ (Figure 2.6). The Northern Profile (NP) AER (Figure 2.2b) identifies similar apparent exhumation rates (>0.2 km/Myr) between ~ 8 and 7 Ma; unfortunately, because the structural configuration around the NP remains poorly constrained (Figure 2.4f+g), this rate may be inaccurate. However, it seems likely that around 10 Ma the MTF became more active, thereby increasing exhumation of the Terskey Range. Furthermore, a more pronounced cooling increase at ~ 10 Ma is identified by thermal models of sample SP4 compared to models of samples NS and SS (Figure 2.3a), suggesting that the Central Terskey Fault (CTF) became active around this time as well. Increases in exhumation and deformation at ~ 10 Ma have been identified throughout the Tien Shan [e.g. Bullen *et al.*, 2001, 2003; Charreau *et al.*, 2005, 2006; Sobel *et al.*, 2006b; Glorie *et al.*, 2010; Jolivet *et al.*, 2010]. Evidently a significant event occurred at ~ 10 Ma that affected deformation in the Tien Shan, possibly as a result of tectonic changes to the south in the Himalayan-Tibetan realm that lead to a significant increase in northward motion of the Tarim basin [e.g. Molnar and Stock, 2009; Sobel *et al.*, 2011].

Interestingly, in contrast to some parts of the Tien Shan, the Terskey Range shows no clear evidence of a significant increase in exhumation at ~ 3 Ma. Thermal models hint at a minor increase in cooling, but this typically occurs below 60°C , where thermal models are less sensitive and the increase is relatively poorly defined. Bullen *et al.* [2003] suggests exhumation rates in the Kyrgyz Range more than doubled at ~ 3 Ma, from <0.3 to ~ 0.8 km/Myr based on a 3.0 ± 0.2 Ma apatite (U-Th)/He (AHe) age. The youngest reliable AHe age identified in the Terskey Range is 6.8 ± 0.2 Ma (NP3-1); therefore, the Terskey Range has not experienced enough exhumation to bring AHe ages <3 Ma to the surface. The magnitude of any <3 Ma exhumational increase in the Terskey Range must be less than that experienced in the Kyrgyz Range, possibly relating to the Terskey Range being located within the relatively arid interior of the Tien Shan rather than along its wetter margins.

2.5. Conclusions

The Terskey Range has a three stage Cenozoic exhumation history (Figure 2.6): (1) virtually no exhumation in the Paleogene (<0.08 km/Myr), (2) an increase to slightly higher exhumation rates at ~ 26 – 20 Ma (<0.12 km/Myr), and (3) a significant increase in exhumation starting at ~ 10 Ma (0.1 – 0.4 km/Myr). We interpret the exhumation increase at ~ 26 – 20 Ma to correspond to the onset of late Cenozoic deformation and the reactivation of the Main Terskey Fault zone (MTF) that lead to the construction of the Terskey Range. The subsequent ~ 10 Ma exhumation increase likely corresponds

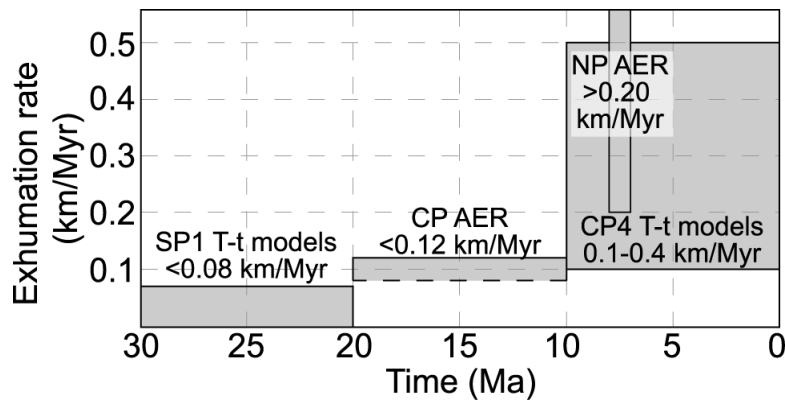


Figure 2.6. Exhumation through time. Dashed lines indicate where the limits are unconstrained and could be lower. Exhumation rates derived from AERs and modelled time-temperature histories (T-t models). Cooling rates converted to exhumation rates by assuming a geothermal gradient of 20–40°C/km; see text for details.

to an intensification in the Terskey Range’s deformation, when the inherited Central Terskey Fault (CTF) and Tyulek Fault (TF) within the range were apparently reactivated.

Paleo-temperature estimates for individual samples at 28 Ma suggest exhumation of the Terskey Range has been spatially variable, with samples near the MTF residing at hotter temperatures prior to the onset of deformation compared to similar elevation samples from farther away. Consequently, exhumation rates determined in one part of the range are not the same as those obtained elsewhere, making it difficult to quantify representative exhumation rates for the different stages. Furthermore, new structural data within the Terskey Range suggests that the present-day elevation of samples is unlikely to equal paleo-structural depth, leading to inaccuracies in apparent exhumation rates derived from age-elevation relationships (AERs).

In this paper, we demonstrate how thermochronological data can provide an insight into recent deformation in settings where suitable geological data is absent. In the Terskey Range, our thermal modelling suggests that a low relief surface preserved in the south of the Terskey Range corresponds to a late Mesozoic–Tertiary basement unconformity that is also found within the nearby Issyk Kul basin. New Cenozoic structural data suggests that the Terskey Range generally dips towards the south; planar structural markers would be required to have been rotated $\sim 5^\circ\text{S}$, while non-planar structural markers could have been folded into a northern anticline and a southern syncline, with most limbs dipping south. We interpret both possibilities as reflecting a decrease in the MTF’s inclination with depth, which has caused either block rotation or fault-bend synclinal folding.

Finally, our thermochronologically-derived structural data provides the first insight into the late Cenozoic deformation responsible for constructing the Terskey Range. Our results suggest that deformation has occurred internally within the Terskey Range, associated with the reactivation of the CTF and TF, and potentially block rotation or basement folding. Although, the contribution of this deformation in accommodating horizontal shortening is likely to be relatively minor in comparison with deformation associated with the MTF, it has had significant consequences on the development of the Terskey Range, altering the magnitude of tectonic rock uplift and influencing exhumation.

Acknowledgements

Funding was provided by an Endeavour Research Fellowship and grant SO 436/4-1 from the German Research Foundation (DFG) to ERS. EAM thanks Universität Potsdam and the Mathematisch-Naturwissenschaftliche Fakultät for additional support. The University of Melbourne thermochronology laboratory receives infrastructure support under the AuScope Program of NCRIS. Helpful comments from Jonas Kley and an anonymous reviewer greatly improved the manuscript.

Chapter 3.

Cenozoic deformation and exhumation history of the Central Kyrgyz Tien Shan

Submitted by **Euan A. Macaulay**, Edward R. Sobel, Alexander Mikolaichuk, Barry Kohn and Finlay M. Stuart (2013) to *Tectonics*. Presently in review.

Abstract

New low-temperature thermochronological data from 80 samples in south-east Kyrgyzstan are combined with previously published data from 61 samples to constrain exhumation in a number of mountain ranges in the Central Kyrgyz Tien Shan. All sampled ranges are found to have a broadly consistent Cenozoic exhumation history, characterised by initially low cooling rates ($<1^{\circ}\text{C}/\text{Myr}$) followed by a series of exhumational increases that occurred diachronously across the region in the late Cenozoic and that are interpreted to record the onset of deformation in different mountain ranges. Combined with geological estimates for the onset of proximal deformation, our data suggests that the Central Kyrgyz Tien Shan started deforming in the Oligocene–early Miocene, leading to the development of several, widely-spaced mountain ranges separated by large intermontane basins. Subsequently, more ranges have been constructed in response to significant shortening increases across the Central Kyrgyz Tien Shan, notably in the late Miocene. The order of range construction is interpreted to reflect variations in the susceptibility of inherited structures to reactivation. Similarly, along strike geometric variations of inherited structures are shown to have influenced the development and growth of individual mountain ranges by altering fault vergence and displacement. Finally, using the sequence of range construction as a framework, we discuss the evolution and partitioning of intermontane basins and the highly time-transgressive onset of late Cenozoic coarse clastic sedimentation.

3.1. Introduction

Intra-continental deformation driven by the India-Eurasian collision initially started in the Tien Shan of Central Asia (Figure 3.1a) during the Oligocene and early Miocene [*Windley et al.*, 1990; *Hendrix et al.*, 1994; *Métivier and Gaudemer*, 1997; *Yin et al.*, 1998; *Sobel and Dumitru*, 1997; *Dumitru et al.*, 2001; *Sobel et al.*, 2006a; *Heermance et al.*, 2007, 2008; *Glorie et al.*, 2011; *De Grave et al.*, 2011a, 2013; *Macaulay et al.*, 2013]. Since then, numerous sub-parallel ranges and intervening basins have developed, forming the world's largest active intra-continental mountain belt – stretching ~2500 km east-west along strike and with widths in excess of 400 km (Figure 3.1b). Based on the available constraints on the timing of deformation, it is clear that the Tien Shan has not grown uniformly by progressively encroaching into the foreland. Instead, as in many other intra-continental mountain belts, deformation is strongly influenced by the numerous pre-existing crustal heterogeneities, inherited from earlier orogenic phases, causing a highly irregular spatiotemporal distribution of deformation [e.g. *Allen and Vincent*, 1997; *Mortimer et al.*, 2007; *Neely and Erslev*, 2009]. Typically, the frictionally weakest, and most preferably orientated structures with respect to the regional stress field, will be reactivated first, driving rock uplift and constructing ranges in their hanging walls [*Holdsworth et al.*, 1997; *Kley et al.*, 2005]. As topography builds in these initial ranges, lithostatic loading will increase and may eventually inhibit deformation, forcing it to migrate to other inherited structures and weaknesses that were previously less suited to reactivation [*Hilley et al.*, 2005]. Unfortunately, across much of the Tien Shan reliable data on the timing of deformation is presently lacking, preventing the sequence of deformation from being constrained. Addressing this deficiency is essential for understanding the complex deformational mechanics of the mountain belt.

In this context, we present new low-temperature thermochronological data from 80 basement samples collected in south-east Kyrgyzstan (Figure 3.1b+c). Our study area spans several mountain ranges of the Central Kyrgyz Tien Shan between Lake Issyk Kul in the north and the Kyrgyz-Chinese border in the south, and extends from $\sim 76^{\circ}\text{E}$ to 80°E , covering an area of $\sim 40,000\text{ km}^2$ (Figure 3.1c). Combined with previously published thermochronological data from 61 samples, this large dataset constrains erosion and exhumation in most ranges within the study area, and can ultimately be used to infer the sequence of range construction. This latter application of the dataset relies on the assumption that the onset of deformation in a particular range will cause an exhumational increase that can be detected in the thermochronological data. Fortunately, the Cenozoic exhumation history of the Central Kyrgyz Tien Shan is well-suited for constraining the onset of deformation, with most ranges following a broadly consistent two-stage exhumation history that involves: (1) low exhumation rates in the early Cenozoic during a phase of tectonic quiescence, and (2) a diachronous exhumational increase in the late Cenozoic. The tectonic quiescence of the early Cenozoic has been well documented in previous studies [e.g. *Trofimov et al.*, 1976; *Makarov*, 1977; *Chediya*, 1986; *Fortuna et al.*, 1994; *Bullen et al.*, 2001; 2003; *Sobel et al.*, 2006b; *De Grave et al.*, 2007; 2013; *Glorie et al.*, 2011]. At this time, topographic relief is assumed to have been significantly reduced and low relief basement unconformities developed that later were overlain by thin, low energy sediments [e.g. *Cobbold et al.*, 1996; *Abdrakmatov et al.*, 2001]. In such a setting, a sudden, increase in exhumation (by an order of magnitude) in the late Cenozoic is most readily explained by the initiation of deformation and the subsequent construction of nearby ranges. Therefore, by dating this initial late Cenozoic exhumation increase in different ranges, and by using geological estimates for the onset of deformation, we are able to determine the sequence of range construction across the Central Kyrgyz Tien Shan for the first time.

Most ranges within the Central Kyrgyz Tien Shan are exclusively composed of Precambrian and Paleozoic basement lithologies that contain no marker beds or other structural data capable of constraining late Cenozoic deformation (Chapter 2) [*Macaulay et al.*, 2013]. Consequently, in these ranges, our thermochronological data provides the first constraints on the spatiotemporal distribution of deformation and the underlying structural architecture; both of which are essential for understanding the development of a particular range through time. Our data identifies ranges that have grown laterally by the along strike propagation of bounding reverse faults, and illustrates how many ranges have expanded into adjacent intermontane basins as main bounding faults migrate along a series of foot wall short-cuts.

Our constraints on the timing of deformation and the spatiotemporal development of ranges provide new insights into the evolution of the Central Kyrgyz Tien Shan. Based on the order of range construction, we are able to identify which intermontane basins were formerly connected and have since been partitioned by out-of-sequence range construction [*Burbank et al.*, 1999]. Furthermore, our data provides a temporal framework of deformation that can be linked to syn-tectonic sedimentation in many intermontane basins, and used to improve our understanding of the Cenozoic sedimentary record, notably the apparent $>10\text{ Myr}$ discrepancy between the onset of coarse clastic sedimentation in different intermontane basins of the Central Kyrgyz Tien Shan (Chapter 4) [*Abdrakhmatov et al.*, 2001; *Wack et al.*, in review]. Finally, we investigate the likely drivers of deformation migrations and the subsequent construction of new ranges.

3.2. Geological setting

Our study area in south-east Kyrgyzstan (Figure 3.1b) is composed of three terranes (Northern, Middle and Southern Tien Shan) that were assembled in the Paleozoic [*Burtman*, 1975, 2010; *Bazhenov et al.*, 2003]. Each terrane has a unique suite of basement lithologies: the Northern Tien Shan predominantly consists of early–mid Paleozoic granitic rocks, while the Middle and Southern

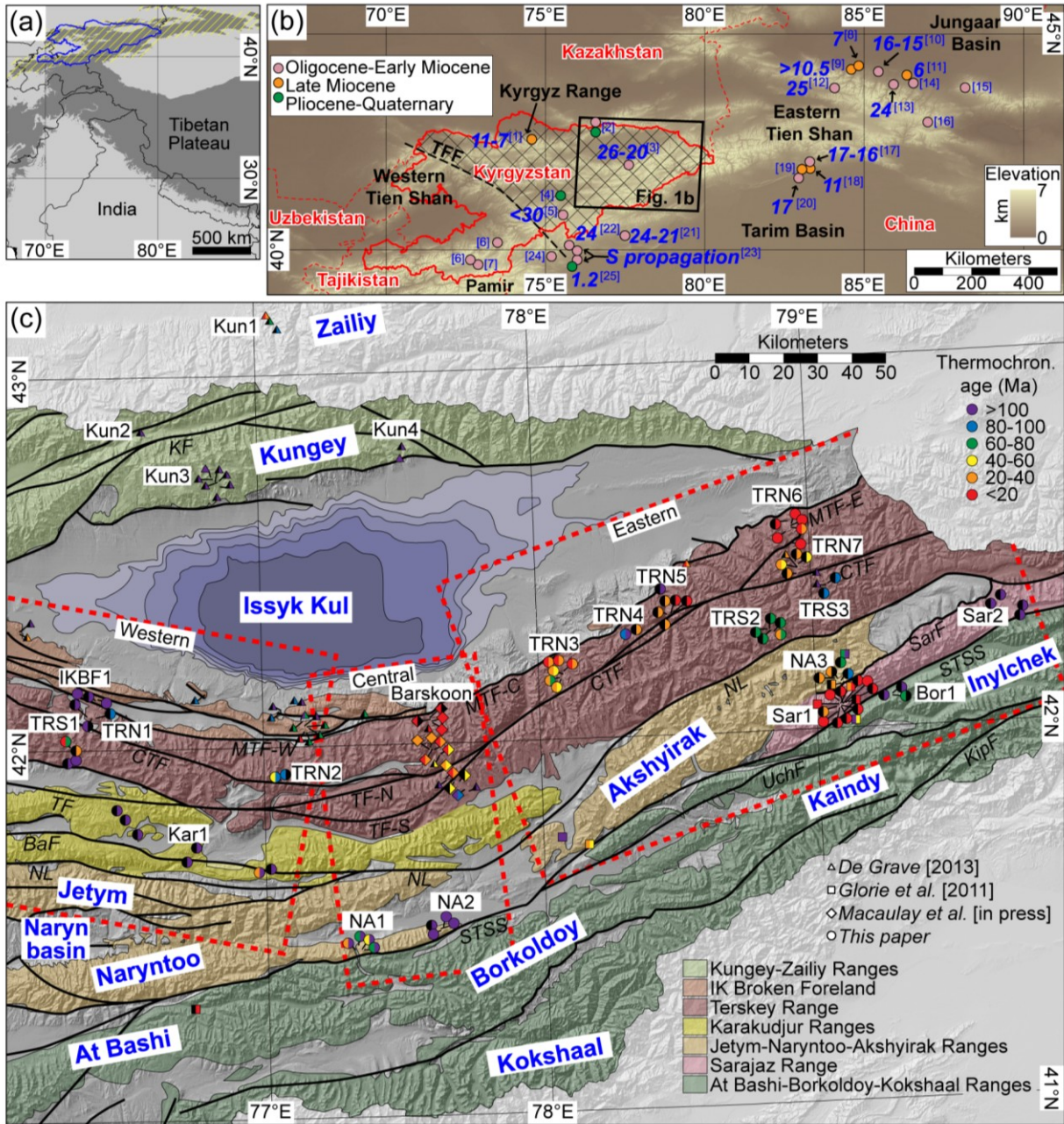


Figure 3.1. (a) Elevation map of Central Asia constructed using GTOPO data. Light grey <2000 m; dark grey >2000 m. Tien Shan highlighted with yellow diagonal lines. Kyrgyzstan outlined in blue. Map in Behrmann projection. (b) Digital elevation model (DEM) of the Tien Shan based on GTOPO90 data. Central Kyrgyz Tien Shan highlighted by hatching. Political boundaries shown in red. TFF= Talas Ferghana Fault. Black box outlines Figure 3.1c. Points and accompanying blue text denote previous estimates for the onset of significant Cenozoic deformation (typically displacements >1 km), colour-coded by age. Corresponding references to superscript numbers. 1: Bullen et al. [2001, 2003], Sobel et al. [2006b]; 2: Selander et al. [2012], De Grave et al. [2013]; 3: Macaulay et al. [2013]; 4: Makarov et al. [2010]; 5: Glorie et al. [2011]; 6: De Grave et al. [2011a]; 7: Coutand et al. [2002]; 8: Sun et al. [2004]; 9: Charreau et al. [2005]; 10: Ji et al. [2008], Charreau et al. [2009a]; 11: Sun and Zhang [2009]; 12: Dumitru et al. [2001], Wang et al. [2009]; 13: Hendrix et al. [1994]; 14: Avouac et al. [1993]; 15: Wang et al. [2008]; 16: Windley et al. [1990]; 17: Huang et al. [2006]; 18: Charreau et al. [2006]; 19: Sun et al. [2009]; 20: Métiévier and Gaudemer [1997]; 21: Yin et al. [1998]; 22: Sobel et al. [2006a]; 23: Heermance et al. [2007, 2008]; 24: Sobel and Dumitru [1997]; 25: Schärer et al. [2004], Chen et al. [2007]. (c) Simplified geological map of Eastern Kyrgyzstan showing distribution of Precambrian and Paleozoic basement (colours) and Meso-Cenozoic sediments (grey). Different colours denote our sub-divisions of the area, discussed in the text. Samples are coloured by age, with different symbols for pre-existing data. Names of individual mountain ranges shown in blue text. Red dashed lines denote location of elevation swath

Figure 3.1. *continued.* profiles shown in Figure 3.4a–c. Thick black lines show locations of major faults. KF: Kungey Fault (Kemin- Chilik Fault slightly to north); MTF: Main Terskey Fault (W,C,E: West, Central, East segments); CTF: Central Terskey Fault; TF: Tyulek Fault; BaF: Baidulla Fault; NL: Nikolaev Line; STSS: Southern Tien Shan Suture; UchF: Uchchat Fault; KipF: Kipchak Fault.

Tien Shan terranes are mostly composed of Paleozoic passive continental margin sedimentary sequences with relatively minor occurrences of Precambrian and late Paleozoic igneous rocks [Bespalov, 1979; Chabdarov, 1962; Knauf, 1965; Pomazkov, 1971; Turchinskiy, 1970; Zhukov, 1969; 1970; 1984]. The Northern and Middle Tien Shan terranes are separated by the Nikolaev Line (NL) – a strike-slip fault with 60 km of late Paleozoic sinistral displacement [Bazhenov and Mikolaichuk, 2004] that likely corresponds to the Narat (Nalati) fault in the Chinese Tien Shan [Jolivet *et al.*, 2010], where high-pressure metamorphic rocks related to a tectonic suture have been identified [e.g. Wang *et al.*, 2010]. The Middle and Southern Tien Shan terranes are separated by the 320–300 Ma Southern Tien Shan Suture (STSS) [Hegner *et al.*, 2010; Seltsmann *et al.*, 2011], which also has accommodated late Paleozoic sinistral strike-slip displacement [Biske, 1995]. This late Paleozoic strike-slip displacement primarily occurred during the Permian, when the Tien Shan experienced significant transpressional deformation [Allen *et al.*, 1995; Bazhenov and Mikolaichuk, 2004; Charvet *et al.*, 2011; Choulet *et al.*, in press]. The Tyulek and Baidulla Faults (TF and BaF) were also active in the Permian, and respectively accommodated 20 and 32 km of sinistral and dextral displacement [Mikolaichuk and Kotov, 1999; Mikolaichuk, 2000].

During the Mesozoic and early Cenozoic, parts of the Tien Shan appear to have been periodically reactivated in response to distal collisions [e.g. Hendrix *et al.*, 1992; Sobel and Dumitru, 1997; Dumitru *et al.*, 2001]. Unfortunately, the Mesozoic and early Cenozoic sedimentary record in the Central Kyrgyz Tien Shan is incomplete [Grishenko, 1985; Severinov, 1990; Mikolaichuk *et al.*, 2008], and the extent and magnitude of any deformation remains poorly constrained. However, based on the available sedimentary record and thermochronological data, it is clear that deformation in the Central Kyrgyz Tien Shan had more or less ceased by the late Mesozoic when the region experienced a >100 Myr period of tectonic quiescence (Chapter 2) [Bullen *et al.*, 2001; 2003; Sobel *et al.*, 2006b; De Grave *et al.*, 2007; 2013; Glorie *et al.*, 2011; Macaulay *et al.*, 2013]. Sediments from this period belong to the thin Kokturpak/Suluterek units (<0.13 km), deposited between the late Cretaceous and Eocene [Fortuna *et al.*, 1994; Sobel and Arnaud, 2000; Simonov *et al.*, 2008]. These deeply weathered, reddish silt and sandstones were significantly reworked and eventually become deposited above a series of low relief basement unconformities or disconformably above thin Jurassic sediments [Afonichev and Vlasov, 1984]. These low relief basement unconformities are often exposed at high elevations within mountain ranges and represent the only reliable structural markers of the subsequent late Cenozoic deformation [Cobbald *et al.*, 1996; Abdrakmatov *et al.*, 2001; Macaulay *et al.*, 2013]; herein these surfaces are collectively termed the late Mesozoic–Tertiary basement unconformities.

Following the deposition of the Kokturpak/Suluterek units, there was an abrupt sedimentary change in the intermontane basins of the Central Kyrgyz Tien Shan, from irregular, limited deposition to much thicker and more continuous red sandstones and conglomerates [Abdrakmatov *et al.*, 2001]. This sedimentary change is interpreted to represent the onset of late Cenozoic deformation. Subsequent sediments are lithostatigraphically grouped into the Shamsi, Chu and Sharpyldak units [Abdrakmatov *et al.*, 2001; Omuraliev and Omuralieva, 2004]. In the Issyk Kul and Naryn basins (Figure 3.1c), the collective thickness of these syn-tectonic sediments is estimated to be ~5 and 3.5 km, respectively [Turchinskiy, 1970; Omuraliev, 1978]. Only the Shamsi unit has been dated in both the Issyk Kul and Naryn basins. Magnetostratigraphy suggests basal ages of 26–22 and ~12 Ma in the Issyk Kul and Naryn basins; upper ages are 13–11 and ~8 Ma (Chapter 4) [Abdrakmatov *et al.*, 2001; Wack *et al.*, in review]. The large age discrepancy between the two basins highlights the dangers of using lithostratigraphy to correlate sediments in different basins of the Central Kyrgyz Tien Shan and suggests that deposition of syn-tectonic sediments is highly time-transgressive across the region. A

similar strongly time-transgressive depositional style has previously been identified for the Xiyu Formation along the southern flank of the Tien Shan, with basal ages ranging from ~15.5 to 0.7 Ma [Heermance *et al.*, 2007].

3.3. Methodology and results

3.3.1. Sample locations

Eighty samples from Precambrian and Paleozoic basement lithologies were analysed using apatite fission track (AFT), apatite and zircon (U-Th)/He (AHe and ZHe) thermochronology. Combined with recently published data from 61 samples [Glorie *et al.*, 2011; De Grave *et al.*, 2013; Macaulay *et al.*, 2013], this large thermochronological dataset contains samples from most mountain ranges in south-east Kyrgyzstan (Figure 3.1c). To aid identification, our samples have been coded by location. The text prefix corresponds to one of seven sub-divided regions, the first number to a sample group, and the second number to the sample position within a group (Table 3.1). From north to south, the sub-divided regions are: Issyk Kul Broken Foreland Ranges (IKBF), Terskey Range North and South (TRN and TRS), Karakudjur Ranges (Kar), Jetym-Naryntoo-Akshyirak Ranges (NA), Sarajaz Range (Sar) and At Bashi-Borkoldoy-Kaindy-Inylchek-Kokshaal Ranges (Bor) (Figure 3.1c). Group numbers increase from west to east within each sub-divided region (Figure 3.1c). Samples within groups are numbered from highest to lowest elevation or from north to south. The complete dataset is summarized in Table 3.1, where locations, ages and basic interpretations are given for each sample. The size of our dataset precludes a detailed discussion of every sample; rather, we use figures to illustrate representative data pattern.

3.3.2. Thermochronological systems

Thermochronological systems are based on temperature-dependent retention of radiogenically produced daughter products (fission tracks for AFT, ^4He for AHe and ZHe). Above a particular temperature, daughter products are not preserved over geological timescales and thermochronological ages are reset to zero. For AFT, this temperature forms the base of a partial annealing zone (PAZ) [Ketcham *et al.*, 1999]; for AHe and ZHe, the respective temperatures correspond to the bottoms of partial retention zones (PRZs) [Wolf *et al.*, 1998; Wolfe and Stockli, 2010]. Within the PAZ, fission tracks are shortened and eventually removed through annealing, while ^4He is partially removed through annealing in the respective PRZs of the AHe and ZHe systems. Temperatures for the PAZ and PRZs depend on the crystal kinetic characteristics and cooling rates [Brandon *et al.*, 1998; Ehlers and Farley, 2003; Reiners *et al.*, 2004; Donelick *et al.*, 2005]; typically the ZHe PRZ extends from ~200 to 130°C [Wolfe and Stockli, 2010], the AFT PAZ from ~140–120 to 60°C [Ketcham *et al.*, 1999] and the AHe PRZ from ~85 to 40°C [Wolf *et al.*, 1998].

For rapidly cooled samples, thermochronological ages correspond to cooling through a particular closure isotherm within the PAZ or PRZs [Ehlers and Farley, 2003; Reiners *et al.*, 2004; Donelick *et al.*, 2005]. Subsequent annealing and diffusion may reduce the apparent thermochronological age. Samples that have cooled slower undergo more annealing and diffusion, and generally have lower closure temperatures. Since fission tracks form at a constant rate over time and initially have the same length, the distribution of AFT lengths can be used to assess the amount of annealing a sample has experienced [Ketcham *et al.*, 1999], which combined with thermochronological age data can be modelled to identify possible cooling pathways.

3.3.2.1. Apatite fission track (AFT)

AFT analysis was carried out on 76 samples and horizontal confined track lengths were measured in 55 of these. Kinetic properties were assessed for every grain counted or containing measured horizontal confined fission tracks by making at least four D_{par} measurement [Donelick *et al.*, 2005] that were subsequently averaged and corrected following Sobel and Seward [2010]. All fission track data, as well as additional details of sample preparation and AFT analytical procedure can be found in Appendix 2 (Table A2.1). AFT ages and chi-squared values were calculated using the MacTrackX

software, following the procedures of *Galbraith* [1981]. Most AFT ages are based on ~20 grains. However, 29 samples contained less than 16 countable grains, resulting in less robust AFT ages with large errors. Ages are reported as pooled ages ($\pm 1\sigma$), unless they fail the chi-squared test (<5%) in which case the central age is reported. New AFT ages range from 6.2 to 260.5 Ma (Table 3.1).

As many horizontal confined fission tracks as possible were measured. Only tracks-in-tracks were measured, except in 5 samples, where this data was supplemented with measurements of tracks-in-cracks. To increase the number of measured horizontal confined tracks, additional mounts of 27 samples were irradiated with either ^{252}Cf [*Carlson et al.*, 1999] or heavy ions [*Jonckheere et al.*, 2007]. The length histograms are included in Appendix 2 (Figure A2.1).

3.3.2.2. Apatite and Zircon (U-Th-Sm)/He analysis (AHe and ZHe)

AHe and ZHe analysis was performed on 37 and 4 samples, respectively (Table 3.1); AFT and AHe data from one of the ZHe samples is presented in Chapter 2 [*Macaulay et al.*, 2013]. At least three aliquots were analysed per sample, except for the AHe analysis of TRN1.2, TRN2.2, TRN7.2 and Sar1.2. AHe analysis was carried out on 15 samples at the University of Melbourne using aliquots of 2–3 grains, and at the Scottish Universities Environmental Research Centre (SUERC) on 22 samples using single grain aliquots. ZHe analysis was carried out at the University of Texas in Austin with single grain aliquots. Corrections are made for the ejection of alpha particles (^4He) produced by the decay of uranium and thorium (and samarium) atoms near the margins of the crystal [*Farley et al.*, 1996]. The correction factor is calculated using the grain size of single aliquots or from the mean grain size of multi-grained aliquots. Anomalous AHe and ZHe aliquots that have been discarded are discussed in Section 3.4.1. Weighted mean AHe ages from the remaining aliquots range from 5.5 to 377.0 Ma, and from 96.2 to 231.7 Ma for ZHe (Table 3.1). Data from all aliquots and additional analytical details can be found in Appendix 2 (Table A2.2).

3.3.3. Thermal modelling

Thermal modelling has been carried out on 42 samples using the HeFTy (v.1.7.5) program [*Ketcham*, 2005]. The HeFTy software models an individual sample's time-temperature history by generating synthetic thermochronological data, which is then compared to the observed data and evaluated using a goodness-of-fit Kuiper's statistic [*Ketcham*, 2005]. Presented time-temperature paths were created using a Monte Carlo search method (inverse modelling).

To ensure the tightest possible temporal constraints, all compatible thermochronological data was incorporated. In many cases, including multiple AHe and ZHe aliquots with slightly different diffusion characteristics allowed time-temperature histories to be more tightly constrained. However, studies into AHe standards reveal a reproducibility of ~6% for uncorrected ages [e.g. *Reiners and Nicolescu*, 2006]; this is generally significantly higher than the AHe analytical error, which were as low as 1.1% of the uncorrected AHe age, and therefore not representative of the uncertainties associated with the method. To address this, the error of many individual AHe aliquots was adjusted to at least 10% of the age, which gives a better approximation of the uncertainty surrounding AHe analysis and also accounts for the uncertainty associated with the Ft correction. Even with this adjusted error, some aliquots were found to be incompatible with either the AFT data or other aliquots from the same sample, and it was often necessary to separate or discard aliquots (Table 3.1). This was an important tool in identifying anomalous aliquots for both AHe and ZHe analysis (Section 3.4.1).

The primary aim of our modelling was to identify and date any cooling rate variations. Typically, this involved multiple models for each sample. Initially, models were run with minimal constraints defined by the user. In some cases, apparent inflection points were identified and subsequently replaced by constraint boxes that were then shifted along the time axis, forcing cooling rate changes to occur earlier or later, thereby testing the model's precision and reliability (Figure 3.2a). In addition to continuous cooling models, samples from the southern Terskey block (TRS), Karakudjur (Kar) and Naryntoo-Akshyirak Ranges (NA) were also forced to undergo reheating in the Oligocene and

Table 3.1. Summary of thermochronological data

No. ^a	Sample	Age/Lith.	Lat.	Long.	Alt., m ^b	ZHe age ^c , Ma	ZHe error	AFT Age, Ma	AFT error, ±1σ	AHe age ^d , Ma	AHe error	Reference	Note
<i>Kun1</i>	ALMA3-03	granite	43.1250	77.0842	2400			70.9	4.0			<i>De Grave et al.</i> [2013]	
<i>Kun1</i>	ALMA3-02	granite	43.1486	77.0592	1960			29.4	1.4			<i>De Grave et al.</i> [2013]	
<i>Kun1</i>	ALMA3-01	granite	43.1633	77.0458	1640			22.9	4.0	14.6	0.9	<i>De Grave et al.</i> [2013]	
<i>Kun2</i>	TS-04	granite	42.8553	76.5775	2360			132.2	6.7			<i>De Grave et al.</i> [2013]	
<i>Kun3</i>	TS-06	granite	42.7264	76.8308	3950			137.4	6.8	159.9	9.6	<i>De Grave et al.</i> [2013]	
<i>Kun3</i>	TS-07	diorite	42.7231	76.8436	3700			147.0	8.0			<i>De Grave et al.</i> [2013]	
<i>Kun3</i>	TS-08	granite	42.7181	76.8439	3515			147.3	6.2			<i>De Grave et al.</i> [2013]	
<i>Kun3</i>	TS-09	granite	42.7169	76.8497	3300			115.9	3.9			<i>De Grave et al.</i> [2013]	
<i>Kun3</i>	TS-10	granite	42.7206	76.8586	3085			134.0	5.3			<i>De Grave et al.</i> [2013]	
<i>Kun3</i>	TS-11	granite	42.7047	76.8642	2860			138.2	7.2			<i>De Grave et al.</i> [2013]	
<i>Kun3</i>	TS-12	granite	42.6778	76.8508	2420			129.7	8.0			<i>De Grave et al.</i> [2013]	
<i>Kun4</i>	TS-14	granite	42.8019	77.5306	2080			153.1	7.9			<i>De Grave et al.</i> [2013]	
<i>Kun4</i>	TS-13	granite	42.7692	77.5236	1850			162.8	8.7	312.3	16.7	<i>De Grave et al.</i> [2013]	
<i>IKBF</i>	AI-88	anorthosite	42.3178	76.1275	1740			101.0	3.5			<i>Issyk Kul Broken Foreland (IKBF)</i>	
<i>IKBF</i>	AI-90	granite	42.3158	76.1283	1725			22.9	4.0			<i>De Grave et al.</i> [2013]	Surprisingly young in comparison nearby ages
<i>IKBF1.1</i>	8TS416	O/granite	42.1371	76.4030	2731			144.4	9.1	147.2	4.2	<i>this paper</i>	AFT < AHe: age inversion likely caused by radiation damage. Acceptable models not sufficiently constrained.
<i>IKBF1.2</i>	8TS417	O/granite	42.1345	76.3999	2538			118.1	6.5			<i>this paper</i>	AFT < AHe: found to be incompatible during modelling
<i>IKBF1.3</i>	8TS418	O/granite	42.1548	76.3322	2122			140.3	10.2	158.1	5.2	<i>this paper</i>	
<i>IKBF</i>	AI-32	granite	42.1481	76.7950	2010							<i>De Grave et al.</i> [2013]	
<i>IKBF</i>	AI-33	granite	42.1458	76.7908	2220			91.0	3.1			<i>De Grave et al.</i> [2013]	
<i>IKBF</i>	Kyr-33	granite	42.0967	77.0683	2030			115.8	20.8			<i>De Grave et al.</i> [2013]	
<i>IKBF</i>	TS-27	granite	42.0947	77.0681	2060			99.4	5.7			<i>De Grave et al.</i> [2013]	
<i>IKBF</i>	TS-19	granite	42.1197	77.1417	2020			107.5	16.5			<i>De Grave et al.</i> [2013]	
<i>IKBF</i>	TS-28	granite	42.1250	77.1167	1700			85.7	10.7			<i>De Grave et al.</i> [2013]	
<i>IKBF</i>	TS-26	granite	42.0706	77.1386	2700			78.4	6.6	183.5	11.0	<i>De Grave et al.</i> [2013]	AFT < AHe: age inversion caused by radiation damage?
<i>IKBF</i>	AI-09	granite	42.0683	77.1444	2940			68.9	7.9			<i>De Grave et al.</i> [2013]	
<i>IKBF</i>	TS-24	granite	42.0544	77.1519	3080			102.6	8.6			<i>De Grave et al.</i> [2013]	
<i>IKBF</i>	TS-23	granite	42.0533	77.1586	3310			72.0	5.0			<i>De Grave et al.</i> [2013]	
<i>IKBF</i>	TS-22	granite	42.0500	77.1653	3500			69.3	7.2			<i>De Grave et al.</i> [2013]	
<i>IKBF</i>	AI-05	granite	42.0425	77.1525	3145			5.0	0.5			<i>De Grave et al.</i> [2013]	Anomalously young in comparison nearby ages - discarded
<i>IKBF</i>	AI-04	granite	42.0411	77.1581	3350			68.2	3.6			<i>De Grave et al.</i> [2013]	
<i>IKBF</i>	TS-20	granite	42.0842	77.3678	2150			61.9	3.9			<i>De Grave et al.</i> [2013]	
TRN1.1	8TS419	S/granite	42.0882	76.3906	3223			87.2	11.8			<i>Terskey Range North (TRN)</i>	
TRN1.2	8TS420	S/granite	42.0909	76.3803	3081					188.8	22.2	<i>this paper</i>	
TRN1.3	8TS421	S/granite	42.0901	76.3662	2853			111.0	10.9			<i>this paper</i>	Modelled – not sufficiently constrained
TRN2.1	9TS474	O/granite	41.9154	77.0680	4054					82.4	0.8	<i>this paper</i>	
TRN2.2	9TS475	O/granodiorite	41.9141	77.0598	3918			87.6	4.7	49.9	0.8	<i>this paper</i>	
TRN	NP1 (9TS492)	S/granite	42.0563	77.6100	2645			17.3	1.4	10.5	3.9	<i>Macaulay et al.</i> [2013]	Modelled – increased cooling in last 25 Ma (Figure A2.3).
TRN	NP2 (9TS493)	S/granite	42.0624	77.6056	2447			17.9	1.7			<i>Macaulay et al.</i> [2013]	
TRN	NP3 (9TS494)	S/granite	42.0650	77.6024	2243					7.5	1.2	<i>Macaulay et al.</i> [2013]	
TRN	NP4 (9TS495)	S/granite	42.0677	77.6026	2184					7.9	0.5	<i>Macaulay et al.</i> [2013]	

Table 3.1. *continued.*

No. ^a	Sample	Age/Lith.	Lat.	Long.	Alt, m ^b	ZHe age ^c , Ma	ZHe error	AFT Age, Ma	AFT error, ±1σ	AHe age ^d , Ma	AHe error	Reference	Note
TRN	Kyr-42	diorite	42.0394	77.5978	2255			17.6	0.8			<i>De Grave et al.</i> [2013]	
TRN	CP1 (TS177)	O/granite	41.9831	77.6009	3520		38.9	2.5	21.9	3.0		<i>Macculay et al.</i> [2013]	
TRN	CP2 (TS176)	O/granite	41.9859	77.6074	3282		27.7	2.2	29.4	2.8		<i>Macculay et al.</i> [2013]	
TRN	CP3 (TS178)	O/granite	41.9842	77.6113	3040		23.3	2.6	14.6	0.1		<i>Macculay et al.</i> [2013]	
TRN	CP4 (TS179)	O/granite	41.9832	77.6163	2839		21.2	1.6	14.3	4.7		<i>Macculay et al.</i> [2013]	
TRN	CP5 (8TS386)	O/granite	41.9766	77.6229	2626		21.8	2.7				<i>Macculay et al.</i> [2013]	
TRN	NS (may105)	O/granite	41.9703	77.6377	2605		28.2	3.8	17.2	6.4		<i>Macculay et al.</i> [2013]	
TRN	Kyr-35	diorite	41.9697	77.6361	2450		38.1	2.0				<i>De Grave et al.</i> [2013]	
TRN	SS (may104)	O/granite	41.9397	77.6564	2721		58.5	6.6	21.3	6.4		<i>Macculay et al.</i> [2013]	Anomalous old compared to nearby ages: not in-situ?
TRN3.1	7TS323	O/granite	42.1613	78.0818	3594		59.1	8.2	28.1	1.7		<i>Macculay et al.</i> [2013]	
TRN3.2	7TS324	O/granite	42.1649	78.0800	3438		64.2	8.4	28.1	1.2		<i>this paper</i>	AFT data and single compatible AHe aliquot modelled: TRN3.1 (young) cooling increase at 29-22 Ma (Figure 3.2a)
TRN3.3	7TS325	O/granite	42.1739	78.0910	3095		51.7	8.7	38.4	1.4		<i>this paper</i>	AFT data and two compatible AHe aliquots modelled: TRN3.4 (young) cooling increase at 10 ± 5 Ma (Figure 3.2b)
TRN3.4	7TS326	O/granite	42.1827	78.0931	2939		29.1	2.8	9.6	0.4		<i>this paper</i>	AFT data and two compatible AHe aliquots modelled: TRN3.5 (young) cooling increase at 10 ± 5 Ma (Figure 3.2b)
TRN3.5	7TS327	O/granite	42.2114	78.0757	2534		21.5	2.7	7.5	0.3		<i>this paper</i>	AFT data and three AHe aliquots modelled in two groups: TRN3.6 (old, young) cooling increase in last 10 Ma (Figure A2.3).
TRN3.6	7TS322	O/granodiorite	42.2240	78.0655	2407		30.2	3.6	8.3	0.3		<i>this paper</i>	
TRN4.1	9TSS02	O/granite	42.2864	78.3605	3445		23.9	2.1				<i>this paper</i>	Anomalous old for lower elevation sample: not in-situ?
TRN4.2	9TSS496	O/granite	42.2745	78.3215	2508		113.2	4.6	93.7	0.9		<i>this paper</i>	Modelled – not sufficiently constrained
TRN5.1	7TSS316	O/granite	42.3238	78.4892	2866		13.4	1.5				<i>this paper</i>	Modelled – not sufficiently constrained
TRN5.2	7TSS317	O/granite	42.3219	78.4820	2752		14.4	2.5				<i>this paper</i>	Modelled – not sufficiently constrained
TRN5.3	7TSS318	O/granite	42.3213	78.4749	2659		20.4	1.9				<i>this paper</i>	Modelled – not sufficiently constrained
TRN5.4	7TSS319	S/granite	42.3139	78.4771	2551		31.9	7.1				<i>this paper</i>	
TRN5.5	7TSS320	O/granite	42.3601	78.4697	2402		39.4	11.8				<i>this paper</i>	
TRN5.6	7TSS321	O/granite	42.3948	78.4532	2188		105.0	5.8				<i>this paper</i>	Modelled – not sufficiently constrained
TRN6.1	IK-13	granite	42.4519	78.5517	1970		26.3	1.3	11.4	0.7		<i>De Grave et al.</i> [2013]	
TRN6.1	7TSS330	O/granite	42.5433	78.9368	3410		21.9	2.2	11.6	0.5		<i>this paper</i>	
TRN6.2	7TSS331	O/granite	42.5476	78.9362	3262		19.1	1.4	10.8	0.5		<i>this paper</i>	AFT data and two compatible AHe aliquot modelled: TRN6.1 (young) not sufficiently constrained.
TRN6.3	7TSS332	O/granite	42.5517	78.9380	3106		15.7	1.7	9.3	0.3		<i>this paper</i>	AFT data and two compatible AHe aliquot modelled: TRN6.2 (young) cooling increase in last 10 Ma (Figure A2.3).
TRN6.4	7TSS333	O/granite	42.5609	78.9268	2704		17.9	1.8	10.9	0.4		<i>this paper</i>	Modelled – increased cooling in last 10 Ma (Figure A2.3).
TRN6.5	SIJC-6	O/granite	42.5322	78.9172	2540		10.7	1.3	7.0	0.3		<i>this paper</i>	Modelled – not sufficiently constrained.
TRN6.6	7TSS328	O/granite	42.5012	78.9362	2719		17.2	1.9	7.9	0.3		<i>this paper</i>	AFT data and two compatible AHe aliquot modelled: TRN6.5 (young) cooling increase in last 10 Ma (Figure A2.3).
TRN7.1	9TSS456	S/granite	42.4436	78.9584	3264		50.2	7.4				<i>this paper</i>	Modelled – increased cooling in last 10 Ma (Figure A2.3).
TRN7.2	SIJC-5	S/granite	42.4345	78.9501	2893		46.7	14.9	29.0	1.3		<i>this paper</i>	
TRN7.3	9TSS458	S/granite	42.4498	78.9476	2875		38.4	5.5				<i>this paper</i>	
TRN7.4	9TSS452	O/granite	42.4173	78.9504	2816		37.9	6.9				<i>this paper</i>	
TRN	IK-12	granite	42.4308	78.9511	2900		38.6	14.4				<i>De Grave et al.</i> [2013]	Modelled – not sufficiently constrained
TRN1.1	8TSS411	O/granite	42.0054	76.3093	3835		64.7	3.7	19.9	0.5		<i>Tersley Range South (TRS)</i> <i>this paper</i>	Modelled – increased cooling in last 30 Ma (Figure A2.3)

Table 3.1. *continued.*

No. ^a	Sample	Age/Lith.	Lat.	Long.	Alt., m ^b	ZHe age ^c , Ma	ZHe error	AFT Age, Ma	AFT error, ±1σ	AHe age ^d , Ma	AHe error	Reference	Note
TRS1.2	8TS413	O/granite	42.0010	76.3199	3558			21	2.3	113.7	2.3	<i>this paper</i>	Modelled – not sufficiently constrained
TRS1.3	8TS414	O/granite	41.9758	76.3235	3274			144.8	10.5	113.7	2.3	<i>this paper</i>	Anomalously old for lower elevation sample: not in-situ?
TRS1.4	8TS410	O/granite	41.9673	76.2935	3145			107.5	9.2	134.2	8.5	<i>this paper</i>	Anomalously old for lower elevation sample: not in-situ?
TRS	SP1 (TS183)	O/granite	41.8735	77.7219	3780	202.4	9.4	92.5	4.9	134.2	8.5	<i>Macaulay et al. [2013]</i>	New ZHe age for this paper: AFT < AHe – radiation damage?
TRS	SP2 (TS171)	PreC/phylite	41.8945	77.6993	3821			40.7	29.5			<i>Macaulay et al. [2013]</i>	
TRS	SP3 (TS172)	PreC/phylite	41.8956	77.6874	3641			40.2	11.3			<i>Macaulay et al. [2013]</i>	
TRS	SP4 (TS173)	O/granite	41.9038	77.6537	3430			26.9	3.4	9.8	4.1	<i>Macaulay et al. [2013]</i>	Anomalously old compared to nearby ages: not in-situ
TRS	Kyr-39	diorite	41.9019	77.6575	3430			110.1	6.6			<i>De Grave et al. [2013]</i>	
TRS	Kyr-38	diorite	41.8708	77.7361	3815			108.4	5.7			<i>De Grave et al. [2013]</i>	
TRS2.1	9TS467	S/granite	42.2718	78.8378	4060			72.9	6.5			<i>this paper</i>	Modelled – not sufficiently constrained
TRS2.2	9TS468	S/granite	42.2717	78.8452	3792			67.4	12.1			<i>this paper</i>	
TRS2.3	9TS469	S/granite	42.2681	78.8495	3616			73.3	10.4			<i>this paper</i>	
TRS2.4	9TS470	S/granite	42.2662	78.8580	3453			70.0	6.8			<i>this paper</i>	
TRS2.5	9TS471	O/granite	42.2566	78.8828	3374			79.4	4.4	39.4	0.4	<i>this paper</i>	Modelled – poorly constrained; reheating possible (Figure A2.3)
TRS	IK-11	sandstone	42.4228	79.0208	3200			129.8	9.1			<i>De Grave et al. [2013]</i>	
TRS	AI-27	tonalite	42.3811	79.0533	3765			122.6	6.7			<i>De Grave et al. [2013]</i>	
TRS3.1	SIJC-4	Pt/granite	42.3888	79.0607	3788			81.0	3.3			<i>this paper</i>	Modelled – not sufficiently constrained
TRS3.2	SIJC-3	Pt/granite	42.3621	79.0455	3393			88.0	3.4			<i>this paper</i>	Modelled – not sufficiently constrained
								<i>Karatajdur Ranges (Kar)</i>					
Karl.1	8TS408	O/granite	41.8388	76.4693	3333			115.3	6.6			<i>this paper</i>	
Karl.2	8TS407	O/granite	41.8121	76.4973	3193			114.6	5.1			<i>this paper</i>	Modelled – not sufficiently constrained
Karl.3	8TS406	O/granite	41.7736	76.5406	2960			130.4	6.3			<i>this paper</i>	
Karl.4	8TS402	O/granite	41.7349	76.7510	2999	184.3	10.5	154.9	6.7			<i>this paper</i>	Modelled – significant cooling between ~200 and 150 Ma (Figure A2.3).
Karl.5	8TS401	O/granite	41.6968	76.7163	2738			124.4	9.6			<i>this paper</i>	
Karl.6	8TS398	Cm/granodiorite	41.6648	76.9755	2988			124.1	7.3	24.4	0.7	<i>this paper</i>	Modelled – poorly constrained; reheating possible (Figure A2.3)
Karl.7	8TS394	O/granite	41.6722	77.0178	3522			125.8	6.6			<i>this paper</i>	Modelled – not sufficiently constrained
								<i>Jetyyn-Naryntoo-Akshyrak Ranges (NA)</i>					
NA1.1	8TS369	C-P/granodiorite	41.4505	77.3417	4061			122.0	6.5	68.5	1.4	<i>this paper</i>	Modelled – poorly constrained; reheating possible (Figure A2.3)
NA1.2	8TS370	C-P/granodiorite	41.4493	77.3357	3855			122.6	7.3	55.7	0.6	<i>this paper</i>	
NA1.3	8TS371	C-P/granodiorite	41.4548	77.3285	3581			121.1	5.8	56.0	1.6	<i>this paper</i>	Modelled – poorly constrained; reheating possible (Figure A2.3)
NA1.4	8TS372	C-P/granodiorite	41.4609	77.3254	3232			107.9	6.7	61.6	1.2	<i>this paper</i>	Modelled – poorly constrained; reheating possible (Figure A2.3)
NA1.5	8TS368	C-P/granodiorite	41.4502	77.3159	3089			218.3	24.4	37.9	0.5	<i>this paper</i>	Modelled – poorly constrained; reheating possible (Figure A2.3)
NA2.1	8TS358	Cm/psammite	41.4968	77.6238	3950			218.3	24.4	372.4	4.6	<i>this paper</i>	All AHe aliquots incompatible with AFT data; models with AFT only are not sufficiently constrained.
NA2.2	8TS359	C-P/granodiorite	41.4986	77.6227	3797	221.2	10.5	155.9	8.7	209.0	2.4	<i>this paper</i>	AFT < AHe: age inversion likely caused by radiation damage. Acceptable models suggest significant cooling at ~200 Ma (Figure 3.2c).
NA2.3	8TS361	C-P/granodiorite	41.5036	77.6298	3482			201.2	9.5	130.3	1.7	<i>this paper</i>	
NA2.4	8TS362	Cm/psammite	41.5108	77.5876	3142			240.7	19.8			<i>this paper</i>	
<i>Akshyrak</i>	AI-31	felsic tuff	41.7367	78.0664	4067			126.1	8.7	107.1	6.4	<i>Glorie et al. [2011]</i>	
<i>Akshyrak</i>	AI-29	mylonite	41.7147	78.1636	3804			56.5	3.9	30.0	1.8	<i>Glorie et al. [2011]</i>	
NA3.1	9TS461	Pt/granite	42.1212	79.0924	3292			88.3	9.5			<i>this paper</i>	Modelled – not sufficiently constrained
NA3.2	9TS463	Pt/granite	42.1261	79.0931	3039			44.7	7.7	23.0	0.6	<i>this paper</i>	
NA3.3	9TS465	Pt/granite	42.1291	79.0800	2679			75.2	7.7	34.7	0.9	<i>this paper</i>	
NA3.4	9TS466	Pt/granite	42.1743	79.0937	2657			23.0	7.7	34.7	0.9	<i>this paper</i>	
<i>Akshyrak</i>	AI-15	granite	42.1111	79.0686	2683	156.5	12.0	23.0	1.3			<i>Glorie et al. [2011]</i>	

Table 3.1. continued.

No. ^a	Sample	Age/Lith.	Lat.	Long.	Alt, m ^b	ZHe age ^c , Ma	ZHe error Ma	AFT Age, Ma	AFT error, ±1σ	AHe age ^d , Ma	AHe error	Reference	Note
<i>Aksytryk</i>	Al-20(1)	granite	42.1998	79.1161	2781			133.5	6.0	57.0	3.4	<i>Glorie et al.</i> [2011]	
<i>Aksytryk</i>	Al-20(2,3)	granite	42.1998	79.1161	2781			133.5	6.0	125.7	7.5	<i>Glorie et al.</i> [2011]	
										<i>Saryqaz Range (Sar)</i>			
Sar1.1	8TS431	P/granite	42.0541	79.1014	3430			16.6	2.2			<i>this paper</i>	Modelled – not sufficiently constrained
Sar1.2	8TS432	P/granite	42.0535	79.0981	3204			21.5	4.8	n/a	n/a	<i>this paper</i>	All AHe ages discarded; Figure A2.3
Sar1.3	8TS433	P/granite	42.0545	79.0944	2992			18.7	4.4			<i>this paper</i>	
Sar1.4	8TS434	P/granite	42.0548	79.0944	2992			15.3	2.8			<i>this paper</i>	
Sar1.5	8TS436	P/granite	42.0545	79.0913	2857			14.6	3.8			<i>this paper</i>	
Sar1.6	8TS435	P/granite	42.0545	79.0912	2857	100.9	4.7	12.4	2.1			<i>this paper</i>	
Sar1.7	8TS437	P/granite	42.0542	79.0847	2698			13.7	3.3			<i>this paper</i>	
Sar1.8	8TS438	P/granite	42.0569	79.0807	2368			23.0	3.7			<i>this paper</i>	Anomalous old for lower elevation sample: not in-situ?
Sar1.9	SITC-1	P/granite	42.0426	79.0758	2611			6.9	0.7	5.9	0.4	<i>this paper</i>	
Sar1.10	SITC-2	P/granite	42.0695	79.0833	2612			11.3	1.7	10.7	0.7	<i>this paper</i>	
<i>Sar</i>	Al-11	granodiorite	42.0420	79.1027	2663			9.8	1.1			<i>Glorie et al.</i> [2011]	
<i>Sar</i>	Al-13(1)	granite	42.0643	79.0872	2660	225.4	18.0	7.9	0.5	6.6	0.4	<i>Glorie et al.</i> [2011]	Anomalous old AHe ages – discarded
<i>Sar</i>	Al-13(2,3)	granite	42.0643	79.0872	2660	225.4	18.0	7.9	0.5	33.8	2.0	<i>Glorie et al.</i> [2011]	Anomalous old AHe ages – discarded
<i>Sar</i>	Al-14(1,2)	granite	42.0624	79.0841	2619			12.8	0.8	14.9	0.9	<i>Glorie et al.</i> [2011]	Anomalous old AHe ages – discarded
<i>Sar</i>	Al-14(3)	granite	42.0624	79.0841	2619			12.8	0.8	50.6	3.0	<i>Glorie et al.</i> [2011]	Anomalous old AHe ages – discarded
Sar2.1	7TSS302	O/granite	42.2772	79.7506	3812			96.1	7.7			<i>this paper</i>	Modelled – not sufficiently constrained
Sar2.2	7TSS305	Pt/granite	42.2998	79.7627	3538			110.9	12			<i>this paper</i>	
Sar2.3	7TSS304	Pt/granite	42.3102	79.6467	3580			200.1	11.5			<i>this paper</i>	Modelled – not sufficiently constrained
Sar2.4	7TSS308	Pt/granite	42.3338	79.6848	3202			161.6	16.2			<i>this paper</i>	
<i>At Bashi</i>	Kyr-21	gneiss	41.2439	76.4072	2615			8.4	0.9			<i>Glorie et al.</i> [2011]	
<i>Borkoldoy</i>	Al-16(1)	granodiorite	42.0198	79.1404	3543	55.4	4.4	58.9	2.7	169.0	10.0	<i>Glorie et al.</i> [2011]	ZHe < AFT < AHe – all discarded.
<i>Borkoldoy</i>	Al-16(2,3)	granodiorite	42.0198	79.1404	3543	55.4	4.4	58.9	2.7	435.0	26.0	<i>Glorie et al.</i> [2011]	Anomalous old AHe ages – discarded
Bor1.1	8TS427	P/granite	42.0782	79.2750	3506			103.1	15.1			<i>this paper</i>	
Bor1.2	8TS428	P/granite	42.0796	79.2755	3367					62.8	1.0	<i>this paper</i>	
Bor1.3	mav65/8	P/granite	42.0814	79.2463	2835			105.2	8.6			<i>this paper</i>	Modelled – not sufficiently constrained

^a Sample name used in text; based on the range a sample was collected from and its location within that range. First number represents the sample group, which increase from west to east, and the second number indicates relative elevation within that sample group – numbers increase from highest to lowest.

^b Altitude (meters) for new samples taken from Shuttle Topography Radar Mission (STRM) dataset.

^c Mean of compatible ZHe aliquots (Figure A2.3).

^d Weighted mean of compatible AHe ages (Figure A2.3).

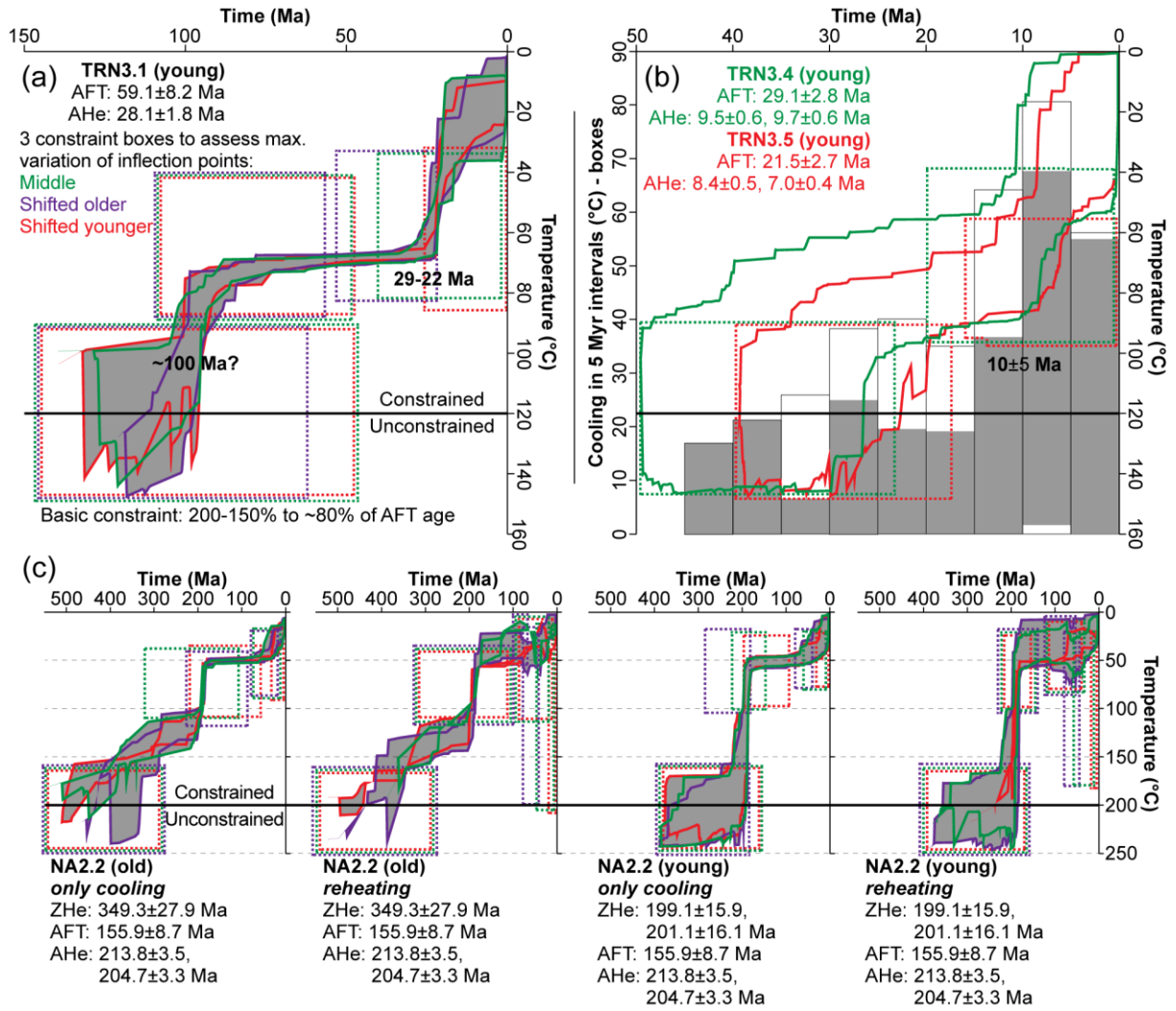


Figure 3.2. Representative time-temperature histories from thermal modelling of individual samples using HeFTy software [Ketcham, 2005]. Annealing and calibration models of Reiners *et al.* [2004], Ketcham *et al.* [2007] and Flowers *et al.* [2009] were used for the ZHe, AFT and AHe data, respectively. AFT lengths were projected to the c-axis [Ketcham *et al.*, 2007], and the ^{252}Cf -irradiation option was used to model the 27 samples that underwent ^{252}Cf or heavy ion irradiation. (a) Acceptable (goodness-of-fit of >0.05) time-temperature pathway envelope for TRN3.1, colour-coded to match input constraints (dashed boxes). Increased cooling after 29–22 Ma. (b) Combined model runs with shifted constraint boxes, as shown in Figure 3.2a, for two samples collected in the same fault bounded block (TRN3.4 and TRN3.5; Figure 3.3c). Grey and white boxes indicate the range cooling achieved by individual acceptable time-temperature pathways; grey corresponds to the overlap in cooling achieved by the two samples. These have been compiled from each acceptable time-temperature history identified by three thermal model runs. Models suggest significant cooling increase at 10 ± 5 Ma. (c) Four different models for the same sample (NA2.2) using different combinations of ZHe data and testing the feasibility of reheating. Significant cooling increase identified in all models at ~ 200 Ma. See text for additional interpretation of these thermal models.

Miocene. These areas often contain outcrops of Cenozoic sediment at high elevation and could have experienced significant burial reheating. The aim of the reheating modelling was to investigate the likely thickness of sediment and further constrain the timing of deposition. Unfortunately, both objectives proved to be beyond the resolution of our data.

Well constrained time-temperature histories were obtained from 14 samples (Table 3.1); all of these models are included in Appendix 2 (Figure A2.3), while model results from four representative samples are shown in Figure 3.2. Thermochronological data from many samples requires a significant Oligocene–early Miocene cooling increase; e.g. thermal models of TRN3.1 identify a 29–22 Ma cooling increase (Figure 3.2a). Interestingly, it is often the case that thermal models from the same

sample group identify two different cooling increases. For example, TRN3.4 and TRN3.5, collected 2.5 and 5.6 km away from TRN3.1, were hotter than the PAZ at 29–22 Ma and therefore could not record this cooling increase. Instead, TRN3.4 and TRN3.5 identify a significant cooling increase at 10 ± 5 Ma (Figure 3.2b); similar late Miocene cooling increases are identified in thermal models from many lower elevation samples collected in the Terskey Range (Figure A2.3). The higher elevation sample from this group (TRN3.1) had cooled below 40°C, where thermal models typically have lower resolution, and the data was unable to tightly constrain the 10 ± 5 Ma inflection point. These three TRN3 samples illustrate why analysing multiple samples collected along a topographic profile yields a more robust thermal history than can be obtained from a single spot sample.

Including the higher temperature thermochronological data from ZHe analysis allows the Mesozoic and early Cenozoic cooling histories to be constrained. The best example is thermal models of NA2.2 (includes ZHe, AFT and AHe data), which shows rapid cooling at ~200 Ma, followed by negligible cooling or reheating up to temperatures of ~80°C in the late Mesozoic, and finally increased cooling in the Cenozoic (Figure 3.2c). Precise timing and details of the ultimate cooling episode cannot be determined, as the sample resided at near-surface temperatures where the thermochronological data was less sensitive to cooling fluctuations. Poorly constrained cooling in the late Cenozoic occurs in many samples from the Issyk Kul Broken Foreland, southern Terskey Range block, Karakudjur and Naryntoo- Akshyirak Ranges (Table 3.1).

3.4. Data interpretation

3.4.1. Data evaluation

Although the vast majority of our thermochronological data are reliable and mutually compatible, some anomalous and unexpected ages were obtained that warrant additional interpretation and discussion. Primarily this relates to some AHe and ZHe aliquots yielding anomalous ages with respect to other aliquots from the same sample or the corresponding AFT age. For the former, some of the ZHe and AHe variability may be related to differences in the diffusion characteristics between aliquots caused by grain size variations [Reiners and Farley, 2001; Reiners *et al.*, 2004], radiation damage [Reiners *et al.*, 2004; Shuster *et al.*, 2006; Flowers *et al.*, 2007; 2009], or for AHe, the number of intact crystal terminations [Brown *et al.*, 2011] (see Table A2.2 for relevant parameters). If so, aliquot age variations could be accurate and potentially be used to further constrain a sample's cooling history during thermal modelling (Section 3.3.3). However, aliquots can also yield erroneous ages due to unrecognised inclusions, ⁴He implantation and U-Th(-Sm) zonation [Farley, 2002; Dobson *et al.*, 2008]. In those cases, ages are not geologically meaningful and need to be removed from the dataset. The problem is identifying erroneous aliquots whilst retaining those that are accurate.

In total we have discarded 2 of 12 ZHe aliquots and 27 of 96 AHe aliquots (Figure 3.3a). The one discarded ZHe aliquot was Kar1.4(3); it yielded a ZHe age of 124.6 ± 10.0 Ma, younger than the sample's 154.9 ± 6.7 Ma AFT age. The remaining two ZHe aliquots from this sample were older than the AFT age and were compatible with the data during thermal modelling. Kar1.4(3), the discarded aliquot, had a uranium concentration of 539.2 ppm and has likely been strongly affected by radiation damage, thus accounting for the anomalously young ZHe age; two ZHe aliquots of sample Sar1.6 also contained high concentrations of uranium, possibly resulting in radiation damage and anomalously young ages, and have been discarded [Guenther *et al.*, 2013]. Thermochronological age inversion also occurred in some samples analysed with both AHe and AFT (AHe > AFT age) (Figure 3.3b). During thermal modelling, 13 AHe aliquots older than the corresponding AFT age were found to produce no acceptable time-temperature histories and have been discarded. However, four AHe aliquots that are older than the corresponding AFT age were found to be compatible during thermal modelling. These all have AHe ages >100 Ma and likely reflect prolonged slow cooling when the

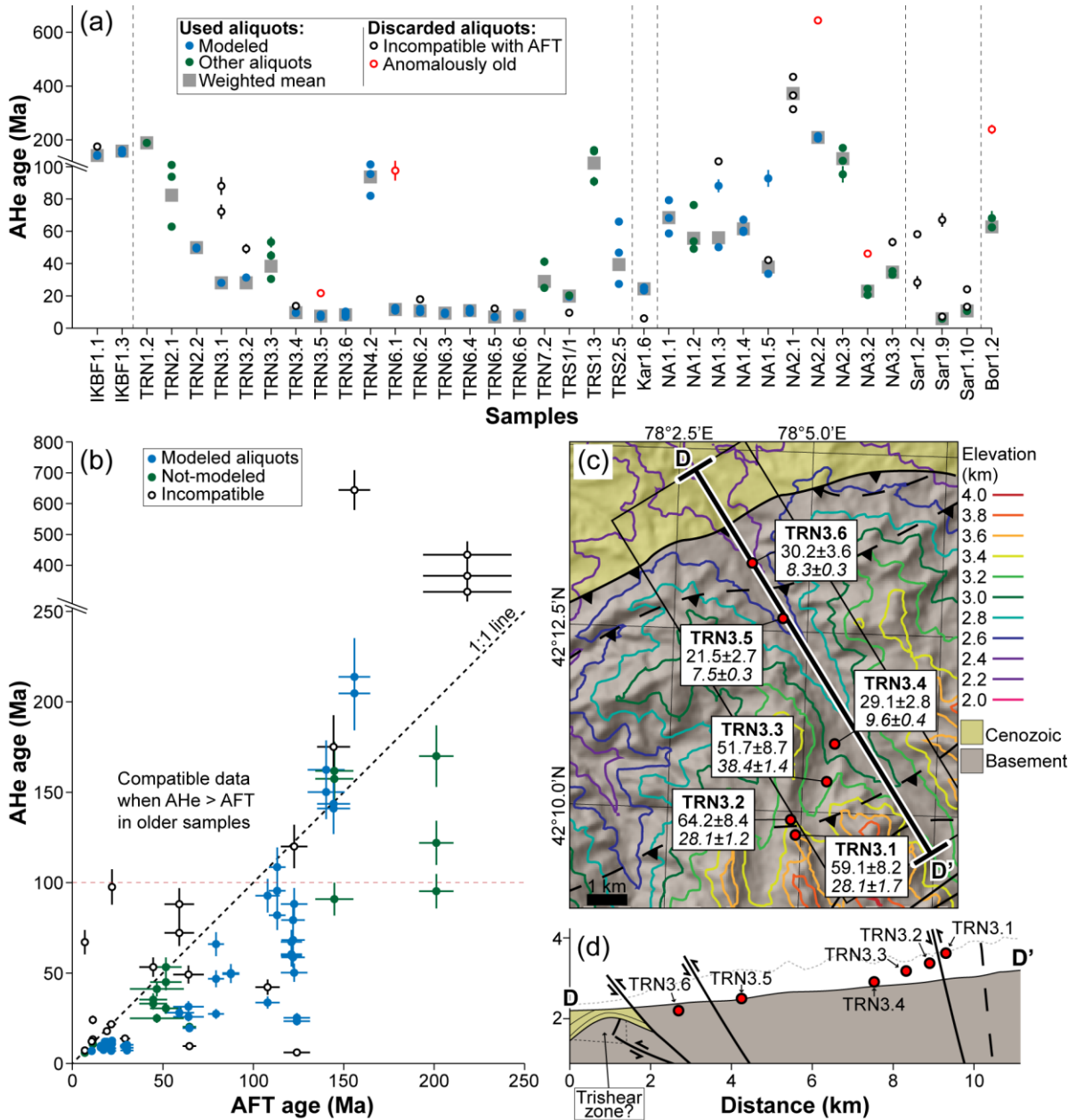


Figure 3.3. (a) All Ft-corrected AHe ages obtained from different samples. Solid symbols denote aliquots that were used to calculate the weighted mean (grey square points); hollow symbols denote discarded aliquots. Colour-coding denotes whether samples were modelled and the reason for discarding. (b) AFT-AHe age plot with 1 to 1 black dashed line. Aliquots are colour coded to show if they were compatible with AFT data during thermal modelling. Many aliquots with AHe ages older than the corresponding AFT age are incompatible and have been discarded; interestingly, this is not always true for AHe aliquots >100 Ma, which have likely been affected by radiation damage and were found to be compatible with the AFT data. (c) Simplified geological map of area where TRN3 samples were collected in the Terskey Range, overlain with colour coded contour lines. Ages for each sample are from AFT (above) and AHe (below). Samples were collected along a topographic profile that crossed two inherited structures. Comparatively old thermochronological ages in the foot wall side suggests that the fault between TRN3.5 and TRN3.6 has been active in the Cenozoic; the fault between TRN3.1 and TRN3.2 might also have been active, although these are unreset samples and the AFT age difference might reflect different annealing properties. (d) Cross section through TRN3 samples, location shown on Figure 3.3c. Dashed grey line = maximum elevation from swath shown in Figure 3.3c. Fault geometries calculated by structural contours derived from Figure 3.3c map. Trishear zone based on the interpretation of *Burgette* [2008].

crystal accumulated radiation damage, leading to a significant reduction in the rate of ^4He diffusion [Flowers *et al.*, 2009]. Of the remaining 14 discarded AHe aliquots, a further 8 aliquots were found to be incompatible with the AFT data during thermal modelling, while the last 6 were discarded because they were significantly older than the sample's other 2 aliquots and likely contain unrecognised inclusions (Figure 3.3a).

Another anomalous aspect of our data is observed when comparing thermochronological ages obtained from nearby samples. In the Central Kyrgyz Tien Shan where topography has dramatically increased during the late Cenozoic, ages at lower elevations ought to be younger than those obtained from samples at higher elevations [e.g. Braun, 2002]. Of our 18 sample groups, 5 contain a lower elevation sample that is older than higher elevation samples. Note this does not include sample groups with Mesozoic and early Cenozoic ages that have cooled slowly through the PAZ or PRZs, and are therefore not necessarily expected to display a positive age-elevation correlation. In some cases (TRN3:Figure 3.3c+d), the samples are separated by inherited structures that were likely reactivated in the late Cenozoic, causing differential exhumation that can account for comparatively old ages at lower elevations. Similarly, unexpectedly old ages from lower elevation samples at TRN5, and possibly at TRS1 as well, can be explained by splays from larger fault zones (Table 3.1). In the other two sample groups with older ages at lower elevations (TRN4 and Sar1), no structural explanation exists to explain these anomalous ages. Instead, it is likely that these samples were not collected in-situ, but reflect large blocks derived from higher elevations. In some areas, accidentally sampling such a rock is hardly surprising given the numerous enormous boulders that are observed.

Finally, in addition to our new data, we have also evaluated previously published thermochronological ages. Based on similar criteria outlined above, we identify at least 5 samples that appear to have inaccurate thermochronological ages and have been discarded from our interpretations. Three of these have inexplicable thermochronological age inversions, and at least one is unlikely to be in-situ (Table 3.1). The last one (Al-05) has an AFT age of 5.0 ± 0.5 Ma [De Grave *et al.*, 2013], which is anomalously young in comparison to the Mesozoic ages derived from nearby samples that were collected in the same fault-bounded block at comparable elevations (<0.2 km altitude difference; Table 3.1). We therefore assume that there were analytical problems leading to an erroneous AFT age.

3.4.2. Spatial distribution of thermochronological ages

Significant variations are observed in the spread of thermochronological ages obtained from different ranges and fault-bounded blocks in the study area (Figure 3.4). To better visualise these age variations and assess whether they reflect differences in the amount of late Cenozoic exhumation, thermochronological ages are sub-divided into those that are less than and more than 25 ± 5 Ma. This value was selected to separate samples that were reset during the late Cenozoic; it is based on the earliest documented late Cenozoic exhumational increases obtained from our thermal models (Section 3.3.3) and age-elevation relationships (Section 3.4.3), as well as previous estimates on the timing of increased exhumation in the study area [Glorie *et al.*, 2011; Wack *et al.*, in review; Macaulay *et al.*, 2013].

The most striking thermochronological age differences are found between ranges. The Terskey and Sarajaz Ranges contain many AFT ages $<25 \pm 5$ Ma; whereas, in the Karakudjur, Naryntoo and Akshyirak Ranges such ages are almost completely absent (Figure 3.4a–c), suggesting that less late Cenozoic exhumation occurred in those ranges. Significant thermochronological age variations are also found within ranges. In the eastern and central swath profiles, reset thermochronological ages young towards the north in the Terskey Range (Figure 3.4a+b), indicating that exhumation increases near the Main Terskey Fault (MTF). In Chapter 2 [Macaulay *et al.*, 2013], this was related to horizontal-axis block rotation or fault-bend synclinal folding caused by a decreasing inclination of the MTF with depth.

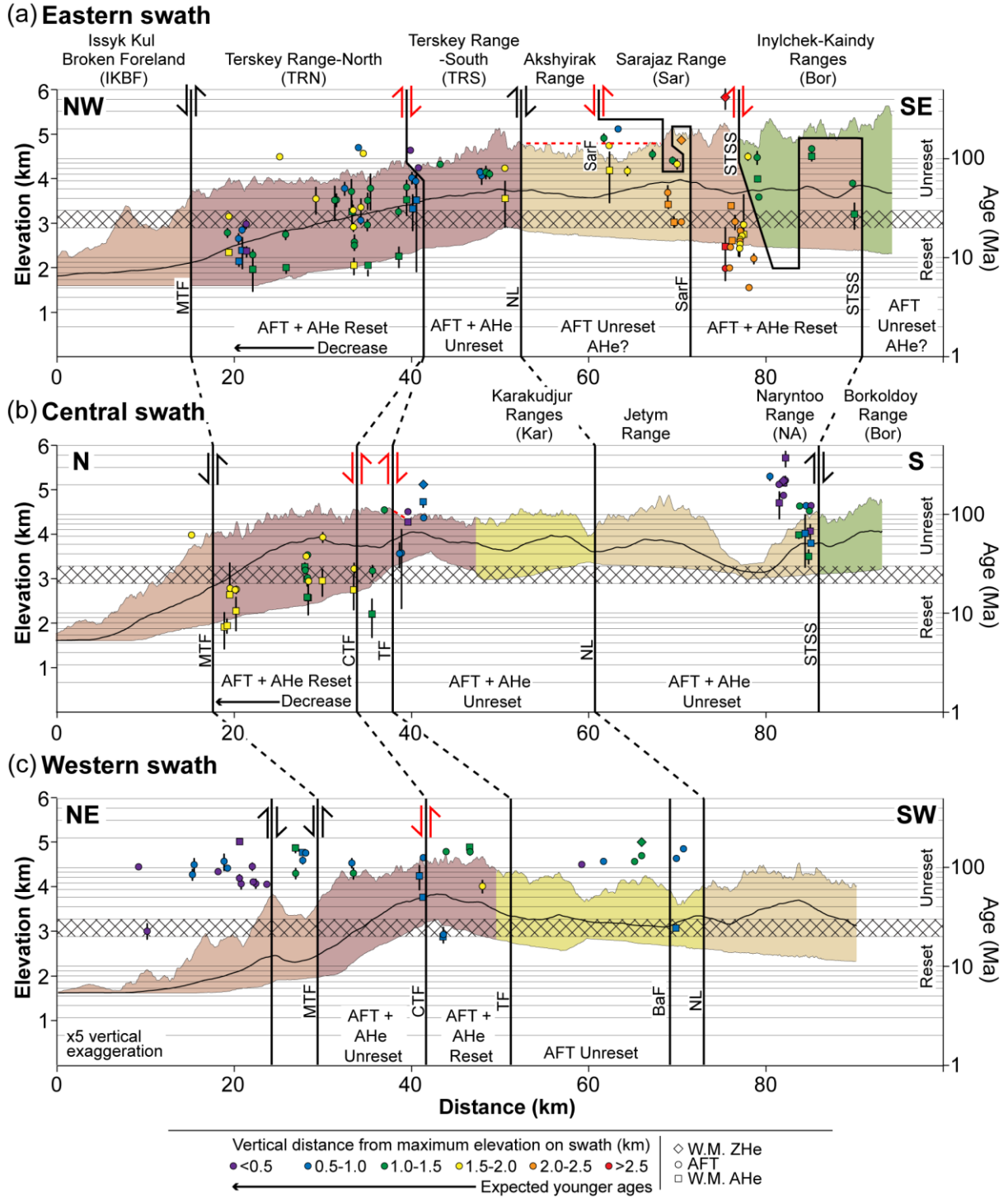


Figure 3.4. Elevation swath profiles through study area, showing minimum, mean and maximum elevations; locations shown on Figure 3.1b. Data is from this study and from *Glorie et al.* [2011], *De Grave et al.* [2013] and *Macaulay et al.* [2013]. Circular points = AFT ages; Square points = AHe ages; Diamond points = ZHe ages. Samples are colour coded to show distance from the maximum swath profile elevation; greater distances (warmer colours) are expected to have younger thermochronological ages (see text for further discussion). Red fault displacement arrows based on offset of thermochronological ages; black fault displacement arrows from geological observations and mapped relationships [*Bespalov*, 1979; *Chabdarov*, 1962; *Knauf*, 1965; *Pomazkov*, 1971; *Turchinskiy*, 1970; *Zhukov*, 1969, 1970, 1984]. Logarithmic scale used for thermochronological ages to improve visualisation. MTF = Main Terskey Fault; CTF = Central Terskey Fault; TF = Tyulek Fault; BaF = Baidulla Fault; NL = Nikolaev Line; STSS = Southern Tien Shan Suture.

Thermochronological age differences between relatively closely spaced samples (<5 km apart) that straddle the Central Terskey Fault (CTF), Tyulek Fault (TF) and Southern Tien Shan Suture (STSS) suggest that these structures have been reactivated in the late Cenozoic with a significant dip-slip component. Based on the differences in thermochronological ages, the up-thrown side can also be identified (Figure 3.4). Interestingly, this reveals that the vergence of the CTF varies along strike. In the eastern Terskey Range, the northern side of the CTF has been up-thrown (Figure 3.4a); in the central and western Terskey Range, the southern side is upthrown, with >0.8 km of vertical displacement accommodated in the Barskoon region (Chapter 2) [Macaulay *et al.*, 2013].

3.4.3. Age-elevation relationships (AERs)

AERs of samples collected at regular elevation intervals (~200 m) along steep topographic profiles are frequently exploited to date exhumational increases and quantify exhumation rates [e.g. Wagner and Reimer, 1972; Fitzgerald *et al.*, 1995; Valla *et al.*, 2010]. Typically, an increase in exhumation will result in a distinctive break-in-slope on age-elevation plots. AFT ages from TRN6 samples collected in the eastern Terskey Range display such a break-in-slope, dating an exhumational increase at 18–16 Ma (Figure 3.5b). A similar exhumational increase is suggested by TRN3 samples, although in this case the break-in-slope is only constrained by one sample and can be placed anywhere between 33 and 19 Ma (Figure 3.5a); however, thermal models refine this estimate to 29–22 Ma (Figure 3.2a). In these AERs, thermochronological ages above the break-in-slope record a combination of earlier exhumation and significant age reduction whilst residing in the AFT PAZ; such ages are commonly referred to as being partially reset or unreset. Samples below the break-in-slope were hotter than the PAZ before the increase in exhumation and have a reset thermochronological age. Another break-in-slope is suggested by the AHe data at TRN3 and TRN6 at ~10 Ma (Figure 3.5a+b). At TRN3, the break-in-slope coincides with a pronounced change in the reproducibility of AHe ages, with samples above (TRN3.2 and TRN3.3) having more AHe age variability than those below (TRN3.4 and TRN3.5). We interpret this as reflecting relatively slow cooling through the PRZ for higher elevation samples compared to the lower two, which has amplified the effects of diffusional differences between aliquots from higher TRN3.2 and TRN3.3 samples, causing more AHe age variation [Reiners, 2007].

The gradient of reset AERs can also be used to calculate the apparent exhumation rate (km/Myr), provided rocks are exhumed vertically and isotherms are horizontal [Stüwe *et al.*, 1994; Mancktelow and Grasemann, 1997; Braun, 2002; Ehlers and Farley, 2003]. Inaccuracies in apparent exhumation rates caused by violating these assumptions typically depend on the orientation of a sampled topographic profile with respect to the lateral transport direction and the geometry of any deflected isotherms [Huntington *et al.*, 2007]. Samples from TRN3 and TRN6 were collected along ~N-S orientated profiles (Figure 3.1c), meaning that any derived rates will be primarily affected by northward lateral exhumation imposed by the north-vergent Main Terskey Fault (MTF) and the topography between the Terskey Range and Issyk Kul (Figure 3.4a). Northward exhumation will cause apparent rates to underestimate true rates [Huntington *et al.*, 2007]; while the impact of the latter depends on whether topographic relief has changed through time. If, as expected, topographic relief between the Terskey Range and Issyk Kul has increased during the late Cenozoic, lower elevation samples will record younger thermochronological ages than would otherwise be the case, thereby decreasing the AER gradient and also underestimating true exhumation rates [Braun, 2002]. Since the combination of lateral transport and increasing relief are likely to cause an underestimation of true exhumation rates, the values obtained from the gradient of reset samples at TRN3 and TRN6 are taken as lower estimates. Therefore, gradients of reset ages from the Terskey Range suggest that exhumation rates were greater than 0.17 km/Myr between ~10 and at least 8 Ma (Figure 3.4a), and 0.31 km/Myr between 18 and 16 Ma (Figure 3.4b).

AFT ages from the western Sarajaz Range (Sar1 samples) plotted against elevation suggest apparent exhumation rates of 0.11 km/Myr between ~19 and 12 Ma (Figure 3.5c). Since this rate is

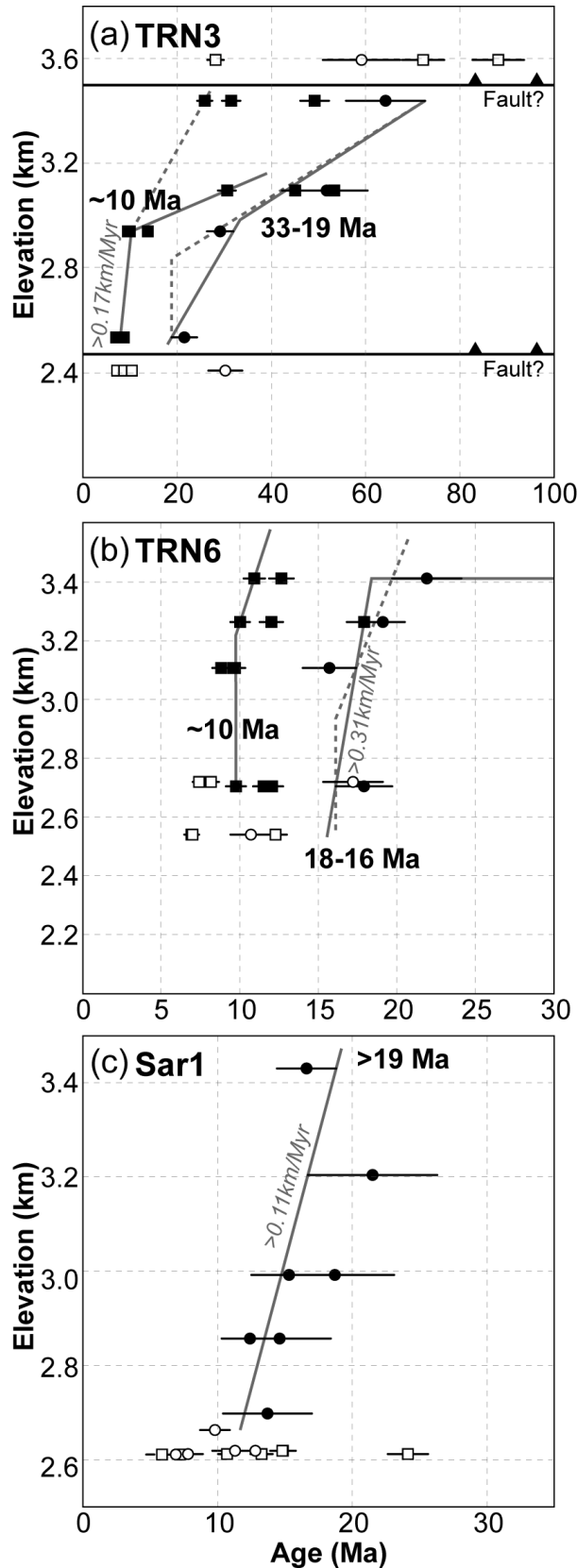


Figure 3.5. Age-elevation relationships (AERs) for three topographic profiles that contain reset thermochronological ages. AFT ages shown by circular points; AHe ages with square points. White points denote samples that were not included when constructing AER trend: (a) white samples are separated by faults; (b–c) sample from bottom of main trunk river and likely affected by incision. Grey lines (solid and dashed) show the range of possible AER trends. Calculated apparent exhumation rates are based on the gradient of these lines and are shown in grey text. Black text denotes timing of break-in-slope and exhumational increases.

comparable with those derived from reset AFT ages in the Terskey Range (TRN3 and TRN6), it is unlikely that these samples are partially reset and we assume that this apparent exhumation rate is valid. However, in contrast to the other topographic profiles discussed, Sar1 samples were collected along an ~E-W orientated topographic profile (Figure 3.1c) on the side of a steep N-S trending gorge. Consequently, rates are unlikely to be significantly affected by N-S long wavelength topography or non-vertical exhumation imposed by the Sarajaz fault and Southern Tien Shan Suture, which bound the range to the north and south, respectively (Figure 3.4a). Instead, the greatest inaccuracies are likely caused by increasing the topographic relief of the gorge, which will lead to an underestimation of the true rates [Braun, 2002]. The derived rate of 0.11 km/Myr is therefore also taken as the possible minimum exhumation.

3.5. Discussion

3.5.1. Mesozoic and Cenozoic exhumation history

At least three phases of Mesozoic intra-continental deformation have been inferred in the Tien Shan from the sedimentary record and thermochronological data [e.g. Hendrix *et al.*, 1992; Dumitru *et al.*, 2001; Jolivet *et al.*, 2010]. These are typically interpreted as delayed responses to the accretion of terranes along the southern Eurasian margin or the Mongol-Okhotsk orogeny. Unfortunately, in the Central Kyrgyz Tien Shan, the sedimentary record for this period is missing and the spatiotemporal distribution of Mesozoic deformation remains poorly constrained. However, recent thermochronological studies have identified multiple, temporally-variable deformation phases in the Mesozoic [De Grave *et al.*, 2007; 2011a; 2011b; 2013; Glorie *et al.*, 2011]. Evidence for these deformation phases comes from clusters of partially reset thermochronological ages and poorly-constrained thermal models, neither of which necessarily require phases of increased exhumation and cooling. More data is therefore required to firstly verify these deformational phases, and secondly, to constrain the spatial extent and magnitude of the associated exhumation.

Our thermochronological data only clearly identifies one significant Mesozoic cooling event, occurring in the early Jurassic. This cooling is particularly well constrained in thermal models that include ZHe data, like NA2.2 (Figure 3.2c) and Kar1.4 (Figure A2.3). Importantly, zircon U-Pb ages of 303 ± 3 and ~ 450 Ma from the sampled igneous bodies [Mikolaichuk *et al.*, 1997; Seltnann *et al.*, 2011] suggest that rapid early Jurassic cooling (~ 200 Ma) is not related to the intrusion of the rocks and instead must represent a period of enhanced exhumation. Similar early Jurassic exhumation increases have been identified in the eastern Tien Shan (Figure 3.1b) and interpreted to relate to intra-continental deformation caused by the accretion of the Qiantang block [Dumitru *et al.*, 2001]. Following this, Mesozoic cooling rates in these two well constrained thermal models remain relatively low ($<1^\circ\text{C}/\text{Myr}$ for NA2.2 in Figure 3.2c) until the Cenozoic. Other Mesozoic phases of elevated cooling are absent or poorly expressed in our thermal models. The only additional Mesozoic increased cooling phase occurs around 100 Ma in models of TRN3.1 (Figure 3.2a); the timing of this phase approximately coincides with some events identified elsewhere in the Central Kyrgyz Tien Shan and may be a delayed response to the accretion of the Lhasa terrane in the early Cretaceous [Glorie *et al.*, 2011; De Grave *et al.*, 2013].

During the Cenozoic, most well constrained thermal models suggest two stages of cooling: (1) universally low rates during the tectonic quiescent period extending from the late Mesozoic through much of the early Cenozoic ($<1^\circ\text{C}/\text{Myr}$ for the overlap of models in Figure 3.6) and (2) increased cooling in the late Cenozoic (Figure 3.6). Importantly, the timing and magnitude of exhumation differ between ranges. In the northern block of the Terskey Range and the Sarajaz Ranges, our age-elevation relationships (AERs) and thermal models suggest continuous exhumation and cooling since the Oligocene–early Miocene (Figure 3.5). In contrast, the data from the Karakudjur and Naryntoo-Akshyirak Ranges is less conclusive and significant heating, associated with sedimentary burial, could have occurred in the late Cenozoic (Figure 3.2c). Unfortunately, thermal modelling is unable to

resolve the magnitude or precise timing of this reheating. However, the lack of late Cenozoic AHe ages ($<25 \pm 5$ Ma) from these ranges (Figure 3.4) suggests that samples were not reheated above the base of the AHe PRZ at 85 to 40°C [Wolf *et al.*, 1998].

The Oligocene–early Miocene cooling history is constrained by many thermal models of higher elevation samples (e.g. TRN3.1; Figure 3.2a) and AERs obtained from the AFT ages of TRN6 samples (18–16 Ma; Figure 3.5b). These exhumation increases are in good agreement with other thermochronological data from the Central Terskey Range (Chapter 2) [Macaulay *et al.*, 2013], and magnetostratigraphic constraints on deposition in the Issyk Kul basin, which dates the onset of coarse clastic sedimentation at 25–22 Ma (Chapter 4) [Wack *et al.*, in review]. Minimum apparent exhumation rates from TRN6 are >0.31 km/Myr in the early Miocene (between 18 and 16 Ma; Figure 3.5b). For this relatively high TRN6 estimate, thermal models suggest that the true exhumation rate cannot be significantly greater than 0.31 km/Myr, as it would require an unrealistically low geothermal gradient of less than 20°C/km (Figure 3.6). Early Miocene exhumation in the eastern Sarajaz Range (Figure 3.1c) is constrained to >0.11 km/Myr between ~19 and 12 Ma by the AER of AFT ages from Sar1 samples (Figure 3.5c). In addition to the Oligocene–early Miocene exhumation increase, many thermal models of lower elevation samples with reset AFT ages identify a second, stronger cooling increase at 10 ± 5 Ma (Figures 2b + 6). This is also suggested by AHe AERs from TRN3 and TRN6 samples (Figure 3.5a+b), and has previously been identified in the Central Terskey Range (Chapter 2) [Macaulay *et al.*, 2013]. The minimum apparent exhumation rate suggested by the TRN3 AER following the ~10 Ma increase is 0.17 km/Myr (Figure 3.5a); note however, that the true rate is likely significantly higher and could be as much as 0.7 km/Myr based the overlap of thermal models of TRN3.4 and TRN3.5 and a geothermal gradient of 20°C/km (Figure 3.2b).

Unfortunately, most other ranges in the study area have not been sufficiently eroded to exhume reset thermochronological ages and AERs cannot be used to constrain the late Cenozoic exhumational increases. These spatial variations in the amount of late Cenozoic exhumation can be attributed to differences in exhumation rates or the duration of active exhumation. As discussed in the next section, geological evidence suggests that much of these spatial exhumation variations relate to differences in the onset of late Cenozoic deformation.

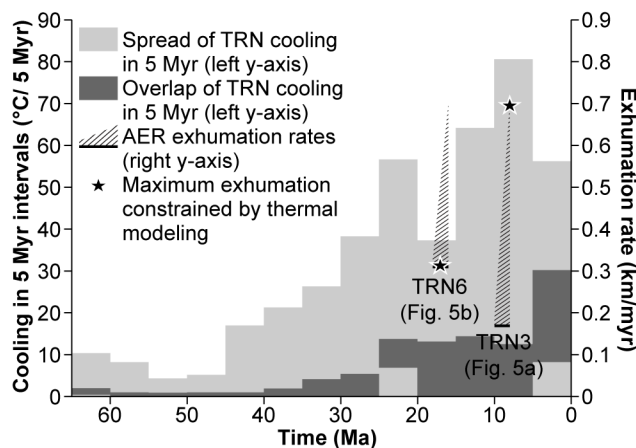


Figure 3.6. Compilation of exhumation and cooling data from the northern Terskey Range (TRN samples). Grey boxes corresponding to the left y-axis show range of cooling achieved in 5 Myr intervals for all well constrained thermal models of TRN samples (9 samples: TRN2.2, 3.1, 4, 5, 6, 6.2, 3, 5, 6). These have been compiled from every acceptable time-temperature history identified by thermal modelling. Darker grey boxes show overlap in cooling achieved in 5 Myr intervals for all samples. AER derived minimum exhumation rates (right y-axis) are shown by thick black lines and hatching. Younger estimates for exhumation increase lead to higher subsequent exhumation rate; preferred rates and onsets (black stars) calculated on the basis of thermal modelling of nearby samples. The right and left y-axis match for a geothermal gradient of 20°C/km; this relatively low geothermal gradient was selected to get maximum constraints on exhumation, which together with the minimum constraints derived from AERs, provides the range of possible exhumation rates.

3.5.2. Onset of late Cenozoic deformation

The timing of late Cenozoic deformation in different ranges can be estimated by assuming that structural reactivation and the onset of deformation will lead to a detectable exhumation increase. As discussed in Section 3.2, prior to the late Cenozoic, the Central Kyrgyz Tien Shan experienced a protracted period of tectonic quiescence, when ranges were not actively exhuming and were likely mantled by thin pre-orogenic sediments of the Kokturpak/Suluterek unit. In this landscape, potential non-tectonic triggers of exhumation increases, such as climatically-induced increases in erosional efficiency, would be ineffective; the only feasible cause for increased exhumation is therefore the onset of deformation. Unfortunately, the lag time between the onset of deformation and the exhumational response cannot be constrained from the available data. Our thermochronologic-derived exhumation constraints therefore provide minimum estimates for the onset of deformation.

In agreement with studies conducted elsewhere in the Tien Shan, our earliest estimates for the onset of deformation are in the Oligocene and early Miocene [e.g. *Windley et al.*, 1990; *Hendrix et al.*, 1994; *Métivier and Gaudemer*, 1997; *Yin et al.*, 1998; *Sobel and Dumitru*, 1997; *Dumitru et al.*, 2001; *Sobel et al.*, 2006a; *Heermance et al.*, 2007, 2008; *Glorie et al.*, 2011; *De Grave et al.*, 2011a, 2013; *Macaulay et al.*, 2013]. Our preferred estimates for the onset of exhumation in the Terskey Range are ~25–20 and 18 Ma at TRN3 and TRn6, respectively. Previous thermochronological and magnetostratigraphy data have suggested similar estimates of ~25 Ma and 22 Ma from the Barskoon region in the central Terskey Range and near the TRN3 samples (Figure 3.7) (Chapters 2 and 4) [*Wack et al.*, in review; *Macaulay et al.*, 2013]. The AER from Sar1 (Figure 3.5c) suggests that the Sarajaz Ranges was actively exhuming by 19 Ma and therefore also must have started deforming by the early Miocene. Furthermore, Oligocene and early Miocene estimates for the onset of deformation have been proposed for the Kokshaal Range in NE China (~25 Ma) and the At Bashi Range (<30 Ma) to the south-west of our study area, and from thermochronological data from the Zailiy Range (Figure 3.1c) [*Sobel et al.*, 2006a; *Glorie et al.*, 2011; *De Grave et al.*, 2013].

Other ranges within the study area lack suitable thermochronological data to constrain exhumation, and the timing of late Cenozoic deformation has to be inferred from geological data. Typically, evidence of proximal deformation can be found in adjacent intermontane basins. However, as mentioned in Section 3.2, constraints on the chronology of these basins are limited and relative ages can only be inferred by lithostratigraphic correlations. These geological-based estimates for the onset of deformation are therefore not as reliable or precise as those obtained from our thermochronological data, and should be interpreted with caution. What follows below is a summary of key geological observations from intermontane basins that we have used to infer the relative age of initial deformation in adjacent mountain ranges.

The Chu unit in the upper Naryn basin contains an abundance of conglomerate clasts sourced from the Middle Tien Shan passive continental margin sedimentary sequence (Appendix 2, Figure A2.4), that were likely derived from the Jetym Range to the north of the basin (Figure 3.7). Nearby, the Chu unit has been magnetostratigraphically dated to <8 Ma [*Abdrakhmatov et al.*, 2001], suggesting that parts of the Jetym Range were sub-aerially eroding at this time, and rock uplift and deformation had started by the late Miocene. In other areas however, the Jetym Range appears to have started deforming in the Pliocene–Pleistocene, during the deposition of the Sharpyldak unit [*Fortuna et al.*, 1994], suggesting that the range developed diachronously.

Bedding measurements along the un-faulted margins of many ranges, where late Cenozoic sediment can be found onlapping Precambrian and Paleozoic basement, can date tectonic rotation and can be used to infer the likely onset of deformation. Above many of Issyk Kul Broken Foreland (IKBF) Ranges for example, the Shamsi and Chu units are separated by slight angular unconformities, indicating that deposition of the Chu unit at <13–11 Ma [*Wack et al.*, in review] was coincident with tectonic rotation in some of the range forming basement blocks. Along the northern, un-faulted

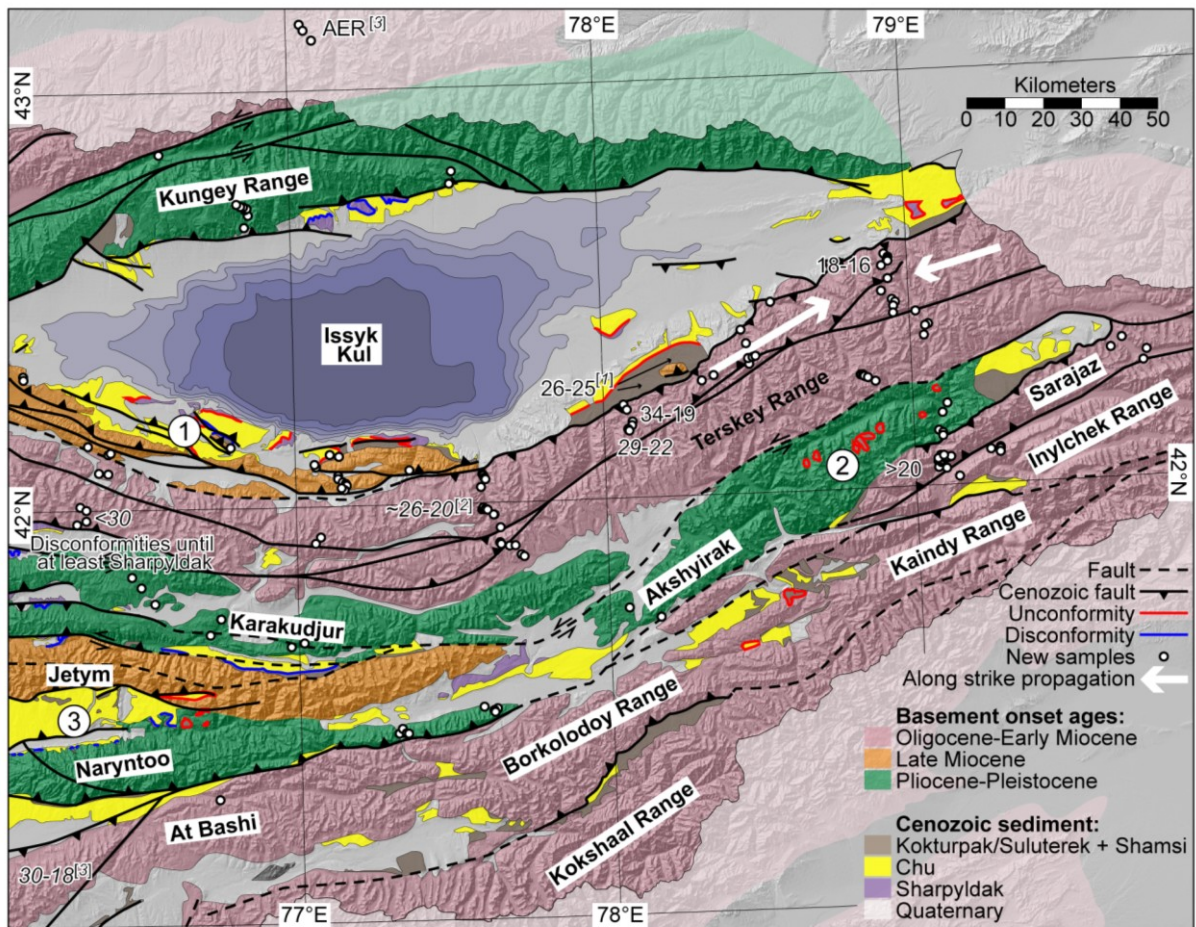


Figure 3.7. Map of study area showing the timing of the initial onset of Late Cenozoic deformation, divided into the three phases of range construction. Distribution of Cenozoic sediments is also shown, with the locations of selected unconformities (red lines) and disconformities (blue lines). White dots show the location of all samples. Key geological evidence of deformation shown by circles and corresponding numbers. 1: Unconformities and growth strata in hanging walls of some IKBF ranges suggest deformation started after 13–11 Ma; 2: Remnants of Cenozoic sediment preserved above relatively flat Late Mesozoic–Tertiary basement unconformities (MTUC); 3: Sediment sourced from Jetym Range suggesting basement sub-aerially exposed before 8 Myr. Data suggesting that sediment in eastern Naryn basin is sourced from Jetym Range can be found in Appendix 2. Corresponding references to superscript italic numbers. 1: *Wack et al.* [in review]; 2: *Macaulay et al.* [2013]; 3: *De Grave et al.* [2013].

margin of the Naryntoo Range, bedding of the Chu unit is sub-parallel to the underlying sediments and the local late Mesozoic–Tertiary basement unconformity (MTUC), implying that no tectonic rotation occurred in the Naryntoo Range until after 8 Ma, when the Chu unit started being deposited [*Abdrakhmatov et al.*, 2001]. If correct, this suggests that the south-vergent reverse fault bounding the south of the range was inactive at the time of deposition, meaning that late Cenozoic rock uplift and deformation started later, probably during the Pliocene–Pleistocene when growth strata is observed in nearby sediments. Similar sub-parallel relationships between the late Mesozoic–Tertiary basement unconformity (MTUC) and much of the overlying late Cenozoic sediments are observed in numerous basins between Karakudjur Ranges, with clear evidence of growth strata and significant angular unconformities only found in the lattermost fill stages. Taken together, this suggests that tectonic rotation and deformation of the Karakudjur Ranges post-date the bulk of sedimentation in these intermontane basins, implying that these ranges are relatively young and probably initiated in the Pliocene–Pleistocene (Figure 3.7). As discussed, a younger onset of deformation in the Karakudjur and Naryntoo Ranges, compared to the thermochronologically-derived Oligocene–early Miocene

estimates for the Terskey and Sarajaz Ranges, at least partly provides an explanation for the observed differences in the amount of late Cenozoic exhumation.

In summary, the combination of thermochronological and geological data suggests at least three stages of range construction: (1) Oligocene–early Miocene when the Terskey, Sarajaz, At Bashi and Kokshaal Ranges developed, (2) late Miocene when deformation started in the Issyk Kul Broken Foreland and Jetyrn Ranges, and (3) the Karakudjur and Naryntoo Ranges in the Pliocene–Pleistocene (Figure 3.7). This only leaves the onset of deformation unassigned in the Akshyirak and Borkolodoy-Kaindy-Inylchek Ranges. However, as discussed there appears to be a correlation between the amount of late Cenozoic exhumation and duration of tectonic activity, thus providing a means of inferring the likely onset of deformation. Based on our thermochronological data, the Akshyirak Range has experienced very little exhumation, and exposures of the late Mesozoic–Tertiary basement unconformities (MTUC) remain relatively undeformed (Figure 3.4). We therefore suggest that such limited deformation and exhumation is indicative with a relatively short duration of tectonic activity and favour a Pliocene–Pleistocene onset of deformation, like the Karakudjur and Naryntoo Ranges. In contrast to these ranges, the late Mesozoic–Tertiary basement unconformities (MTUC) appear to have been completely removed in the Borkolodoy-Kaindy-Inylchek Ranges (Figure 3.4a), suggesting significantly more exhumation has occurred, and deformation likely started earlier, possibly in the Oligocene–early Miocene.

3.5.3. Geological history

Thermochronological and geological data suggest that ranges within the study area have developed out-of-sequence (Figure 3.7). In this section, using our constraints for the onset of deformation as a temporal framework, we first discuss the evolution of the Central Kyrgyz Tien Shan: describing the structural architecture and discussing the likely causes of deformation migration, from the construction of the earliest ranges in the Oligocene–early Miocene to the present-day (Figure 3.8). Finally, we relate the structural evolution of the Central Kyrgyz Tien Shan and the out-of-sequence range construction to the sedimentary record of intermontane basins.

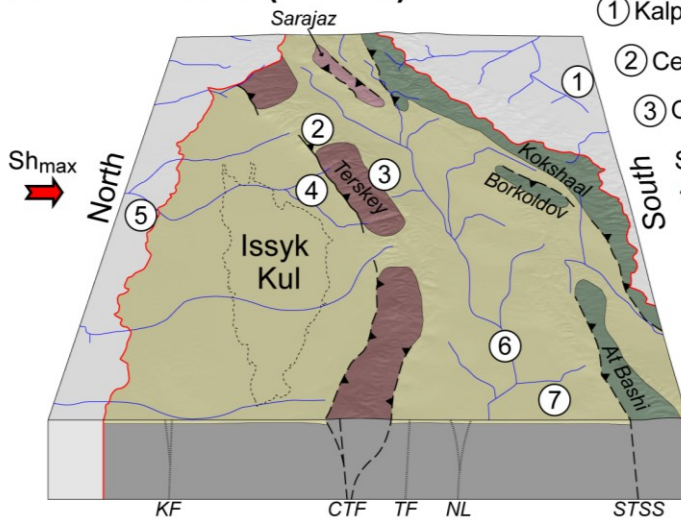
As discussed in Section 3.5.2, the Zailiy, Terskey, Sarajaz, At Bashi, Kokshaal Ranges and possibly the Borkolodoy-Kaindy-Inylchek Ranges were the first to be constructed in the Central Kyrgyz Tien Shan. The construction of these ranges in the Oligocene–early Miocene likely reflects the first manifestation of intra-continental deformation in the Central Kyrgyz Tien Shan, following the India-Eurasian collision and subsequent transfer of compressional stresses into the Asian continent. Typically, these early ranges are bounded on at least one side by a pre-existing structure that has been reactivated as a high angle reverse fault [e.g. *Tozer, 2004; Macaulay et al., 2013*]. Interestingly, this contrasts with many younger ranges, where bounding faults appear to have only developed in the late Cenozoic; for instance, the high-angle reverse faults along the southern margin of the Kungey Range that initiated in the Pliocene–Pleistocene [*Selander et al., 2012*]. Clearly, the locations of these early ranges must reflect the distribution of inherited structures that were predisposed to being reactivated as high angle reverse faults, suggesting that differences in the susceptibility of structures to reactivation have facilitated the observed out-of-sequence range construction. However, from the available data, the precise controls on what makes some inherited structure more suited to late Cenozoic reactivation remains unclear, although it probably relates in some way to the strength and orientation of these structures [e.g. *Holdsworth et al., 1997; Kley et al., 2005*]. For example, many ~E-W trending, Permian strike-slip faults have near vertical inclinations that are not well suited to accommodating significant amounts of ~N-S horizontal shortening and have therefore only been reactivated in a few locations with a dip-slip component. Interestingly, where these faults have been reactivated, their steep inclinations have meant that even minor along strike variations have drastically altered the sense and magnitude of post-reactivation displacement. As discussed in Section 3.4.2, this provides an explanation for the observed along strike changes in the late Cenozoic vergence of the Central Terskey Fault (CTF) (Figure 3.4a–c). Similarly, in our study area, only the eastern part of the Nikolaev Line

(NL) appears to have been reactivated with a significant dip-slip component (Figure 3.4a–c). Therefore, although the late Cenozoic displacements on these Permian strike-slip faults are usually relatively minor [e.g. *Macaulay et al.*, 2013], these structures have likely had a pronounced effect on the development of ranges and in some younger ranges that are not bounded by inherited structures, like the Kungey Range, may have assisted deformation [e.g. *Selander et al.*, 2012].

Some of these early, Oligocene–early Miocene ranges appear to have grown laterally along strike, possibly reflecting the propagation of bounding structures away from areas that were the best suited to reactivation. In the Terskey Range, our estimates for the onset of deformation vary along strike (Figure 3.7), suggesting that like the Kyrgyz Range to the north-west of our study area [*Sobel et al.*, 2006b], the range grew laterally as fault propagated along strike. In the Terskey Range however, this lateral propagation is complicated by the segmentation of the Main Terskey Fault zone (MTF), which bounds the range to the north and primarily drives rock uplift (Figure 3.1c) (Chapter 2) [*Macaulay et al.*, 2013]. Each fault segment is likely to have commenced independently before coalescing; the 18–16 Ma estimate for activity along the eastern segment, obtained from TRN6 samples, therefore reflects a different propagation history to the trend established by estimates from the central segment (Figure 3.7).

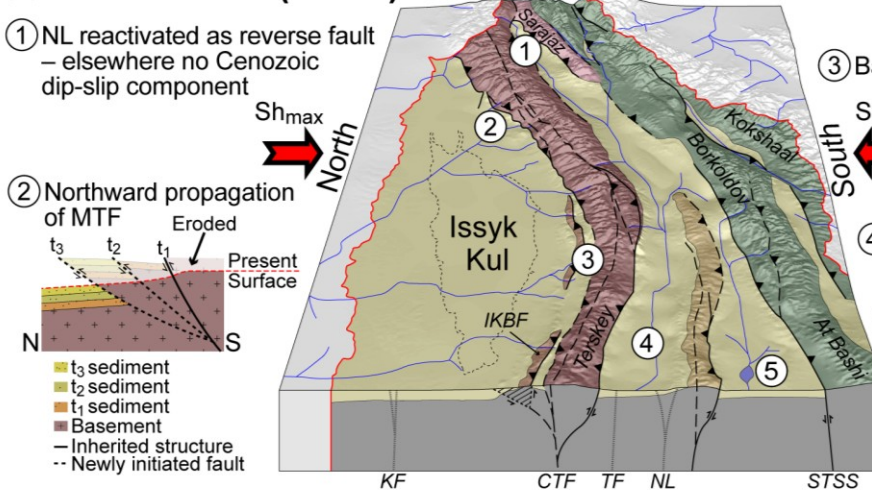
In the late Miocene, the Issyk Kul Broken Foreland (IKBF) Ranges started developing along a series of predominantly south-vergent reverse faults (Figure 3.7). Paradoxically, these reverse faults appear to collectively up-throw the Issyk Kul basin rather than the Terskey Range to south. *Burgette* [2008] addressed this problem and suggested that these structures lie on inherited weaknesses that were reactivated by trishear deformation ahead of a north-vergent reverse fault at depth (Figure 3.8a). If this interpretation is correct, it is likely that the north-vergent reverse fault at depth corresponds to a foot wall short-cut of the MTF. Also in the late Miocene, deformation started in the Jetym Range (Figure 3.7), and other ranges in the Central Kyrgyz Tien Shan such as the Kyrgyz Range to the north-west of our study area (Figure 3.1b) [*Bullen et al.*, 2001, 2003; *Sobel et al.*, 2006b]. Importantly, the construction of these younger ranges does not coincide with a decrease in the exhumation of those ranges that initiated earlier, in the Oligocene–early Miocene. Such a decrease would be expected if the locus of deformation had shifted in the late Miocene and the overall magnitude of crustal shortening had remained constant, as a cessation or reduction in deformation across pre-existing ranges would lead to less rock uplift and presumably exhumation of older, Oligocene–early Miocene ranges, like the Terskey Range. Instead, exhumation in the Terskey Range actually increases in the late Miocene (Figure 3.6), and possibly also increased in the At Bashi Range at ~10 Ma [*Glorie et al.*, 2011]. These changes can be interpreted to reflect an increase in either rock uplift or erosional efficiency. The former possibility would suggest an overall intensification of deformational processes in the Terskey and At Bashi Ranges at the same time as the initiation of deformation in the IKBF, Jetym and Kyrgyz Ranges, implying that shortening across the Central Kyrgyz Tien Shan must have increased. On the other hand, if the late Miocene exhumational increases were caused by more efficient erosion, then topographic and lithostatic loading within the pre-existing Terskey and At Bashi Ranges ought to decrease, allowing more deformation to occur and reducing the requirement for deformation to migrate elsewhere [*Hilley et al.*, 2005]. In this scenario, rock uplift in the Terskey and At Bash Range must have significantly outpaced erosion, such that it was still necessary to construct new ranges. Again, this suggests that construction of new ranges in the late Miocene is driven by an overall shortening increase across the Central Kyrgyz Tien Shan. The idea that deformation and shortening in the Tien Shan intensified in the late Miocene has previously been suggested [e.g. *Abdrakhmatov et al.*, 2001; *Sobel et al.*, 2006a; *Glorie et al.*, 2010, 2011]. Furthermore, a late Miocene (~10 Ma) age for the onset of deformation in the Central Kyrgyz Tien Shan has even been inferred by calculating the time taken to accommodate the total Cenozoic shortening of 203 ± 50 km, determined from the amount of the crustal thickening [*Avouac et al.*, 1993], with the present GPS-derived convergence rates (20 ± 2 mm/yr) [e.g. *Abdrakhmatov et al.*, 1996; *Zubovich et al.*, 2010].

(a) Mid Miocene (~15 Ma)



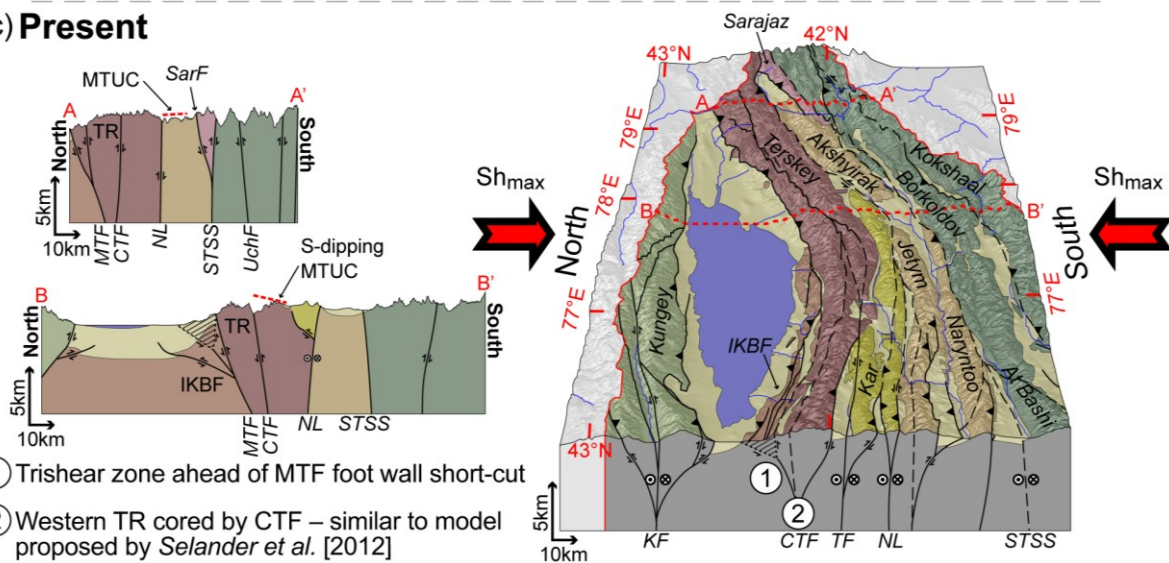
- ① Kalpin Tagh onset at 22-20 Ma [Chang et al., 2012]
- ② Central MTF segment propagating eastward
- ③ Onlapping sediment
- ④ Low sedimentation rate (<0.1 km/Myr) for Shamsi unit in Issyk Kul [Wack et al., in review]
- ⑤ Possible Late Oligocene-Early Miocene onset for Zailiy Range – based on AFT data [De Grave et al., 2013]
- ⑥ W-directed paleocurrent directions [Abdrakhmatov et al., 2001]
- ⑦ Syn-tectonic sediments (Shamsi unit) younger in Naryn than Issyk Kul – highly time-transgressive deposition.

(b) Late Miocene (~8 Ma)



- ① NL reactivated as reverse fault – elsewhere no Cenozoic dip-slip component
- ② Northward propagation of MTF
- ③ Basin progressively overthrust
- ④ Basin later partitioned by Karakudjur Ranges
- ⑤ More lacustrine sediment in Chu, possibly indicating a less connected fluvial system after the construction of new ranges [Abdrakhmatov et al., 2001].

(c) Present



- ① Trishear zone ahead of MTF foot wall short-cut
- ② Western TR cored by CTF – similar to model proposed by Selander et al. [2012]

Figure 3.8. Conceptual model of the geological history of the Central Kyrgyz Tien Shan, based on the available constraints and geological data. Red arrows represent the inferred qualitative magnitude of shortening across the region. Numbers in white circles correspond to explanatory comments. Kyrgyz border and position of Issyk Kul are kept throughout for reference. Solid black line denotes location of Cenozoic faults; dashed line shows faults where Cenozoic activity is unclear. (a–b) Mid-Miocene and late Miocene: Grey lines with short dashes show location of pre-existing structures (Permian Strike-slip faults) that are interpreted to subsequently core Pliocene–Pleistocene ranges. (c) Present-day illustration of Central Kyrgyz Tien Shan. Positions of cross section A–A’ and B–B’ shown on block illustration. Sub-surface structure modified after *Selander et al.* [2012] for the Kungey Range, *Burgette* [2008] for the Issyk Kul Broken Foreland (IKBF) Ranges, and *Goode et al.* [2011] for the Jetym Range and Naryn basin.

Taken together this suggests that, although crustal shortening across the Central Kyrgyz Tien Shan started in the Oligocene–early Miocene, rates must have significantly increased in the late Miocene. Additionally, this increase is supported by a late Miocene increase in the northward motion of the Tarim basin, which has been inferred from the deceleration of strike-slip faulting along the basins western boundary with the Pamir [*Sobel et al.*, 2011]. Therefore, it seems likely that the significant shortening increase identified in the Central Kyrgyz Tien Shan was part of a much larger geodynamical change in the late Miocene that affected much of Central Asia, possibly relating to the proposed delamination of lithospheric mantle under the Tibetan Plateau [*Molnar et al.*, 1993; *Molnar and Stock*, 2009] or in the Tien Shan [*Li et al.*, 2009].

In terms of the sedimentary record, the first episode of deformation in the Oligocene–early Miocene is recorded by the deposition of the Shamsi unit. As this unit overlies a hiatus in sedimentation, it is not surprising that the onset of deformation and exhumation in the ranges and Shamsi deposition are temporally linked. However, as mentioned in Section 3.2, the basal age of the Shamsi unit varies by >10 Myr between the Naryn and Issyk Kul basins (Chapter 4) [*Abdrakhmatov et al.*, 2001]. We suggest that this time lag reflects the highly time-transgressive deposition of the initial syn-tectonic sediments, and has been exacerbated by the sheer size of the basin that extended between the Terskey and At Bashi Ranges until the late Miocene (Figure 3.8c). The older ages from the Issyk Kul basin (26–25 Ma) were obtained from a proximal setting, presently located within <10 km of the Terskey Range, and therefore experienced a minimal time lag. In contrast, the younger basal ages (~12 Ma) from the Naryn basin, were obtained from sections that would have been located roughly in the middle of the formerly large basin between the Terskey and At Bashi Range (Figure 3.8c), and therefore likely have a significantly delayed onset of syn-tectonic sedimentation. Furthermore, in this part of the Naryn basin, without the tectonic loading of adjacent ranges, it is unlikely that significant accommodation space would have been generated [e.g. *Strecker et al.*, 2011], and could potentially explain the relatively thin Shamsi unit (~200 m thick) [*Omuraliev*, 1978; *Goode et al.*, 2011] (Figure 3.8c).

Despite only being constrained at a few localities [*Abdrakhmatov et al.*, 2001], the basal ages of the Chu unit are approximately coincident with the late Miocene intensification of deformation, discussed above. We therefore favor a tectonic driver, over a possible change in regional climate, to explain the onset of Chu deposition, and suggest that changes in the lithostratigraphic record for these two units primarily reflect the evolution of tectonism in the Central Kyrgyz Tien Shan. Either way, the onset of deformation in the IKBF and Jetym Ranges in the late Miocene would have led to the removal of the overlying sediments. Such an influx of reworked sediments could at least partly explain the observed increase in the textural and mineralogical maturity of the Chu unit compared to the underlying Shamsi [e.g. *Abdrakhmatov et al.*, 2001]. Out-of-sequence range construction in the Central Kyrgyz Tien Shan has therefore had pronounced impacts on sedimentary routing and basin development that need to be further explored to fully understand the geological evolution of the region. In accordance with earlier studies [*Cobbold et al.*, 1996; *Burbank et al.*, 1999; *Abdrakhmatov et al.*, 2001], our data suggests that many intermontane basins have been partitioned by the construction of new ranges and further decreased in size as their margins were overthrust by the

surrounding ranges and range bounding fault systems encroached into basins along foot wall short-cuts.

3.6. Conclusions

We present new thermochronological data that constrains Late Cenozoic exhumation of various mountain ranges within the Central Kyrgyz Tien Shan. Age-elevation relationships and thermal modelling reveal a three stage exhumation history for the Terskey Range in the north of our study area (Figure 3.1c): (1) low cooling rates and exhumation in the Early Cenozoic ($<1^{\circ}\text{C}/\text{Myr}$), (2) increased exhumation likely occurring between ~ 25 and 18 Ma to rates of $0.2\text{--}0.3\text{ km}/\text{Myr}$, and (3) a second exhumation increase at 10 ± 5 Ma (Figure 3.6). Exhumation rates of $>0.11\text{ km}/\text{Myr}$ between ~ 19 and 12 Ma are also constrained in the Sarajaz Range by a new age-elevation relationship (Figure 3.5c). Other sampled ranges typically have experienced insufficient exhumation to bring reset thermochronological ages to the surface and the timing of exhumation increases cannot be precisely constrained. However, thermal modelling from these ranges indicates that cooling rates have increased in the Late Cenozoic (e.g. Figure 3.2c). By using geological data from these ranges and by interpreting the initial Late Cenozoic exhumation increase as reflecting the onset of deformation, we have constrained the order of range construction for the first time, and can show that out-of-sequence deformation has occurred (Figure 3.7). The first phase of range construction occurred in the Oligocene–Early Miocene, when the Zailiy, Terskey, Sarajaz, At Bashi, Borkoldoy and Kokshaal Ranges developed. Subsequently in the Late Miocene, the Issyk Kul Broken Foreland and Jetym Ranges started forming, and then in the Pliocene–Pleistocene, the Kungey, Karakudjur, Naryntoo and Akshyirak Ranges were constructed (Figure 3.7). This order of range construction presumably relates to the susceptibility of pre-existing structures to reactivation, implying that the Main Terskey Fault (MTF), Sarajaz Fault (SarF) and parts of the Southern Tien Shan Suture (STSS) were the most suited to accommodating $\sim\text{N-S}$ horizontal shortening.

Following structural reactivation, our data suggest that some ranges have grown laterally along strike (Figure 3.7), and possibly coalesced with other fault segments (Figure 3.8). Furthermore, parts of the Terskey Range have propagated into the foreland along foot wall short-cuts (e.g. Figure 3.3d); other ranges are likely to have expanded similarly. Therefore, over time, intermontane basins get smaller, with overthrusting around the margins as well as the partitioning and subsequent removal of sediments by following the out-of-sequence construction of ranges (Figure 3.8). Based on our inferred order of range construction, we suggest that the Naryn basin was formally much larger, extending between the Terskey Range in the north and the At Bashi-Bordolodoy Range to the south. Our constraints on the timing of deformation provide a temporal framework that will allow future studies to further investigate the geological evolution of the Central Kyrgyz Tien Shan and better understand the development of intermontane basins.

Finally, the timing of the three phases of range construction (Oligocene–Early Miocene, Late Miocene and Pliocene–Pleistocene) is interpreted to relate to shortening increases across the Central Kyrgyz Tien Shan. Our data indicates that younger ranges have not been constructed at the expense of deformation and rock uplift in older pre-existing ranges, which suggests that the locus of deformation has not simply migrated between ranges and instead requires an overall increase in shortening. In particular, we suggest that a significant shortening increase in the Late Miocene is required to account for the increased exhumation of the Terskey Range at a time when new ranges were being constructed in the study area and elsewhere in the Central Kyrgyz Tien Shan.

Acknowledgements

Funding was provided by an Endeavour Research Fellowship and grant SO 436/4-1 from the German Research Foundation (DFG) to ERS. EAM thanks Universität Potsdam and the Mathematisch-Naturwissenschaftliche Fakultät for additional support. AM thanks the German Academic Exchange

Service (DAAD) for supporting three visits to Germany. The University of Melbourne thermochronology laboratory receives infrastructure support under the AuScope Program of NCRIS. Douglas Burbank and Mike Oskin are thanked for providing 6 samples. We thank Christina Trautmann for her help with heavy ion irradiations performed at GSI Helmholtzzentrum für Schwerionenforschung in Darmstadt. Markus Safaricz, Misha Yaremovich, Andryj Derzhulo and Vasyl Hyshchyn are thanked for providing field assistance.

Chapter 4.

Cenozoic magnetostratigraphy and rock magnetism of the southern Issyk-Kul basin, Kyrgyzstan

Submitted by **Michael R. Wack**, Stuart A. Gilder, Euan A. Macaulay, Edward R. Sobel, Julien Charreau and Alexander Mikolaichuk (2013) to *Tectonophysics*.

Abstract

We present paleomagnetic data from the northern flank of the Tien Shan mountain belt, southeast of Lake Issyk-Kul (Kyrgyzstan). 613 cores were collected in two parallel sections with a total thickness of 960 m (Chon Kyzylsuu, CK) and 990 m (Jeti Oguz, JO), as well as 48 cores at six sites in a nearby anticline. Rock magnetic analyses identify both magnetite and hematite in the fluvial-lacustrine sediments. The concentration of both minerals, the magnetite:hematite ratio, and the average magnetite grain size increase upward in both sections. Anisotropy of anhysteretic remanent magnetization defines a tectonic fabric with sub-horizontal maximum axes that are parallel to the strike direction together with intermediate and minimum axes that streak out about a great circle orthogonal to the maximum axes. Stepwise thermal demagnetization isolates interpretable magnetization components in 284 samples that define 26 polarity chrons in CK and 19 in JO. A positive fold test, dual polarities and systematic changes in rock-magnetic parameters with depth suggest that the high temperature magnetization component was acquired coevally with deposition. An age model based on a visual magnetostratigraphic correlation of both sections with the geomagnetic polarity time scale defines absolute ages from 26.0 to 13.3 Ma, with a fairly constant sedimentation rate of 9–10 cm/ka. A correlation based on a numerical algorithm arrives at a slightly different conclusion, with deposition ages from 25.2 to 11.0 Ma and sedimentation rates from 5–8 cm/ka. In comparison with sedimentation rates found at other magnetostratigraphic sections in the Tien Shan realm, we infer that the sedimentary record in this part of the Issyk-Kul Basin preceded the more rapid phase of uplift of the Kyrgyz Tien Shan. The onset of deposition and concomitant erosion of the adjacent Terskey Range is in good agreement with independent assessments of the exhumation history of this mountain range, with erosion increasing at 25–20 Ma and accelerating after 11–13 Ma.

4.1. Introduction

The 2500 km long Tien Shan mountain belt in Central Asia is a product of deformation driven by the India-Asia continental collision superimposed on older episodes of Paleozoic orogenesis [Molnar and Tapponnier, 1975; Tapponnier and Molnar, 1979; Cobbold *et al.*, 1993; Mikolaichuk *et al.*, 1997; Burtman, 2006]. Its imposing topography, with peaks up to 7000 m, and plethora of exposures in a fairly arid environment provide exceptional conditions to study tectonic deformation and mountain building processes. Late Quaternary slip rates and present GPS data suggest that deformation is distributed across the central Tien Shan [Thompson *et al.*, 2002; Zubovich *et al.*, 2010]. While the overall compressional deformation regime is evident, the timing and mode of local deformation are much less well understood.

One way to study the uplift and erosion history of a mountain range is to examine the sediments shed from it. Deriving two-dimensional accumulation rates from the sediments and extrapolating them into a three-dimensional volume quantifies the amount and timing of mass removal from the system. For this reason, magnetostratigraphic studies can be extremely useful to develop a precise chronology of otherwise fossil-poor sediments, and ultimately to derive deposition rates. Complimented with ancillary rock magnetic analyses, clues on sediment source and the hydrodynamic regime acting during sedimentation can also be ascertained [Gilder *et al.*, 2001]. Such studies are becoming commonplace in the Tien Shan range [Bullen *et al.*, 2001; Charreau *et al.*, 2005, 2006,

2009a,b, 2011; *Heermance et al.*, 2008; *Huang et al.*, 2006; *Sun et al.*, 2004, 2009; *Sun and Zhang*, 2009]. Together with fission track cooling ages, these studies converge on the interpretation that the modern phase of Tien Shan growth began at around 25 Ma and accelerated around 11 Ma (Chapters 2 and 3) [*Abdrakhmatov et al.*, 2001; *Bullen et al.*, 2001; *Charreau et al.*, 2006; *Sobel et al.*, 2006a; 2006b; *Heermance et al.*, 2008; *Li et al.*, 2011; *Macaulay et al.*, in review]. Exceptions naturally exist and most of the work has taken place within the Chinese portion of the Tien Shan.

To better understand the Cenozoic uplift history of the central part of the Tien Shan range, we studied fluvial-lacustrine sediments deposited within the Issyk-Kul basin, Kyrgyzstan. Our intention was to date the fossil-poor strata via magnetostratigraphy and use the magnetostratigraphy to establish sedimentation rates. A suite of rock magnetic experiments on the same rocks were carried out to constrain the magnetic remanence carriers and identify potential changes in sediment composition and depositional environment, and to establish the extent that deformation or compaction may have affected the sediments and paleomagnetic directions. The results from this work are described below.

4.2. Geology, Sampling and Methodology

We sampled two parallel sections in the Tien Shan Mountains, southeast of Lake Issyk-Kul in Kyrgyzstan (Figure 4.1). The sections are located in NNW-trending river valleys, separated by ~13 km. The western section lies close to Chon Kyzylsuu village and the eastern section near the village of Jeti Oguz (Dzhety-Ogyuz). We assigned them the abbreviated names of CK and JO, respectively. Both sections have similar stratigraphies, consisting of fluvio-lacustrine siltstone, sandstone and conglomerate. They have a distinct red pigment near the base that gradually fades towards the top (Figure 4.1c). We use the naming scheme proposed by *Abdrakhmatov et al.* [2001] for the various Mesozoic and Cenozoic formations of separate basins in Kyrgyzstan (i.e. four units: Kokturpak/Suluterek, Shamsi, Chu and Sharpyldak). Local formation names are appended in brackets below and shown in the stratigraphic column (Figure 4.2). Both sections begin at the base of a coarse clastic unit which directly overlies an apparently fine grained, covered unit which is interpreted to represent the Chonkurchak Formation, lithostratigraphically equivalent to the Kokturpak/Suluterek unit. Regional geological maps [*Knauf*, 1965] place the JO section wholly within the Shamsi group (local Dzhety-Oguz formation, upper Paleogene to lower Neogene, Pg₃?+N₁kr₁₊₂) while CK is mapped as extending into the Chu group (local Issyk-Kul or Soguty/Djunky formation, N₂is₁₊₂), although no correlative lithologic change was noted (Figure 4.1b). Two tortoise shells (A and B in Figure 4.1b) constrain the published age of the sediments. Shell A, found within the sediments of our JO section, was dated as Oligocene – Early Miocene [*Ryabinin*, 1927]; shell B, found above our JO section, was dated as Middle Pliocene [*Kuznetsov et al.*, 1964]. The JO section spans nearly the entire Dzhety-Ogyuz Formation as defined by *Cobbold et al.* [1996], which belongs to the Shamsi (Kyrgyz) group (Figure 4.2). It is overlain by the Chu (Issyk- Kul) group and underlain by the Kokturpak (Chonkurchak) Formation, which marks the basal portion of Tertiary sediments that unconformably overlie Jurassic quartzite [*Cobbold et al.*, 1996]. No significant discontinuity or unconformity was identified in either section. Strike directions between the sections together with their similar lithologies suggest significant stratigraphic overlap exists between the two. *Thomas et al.* [1993] reported paleomagnetic and anisotropy of magnetic susceptibility data from 5 sites collected in the JO section.

Two 24 mm diameter cores per horizon were collected using gasoline-powered or slowly rotating battery-powered drills. The cores were oriented using magnetic and, whenever possible, sun compass measurements with an automated orientation sensor linked to a small portable computer. The average measured magnetic declination anomaly of $4.0^{\circ} \pm 1.7^{\circ}$ (N= 341) conforms well with that predicted by the international geomagnetic reference field (4.3°). The measured values were used to correct dip directions and core azimuths. Bedding orientations (N= 146 for CK; N= 129 for JO) define an average dip direction of $338^{\circ} \pm 19^{\circ}$ for CK and $355^{\circ} \pm 13^{\circ}$ for JO; dip angles change with stratigraphic

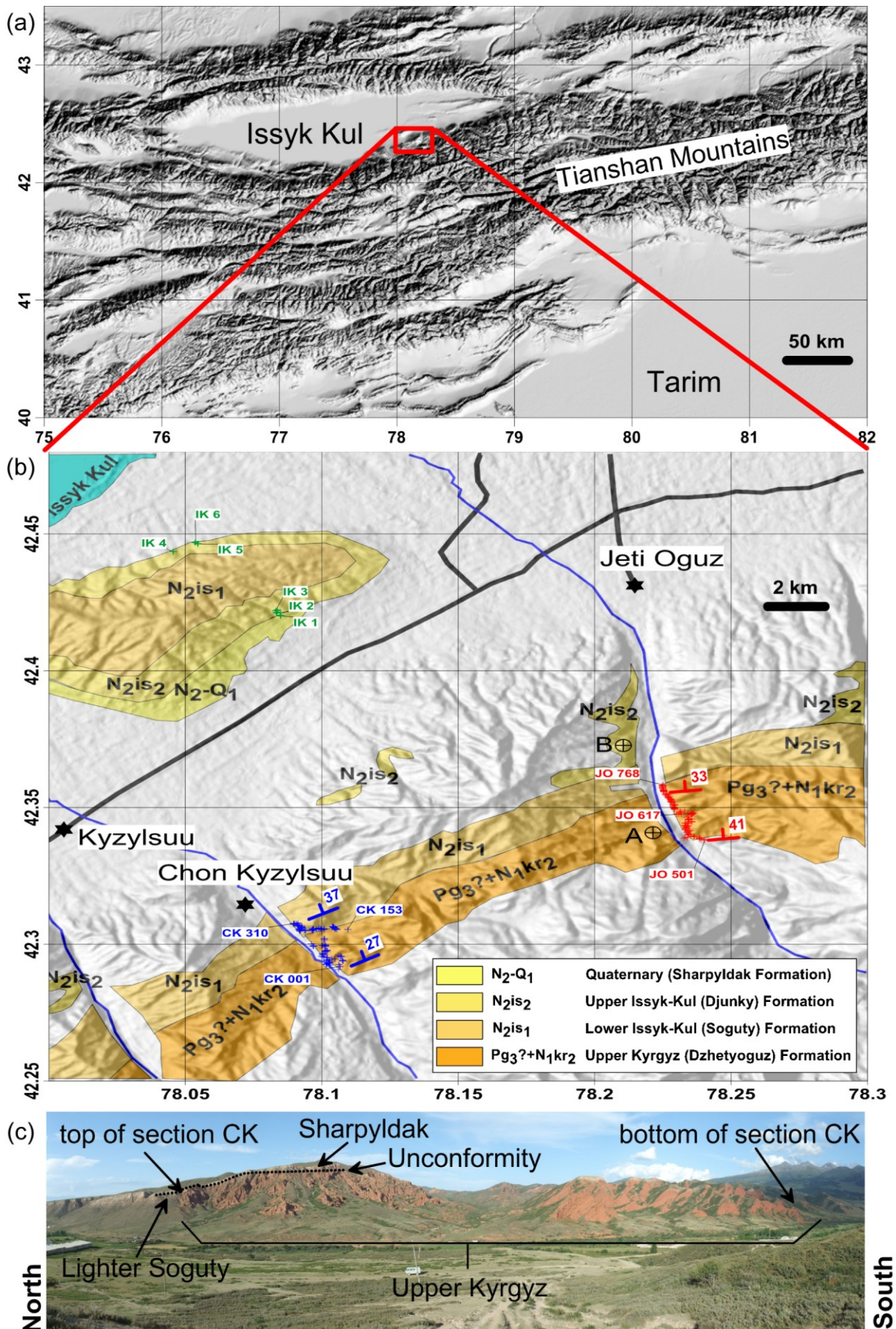


Figure 4.1. (a) Topographic map of the Tien Shan based on the ASTER GDEM model from METI and NASA. (b) Cenozoic geologic map of the sampling area indicated in (a). The location of every second core from the Chon Kyzylsuu (CK) and Jeti Oguz (JO) magnetostratigraphic sections are shown in blue and red, respectively. Locations of six sampling sites in the anticline north of Chon Kyzylsuu are labeled IK. Formation boundaries follow the regional geological map of *Knauf* [1965]. Pg= Paleogene, N= Neogene, Q= Quaternary, 2 and 3= late, 1= early. A more detailed stratigraphic column is given in Figure 4.2. A and B indicate sampling localities of tortoise fossils that constrain the age of sediments [*Ryabinin*, 1927; *Kuznetsov et al.*, 1964]. (c) Panoramic photo of the Chon Kyzylsuu section (view toward the east).

position. At CK, dips steepen from 27° at the bottom to 37° at the top, whereas at JO they flatten from 41° at the bottom to 33° at the top. *Cobbold et al.* [1996] also observed a flattening in dip at JO. One interpretation of the bedding attitudes is that both sections belong to the same anticlinal structure with CK located closer to the fold axis. In this way, the shallowing in bedding dip at JO does not reflect syn-sedimentary folding and concomitant deposition.

To average out measurement errors, we linearly interpolated dip and dip direction along stratigraphic height which mimics a running average of 25 data points. Stratigraphic depth was measured relative to the lowest core in each section. When direct measurements were not feasible because the lateral distance between drilling sites was too large, we calculated the stratigraphic distance from bedding attitude and GPS locations. Samples were selected from the finest-grained horizons available with an average spacing of six and seven meters over a total thickness of 960 and 990 meters for CK and JO, respectively.

To perform a fold test, we sampled six sites (IK1–6) of light gray, fine-grained, lacustrine sediments (mapped as Pliocene) on both limbs of an anticline that lies 14 km north of the CK section (Figure 4.1). At each site we drilled eight cores spread over three to nine meters of stratigraphic thickness. Table A3.1 lists the GPS coordinates, the number of cores obtained and the bedding orientations for all sites. Cores were cut into 22 mm-high specimens. The specimens from the deepest part of the cores were assigned an “A” sub-designation and the shallower core, if available, a “B” sub designation. One “A” specimen per horizon was thermally demagnetized while “B” cores were used for alternating field (AF) demagnetization and anhysteretic remanent magnetization (ARM) experiments. Small chips from the deepest part of the core were used for rock magnetic measurements.

Thermal demagnetization was done with an ASC Scientific TD-48 oven over approximately 20 steps up to 685°C. We placed the samples at the same location inside the oven and flipped the samples’ z-axes each heating step to identify potential stray field contamination (none was detected). We used our homemade automated system, called the SushiBar [*Wack and Gilder*, 2012], which facilitates AF demagnetization and ARM acquisition experiments and measures the magnetic moment of the samples with a 2G Enterprises, three-axis superconducting magnetometer [software after *Wack*, 2010]. The oven and SushiBar are housed in a magnetically shielded (~500 nT) room at Ludwig Maximilians Universität (LMU), Munich. The performed principal component analysis is from *Kirschvink* [1980], the statistical analyses are from *Fisher* [1953] and VGP (virtual geomagnetic pole) calculations were performed with PMGSC 4.2 [*R. J. Enkin*, unpublished] and PaleoMac [*Cogné*, 2003]. Rock magnetic experiments were carried out with a Petersen Instruments, variable field translation balance (at LMU) [*Krasa et al.*, 2007] using the RockMagAnalyzer [*Leonhardt*, 2006] for data interpretation.

4.3. Results

4.3.1. Magnetic Mineralogy

To constrain the unblocking temperatures of the minerals present in the rock, we imparted an artificial TRM on six samples from the JO section by exposing them to a 40 μT field during cooling from 700°C to room temperature. The resulting magnetizations are $1.1 \pm 0.3 \cdot 10^{-6} \text{ Am}^2$ with a

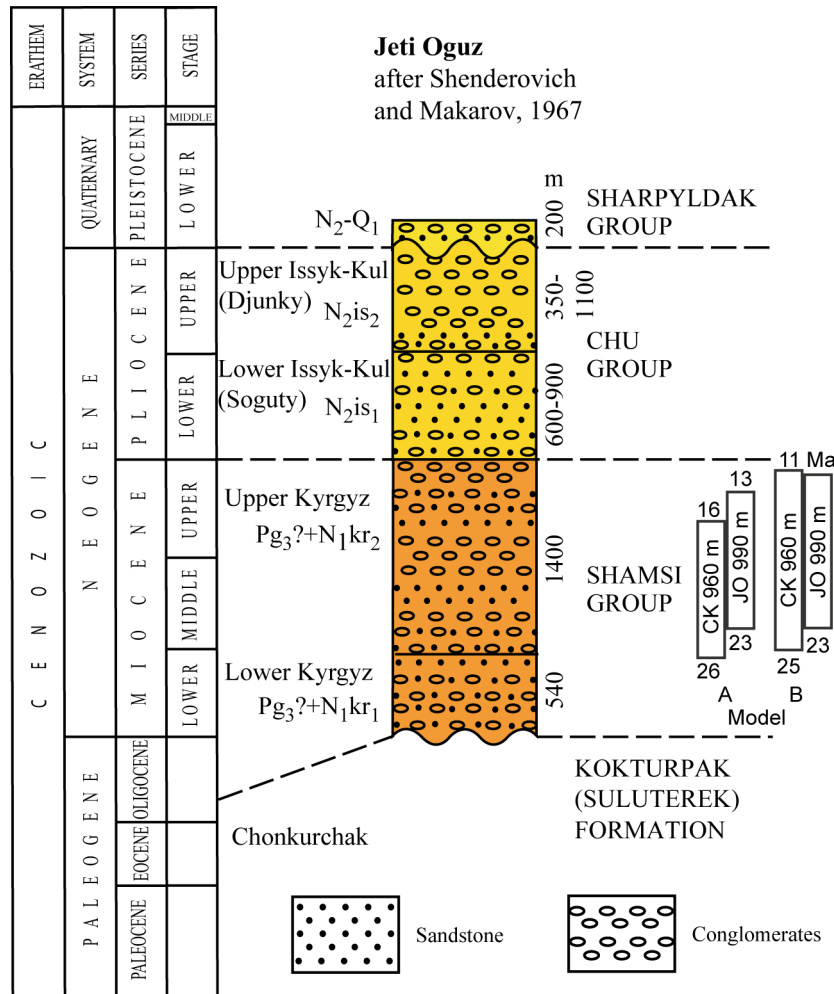


Figure 4.2. Stratigraphic column of Cenozoic sediments in the Jeti Oguz area drawn after *Shenderovich and Makarov* [1967]. Estimated stratigraphic placement of the CK and JO sections for both proposed age models is shown on the right. Names of sedimentary units proposed by *Abdrakhmatov et al.* [2001] are shown right and corresponding local names left of the stratigraphic column. Thicknesses were calculated from bedding dips and distances.

tendency of higher magnetization toward the top of the section. Subsequently, we exposed the specimens to the same 20-step thermal demagnetization procedure that was used to demagnetize the natural remanent magnetizations (NRM) of the specimens (Figure 4.3). Figure 4.3 reveals two Curie temperatures with a broad decay from 400 to 580°C, followed by a kink at 580°C, the Curie temperature of stoichiometric magnetite, then a sharp drop in magnetization at 680°C, the Curie temperature of stoichiometric hematite.

With the variable field translation balance, we measured thermomagnetic curves, hysteresis loops, isothermal remanent magnetization (IRM) acquisition and backfield curves on 21 specimens distributed along the two sections (Figure 4.4). IRM acquisition curves (Figures 4.4a+c) rise quickly in fields below 150 mT, which indicates a low coercivity mineral, although saturation is not reached even at the highest fields of 0.81 T, due to the presence of a magnetic phase with high coercivity. Samples towards the top of both sections show a faster increase in IRM acquisition, and a flatter acquisition profile at higher fields, which likely reflects an increasing magnetite concentration with stratigraphic height. Thermomagnetic curves were measured with an applied field of 600 mT for CK samples and 60 mT for JO samples (Figures 4.4b+d). Despite differences in the magnetizations between the cooling 160 and heating curves as a function of applied field strength, both reveal Curie temperatures around 580°C followed by a gently decay to 680°C – typical of magnetite and hematite.

We speculate that 600 mT fields are strong enough to partially magnetize a high coercivity phase that transforms to a non-magnetic phase with increasing temperature; 60 mT are insufficient to magnetize the high coercivity phase thus obscuring the transformation.

Coercive force (B_c), saturation magnetization (M_s), saturation remanent magnetization (M_{rs}) and coercivity of remanence (B_{cr}) were determined from hysteresis loops (Figure 4.4e) and backfield curves (Figure 4.4f) for 21 samples. Hysteresis parameters show general trends with stratigraphic height, with B_c and B_{cr} decreasing and M_{rs} and M_s (M_s defined as the magnetic moment at 810 mT) increasing toward the top of both sections; the remanence ratio (M_{rs}/M_s) decreases toward the top. Bulk susceptibility (X), ARM moment (90 mT AF field, 0.1 mT bias field), room temperature moment (also called natural remanent magnetization, NRM) as well as the moment remaining after AF demagnetization in a 90 mT peak field from the CK (99 B-cores) and JO (65 B-cores) sections all increase towards the top of the section (Figure 4.5). These data indicate that magnetite (best reflected by X and ARM) and hematite concentrations (best reflected by moment remaining after AF demagnetization) increase upward in both sections. The intensity of red pigment does not correlate with hematite content. An abrupt increase in several rock magnetic parameters occurs around the 700 m level in JO and the 600 m level in CK (Figure 4.5) that can potentially help tie the two sections together during magnetostratigraphic correlation.

In order to examine potential changes in magnetite grain size with depth, we measured the partial ARM spectra of 164 samples (Figure 4.6). While peak ARM moments increase toward the top, the peak coercivity shifts slightly towards lower fields, which indicates an increase in median magnetite grain size from about 3 μm at the bottom to 4 μm at the top [Jackson, 1991]. The narrowing of the pARM spectra towards the top could reflect an increase in the magnetite to hematite ratio, even though the absolute concentrations of both phases increase; e.g., lower magnetite to hematite ratios widen the ARM spectra toward the bottom of the sections.

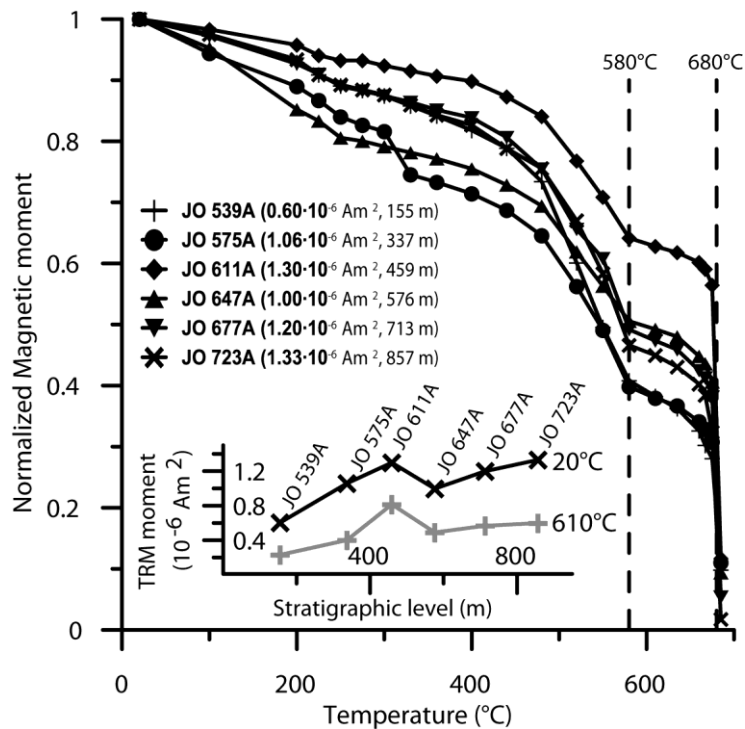


Figure 4.3. Normalized magnetic moments of stepwise thermal demagnetization of an artificial thermoremanent magnetization imparted to six samples from the Jeti Oguz (JO) section. Initial magnetic moments used for normalization are given in the inset diagram.

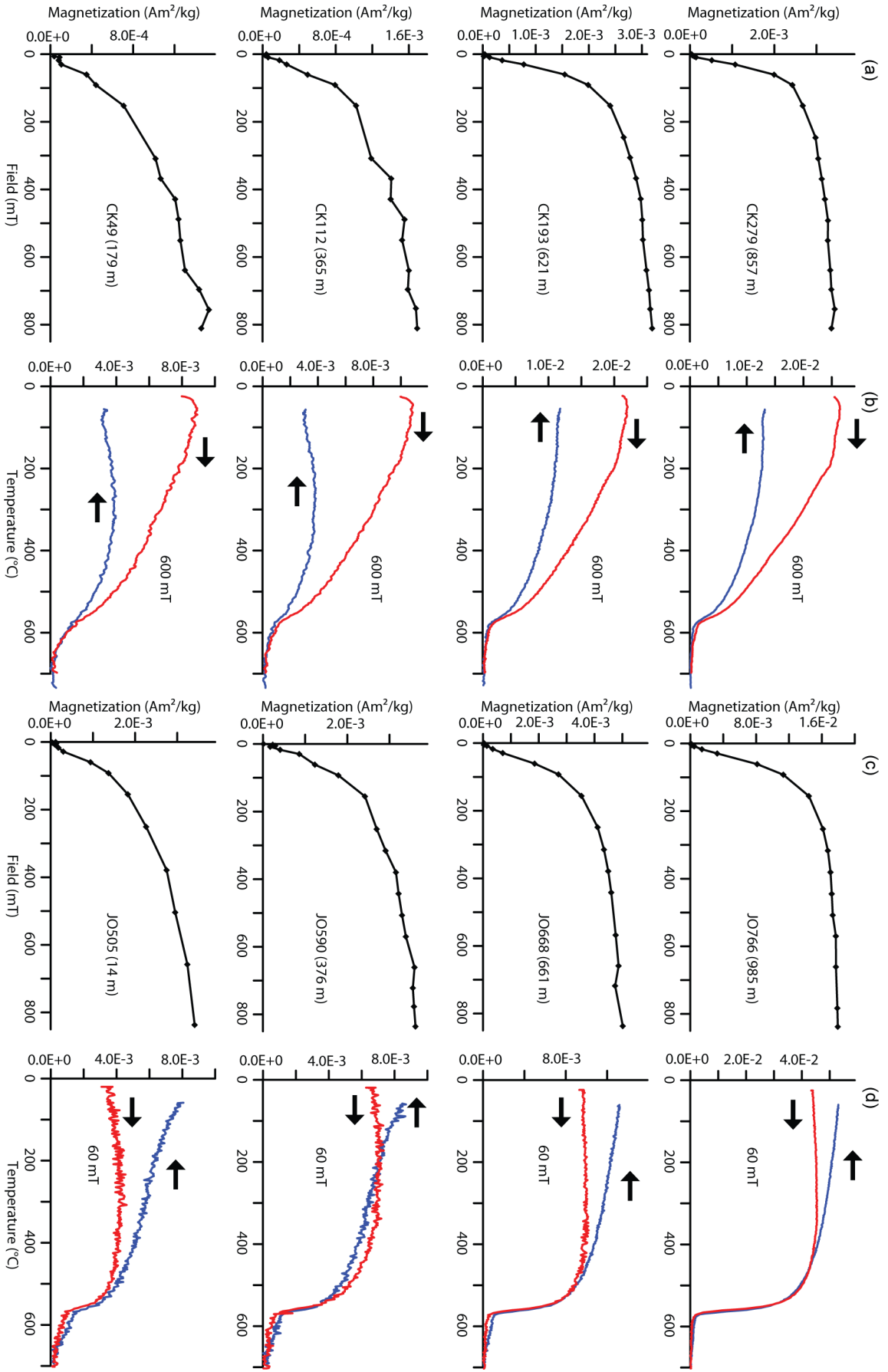


Figure 4.4.

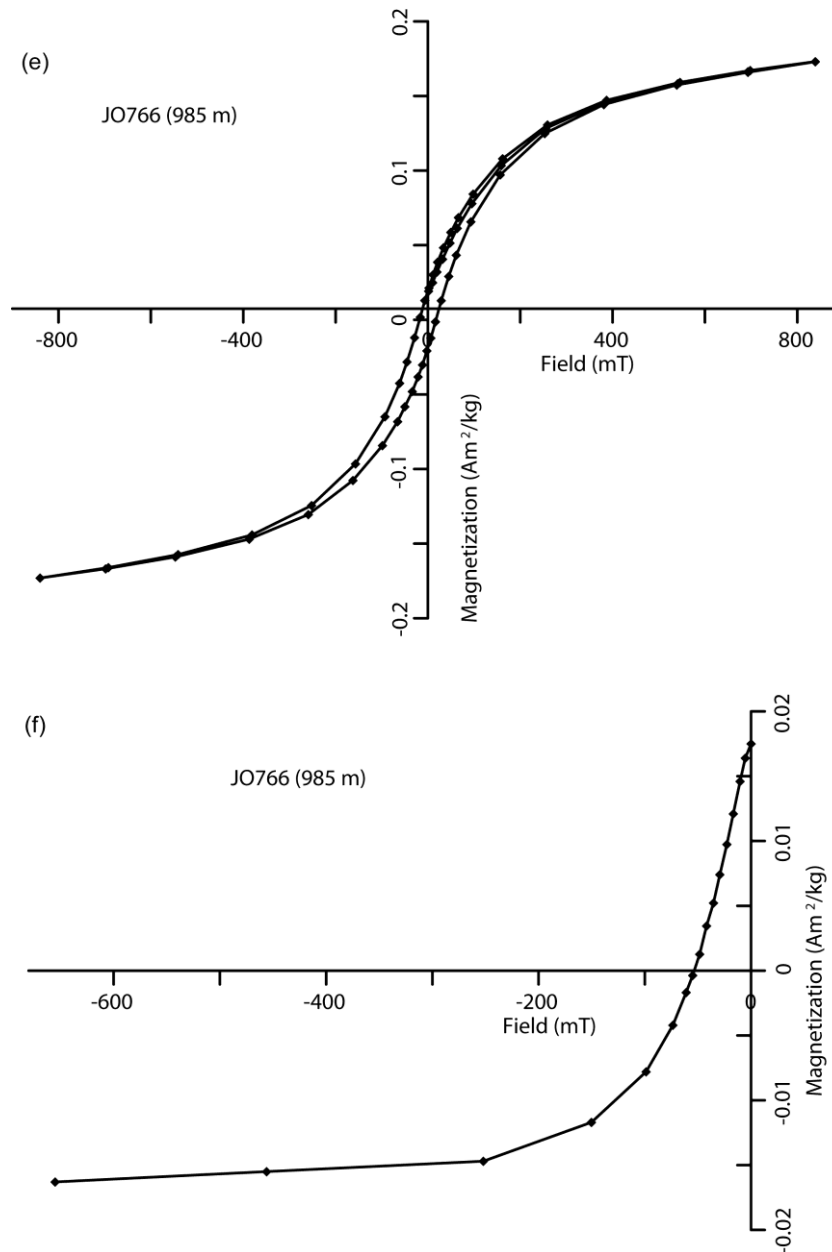


Figure 4.4. *continued.* Representative strong-field magnetization measurements of samples from the Chon Kyzylsuu (CK) and Jeti Oguz (JO) sections. (a + c) Isothermal remanent magnetization acquisition. (b + d) Thermomagnetic curves for the same samples as in (a + c). Heating curves are shown in red, cooling curves in blue. (e + f) hysteresis loop and backfield curve for sample JO766. Thermomagnetic curves were corrected for paramagnetic contributions with the RockMagAnalyzer software [Leonhardt, 2006]. Stratigraphic level is given in brackets following the sample name; samples with higher numbers lie toward the top of the sections.

4.3.2. Anisotropy of Anhysteretic Remanence

We measured ARM acquisition using a switching field window from 20 to 0 mT with a DC bias field of 0.1 mT in 12 independent directions for 60 and 98 B-cores from the JO and CK sections, respectively. Magnetic moments of the three components from the 12 experiments were converted to anisotropy tensors to then calculate eigenvector directions [Wack and Gilder, 2012]. Maximum (k1) principal axis directions of the remanent anisotropy ellipsoids are well defined, lying predominantly in the horizontal plane parallel to the strike direction (Figure 4.7; Table A3.2). Intermediate (k2) and minimum (k3) axis directions are streaked along a great circle, orthogonal to k1 and the maximum stress axis of deformation, characteristic of prolate, tectonic fabrics [Graham, 1966; Borradaile and

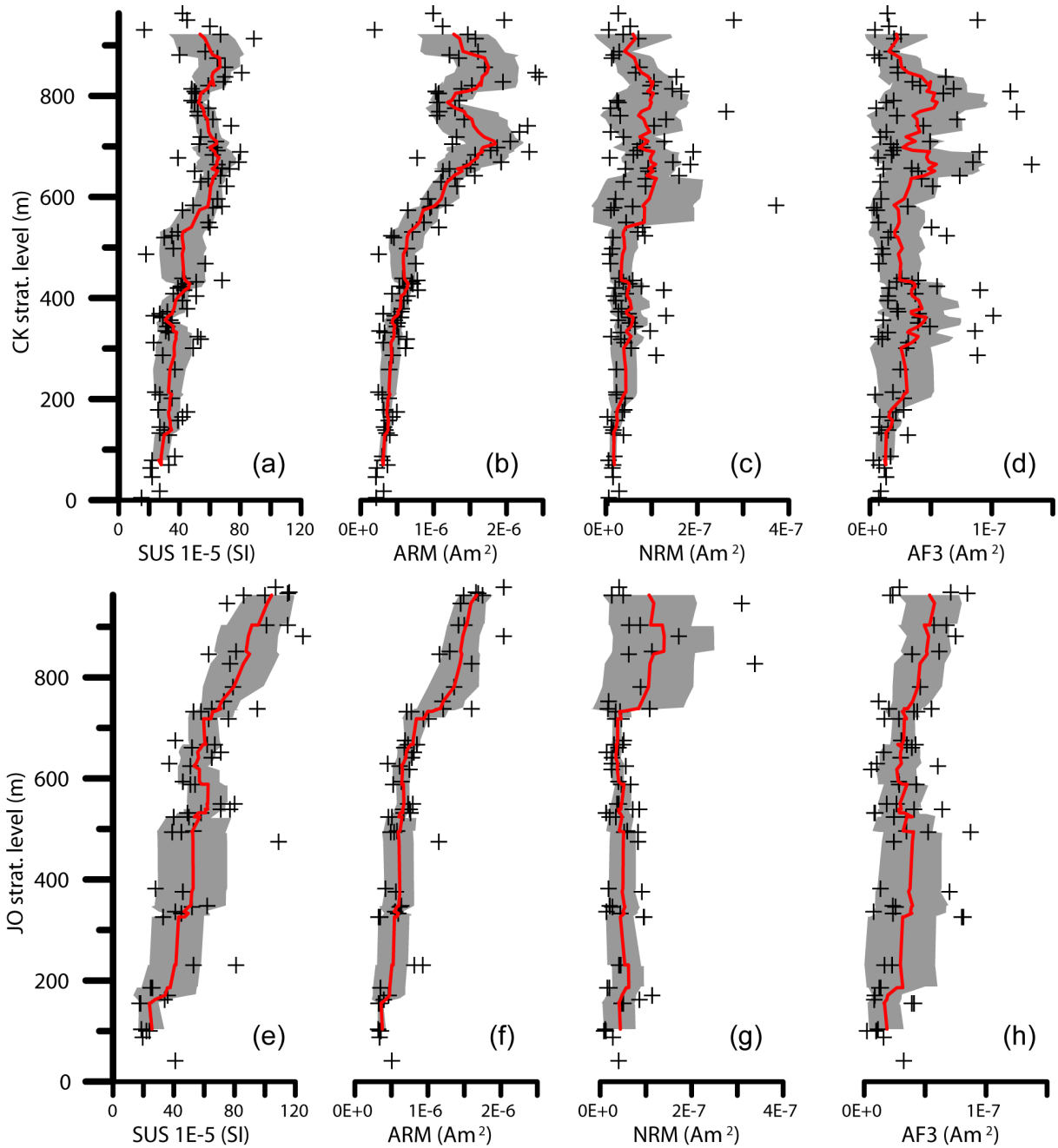


Figure 4.5. Stratigraphic variation of (a + e) bulk susceptibility (SUS), (b + f) anhysteretic remanent magnetization (ARM) (90–0 mT peak AF field, 0.1 mT bias field), (c + g) natural remanent magnetization (NRM) and (d + h) moment remaining after 3 axis 90 mT peak field alternating field demagnetization (AF3) from the Chon Kyzylsuu (CK- a–d, 99 cores) and Jety Oguz (JO- e–h, 65 cores) sections (5 points omitted to better see trends). Red lines are running averages with window width of 9 points. 1σ uncertainties in gray.

Tarling, 1981; Hrouda, 1982; Winkler *et al.*, 1997]. Principal axis directions lower in the sections define triaxial fabrics, with those in JO shifted toward oblate fabrics with well-grouped k3 directions and k1 and k2 directions that streak along a great circle. Anisotropy of magnetic susceptibility (AMS) measured by Thomas *et al.* [1993] from sites surrounding the Issyk-Kul basin including JO yield a virtually identical k1 axis direction yet the k3 axes are vertical. They argued that the AMS data fabrics originate from the alignment of hematite grains. We think that both the AMS and ARM fabrics stem from magnetite due to its higher susceptibility and lower coercivity compared to hematite, although hematite likely influences ARM more than AMS.

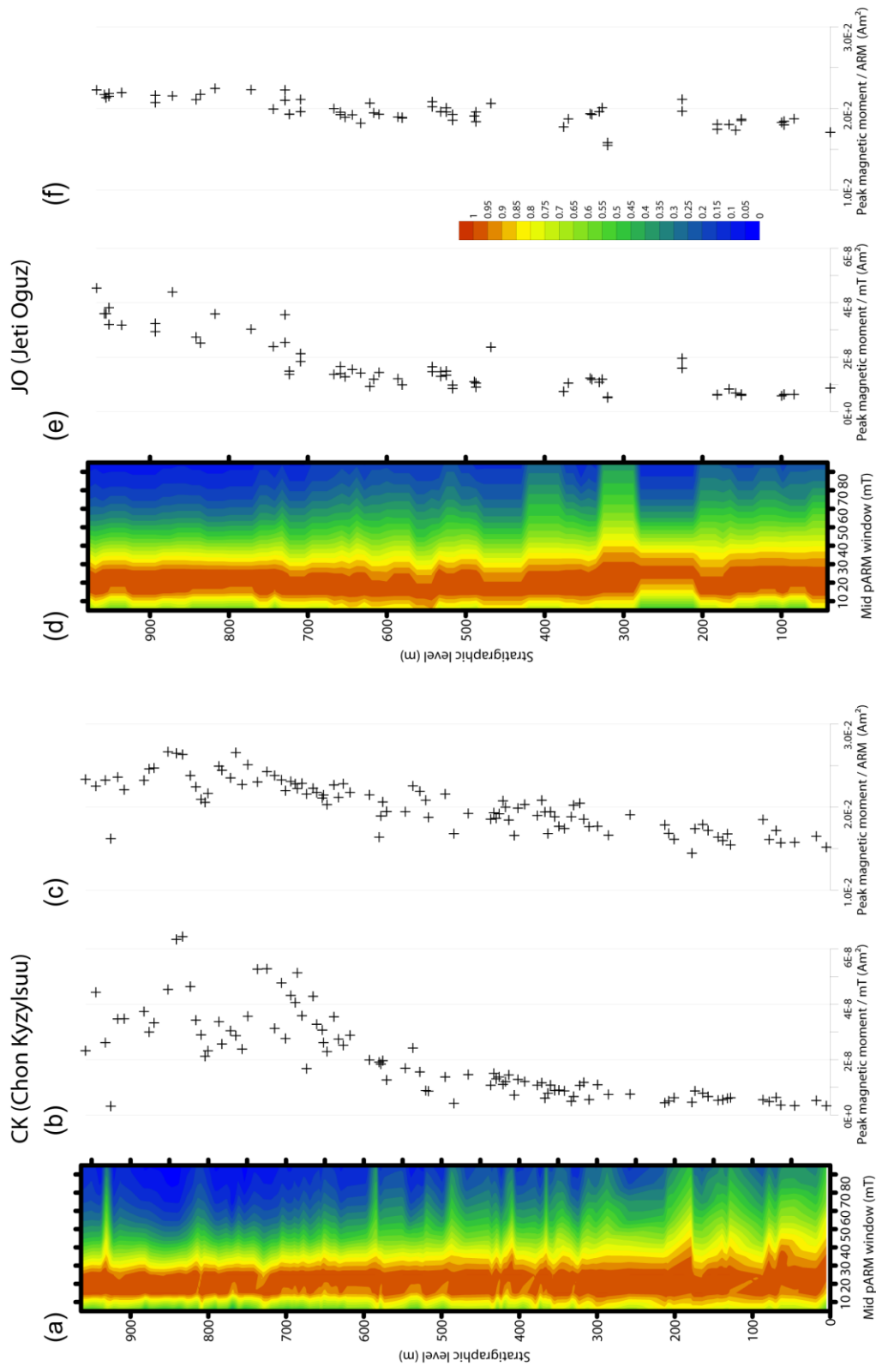


Figure 4.6. Partial anhysteretic remanent magnetization (pARM) spectra as a function of depth for the Chon Kyzylsuu (CK) (a–c, 99 cores) and Jeti Oguz (JO) (d–f, 65 cores) sections. (a + d) Contoured pARM spectra for all samples: red ridges represent the coercivity range of the maximum ARM moments; each spectrum is normalized to its peak value, which is shown in (b + e). (c + f) Ratios of peak pARM moment to total ARM moment. Note the increase in total moment and slight decrease in peak coercivity window towards the top of both sections.

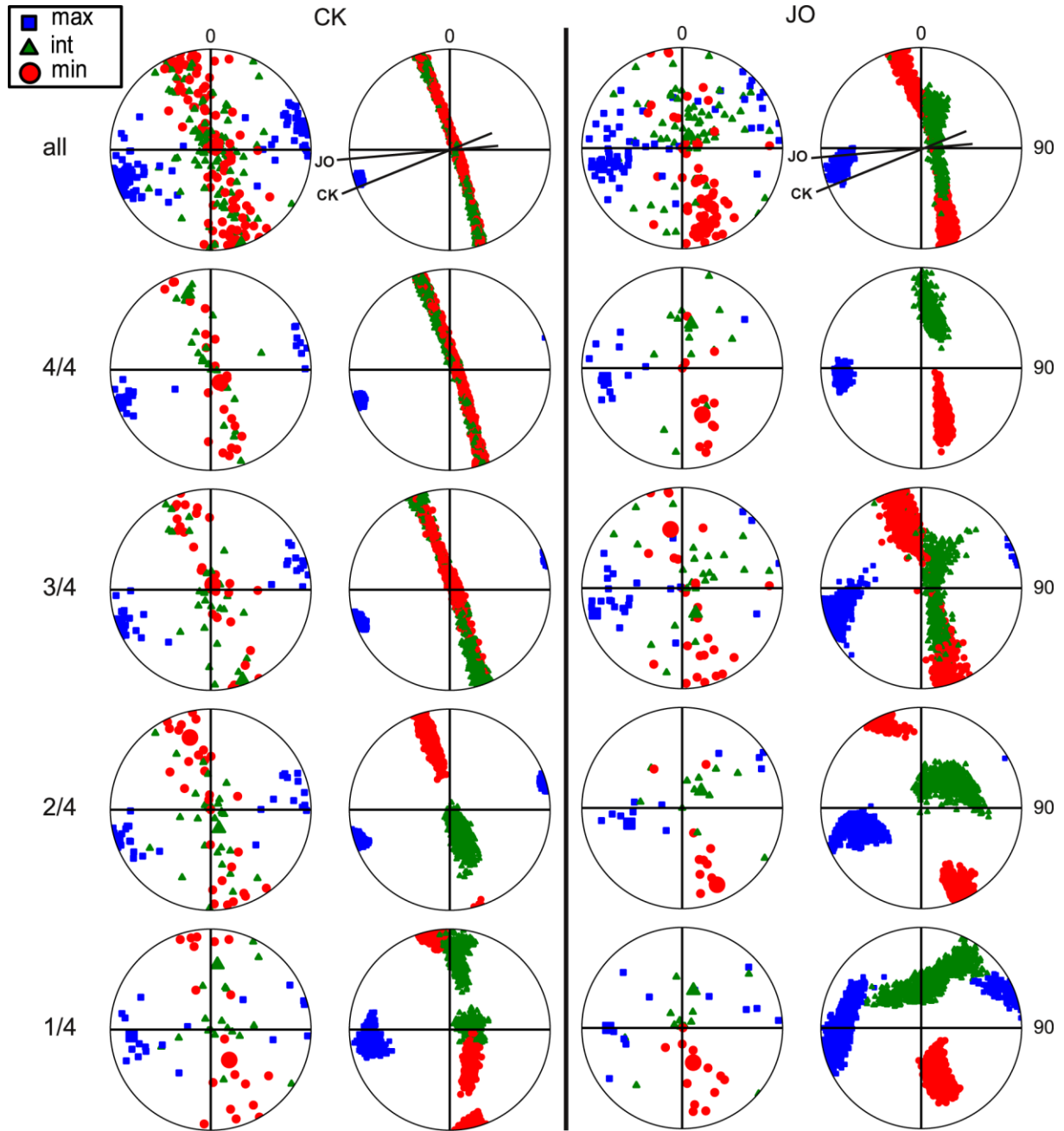


Figure 4.7. Principal directions for anisotropy of anhysteretic remanent magnetization (AARM) tensors for the Chon Kyzylsuu (CK) and Jeti Oguz (JO) sections in bedding corrected coordinates. All data are shown twice: original (left) and bootstrapped (right). Geographic north is up, east to the right; directions are plotted on the lower hemisphere. First row shows the entire data set from each section (strike lines of both sections provided for comparison). Subsequent rows show data from each fourth of the section: 1/4 is the bottom and 4/4 is top. Large symbols are the average direction based on the mean of the normalized individual tensors.

Following *Jelinek* [1981], we calculated the degree of anisotropy (P), the shape parameter (T: -1 prolate; 0 triaxial; +1 oblate), the lination (L), and the foliation (F), and plotted them as a function of stratigraphic position (Figure A3.1). The degree of anisotropy ($7.8 \pm 2.4\%$ for JO and $7.6 \pm 2.8\%$ for CK) remains constant in both sections. Although individual shape parameters show considerable scatter (CK= -0.15 ± 0.41 , JO= 0.01 ± 0.43), nine-point running averages for CK are fairly constant at -0.15, whereas those from JO change from oblate (T ~ 0.2) at the bottom to prolate (T ~ -0.4) towards the top. CK has both constant L and F, while the change in T in JO is roughly mimicked by a decrease in F and increase in L. *Flinn* [1962] diagrams of the data show a high degree

of scatter for individual samples (Figure A3.2). Average values for each quarter of the sections are closely clustered and solely prolate for the CK section, yet vary systematically from oblate/triaxial to prolate for the JO section towards the top as seen in T and in Figure 4.7. Taken together the anisotropy data are best interpreted as the remnants of a sedimentary fabric near the base of the sections that gets systematically more overprinted by a tectonic fabric towards the top. This interpretation is consistent with the evolution seen on the Flinn diagram for the JO section when compared with the progressive superimposition of two such fabrics from numerical simulations [Housen *et al.*, 1993]. The increase in tectonic fabric with stratigraphic height likely does not reflect an increase in stress from the top down, but rather the propensity for the strata to strain under a given stress, such as a systematic change in clay content or clay type. In this way, the amount of red pigment inversely correlates with the degree of tectonic fabric.

4.3.3. Magnetic Remanence

Magnetization component directions were isolated via stepwise thermal demagnetization up to 685°C and alternating field demagnetization up to 90 mT. Owing to the presence of hematite, alternating field demagnetization removed only a minor fraction of the NRM in most cases (on average 28% for JO, 24% for lower half of CK and 53% for upper half of CK) and did not yield interpretable *Zijderveld* [1967] plots. NRM moments range from $5.2 \cdot 10^{-9}$ to $4.0 \cdot 10^{-7}$ for CK and from $2.7 \cdot 10^{-9}$ to $1.3 \cdot 10^{-6}$ Am² for JO, with averages of $5.1 \pm 5.6 \cdot 10^{-8}$ and $1.1 \pm 2.3 \cdot 10^{-7}$ Am², respectively. The samples exhibit a wide variety of demagnetization behavior as follows: well defined single component demagnetization trajectories of normal or reverse polarity that decay toward the origin (Figures 4.8a+b), two well-defined magnetization components, one that does not trend toward the origin at low temperatures (<300–400°C) and another that does at higher temperatures (Figure 4.8c), demagnetization trajectories that follow great circle paths that might or might not reach a stable endpoint (Figure 4.8d) and noisy data that cannot be interpreted (Figure 4.8e).

Of note is that the unblocking temperatures indicative of the magnetite and hematite fractions yield the same direction (i.e. directions above and below 580°C are coherent), which suggests that both magnetic phases recorded the same paleofield and argues against the secondary growth of one of the magnetic phases. The tectonic correction and relatively high degree of scatter among the samples' directions make it difficult to unambiguously distinguish overprints along the present Earth's magnetic field direction (IGRF: D= 4.3°, I= 62.2°; geocentric axial dipole: D= 0°, I= 61.2°) from a primary signal in samples with normal polarity. Because the low temperature overprint component in the samples with reversed polarity was removed around 300°C, we assume the same is true for the samples with normal polarity and hence did not exclude any samples with north and down directed magnetization components at high temperature. Altogether, 133 (CK) and 99 (JO) high temperature magnetization component directions were determined by principal component analysis [Kirschvink, 1980] (Figure 4.9). For both sections, inclinations from samples with reverse polarity are ~7° steeper than those with normal polarity, which we attribute to unremoved present day field overprints. The overall tilt corrected mean directions from both sections are indistinguishable at 95% confidence limits; the tilt corrected mean direction of the JO section (D= 4.3°, I= 44.7°, a95= 4.9°) is indistinguishable within 95% confidence limits of that obtained by *Thomas et al.* [1993] (D= 0°, I= 44°, a95= 11°, N= 5 sites).

Stepwise demagnetization of the samples from the anticline north of the magnetostratigraphic sections yielded well defined linear magnetization components with coherent magnetization directions (Figure 4.8 - IK samples) except for sites IK3 and IK5 that have high dispersion with a95s >15° (Table A3.3). To apply the fold test, we considered the mean normal and reverse polarity directions from each magnetostratigraphic section as a site and used the site mean directions from the anticline whose a95s are <15° (Figure A3.3 and Table A3.3). The direction-correction fold test [Enkin, 2003] is positive with an optimum degree of untilting of $111.6 \pm 18.6\%$. The parametric simulation fold test [Watson and Enkin, 1993] yields an optimum degree of untilting at $95.5 \pm 5.9\%$. We conclude that the

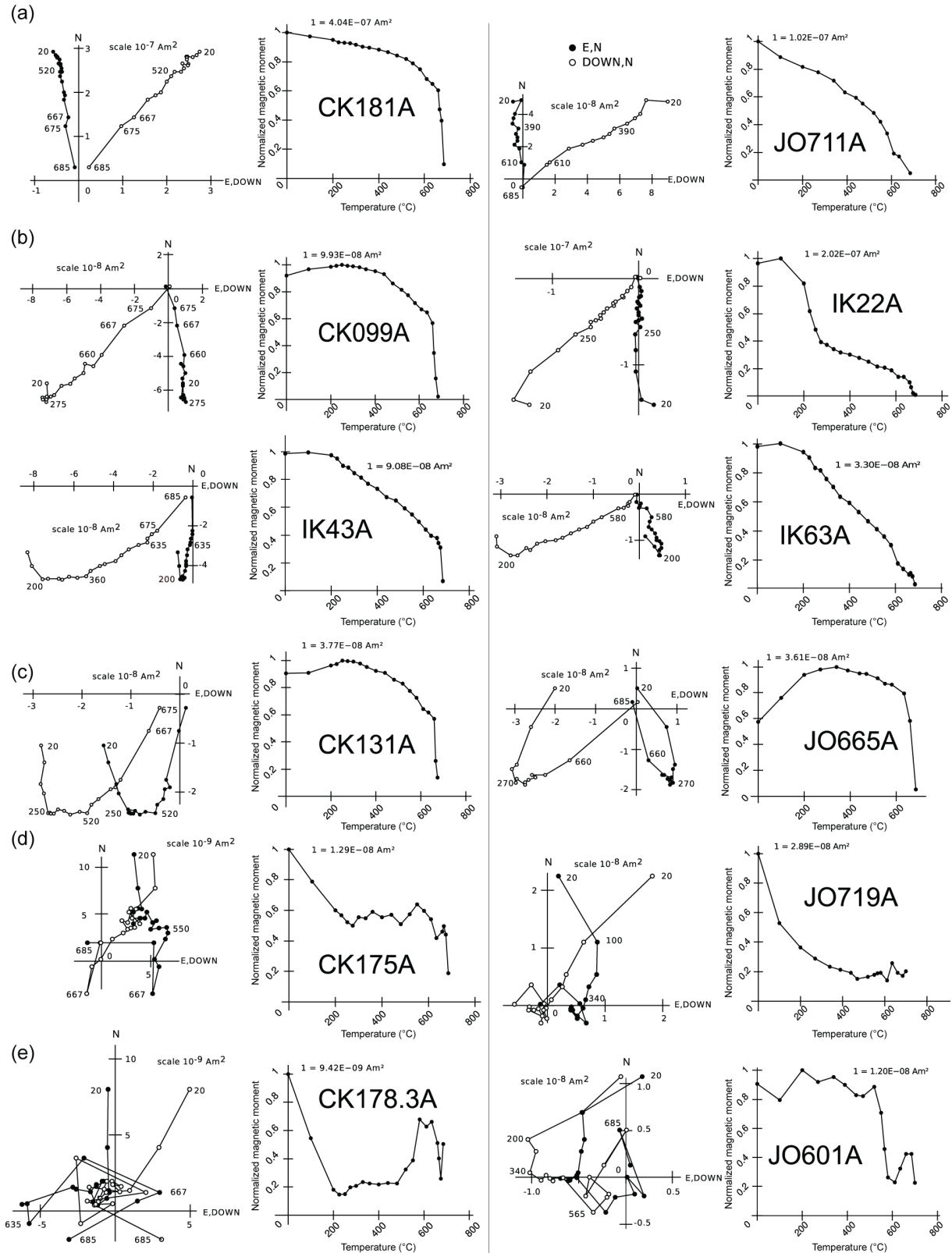


Figure 4.8. Representative thermal demagnetization data of 12 samples. For each sample a Zijderveld plot in tilt corrected coordinates (left) and the decay of normalized magnetic moment with temperature (right) are shown. (a) A single magnetization component with normal polarity. (b) a single magnetization component with reverse polarity. (c) reversed polarity high temperature magnetization component with low temperature magnetization component. (d) magnetization directions do not decay toward the origin and become unstable at high temperatures - polarity can be inferred by great circle fitting. (e) data not interpretable. JO, CK and IK designate samples from Jeti Oguz, Chon Kyzylsuu and Issyk-Kul anticline sections, respectively.

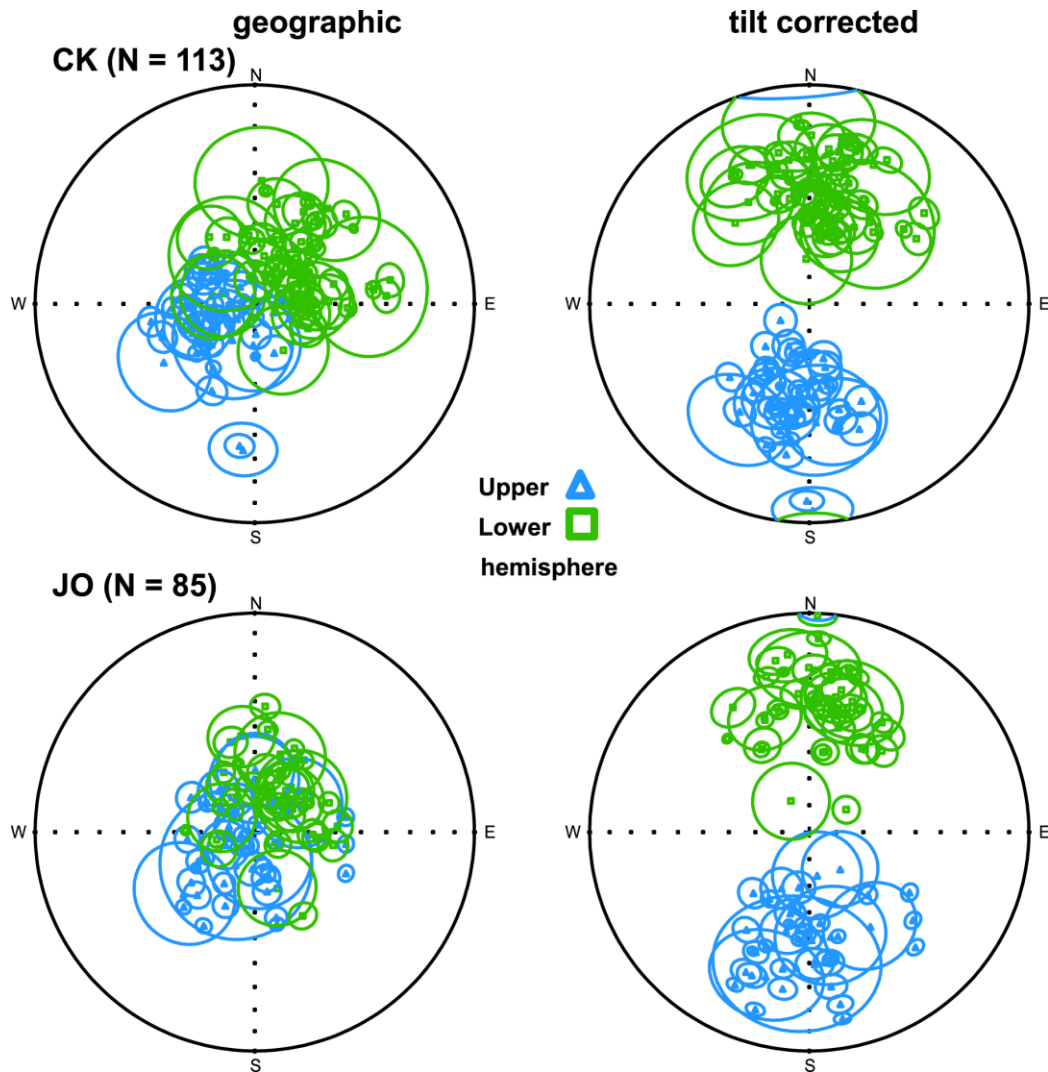


Figure 4.9. Characteristic high temperature magnetization directions isolated by stepwise thermal demagnetization. Circles are maximum angular deviation uncertainties on the best-fit line segments. Directions identified as positive or negative polarity for the CK (113 specimens) and JO 557 (85 specimens) sections are shown in geographic (left) and tilt corrected (right) coordinates. Blue points have upward-directed inclinations, green points downward inclinations.

remance was acquired before folding, which occurred after the Pliocene. The mean direction of all sites ($D= 2.7^\circ$, $I= 52.0^\circ$, $a95= 6.2^\circ$) is indistinguishable within 95% confidence limits of the mean direction obtained by *Thomas et al.* [1993] for the entire Issyk-Kul basin ($D= 2^\circ$, $I= 49^\circ$, $a95= 6^\circ$, $N= 13$ sites). Comparison of our results with the synthetic 20 Ma paleomagnetic pole of Eurasia [*Besse and Courtillot*, 2002] reveals an insignificant counterclockwise rotation of $6 \pm 7^\circ$ and a paleolatitude difference of $10 \pm 5^\circ$ that implies a 1100 ± 500 km translation towards the north. The paleolatitude difference likely stems from an artifact due to inclination shallowing, which is frequently observed in sedimentary rocks in central Asia [e.g. *Gilder et al.*, 2001, 2003; *Tan et al.*, 2003; *Yan et al.*, 2005]. Interestingly, the remance directions of magnetite and hematite are shallowed to the same extent.

4.3.4. Magnetostratigraphy

Great circles were fit to 52 samples that did not reach stable end points. Polarities were assigned to them depending on the trend during progressive demagnetization. Together with the best-fit data, we classified the 284 paleomagnetic demagnetization data into three categories: normal, reverse or intermediate—the latter being a direction that deviates more than 45° away from the normal or

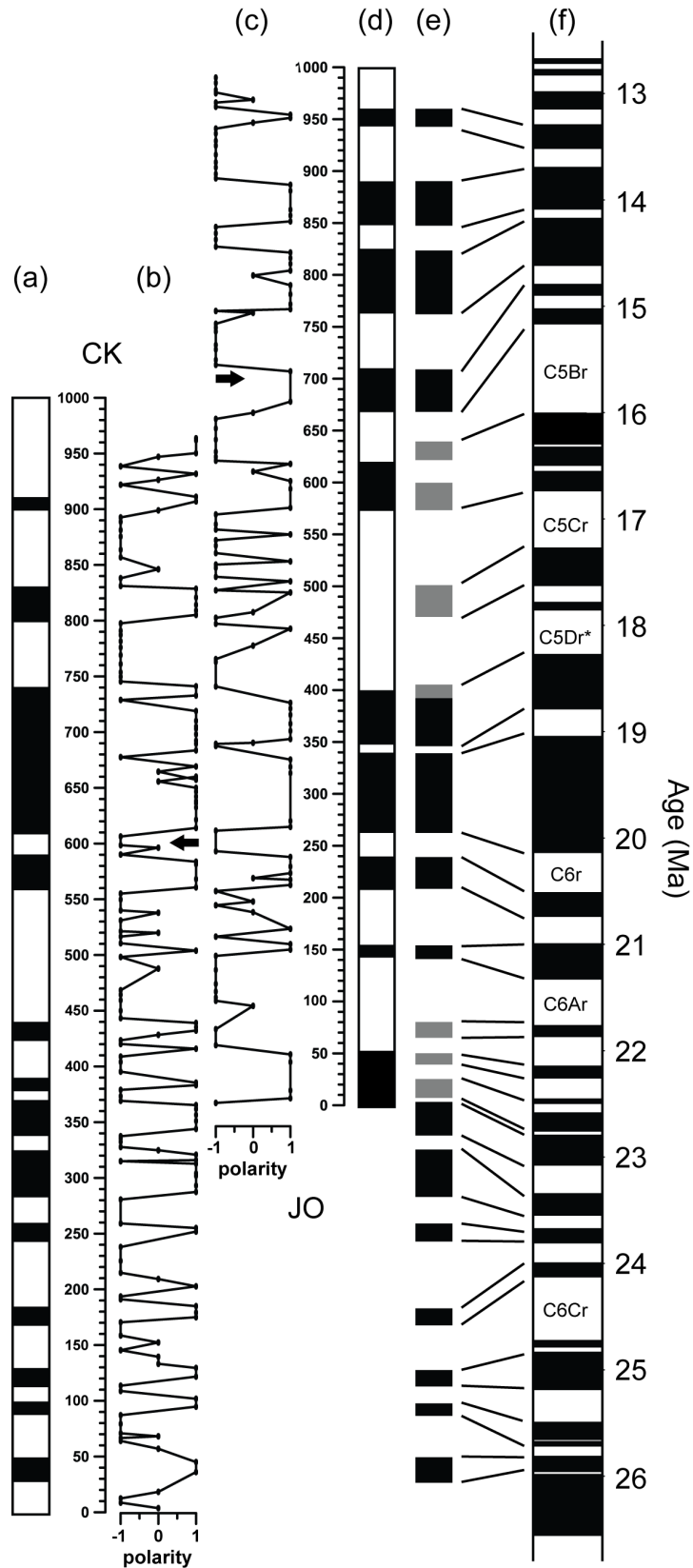


Figure 4.10. Polarity chrons (a + d) based on principal component analysis and great circle fitting (b + c) for the Chon Kyzylsuu (CK) and Jeti Oguz (JO) sections (a + d) plotted as a function of depth. Both (a) and (d) were combined into a composite magnetostratigraphic column (e) that was then visually correlated with the geomagnetic polarity timescale (f) from *Gradstein and Ogg* [2004], referred to as “Model A”. Gray chrons were not used to match the magnetostratigraphies between both sections but they were considered when correlating the composite magnetostratigraphy with the reference scale. Arrows indicate the stratigraphic levels of the sudden rise in ARM acquisition.

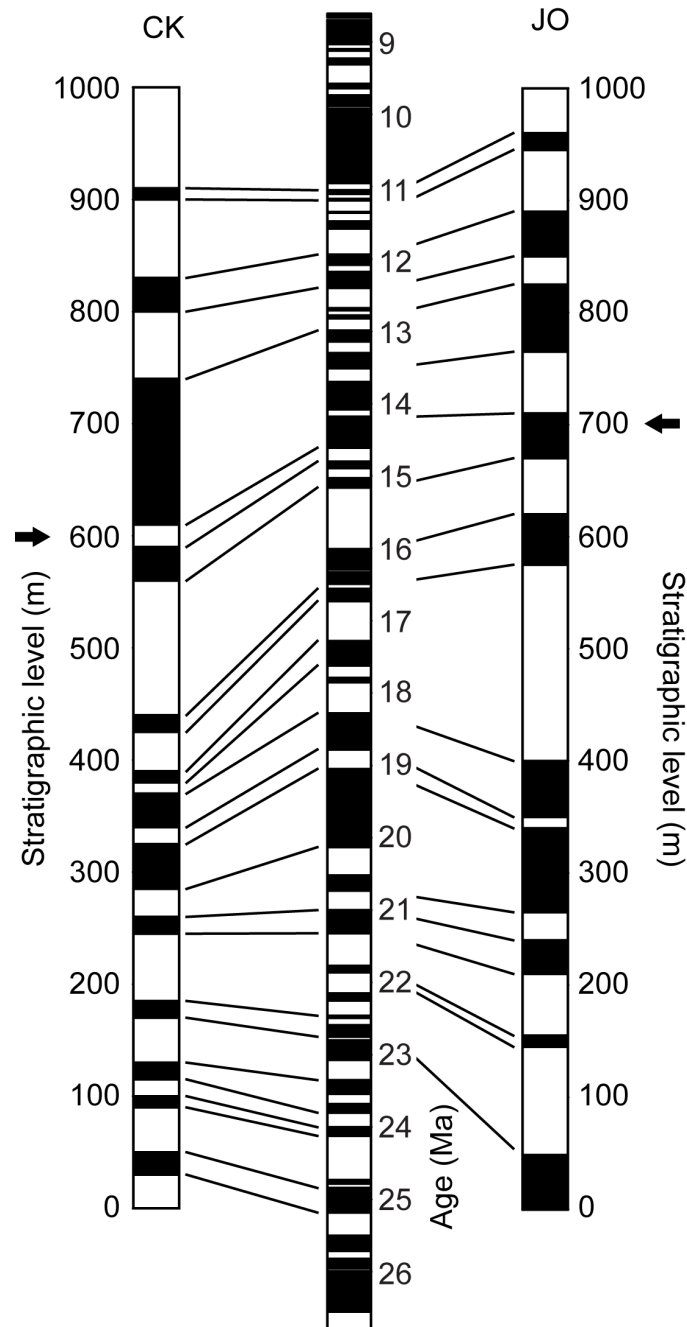


Figure 4.11. Polarity chron mapping of the Chon Kyzylsuu (CK) and Jeti Oguz (JO) sections with the geomagnetic polarity timescale from *Gradstein and Ogg* [2004] based on the two consistent correlations found by the Cupydon computer program of *Lallier et al.* [2013], referred to as “Model B”. Arrows indicate the stratigraphic levels of the sudden rise in ARM acquisition.

reversed polarity mean direction. The former two were used to define 26 and 19 polarity chrons in the CK and JO sections, respectively (Figure 4.10).

From the measured strike directions, geographic position of the samples and lithologic similarities, we expect a significant stratigraphic overlap between the two sections. Based on this assumption we propose two potential age models (A and B – Figures 4.10 and 4.11) and their corresponding sedimentation rates (Figure 4.12). Model A represents our best eyeball match of the polarity patterns (Figure 4.10e). When correlating the sections, we sometimes ignored short (< 100 ka) polarity chrons and neglected chrons defined by a single sample. Minor local hiatuses and/or incomplete sampling can explain the incoherency in chron matching between the two sections, as indicated in gray in Figure 4.10. These discrepant chrons were not used to correlate the two sections

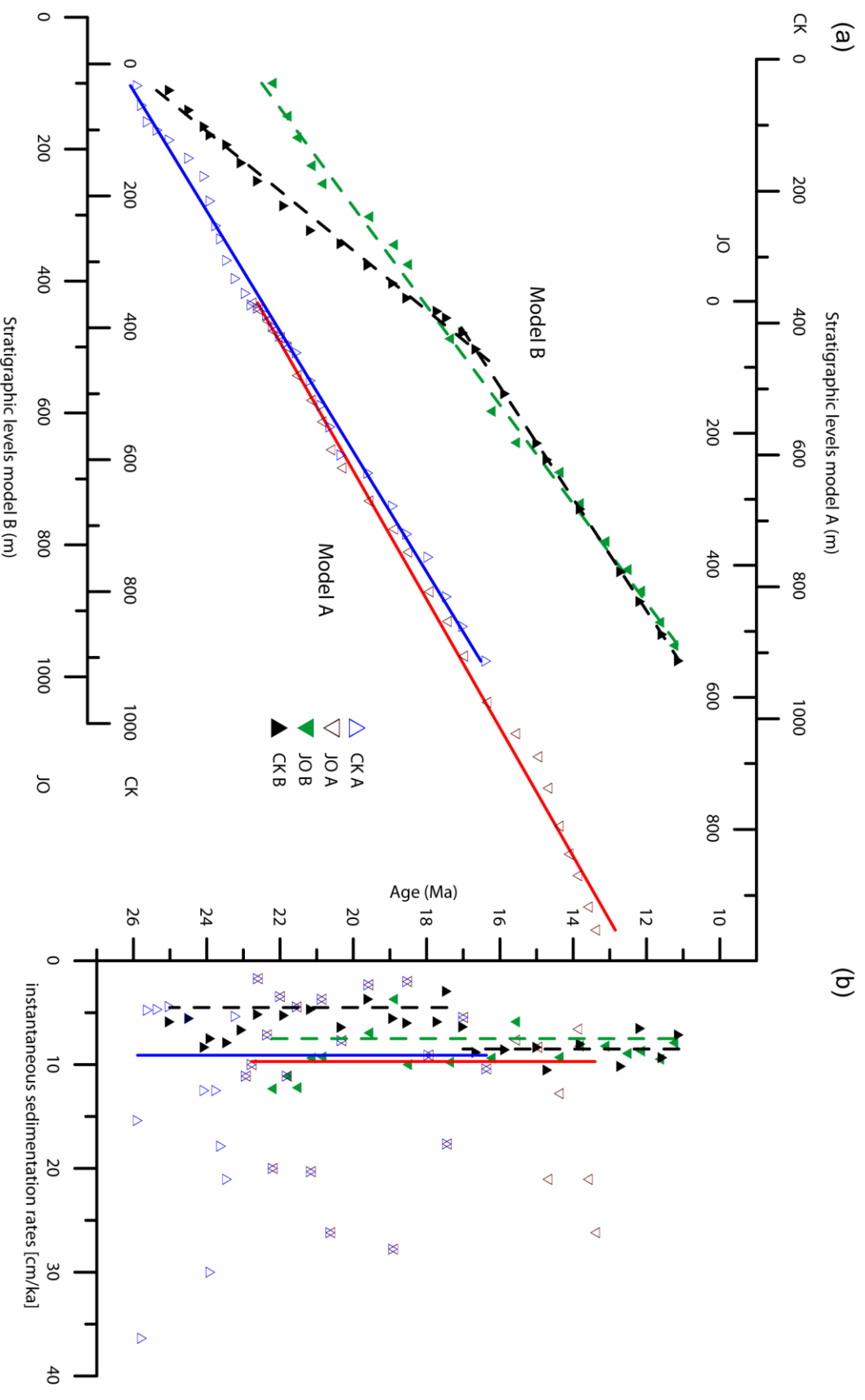


Figure 4.12. Sedimentation rates derived from models A and B. Sedimentation rates (in cm/ka) derived by linear regression as shown in (a) are 9.7 ± 0.4 for JO(A), 9.1 ± 0.4 for CK(A), 7.5 ± 0.6 for JO(B), 8.5 ± 1.6 for CK(B), stratigraphic level 0–400 m) resp. 4.5 ± 0.8 cm/ka for the remaining part of CK(B). Instantaneous sedimentation rates for each polarity chron as well as fitted slopes are shown in (b). One point was omitted in (b) for better scaling.

but they were considered when comparing against the reference polarity timescale of *Gradstein and Ogg* [2004] (Figure 4.10f). Model A, which lacks only five chrons versus the reference scale, yields absolute sedimentation ages ranging from 26.0 to 16.2 Ma for CK and 22.8 to 13.3 Ma for JO. If true, this correlation imposes a 4 Myr time difference in the sudden rise in ARM between the two sections, which reflect a significant amount of along-strike progradation. Model A implies similar and largely constant sedimentation rates of 9.1 ± 0.4 cm/ka for CK and 9.7 ± 0.4 cm/ka for JO (Figure 4.12), which are in good agreement with published estimates of ~ 7 cm/ka for the Issyk-Kul Basin [*Trifonov et al.*, 2008].

Model B was constrained by a numerical magnetostratigraphic correlation method based on the Dynamic Time Warping algorithm [*Lallier et al.*, 2013]. Since the algorithm only considers missing chrons in the stratigraphic record, but not in the reference polarity scale, this method could not be used to directly correlate the two sections. Therefore we ran the program independently for each section to find 5000 potential matches with the timescale of *Gradstein and Ogg* [2004]. From a plot of the least expensive (i.e. best matching) correlations for each section, we picked the ones that have the highest probability, significant temporal overlap and compatible sedimentation rates (Figure A3.4), which leaves only one option (Figure 4.11), resulting in absolute ages from 25.2 to 11.0 Ma for CK and 22.2 to 11.1 Ma for JO. Sedimentation rates are constant at 7.5 ± 0.6 cm/ka for JO, whereas an increase from 4.5 ± 0.8 to 8.5 ± 1.6 cm/ka occurs around 16.5 Ma in CK (Figure 4.12). The lower scatter in sedimentation rates among individual chrons in Model B than in Model A (Figure 4.12b) is expected because the algorithm specifically minimizes variations in sedimentation rate. On the other hand, the algorithm correlation results in a much higher number of missing chrons (20 for CK, 14 for JO) in the magnetostratigraphic record.

4.4. Discussion and Conclusions

Hematite and magnetite carry the magnetic remanence in the sediments of the two magnetostratigraphic sections. Stepwise demagnetization isolates a high temperature component, encompassing the unblocking spectra of both magnetic minerals, with dual polarities that passes the fold test. Rock magnetic parameters show systematic differences with stratigraphic height. The overall mean direction for both sections and the nearby anticline are indistinguishable at 95% confidence limits with an earlier study by *Thomas et al.* [1993]. The sum of these observations leads us to conclude the high temperature magnetization component represents a primary, detrital remanent magnetization.

The polarity chrons defined by the high temperature component do not lead to a straightforward correlation — either with respect to each section or with respect to the reference geomagnetic polarity timescale. Two independent correlation methods yield sedimentation ages ranging from 26.0 to 13.3 Ma (Model A) or from 25.2 to 11.0 Ma (Model B). Model A, based on visual matching, requires a 4 Myr offset in the sudden rise in magnetite concentration (ARM moments) between the two sections. The five, rather short (<100 ka) missing chrons in the stratigraphic polarity pattern are plausible when considering the time resolution of the record. Model B identifies the highest likelihood correlations defined by the numerical algorithm of *Lallier et al.* [2013]. It predicts more homogeneous sedimentation rates for individual polarity intervals and requires only a small stratigraphic offset between the two sections, matching the magnetite increase to within less than 1 Myr. Conversely, it implies many chrons were missed (20 and 14), one up to 340 ka in duration (C5Dn), which seems unlikely given the sampling density and reversal frequency. Moreover, Model B shows a sudden increase in sedimentation rate in the CK section from 4.5 to 8.5 cm/ka at ~ 16.5 Ma which is not seen in the JO section, which has a fairly constant sedimentation rate of 7.5 cm/ka. Despite the ambiguity in the correlations derived from Models A and B, both give relatively comparable age estimates and sedimentation rates, thus conclusions drawn from either one would yield similar interpretations. So,

we can reasonably conclude the Chon Kyzylsuu and Jeti Oguz sections lie within 26 to 11 Ma with sedimentation rates on the order of 5 to 10 cm/ka. A finer interpretation would be unwarranted.

Geological maps suggest that the top of the CK section reaches into the Chu group (Figures 4.1b and 4.2), which is not supported by our lithological observations (Figure 4.1c). Indeed, our field observations suggest that the stratigraphic transition occurs up-section of the youngest CK sample. Therefore, we infer that the base of the Chu group at Issyk-Kul is younger than ~11.0 Ma. Previous age constraints on the sediments are based on low resolution biostratigraphy from tortoise shell remnants or from lithostratigraphic correlation [Afonichev and Vlasov, 1984; Krilov, 1960; Simonov *et al.*, 2008] – both of which have large uncertainties (for the latter see below) and therefore can only provide a rough timeframe. The ages proposed for the base of the sections in our study (26 to 23 Ma) are compatible with estimates for the initiation of exhumation in the Oligo–Miocene of the source mountains, namely the Eastern Terskey Range (Chapter 3) [Macaulay *et al.*, in review]. Magnetostratigraphy of other intermontane basins in the Tien Shan (e.g., Naryn ~200 km to the southwest of our sections) find younger deposition ages of ~12 to 8 Ma for the Shamsi group [Abdrakhmatov *et al.*, 2001]. However, farther east in the Tien Shan within China, seemingly identical lithostratigraphies can have age differences exceeding 10 Myr from basin to basin [e.g., Heermance *et al.*, 2008]. A 3 Myr difference for the base of the Xiyu Formation, which is a thick conglomerate unit found throughout the Tien Shan realm, was found for two sections lying 60 km apart [Charreau *et al.*, 2009b]. Thus any conclusions based on lithostratigraphic correlation should be exercised with caution. Likely the depositional history of individual basins is more representative of local deformation, i.e. the formation of adjacent ranges.

Calculated sedimentation rates of 5 to 10 cm/ka are low compared with rates of 20–30 cm/ka published for the front of active mountain ranges in central Asia [e.g., Gilder *et al.*, 2001; Charreau *et al.*, 2005, 2006, 2009b, 2011; Sun *et al.*, 2009]. The growing consensus is that the Tien Shan underwent an accelerated phase of exhumation around 11 Ma (Chapter 3) [Abdrakhmatov *et al.*, 2001; Bullen *et al.*, 2003; Charreau *et al.*, 2005, 2006, 2009b, 2011; Heermance *et al.*, 2008; Macaulay *et al.*, in review]. Rates of 5 to 10 cm/ka are similar to those reported of sediments older than 15 Ma from the Jingou River section in the Tien Shan [Charreau *et al.*, 2009a]. Hence, we infer that the Chon Kyzylsuu and Jeti Oguz sediments likely pre-date the most active phase of uplift of the Kyrgyz Tien Shan. This interpretation agrees with thermochronologic results obtained from the Terskey range (Chapter 3) [Macaulay *et al.*, in review], directly south of our study area.

Acknowledgments

Funding was provided by Deutsche Forschungsgemeinschaft projects GI712-1/1 and 436 KIR 113/2/0-1. We thank the Central-Asian Institute of Applied Geosciences (CAIAG), Vasyl Hyshchyn, Ivan Andreev, Tobias Wurft, Martin Leberer and Denise Schmidt for their support of the field work and help in the laboratory.

Chapter 5.

The sedimentary record of the Issyk Kul basin, Kyrgyzstan: climatic and tectonic inferences

Submitted by Euan A. Macaulay, Edward R. Sobel, Alexander Mikolaichuk, Michael Wack, Stuart Gilder, Andreas Mulch, Alla B. Fortuna, Scott Hynek and Farid Apayarov (2013) to *Basin Research*.

Abstract

A broad array of new provenance and stable isotope data are presented from two magnetostratigraphically dated sections in the south-eastern Issyk Kul basin of the Central Kyrgyz Tien Shan (presented in Chapter 4) [Wack *et al.*, in review]. A combination of zircon U-Pb provenance, paleocurrent and conglomerate clast count analyses are used to determine sediment provenance. Importantly, this analysis reveals that the first coarse-grained, syn-tectonic sediments (Dzhety Oguz formation) were sourced from the nearby Terskey Range, supporting previous thermochronology-based estimates of ~29–26 Ma for the onset of deformation in the range. Climate variations are identified using stable isotope ($\delta^{18}\text{O}$ and $\delta^{13}\text{C}$) data from 53 samples collected in the two sections and are compared to the compositions of modern water from 128 samples. Two key features are identified in the stable isotope dataset derived from the sediments: (1) isotope values, in particular $\delta^{13}\text{C}$, decrease between ~26.0 and 23.6 Ma, and (2) the scatter of $\delta^{18}\text{O}$ values increased significantly after ~22.6 Ma. The first feature is interpreted to reflect progressively wetter conditions. Based on the fact that this feature slightly post-dates the onset of deformation in the Terskey Range, we suggest that it has been caused by orographically enhanced precipitation. This provides the first solid evidence that surface uplift accompanied late Cenozoic deformation and rock uplift in the Terskey Range. We interpret the increased scatter of the second feature to reflect variable moisture source or availability caused by global climate change following the onset of Miocene glaciations at ~22.6 Ma.

5.1. Introduction

The sedimentary record preserved in basins linked to the Tien Shan mountain of Central Asia (Figure 5.1a) contains important clues about how regional climate has varied over millions of years [e.g. Graham *et al.*, 2005; Sun and Zhang, 2008; Charreau *et al.*, 2012]. Previous work exploiting this sedimentary record has suggested that the Central Asian climate has often deviated from the overall global trend [Akhmetiev *et al.*, 2005], and that the development of the Tien Shan and other mountain belts in Central Asia have altered atmospheric circulation and affected the regional climate during the Cenozoic [Kent-Corson *et al.*, 2009; Bershaw *et al.*, 2012]. However, most of these studies were based in the foreland basins to the north and south of the Tien Shan, leaving a large gap in our understanding of how climate has varied over million year timescales within the orogen. In particular, the climate of these foreland settings has been influenced by the growth of multiple mountain ranges and the signal cannot easily be disentangled to investigate the surface uplift history of one specific mountain range. Furthermore, although the timing of deformation has been inferred in many locations, it has usually been based on coincident exhumational increases identified through thermochronological or sedimentary data, and provides no indication of the magnitude of surface uplift [e.g. Hendrix *et al.*, 1994; Charreau *et al.*, 2005; 2006; 2009a; Heermance *et al.*, 2007; 2008; Jolivet *et al.*, 2010; Macaulay *et al.*, 2013; in review]. Consequently, constraints on the surface uplift history of individual mountain ranges are relatively rare.

The sedimentary record of the numerous intermontane basins within the Tien Shan could supply unique insights into the effects of global and regional climate changes within the orogen and could contain vital clues about the surface uplift histories of surrounding mountain ranges. The Issyk Kul basin in eastern Kyrgyzstan is one of the largest of these intermontane basins (Figure 5.1a). Today,

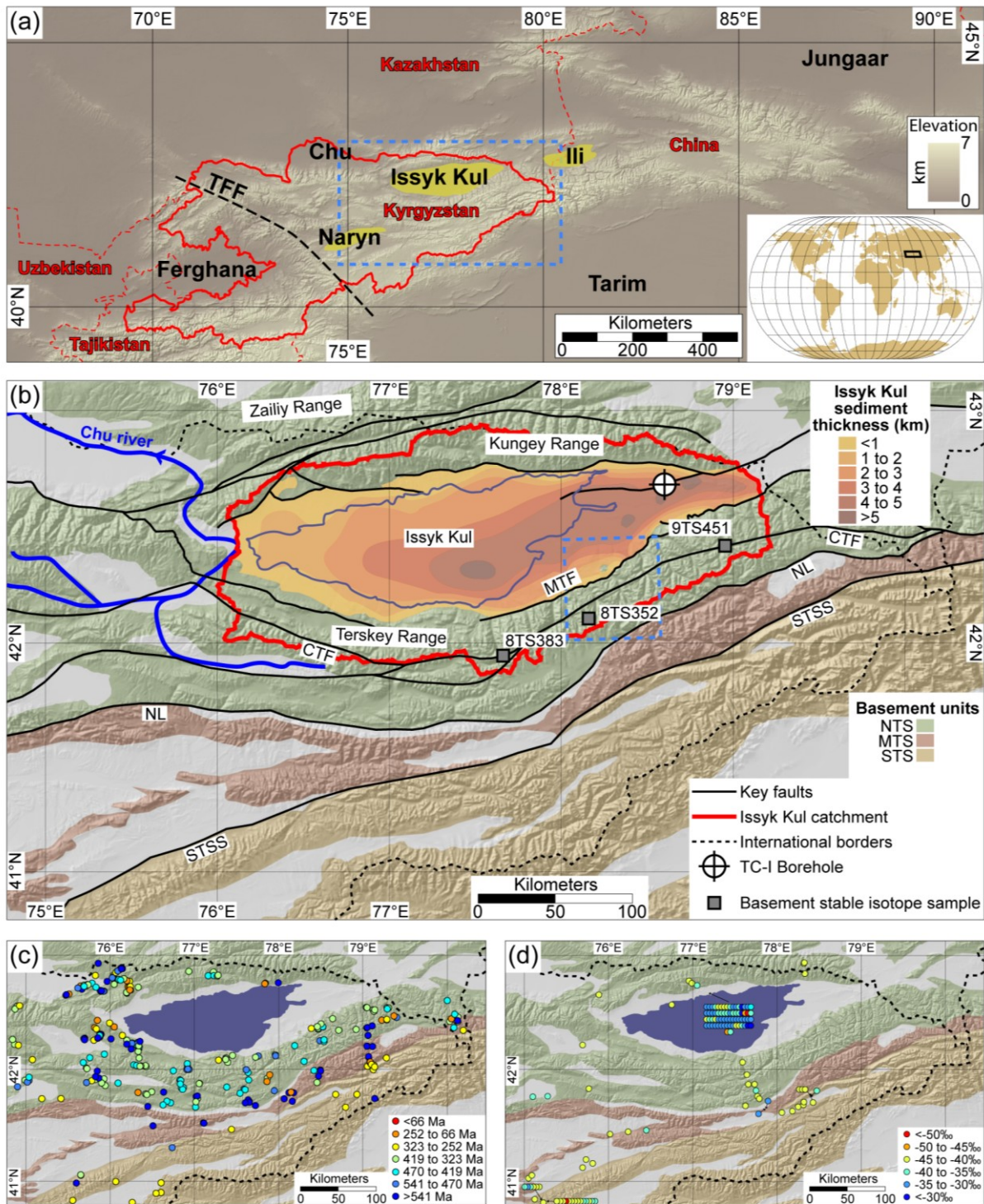


Figure 5.1. (a) Digital elevation model (DEM) of the Tien Shan based on GTOPO90 dataset. Selected large intermontane basins highlighted in yellow. Major sedimentary basins labelled with black text. TFF = Talas-Ferghana Fault, which separates Eastern and Central Kyrgyz Tien Shan. Political boundaries shown in red. Blue dashed box outlines extent of Figure 5.1b. (b) Geological map of Eastern Kyrgyzstan showing distribution of Precambrian and Paleozoic basement assemblages (coloured coded by terrane) and Meso-Cenozoic sediments (grey). NTS: Northern Tien Shan terrane; MTS: Middle Tien Shan terrane; STS: Southern Tien Shan terrane. Isochore map from the Issyk Kul basin based on a spline interpolation of depth to Precambrian and Paleozoic basement map [Omuraliev, 1988]; corresponds to a total Meso-Cenozoic sediment volume of 32590 km³. Extent of Lake Issyk Kul shown in blue. Watershed of Issyk Kul basin delineated with red line. Main faults shown with black lines; MTF: Main Terskey Fault; CTF: Central Terskey Fault; NL: Nikolaev Line.

Figure 5.1. *continued.* STSS: Southern Tien Shan Suture. Political boundaries shown with dashed black lines. Extent of Figure 5.2 shown by blue dashed box. (c) Map showing available zircon U-Pb ages; samples were predominantly collected from intrusive igneous rocks and have been coloured by age (see Appendix 4 Table A4.2). (d) Map showing distribution of modern water samples, coloured by $\delta^{18}\text{O}$ value.

the basin has a semi-arid climate [Aizen *et al.*, 1997] that is controlled by the Central Asian and Arctic air masses [Araguas-Araguas *et al.*, 1998]. Most precipitation falls in the summer months, when the Siberian High Pressure Cell migrates northward, allowing moisture-bearing air masses from the west to reach the Central Kyrgyz Tien Shan [Aizen *et al.*, 1995]. This moisture is originally sourced from the Atlantic and Mediterranean and is recharged by evaporation from intervening water bodies, such as the Black and Caspian Seas [Aizen *et al.*, 2001]. Presently, the basin is internally drained and contains a large lake with a hydrological catchment area of $\sim 39370 \text{ km}^2$ (Figure 5.1b). However, this has not always been the case, and there were wetter periods in the past when the lake was higher and the basin was connected to the foreland via the Chu river, which presently is located a few kilometers west of the basin [Ricketts *et al.*, 2001].

The preserved sedimentary record of the Issyk Kul basin was deposited intermittently in the Mesozoic and Cenozoic [e.g. Cobbold *et al.*, 1996; Abdrakhmatov *et al.*, 2001]. In places, these sediments can reach thicknesses of 5 km [Knauf, 1965; Turchinskiy, 1970; Fortuna, 1983]. Until recently, the fossil-poor sediments of the basin could not be precisely dated, preventing the full potential of the sedimentary record from being utilised. The magnetostratigraphic correlations from two adjacent sections presented in Chapter 4 [Wack *et al.*, in review] represent the first age controls for a kilometer-thick portion of the stratigraphy. These magnetostratigraphically derived ages provide a temporal framework for the new data presented herein.

In this paper, we present a broad array of new data to investigate the climatic and tectonic evolution of the Issyk Kul basin and the surrounding region over million year timescales. Climate variations are primarily identified by using stable isotopic ($\delta^{18}\text{O}$ and $\delta^{13}\text{C}$) data from authigenic carbonate in the two adjacent magnetostratigraphically-dated sections. Additionally, $\delta^{18}\text{O}$ data from 128 modern water samples are presented and found to be relatively consistent with the values derived from sediments. This climate proxy dataset is supplemented with previously published pollen data [Fortuna, 1983], and used to infer climate changes between the main Cenozoic stratigraphic formations of the Issyk Kul basin (Section 5.2.3). New paleocurrent, conglomerate composition and zircon U-Pb provenance data are also presented and used to determine sediment sources and the location of drainage divides through time. This provenance data provides constraints on the timing of active exhumation in mountain ranges and can be used to infer the local onset of late Cenozoic deformation. Based on the inferred onsets of local deformation and our climate proxy data, we are able to constrain the timing of surface uplift in the mountain range to the south of the basin. Together with sedimentological data, these new constraints on provenance, climate changes and surface uplift provide important insights into many aspects of the development of the Issyk Kul basin and surrounding region, and allow the interactions between tectonic deformation, climate and surface processes to be investigated.

5.2. Setting

5.2.1. Tectonic history of the Central Kyrgyz Tien Shan

The Issyk Kul basin is located in the Central Kyrgyz Tien Shan. At these longitudes ($70\text{--}80^\circ\text{E}$), the Tien Shan presently accommodates $\sim 20 \text{ mm/a}$ of north-south horizontal crustal shortening, equivalent to nearly two-thirds of the total India-Eurasian convergence [Zubovich *et al.*, 2010]. The present deformation phase represents the latest in a series of orogenic events in the Tien Shan, stretching back to the Paleozoic, when the terranes of the region were first assembled [Korolev, 1956; Knauf, 1972; Burtman, 1975; Bakirov and Maksumova, 2001; Bazhenov *et al.*, 2003].

The Central Kyrgyz Tien Shan is composed of three Paleozoic terranes (Northern, Middle and Southern Tien Shan terranes), each of which contain a distinctive suite of basement lithologies. The Issyk Kul basin is located in the Northern Tien Shan terrane (Figure 5.1b). This terrane predominantly consists of subduction-related granitoids, which typically yield Ordovician and Silurian zircon U/Pb ages (Figure 5.1c). Minor occurrences of Precambrian metamorphic rocks, as well as other Paleozoic igneous and sediments, are also found in the terrane (e.g. Figure 5.2). In contrast, the igneous bodies of the Middle and Southern Tien Shan terranes mostly have Precambrian and Devonian–Permian zircon U/Pb ages (Figure 5.1c). Additionally, these two terranes contain large Paleozoic passive continental margin sequences. The Northern and Middle Tien Shan terranes are separated by the Nikolaev Line, while the Middle and Southern Tien Shan terranes are separated by the 320–300 Ma Southern Tien Shan Suture [Bakirov and Burtman, 1984; Hegner *et al.*, 2010; Seltmann *et al.*, 2011]. Both terrane boundaries were exploited in the Permian when a system of large strike-slip faults developed across the region, which also included the Central Terskey Fault (Figure 5.1b) [Bazhenov and Mikolaichuk, 2004].

In the Mesozoic and early Cenozoic, parts of the Tien Shan were reactivated in response to distal collisions [e.g. Hendrix *et al.*, 1992; Sobel and Dumitru, 1997; Dumitru *et al.*, 2001]. In the Central Kyrgyz Tien Shan, conclusive evidence of Mesozoic and early Cenozoic deformation has not been identified in the sedimentary record, although increased cooling indicative of active deformation has been suggested by some models of thermochronologic data [e.g. Glorie *et al.*, 2011; De Grave *et al.*, 2013]. Instead, most of the available data suggests that between the late Mesozoic and the early Oligocene, the Central Kyrgyz Tien Shan experienced very little erosion and likely experienced a prolonged (>100 Myr) period of tectonic quiescence (Chapters 2 and 3) [Chediya, 1986; Fortuna *et al.*, 1994; Bullen *et al.*, 2001; 2003; Sobel *et al.*, 2006b; Macaulay *et al.*, in review].

Subsequently in the late Cenozoic, deformation occurred throughout the region. Initially, numerous Paleozoic structures were reactivated, building a series of widely-spaced mountain ranges separated by large intermontane basins. Since then, many more ranges have been constructed in an out-of-sequence fashion [Macaulay *et al.*, in review], leading to the partitioning of these large intermontane basins (Chapter 3) [Makarov, 1977; Cobbold *et al.*, 1996; Burbank *et al.*, 1999]. Thermochronological data from the region suggests that the Terskey Range, located immediately south of the Issyk Kul basin (Figure 5.1b), was one of the first ranges in the Central Kyrgyz Tien Shan to start deforming. This data has identified a series of late Oligocene–early Miocene exhumational increases (29–16 Ma) that have been interpreted to record increased rock uplift following the initial onset of late Cenozoic deformation and the along strike propagation of range-bounding faults. Similar late Oligocene–early Miocene onset ages have also been inferred for many ranges in the Southern Tien Shan terrane (Section 3.5.2) [Macaulay *et al.*, in review]. In contrast, most of the mountain ranges composed of basement belonging to the Middle Tien Shan terrane have younger onset ages and appear to have developed out-of-sequence. North of the Issyk Kul basin, deformation in the Kungey Range has been inferred to have initiated in the Pliocene–Pleistocene on the basis of paleocurrent data [Selander *et al.*, 2012]. Farther north in the Zailiy Range (Figure 5.1b), thermochronological data suggests that deformation started in the late Oligocene–early Miocene [De Grave *et al.*, 2013]. If correct, this implies that the Issyk Kul basin has been an intermontane basin since the late Oligocene–early Miocene; this earlier basin was later reduced in size in the Pliocene–Pleistocene by the development of the Kungey Range.

5.2.2. Issyk Kul basin stratigraphy

In the past, a lack of precise age control meant that the Cenozoic strata of the different intermontane basins in the Central Kyrgyz Tien Shan could only be correlated by lithostratigraphy. This was primarily based on colour and average grain size, leading to four regionally correlated lithostratigraphic groups: the Kakturpak/Suluterek, Shamsi, Chu and Sharpyldak groups [Abdrakhmatov *et al.*, 2001]. However, new magnetostratigraphically-derived age constraints have

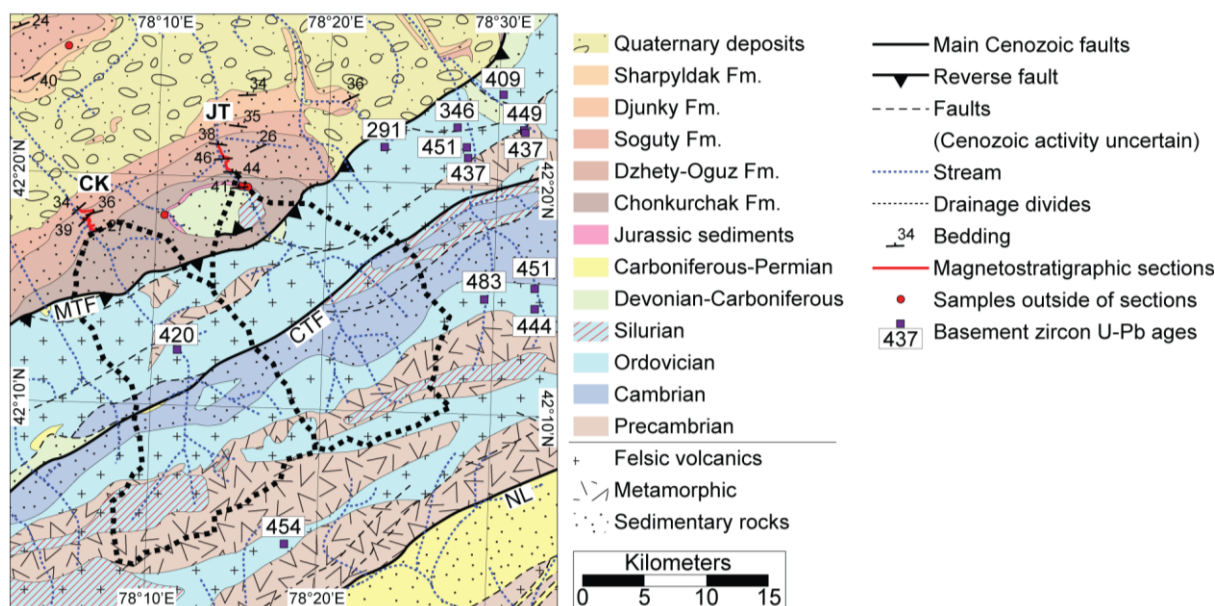


Figure 5.2. Geological map of study area in the south-east corner of the Issyk Kul basin, adapted from *Knauf* [1965]. Dashed black lines denote the modern up-stream catchment areas of the Chon Kyzylsu and Jeti Oguz sections.

revealed significant temporal discrepancies between lithostratigraphically correlated groups in different basins [*Abdrakhmatov et al.*, 2001; *Wack et al.*, in review], suggesting that deposition of these groups could be highly diachronous (Chapter 3) [e.g. *Macaulay et al.*, in review]. Therefore, local formation names [*Omuraliev and Omuralieva*, 2004] are used herein for the stratigraphy of the Issyk Kul basin; the four lithostratigraphic groups are replaced by the Chonkurchak, Dzhety Oguz, Soguty/Djunky and Sharpyldak formations, respectively (Figure 5.3a).

The Chonkurchak formation has a late Cretaceous to early Oligocene depositional age [*Afonichev and Vlasov*, 1984]. Despite the relatively long duration of deposition (>45 Myr), the Chonkurchak formation is usually only tens of meters thick, suggesting that sedimentation rates were extremely low and probably intermittent. Low sediment input is also supported by cooling histories obtained from modelling of basement thermochronological data from the region, which suggest uniformly low erosion rates during this time interval [*De Grave et al.*, 2013; *Macaulay et al.*, 2013; in review]. Deposition of the Chonkurchak formation is coincident with the >100 Myr period of tectonic quiescence between the late Mesozoic and the early Oligocene (Section 5.2.1). At this time, it is believed that a relatively flat, steppe-like landscape developed [*Chediya*, 1986; *Fortuna et al.*, 1994; *Burgette*, 2008]. The Chonkurchak formation is therefore pre-orogenic, reflecting sedimentation during the tectonic quiescent period that was deposited above low relief basement unconformities or disconformably above a ~120 m thick sequence of Jurassic arkosic sandstones and lacustrine sediments [*Knauf*, 1965]. Based on the thickest and most complete sections, the Chonkurchak formation has been sub-divided into two units. The basal unit consists mostly of thin paleosols and lacustrine deposits, while the upper unit is predominantly reddish silt and sandstones [*Fortuna*, 1983; *Selander et al.*, 2012].

In many basins within the Central Kyrgyz Tien Shan, the deposition of the lithostratigraphically correlated Shamsi group marks the onset of syn-orogenic sedimentation [*Abdrakhmatov et al.* 2001]. In the Issyk Kul basin, the irregular and limited deposition of the fine grained, pre-orogenic Chonkurchak formation is replaced by the more continuous, coarser grained sandstones and conglomerates of the Dzhety Oguz formation (Shamsi group). A complete section through the Dzhety Oguz formation is exposed at the type-locality, near the village of Jeti Oguz in the south-eastern Issyk

Kul basin. There, the Dzhety Oguz formation is a ~1 km thick sequence predominantly consisting of poorly sorted clast-supported conglomerates, attesting to a high energy, braided river depositional environment [Cobbald *et al.*, 1996] (Figure 5.3d).

The section near Jety Oguz, and a similar section near the village of Chon Kyzylsu, ~15 km to the west, have been dated using magnetostratigraphy (Chapter 4) [Wack *et al.*, in review] (Figure 5.2). At these locations, the Dzhety Oguz formation is extensively exposed. The base of these sections coincide with a distinctive break-in-slope. Below the sections, the underlying sedimentary units are generally covered by thick, recent soil deposits and rarely outcrop. This likely reflects the greater erodibility of the finer grained underlying sediments of the Jurassic and Chonkurchak formations compared to the coarser grained sandstones and conglomerates of the Dzhety Oguz formation. Therefore, the deposition of the Dzhety Oguz formation marks a distinctive change in the sedimentation history of this part of the Issyk Kul basin. From the magnetostratigraphic data, two slightly different age models were proposed; one based on the best visual magnetostratigraphic correlation (model A) and the other using a numerical algorithm that minimizes misfit (model B). At the Jety Oguz section, the age models suggest that deposition of the formation started either at 22.8 or 22.1 Ma, ended at 13.3 or 11.1 Ma, and had sedimentation rates of 9.7 ± 0.4 or 7.5 ± 0.6 cm/ka, respectively. At the Chon Kyzylsu section, both models have slightly older basal ages for the formation of 26.0 and 25.2 Ma, and have upper ages of 16.2 and 11.0 Ma; sedimentation rates for model A are 9.1 ± 0.4 cm/ka, while for model B they increase from 4.5 ± 0.8 to 8.5 ± 1.6 cm/ka at around 16.5 Ma.

Above the Dzhety Oguz formation is the Soguty formation; unfortunately, the time gap separating the two formations is presently unconstrained. In the lithostratigraphic scheme, the Soguty and Djunky formations of the Issyk Kul basin (also referred to as the Issyk Kul formation) belong to the Chu group, which elsewhere in the Central Kyrgyz Tien Shan is assigned a late Miocene–early Pliocene age [Omuraliev and Omuralieva, 2004]. In most intermontane basins, the Chu group is usually the main basin filling unit [Abdrakhmatov *et al.*, 2001]. In the Issyk Kul basin, the Soguty and Djunky formations reach thicknesses of 2.5 km and often represents ~50% of the preserved Meso–Cenozoic sedimentary sequence [Fortuna, 1983]. If the late Miocene–early Pliocene age and inferred duration of ~8 Myr is correct, this suggests that the Soguty and Djunky formations have a much higher sedimentation rate (~31 cm/ka) than the underlying Dzhety Oguz formation (4–10 cm/ka). Moreover, the Soguty and Djunky formations deposited by meandering river systems are generally finer grained, lighter in colour and better sorted than the underlying Dzhety Oguz formation (Figure 5.3e) [Abdrakhmatov *et al.*, 2001; Burgette, 2008]. Conceivably, the decrease in the overall grain size and the increase in sedimentation rate between the Dzhety Oguz to Soguty and Djunky formations could be caused by either tectonic or climatic changes [Allen *et al.*, 2013]. For the former, the likely driver might relate to an overall late Miocene increase in horizontal crustal shortening (Chapter 3) [Macaulay *et al.*, in review], which is approximately coincident with the time the Soguty formation started being deposited. This late Miocene increase in the magnitude of deformation has also been suggested elsewhere in the Central Kyrgyz Tien Shan [Abdrakhmatov *et al.*, 1996; 2001; Sobel *et al.*, 2006a; Glorie *et al.*, 2010; 2011] and has been linked to a regional change in Central Asian deformation [Sobel *et al.*, 2011]. Potentially, this increase in shortening could have promoted more tectonic subsidence within intermontane basins, thus explaining the higher sedimentation rate of the Soguty and Djunky formations compared to the Dzhety Oguz formation. Furthermore, if sediment supply did not significantly outpace basin subsidence, the increased tectonic subsidence could also have caused a facies retrogradation, whereby the coarser grained deposits of the Dzhety Oguz formation at a particular location are replaced by the finer grained sediments of the overlying Soguty and Djunky formations. Alternatively, this retrogradation of sedimentary facies could reflect a climatically-induced decrease in the amount of sediment supplied to the basin. If this did occur, then the sedimentation rate should have decreased and an associated exhumational decrease ought to be

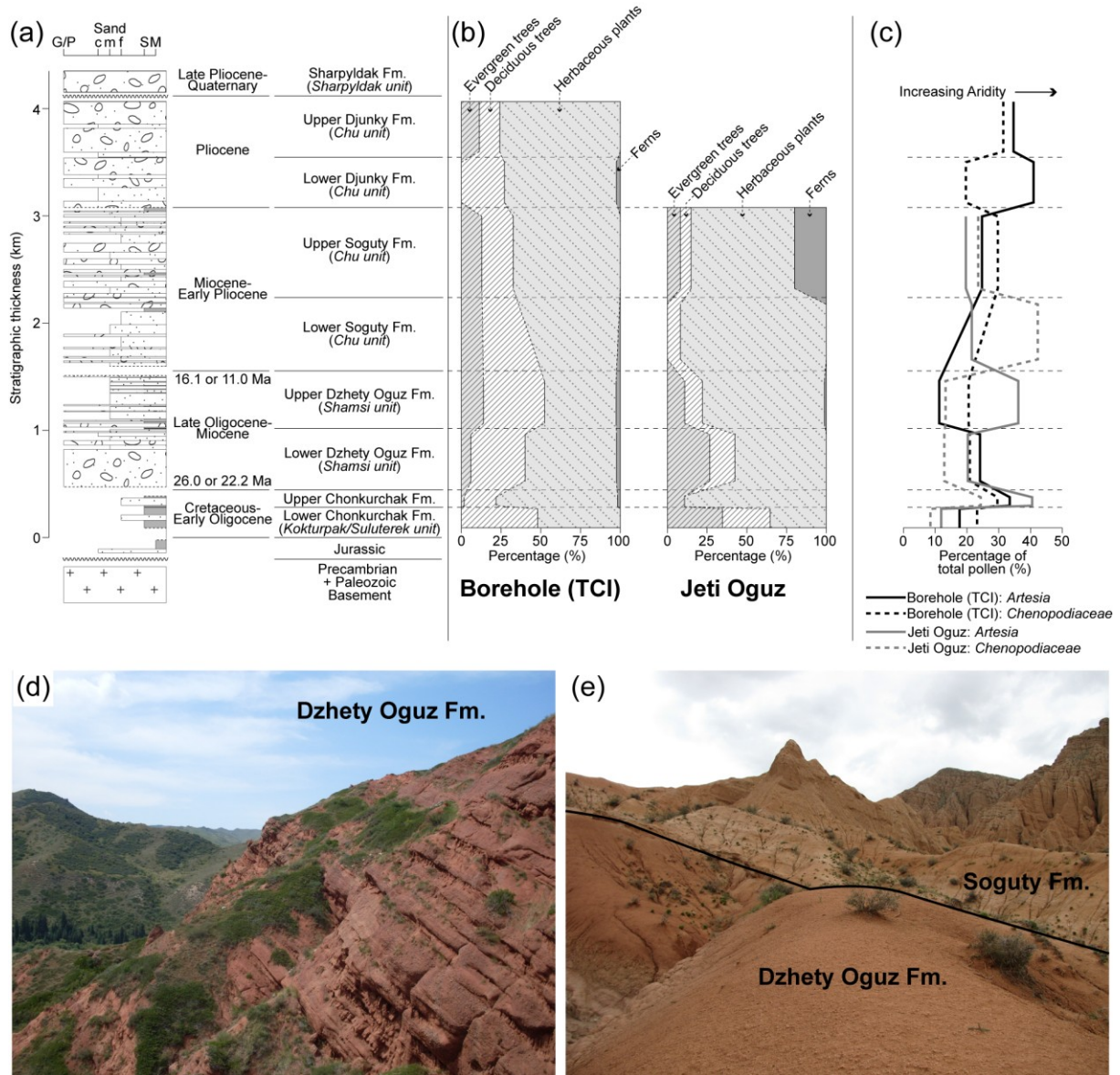


Figure 5.3. (a) Simplified stratigraphic column of the Meso-Cenozoic sedimentary sequence preserved in the Issyk Kul basin, adapted from *Knauf* [1965] and *Fortuna* [1983]. Age estimates from Chapter 4 [*Wack et al.*, in review]; lithostratigraphic correlations adapted from *Abdrakhmatov et al.* [2001], *Omuraliev and Omuralieva* [2004] and *Selander et al.* [2012]. G/P: Gravel and pebble conglomerates; c, m, f sand: coarse, medium and fine sands; S: silt; M: mudstone. (b) Medians of pollen composition abundances for different stratigraphic units separated by plant type, based on data from the TC-I borehole (42.683°N 78.6°E; Figure 5.1b) and from near the the Jety Oguz section (Figure 5.2) [*Fortuna*, 1983]. (c) Median proportions of *Artesia* and *Chenopodiaceae* through time from the borehole data and from around the Jety Oguz section [*Fortuna*, 1983]. *Artesia* and *Chenopodiaceae* are drought tolerant herbaceous taxa; increasing abundances of these taxa is often viewed as indicating more arid conditions [e.g. *Sun and Zhang*, 2008]. (d) Photograph of the Dzhety Oguz formation at the Jety Oguz section (Figure 5.2). (e) Photograph of the contact between the Dzhety Oguz and Soguty formation at 42.169°N 76.795°E.

observed in the surrounding mountain ranges. Since such decreases are not observed in the basin or in thermochronologically-derived exhumation histories for the Terskey and Zailiy Ranges [*De Grave et al.*, 2013; *Macaulay et al.*, 2013; in review], we favour the tectonic explanation for the transition from the Dzhety Oguz to Soguty formations.

During the deposition of the overlying Sharpyldak formation, sedimentation is again dominated by poorly sorted conglomerates, which were delivered to the basin by high energy river systems. In

the Issyk Kul basin, this transition between the Djunky and Sharpyldak formation has not been dated. However, in the Chu basin (Figure 5.1a), the transition between the lithostratigraphic equivalents of these formation has been constrained to < 3 Ma by magnetostratigraphy [Bullen *et al.*, 2001]. Similar late Pliocene–Pleistocene estimates have been inferred elsewhere in the Central Kyrgyz Tien Shan, leading to the suggestion that the Sharpyldak group could reflect either a regionally extensive deformational increase or climatically-enhanced erosion [Bullen *et al.*, 2003; Sobel *et al.*, 2006b; Burgette, 2008; Trifonov *et al.*, 2008]. Interestingly, the nature of the contact between the formations varies within the Issyk Kul basin. In the south, the Sharpyldak formation is deposited above an angular unconformity [Burgette, 2008], whereas to the north, the Djunky and Sharpyldak formations are separated by a disconformity [Selander *et al.*, 2012]. This difference is related to numerous structures that propagated into the southern part of the basin during the deposition of the Sharpyldak formation, rotating older sediments and causing rock uplift. Subsequent erosion and incision into these older sediments would have generated topographic relief in the south of basin, thus explaining the variability in the thickness of the Sharpyldak formation (10–500 m) [Knauf, 1965; Turchinskiy, 1970; Fortuna, 1983; Selander *et al.*, 2012].

5.2.3. Pollen data

Published pollen data provides an indication of climatic variations between the main sedimentary units (Figure 5.3b+c). Here, we focus on pollen data from the Jety Oguz section (Figure 5.2) and samples from a borehole (Figure 5.1b), and use fluctuations in the medians of different plant types or the content of two drought tolerant herbaceous taxa (*Artesia* and *Chenopodiaceae*) [Sun and Zhang, 2008] to identify two key climate changes in Issyk Kul stratigraphy.

Firstly, the basal unit of the Chonkurchak formation has a higher abundance of deciduous trees and contains less drought-tolerant species (Figure 5.3b+c) than the upper unit. Taken together, this suggests that the lower unit was deposited during comparatively wet conditions. The associated change in sedimentation from the thin paleosol and lacustrine deposits of the lower unit to the reddish silt and sandstones of the upper, was likely caused by this increase in aridity. The second feature identified in the pollen record is that the basin has become progressively more arid since the late Miocene (Figure 5.3c) [Fortuna, 1983]. Interestingly, a similar Neogene intensification of aridity is seen elsewhere in Central Asia [Kent-Corson *et al.*, 2009; Zhuang *et al.*, 2011].

5.3. Methodology and results

5.3.1. Sedimentological analysis

Detailed outcrop-based analyses were performed throughout the Chon Kyzylsu and Jety Oguz sections (Figure 5.2) to determine paleocurrent directions, grain size, and conglomerate clast compositions (Figure 5.4). Paleocurrent directions calculated from measurements of 10–20 imbricated clasts at 22 locations suggests that the river system was directly roughly northwards during the deposition of the Dzhety Oguz formation; the same paleocurrent direction was determined by Cobbold *et al.* [1996]. Grain sizes were measured and classified using the Wentworth scale for every measured bed in both sections [Wentworth, 1922]: 1115 for the Chon Kyzylsu section and 917 at Jety Oguz. In order to better visual this data and identify variations through time, moving averages of the grain size classifications have been calculated throughout the sections. Despite considerable scatter, these plots indicate that average grain sizes remain relatively constant through both sections, except for the gradual up-section decrease in the lowermost ~250 m of the Chon Kyzylsu section (Figure 5.4b). Conglomerate clast abundances were characterised by counting at least 100 clasts using a 1 x 1 m grid at 12 regularly-spaced (~150 m) intervals throughout both sections. The results of this analysis reveals that clast proportions have remained relatively constant during the deposition of the Dzhety Oguz formation and are similar in both sections. Most clasts have granitic or metasedimentary compositions; clasts of diorites, marbles, limestones, clastic sedimentary rocks and quartzites were also found (Figure 5.4c).

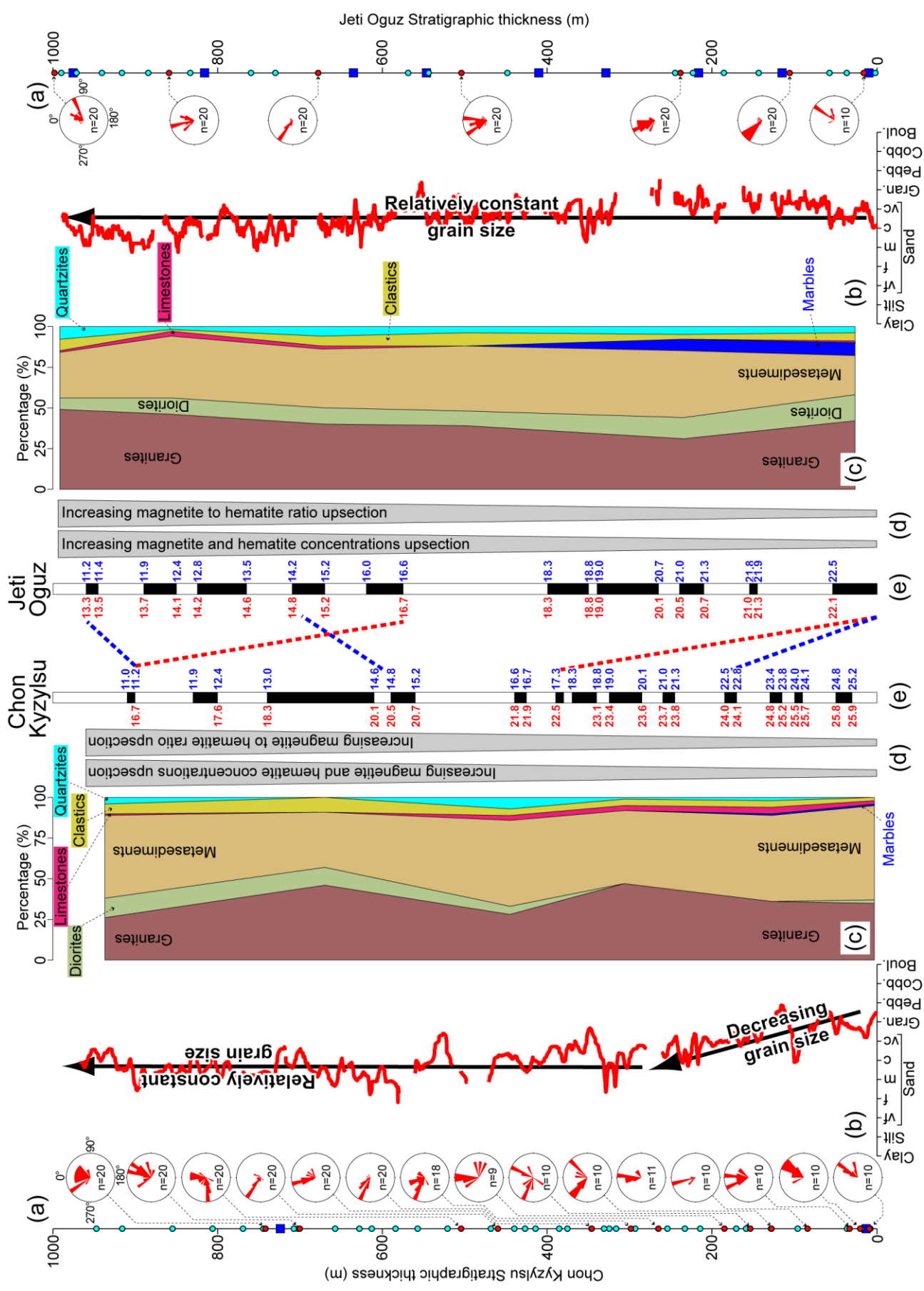


Figure 5.4. Sedimentologic data for the Dzhety Oguz formation from the Chon Kyzylsu (left) and Jeti Oguz (right) sections. (a) Rose diagrams of imbricated clast orientations, showing paleocurrent flow directions towards the north; n = number of measurements. Stratigraphic positions of measurements indicated with red dots. Light blue dots show positions of stable isotope samples; dark blue squares show zircon samples. (b) Average grain sizes, determined with a 21-point moving average. (c) Compositions of conglomerate determined from >100 clasts per site. (d) Changes in the composition of the sediment inferred from variations in magnetic parameters, inferred from the bulk susceptibility, anhysteretic remanence (ARM) spectra, and the natural remnant magnetization (NRM) (Chapter 4) [Wack *et al.*, in review]. (e) Magnetostratigraphic correlations from age model A (red) and B (blue) (Section 4.3.4) [Wack *et al.*, in review].

5.3.2. Zircon U-Pb provenance analysis

Zircon U-Pb provenance analysis was carried out at Birkbeck University of London on fifteen samples collected from most of the main stratigraphic units in the Issyk Kul basin (details of the analytical procedure are found in Table 5.1). Near the Jeti Oguz section, single samples of Jurassic quartzite (JJZ1) and present-day river sands (11TS02) were collected (Figure 5.2); nine samples (JTZ50–66) were collected at ~100 m intervals through the magnetostratigraphically-dated Dzhety Oguz formation at this location (Figure 5.4). At the Chon Kyzylsu section, samples were taken near the bottom and top of the Dzhety Oguz formation at stratigraphic levels of ~10 m (CKZ1) and ~725 m (CKZ17). Additionally, the Djunky formation was sampled at an anticline ~15 km north-west of the section (9TS511) (Figure 5.2). For each sample, 76–133 zircon crystals were dated using LA-ICP-MS. Analyses with >20% discordance were excluded, leaving 54–124 zircon U-Pb ages per sample (Table 5.1).

Probability density functions (PDFs) showing the distribution of zircon U/Pb ages in the Phanerozoic reveal that most samples have a single dominant peak between ~440 and 465 Ma (Figure 5.5a). However, two samples located near the top of the Dzhety Oguz formation (JTZ64 and JTZ66) exhibit different distributions. The lower sample (JTZ64) at a stratigraphic level of 815 m has a younger maximum peak at ~360 Ma; the upper sample (JTZ66) at a level of 980 m has bimodal distribution with a maximum peak at 414 Ma and a lesser one at ~323 Ma. The complete dataset including ages from all of analysed zircon grains can be found in appendix 4 (Table A4.1).

In addition to the zircon U-Pb ages from sediments, we have compiled the available data from basement lithologies in the surrounding region (Figure 5.1c and Table A4.2). The analysed samples were predominantly collected from igneous intrusive bodies. As discussed in Section 5.2.1, each of the terranes that make up the Central Kyrgyz Tien Shan has a different Paleozoic history, which is reflected in the variable ages of the sampled intrusions (Figure 5.1c and 5.5c). Despite the non-random selection of these previously analysed samples, this dataset provides a means of assessing sedimentary provenance and differentiating between the three terranes (Section 5.4.1).

5.3.3. Oxygen and carbon isotopes

Oxygen ($\delta^{18}\text{O}$) and carbon ($\delta^{13}\text{C}$) isotope analyses were performed on 53 mudstone and siltstone samples collected throughout the Dzhety Oguz formation at the Chon Kyzylsu and Jeti Oguz sections (Figure 5.6 and Table 5.2). Field observations indicate that these sediments represent over-bank deposits. $\delta^{18}\text{O}$ and $\delta^{13}\text{C}$ analyses were also performed on three carbonate-bearing basement samples from the Terskey Range (Figure 5.1b) to investigate the potential influence of detrital carbonate on the isotopic values obtained from the sediments (Section 5.4.2.2). Furthermore, $\delta^{18}\text{O}$ values from 128 modern water samples were also obtained. All isotopic ratios are reported relative to the Pee Dee Belemnite (PDB) standard; consult Table 5.2 for further details regarding the analytical procedures.

For the sediment samples, we obtained $\delta^{18}\text{O}$ and $\delta^{13}\text{C}$ values ranging between -15.3 to -9.0‰ and -9.4 to -3.0‰, respectively. Despite a high degree of scatter in the data from the sediments, significant variations can be detected in both sections, particularly in the calculated moving averages from the more densely sampled Chon Kyzylsu section (Figure 5.6a+b). Arguably the most obvious feature occurs in the lowermost ~250 m of the Chon Kyzylsu section, where $\delta^{13}\text{C}$ values of 10 samples gradually decreases up-section from -4.8 to -9.4‰ (Figure 5.6a). Another noticeable feature of the

data from the Chon Kyzylsu section is that the scatter of $\delta^{18}\text{O}$ increases above ~420 m (Figure 5.6a); the lower 18 samples have a standard deviation of 0.6‰, compared to 0.8‰ for the 17 samples above 420 m.

For each basement sample, stable isotope analyses were performed on the carbonate-bearing host rock and calcite veins (Table 5.2). $\delta^{13}\text{C}$ values were relatively consistent, and were found to range between -2.89 to 1.2‰; furthermore, in each sample, the two analysed components were also found to be similar, varying by <0.6‰. On the other hand, $\delta^{18}\text{O}$ values were much more scattered (ranging between -23.6 to -9.4‰) and with significant variations between the two analysed components (up to 5.0‰) (Table 5.2). Compared to the stable isotope ratios obtained from the sediment samples, the $\delta^{13}\text{C}$ values from basement samples were significantly higher, while the $\delta^{18}\text{O}$ of sediments lies within the wide range of values derived from the basement samples. Analysis of the $\delta^{18}\text{O}$ values of modern water samples reveals a large degree of scatter; values ranging between -51.1 to -28.5‰, with a mean of -37.8‰ (Table 5.2). If authigenic calcite were to precipitate from these modern water samples at surface temperatures (~20°C), the $\delta^{18}\text{O}$ values would increase by ~29.1‰ and range between -22.0 and 0.6‰ [Kim and O’Neil, 1997]. $\delta^{18}\text{O}$ values from the sediments fall within this range (-15.3 to -9.0‰).

Table 5.1. Summary of samples that underwent zircon U/Pb provenance analysis^a

Sample	Latitude	Longitude	Formation/Section strat. position (m) ^b	Total no. of grains	No. of concordant grains (<20%) ^c
JJZ1	42.3273	78.2466	Jurassic	102	86
9TS506	42.3048	78.1747	Chonkurchak	130	124
JTZ50	42.3381	78.2404	JT (4.5)	100	88
JTZ52	42.3400	78.2344	JT (110.1)	107	78
JTZ54	42.3425	78.2334	JT (212.4)	106	72
JTZ56	42.3443	78.2332	JT (324.0)	112	108
JTZ58	42.3457	78.2355	JT (405.7)	76	54
JTZ60	42.3480	78.2316	JT (542.1)	114	88
JTZ62	42.3520	78.2280	JT (630.2)	122	99
JTZ64	42.3538	78.2270	JT (810.9)	124	109
JTZ66	42.3583	78.2250	JT (995.6)	124	100
CKZ1	42.2924	78.1087	CK (7.4)	133	90
CKZ17	42.3050	78.0938	CK (719.0)	92	67
9TS511	42.4463	78.0545	Djunky	102	86
11TS02	42.3273	78.2439	Modern sand	123	108

^a Samples were analysed by LA-ICPMS using a New Wave 213 aperture imaged frequency quintupled laser ablation system (213 nm) coupled to an Agilent 750a quadrupole-based ICP-MS. Real time data were processed using GLITTER. Repeated measurements of external zircon standard PLESOVIC (TIMS reference age of 337.13 ± 0.37 Ma) [Slama et al., 2008] and NIST 612 silicate glass [Pearce et al., 1997] were used to correct instrumental mass bias and depth dependent inter-element fractionation of Pb, Th and U. Data were processed using Isoplot [Ludwig, 2003] following the recommended procedures of an international workshop convened to consider data handling [Horstwood et al., 2009].

^b Formation that sample was collected from. Except for samples from the Jeti Oguz (JT) and Chon Kyzylsu (CK) sections through the Dzhety Oguz formation. For those samples the stratigraphic position in meters is displayed in brackets.

^c Zircon U/Pb ages were deemed to be concordant when the difference between the 207/206 and 206/238 ages were <20% of the 206/238 age. The complete dataset can be found in the supplementary material (Table A4.1).

Table 5.2. Stable isotope data

Sample ^a	Latitude	Longitude	Strat. position (m) /Lithology/water source ^b	Age model A (Ma) /Unit age ^c	Age model B (Ma) /Date collected ^d	$\delta^{18}\text{O}$, ‰ (PDB) ^e	$\delta^{13}\text{C}$, ‰ (PDB)
<i>Chon Kyzylsu section (CK)</i>							
CKP01	42.2924	78.1087	8	26.0	25.6	-10.8	-4.8
CKP02	42.2920	78.1066	18	26.0	25.4	-11.6	-4.4
CKP03	42.2925	78.1064	36	25.9	25.1	-11.9	-4.3
CKP04	42.2956	78.1069	96	25.6	24.1	-12.7	-7.5
CKP05	42.2925	78.1019	128	24.8	23.4	-11.6	-5.7
CKP07	42.2927	78.1026	159	24.1	22.8	-12.3	-6.0
CKP06	42.2932	78.1025	171	24.3	23.0	-12.4	-6.7
CKP08	42.2940	78.1019	214	23.9	21.9	-11.8	-8.1
CKP09	42.2949	78.1018	233	23.8	21.5	-13.4	-7.7
CKP10	42.2954	78.1017	254	23.8	21.1	-13.0	-9.4
CKP11	42.2961	78.1005	293	23.6	19.9	-13.0	-6.8
CKP12	42.2964	78.1005	316	23.4	19.2	-12.2	-6.8
CKP13	42.2974	78.1014	325	23.4	19.0	-12.6	-5.4

Table 5.2. continued.

Sample ^a	Latitude	Longitude	Strat. position (m) /Lithology/water source ^b	Age model A (Ma) /Unit age ^c	Age model B (Ma) /Date collected ^d	$\delta^{18}\text{O}$, ‰ (PDB) ^e	$\delta^{13}\text{C}$, ‰ (PDB)
CKP14	42.2974	78.1012	331	23.3	18.9	-12.7	-6.1
CKP15	42.2979	78.1021	346	23.0	18.7	-12.8	-6.4
CKP17	42.2998	78.1014	375	22.7	18.0	-12.9	-6.9
CKP18	42.2990	78.0985	385	22.6	17.4	-11.8	-6.7
CKP19	42.2991	78.0970	414	22.2	16.8	-12.4	-6.3
CKP20	42.2996	78.0964	427	21.9	16.7	-12.4	-6.6
CKP21	42.2997	78.0961	440	21.8	16.6	-12.7	-7.2
CKP22	42.3021	78.1007	468	21.5	16.3	-11.1	-7.9
CKP23	42.3056	78.1048	521	21.1	15.7	-13.0	-8.6
CKP24	42.3063	78.1043	557	20.7	15.2	-11.2	-5.4
CKP25	42.3056	78.1008	584	20.6	14.9	-12.5	-6.1
CKP26	42.3056	78.0996	613	20.1	14.6	-11.0	-7.0
CKP27	42.3057	78.0989	628	19.9	14.4	-11.3	-7.8
CKP28	42.3050	78.0966	657	19.5	14.0	-13.5	-8.2
CKP29	42.3055	78.0965	703	18.9	13.5	-12.8	-8.3
CKP30	42.3050	78.0938	707	18.8	13.4	-12.5	-8.2
CKP31	42.3048	78.0919	744	18.2	12.9	-12.6	-6.2
CKP32	42.3052	78.0917	769	18.0	12.7	-12.7	-6.8
CKP33	42.3060	78.0923	806	17.5	12.3	-13.7	-6.5
CKP34	42.3066	78.0927	855	17.1	11.6	-12.5	-8.2
CKP35	42.3070	78.0918	916	16.5	10.9	-11.5	-8.2
CKP41	42.3075	78.0897	947	16.3	10.2	-11.7	-7.2
<i>Jeti Oguz section (JT)</i>							
JTP50	42.3381	78.2404	2	22.50	23.02	-9.0	-5.8
JTP51	42.3385	78.2386	37	22.26	22.74	-9.3	-3.0
JTP52	42.3390	78.2384	58	22.06	22.57	-10.4	-5.0
JTP54	42.3407	78.2341	144	21.30	21.90	-13.4	-5.1
JTP55	42.3415	78.2342	186	20.80	21.50	-12.5	-5.9
JTP56	42.3439	78.2337	224	20.60	21.15	-12.3	-7.2
JTP57	42.3435	78.2331	245	20.40	20.90	-11.4	-6.0
JTP62	42.3476	78.2355	449	17.87	17.84	-12.5	-6.5
JTP67	42.3483	78.2313	544	16.98	16.91	-12.5	-6.6
JTP68	42.3482	78.2328	569	16.76	16.67	-15.3	-6.0
JTP74	42.3521	78.2282	730	14.75	14.03	-12.7	-6.0
JTP75	42.3529	78.2279	760	14.60	13.60	-14.2	-7.2
JTP77	42.3544	78.2265	834	14.17	12.60	-12.1	-6.6
JTP78	42.3557	78.2253	885	13.75	11.95	-13.7	-7.0
JTP79	42.3564	78.2253	916	13.60	11.65	-14.1	-7.1
JTP80	42.3572	78.2246	941	13.50	11.40	-13.0	-8.2
JTP81	42.3578	78.2247	972	13.10	11.00	-13.5	-7.2
JTP82	42.3583	78.2250	990	12.90	10.80	-13.8	-7.3
<i>Basement samples</i>							
9TS451	42.4149	78.9529	Green Marble	Cambrian		-23.6	-2.5
9TS451	42.4149	78.9529	Calcite vein	Cambrian		-18.6	-2.9
8TS383	41.9347	77.6609	Calcite vein	Cambrian		-9.4	1.2
8TS383	41.9347	77.6609	Grey Marble	Cambrian		-10.8	0.6
8TS352	42.0977	78.1591	Calcite vein	Precambrian		-14.8	0.2
8TS352	42.0977	78.1591	Dark Marble	Precambrian		-11.0	0.7
<i>Modern water samples</i>							
06-TP-60	40.8238	75.2901	Snow		winter 05/06	-51.1	
IK-26	42.6606	77.2026	Snow		11/8/03	-50.1	
IK-27	42.6606	77.2026	Snow		11/17/03	-48.1	
05-IK-75	42.6587	77.2032	Snow		11/26/2005	-45.5	
05-IK-74	42.6587	77.2032	Snow		11/25/2005	-44.4	
05-AB-81	40.8237	75.2901	Snow		10/15/05	-44.1	
05-IK-73	42.6587	77.2032	Snow		11/25/2005	-43.0	
05-AB-23	40.8112	75.2330	Stream water		7/21/05	-43.0	
04-CTS-05	41.7133	78.3218	Stream water		7/28/04	-42.9	
04-WA-70	41.1279	75.6972	well water		June/July 2004	-42.9	
04-CTS-08	41.7742	78.3999	Snow		7/29/04	-42.8	
04-AB-12	40.7511	75.2592	Snow		7/17/04	-42.8	
KYR07-52	40.8439	75.1292	Stream water			-42.8	
04-CTS-03	41.6696	78.2542	Stream water		7/28/04	-42.8	
05-AB-25	40.8249	75.2911	Stream water		7/23/05	-42.5	
04-CTS-04	41.6847	78.3165	Stream water		7/28/04	-42.3	
04-CTS-28	41.7635	77.7678	Stream water		7/31/04	-42.3	
04-CTS-26	41.6776	77.6295	River water		7/31/04	-42.2	
04-WA-73	41.4491	76.2365	Well water		June/July 2004	-42.1	
04-AB-01	41.1649	75.8182	River water		7/14/04	-41.9	
KYR07-04	40.8136	75.2295	Stream water			-41.7	
04-CTS-27	41.7414	77.7926	Stream water		7/31/04	-41.7	
04-NO-02	42.2183	75.6998	River water		7/24/04	-41.7	
04-CTS-01	41.6203	78.0602	River		7/28/04	-41.6	

Table 5.2. *continued.*

Sample ^a	Latitude	Longitude	Strat. position (m) /Lithology/water source ^b	Age model A (Ma) /Unit age ^c	Age model B (Ma) /Date collected ^d	$\delta^{18}\text{O}$, ‰ (PDB) ^e	$\delta^{13}\text{C}$, ‰ (PDB)
04-AB-02	40.8282	75.2121	Stream water		7/14/04	-41.6	
KYR07-71	41.2001	75.7367	River water			-41.5	
KB-08	42.9391	78.3258	River		7/1/03	-41.4	
04-CTS-06	41.7702	78.4063	Glacial melt		7/29/04	-41.3	
04-NO-01	41.8316	75.7716	River water		7/18/04	-41.3	
04-WA-66	41.4587	76.4511	River water		June/July 2004	-41.2	
04-CTS-33	42.0660	77.5941	River water		8/1/04	-41.2	
04-IK-41	42.5699	76.7540	Tap water		8/18/04	-41.2	
05-AB-80	40.8249	75.2911	Stream water		9/10/05	-41.1	
Bos-Prec-15	42.6587	77.2031	Rain water		11/23/04	-41.1	
KYR07-51	41.0333	75.0564	Stream water			-41.0	
04-CTS-17	41.7474	78.4204	Spring water		7/30/04	-41.0	
04-CH-01	42.6595	75.8881	Spring water		8/7/04	-41.0	
04-AB-17	40.8231	75.2893	Stream water		7/17/04	-41.0	
IK-21	42.6606	77.2026			9/15/03	-40.9	
05-AB-29	40.8403	75.2152	Stream water		9/5/05	-40.9	
05-AB-21	40.8111	75.2298	Stream water		7/21/05	-40.9	
KYR07-50	41.0555	75.0974	Stream water			-40.8	
KB-10	42.8432	78.3331	River		7/1/03	-40.8	
06-TP-66	40.8238	75.2901	Stream		winter 05/06	-40.7	
05-AB-82	40.8237	75.2901	Stream water		10/15/05	-40.6	
06-AB-44	40.8238	75.2901	Stream water		7/28/06	-40.6	
KB-06	42.9308	78.3228	River		6/29/03	-40.4	
KYR07-83	42.6493	77.1991	Spring water			-40.4	
06-AB-44	40.8238	75.2901	Stream water		7/28/06	-40.4	
05-AB-03	40.8415	75.2149	Stream water		7/19/05	-40.3	
IK-24	42.6468	77.2010	Spring water		10/23/03	-40.3	
04-CTS-32	41.8681	77.7384	Lake water		8/1/04	-40.2	
KYR05-AB99	40.8236	75.2901	Stream		10/18/05	-40.2	
IK-14	41.9553	77.6479	River		8/30/03	-40.2	
IK-08	42.7586	76.9896	Glacial melt		8/19/03	-40.2	
04-CTS-02	41.6298	78.1864	River water		7/28/04	-40.2	
KYR07-72	41.4241	76.0207	River water			-40.1	
KYR07-84	42.6654	77.2090	Tap water			-40.1	
IK-07	42.7801	76.9598	Glacial melt		8/19/03	-40.1	
IK-12	41.8686	77.6645	Glacial melt		8/29/03	-40.0	
IK-20	42.6606	77.2026	Tap water		9/15/03	-40.0	
Bos-Prec-03	42.6587	77.2031	Rain water		3/17/04	-39.8	
TR-01	40.8231	75.2893	River		8/12/03	-39.7	
KYR07-30	40.8236	75.2900	Stream water			-39.6	
IK-32	42.6587	77.2031	Snow		2/17/04	-39.6	
KYR07-69	40.8234	75.2898	Stream water			-39.6	
KYR07-85	42.6705	77.2068	Irrigation water			-39.5	
05-AB-84	40.8393	75.2155	Stream water		10/15/05	-39.4	
05-IK-03	42.6706	77.2068	Rain water			-39.0	
04-CTS-10	41.7662	78.4097	Spring water		7/30/04	-38.9	
04-AB-10	40.7511	75.2592	Snow		7/16/04	-38.6	
04-WA-75	41.7643	75.2801	Rain water		June/July 2004	-38.6	
KYR07-01	40.8386	75.2154	Stream water			-38.2	
04-IK-34	42.6453	77.2080	Pond water		8/12/04	-38.1	
Bos-Prec-02	42.6587	77.2031	Rain water		3/16/04	-38.1	
KYR07-80	42.6448	77.2120	Pond water			-38.0	
Bos-Prec-14	42.6587	77.2031	Rain water		10/27/04	-37.8	
04-WA-72	41.7568	75.1089	Rain water		June/July 2004	-37.4	
04-WA-79	40.8231	75.2893	Rain water		June/July 2004	-37.3	
Bos-Prec-07	42.6587	77.2031	Rain water		5/24/04	-36.8	
IK-19	42.6606	77.2026	Rain		9/15/03	-36.6	
05-IK-66	42.6591	77.2030	Rain		9/29/2005	-36.5	
05-IK-68	42.6591	77.2030	Rainwater		10/11/05	-36.1	
05-IK-67	42.6591	77.2030	Rainwater		10/24/2005	-35.7	
04-CTS-31	41.8155	77.7528	Hail		7/31/04	-35.6	
Bos-Prec-01	42.6587	77.2031	Snow		3/11/04	-35.4	
04-WA-71	41.4587	76.4511	Rain water		June/July 2004	-35.1	
Bos-Prec-11	42.6587	77.2031	Rain water		9/16/04	-35.0	
Bos-Prec-05	42.6587	77.2031	Rain water		4/22/04	-34.9	
Bos-Prec-04	42.6587	77.2031	Snow/Rain		3/22/04	-34.8	
Bos-Prec-12	42.6587	77.2031	Rain water		9/21/04	-34.8	
Bos-Prec-06	42.6587	77.2031	Rain water		5/7/04	-34.5	
IK-01	42.6606	77.2026	Rain		7/5/03	-34.2	
04-CTS-25	41.6541	77.8473	Pond water		7/31/04	-33.8	
Bos-Prec-09	42.6587	77.2031	Rain water		8/30/04	-33.5	
05-IK-05	42.6706	77.2068	Rain water		8/24/2005	-33.4	
05-IK-18	42.6706	77.2068	Rain water		8/26/2005	-32.7	

Table 5.2. continued.

Sample ^a	Latitude	Longitude	Strat. position (m) /Lithology/water source ^b	Age model A (Ma) /Unit age ^c	Age model B (Ma) /Date collected ^d	$\delta^{18}\text{O}$, ‰ (PDB) ^e	$\delta^{13}\text{C}$, ‰ (PDB)
KYR07-02	40.8194	75.2281	Hail/Snow			-32.7	
IK-02	42.6606	77.2026	Rain		7/10/03	-32.6	
04-IK-35	42.6438	77.2118	pond water		8/12/04	-32.6	
Bos-Prec-13	42.6587	77.2031	Rain water		10/7/04	-32.5	
05-IK-01	42.6706	77.2068	Rain water		7/30/05	-32.4	
05-IK-02	42.6706	77.2068	Rain water		2/8/05	-32.3	
KB-04	42.9391	78.3258	Rain		6/28/03	-32.2	
Bos-Prec-08	42.6587	77.2031	Rain water		5/30/04	-31.5	
04-IK-44	42.6685	77.2712	Rain water		8/21/04	-31.3	
05-IK-20	42.6591	77.2030	Rain water		1/9/05	-31.1	
04-IK-04	42.6468	77.2010	Issyk Kul		5/9/04	-31.1	
04-IK-06	42.6468	77.2010	Issyk Kul		5/29/04	-31.0	
04-IK-05	42.6468	77.2010	Issyk Kul		5/19/04	-30.9	
04-IK-12	42.6468	77.2010	Issyk Kul		8/11/04	-30.9	
04-IK-03	42.6468	77.2010	Issyk Kul		4/21/04	-30.9	
IK-28	42.6468	77.2010	Issyk Kul		11/22/03	-30.8	
KYR07-82	42.6469	77.2013	lake water			-30.8	
04-IK-07	42.6468	77.2010	Issyk Kul		6/10/04	-30.8	
04-IK-11	42.6468	77.2010	Issyk Kul		8/4/04	-30.8	
KYR05-IK35	42.6469	77.2012	Lake		11/27/05	-30.7	
IK-25	42.6468	77.2010	Issyk Kul		11/1/03	-30.7	
05-AB-65	40.7082	75.3815	Lake water		9/8/05	-30.6	
04-IK-02	42.6468	77.2010	Issyk Kul		4/1/04	-30.6	
IK-04	42.6606	77.2026	Rain		8/4/03	-30.5	
04-IK-08	42.6468	77.2010	Issyk Kul		6/20/04	-30.5	
04-IK-10	42.6468	77.2010	Issyk Kul		7/19/04	-30.5	
04-CTS-24	41.6480	77.8585	Pond water		7/31/04	-30.3	
IK-30	42.6468	77.2010	Issyk Kul		12/21/03	-30.3	
04-IK-30	42.6595	77.2028	Rain water			-29.8	
Bos-Prec-10	42.6587	77.2031	Rain water		9/3/04	-29.1	
04-IK-01	42.6468	77.2010	Issyk Kul		3/11/04	-28.5	

^a 53 carbonate-bearing mudstone and siltstone samples and 3 carbonate-bearing basement samples were powdered using a dental drill. Between 0.18 and 0.60 mg of these powders were loaded into sealed reactivation vessels, flushed with helium gas and reacted at 72°C with phosphoric acid using a Thermo GasBench II. Isotope ratios were measured in continuous flow mode using a MAT253 gas mass spectrometer in the Goethe University-BiK-F Stable Isotope Laboratory in Frankfurt. Due to the variable carbonate contents of the samples, we adjusted the sample sizes to match standard sample size during the mass spectrometric measurements. Based on repeated analyses of reference materials NBS-19 and two different in-house standards analytical precision was determined to be <0.1‰ for both $\delta^{13}\text{C}$ and $\delta^{18}\text{O}$. Random samples were duplicated and tested for consistency and the raw isotope data were corrected for mass bias, signal size, and offset from the certified reference values similar to methods described in *Spötl and Vennemann* [2003].

The $\delta^{18}\text{O}$ values of 128 modern water samples were measured at the the University of Utah by three different methods; CO_2 equilibration via GC-IRMS using a Finnigan MAT 252, pyrolyzation in a thermochemical elemental analyzer furnace (TCEA; ThermoFinnigan) prior to IRMS analysis in continuous flow mode (ThermoFinnigan Delta Plus XL), and wavelength-scanned cavity ring down spectroscopy (Picarro L1102-i). Data quality was assured by replicate analyses of unknowns and by extensive analysis of three internal standards intercalibrated with VSMOW and SLAP.

^b Stratigraphic position of sediment sample in meters. Lithology of basement samples. Water source for modern water samples.

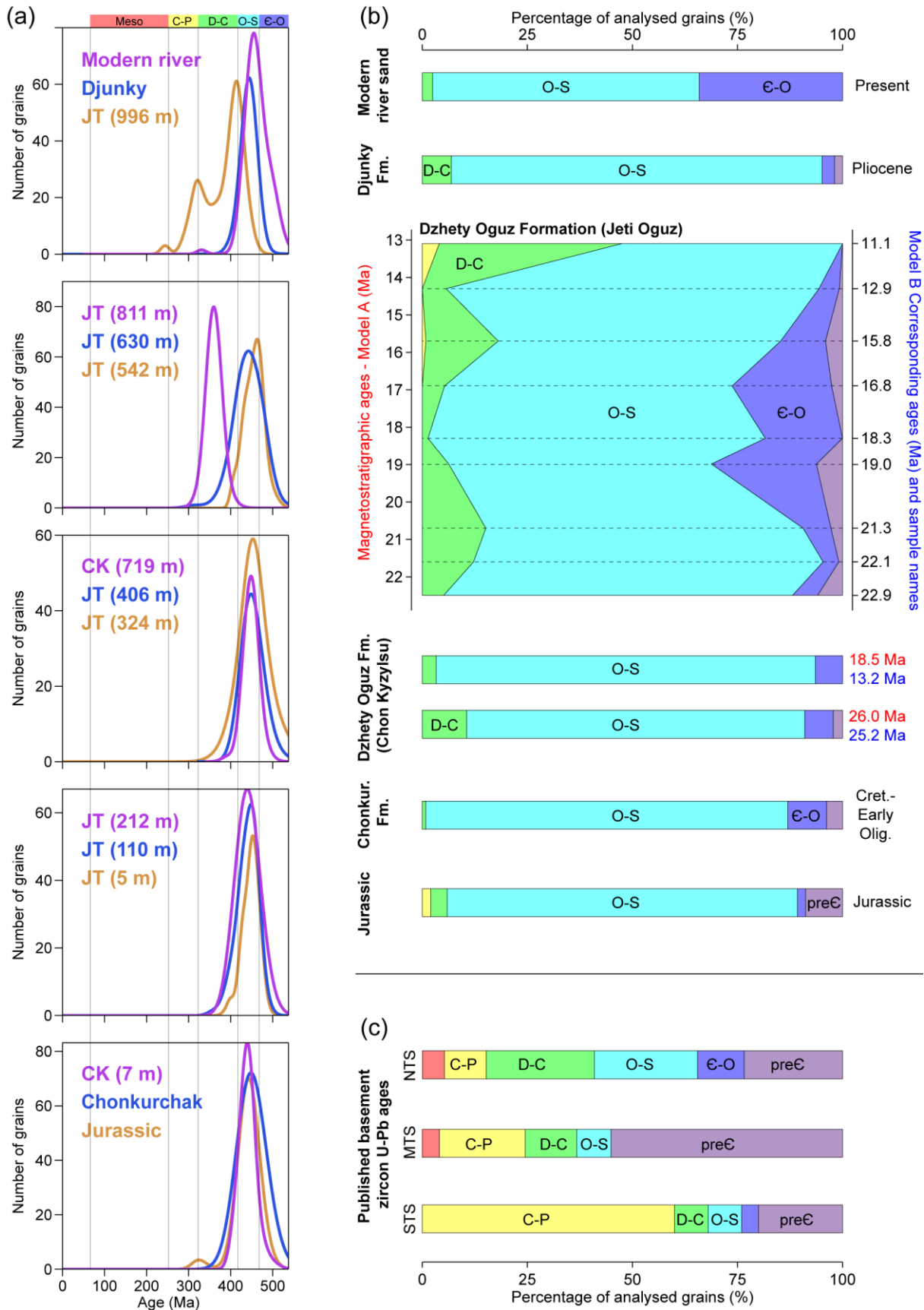
^c For sediment samples the age from model A is stated. For basement samples the age of the unit from [Knauf, 1965; Turchinsky, 1970] is stated.

^d For sediment samples the age from model B is stated. For modern water samples the date of collection is given; typically as month/day/year.

^e The $\delta^{18}\text{O}$ values for basement and modern water samples were measured with respect to the Standard Mean Ocean Water (SMOW) standard. These values were converted to the Pee Dee Belemnite (PDB) standard using the equation of *Friedmann and O'Neil* [1977], which is stated below.

$$\delta^{18}\text{O}_{\text{PDB}} = 0.97006 * \delta^{18}\text{O}_{\text{SMOW}} - 29.94$$

Figure 5.5. (a) Phanerozoic probability density functions (PDF) of zircon U-Pb ages. Calculated using Isoplot [Ludwig, 2003]. See supplementary material for complete dataset. (b) Percentages of zircon ages from different age groups, which are based on the available ages for intrusions across the region (Figure 5.1c). preC: Precambrian (>541 Ma); E-O: Cambrian-Early Ordovician (541-470 Ma); O-S: Middle Ordovician-Silurian (470-419 Ma); D-C: Devonian-Carboniferous (419-323 Ma); Meso: Mesozoic (252-66 Ma). (c) Percentages of different age populations from basement zircon ages from different terranes south of the Issyk Kul basin (Figure 5.1c). NTS: North Tien Shan terrane; MTS: Middle Tien Shan terrane; STS: Southern Tien Shan terrane.



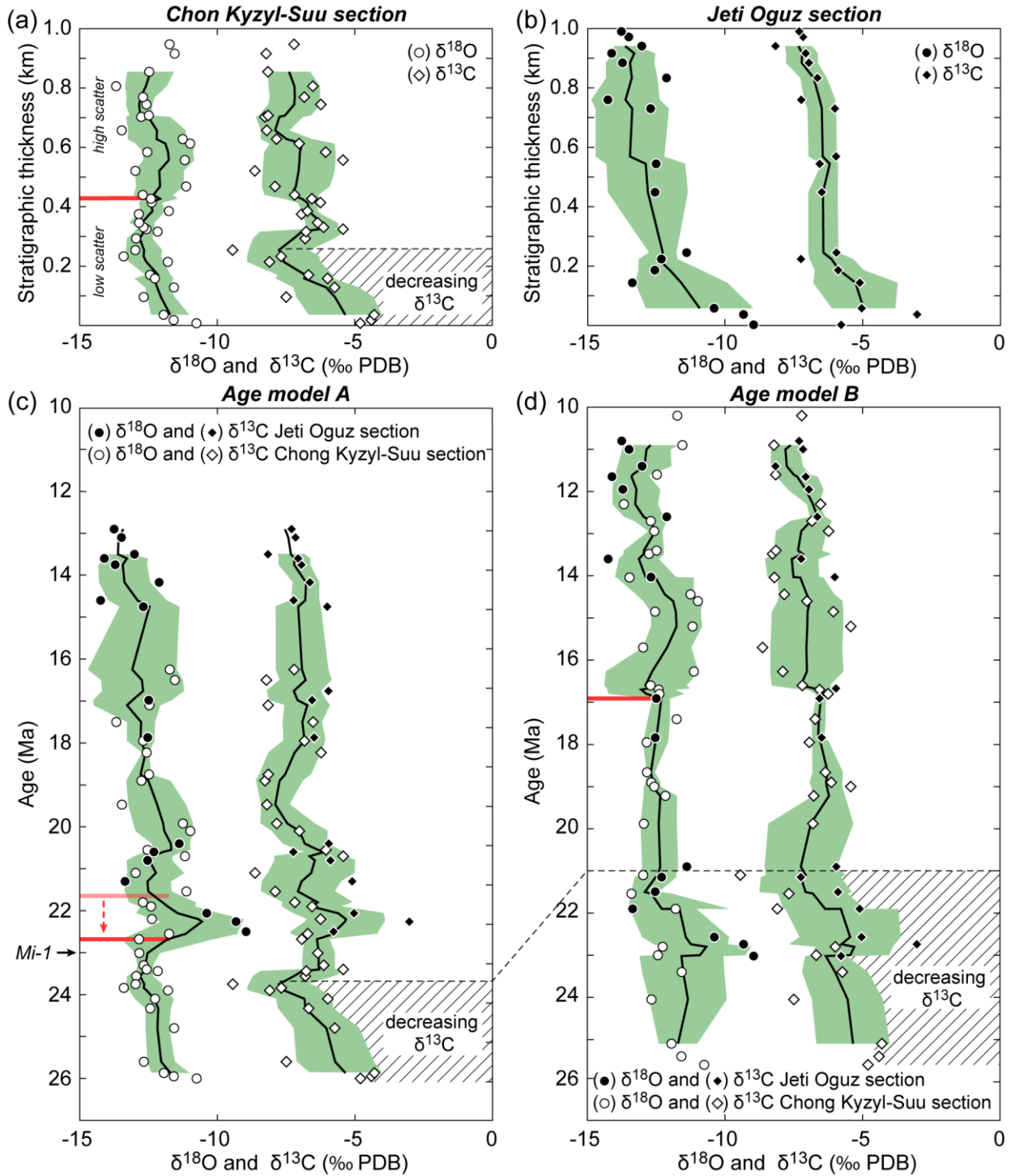


Figure 5.6. (a-b) $\delta^{18}\text{O}$ and $\delta^{13}\text{C}$ values plotted against stratigraphic positions from the Chon Kyzylsu (left) and Jeti Oguz (right) sections. Black lines and green areas represent a 5-point moving mean and the associated standard deviations, respectively. (c-d) $\delta^{18}\text{O}$ and $\delta^{13}\text{C}$ values plotted against age from the two different magnetostratigraphically derived age models. Note the adjusted position of the red line denoting increase $\delta^{18}\text{O}$ scatter.

5.4. Discussion

5.4.1. Sediment provenance

Imbricated clasts from the Dzhety Oguz formation indicate that the fluvial system drained northwards (Figure 5.4a). Furthermore, the conglomerates are dominated by granitic and metasedimentary clasts (Figure 5.4c), both of which are widespread in the Terskey Range,

immediately to the south of the basin (Figure 5.2). These observations imply that the Dzhety Oguz formation in the south-east part of the basin was sourced from the south.

As discussed in Section 5.2.2, each of the three Paleozoic terranes (Northern, Middle and Southern Tien Shan terranes) contains igneous intrusions with different ages. Comparison between zircon U-Pb ages obtained from the sediments and basement lithologies provides a means to assess the contribution of these terranes to sediments in the Issyk Kul basin. For example, the significant amount (up to 25% in the Dzhety Oguz formation) of Cambrian–Early Ordovician zircons ages (541–470 Ma) obtained from the sediments have likely been sourced from the Northern Tien Shan, as the available basement data suggests that igneous bodies with a similar age are absent from the Middle Tien Shan and relatively rare in the Southern Tien Shan (Figures 5.1c and 5.5c). Although the other age populations could have come from any of the three terranes, their relative abundances are generally not consistent with either a Middle or Southern Tien Shan source. The middle Ordovician–Silurian ages (470–419 Ma), which account for the majority of analysed zircons in most samples (Figure 5.5b) are most abundant in the Northern Tien Shan terrane, and are particularly common in the modern catchments of the Jety Oguz and Chon Kyzylsu sections (Figure 5.2). More significantly, very few Precambrian ages were obtained from the sediments (<9%). In contrast, >50% of the analyses performed on igneous bodies from the Middle Tien Shan terrane yielded Precambrian U-Pb ages (Figure 5.5c), implying that the Middle Tien Shan terrane was not a significant source. Rather, we suggest that the few Precambrian grains found in the Issyk Kul basin are recycled from zircon-bearing Precambrian metasedimentary sequences in the North Tien Shan terrane. It therefore seems likely that the sediments of the Issyk Kul basin were sourced exclusively from the Northern Tien Shan basement lithologies in the Terskey Range. This suggests that the drainage divide has remained near the present location since before the onset of late Cenozoic deformation in the Terskey Range, possibly reflecting some residual topography across the region. Importantly, this means that the proximal, coarse-grained sediments of the Dzhety Oguz formation have been sourced from the Terskey Range, supporting the 29–22 Ma onset of deformation inferred from the available thermochronological data (Chapters 2 and 3) [Macaulay *et al.*, 2013; in review], and further constraining it to before 26 Ma.

5.4.2. Stable isotopes

Variations in the $\delta^{18}\text{O}$ and $\delta^{13}\text{C}$ obtained from authigenic carbonates are increasingly used in Central Asia to identify changes in the isotopic value of moisture delivered to an area, and the type and amount of vegetation cover [e.g. Graham *et al.*, 2005; Kent-Corson *et al.*, 2009; Bershaw *et al.*, 2012; Charreau *et al.*, 2012]. Ultimately, these changes could be driven by global or regional climatic variations, topographic changes or shifting moisture sources [e.g. Cole *et al.*, 1999; Blisniuk and Stern, 2005]. These mechanisms seldom operate in isolation, and the isotopic signal usually reflects the cumulative effects of multiple competing factors. Understanding the respective roles and magnitudes of potential drivers, as well as any feedback relationships between them, is therefore essential for interpreting stable isotope data and identifying the likely causes of variations. In this section, we first discuss the initial isotopic signal from over-bank deposits (Section 5.4.2.1); before discussing potentially contamination of this initial signal (Section 5.4.2.2) and the effects of different vegetation on the $\delta^{13}\text{C}$ signal (Section 5.4.2.3). Subsequently, in Section 5.4.2.4, stable isotope data from the sediments are used to differentiate between the two age models derived from magnetostratigraphy (Chapter 4) [Wack *et al.*, in review]. Finally, in Sections 5.4.2.5 and 5.4.2.6, the two distinctive features observed in the Chon Kyzylsu section (Section 5.3.3) are discussed and interpreted.

5.4.2.1. Isotopic signal from over-bank deposits

$\delta^{18}\text{O}$ analysis of carbonate in paleosols usually aims to estimate the isotopic composition of water that infiltrated the sampled sediments soon after deposition. Typically, this carbonate accumulates over tens of thousands of years and the derived $\delta^{18}\text{O}$ values represent a time-averaged signal of soil water [Rowley and Garzzone, 2007]. This in turn is interpreted to reflect the long-term isotopic

composition of local precipitation [Quade *et al.*, 2007]. In contrast, $\delta^{18}\text{O}$ values obtained from lacustrine sediments will ideally reflect the isotopic composition of lake water, and therefore the derived values are controlled by precipitation delivered across the whole catchment and from the hydraulic balance of the lake [Leng *et al.*, 2006]. Similarly, $\delta^{13}\text{C}$ values from paleosols and lacustrine samples reflect carbon input into the soils from organic material that was either sourced locally or from the entire catchment area, which underwent decomposition in the soil or at the bottom of the lake [Leng *et al.*, 2006; Quade *et al.*, 2007]. For further comparison between the isotopic signals derived from paleosol and lacustrine samples see Ballato *et al.* [2010].

In the Dzhety Oguz formation neither lacustrine sediments nor paleosol horizons were available, and samples were instead collected from over-bank deposits (Section 5.3.3). In these settings, the initial $\delta^{18}\text{O}$ values of authigenic carbonate likely reflects moisture delivered to the upstream portion of the catchment area that accumulated during periods of flooding, as well as the effects of any subsequent evaporation. Similarly, $\delta^{13}\text{C}$ values of the sampled sediments likely reflect a combination of organic matter derived from upstream within the catchment that was deposited during flooding of the river system and vegetation that subsequently grew on the flood plain. Therefore, the initial isotopic signal obtained from over-bank deposits is likely to be controlled by moisture and vegetation from the entire catchment area, as it is in lacustrine settings.

5.4.2.2. Potential contamination of initial authigenic isotopic signal

Ideally, the derived isotopic values will reflect authigenic carbonate that precipitated from surficial water and vegetation around the time of deposition. However, this initial isotopic signal may become obscured by recrystallisation of carbonate during burial and diagenesis. The magnitude of this modification depends on the diagenetic history of the sediment, with higher temperature recrystallisation and fluid-mineral interaction being the most detrimental to the preservation of the initial signal [Garzzone *et al.*, 2004]. Diagenetic modification is particularly problematic for the $\delta^{18}\text{O}$ values, which can be altered by the interaction with considerably smaller volumes of fluid compared to the $\delta^{13}\text{C}$ values [Banner and Hanson, 1990; Leier *et al.*, 2009]. However, if this did occur, the $\delta^{18}\text{O}$ values are likely to become homogeneous over closely spaced samples. Therefore, given the significant isotopic variations identified between samples in relatively close proximity from the Chon Kyzylsu section (Figure 5.6a), a major diagenetic overprint seems unlikely. Furthermore, no evidence of veining or sparry calcite was identified in the field or in thin sections of samples, suggesting that diagenetic overprint and secondary calcite growth have not occurred.

Another potential source of carbonate that could lead to the analyzed sediment stable isotope values that are not representative of syn-depositional surficial waters and vegetation is detrital carbonate sourced from basement lithologies. As discussed in Section 5.4.1, sediments of the Dzhety Oguz formation are sourced from the Terskey Range, which contains some carbonate-bearing Precambrian metasediments and Paleozoic sediments. Despite sampling the sedimentary matrix and avoiding detrital clasts, it is possible that some detrital carbonate could have been sampled. However, if that were to be the case, the $\delta^{13}\text{C}$ values obtained from the sediments (between -9 and -3‰) should be significantly higher, as basement samples yielded values from -2.89 to 1.2‰. Moreover, fluctuations in $\delta^{13}\text{C}$ values cannot be correlated with any change in sedimentary provenance and therefore are unlikely to reflect variations in the contributions of different carbonate-bearing basement sources. Furthermore, the red pigmentation of the sediments indicates that deposition occurred under oxidizing conditions [e.g. Walker, 1967]. This is significant as it suggests that groundwater around the time of deposition did not become isolated from soil CO_2 , leading to sulphate reducing conditions or methanogenesis, both of which involve exchanges between the initial carbonates and other carbonate reservoirs, such as detrital carbonate rocks or methane gas [Quade and Roe, 1999]. For these reasons, we suggest that our derived isotopic signals from the over-bank deposits reflect the early groundwater conditions, and that these values can be used to reconstruct paleo-climate and environmental conditions [e.g. Quade and Roe, 1999].

5.4.2.3. Vegetation inferences

$\delta^{13}\text{C}$ values are influenced by the composition of the local vegetation present at the time of deposition, in particular the relative abundances of C3 versus C4 plants and soil respiration [Cerling *et al.*, 1993]. Environments dominated by C3 plants precipitate carbonate with $\delta^{13}\text{C}$ values of *ca.* -12.2‰, compared to values of ~2‰ in C4 dominated areas [Quade *et al.*, 1995]. $\delta^{13}\text{C}$ values from the Dzhety Oguz Formation range between -9.4 and -3.0‰, with a mean value of -6.7‰ (Table 5.2). Therefore, our results are intermediate between the two end members, and could reflect the presence of both C3 and C4 plants in the catchment area, or C3-dominated vegetation that was either under water stress caused by seasonal precipitation or had low soil respiration rates, whereby atmospheric CO_2 had a significant effect on the derived isotopic values [Charreau *et al.*, 2012]. However, the available pollen data suggests that the vegetation cover at the time of deposition was dominated by C3 plants [Fortuna, 1983]. Furthermore, globally and within Central Asia, most data suggest that the expansion of C4 plants occurred after ~8 Ma [Cerling *et al.*, 1993; 1997; Molnar, 2005; Zhang *et al.*, 2009], and therefore, significantly post-dates the 26–11 Ma ages of the sampled Dzhety Oguz formation. Consequently, our results are consistent with C3-dominated vegetation which were either affected by highly seasonal precipitation or low soil respiration rates, rather than a mixture of C3 and C4 plants.

5.4.2.4. Stable isotope values over time

Key features identified in the isotopic record can be used to correlate the two sections, providing a means of evaluating and discriminating between the two different magnetostratigraphic age models derived from magnetostratigraphic correlations (Figure 5.4e). The most useful of these is the decreasing $\delta^{13}\text{C}$ trend identified in the lowermost ~250 m in the Chon Kyzylsu section, which is discussed and interpreted in Section 5.4.2.5. In model A, the lowermost sample from the Jety Oguz section (JTP50) has an inferred age of 22.5 Ma and therefore postdates the interval of decreasing $\delta^{13}\text{C}$ values observed at the Chon Kyzylsu section (~26–23.6 Ma). In contrast, model B suggests that the same sample has an age of 23 Ma, and overlaps by 2 Myr with the interval of decreasing $\delta^{13}\text{C}$ values. In total, six samples from the Jety Oguz section overlap with the negative $\delta^{13}\text{C}$ trend in model B; $\delta^{13}\text{C}$ values from these samples are offset by ~1 to 4‰ from Chon Kyzylsu section samples of similar age (Figure 5.6d). Importantly, four of these samples also show similar offsets when the data from the Chon Kyzylsu and Jety Oguz sections are plotted against model A. Such an isotopic offset between the Chon Kyzylsu and Jety Oguz sections is unlikely to relate to climatic or environmental differences between two sections separated by only 15 km along depositional strike. Furthermore, provenance data suggests that the catchments have not changed significantly in size during the deposition of the Dzhety Oguz formation (Section 5.4.1) and the hyposmetries of similarly sized, adjacent catchments would probably have been consistent. Instead, the discrepancies likely relates to fluctuations in moisture availability, sources of moisture, seasonality or amount of evaporation that are beyond the resolution of our dataset. This interpretation seems to be more consistent with age model A, as the four offset samples are found when $\delta^{13}\text{C}$ and $\delta^{18}\text{O}$ values from Chon Kyzylsu are more scattered (Figure 5.6a+c). In contrast, in model B the offset samples are located where stable isotope data from Chon Kyzylsu are less variable (Figure 5.6a+d). Additionally, the 3.2 Myr age difference between the base of the Chon Kyzylsu and Jety Oguz sections in model A also explains the lack of the decreasing average grain size trend in the Jety Oguz section and the absence of a decrease $\delta^{13}\text{C}$ trend of similar magnitude to that observed at the Chon Kyzylsu section (Figures 5.4b and 5.6a+b). The significance of this grain size reduction in terms of the depositional history of the basin is discussed in Section 5.4.2.5. For the reasons outlined above, we favour model A.

5.4.2.5. Decreasing $\delta^{13}\text{C}$ values between 0 and 250 m in the Chon Kyzylsu section

The decreasing $\delta^{13}\text{C}$ trend could reflect either decreasing hydraulic stress on the C3-dominated vegetation, progressively higher soil respiration rates, or reduced influence of atmospheric CO_2 caused by an up-section decrease in porosity and permeability brought about by the observed decrease in the

grain size (Figure 5.3b). However, for this latter interpretation, it is worth bearing in mind that the observed decrease in grain size relates to the averages of every measured bed, and not the over-bank deposits from which stable isotope samples were collected. The porosity and permeability of these beds appears to remain relatively consistent throughout the section, suggesting that the interaction between soil and atmospheric CO₂ has not significantly varied and cannot account for the decreasing $\delta^{13}\text{C}$ values in the lowermost ~250 m. The remaining two interpretations both point to wetter conditions during the deposition of this portion of the section. Plotting the $\delta^{13}\text{C}$ values against the preferred age model A (Section 5.4.2.4) suggests that the Chon Kyzylsu catchment was getting progressively wetter between ~26.0 and 23.6 Ma (Figure 5.6c). Importantly, previously published pollen data from a similar time interval in the Kazakh Shield (Figure 5.1a) suggests that precipitation decreased between ~25 and 20 Ma (Figure 5.7) [Akhmet'ev *et al.*, 2005]. The occurrence of this precipitation decrease in low relief regions of Central Asia implies that the progressively wetter conditions inferred from our data is unlikely to reflect global or even regional climatic changes. Instead, we suggest that the progressively wetter conditions in the Issyk Kul basin is linked to surface uplift in the Terskey Range to the south. An onset age of 29–26 Ma has been inferred for deformation and rock uplift in the Terskey Range on the basis of thermochronological data (Section 3.5.2) [Macaulay *et al.*, in review] and refined with magnetostratigraphic and sediment provenance data (Chapter 4) [Wack *et al.*, in review] (Section 5.4.1). If our interpretation is correct, this suggests that sufficient topography had developed within the Terskey Range within 3 Myr such that further surface uplift influenced local precipitation. This progressive increase in orographic precipitation need not reflect significant, kilometer-scale topographic relief, and could feasibly relate to relatively minor elevation differences between the Terskey Range and the Issyk Kul basin.

Surface uplift in the Terskey Range also provides an explanation for the coincident decrease in the average grain size that has been observed in the lowermost ~250 m portion of the Chon Kyzylsu section (Figure 5.3b). Crustal shortening accompanied by surface uplift within the range would increase the topographic load, promoting more flexural subsidence in the basin, which turn could have induced a gradual facies retrogradation, whereby coarser grained sediments are replaced by progressively smaller grain sizes at a particular position within the basin. Furthermore, higher flexural subsidence is potentially supported by the instantaneous sedimentation rates derived from magnetostratigraphic data, which despite considerable scatter, suggest that the highest rates are found in the lowermost portion of the Chon Kyzylsu section in model A (Chapter 4) [Wack *et al.*, in review].

5.4.2.6. Increased $\delta^{18}\text{O}$ scatter after ~420 m in the Chon Kyzylsu section

The second stable isotope feature observed at Chon Kyzylsu involves increased $\delta^{18}\text{O}$ scatter at ~420 m (Figure 5.6a), corresponding to ~21.7 Ma in model A (Figure 5.6c). However, the addition of samples from the Jety Oguz section suggests that this increased scatter could have started slightly earlier at ~22.6 Ma (Figure 5.6c). Increased scatter in the ^{18}O values could be caused by short-term fluctuations in moisture availability, sources of moisture, seasonality or amount of evaporation. Interestingly, this adjusted age (~22.6 Ma) is approximately coincident with the global transition from the late Oligocene warm period to the Mi-1 glaciations at ~23 Ma [Zachos *et al.*, 2001]. Following this transition, there were a series of small, intermittent glaciations, each of which would have presumably led to fluctuations in the availability of moisture or a reorganisation of atmospheric circulation leading to changing moisture sources. Therefore, we suggest that the onset of these Miocene glaciations explains the increased scatter of the $\delta^{18}\text{O}$ data at ~22.6 Ma, although at the moment we lack the temporal resolution to determine the associated climatic changes in the Issyk Kul basin.

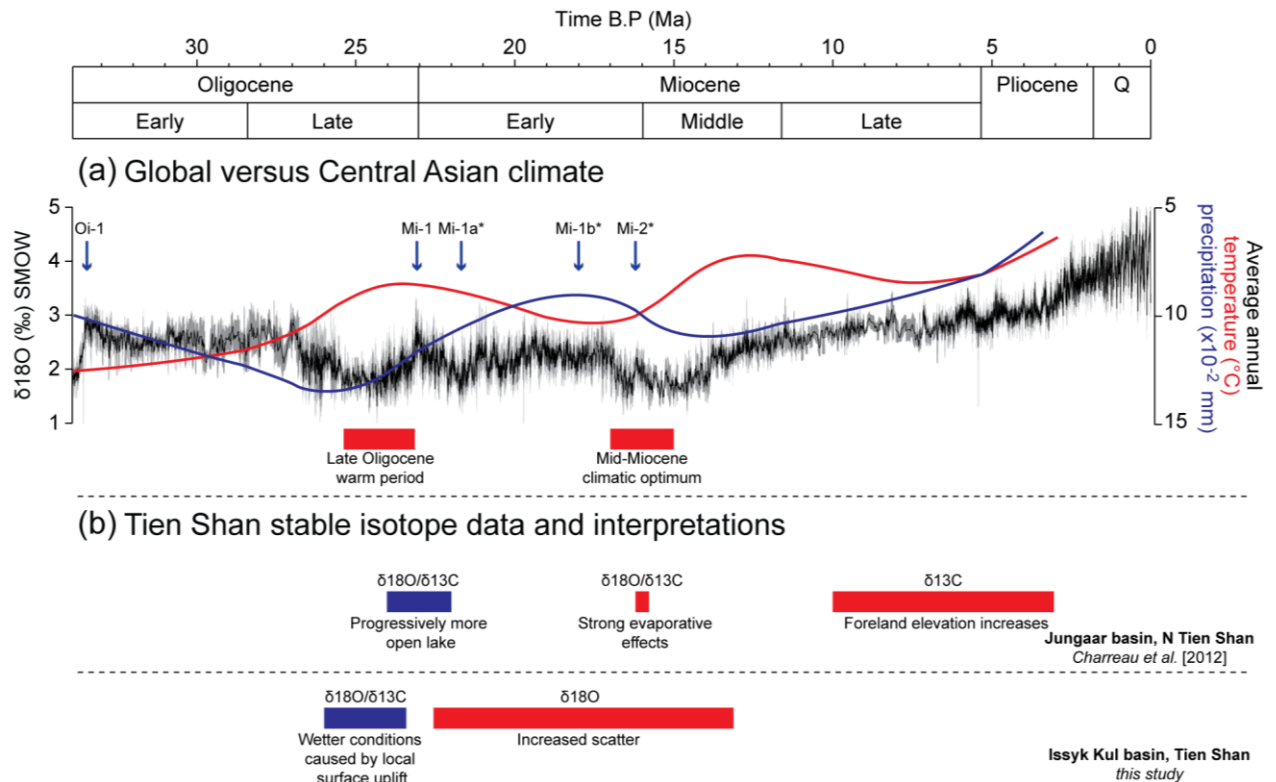


Figure 5.7. (a) Comparison between global and Central Asian climate. Compilation of global $\delta^{18}\text{O}$ records [Zachos *et al.*, 2001] shown by black line and grey swath, which are plotted against the left y-axis and denote a 5-point moving average and the standard deviation, respectively. Trends of annual temperature and precipitation in Central Asia shown by red and blue lines [Akhmet'ev *et al.*, 2005]. These trends have been inferred from pollen data in the Zaisanskaya depression of eastern Kazakhstan (Figure 5.1a). Timing of glaciations (Oi-1 and Mi-1), the Late Oligocene warm period and the Mid-Miocene climatic optimum from Zachos *et al.* [2001]; other glaciations marked with asterisk (Mi-1a, Mi-1b and Mi-2) from Billups *et al.* [2002]. (b) Inferences from stable isotope in and around the Tien Shan. Blue denotes periods when stable isotope values decrease, while red indicates either higher stable isotope values or more scatter in data.

5.5. Conclusions

Zircon U-Pb provenance ages, conglomerate clast analysis and paleocurrent data identify the Terskey Range as the dominant source of sediment in the south-eastern Issyk Kul basin. Crucially, this includes the first syn-tectonic sediments to be deposited (Dzhety Oguz formation), supporting and refining the available thermochronology-based estimates for the onset of deformation in the nearby Terskey Range to 29–26 Ma.

Over-bank deposits from the Dzhety Oguz formation provide the first stable isotope record of climate from an intermontane basin within the Tien Shan. Firstly, this stable isotope data from the two adjacent sections can be compared and used to evaluate accuracy of the two magnetostratigraphic age models. Based on this comparison, we prefer ages from the visual magnetostratigraphic correlation (model A), where the Dzhety Oguz formation was deposited from 26.0 to 16.2 Ma at Chon Kyzylsu and 22.8 to 13.3 Ma at the Jety Oguz section (Chapter 4) [Wack *et al.*, in review]. The $\delta^{18}\text{O}$ values from these sediments are relatively consistent with that expected from calcite precipitates from the modern water samples, and likely reflects the fact that moisture delivered to the region has had to travel great distances and become depleted in ^{18}O . Within our stable isotope record, we have identified two key features. The first is a progressive decrease in $\delta^{13}\text{C}$ values in the lowermost ~250 m of the Dzhety Oguz formation at Chon Kyzylsu (Figure 5.6a), which is interpreted to reflect the region becoming gradually wetter between ~26.0 and 23.6 Ma (Figure 5.6c), as a result of progressively more orographic precipitation as the topography of the Terskey Range increased after the onset of

deformation at 29–26 Ma. Importantly, this provides the first solid evidence that surface uplift accompanied late Cenozoic deformation and rock uplift in the Terskey Range. Subsequently at ~22.6 Ma, the second key feature occurs, where scatter in the stable isotopic data increases. We interpret this change to reflect more variability in moisture availability or sources caused by global climate fluctuations following the transition from the late Oligocene warm period to the early Miocene glaciations (Figure 5.7). Although our climate interpretations are admittedly speculative because our database is small, the sediments stored in the Issyk Kul basin and other intermontane basins within the Tien Shan clearly represent an important archive for understanding climate variations in high elevation, intra-continental settings and for constraining the spatiotemporal distribution of surface uplift.

Acknowledgements

Funding was provided through the Deutsche Forschungsgemeinschaft (DFG) projects SO 436/4-1 and 436 KIR 113/2/0-1. EAM thanks Universität Potsdam and the Mathematisch-Naturwissenschaftliche Fakultät for additional support.

AM acknowledges support through the LOEWE funding program (Landes Offensive zur Entwicklung Wissenschaftlich ökonomischer Exzellenz) of Hesse's Ministry of Higher Education, Research, and the Arts.

Chapter 6.

Discussion and conclusions

The main objective of this thesis has been to identify and date changes in tectonic deformation, climate and surface processes in order to better understand the orogenic evolution of the Central Kyrgyz Tien Shan. This goal has largely been achieved by using a diverse collection of datasets to constrain and infer the exhumation, sedimentation, deformation and climatic histories of many mountain ranges and intermontane basins in the Central Kyrgyz Tien Shan. In doing so, I have been able to constrain the timing of deformation in a transect through the Tien Shan for the first time, and identify variations in the amount of horizontal crustal shortening, which in turn significantly affected exhumation and sedimentation across the region.

In Section 6.1, I first integrate new observations and constraints based on thermochronological, geological, magnetostratigraphic, sedimentological, and paleo-climate proxy data, and summarize the key events in the orogenic evolution of the Central Kyrgyz Tien Shan. In particular, I discuss possible links and feedbacks between the tectonic, climatic and surface processes. These key events are presented in a summary diagram (Figure 6.1). Subsequently, in Section 6.2, I discuss new constraints on the structural architecture of the region and make inferences about how mountain ranges and intermontane basins have grown and developed. Finally, in Section 6.3, I discuss some of the key unresolved questions that have arisen during this study and future research directions that could answer these questions and further improve our understanding of the Tien Shan's orogenic evolution.

6.1. Late Cenozoic orogenic evolution of the Central Kyrgyz Tien Shan

The thermochronologic data presented in this thesis suggest at least two stages of Cenozoic cooling occurred in most of the region's mountain ranges: (1) initially low cooling rates ($<1^{\circ}\text{C}/\text{Myr}$) during the tectonic quiescent period and (2) increased cooling in the late Cenozoic, which occurs diachronously and with variable magnitude in different ranges (Section 3.5.1, Figure 3.6). This second cooling stage is interpreted to represent increased erosion caused by active deformation. Together with geological estimates for the timing of deformation, the timing of this second cooling stage allows the onset of deformation to be constrained in a transect through the Tien Shan for the first time (Chapter 3).

The earliest estimates I have obtained for the onset of deformation are in the late Oligocene and early Miocene; these are found in the Terskey Range (~29–18 Ma) and Sarajaz Range (>19 Ma) (Figure 6.1a). Similar estimates are proposed for the Borkolodoy, Kaindy and Inylchek Ranges based on the amount of late Cenozoic exhumation (Section 3.5.2). In previous studies, late Oligocene–early Miocene estimates have been suggested for the Zailiy Range [De Grave *et al.*, 2013], At Bashi Range [Glorie *et al.*, 2011] and Kokshaal Range [Sobel *et al.*, 2006a] (see Figure 6.1a for locations of ranges). This initial deformation represents the first manifestation of tectonic forces related to the India-Eurasia collision in the Central Kyrgyz Tien Shan, and likely involved the reactivation of the frictionally weakest and most suitably orientated inherited structures available for accommodating north-south directed horizontal shortening.

In the Terskey Range, this late Oligocene–early Miocene estimate of deformation is supported by new magnetostratigraphic age constraints on the sedimentary record of the adjacent Issyk Kul basin (Chapter 4). These data suggest that the first coarse grained sediments indicative of a proximal, actively deforming source started being deposited at 26 Ma (Section 4.3.4). Interestingly, the basal ages of this first syn-tectonic sedimentary unit differs by 3.2 Myr between two sections located <15 km apart (Figure 6.1a). Such diachronous deposition could reflect the eastward propagation of deformation in the Terskey Range, which is also observed in thermochronologically-derived estimates (Section 3.5.3). Alternatively, the diachroneity could be explained by minor topographic differences

(<0.3 km) in the basin that took 3.2 Myr to be infilled because of the low sedimentation rates (~0.09 km/Myr). Either way, the deposition of this sedimentary unit was highly time-transgressive.

Comparing the available absolute ages for initial syn-tectonic sediments in different intermontane basins reveals even larger time variations, at least as the locations where magnetostratigraphic studies have been conducted. Deposition of these first syn-tectonic sediments started >13 Myr earlier in the Issyk Kul basin than the Naryn basin (Figure 6.2a). This large time difference likely relates in part to the position of the sampled sections with respect to actively deforming mountain ranges. In the Issyk Kul basin, the magnetostratigraphically-derived basal ages presented in this thesis are presently located <10 km from the source area in the Terskey Range. In contrast, the younger ages from the Naryn basin were obtained from more distal settings [Abdrakhmatov *et al.*, 2001]. Furthermore, many of the mountain ranges that presently surround the Naryn basin were not actively deforming during the deposition of the first syn-tectonic unit and the dated sections were likely located in the middle of a large intermontane basin extending between the Terskey Range to the north and the At Bashi Range to the south. Therefore, it is not surprising that such a large time variation is observed.

In the Issyk Kul basin, stable isotope data were collected from the two parallel magnetostratigraphically-dated sections (Chapter 5). These data suggest that following the onset of deformation in the Terskey Range, the region became progressively wetter (Figure 5.5). In Section 5.4.2.5, I have suggested that this reflects increased orographic precipitation within the Terskey Range. These data provide the first evidence that surface uplift accompanied late Cenozoic deformation and rock uplift in the Terskey Range; this is the first time a link between the development of a specific mountain range and orographically enhanced precipitation has been documented in the Tien Shan on the basis of climatic data. Moreover, sedimentological data reveals that this period of surface uplift and wetter conditions coincided with a decrease in the average grain size, possibly reflecting progressively more flexural subsidence in the basin caused by an increasing topographic load (Section 5.4.2.5). If similar records were to become available for other intermontane basins, it could provide an important tool for assessing surface uplift histories of individual mountain ranges and investigating the interactions of tectonic, climatic and surface processes.

Subsequently, in the late Miocene (~12–5 Ma), deformation started in the Issyk Kul Broken Foreland and Jetym Ranges. Importantly, the onset of deformation in these ranges does not coincide with a decrease in exhumation of ranges that had started deforming earlier. Based on this observation, I have suggested in Section 3.5.3 that the locus of deformation cannot have shifted in the late Miocene; if this had occurred, there should have been a cessation or reduction in deformation and presumably exhumation in the ranges that formed earlier to maintain the same bulk crustal shortening. Instead, thermochronological data from the Terskey Range, which started deforming earlier at ~29–18 Ma, shows that exhumation actually increased in the late Miocene (Figure 3.6). Also at this time, activity appears to have started on the Central Terskey Fault (CTF) (Section 2.4.3). Collectively, the approximately coincident onset of deformation in the Issyk Kul Broken Foreland and Jetym Ranges, the reactivation of the Central Terskey Fault, and the increased exhumation of the Terskey Range suggests that there must have been an overall increase in the rate of horizontal crustal shortening. Similar late Miocene increases in magnitude deformation have been proposed in numerous locations within the Tien Shan [Abdrakhmatov *et al.*, 1996; 2001; Sobel *et al.*, 2006a; Glorie *et al.*, 2010; 2011] and has been linked to a regional change in Central Asian deformation [Sobel *et al.*, 2011].

This late Miocene increase in the magnitude of deformation is approximately synchronous with an inferred increase in sedimentation rate and a significant fining upwards change in sedimentary facies distribution (Section 5.2). This change involves the transition between the first syn-tectonic unit (Shamsi group) to the lighter coloured, better sorted and generally more fine-grained channelized sand and conglomerates of the Chu group, which forms the main basin filling unit of the Central Kyrgyz Tien Shan [Abdrakhmatov *et al.*, 2001]. Such a change in sedimentation rates and facies distribution could conceivably be caused by tectonic or climatic changes [e.g. Allen *et al.*, 2013]. In the former

case, increased shortening across the Central Kyrgyz Tien Shan could have promoted increased tectonic subsidence within intermontane basins, thus explaining the increased sedimentation rates. Moreover, provided that the sediment supply did not significantly outpace basin subsidence, increased tectonic subsidence could also account for the retrogradation of sedimentary facies, which has been observed at numerous locations between the Shamsi and Chu groups [Abdrakhmatov *et al.*, 2001; Burgette, 2008; Selander *et al.*, 2012]. Alternatively, pollen data suggest that since the late Miocene, the Central Kyrgyz Tien Shan became more arid [Fortuna, 1983], which could potentially have reduced sediment supply into the basin and caused facies retrogradation. However, in the thermochronological data from the Terskey Range, the decrease in exhumation that would be expected to accompany a reduction in the supply of sediment is not observed (Chapter 2 and 3). For this reason, I favour the former interpretation where the sedimentary change is tectonically driven.

The last stage in the orogenic evolution of the Central Kyrgyz Tien Shan involves the onset of deformation in the Kungey [Selander *et al.*, 2012], Karakudjur, Naryntoo and Akshyirak Ranges (Chapter 3) in the Pliocene–Pleistocene. The onset of deformation in these ranges also seems to approximately coincide with a significant sedimentary change, although the precise timing remains poorly constrained. This change involves the well-sorted channelized sand and conglomerate deposits of the Chu group which are replaced by the poorly sorted conglomerates of the Sharpyldak group [Abdrakhmatov *et al.*, 2001]. Once again, this change could feasibly be caused by tectonic or climatic forcing, which cannot presently be differentiated [Bullen *et al.*, 2003; Sobel *et al.*, 2006b; Burgette, 2008; Trifonov *et al.*, 2008]. The summary of key events outlined above represents a significant step forward in understanding the orogenic evolution of the Central Kyrgyz Tien Shan and provides a solid framework for future studies that may uncover further details in the coupled tectonic and climatic evolution of the region.

6.2. Structural architecture of the Central Kyrgyz Tien Shan

In addition to identifying and dating key events in the orogenic evolution of the Central Kyrgyz Tien Shan, data presented in this thesis have also provided numerous new insights into the underlying structural architecture of the region and the roles of individual structures in creating mountain ranges and intermontane basins. Arguably, the most significant of these insights is determining which inherited structures have been reactivated in the late Cenozoic and identifying their sense of displacement. Many of these structures are located within mountain ranges and have basement lithologies exposed on both sides. Therefore, field evidence of late Cenozoic reactivation is relatively hard to come by, and in many cases, it was previously unclear whether many of these structures had been reactivated. Based on the offset of thermochronological ages presented in this thesis, I have been able to show that the Central Terskey Fault (CTF), Tyulek Fault (TF) and Southern Tien Shan Suture (STSS) were reactivated in the late Cenozoic (Figure 6.1a); furthermore, I have been able to identify the late Cenozoic relative sense of vertical displacement for the first time (Figure 3.4). Interestingly, my thermochronological data suggests that the sense of vertical displacement often varies along strike. For example, in the west, the Central Terskey Fault (CTF) has up-thrown its southern side, whereas in the east, the northern side is up-thrown (Section 3.4.2). Similarly, other structures, like the Nikolaev Line (NL), have only been reactivated in certain parts (Figure 6.1a). Most of the structures, in which along-strike variations in vergence and the magnitude of displacement have been identified correspond to steeply dipping Permian strike-slip faults [Bazhenov and Mikolaichuk, 2004]. For these steeply dipping structures, even minor along-strike differences in the inherited geometry could result in a change of vergence or the ability to accommodate dip-slip displacement, potentially providing an explanation for the observed variations. The slip of most of these steeply dipping structures is directed vertically, meaning that they can have a disproportionate influence of tectonically-driven rock uplift and exhumation within a mountain range. Consequently, the along strike differences in the vergence of the Central Terskey Fault (CTF) have significantly affected the magnitudes rock uplift and

exhumation, which will have undoubtedly influenced the development of the Terskey Range. Nevertheless, the contribution of these steeply dipping structures to horizontal shortening across the Central Kyrgyz Tien Shan is negligible.

The vast majority of horizontal shortening appears to have been accommodated by range-bounding faults (Chapter 2). In the Terskey Range, based on thermochronologically-derived structural markers, I have suggested that the inclination of the range-bounding fault system to the north of the range decreases with depth, causing block rotation or fault-bend folding within the range (Chapter 2). Furthermore, new fault kinematic data from this range-bounding fault system suggests that it initially developed around a reactivated structure, and then propagated northwards along newly initiated foot wall short-cuts. A similar model involving the basin-ward propagation of range-bounding structures has been proposed for the Kungey Range to the north of the Issyk Kul basin by *Selander et al.* [2012]. However, in the Kungey Range, the range-bounding faults have not reactivated inherited structures, although their initiation may have been assisted by the Kungey and Kemin-Chilik Faults (KF) in the middle of the range. The presence of the inherited structure within the fault system bounding the Terskey Range can potentially explain why deformation started earlier there than in the Kungey Range. Therefore, it seems likely that the inherited structures within the Central Kyrgyz Tien Shan have dictated the spatiotemporal distribution of deformation, controlling the timing and locations of range and basin development, and strongly influencing the pattern of exhumation within many basement-cored ranges.

6.3. Remaining research questions and future directions

Despite the many new insights and constraints on the orogenic evolution of the Central Kyrgyz Tien Shan derived from the data presented in this thesis, many important questions remain. To my mind, arguably the most significant of these questions is what makes a particular inherited structure, or part of the structure, more prone to tectonic reactivation? In this thesis, I have suggested that some of the irregularities in the orogenic evolution of the Central Kyrgyz Tien Shan during the late Cenozoic, such as the out-of-sequence onset of deformation (Chapter 3), relate to differences in the suitability and susceptibility of inherited structures to tectonic reactivation. Crucially, however, the data presented here are not able to identify why some structures are more prone to reactivation. If this could be resolved by collecting detailed geological data from fault zones and determining the pre-activation geometry of the structures, it would lead to a much more complete understanding of orogenic development within the Central Kyrgyz Tien Shan and potentially other intra-continental settings around the world.

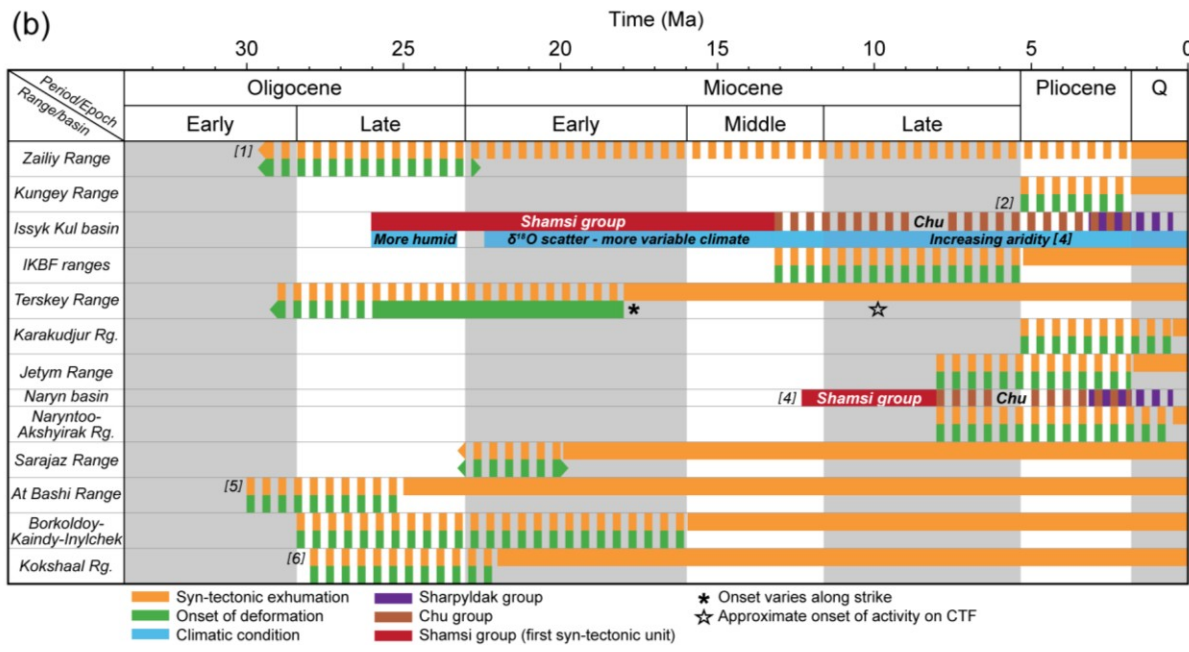
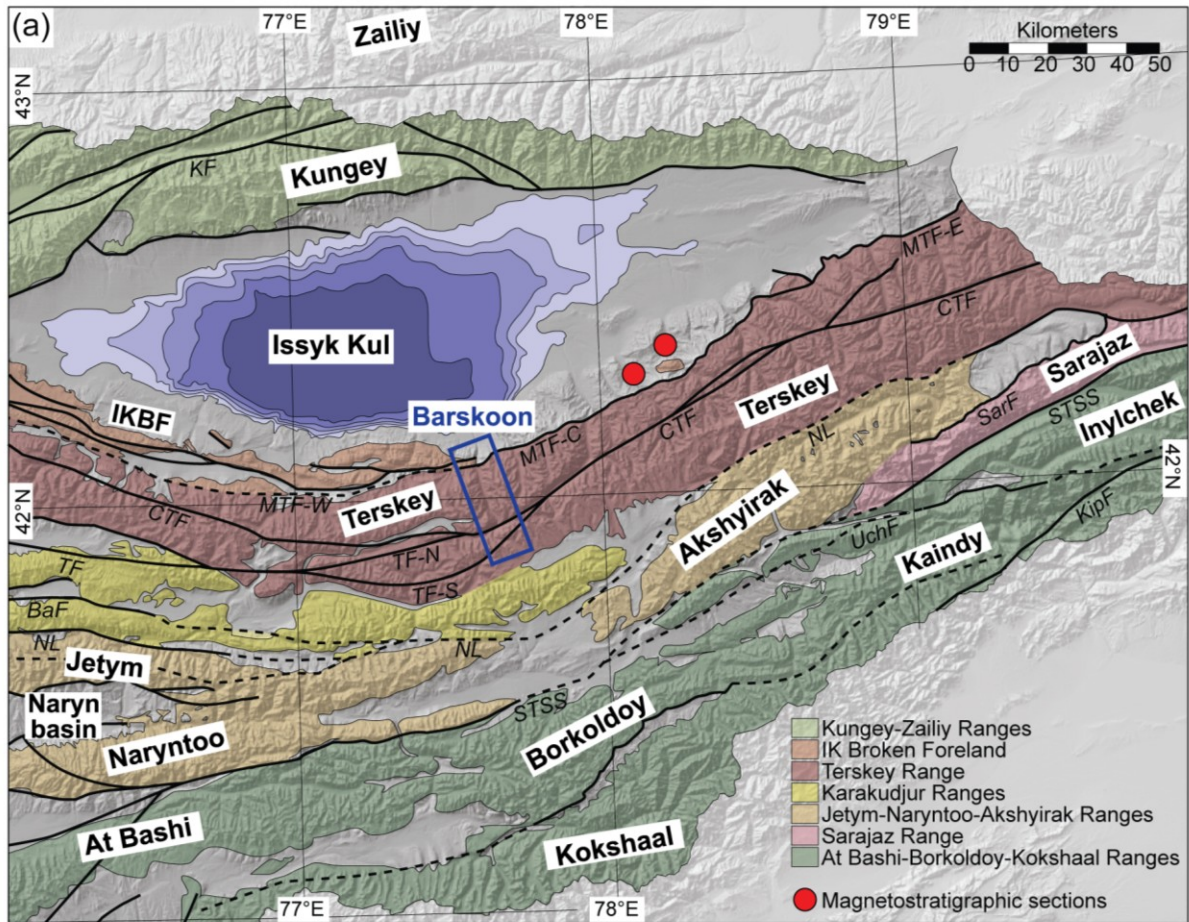
In general, more quantitative constraints on deformation in the Central Kyrgyz Tien Shan are needed to address many fundamental questions about the mechanics of tectonic processes in this intra-continental setting. For example, constraining the timing and displacements of individual range-bounding faults could provide valuable information about whether the initiation of new foot wall short-cuts from a reactivated structure, as observed in the Terskey Range (Chapter 2), relates to a decrease in the efficiency of slip on inherited structures or an erosional decrease across the mountain range, as predicted from critical Coulomb wedge mechanics [*Davis et al.*, 1983; *Dahlen et al.*, 1984; *Dahlen*, 1990]. Another potentially valuable source of information is the sedimentary record of intermontane basins, which remains poorly constrained. Furthermore, if these age controls were combined with stable isotope or other climatic proxy data, as in Chapter 5, the surface uplift history of adjacent mountain ranges could also be inferred, providing important insights into the orogenic evolution of the region. In particular, the comparison of climate conditions inferred from pre-tectonic sediments of the Koktorpak/Suluterek group at multiple locations in both modern basins and mountain ranges could provide an indication of any differences in elevation that may have existed in the early Cenozoic, testing the hypothesis that during the period of tectonic quiescence the Central Kyrgyz Tien

Shan had a relatively low relief [e.g. *Chediya*, 1986; *Fortuna et al.*, 1994; *Bullen et al.*, 2001; 2003; *Sobel et al.*, 2006b; *De Grave et al.*, 2007; 2013; *Glorie et al.*, 2011; *Macaulay et al.*, 2013; in review].

Indeed, although this thesis has focussed on the late Cenozoic orogenic evolution of the Central Kyrgyz Tien Shan, some of the data presented here have important implications for the earlier history of the region, and have posed many new questions that I believe could prove to be fruitful avenues of research. Potentially one of the most interesting and important unresolved questions concerns the spatiotemporal distribution of Mesozoic deformation. Time-temperature modelling of thermochronological data presented in this thesis suggests that the most pronounced Mesozoic cooling occurred in the early Jurassic (Figure 3.2c). I have interpreted this increased cooling to reflect active deformation in the Central Kyrgyz Tien Shan. However, the spatial extent of this deformation remains poorly constrained. This could be addressed by obtaining more zircon (U-Th-Sm)/He data, which would allow the higher temperature portion of the cooling histories to be better constrained in more samples, and provide an indication as to whether increased cooling in the early Jurassic was geographically widespread across the Tien Shan. Constraining the timing and location of this early Jurassic deformational phase as well as other proposed Mesozoic–early Cenozoic deformation phases [*Sobel and Dumitru*, 1997; *Dumitru et al.*, 2001; *De Grave et al.*, 2007; 2011a; 2011b; 2013; *Glorie et al.*, 2011] is essential to identify the causative mechanisms of active deformation at those times. In particular, such data may clarify whether the various phases of Mesozoic deformation reflect delayed responses to the accretion of terranes (e.g. the Qiantang, Lhasa and Kohistan-Dras collisions) along the southern Eurasian margin or the closure of the Mongol-Okhotsk ocean to the east [*Hendrix et al.*, 1992; *Dumitru et al.*, 2001; *Jolivet et al.*, 2010].

In summary, although this study has merely scratched the surface in terms of understanding the complex and highly irregular orogenic evolution of the Central Kyrgyz Tien Shan, I have provided a strong temporal framework and chronology of key events upon which future work can build. Furthermore, as I have shown in this thesis, by collecting numerous different robust datasets that integrate tectonic deformation, climate, exhumation and sedimentation, it is possible to unravel the complex evolution of the Central Kyrgyz Tien Shan and constrain the processes that have shaped its development.

Figure 6.1. (a) Simplified geological map of Eastern Kyrgyzstan showing distribution of Precambrian and Paleozoic basement (colours) and Mesozoic–Cenozoic sediments (grey). Different basement-cored ranges are coloured, see legend for names. Names of ranges and intermontane basins are also shown by blue labels. Blue outlined box shows the Barskoon region (Chapter 2). Red dots are the locations of magnetostratigraphic sections (Chapters 4 and 5). Thick blue lines show location of major faults. Solid lines = active in late Cenozoic; dashed line = non-active in late Cenozoic. KF: Kungey Fault and Kemin Chilik Fault; MTF: Main Terskey Fault (W, C, E: West, Central and East segments); CTF: Central Terskey Fault; TF: Tyulek Fault; BaF: Baidulla Fault; NL: Nikolaev Line; STSS: Southern Tien Shan Suture; UchF: Uchchat; KipF: Kipchak Fault. (b) Summary diagram of exhumation, deformation, sedimentation and climate data from the Central Kyrgyz Tien Shan. Timing inferred from previously published data shown by numbers in square brackets. 1: *De Grave et al.* [2013]; 2: *Selander et al.* [2012]; 3: *Fortuna* [1983]; 4: *Abdrakhmatov et al.* [2001]; 5: *Glorie et al.* [2011]; 6: *Sobel et al.* [2006a].



References

- Abdrachmatov, K. E., D. Delvaux, and K. D. Djanuzakov (2002), Active tectonics and seismic hazard of the Issyk-Kul Basin in the Kyrgyz Tian-Shan, in *Lake Issyk-Kul: Its natural environment*, vol. IV. Earth and Environmental Sciences, v.13, edited by J. Klerx and B. Imanackunov, pp. 147-160, NATO Science Series, IOS Press, Amsterdam.
- Abdrakhmatov, K. Y., S. A. Aldazhanov, B. H. Hager, M. W. Hamburger, T. A. Herring, K. B. Kalabaev, K. B. Kalabayev, V. I. Makarov, P. Molnar, S. V. Panasyuk, M. T. Prilepin, R. E. Reilinger, I. S. Sadybakasov, B. J. Souter, Y. A. Trapeznikov, V. Y. Tsurkov, and A. V. Zubovich (1996), Relatively recent construction of the Tien Shan inferred from GPS measurements of present-day crustal deformation rates, *Nature*, 384(6608) 450-453, doi: 10.1038/384450a0.
- Abdrakhmatov, K. E., R. Weldon, S. Thompson, D. Burbank, C. Rubin, M. Miller, and P. Molnar (2001), Origin, direction, and rate of modern compression in the central Tien Shan, Kyrgyzstan, *Geologiya i Geofizika (Russian Geology and Geophysics)*, 42, 1585-1609.
- Afonichev, N. A., and H. G. Vlasov (1984), Geologicheskaya karta Kazakhstana i Sredney Azii (so stratigraficheskimi kolonkami), Mashtab: 1:1,500,000 (Geological map of Kazakhstan and Middle Asia (with stratigraphic columns), scale 1:1,500,000).
- Aizen, E. M., V. B. Aizen, J. M. Melack, T. Nakamura, and T. Ohta (2001), Precipitation and atmospheric circulation patterns at mid-latitudes of Asia, *International Journal of Climatology*, 21, 535-556, doi: 10.1002/joc.626.
- Aizen, V. B., E. M. Aizen, and J. M. Melack (1995), Climate, snow cover, glaciers and runoff in the Tien Shan, Central Asia, *Water Resources Bulletin*, 31(6), doi: 10.1111/j.1752-1688.1995.tb03426.x.
- Aizen, V. B., E. M. Aizen, J. M. Melack, and J. Dozier (1997), Climatic and hydrologic changes in the Tien Shan, Central Asia. *Journal of Climate*, 10(6), 1393-1404, doi: 10.1175/1520-0442(1997)010<1393:CAHCIT>2.0.CO;2.
- Akhmeteyev, M. A., A. E. Dodoniv, M. V. Somikova, I. I. Spasskaya, K. V. Kremenetsky, and V. A. Klimanov (2005), Kazakhstan and Central Asia (plains and foothills). *Geological Society of America Special Papers*, 382, 139-161, doi: 10.1130/0-8137-2382-5.139.
- Alekseev, D. V., K. E. Degtyarev, A. B. Kotov, E. B. Sal'nikova, A. A. Tret'yakov, S. Z. Yakovleva, I. V. Anisimova, and K. N. Shatagin (2009), Late Paleozoic Subductional and Collisional Igneous Complexes in the Naryn Segment of the Middle Tien Shan (Kyrgyzstan), *Doklady Earth Sciences*, 427(5), 760-763.
- Allen, M. B., and S. J. Vincent (1997), Fault reactivation in the Junggar region, northwest China: The role of basement structures during Mesozoic-Cenozoic compression, *J. Geol. Soc.*, 154, 151-155, doi: 10.1144/gsjgs.154.1.0151.
- Allen, M. B., A. M. C. Sengör, B. A. Natal'in (1995), Junggar, Turfan and Alakol basins as Late Permian to ?Early Triassic extensional structures in a sinistral shear zone in the Altaid orogenic collage, Central Asia, *Journal of the Geological Society*, 152(2), 327-338, doi: 10.1144/gsjgs.152.2.0327.
- Allen, P. A., J. J. Armitage, A. Carter, R. A. Duller, N. A. Michael, H. D. Sinclair, A. L. Whitchurch, and A. C. Whittaker (2013), The Qs problem: Sediment volumetric balance of proximal foreland basin systems, *Sedimentology*, 60(1), 102-130, doi: 10.1111/sed.12015.
- Allmendinger, R. W., N. Cardozo, and D. Fisher (2012), *Structural geology algorithms: Vectors and tensors in structural geology*, Cambridge University Press, Cambridge, UK.
- Apayarov, F. K. (2002), Kumyshtag intrusion as an age reference point in Talas Alatau (Northern Tien Shan, in *Environmental problems of development of mineral - raw material resources of mountains of Tien Shan* (In Russian), edited, pp. 67-71, Bishkek.
- Apayarov, F. K. E. (2007), Geological research of 1:200 000 scale on the near-boundary territory at the western part of the Kyrgyz Ridge within K-42-XII, K-42-XVIII, K-43-VII, K-43-VIII, K-43-XIII, K-43-XIV sheets, *Archives of the ministry of natural resources of the Kyrgyz Republic*, Ivanovka.
- Apayarov, F. K. (2009), Almalsaiskiy massif (structure, composition and age) and its significance as a regional reference point for the Tien Shan Caledonides, in *Geology and mineral deposits* (In Russian), edited by K. Z. Kurmanaliev, pp. 141-151, Bishkek.
- Apayarov, F. K. (2010), Early Devonian intrusives of Northern Tien Shan (in Russian), *Natural Resources: Journal of ministry of natural resources of Kyrgyz Republic*, 1, 14-21.
- Araguás-Araguás, L., K. Froehlich, and K. Rozanski (1998), Stable isotope composition of precipitation over southeast Asia, *Journal of Geophysical Research: Atmospheres (1984-2012)*, 103(D22), 28721-28742, doi: 10.1029/98JD02582.
- Avouac, J. P., P. Tapponnier, M. Bai, H. You, and G. Wang (1993), Active thrusting and folding along the northern Tien Shan and late Cenozoic rotation of the Tarim relative to Dzungaria and Kazakhstan, *Journal of Geophysical Research*, 98, 6755-6804, doi: 10.1029/92JB01963.
- Avouac, J. P., and E. B. Burov (1996), Erosion as a driving mechanism of intracontinental mountain growth, *Journal of Geophysical Research*, 101(B8), 17747-17, doi: 10.1029/96JB01344.
- Baev, D. G., V. I. Chernov, and A. P. Bashkirov (1989), Geological structure and minerals of Ak-Shyirak (east) Range (K-44-61-G-v,g; K-44-73-A,B,V,G sheets). Report of the Akbel party on geological survey and exploration activity at a scale 1:50 000 carried out in 1983-1989 years, *Archives of the State Geological Agency of the Kyrgyz Republic*, Frunze.
- Bakirov A. B., and V. S. Burtman (1984), Tectonic history of the Turkestan Paleoocean, in *Tectonics of the Tien Shan Variscides: Guidebook for excursion 27th International Geological Congress*, pp. 19-23, Bishkek, Kyrgyzstan.
- Bakirov, A. B., and R. A. Maksumova (2001), Geodynamic evolution of the Tien Shan lithosphere, *Russian Geology and Geophysics*, 42(10), 435-443.
- Ballato, P., A. Mulch, A. Landgraf, A., M. R. Strecker, M. C. Dalconi, A. Friedrich, and S. H. Tabatabaei (2010), Middle to late Miocene Middle Eastern climate from stable oxygen and carbon isotope data, southern Alborz mountains, N Iran, *Earth and Planetary Science Letters*, 300(1), 125-138, doi: 10.1016/j.epsl.2010.09.043.
- Banner, J. L., and G. N. Hanson (1990), Calculation of simultaneous isotopic and trace element variations during water-rock interaction with applications to carbonate diagenesis, *Geochimica et Cosmochimica Acta*, 54(11), 3123-3137, doi: 10.1016/0016-7037(90)90128-8.
- Bazhenov, M. L., and A. V. Mikolaichuk (2004), Structural Evolution of Central Asia to the North of Tibet: A Synthesis of Paleomagnetic and Geological Data, *Geotectonics*, 38(5), 379-393.
- Bazhenov, M. L., A. Q. Collins, K. E. Degtyarev, N. M. Levashova, A. V. Mikolaichuk, V. E. Pavlov, and R. Van der Voo (2003), Paleozoic northward drift of the North Tien Shan (Central Asia) as revealed by Ordovician and Carboniferous paleomagnetism, *Tectonophysics*, 366, 113-141, doi: 10.1016/S0040-1951.
- Berger, A. L., S. P. Gulick, J. A. Spotila, P. Upton, J. M. Jaeger, J. B. Chapman, L. A. Worthington, T. L. Pavlis, K. D. Ridgway, B. A. Willems, and R. J. McAleer (2008), Quaternary tectonic response to intensified glacial erosion in an orogenic wedge, *Nature Geoscience*, 1(11), 793-799, doi: 10.1038/ngeo334.
- Bershaw, J., C. N. Garzzone, L. Schoenbohm, G. Gehrels, and L. Tao (2012), Cenozoic evolution of the Pamir plateau based on stratigraphy, zircon provenance, and stable isotopes of foreland basin sediments at Oyttag (Wuyitake) in the Tarim Basin (west China), *Journal of Asian Earth Sciences*, 44, 136-148, doi: 10.1016/j.jseas.2011.04.020.
- Bespalov, V. P. (editor) (1979), Geological Map of the USSR of 1:200000 scales, Northern Tien-Shan series, *Sheet K-43-XI*, Russian Geological Research Institute (VSEGEI), Nedra, Moscow.
- Besse, J., and V. Courtillot (2002), Apparent and true polar wander and the geometry of the geomagnetic field over the last 200 Myr, *Journal of Geophysical Research*, 107, 2300.

- Billups, K., J. E. T. Channell, and J. Zachos (2002), Late Oligocene to early Miocene geochronology and paleoceanography from the subantarctic South Atlantic, *Paleoceanography*, *17*(1), 4-1, doi: 10.1029/2000PA000568.
- Biske, G. S. (1995), Late Paleozoic Collision of the Tarim and Kyrgyz-Kazakhstan Paleococontinents, *Geotektonika*, *30*(1), 31-39.
- Blisniuk, P. M., and L. A. Stern (2005), Stable isotope paleoaltimetry: A critical review. *American Journal of Science*, *305*(10), 1033-1074, doi: 10.2475/ajs.305.10.1033.
- Borradaile, G. J., and D. H. Tarling (1981), The influence of deformation mechanisms on magnetic fabrics in weakly deformed rocks, *Tectonophysics*, *77*, 151-168.
- Brandon, M. T., M. K. Roden-Tice, and J. I. Garver (1998), Late Cenozoic exhumation of the Cascadia accretionary wedge in the Olympic Mountains, northwest Washington State, *Geol. Soc. Am. Bull.*, *110*, 985-1009, doi: 10.1130/0016-7606(1998)110<0985:1CEOTC>2.3.CO;2.
- Braun, J. (2002), Quantifying the effect of recent relief changes on age-elevation relationships, *Earth and Planetary Science Letters*, *200*, 331-343, doi: 10.1016/S0012-821X(02)00638-6.
- Brown, R. W., R. Beucher, K. Gallagher, C. Persano, F. Stuart, and P. Fitzgerald (2011), A new approach to deriving thermal history information from apatite (U-Th)/He analyses which exploits the natural dispersion of single grain age determinations, *Geophysical Research Abstracts*, *13*, EGU2011-8194-3.
- Bullen, M. E., D. W. Burbank, J. I. Garver, and K. Y. Abdрахmatov (2001), Late Cenozoic tectonic evolution of the northwestern Tien Shan: New age estimates for the initiation of mountain building, *Geological Society of America Bulletin*, *113*(12), 1544-1559, doi: 10.1130/0016-7606(2001)113<1544:1CTEOT>2.0.CO;2.
- Bullen, M. E., D. W. Burbank, and J. I. Garver (2003), Building the Northern Tien Shan: Integrated thermal, structural, and topographic constraints, *Journal of Geology*, *111*(2), 149-165, doi: 10.1086/345840.
- Burbank, D. W. (1992), Causes of recent Himalayan uplift deduced from deposited patterns in the Ganges basin, *Nature*, *357*(6380), 680-683, doi: 10.1038/357680a0.
- Burbank, D. W., J. K. McLean, M. Bullen, K. Y. Abdрахmatov and M. M. Miller (1999), Partitioning of intermontane basins by thrust-related folding, Tien Shan, Kyrgyzstan, *Basin Research*, *11*, 75-92, doi: 10.1046/j.1365-2117.1999.00086.x
- Burgette, R. J. (2008), Uplift in response to tectonic convergence: The Kyrgyz Tien Shan and Cascadia subduction zone, PhD thesis, Department of Geological Sciences, University of Oregon, USA.
- Burtman, V. S. (1975), Structural geology of Variscan Tien Shan, USSR, *American Journal of Science*, *275-A*, 157-186
- Burtman, B. S. (2006), The Tien Shan Early Paleozoic tectonics and geodynamics, *Russian Journal of Earth Sciences*, *8*, 1-23.
- Burtman, V. S. (2010), Tien Shan, Pamir, and Tibet: history and geodynamics of Phanerozoic oceanic basins, *Geotectonics*, *44*(5), 388-404, doi: 10.1134/S001685211005002X.
- Carlson, W. D., R. A. Donelick, and R. A. Ketcham (1999), Variability of apatite fission-track annealing kinetics: I. Experimental results, *American Mineralogist*, *84*(9), 1213-1223.
- Cerling, T. E., Y. Wang, and J. Quade (1993), Expansion of C4 ecosystems as an indicator of global ecological change in the late Miocene, *Nature*, *361*(6410), 344-345, doi: 10.1038/361344a0.
- Cerling, T. E., J. M. Harris, B. J. MacFadden, M. G. Leakey, J. Quade, V. Eisenmann, and J. R. Ehleringer (1997), Global vegetation change through the Miocene/Pliocene boundary, *Nature*, *389*(6647), 153-158, doi: 10.1038/38229.
- Chabdarov, N. M. (editor) (1962) Geological Map of the USSR of 1:200000 scales, Northern Tien-Shan series, *Sheet K-44-VII*, Russian Geological Research Institute (VSEGEI), Nedra, Moscow.
- Charreau, J., Y. Chen, S. Gilder, S. Dominguez, J. P. Avouac, S. Sen, D. Sun, Y. Li, and W. M. Wang (2005), Magnetostratigraphy and rock magnetism of the Neogene Kuitun He section (northwest China): implications for Late Cenozoic uplift of the Tianshan mountains, *Earth and Planetary Science Letters*, *230*, 177-192, doi: 10.1016/j.epsl.2004.11.002.
- Charreau, J., S. Gilder, Y. Chen, S. Dominguez, J. P. Avouac, S. Sen, M. Jolivet, Y. Li, and W. M. Wang (2006), Magnetostratigraphy of the Yaha section, Tarim Basin (China): 11 Ma acceleration in erosion and uplift of the Tianshan Mountains, *Geology*, *34*(3), 181-184, doi: 10.1130/G22106.1.
- Charreau, J., Y. Chen, S. Gilder, L. Barrier, S. Dominguez, R. Augier, S. Sen, J. P. Avouac, A. Galland, F. Graveleau, and Q. Wang (2009a), Neogene uplift of the Tian Shan Mountains observed in the magnetic record of the Jingou River section (northwest China), *Tectonics*, *28*, TC2008, doi:10.1029/2007TC002137.
- Charreau, J., C. Gumiaux, J. P. Avouac, R. Augier, Y. Chen, L. Barrier, S. Gilder, S. Dominguez, N. Charles, and Q. Wang (2009b), The Neogene Xiyu Formation, a diachronous prograding gravel wedge at front of the Tianshan: Climatic and tectonic implications, *Earth and Planetary Science Letters*, *287*, 298-310.
- Charreau, J., P. H. Blard, N. Puchol, J. P. Avouac, E. Lallier-Vergès, D. Bourlès, R. Braucher, A. Galland, R. Finkel, M. Jolivet, Y. Chen, and P. Roy (2011), Paleo-erosion rates in Central Asia since 9 Ma: A transient increase at the onset of Quaternary glaciations?, *Earth and Planetary Science Letters*, *304*, 85-92.
- Charreau, J., M. L. Kent-Corson, L. Barrier, R. Augier, B. D. Ritts, Y. Chen, C. France-Lannord, and C. Guilmette (2012), A high-resolution stable isotopic record from the Junggar Basin (NW China): Implications for the paleotopographic evolution of the Tianshan Mountains, *Earth and Planetary Science Letters*, *341*, 158-169, doi: 10.1016/j.epsl.2012.05.033.
- Charvet, J., L. Shu, S. Laurent-Charvet, B. Wang, M. Faure, D. Cluzel, Y. Chen, and K. De Jong (2011), Palaeozoic tectonic evolution of the Tianshan belt, NW China, *Sci China Earth Sci*, *54*, 166-184, doi: 10.1007/s11430-010-4138-1
- Chediya, O. K. (1986), *Morfostruktury i noveishii tektonogenez Tyan'-Shanya (Morfostructures and Neotectonics of the Tien Shan)*, 314 pp., Ilim, Frunze (Bishkek), Kyrgyzstan.
- Chen, J., R. Heermance, D. W. Burbank, K. M. Scharer, J. Miao, and C. Wang (2007), Quantification of growth and lateral propagation of the Kashi anticline, southwest Chinese Tian Shan, *J. Geophys. Res.*, *112*, B03S16, doi:10.1029/2006JB004345.
- Choulet, F., Y. Chen, J. P. Cogné, A. Rabillard, B. Wang, W. Lin, M. Faure, and D. Cluzel (2013), First Triassic palaeomagnetic constraints from Junggar (NW China) and their implications for the Mesozoic tectonics in Central Asia, *Journal of Asian Earth Sciences*, doi: 10.1016/j.jseas.2013.01.023, in press.
- Cobbold, P. R., P. Davy, D. Gapais, E. A. Rossello, E. Sadybakasov, J. C. Thomas, J. J. Tondji Biyo, and M. de Urreiztieta (1993), Sedimentary basins and crustal thickening, *Sedimentary Geology*, *86*, 77-89.
- Cobbold, P. R., E. Sadybakasov, and J. C. Thomas (1996), Cenozoic transpression and basin development, Kyrgyz Tien Shan, central Asia, in *Geodynamic Evolution of Sedimentary Basins*, edited by F. Roure, N. Ellouz, V.S. Shein and I. Skvortsov, pp. 181-202, Editions Technip, Paris.
- Cogné, J. P. (2003), PaleoMac: A Macintosh application for treating paleomagnetic data and making plate reconstructions, *Geochemistry Geophysics Geosystems*, *4*, 1-8.
- Cole, J. E., D. Rind, R. S. Webb, J. Jouzel, and R. Healy (1999), Climatic controls on interannual variability of precipitation $\delta^{18}\text{O}$: Simulated influence of temperature, precipitation amount, and vapor source region, *Journal of Geophysical Research*, *104*(D12), 14223-14235, doi: 10.1029/1999JD900182.
- Coutand, I., M. R. Strecker, J. R. Arrowsmith, G. Hilley, R. C. Thiede, A. Korjenkov, and M. Omuraliev (2002), Late Cenozoic tectonic development of the intramontane Alai Valley, (Pamir-Tien Shan region, central Asia): An example of intracontinental deformation due to the Indo-Eurasia collision, *Tectonics*, *21*(6), 1053, doi:10.1029/2002TC001358.
- Dahlen, F. A., J. Suppe, and D. Davis (1984), Mechanics of fold-and-thrust belts and accretionary wedges: Cohesive

- Coulomb theory, *Journal of Geophysical Research: Solid Earth* (1978–2012), 89(B12), 10087-10101, doi: 10.1029/JB089iB12p10087.
- Dahlen, F. A. (1990), Critical taper model of fold-and-thrust belts and accretionary wedges, *Annual Review of Earth and Planetary Sciences*, 18, 55, doi: 10.1146/annurev.earth.18.050190.000415.
- Davis, D., J. Suppe, and F. A. Dahlen (1983), Mechanics of fold-and-thrust belts and accretionary wedges, *Journal of Geophysical Research: Solid Earth* (1978–2012), 88(B2), 1153-1172, doi: 10.1029/JB088iB02p01153.
- De Grave, J., M. M. Buslov, and P. Van den Haute (2007), Distant effects of India-Eurasia convergence and Mesozoic intracontinental deformation in Central Asia: Constraints from apatite fission-track thermochronology, *Journal of Asian Earth Sciences*, 29, 188-204, doi: 10.1016/j.jseaeas.2006.03.001.
- De Grave, J., S. Glorie, A. Ryabinin, F. Zhimulev, M. M. Buslov, A. Izmer, M. Elburg, F. Vanhaecke, and P. Van den haute (2011a), Late Palaeozoic and Meso-Cenozoic tectonic evolution of the Southern Kyrgyz Tien Shan: constraints from multi-method thermochronology in the Trans-Alai, Turkestan-Alai Section and the Southeastern Ferghana Basin, *Journal of Asian Earth Sciences*, 40, 149-168, doi: 10.1016/j.jseaeas.2011.04.019.
- De Grave, J., S. Glorie, M. M. Buslov, A. Izmer, A. Fournier-Carrie, V. Y. Batalev, F. Vanhaecke, and M. Elburg (2011b), The thermo-tectonic history of the Song-Kul plateau, Kyrgyz Tien Shan: Constraints by apatite and titanite thermochronometry and zircon U/Pb dating, *Gondwana Research*, 20(4), 745-763, doi: 10.1016/j.gr.2011.03.011.
- De Grave, J., S. Glorie, M. M. Buslov, D. F. Stockli, M. O. McWilliams, V. Y. Batalev, P. Van den haute (2013), Thermo-tectonic history of the Issyk Kul basement (Kyrgyz Northern Tien Shan, Central Asia), *Gondwana Research*, 23(3), 998-1020, doi: 10.1016/j.gr.2012.06.014.
- Dobson, K. J., F. M. Stuart, and T. J. Dempster (2008), U and Th zonation in Fish Canyon Tuff zircons: Implications for a zircon (U-Th)/He standard, *Geochimica et Cosmochimica Acta*, 72(19), 4745-4755, doi: 10.1016/j.gca.2008.07.015.
- Donelick, R. A., R. A. Ketcham, and W. D. Carlson (1999), Variability of apatite fission-track annealing kinetics: II. Crystallographic orientation effects, *American Mineralogist*, 84(9), 1224-1234.
- Donelick, R. A., P. B. O'Sullivan, and R. A. Ketcham (2005), Apatite Fission-Track Analysis, *Reviews in Mineralogy & Geochemistry*, 58, 49-94, doi: 10.2138/rmg.2005.58.3.
- Dumitru, T. A. (1993), A new computer automated microscope stage system for fission track analysis, *Nuclear tracks*, 21(4), 575-580, doi: 10.1016/1359-0189(93)90198-I.
- Dumitru, T. A., D. Zhou, E. Z. Chang, S. A. Graham, M. S. Hendrix, E. R. Sobel, and A. R. Carroll (2001), Uplift, exhumation, and deformation in the Chinese Tien Shan, in *Paleozoic and Mesozoic Tectonic Evolution of Central and Eastern Asia: From Continental Assembly to Intracontinental Deformation*, edited by M. S. Hendrix and G. A. Davis, *Mem. Geol. Soc. Am.*, 194, 71-99.
- Ehlers, T. A., and K. A. Farley (2003), Apatite (U - Th)/He thermochronometry: Methods and applications to problems in tectonic and surface processes, *Earth Planet. Sci. Lett.*, 2061 - 14, doi: 10.1016/S0012-821X.
- Enkin, R. (2003), The direction-correction tilt test: an all-purpose tilt/fold test for paleomagnetic studies, *Earth and Planetary Science Letters*, 212, 151-166.
- Erslev, E. A. (1986), Basement balancing of Rocky Mountain foreland uplifts, *Geology*, 14, 259-262, doi: 10.1130/0091-7613(1986)14<259:BBORMF> 2.0.CO;2.
- Esmintsev A.N. (1989), Report on the geological survey and search within the Jarkulak-Donarcha gold-bearing zone, "Geoinform", Republic Kazakhstan, Kokchetav.
- Farley, K.A. (2000), Helium diffusion from apatite: general behavior as illustrated by Durango fluorapatite, *J. Geophys. Res.*, 105(B2), 2903-2914, doi: 10.1029/1999JB900348.
- Farley, K. A. (2002), (U-Th)/He dating: techniques, calibrations, and applications, *Reviews in Mineralogy and Geochemistry*, 47, 819-843, doi: 10.2138/rmg.2002.47.18.
- Farley, K. A., R. A. Wolf, and L. T. Silver (1996), The effects of long alpha-stopping distances on (U-Th)/He ages, *Geochimica et Cosmochimica Acta*, 60(21), 4223-4229, doi: 10.1016/S0016-7037(96)00193-7.
- Fisher, R. (1953), Dispersion on a sphere, *Proceedings of the Royal Society*, 305, 295-305.
- Fitzgerald, P. G., R. B. Sorkhabi, T. F. Redfield, and E. Stump (1995), Uplift and denudation of the central Alaska Range; a case study in the use of apatite fission track thermochronology to determine absolute uplift parameters, *Journal of Geophysical Research*, 100(B10), 20,175-20,191, doi: 10.1029/95JB02150.
- Flinn, D. (1962), On Folding During Three-Dimensional Progressive Deformation, *Quarterly Journal of the Geological Society*, 118, 385-428.
- Flowers, R. M., D. L. Shuster, B. P. Wernicke, and K. A. Farley (2007), Radiation damage control on apatite (U-Th)/He dates from the Grand Canyon region, Colorado Plateau, *Geology*, 35(5), 447-450, doi: 10.1130/G23471A.1.
- Flowers, R., R. A. Ketcham, D. Shuster, and K. A. Farley (2009), Apatite (U-Th)/He thermochronology using a radiation damage accumulation and annealing model, *Geochim. Cosmochim. Acta*, 73, 2347-2365, doi: 10.1016/j.gca.2009.01.015.
- Foeken, J.P.T., F. M. Stuart, K. J. Dobson, C. Persano, and D. Vilbert (2006), A diode laser system for heating minerals for (U-Th)/He chronometry, *Geochem. Geophys. Geosyst.*, 7, Q04015, doi:10.1029/2005GC001190.
- Fortuna, A. B. (1983), Spore and pollen complexes and stratigraphy of the Paleogene and Neogene sediments of the northern Tien Shan (in Russian), Candidate of Science thesis, Institute of Seismology of the Academy of Sciences of the Kyrgyz SSR, Dushanbe, Tajikistan.
- Fortuna, A. B., C. K. Kerimbekov, S. I. Kyzikov, and A. V. Mikolaichuk (1994), Lithostratigraphic and palynologic data of Cenozoic deposits of Tessik-Sarybulak depression, in *Geology of Cenozoic and Seismotectonics of the Tien Shan* (in Russian), pp. 26-39, Ilim, Bishkek, Kyrgyzstan.
- Friedman, I., and J. R. O'Neil (1977), *Compilation of stable isotope fractionation factors of geochemical interest*, 440, USGPO.
- Galbraith, R. F. (1981), On statistical models for fission track counts, *Mathematical Geology*, 13, 471-478, doi: 10.1007/BF01034498.
- Garcia, P. E., and G. H. Davis (2004), Evidence and mechanisms for folding of granite, Sierra de Hualfin basement-cored uplift, northwest Argentina, *AAPG bulletin*, 88, 1255-1276, doi: 10.1306/04290403092.Gautheron, C., L. Tassan-Got, J. Barbarand, and M. Pagel (2009), Effect of alpha-damage annealing on apatite (U-Th)/He thermochronology, *Chemical Geology*, 266, 157-170, doi: 10.1016/j.chemgeo.2009.06.001.
- Garzzone, C. N., D. L. Dettman, and B. K. Horton (2004), Carbonate oxygen isotope paleoaltimetry: evaluating the effect of diagenesis on paleoelevation estimates for the Tibetan plateau, *Palaeogeography, Palaeoclimatology, Palaeoecology*, 212(1), 119-140, doi: 10.1016/j.palaeo.2004.05.020.
- Gilder, S., Y. Chen, and S. Sen (2001), Oligo-Miocene magnetostratigraphy and rock magnetism of the Xishuigou section, Subei (Gansu Province, western China) and implications for shallow inclinations in central Asia, *Journal of Geophysical*, 106, 30505- 30521.
- Gilder, S., Y. Chen, J. P. Cogné, X. Tan, V. Courtillot, D. Sun, and Y. Li (2003), Paleomagnetism of Upper Jurassic to Lower Cretaceous volcanic and sedimentary rocks from the western Tarim Basin and implications for inclination shallowing and absolute dating of the M-0 (ISEA?) chron, *Earth and Planetary Science Letters*, 206, 587-600.
- Glorie, S., J. De Grave, M. M. Buslov, M. A. Elburg, D. F. Stockli, A. Gerdes, and P. Van den haute (2010), Multi-method chronometric constraints on the evolution of the Northern Kyrgyz Tien Shan granitoids (Central Asian Orogenic Belt): From emplacement to exhumation, *J. Asian Earth Sci.*, 38(3-4), 131-146, doi:10.1016/j.jseaeas.2009.12.009.
- Glorie, S., J. De Grave, M. M. Buslov, F. I. Zhimulev, D. F. Stockli, V. Y. Batalev, A. Izmer, P. Van den haute, F. Vanhaecke, and M.A. Elburg (2011), Tectonic history of the Kyrgyz South Tien Shan (Atbashi-Inylchek) suture zone: The role of

- inherited structures during deformation-propagation, *Tectonics*, 30, TC6016, doi:10.1029/2011TC002949.
- Goode, J. K., D. W. Burbank, and B. Bookhagen (2011), Basin width control of faulting in the Naryn Basin, south-central Kyrgyzstan, *Tectonics*, 30, TC6009, doi:10.1029/2011TC002910.
- Gradstein, F., and J. Ogg (2004), Geologic Time Scale 2004 - why, how, and where next!, *Lethaia*, 37, 175-181.
- Graham, J. W. (1966), Significance of magnetic anisotropy in Appalachian sedimentary rocks, *The earth beneath the continents*, 10, 627-648.
- Graham, S. A., C. P. Chamberlain, Y. Yue, B. D. Ritts, A. D. Hanson, T. W. Horton, J. R. Waldbauer, M. A. Poage, and X. Feng (2005), Stable isotope records of Cenozoic climate and topography, Tibetan Plateau and Tarim Basin, *American Journal of Science*, 305(2), 101-118, doi: 10.2475/ajs.305.2.101.
- Green, P.F. (1981), A new look at statistics in fission-track dating, *Nuclear Tracks*, 5, 77-86, doi: 10.1016/0191-278X(81)90029-9.
- Green, P. F., I. R. Duddy, G. M. Laslett, K. A. Hegarty, A. J. W. Gleadow, and J. F. Lovering (1989), Thermal annealing of fission tracks in apatite, 4, Quantitative modeling techniques and extension to geological timescales, *Chem. Geol. (Isotope Geosci. Sec.)*, 79, 155-182, doi: 10.1016/0168-9622(89)90018-3.
- Grishenko, V. A. (1985), Geological survey at a scale 1:50 000 within the Saryjazyk area: Final report of the Ottuk Department on researches carried out in 1980-1985 [in Russian], report, Arch. of the State Geol. Agency of the Kyrgyz Repub., Frunze, U.S.S.R.
- Guenther, W. R., P. W. Reiners, R. A. Ketcham, L. Nasdala, and G. Giester (2013), Helium diffusion in natural zircon: radiation damage, anisotropy, and the interpretation of zircon (U-Th)/He thermochronology, *American Journal of Science*, 313(3), 145-198, doi: 10.2475/03.2013.01.
- Heermance, R. V., J. Chen, D. W. Burbank, and C. S. Wang (2007), Tectonic control on gravel progradation and the significance of upward coarsening stratigraphy in the evolving southwestern Chinese Tian Shan foreland, *Basin Research*, 19, 599 - 632, doi:10.1111/j.1365-2117.2007.00339.x.
- Heermance, R. V., J. Chen, D. W. Burbank, and J. Miao (2008), Temporal constraints and pulsed Late Cenozoic deformation during the structural disruption of the active Kashi foreland, northwest China, *Tectonics*, 27, TC6012, doi:10.1029/2007TC002226.
- Hegner, E., R. Klemd, A. Kröner, M. Corsini, D. V. Alexeiev, L. M. Iaccheri, T. Zack, P. Dulski, X. Xia, and B. F. Windley (2010), Mineral ages and P-T conditions of Late Paleozoic high-pressure eclogite and provenance of mélange sediments from Atbashi in the south Tianshan orogen of Kyrgyzstan, *Am. J. Sci.*, 310, 916-950, doi:10.2475/09.2010.07.
- Hendrix, M. S., S. A. Graham, A. R. Carroll, E. R. Sobel, C. L. McKnight, B. J. Schuelein, and Z. Wang (1992), Sedimentary record and climatic implications of recurrent deformation in the Tian Shan: Evidence from Mesozoic strata of the north Tarim, south Junggar, and Turpan basins, Northwest China, *Geological Society of America Bulletin*, 104(1), 53-79, doi: 10.1130/0016-7606(1992)104<0053:SRACIO> 2.3.CO;2.
- Hendrix, M. S., T. A. Dumitru, and S. A. Graham (1994), Late Oligocene-Early Miocene unroofing in the Chinese Tian Shan: An early effect of the India-Asia collision, *Geology*, 22, 487-490, doi: 10.1130/0091-7613(1994)022<0487:LOEMUI> 2.3.CO;2.
- Hilley, G., P. M. Blisniuk, and M. R. Strecker (2005), Mechanics and erosion of basement-cored uplift provinces, *J. Geophys. Res.*, 110, B12409, doi:10.1029/2005JB003704.
- Holdsworth, R. E., C. A. Butler, and A. M. Roberts (1997), The recognition of reactivation during continental deformation, *J. Geol. Soc.*, 154(1), 73-78, doi: 10.1144/gsjgs.154.1.0073.
- Horstwood, M., J. Kosiński, S. Jackson, N. Pearson, and P. Sylvester (2009), Investigating Age Resolution in Laser Ablation Geochronology, *Eos, Transactions American Geophysical Union*, 90, 6, pp.47, doi: 10.1029/2009EO60004.
- Housen, B. A., C. Richter, and B. A. van Der Pluijm (1993), Composite magnetic anisotropy fabrics: experiments, numerical models and implications for the quantification of rock fabrics, *Tectonophysics*, 220, 1-12.
- Hrouda, F. (1982), Magnetic anisotropy of rocks and its application in geology and geophysics, *Surveys in Geophysics*, 5, 37- 82.
- Huang, B., J. D. A. Piper, S. Peng, T. Liu, Z. Li, Q. Wang, and R. Zhu (2006), Magnetostratigraphic study of the Kuche Depression, Tarim Basin, and Cenozoic uplift of the Tian Shan range, western China, *Earth and Planetary Science Letters* 251, no. 3 (2006): 346-364, doi:10.1016/j.epsl.2006.09.020.
- Huntington, K. W., T. A. Ehlers, K. V. Hodges, and D. M. W. Jr. (2007), Topography, exhumation pathway, age uncertainties, and the interpretation of thermochronometer data, *Tectonics*, 26, TC4012, doi:10.1029/2007TC002108.
- Hurford, A.J., and P.F. Green (1983), The zeta age calibration of fission-track dating, *Chemical Geology*, 41(4), 285-317, doi: 10.1016/S0009-2541(83)80026-6.
- Jackson, M. (1991), Anisotropy of magnetic remanence: a brief review of mineralogical sources, physical origins, and geological applications, and comparison with susceptibility anisotropy, *Pure and Applied Geophysics*, 136, 1-28.
- Jelinek, V. (1981), Characterization of the magnetic fabric of rocks, *Tectonophysics*, 79, T63-T67.
- Ji, J., P. Luo, P. White, H. Jiang, L. Gao, and Z. Ding (2008), Episodic uplift of the Tianshan Mountains since the late Oligocene constrained by magnetostratigraphy of the Jingou River section, in the southern margin of the Junggar Basin, China, *J. Geophys. Res.*, 113, B05102, doi:10.1029/2007JB005064.
- Jolivet, M., S. Dominguez, J. Charreau, Y. Chen, Y. Li, and Q. Wang (2010), Mesozoic and Cenozoic tectonic history of the central Chinese Tian Shan: Reactivated tectonic structures and active deformation, *Tectonics*, 29, TC6019, doi:10.1029/2010TC002712.
- Jonckheere, R., E. Enkelmann, M. Min, C. Trautmann, and L. Ratschbacher (2007), Confined fission tracks in ion-irradiated and step-etched prismatic sections of Durango apatite, *Chemical Geology*, 242(1), 202-217, doi: 10.1016/j.chemgeo.2007.03.015.
- Jordan, T.E., and R.W. Allmendinger (1986), The Sierras Pampeanas of Argentina, a modern analogue of Rocky Mountain foreland deformation, *Amer. J. Earth Sci.*, 286, 737-764, doi: 10.2475/ajs.286.10.737.
- Kent-Corson, M. L., B. D. Ritts, G. Zhuang, P. M. Bovet, S. A. Graham, S. A., and C. Page Chamberlain (2009), Stable isotopic constraints on the tectonic, topographic, and climatic evolution of the northern margin of the Tibetan Plateau, *Earth and Planetary Science Letters*, 282(1), 158-166, doi: 10.1016/j.epsl.2009.03.011.
- Ketcham, R.A. (2005), HeFTy: Forward and inverse modeling thermochronometer systems, in *Low-temperature thermochronology: Techniques, interpretations, and applications*, vol. 58, *Reviews in Mineralogy and Geochemistry*, edited by P.W. Reiners and T.A. Ehlers, pp. 596-597, The Mineralogical Society of America, Chantilly, VA, USA.
- Ketcham, R.A., R.A. Donelick, and W.D. Carlson (1999), Variability of apatite fission-track annealing kinetics: III. Extrapolation to geological time scales, *American Mineralogist*, 84(9), 1235-1255.
- Ketcham, R.A., A.C. Carter, R.A. Donelick, J. Barbarand, and A.J. Hurford (2007), Improved modeling of fission-track annealing in apatite, *American Mineralogist*, 92, 799-810, doi: 10.2138/am.2007.2281.
- Kim, S. T., and J. R. O'Neil (1997), Equilibrium and nonequilibrium oxygen isotope effects in synthetic carbonates, *Geochimica et Cosmochimica Acta*, 61(16), 3461-3475, doi: 10.1016/S0016-7037(97)00169-5.
- Kirschvink, J. L. (1980), The least-squares line and plane and the analysis of palaeomagnetic data, *Geophysical Journal of the Royal Astronomical Society*, 62, 699-718.
- Kiselev, V. V. (1999), Uranium-lead (zircon) geochronology of magmatic formations of the Northern Tien Shan (in Russian), in *Proceedings (Izvestia) of the National Academy of Science of Kyrgyz Republic*, edited, pp. 21-33, Ilim, Bishkek.

- Kiselev, V. V., F. K. Apayarov, V. T. Komarevtsev, E. N. Tsyganok, and E. M. Lukashova (1993), Isotope age of zircons of the Tien Shan crystalline complexes (in Russian), in *The Early Pre-Cambrian of Central Asian fold belt*, edited, pp. 99-115, Nauka, St. Petersburg.
- Kley, J., E. A. Rossello, C. R. Monaldi, and B. Habighorst (2005), Seismic and field evidence for selective inversion of Cretaceous normal faults, Salta rift, northwest Argentina, *Tectonophysics*, 399(1), 155-172, doi: 10.1016/j.tecto.2004.12.020.
- Knauf, V. I. (editor) (1965), Geological Map of the USSR of 1:200000 scales, Northern Tien-Shan series, *Sheet K-44-XIII*, Russian Geological Research Institute (VSEGEI), Nedra, Moscow.
- Knauf, V.I. (editor) (1972), Geology of USSR. Volume XXV. Kyrgyz SSR, *Book 2*, pp. 156–280, Nedra, Moscow.
- Konopelko, D., G. Biske, R. Seltmann, O. Eklund, and B. Belyatsky (2007), Post-collisional granites of the Kokshaal Range, Southern Tien Shan, Kyrgyzstan: Age, petrogenesis and regional tectonic implications, *Lithos*, 97, 140-160.
- Konopelko, D., R. Seltmann, G. Biske, M. Kiseleva, D. Matukov, and S. Sergeev (2008), Deciphering Caledonian events: timing and geochemistry of the Caledonian magmatic arc in the Kyrgyz Tien Shan, *Journal of Asian Earth Sciences*, 32, 131–141.
- Konopelko, D., R. Seltmann, G. Biske, E. Lepekhina, and S. Sergeev (2009), Possible source dichotomy of contemporaneous post-collisional barren I-type versus tin-bearing A-type granites, lying on opposite sides of the South Tien Shan suture, *Ore Geology Reviews*, 35, 206–216.
- Koons, P. O. (1987), Some thermal and mechanical consequences of rapid uplift: an example from the Southern Alps, New Zealand, *Earth and planetary science letters*, 86(2), 307-319, doi: 10.1016/0012-821X(87)90228-7.
- Koons, P. O. (1990), Two-sided orogen: Collision and erosion from the sandbox to the Southern Alps, New Zealand, *Geology*, 18(8), 679-682, doi: 10.1130/0091-7613(1990)018<0679:TSOCAE>2.3.CO;2.
- Korolov, V. G. (1956), In the inherited nature of some of the Mesozoic-Cenozoic basins of the Northern Tien Shan (in Russian), *Proceedings of the Institute of Geology, Academy of Sciences of the Kyrgyz SSR*, 7, Frunze, Publishing House of Kyrgyz Academy of Sciences. pp.87-94.
- Krasa, D., K. Petersen, and N. Petersen (2007), The variable field translation balance, in *Encyclopedia of Geomagnetism and Paleomagnetism*, edited by Gubbins, D., and E. Herrero-Bervera, Springer, Dordrecht, pp. 977-979.
- Krilov, A. Y. (1960), Absolute age of the rocks of the central Tien Shan and application of Argon methods to metamorphic and sedimentary sediments, in *Determination of the Absolute Age of Pre-Quaternary Formations*, edited by Starik, I. E., Nedra, Moscow, pp. 222-224.
- Kröner, A., D. V. Alexeiev, E. Hegner, Y. Rojas-Agramonte, M. Corsini, Y. Chao, J. Wong, B. F. Windley, D. Liu, and A. A. Tretyako (2012), Zircon and muscovite ages, geochemistry, and Nd–Hf isotopes for the Aktyuz metamorphic terrane: Evidence for an Early Ordovician collisional belt in the northern Tianshan of Kyrgyzstan, *Gondwana Research*, 21, 901–927.
- Kröner, A., D. V. Alexeiev, Y. Rojas-Agramonte, E. Hegner, J. Wong, X. Xia, E. Belousova, A. V. Mikolaichuk, R. Seltmann, D. Liu, and V. V. Kiselev (2013), Mesoproterozoic (Grenville-age) terranes in the Kyrgyz North Tianshan: Zircon ages and Nd–Hf isotopic constraints on the origin and evolution of basement blocks in the southern Central Asian Orogen, *Gondwana Research*, 23, 272–295.
- Kuznetsov V. D., K. K. Karabalaev, I. M. Ibragimov (1964), The fossil land tortoise from Kyrgyzstan, in *Materials on the geology of the Tien Shan*. Ilim Publishing house, Frunze, pp. 135-146 (in Russian).
- Lallier, F., C. Antoine, J. Charreau, G. Caumon, J. Ruiu (2013), Management of ambiguities in magnetostratigraphic correlation, *Earth and Planetary Science Letters*, in press, 2013.
- Leier, A., J. Quade, P. DeCelles, and P. Kapp (2009), Stable isotopic results from paleosol carbonate in South Asia: paleoenvironmental reconstructions and selective alteration, *Earth and Planetary Science Letters*, 279(3), 242-254, doi: 10.1016/j.epsl.2008.12.044.
- Leng, M. J. (editor) (2006), *Isotopes in palaeoenvironmental research*, 10, Springer.
- Leonhardt, R. (2006), Analyzing rock magnetic measurements: The RockMagAnalyzer 1.0 software, *Computers & Geosciences*, 32, 1420-1431.
- Li, C., Z. Guo, G. Dupont-Nivet (2011), Late Cenozoic tectonic deformation across the northern foreland of the Chinese Tien Shan, *Journal of Asian Earth Sciences*, 42, 1066-1073.
- Li, Z., S. Roecker, Z. Li, B. Wei, H. Wang, G. Schelochkov, and V. Bragin (2009), Tomographic image of the crust and upper mantle beneath the western Tien Shan from the MANAS broadband deployment: Possible evidence for lithospheric delamination, *Tectonophysics*, 477(1), 49-57, doi: 10.1016/j.tecto.2009.05.007.
- Ludwig, K. (2003), User's manual for Isoplot 3.00: a geochronological toolkit for Microsoft Excel, *Berkeley Geochronology Center Special Publication*, 4, 70.
- Macaulay, E. A., E. R. Sobel, A. Mikolaichuk, A. Landgraf, B. Kohn, and F. Stuart (2013), Thermochronologic insight into late Cenozoic deformation in the basement-cored Terskey Range, Kyrgyz Tien Shan, *Tectonics*, 32, 1-4, doi:10.1002/tect.20040.
- Macaulay, E. A., E. R. Sobel, A. Mikolaichuk, B. Kohn, and F. M. Stuart (in review), Cenozoic deformation and exhumation history of the Central Kyrgyz Tien Shan, *Tectonics*, in review.
- Makarov V.I. (1977), New tectonic structure of the Central Tien Shan (in Russian), Nauka, Moscow.
- Makarov, V. I., D. V. Alekseev, V. Yu Batalev, E. A. Bataleva, I. V. Belyaev, V. D. Bragin, N. T. Dergunov, N. N. Efimova, M. G. Leonov, L. M. Munirova, A. D. Pavlenkin, S. Roecker, Y. V. Roslov, A. K. Rybin, and G. G. Shchelochkov (2010), Underthrusting of Tarim beneath the Tien Shan and deep structure of their junction zone: Main results of seismic experiment along MANAS Profile Kashgar-Song-Köl, *Geotectonics*, 44(2), 102-126, doi: 10.1134/S0016852110020020.
- Mancktelow, N. S., and B. Grasemann (1997), Time-dependent effects of heat advection and topography on cooling histories during erosion, *Tectonophysics*, 270, 167-195, doi: 10.1016/S0040-1951(96)00279-X.
- Marrett, R. A., and R. W. Allmendinger (1990), Kinematic analysis of fault-slip data, *Journal of Structural Geology*, 12, 973-986, doi: 10.1016/0191-8141(90)90093.
- Meesters, A.G.C.A., and T.J. Dunai (2002), Solving the production–diffusion equation for finite diffusion domains of various shapes Part I. Implications for low-temperature (U–Th)/He thermochronology, *Chemical Geology*, 186, 333–344, doi: 10.1016/S0009-2541(02)00073-6.
- Métivier, F., and Y. Gaudemer (1997), Mass transfer between eastern Tien Shan and adjacent basins (central Asia): Constraints on regional tectonics and topography, *Geophysical Journal International*, 128(1), 1-17, doi: 10.1111/j.1365-246X.1997.tb04068.x.
- Mikolaichuk, A. V., V. I. Rubtsov, and a. Z. I. Afimov (1994), Geological structure and minerals of K-43-80-B, G; K-43-81-A-a,v, V, G sheets (Sultansary area). Report of the Suek party on researches at a scale 1:50 000 carried out in 1988-1993 years, *Archives of the State Geological Agency of the Kyrgyz Republic*, Ivanovka.
- Mikolaichuk, A. V. (2000), The structural position of thrusts in the recent orogen of the central Tien Shan, *Russian Geology and Geophysics*, 41(7), 961-970.
- Mikolaichuk, A. V., and V. V. Kotov (1999), Late Caledonian Granite-Gneiss Dome in the Karakudzhur River Basin, in *Geology and Geography of the Kyrgyz Republic* [in Russian], pp. 43-46, Bishkek.
- Mikolaichuk A. V., Buchroithner M. F. (editors) (2008), Digital Geological Map of the Khan Tengri Massif (Kyrgyzstan), ISTC (Project No. KR-920).
- Mikolaichuk, A. V., S. A. Kurenkov, K. E. Degtyarev, and V. I. Rubtsov (1997), Northern Tien Shan: Main Stages of Geodynamic Evolution in the Late Precambrian-Early Paleozoic, *Geotectonics*, 31(6), 445-462.

- Molnar, P. (2005), Mio-Pliocene Growth of the Tibetan Plateau and Evolution of East Asian Climate, *Palaeontologia Electronica*, 8, 1; 2A:23p.
- Molnar, P., and P. Tapponnier (1975), Cenozoic tectonics of Asia: Effects of a continental collision, *Science*, 189(4201), 419-426.
- Molnar, P., and P. England (1990), Late Cenozoic uplift of mountain ranges and global climate change: chicken or egg?, *Nature*, 346(6279), 29-34, doi: 10.1038/346029a0.
- Molnar, P., and J. M. Stock (2009), Slowing of India's convergence with Eurasia since 20 Ma and its implications for Tibetan mantle dynamics, *Tectonics*, 28, TC3001, doi:10.1029/2008TC002271.
- Molnar, P., P. England, and J. Martinod (1993), Mantle dynamics, uplift of the Tibetan Plateau, and the Indian monsoon, *Reviews of Geophysics*, 31(4), 357-396, doi: 10.1029/93RG02030.
- Morozov, V. P., and A. G. Razboinikov (1993), Geological structure and minerals of Aktyuz-Boordu ore area on the area of sheets K-43-44-B-v-2, 4; K-43-44-V; K-43-44-G; K-43-45-A-v, g; K-43-45-V; K-43-56-A-a. Report of the Kemin party on works 1986-1993 years, *Archives of the ministry of natural resources of the Kyrgyz Republic*, Ivanovka.
- Mortimer, E., B. Carrapa, I. Coutand, L. Schoenbohm, E. R. Sobel, J. S. Gomez, and M. R. Strecker (2007), Fragmentation of a foreland basin in response to out-of-sequence basement uplifts and structural reactivation: El Cajón-Campo del Arenal basin, NW Argentina, *Geological Society of America Bulletin*, 119(5-6), 637-653, doi: 10.1130/B25884.1.
- Narr, W., and J. Suppe (1994), Kinematics of basement-involved compressive structures, *American Journal of Science*, 294, 802-860, doi: 10.2475/ajs.294.7.802.
- Neely, T. G., and E. A. Erslev (2009), The interplay of fold mechanisms and basement weaknesses at the transition between Laramide basement-involved arches, north-central Wyoming, USA, *Journal of Structural Geology*, 31(9), 1012-1027, doi: 10.1016/j.jsg.2009.03.008.
- Nielsen, S. B., K. Gallagher, C. Leighton, N. Balling, L. Svenningsen, B. H. Jacobsen, E. Thomsen, O. B. Nielsen, C. Heilmann-Clausen, D. L. Egholm, M. A. Summerfield, O. R. Clausen, J. A. Piotrowski, M. R. Thorsen, M. Huuse, N. Abrahamsen, C. King, H. Lykke-Andersen (2009), The evolution of western Scandinavian topography: A review of Neogene uplift versus the ICE (isostasy-climate-erosion) hypothesis, *Journal of Geodynamics*, 47(2-3), 72-95, doi: 10.1016/j.jog.2008.09.001.
- Omuraliev, M. (1978), Geology and tectonic features of the Cenozoic Alabuga-Naryn Basin (central Tien Shan), Ph.D. thesis, Inst. of Geophys. and Seismol., Acad. of Sci. of the Kirghiz SSR, Frunze, U.S.S.R.
- Omuraliev, M. (1988), Map of the newest tectonics of Kyrgyz Republic, 1:500 000, Natural resource of Kyrgyz SSR, Kartofarika, Tashkent.
- Omuraliev, M., and A. Omuralieva (2004), *Late Cenozoic tectonics of the Tien Shan*, Bishkek.
- Pearce, N. J. G., W. T. Perkins, J. A. Westgate, M. P. Gorton, S. E. Jackson, C. R. Neal, S. P. Chenery (1997), A compilation of new and published major and trace element data for NIST SRM 610 and NIST SRM 612 glass reference materials, *Geostandards Newsletter*, 21, 115-144, doi: 10.1111/j.1751-908X.1997.tb00538.x.
- Petit, J. P. (1987), Criteria for the sense of movement on fault surfaces in brittle rocks, *Journal of Structural Geology*, 9(5-6), 597-608, doi: 10.1016/0191-8141(87)90145-3.
- Pomazkov, K. D. (editor) (1971) Geological Map of the USSR of 1:200000 scales, Northern Tien-Shan series, *Sheet K-43-XVII*, Russian Geological Research Institute (VSEGEI), Nedra, Moscow.
- Pomazkov, K. D. (1972), Geology of USSR, vol. XXV Kyrgyz SSR, pp. 280, Nedra, Moscow, Russia.
- Quade, J., and L. J. Roe (1999), The stable-isotope composition of early ground-water cements from sandstone in paleoecological reconstruction, *Journal of Sedimentary Research*, 69(3), 667-674, doi: 10.2110/jsr.69.667.
- Quade, J., J. M. Cater, T. P. Ojha, J. Adam, and T. M. Harrison (1995), Late Miocene environmental change in Nepal and the northern Indian subcontinent: Stable isotopic evidence from paleosols, *Geological Society of America Bulletin*, 107(12), 1381-1397, doi: 10.1130/0016-7606(1995)107<1381:LMECIN>2.3.CO;2.
- Quade, J., C. Garzzone, and J. Eiler (2007), Paleoelevation reconstruction using pedogenic carbonates, *Reviews in Mineralogy and Geochemistry*, 66(1), 53-87, doi: 10.2138/rmg.2007.66.3.
- Reiners, P. W. (2007), Thermochronologic Approaches to Paleotopography, in *Paleoaltimetry: Geochemical and Thermodynamic Approaches*, *Reviews in Mineralogy and Geochemistry*, vol. 66, edited by Kohn, M.J., pp. 243-267, doi: 10.2138/rmg.2007.66.10.
- Reiners, P. W., and K. A. Farley, (2001), Influence of crystal size on apatite (U-Th)/He thermochronology: an example from the Bighorn Mountains, Wyoming, *Earth and Planetary Science Letters*, 188(3), 413-420, doi: 10.1016/S0012-821X(01)00341-7.
- Reiners, P. W., and S. Nicolescu (2006), Measurement of parent nuclides for (U-Th)/He chronometry by solution sector ICP-MS, ARHDL Report 1, <http://www.geo.arizona.edu/~reiners/arhdl/arhdl.htm>
- Reiners, P. W., T. L. Spell, S. Nicolescu, and K. A. Zanetti (2004), Zircon (U-Th)/He thermochronometry: He diffusion and comparisons with ⁴⁰Ar/³⁹Ar dating, *Geochimica et Cosmochimica Acta*, 68(8), 1857-1887, doi: 10.1016/j.gca.2003.10.021.
- Ricketts, R. D., T. C. Johnson, E. T. Brown, K. A. Rasmussen, and V. V. Romanovsky (2001), The Holocene paleolimnology of Lake Issyk-Kul, Kyrgyzstan: Trace element and stable isotope composition of ostracodes, *Palaeogeography, Palaeoclimatology, Palaeoecology*, 176(1), 207-227, doi: 10.1016/S0031-0182(01)00339-X.
- Rowley, D. B., and C. N. Garzzone (2007), Stable Isotope-based Palealtimetry, *Annual Review of Earth and Planetary Sciences*, 35, 463-508, doi: 10.1146/annurev.earth.35.031306.140155.
- Rubtsov, V. I., and A. F. Lopin (1984), Geological structure and minerals of K-43-71-A, B, V, G; K-43-72-A, B, V, G; K-43-83-A, B, V, G; K-43-84-A, B, V, G sheets. Report of the Jilusu party on geological survey at a scale 1:50 000 carried out in 1977-1983 years, *Archives of the State Geological Agency of the Kyrgyz Republic*, Frunze.
- Rubtsov, V. I. E. (1999), Geological structure and minerals of the Tyundyuk area. Report of a Suek party about results of geological research and general searches of scale 1:50000 on the area of sheets K-43-56-A-v,g; K-43-56-B-v; K-43-56-V,G; K-43-57-V-a,v; K-43-68-A-a,b; K-43-68-B-a,b,g; K-43-69-A, carried out at 1993-1999 years, *Archives of the ministry of natural resources of the Kyrgyz Republic*, Ivanovka.
- Ryabinin, A.N. (1927), New turtle of Lower Tertiary sediments from Semirech'e Province, *Proceedings of Geolkom (Geological Committee)*, 46, 193-200 (in Russian).
- Scharer, K. M., D. W. Burbank, J. Chen, R. J. Weldon, C. Rubin, R. Zhao, and J. Shen (2004), Detachment folding in the Southwestern Tien Shan-Tarim foreland, China: shortening estimates and rates, *Journal of structural Geology*, 26(11), 2119-2137, doi: 10.1016/j.jsg.2004.02.016.
- Schmidt, C. J., P. W. Genovese, and R. B. Chase (1993), Role of basement fabric and cover-rock lithology on the geometry and kinematics of twelve folds in the Rocky Mountain foreland, in *Laramide basement deformation in the Rocky Mountain foreland of the Western United States*, vol. 280, *Special Paper*, edited by C.J. Schmidt, et al., pp. 1-44, Geological Society of America, Boulder, CO.
- Selander, J., M. Oskin, C. Ormukov, and K. Abdrakhmatov (2012), Inherited strike-slip faults as an origin for basement-cored uplifts: Example of the Kungey and Zailiskey Ranges, northern Tien Shan, *Tectonics*, 31, TC4026, doi:10.1029/2011TC003002.
- Seltmann, R., D. Konopelko, G. Biske, F. Divaev, and S. Sergeev (2011), Hercynian post-collisional magmatism in the context of Paleozoic magmatic evolution of the Tien Shan orogenic belt, *Journal of Asian Earth Sciences*, 42, 821-838.
- Semenov, B. V., and A. F. Lopin (1987), Geological structure and minerals of the western part of the Terskei Ala-Too Ridge. Report of the Bolgart party on researches of a scale 1:50000

- on area of sheets K-43-69-B-v, G; K-43-70-V-v,g; G-v,g; K-43-82-B, G carried out at 1983-1987 years, *Archives of the ministry of natural resources of the Kyrgyz Republic*, Frunze.
- Severinov, V.A.E. (1990), Geological structure and mineral resources within the Karkara area: Report on the geological survey at a scale 1:50 000 carried out in 1985-1989 (in Russian), *Archives of the State Geological Agency of the Kyrgyz Republic*, Bishkek, Kyrgyzstan.
- Shenderovich, D. M., B. A. Makarov (1967), Geological map of the USSR, Northern Tien-Shan series., Sheet K-44-XIII. 1:200000 scales. Nedra (in Russian).
- Shirvell, C. R., D. F. Stockli, G. J. Axen, and M. Grove (2009), Miocene-Pliocene exhumation along the west Salton detachment fault, southern California, from (U-Th)/He thermochronometry of apatite and zircon, *Tectonics*, 28(2), doi: 10.1029/2007TC002172.
- Shuster, D. L., R. M. Flowers, and K. A. Farley (2006), The influence of natural radiation damage on helium diffusion kinetics in apatite, *Earth and Planetary Science Letters*, 249(3), 148-161, doi: 10.1016/j.epsl.2006.07.028.
- Sibson, R. H. (1985), A note of fault reactivation, *Journal of Structural Geology*, 7(6), 751-754, doi: 10.1016/0191-8141(85)90150-6.
- Simonov, V. A., A. V. Mikolaichuk, S. V. Rasskazov, S. V. Kovyazin (2008), Cretaceous-Paleogene within plate magmatism in Central Asia: data from the Tien Shan basalts, *Russian Geology and Geophysics*, 49(7), 520-533.
- Simpson, G. D. (2006), Modelling interactions between fold-thrust belt deformation, foreland flexure and surface mass transport, *Basin Research*, 18(2), 125-143, doi: 10.1111/j.1365-2117.2006.00287.x.
- Sláma, J., J. Košler, D. J. Condon, J. L. Crowley, A. Gerdes, J. M. Hanchar, M. S. A. Horstwood, G. A. Morris, L. Masdala, N. Norberg, U. Schaltegger, B. Schoene, M. N. Tubrett, and M. J. Whitehouse (2008), Plešovice zircon—a new natural reference material for U–Pb and Hf isotopic microanalysis. *Chemical Geology*, 249(1), 1-35, doi: 10.1016/j.chemgeo.2007.11.005.
- Sobel, E. R., and T. A. Dumitru (1997), Thrusting and exhumation around the margins of the western Tarim basin during the India-Asia collision, *Journal of Geophysical Research*, 102(B3), 5043-5063, doi: 10.1029/96JB03267.
- Sobel, E. R., and N. Arnaud (2000), Cretaceous - Paleogene basaltic rocks of the Tuyon basin, NW China and the Kyrgyz Tian Shan: The trace of a small plume, *Lithos*, 50(1-3), 191-215, doi: 10.1016/S0024-4937(99)00046-8.
- Sobel, E. R., G. E. Hilley, and M. R. Strecker (2003a), Formation of internally drained contractional basins by aridity-limited bedrock incision, *Journal of Geophysical Research: Solid Earth* (1978–2012), 108(B7), doi: 10.1029/2002JB001883.
- Sobel, E.R., and M.R. Strecker (2003b), Uplift, exhumation, and precipitation: Tectonic and climatic control of Late Cenozoic landscape evolution in the northern Sierras Pampeanas, Argentina, *Basin Research*, 15(4), 431-451, doi: 10.1046/j.1365-2117.2003.00214.x.
- Sobel, E. R., J. Chen, and R. V. Heermance (2006a), Late Oligocene - Early Miocene initiation of shortening in the Southwestern Chinese Tian Shan: Implications for Neogene shortening rate variations, *Earth and Planetary Science Letters*, 247, 70-81, doi: 10.1016/j.epsl.2006.03.048.
- Sobel, E. R., M. Oskin, D. Burbank, and A. Mikolaichuk (2006b), Exhumation of basement-cored uplifts: Example of the Kyrgyz Range quantified with apatite fission-track thermochronology, *Tectonics*, 25, TC2008, doi:10.1029/2005TC001809.
- Sobel, E. R., and D. Seward (2010), Influence of etching conditions on apatite fission-track etch pit diameter, *Chemical Geology*, 271, 59-69, doi:10.1016/j.chemgeo.2009.12.012.
- Sobel, E. R., L. M. Schoenbohm, J. Chen, R. Thiede, D. F. Stockli, M. Sudo, and M. R. Strecker (2011), Late Miocene–Pliocene deceleration of dextral slip between Pamir and Tarim: Implications for Pamir orogenesis, *Earth and Planetary Science Letters*, 304, 369-378, doi: 10.1016/j.epsl.2011.02.012.
- Spiegel, C., B. Kohn, D. Belton, Z. Berner, A. Gleadow (2009), Apatite (U-Th-Sm)/He thermochronology of rapidly cooled samples: The effect of He implantation, *Earth and Planetary Science Letters*, 285(1-2), 105-114, doi: 10.1016/j.epsl.2009.05.045.
- Spötl, C., and T. W. Vennemann (2003), Continuous-flow isotope ratio mass spectrometric analysis of carbonate minerals, *Rapid Communications in Mass Spectrometry*, 17(9), 1004-1006, doi: 10.1002/rcm.1010.
- Strecker, M.R., G.E. Hilley, B. Bookhagen, and E. R. Sobel (2011), Structural, geomorphic, and depositional characteristics of contiguous and broken foreland basins: examples from the eastern flanks of the central Andes in Bolivia and NW Argentina, in *Tectonics of Sedimentary Basins: Recent Advances*, edited by C. Busby and A. Azor, pp. 508-521, John Wiley & Sons Ltd, Chichester, UK. doi: 10.1002/9781444347166.ch25.
- Stüwe, K., L. White, and R. Brown (1994), The influence of eroding topography on steady-state isotherms; application to fission track analysis, *Earth and Planetary Science Letters*, 124(1-4), 63-74, doi: 10.1016/0012-821X(94)00068-9.
- Sun, J., and Z. Zhang (2008), Palynological evidence for the mid-Miocene climatic optimum recorded in Cenozoic sediments of the Tian Shan Range, northwestern China, *Global and Planetary Change*, 64(1), 53-68, doi: 10.1016/j.gloplacha.2008.09.001.
- Sun, J., and Z. Zhang (2009), Syntectonic growth strata and implications for late Cenozoic tectonic uplift in the northern Tian Shan, China, *Tectonophysics*, 463(1), 60-68, doi: 10.1016/j.tecto.2008.09.008.
- Sun, J., R. Zhu, and J. Bowler (2004), Timing of the Tianshan Mountains uplift constrained by magnetostratigraphic analysis of molasse deposits, *Earth and Planetary Science Letters*, 219(3), 239-253, doi: 10.1016/S0012-821X(04)00008-1.
- Sun, J., Y. Li, Z. Zhang, and B. Fu (2009), Magnetostratigraphic data on Neogene growth folding in the foreland basin of the southern Tianshan Mountains, *Geology*, 37(11), 1051-1054, doi: 10.1130/G30278A.1.
- Suppe, J. (1983), Geometry and kinematics of fault-bend folding, *American Journal of Science*, 283(7), 684-721, doi: 10.2475/ajs.283.7.684.
- Tan, X., K. P. Kodama, H. L. Chen, D. Fang, D. Sun, Y. Li (2003), Paleomagnetism and magnetic anisotropy of Cretaceous red beds from the Tarim basin, northwest China: Evidence for a rock magnetic cause of anomalously shallow paleomagnetic inclinations from central Asia, *Journal of Geophysical Research*, 108, EPM 10-1–EPM 10-20.
- Tapponnier, P., and P. Molnar (1979), Active faulting and Cenozoic tectonics of the Tien Shan, Mongolia, and Baykal regions, *Journal of Geophysical Research*, 84(B7), 3425-3459, doi: 10.1029/JB084iB07p03425.
- Thiede, R. C., B. Bookhagen, J. R. Arrowsmith, E. R. Sobel, and M. R. Strecker (2004), Climatic control on rapid exhumation along the Southern Himalayan Front, *Earth and Planetary Science Letters*, 222(3), 791-806, doi: 10.1016/j.epsl.2004.03.015.
- Thomas, J. C., H. Perroud, P. R. Cobbold, M. L. Bazhenov, V. S. Burtman, A. Chauvin, and E. Sadybakasov (1993), A paleomagnetic study of Tertiary formations from the Kyrgyz Tien-Shan and its tectonic implications, *Journal of Geophysical Research*, 98, 9571-9589.
- Thompson, S., R. Weldon, C. Rubin, K. Abdrakhmatov, P. Molnar, P., and G. Berger (2002), Late Quaternary slip rates across the central Tien Shan, Kyrgyzstan, central Asia, *Journal of Geophysical Research*, 107, ETG 7-1–ETG 7-32.
- Thomson, S. N., M. T. Brandon, P. W. Reiners, M. Zattin, P. J. Isaacson, M. L. Balestrieri (2010), Thermochronologic evidence for orogen-parallel variability in wedge kinematics during extending convergent orogenesis of the northern Apennines, Italy, *GSA Bulletin*, 122(7/8), 1160-1179, doi: 10.1130/B26573.1.
- Tozer, C. H. (2004), The influence of inherited structures on the Cenozoic orogeny of the Kyrgyz Tien Shan, PhD thesis, Department of Geological Sciences, University of Oregon, USA.
- Trifonov, V. G., E. V. Artyushkov, A. E. Dodonov, D. M. Bachmanov, A. V. Mikolaichuk, and F. A. Vishnyakov (2008), Pliocene-quaternary orogeny in the Central Tien

- Shan, *Russian Geology and Geophysics*, 49(2), 98-112, doi: 10.1016/j.rgg.2007.06.012
- Trofimov, A. K., N. F. Udalov, N. G. Utkina, F. B. Fortuna, O. K. Chediya, and V. M. Yazovskii (1976), *Cenozoic Geology of the Chu Depression and Its Mountainous Surroundings* [in Russian], 128 pp., Nauka, St. Petersburg, Russia.
- Turchinskiy, V. P. (1970), Geological map of the USSR of 1:200 000 scales. Northern Tien Shan series, *Sheet K-43-XVIII*, Russian Geological Research Institute (VSEGEI), Nedra, Moscow, Russia.
- Vakhrameev V. A. (1964), Jurassic and Early Cretaceous floras of Eurasia and the paleofloristic provinces of this period (in Russian), *Transactions Geol. Inst. Moscow*, 102, 1-263.
- Valla, P. G., F. Herman, P. A. Van Der Beek, and J. Braun (2010), Inversion of thermochronological age-elevation profiles to extract independent estimates of denudation and relief history—I: Theory and conceptual model, *Earth and Planetary Science Letters*, 295(3), 511-522, doi: 10.1016/j.epsl.2010.04.033.
- Wack, M. (2010), A new software for the measurement of magnetic moments using SQUID and spinner magnetometers, *Computers & Geosciences*, 36, 1178-1184.
- Wack, M. R., and S. A. Gilder (2012), The SushiBar: An automated system for paleomagnetic investigations, *Geochemistry Geophysics Geosystems*, 13, Q12Z38.
- Wack, M. R., S. A. Gilder, E. A. Macaulay, E. R. Sobel, J. Charreau, and A. Mikolaichuk (in review), Cenozoic magnetostratigraphy and rock magnetism of the southern Issyk-Kul basin, Kyrgyzstan, *Tectonophysics: A tribute to Graham Borradaile*, in review.
- Wagner, G. A., and G. M. Reimer (1972), Fission track tectonics: the tectonic interpretation of fission track apatite ages, *Earth and Planetary Science Letters*, 14(2), 263-268, doi: 10.1016/0012-821X(72)90018-0.
- Walker, T. R. (1967), Formation of red beds in modern and ancient deserts, *Geological Society of America Bulletin*, 78(3), 353-368, doi: 10.1130/0016-7606(1967)78[353:FORBIM]2.0.CO;2.
- Wang, B., M. Faure, L. Shu, K. de Jong, J. Charvet, D. Cluzel, B. Jahn, Y. Chen, and G. Ruffet (2010), Structural and geochronological study of high-pressure metamorphic rocks in the Kekesu section (northwestern China): Implications for the late Paleozoic tectonics of the Southern Tianshan, *The Journal of Geology*, 118(1), 59-77, doi: 10.1086/648531.
- Wang, Q., S. Li, and Z. Du (2009), Differential uplift of the Chinese Tianshan since the Cretaceous: constraints from sedimentary petrography and apatite fission-track dating, *International Journal of Earth Sciences*, 98(6), 1341-1363, doi: 10.1007/s00531-009-0436-2.
- Wang, Z., T. Li, J. Zhang, Y. Liu, and Z. Ma (2008), The uplifting process of the Bogda Mountain during the Cenozoic and its tectonic implication, *Science in China Series D: Earth Sciences*, 51(4), 579-593, doi: 10.1007/s11430-008-0038-z.
- Watson, G., and R. Enkin (1993), The fold test in paleomagnetism as a parameter estimation problem, *Geophysical Research Letters*, 20, 2135-2137.
- Wentworth, C. K. (1922), A scale of grade and class terms for clastic sediments, *The Journal of Geology*, 30(5), 377-392.
- Whipple, K. X. (2009), The influence of climate on the tectonic evolution of mountain belts, *Nature Geoscience*, 2(2), 97-104, doi: 10.1038/ngeo413.
- Whipple, K. X., and B. J. Meade (2006), Orogen response to changes in climatic and tectonic forcing, *Earth and Planetary Science Letters*, 243(1), 218-228, doi: 10.1016/j.epsl.2005.12.022.
- Willett, S. D. (1999), Rheological dependence of extension in wedge models of convergent orogens, *Tectonophysics*, 305(4), 419-435, doi: 10.1016/S0040-1951(99)00034-7.
- Willett, S., C. Beaumont, and P. Fullsack (1993), Mechanical model for the tectonics of doubly vergent compressional orogens, *Geology*, 21(4), 371-374, doi: 10.1130/0091-7613(1993)021<0371:MMFTTO>2.3.CO;2.
- Windley, B. F., M. B. Allen, C. Zhang, Z. Y. Zhao, and G. R. Wang (1990), Paleozoic accretion and Cenozoic reformation of the Chinese Tien Shan range, central Asia, *Geology*, 18(2), 128-131, doi: 10.1130/0091-7613(1990)018<0128:PAACRO>2.3.CO;2.
- Winkler, A., L. Alfonsi, F. Florindo, L. Sagnotti, F. Speranza (1997), The magnetic anisotropy of rocks: principles, techniques and geodynamic applications in the Italian peninsula, *Annals of Geophysics*, 40, 729-740.
- Wolf, R. A., K. A. Farley, and D. M. Kass (1998), Modeling of the temperature sensitivity of the apatite (U-Th)/He thermochronometer, *Chemical Geology*, 148(1), 105-114, doi: 10.1016/S0009-2541(98)00024-2.
- Wolfe, M. R., and D. F. Stockli (2010), Zircon (U-Th)/He thermochronometry in the KTB drill hole, Germany, and its implications for bulk He diffusion kinetics in zircon, *Earth and Planetary Science Letters*, 295(1), 69-82, doi: 10.1016/j.epsl.2010.03.025.
- Yan, M., R. van der Voo, L. Tauxe (2005), Shallow bias in Neogene palaeomagnetic directions from the Guide Basin, NE Tibet, caused by inclination error, *Geophysical Journal*, 163, 944-948.
- Yin, A., S. Nie, P. Craig, T. M. Harrison, F. J. Ryerson, Q. Xianglin, and Y. Geng (1998), Late Cenozoic tectonic evolution of the southern Chinese Tien Shan, *Tectonics*, 17(1), 1-27, doi: 10.1029/97TC03140.
- Zachos, J., M. Pagani, L. Sloan, E. Thomas, and K. Billups (2001), Trends, rhythms, and aberrations in global climate 65 Ma to present, *Science*, 292(5517), 686-693, doi: 10.1126/science.1059412.
- Zakharov, I. L., and M. P. Khristova (1986), Legend compilations to the geological maps of the Kyrgyz range mountain system (report of a Alamedin party on researches at 1983-1986), *Archives of the ministry of natural resources of the Kyrgyz Republic*, Frunze.
- Zamaletdinov T.S., and T. V. A. .. (1994), Deep forecast mapping on Kyrgyz geodynamic site. The report of the Geodynamic party on results of the works carried out at 1989-1994 years, *Archives of the ministry of natural resources of the Kyrgyz Republic*, Bishkek.
- Zhang, C., Y. Wang, T. Deng, X. Wang, D. Biasatti, Y. Xu, and Q. Li (2009), C4 expansion in the central Inner Mongolia during the latest Miocene and early Pliocene, *Earth and Planetary Science Letters*, 287(3), 311-319, doi: 10.1016/j.epsl.2009.08.025.
- Zhuang, G., J. K. Hourigan, P. L. Koch, B. D. Ritts and M.L. Kent-Corson (2011), Isotopic constraints on intensified aridity in Central Asia around 12Ma, *Earth and Planetary Science Letters*, 312(1), 152-163, doi: 10.1016/j.epsl.2011.10.005.
- Zhukov, Y. V. (editor) (1969) Geological Map of the USSR of 1:200000 scales, Northern Tien-Shan series, *Sheet K-44-XXIV*, Russian Geological Research Institute (VSEGEI), Nedra, Moscow.
- Zhukov, Y. V. (editor) (1970) Geological Map of the USSR of 1:200000 scales, Northern Tien-Shan series, *Sheet K-43-XXIII*, Russian Geological Research Institute (VSEGEI), Nedra, Moscow.
- Zhukov, Y. V. (editor) (1984) Geological Map of the USSR of 1:200000 scales, Northern Tien-Shan series, *Sheet K-43-XII*, Russian Geological Research Institute (VSEGEI), Nedra, Moscow.
- Zijderveld, J. D. A. (1967), A.C. demagnetization of rocks: Analysis of results, in *Methods in Palaeomagnetism* edited by Collinson, D. W., K. M. Creer, S. K. Runcorn., Elsevier, Amsterdam, pp. 254-286.
- Zubovich, A.V., X.q. Wang, Y.G. Scherba, G.G. Schelochkov, R. Reilinger, C. Reigber, O.I. Mosienko, P. Molnar, W. Michajljow, V.I. Makarov, J. Li, S.I. Kuzikov, T.A. Herring, M.W. Hamburger, B.H. Hager, Y.m. Dang, V.D. Bragin, and R.T. Beisenbaev (2010), GPS velocity field for the Tien Shan and surrounding regions, *Tectonics*, 29, TC6014, doi:10.1029/2010TC002772.

Appendix 1.

Thermochronological data from the Barskoon transect (Supplementary material for Chapter 2)

In this appendix the thermochronological data from the 15 new samples used in Chapter 2 is presented. In section A1.1, the methodology and procedures involved in thermochronological analysis and thermal modelling are outlined. Apatite fission track (AFT) and (U-Th)/He (AHe) data are presented in Tables A1.1 and A1.2, respectively. Thermal modelling results are presented in Figure A1.2. Then in Section 1.2, the variability of AHe ages derived from the aliquots of the same sample is discussed and evaluated using plots of AHe age against effective uranium (eU) and grain size (radius of equivalent sphere) (Figure A1.3).

A1.1. Thermochronological methodology

A1.1.1. AFT methodology

Thirteen samples were analysed using AFT, following preparation and analytical procedure presented in Table A1.1. To increase the number of horizontal confined AFT length measured, additional mounts of four samples were irradiated using ^{252}Cf [Carlson *et al.*, 1999]. Fission track length histograms for all samples are presented in Figure A1.1.

AFT ages were determined using 13 to 25 grains per sample, except for two samples (SP2 and SP3; Table A1.1) that contained insufficient countable grains. These samples failed the chi-squared test and are reported as central ages ($\pm 1\sigma$) (Table A1.1). All other samples pass chi-squared and are reported as pooled ages ($\pm 1\sigma$) (Table A1.1). Statistics were calculated using the MacTrackX software; following procedures of Galbraith [1981]. Kinetic properties for every grain dated and measured were assessed by making at least four Dpar measurements [Ketcham, 1999], averaged and corrected following Sobel and Seward [2010].

A1.1.2. AHe methodology

AHe ages were determined for 2-5 aliquots per sample; all data is presented in Table A1.2. Eight samples were analysed at the University of Melbourne, typically using 3 grain aliquots. A further 4 samples were analysed at the Scottish Universities Environmental Research Centre (SUERC) using single grain aliquots. Corrections are made for the ejection of alpha particles (^4He) produced by the decay of uranium and thorium (and samarium) atoms near the margins of a crystal [Farley *et al.*, 1996]. The correction factor is calculated on the basis of grain size for single aliquots analysed at SUERC, or by taking the mean grain size for multiple grain aliquots analysed at the University of Melbourne. Helium was released during degassing experiments on all aliquots, except for NP2-1 and NP4-1 where helium levels did not increase beyond the background level; these aliquots are therefore discarded and not considered.

A1.1.3. Thermal modelling

Thermal modelling of individual samples was carried out using the HeFTy program [Ketcham, 2005]. The AFT annealing model of Ketcham *et al.* [2007] and the AHe calibration of Flowers *et al.* [2009] were used. Inputs included AFT lengths, single grain AFT ages, kinetic parameters (Dpar) and selected AHe aliquots. AFT lengths were adjusted for their angle to the crystallographic axis, and the ^{252}Cf -irradiation option was used where appropriate. The program generates synthetic thermochronologic data for a particular time-temperature history using a Monte Carlo approach that is then compared with the observed data and evaluated to determine goodness-of-fit using a Kuiper's statistic. Acceptable fits (goodness-of-fit >0.05) were used for interpretations. Thermal models are only interpreted below $\sim 110^\circ\text{C}$.

The input error for individual AHe aliquots for the thermal modelling is taken to be either 10% of the uncorrected age or the analytical error, depending on which is higher. Where possible, multiple

AHe aliquots were modelled simultaneously to more tightly constrain modelled time-temperature histories; NP2-1 and aliquots from CP2 were not included in any thermal models (see sections 2.3.1 and 2.3.3 for explanations). Including some AHe aliquots meant no time-temperature histories could be identified that fit the AFT and AHe data acceptably (goodness-of-fit >0.05). For example, acceptable fits were not found when any AHe aliquots were included that had a corrected age older than or equal to the AFT age within error (NP1-1, NP2-2, NP2-3, CP4-2, SP1-1,2,3; Tables A1.1 and 1.2). Samples NS, SS and SP4 have groups of two aliquots that reproduce well and one anomalously old aliquot (NS-3, SS-3 and SP4-5; Table A1.2). For these samples, and for the remaining aliquots of NP1 and CP4, thermal models were divided into those with younger AHe aliquots and those with the older aliquots. For CP4 and NS, good fitting time-temperature histories were identified when only young AHe aliquots were included in thermal models; older aliquots did not yield good fits. AHe aliquots and a summary of the AFT data used in different thermal models for each sample are listed in Table A1.2. Thermal model results are shown in Figure A1.2.

The goal of the thermal modelling was to identify any increases in cooling and to constrain as accurately as possible a range of paleo-temperatures prior to the onset of Cenozoic deformation. To achieve these goals, different constraint boxes were constructed that modelled time-temperature pathways had to pass through. The first thermal models were only constrained at the present day at surface temperatures of $10 \pm 10^\circ\text{C}$ and with a large box with temperatures in excess of the $\sim 110^\circ\text{C}$ assumed to be the total AFT annealing temperature ranging from $\sim 200\%$ and 90% of the sample's AFT age. These constraints provided a preliminary indication of the likely time-temperature pathways that would agree with a sample's data. However, even with these minimal constraints, some thermal models clearly show that cooling must have increased in the last 25 Ma (CP1, NS, SS and SP4; Figure 2.4). To more precisely date the timing of this cooling increase, additional constraints were added to the thermal models, forcing generated time-temperature histories to cool at a particular time to test the feasibility of different cooling increases. Three sets of thermal models have been run, each with an additional constraint box between ~ 26 and 20 Ma, ~ 15 and 5 Ma, or 5 and 0 Ma (Figure 2.4). The initial constraints of the present-day surface temperature and the large box remain constant during these thermal models, except in CP2 and NS where the lower time constraint was increased to allow the 26-20 Ma box to be constructed. The additional constraints were selected because there is evidence from the Terskey Range or elsewhere in the Tien Shan that exhumation and therefore cooling could have increased during each of these periods. The ~ 26 and 20 Ma constraint tests whether the increase in exhumation observed in our AERs (section 2.3.3) and the onset of Cenozoic deformation suggested by *Wack et al.*, [in review] can be identified via thermal modelling, and if it is possible to more precisely constrain the timing of this event. The ~ 15 - 5 and <5 Ma constraints were selected to determine whether similar increase in exhumation identified elsewhere in the Tien Shan, notably the Kyrgyz Range (Figure 2.1a) [*Bullen et al.*, 2001; 2003; *Sobel et al.*, 2006b] occurred in the Terskey Range.

A1.2. AHe age variability

In many cases AHe ages were not reproduced in different aliquots from the same sample. Some of this age variation is interpreted to relate to differences in the diffusion of ^4He . Grain size displays a positive correlation with AHe age aliquots in 6 samples (NP4, CP1, CP3, NS and SP4; Table A1.2 and Figure A1.3), suggesting in those cases that size has a strong control on diffusion [*Farley*, 2000]. A positive correlation is also found between effective uranium (eU) and the AHe age of aliquots in 2 samples (NS and CP3). Grain size- and eU-AHe age plots for all samples can be found in the Figure A1.3. Aliquots with higher eU are more likely to be affected by radiation damage, which leads to increased helium retention and older AHe ages [*Flowers et al.*, 2009]. Aliquots ages of samples are only compared or used in age-elevation relationships (AERs) when they have similar grain sizes and eU concentrations. In samples where AHe ages do not correlate with either grain size or eU, the

reason for age variability is unclear and difficult to interpret. One possibility is that age variation relates to grain breakages during the mineral separation process. Another possibility is anomalously old AHe aliquots contain unidentified inclusions within some crystals which produced anomalously old aliquots [Farley, 2002]. Interestingly when aliquots with anomalously old AHe ages are discarded, correlations can be found between AHe age and eU in a further 2 samples (CP4 and SP1; see supplementary material). Additional helium implantation from sources outside the crystal or uranium and thorium zonation within crystals [Farley, 2002] may also be responsible for anomalously old aliquots.

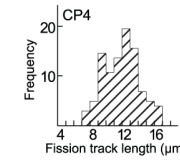
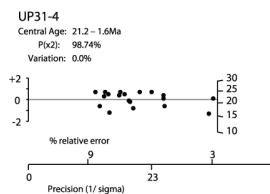
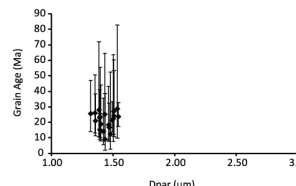
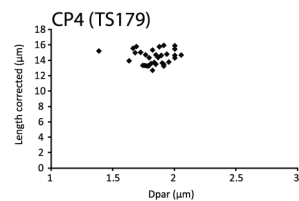
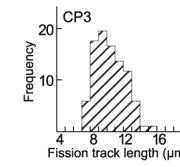
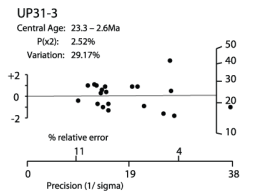
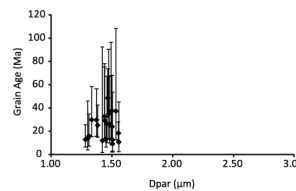
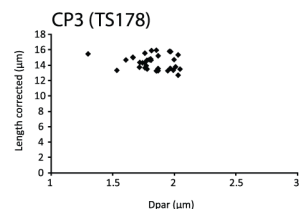
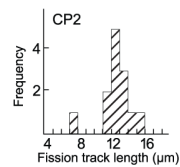
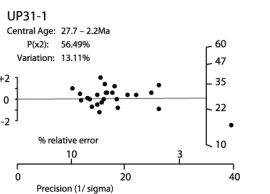
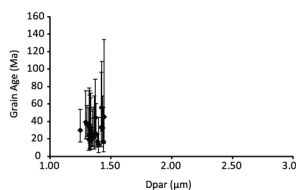
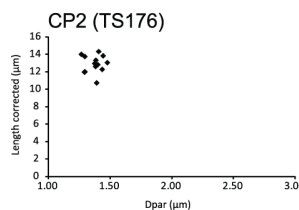
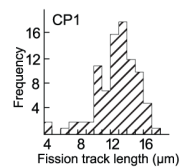
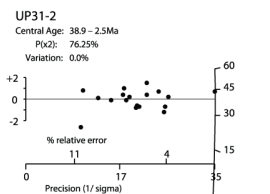
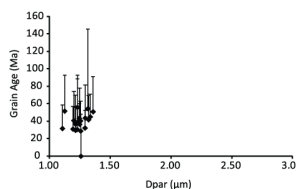
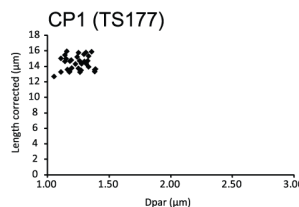
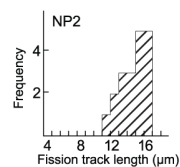
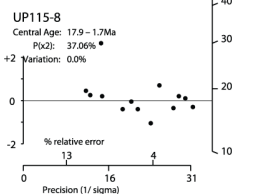
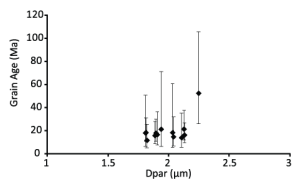
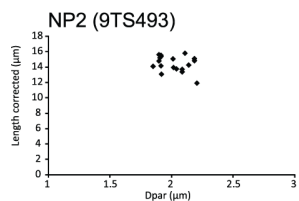
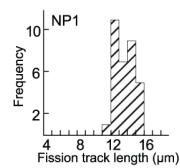
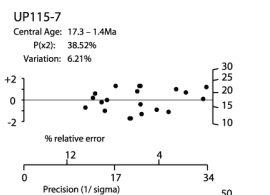
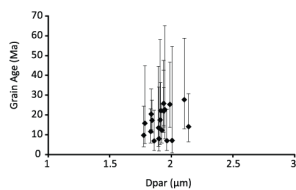
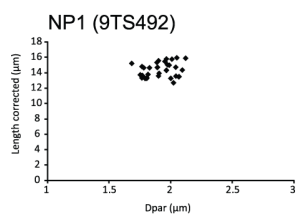
Table A1.1. Apatite fission track (AFTD) data from the Terskey Range^a

Sample ^b	Code	Age/ Lithology	Latitude	Longitude	Altitude, m ^e	Xf ^d	Rho-S ^e x10 ⁶	NS ^f	RhoI ^e x10 ⁵	NI ^f	P(χ^2) ^g %	RhoD ^h x10 ⁶	ND ⁱ	Age, Ma $\pm 1\sigma$	Dpar ^j , μm	SD, μm	Mean length, μm	Error, μm	SD, μm	No. Lengths ^k	Analyst ^l	
NP1	9T5492	S/granite	42.0563	77.6100	2645	20	3.925	177	3.062	2269	38.5	1.246	5060	17.3	1.4	1.92	0.11	13.66	2.38	1.23	33	EM
NP2	9T5493	S/granite	42.0624	77.6056	2447	13	7.801	123	6.308	1521	37.1	1.239	5060	17.9	1.7	2.00	0.13	13.75	3.15	1.45	19	EM
CP1	TS177	O3/granite	41.9831	77.6009	3520	20	1.715	299	2.655	1931	76.3	1.365	5710	38.9	2.5	1.36	0.06	11.77	1.25	2.49	89	ES
CP2	TS176	O3/granite	41.9859	77.6074	3282	25	1.491	218	1.617	2011	56.5	1.360	5710	27.7	2.2	1.24	0.08	11.64	3.23	1.92	13	ES
CP3	TS178	O3/granite	41.9842	77.6113	3040	21	2.174	162	1.969	1789	31.3	1.369	5710	23.3	2.6	1.71	0.19	9.40	0.96	1.80	96*	ES
CP4	TS179	O3/granite	41.9832	77.6163	2839	20	1.330	200	1.113	2389	98.7	1.374	5710	21.2	1.6	1.76	0.19	10.92	1.09	2.21	84*	ES
CP5	8T5386	O3/granite	41.9766	77.6229	2626	20	1.388	76	1.496	705	5.0	1.134	4734	21.8	2.7	1.81	0.18	-	-	-	-	EM
NS	may105	O3/granite	41.9703	77.6377	2605	20	1.188	64	1.351	563	90.0	1.392	5562	28.2	3.8	1.78	0.16	11.78	1.86	1.63	40*	EM
SS	may104	O3/granite	41.9397	77.6564	2721	23	0.937	103	2.220	435	7.6	1.397	5562	58.5	6.6	1.89	0.14	12.64	4.78	2.40	7	EM
SP1	TS183	O3/granite	41.8735	77.7219	3780	20	1.123	541	4.667	1302	83.4	1.214	5034	92.5	4.9	1.40	0.09	13.12	1.34	1.81	96	ES
SP2	TS171	PreC/phyllite	41.8945	77.6993	3821	7	2.506	507	16.939	750	0.0	1.264	5034	40.7	29.5	1.85	0.39	12.72	5.69	1.53	5	ES
SP3	TS172	PreC/phyllite	41.8956	77.6874	3641	5	1.356	35	2.409	197	3.9	1.274	5034	40.2	11.3	1.48	0.09	14.66	-	-	1	ES
SP4	TS173	O3/granite	41.9038	77.6537	3430	18	1.340	72	1.561	618	99.7	1.294	4981	26.9	3.4	1.80	0.12	10.25	1.97	2.49	27*	EM

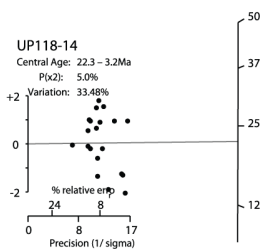
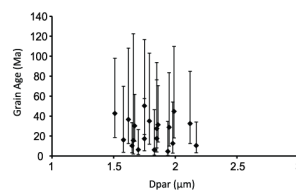
^a Sample preparation and analysis were similar to that outlined by Sobel and Strecker [2003b]. All apatites were etched in 5.5 mol Nitric acid for 20 seconds at 21°C. Samples were analyzed with a Leica DMRM microscope with drawing tube located above a digitizing tablet and a Kinetek computer-controlled stage driven by the FTStage program [Dumitru, 1993]. Analysis was performed with reflected and transmitted light at 1250X magnification. Samples were irradiated at Oregon State University. Following irradiation, the mica external detectors were etched with 21°C, 40% hydrofluoric acid for 45 minutes. The pooled age (central age) is reported for samples with P(χ^2) greater than (less than) 5% as they pass (fail) the χ^2 test. Age errors are presented as one sigma, calculated using the zeta calibration method [Hurford and Green, 1983]. Note that two slides were combined for sample TS172.

^b Sample name used in text.
^c Altitude (meters) taken from STRM dataset.
^d Xfs is the number of individual crystals dated.
^e Rho-S and Rho-I are spontaneous and induced track density; both measured in (tracks/cm²).
^f NS and NI are the number of spontaneous and induced tracks counted, respectively.
^g P(χ^2) (%) is the chi-squared probability [Galbraith, 1981; Green, 1981].
^h Rho-D is the induced track density in external detector adjacent to CNS dosimetry glass (tracks/cm²).
ⁱ ND is the number of tracks counted in determining Rho-D.
^j Mean of at least four Dpar measurements. The correction factor [Sobel and Seward, 2010] was found to 1 with respect to the Durango apatite standard [Donelick et al., 1999].
^k Samples with asterisk (*) indicates track lengths measured from ²⁵²Cf-irradiation slide.
^l Zeta calibration used for apatite: EM: 357.2 \pm 8 (E. Mccaulley, unpublished, 2011); ES: 369.6 \pm 7.6 (E. Sobel, unpublished data, 2003). All lengths were measured by EM. The correction factor [Sobel and Seward, 2010] compared to Durango and FCT apatites [Donelick et al., 1999] were found to be 1.0 for EM and 0.8 for ES.

^{Spot samples}
Northern profile
Central profile
Southern profile



CP5 (8TS386)



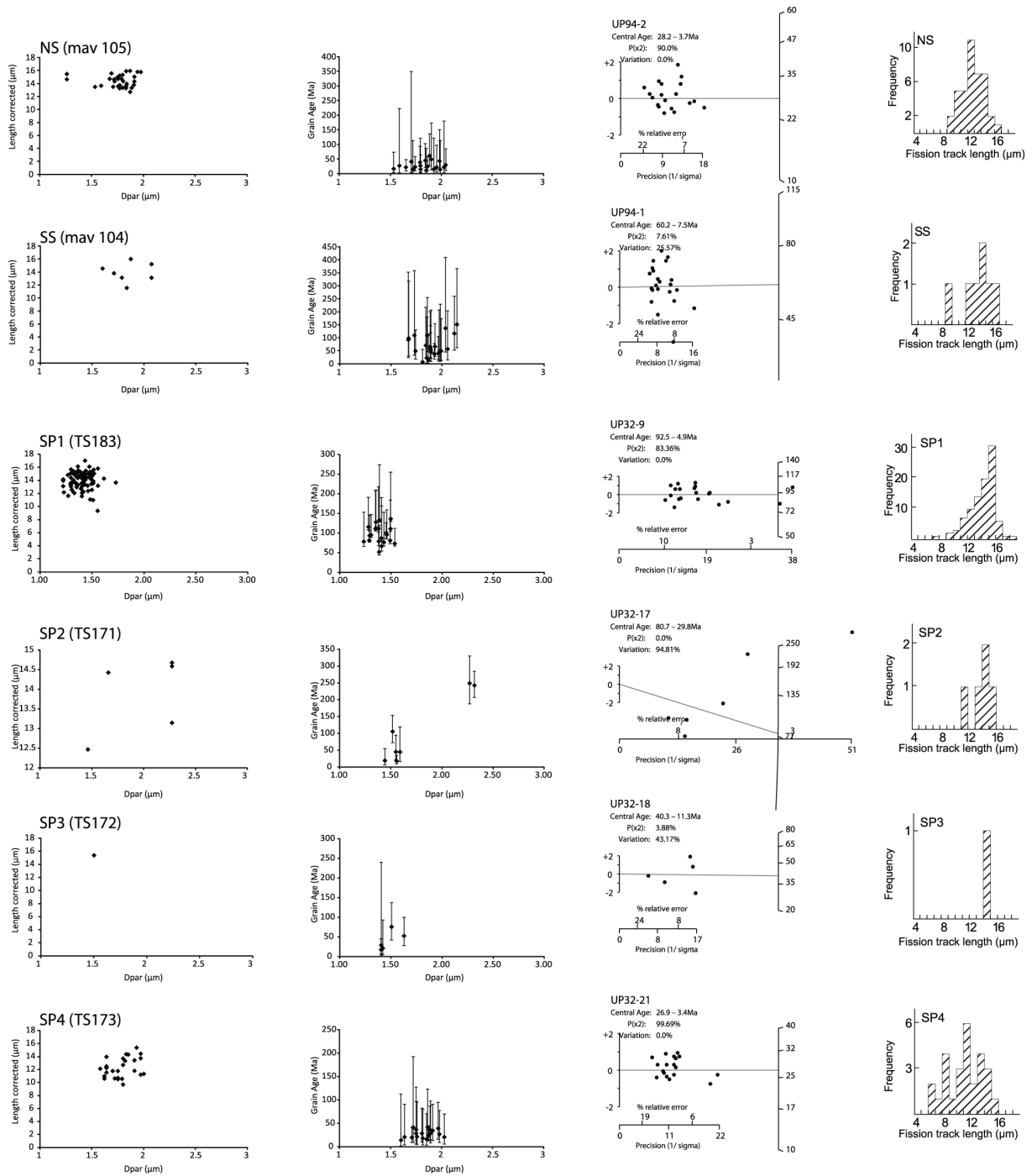


Figure A1.1. Plots of AFT data for all 12 samples analysed. From left to right: Dpar (μm) versus HeFTy corrected AFT lengths (μm), Dpar (μm) versus Grain age (Ma) (errors are $\pm 95\%$ uncertainty limits), radial plots for AFT ages, and AFT length histograms.

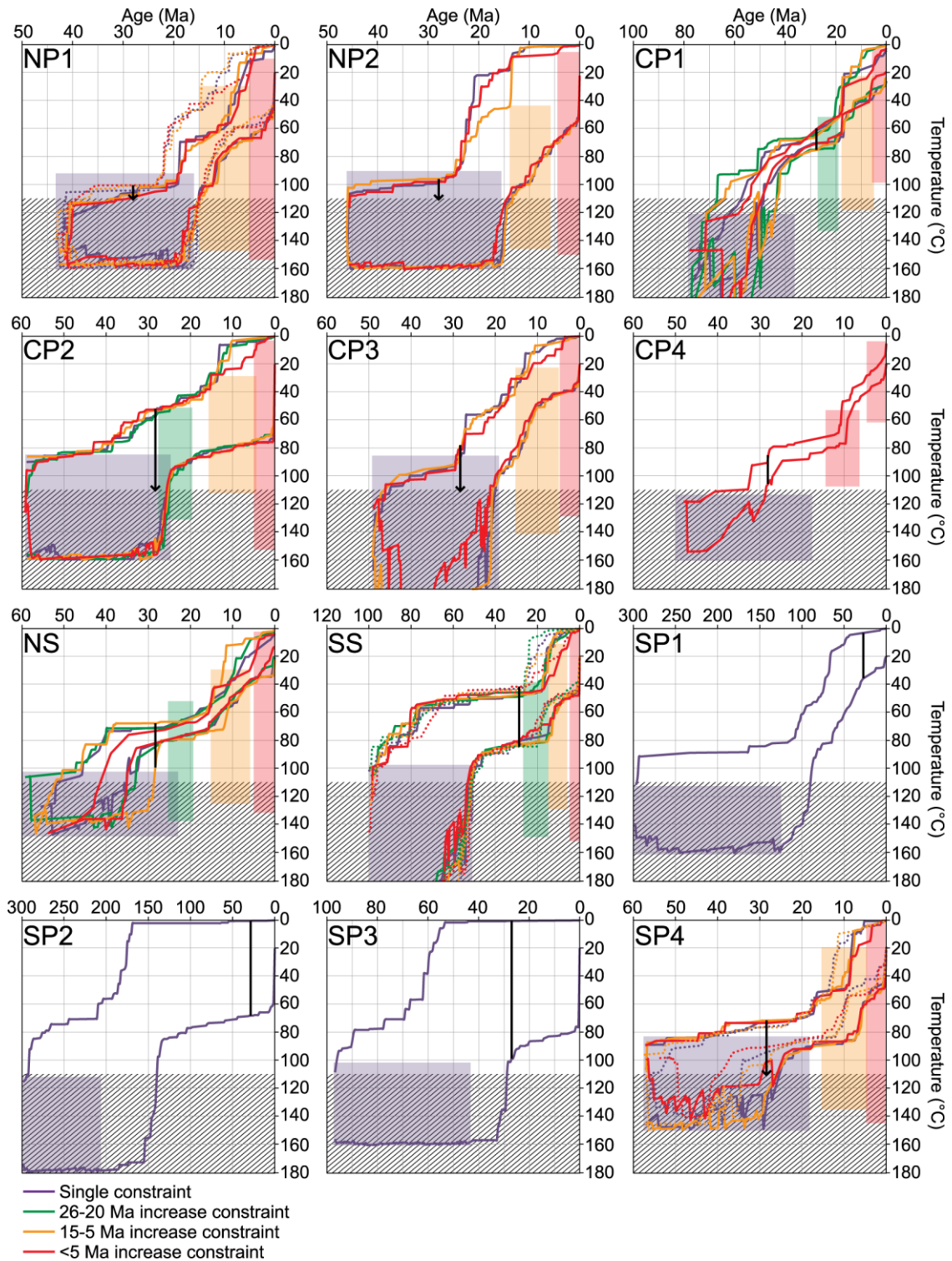


Figure A1.2. Time-temperature histories derived from thermal modelling of individual samples using HeFTy software [Ketcham, 2005]. AFT and AHe input data for thermal models is summarized in Table A1.3. Histograms of AFT track lengths are in the data repository. Acceptable time-temperature pathway envelopes are colour coded to match the input constraints (faded boxes), see key at bottom for list. Dotted lines = thermal models including old AHe aliquot component; Solid lines = remaining AHe component. Diagonal lines = portion of time-temperature histories above the assumed total AFT annealing temperature ($\sim 110^{\circ}\text{C}$); not constrained by thermochronological data. Black lines indicate possible temperature range at 28 Ma.

Table A1.2. continued

Sample ^b	Xls ^c	Lithology	Latitude	Longitude	Alt ^d (m)	U ^e	Th ^e	Sm, ppm	He ^f x10 ⁻⁹ cc	eU ^g	Length ^h , µm	Width ^h , µm	Rs ⁱ , µm	Term ^j	Uncorrected age ^k (Ma)	Error	Model error ^l	F ^m	Corrected age (Ma)	Error	Notes	
SP1-2	3	O3/granite	41.8735	77.7219	3780	5.8	19.0	470.8	0.79	10.3	137	102	51	3	86.9	0.7	n/a	0.69	126.0	7.8	Incompatible with AFT data (modelling)	
SP1-3	3	O3/granite	41.8735	77.7219	3780	7.4	24.9	597.9	1.47	13.3	197	92	46	4	92.1	0.7	n/a	0.68	135.7	8.4	Incompatible with AFT data (modelling)	
<i>W. Mean</i>																						
SP4-1	3	O3/granite	41.9038	77.6537	3430	17.3	50.3	352.6	0.41	29.1	198	103	52	2	9.2	0.7	0.9	0.72	12.8	0.8	Old component – modelled with AFT	
SP4-2	3	O3/granite	41.9038	77.6537	3430	17.5	47.0	320.5	0.11	28.5	164	79	40	3	5.0	0.6	0.6	0.64	7.8	0.5	Young component – modelled with AFT	
SP4-3	3	O3/granite	41.9038	77.6537	3430	7.6	12.9	125.2	0.18	22.8	156	103	51	1	5.9	0.8	0.8	0.76	7.8	0.5	Young component – modelled with AFT	
SP4-3	3	O3/granite	41.9038	77.6537	3430	14.0	37.5	246.7	0.30	23.4	1178	125	63	1	9.1	0.7	0.9	0.68	13.4	0.8	Old component – modelled with AFT	
SP4-5	3	O3/granite	41.9038	77.6537	3430	14.0	39.9	247.9	0.26	10.6	198	90	45	3	12.4	0.7	n/a	0.71	17.4	0.8	Incompatible with AFT data (modelling)	
<i>W. Mean</i>																						
																						Positive grain size-AHe age correlation

^a Sample analysis was similar to that outlined by *Foeken et al.* [2006] for single grained aliquots and *Spiegel et al.*, [2009] for multiple grain aliquots. Grains were placed in platinum tubes and outgassed using a laser.

^b W. Mean is the weighted mean of all the aliquots from the above samples; the corrected age error for weighted mean is the standard deviation between the aliquots. Samples with strikethrough did not release any helium on degassing and are not included in weighted mean calculations.

^c Xls is the number of individual crystals in one aliquot; single crystal aliquots were analysed at SUERC and multiple crystal aliquots were analysed at the University of Melbourne.

^d Alt: Altitude of sample. Taken from SRIM dataset.

^e Uranium and Thorium content in parts per million (ppm); unless marked by asterisk (*) in which case content in nanograms (ng)

^f Helium volume in nano-cubic centimeters (ncc): 10⁹ cubic centimeters.

^g Effective uranium calculated by U + (0.235 x Th) [Flowers et al., 2009]. Values stated as parts per million (ppm); unless marked by asterisk (*) in which case content in nanograms (ng).

^h Length (Len) and width (Wid) of crystals in aliquots. For multiple grained aliquots this is the mean of all crystals.

ⁱ Radius of a sphere with the equivalent surface-area-to-volume ratio as cylindrical crystals [Meesters and Dunai, 2002].

^j The number of complete terminations preserved within an aliquot.

^k Age calculations following *Meesters and Dunai* [2002] for single-grained aliquots and *Farley et al.* [1996] for multiple grained aliquots.

^l Model error used for thermal modelling. Taken to be 10% of uncorrected age or the analytical error, depending on which is higher.

^m α -ejection correction [Farley et al., 1996] calculated using mass-weighted average radii.

Table A1.3. Thermal modelling of thermochronologic data from the Terskey Range^a

Sample ^b	AFT data used ^c	AHe aliquots used ^d	Cooling increases ^e , Ma	Min. temp. at 28 Ma ^f , °C	Max. temp. at 28 Ma, °C	Exhumation ^g , km
NP1-old	20 AFTa, 33 AFTI	NP1-2	Poorly defined	100	>110	3.2 – >4.4
NP1-young	20 AFTa, 33 AFTI	NP1-3	Poorly defined	105	>110	3.4 – >4.4
NP2	13 AFTa, 19 AFTI	none	Poorly defined	95	>110	3.0 – >4.4
CP1	20 AFTa, 89AFTI	CP1-1,2,3,4,5	~20	61	75	1.6 – 3.0
CP2	25 AFTa, 13AFTI	none	Poorly defined	52	>110	1.3 – >4.4
CP3	21 AFTa, 96 AFTI*	CP3-1,2	Poorly defined	78	>110	2.3 – > 4.4
CP4-old	20 AFTa, 84 AFTI*	CP4-3	No acceptable fits	n/a	n/a	n/a
CP4-young	20 AFTa, 84 AFTI*	CP4-1	~10	90	106	2.8 – 4.2
NS-old	20 AFTa, 40 AFTI*	NS-1,4	No acceptable fits	n/a	n/a	n/a
NS-young	20 AFTa, 40 AFTI*	NS-2,5	20-10	68	94	1.9 – 3.8
SS-old	23 AFTa, 7 AFTI	SS-1,4	~20	41	84	0.8 – 3.4
SS-young	23 AFTa, 7 AFTI	SS-2	<20	45	83	1.0 – 3.3
SP1	20 AFTa, 96 AFTI	none	Poorly defined	3	37	<1.5
SP2	7AFTa, 5AFTI	none	Poorly defined	0	68	<2.7
SP3	5AFTa, 1AFTI	none	Poorly defined	0	101	<4.0
SP4-old	18AFTa, 27 AFTI	SP4-1,4	<20	76	102	2.2 – 4.1
SP4-young	18AFTa, 27 AFTI	SP4-2,3	15-5	71	>110	2.0 – >4.4

^a Thermal modelling of individual samples carried out using HeFTy version 1.7.4 (see supplementary material for time-temperature plots). *Ketcham et al.* [2007] annealing model and 5.5 mol C-axis projection were used for AFT lengths. Calibration used for AHe is from *Flowers et al.* [2009], while the stopping distance and alpha correction is from *Ketcham* [2009].

^b Samples used in different thermal models. Models that use the old or young component of AHe ages are stated.

^c Thermochronologic data used in thermal modelling. AFTa: number of apatite crystals counted and dated. AFTI: number of AFT lengths measured (asterisk denotes when Cf-irradiation was used).

^d AHe aliquots used in models; explanations are provide in text for why particular aliquots were selected. HeFTy inputs of the uncorrected age and errors for individual aliquots are listed in Table A1.2.

^e Timing of most significant cooling rate increase observed in thermal modelling. For models showing monotonic cooling with no increase, this is not applicable (n/a).

^f Paleo-temperature at 28 Ma derived from thermal models; stated as median (Med.) temperature and associated uncertainty. Incorporates acceptable fits as well as good fits, and represents the widest possible spread of temperatures.

^g Range of total exhumation experienced by individual samples since 28 Ma, calculated for an assumed paleo-geothermal gradient of 25 °C/km and surface temperatures of 10 ± 10°C.

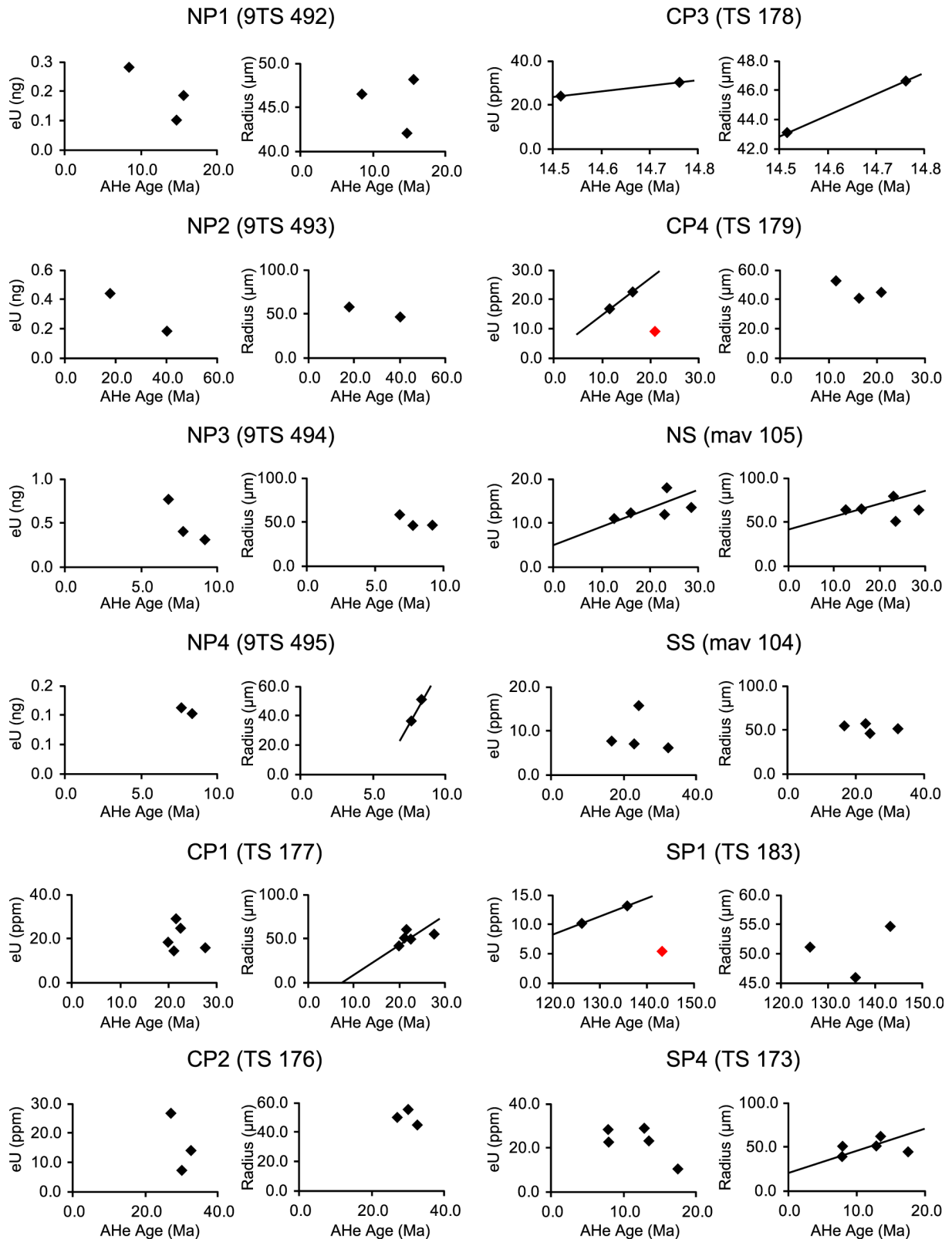


Figure A1.3. eU-AHe age and grain size-AHe age plots for all samples. Black trend lines connect samples where a possible correlation exists between AHe age and either eU or grain size. These trend lines have been constructed by eye. Red points indicate aliquots that if rejected allow a correlation to exist with the remaining aliquots.

Appendix 2.

Thermochronological data from the Central Kyrgyz Tien Shan (Supplementary material for Chapter 3)

This appendix presents the new thermochronological data used in Chapter 3 and the conglomerate clast count data from the Upper Naryn basin, which is used to infer a Late Miocene onset age for the Jetym Range (Section 3.5.2). In the sections A2.1, A2.2 and A2.3, the apatite fission track (AFT), (U-Th)/He (AHe) and zircon (U-Th)/He (ZHe) data are presented. Subsequently, in Figure A2.3, various tightly constrained thermal models are provided. Finally, Figure A2.4 presents the conglomerate clast count data.

A2.1. Apatite fission track (AFT) data

The dataset presented in chapter 3 contains new AFT ages, lengths and D_{par} measurements from 76 samples collected throughout the Central Kyrgyz Tien Shan. Samples were analysed between 2009 and 2012 at the Universität Potsdam. Mineral separation and analytical procedures are the same outlined in Appendix 1. Further details can be found in Section 3.3.2.1 and in Table A2.1. In this appendix, AFT data (Table A2.1) and a series of plots from every analysed sample (Figure A2.1) is provided.

A2.2. Apatite (U-Th)/He (AHe) data

Chapter 3 contains new AHe data from 37 samples. Multi-grained aliquots from 15 samples were analysed at the University of Melbourne in 2008, and single grained aliquots from 22 samples were analysed at the Scottish Universities Environmental Research Centre (SUERC) in 2011. Mineral separation and analytical procedures are the same as that outlined in Appendix 1. Further details can be found in Section 3.3.2.2 and in Table A2.2. In this appendix the complete dataset is provided in Table A2.2 and plots are provided for each sample showing AHe ages from different aliquots against the effective uranium (eU) and the equivalent spherical radius (grain size) (Figure A2.2). These plots were used to identify anomalous aliquots and better understand the AHe age variability (see Appendix 1 Section A1.2 for more details).

A2.3. Zircon (U-Th)/He (ZHe) data

Chapter 3 contains new ZHe data from 4 samples. This analysis was carried out at the University of Texas in Austin on single grain aliquots in 2012. Table A2.3 contains the complete dataset.

^g $P(\chi^2)$ (%) is the chi-squared probability [Galbraith, 1981; Green, 1981].

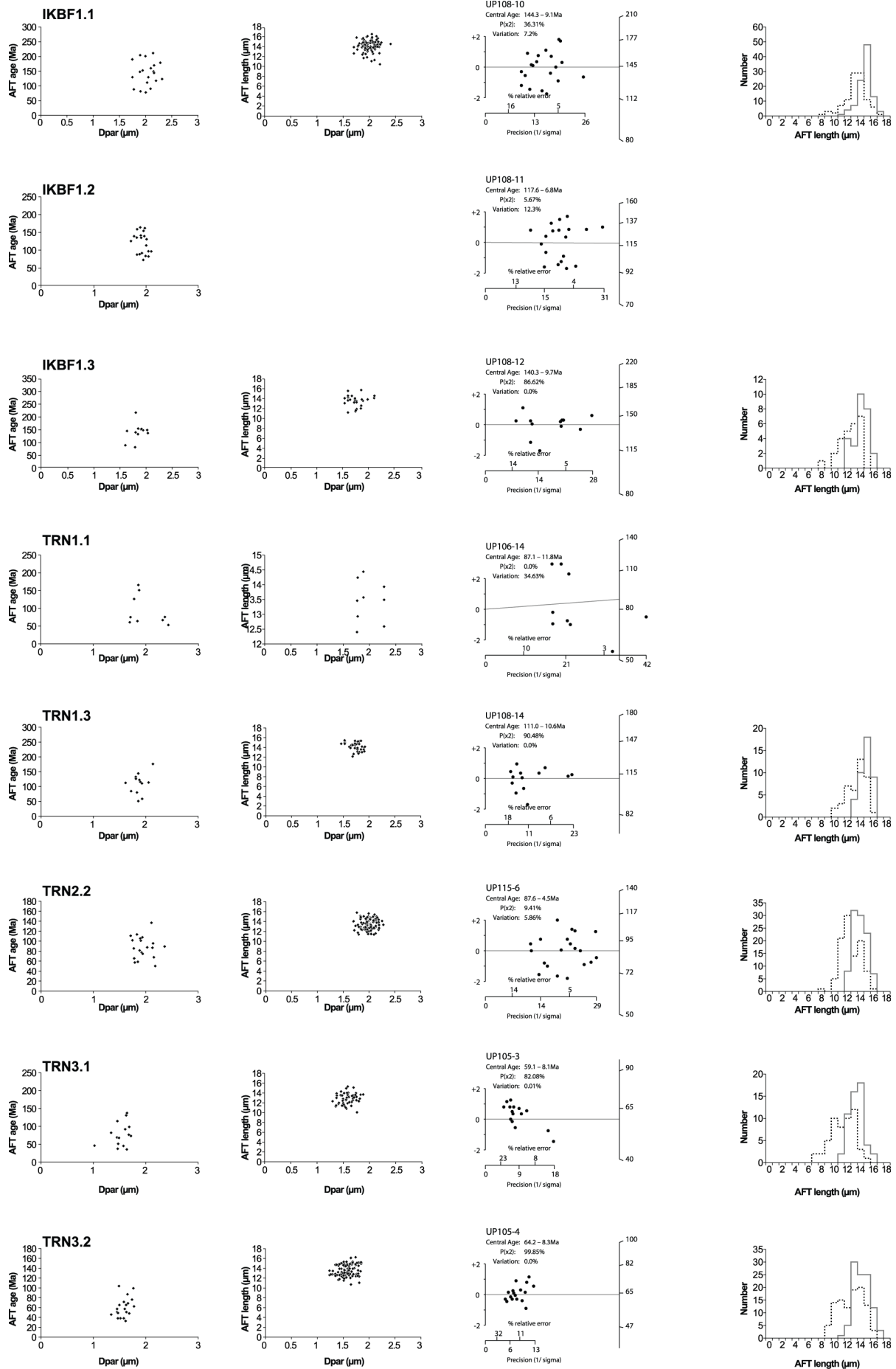
^h Rho-D is the induced track density in external detector adjacent to CN5 dosimetry glass (tracks/cm²).

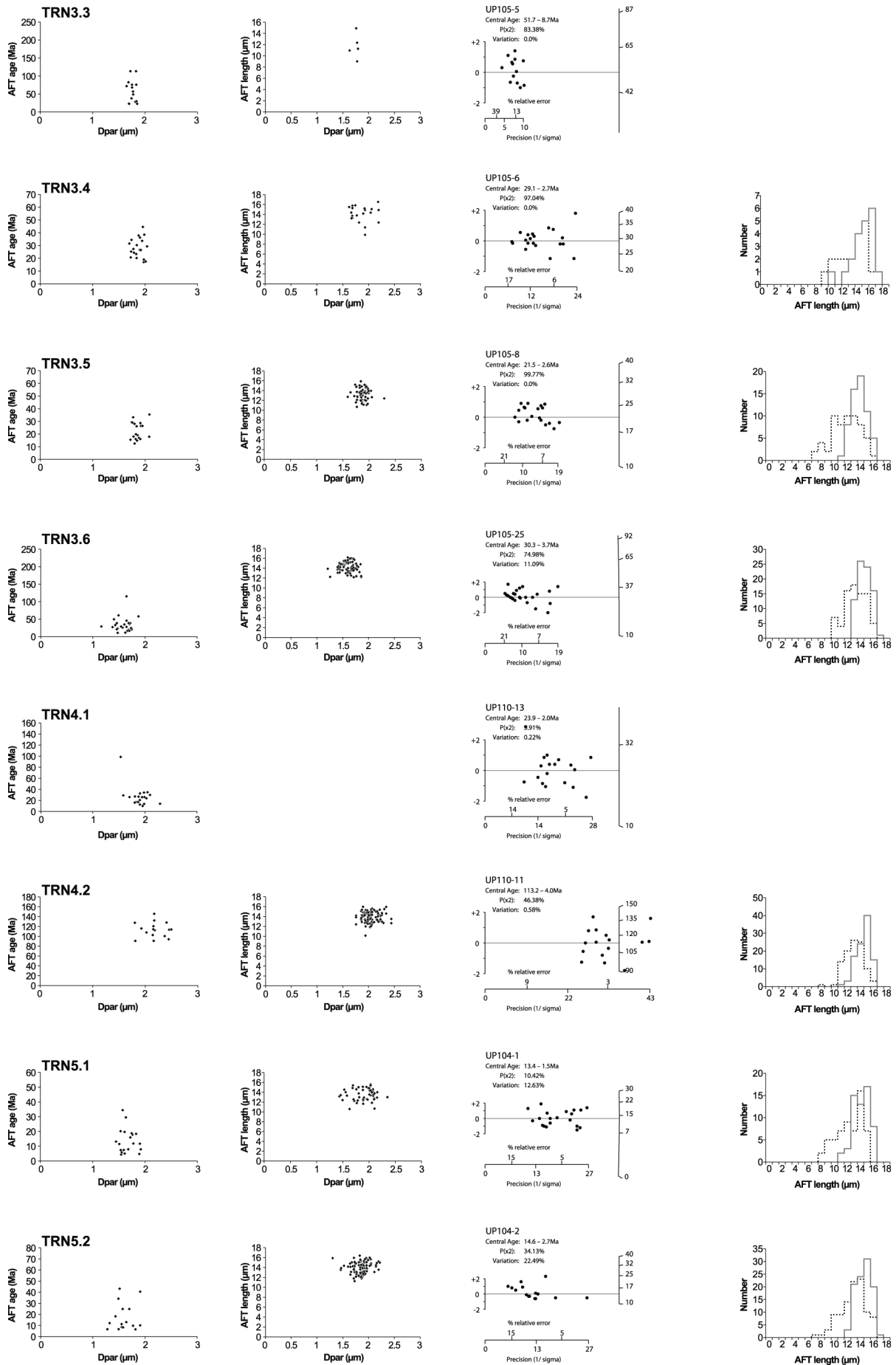
ⁱ ND is the number of tracks counted in determining Rho-D.

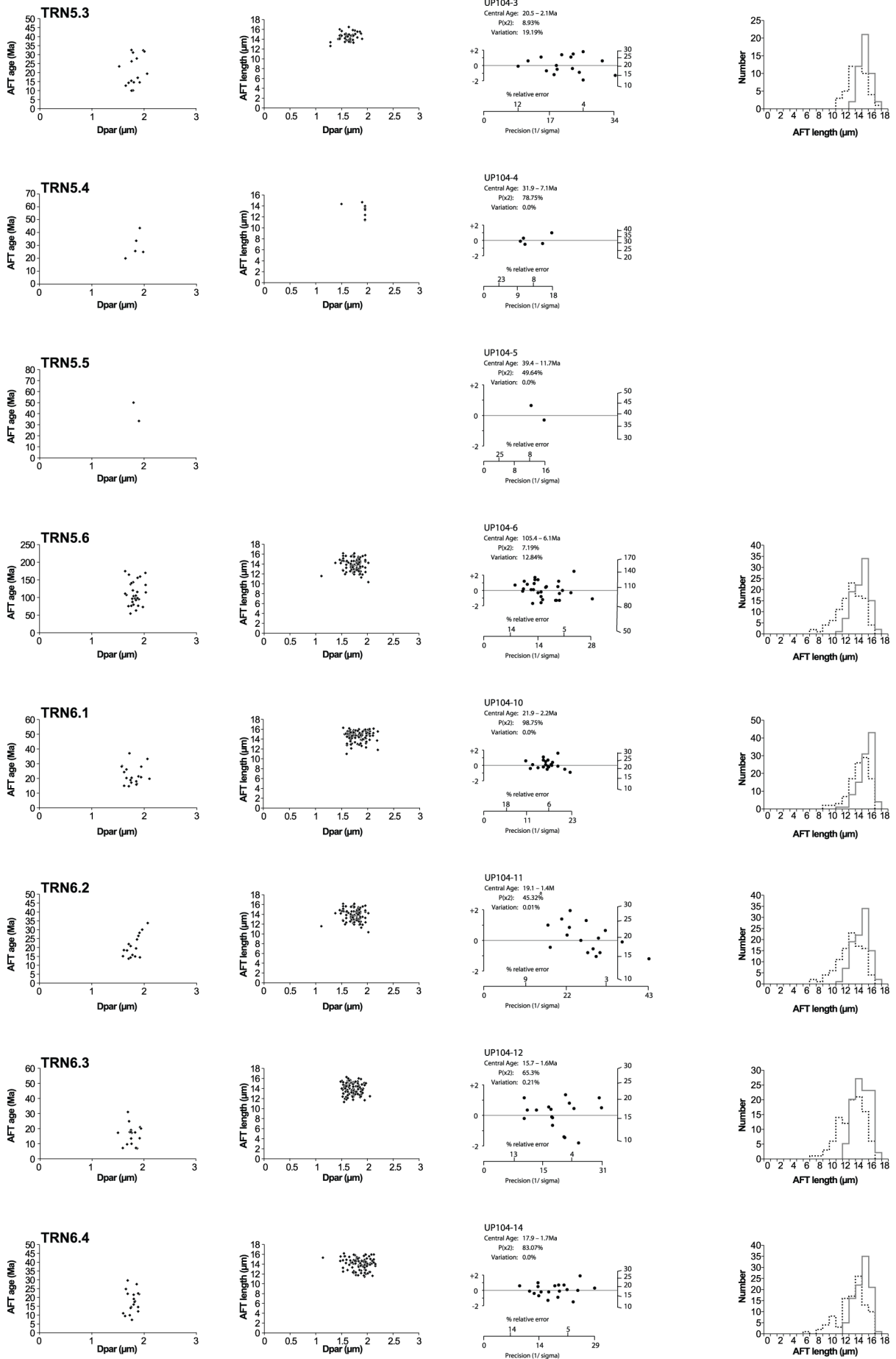
^j Mean of at least four Dpar measurements. The correction factor [Sobel and Seward, 2010] was found to 1 with respect to the Durango apatite standard [Donelick et al., 1999].

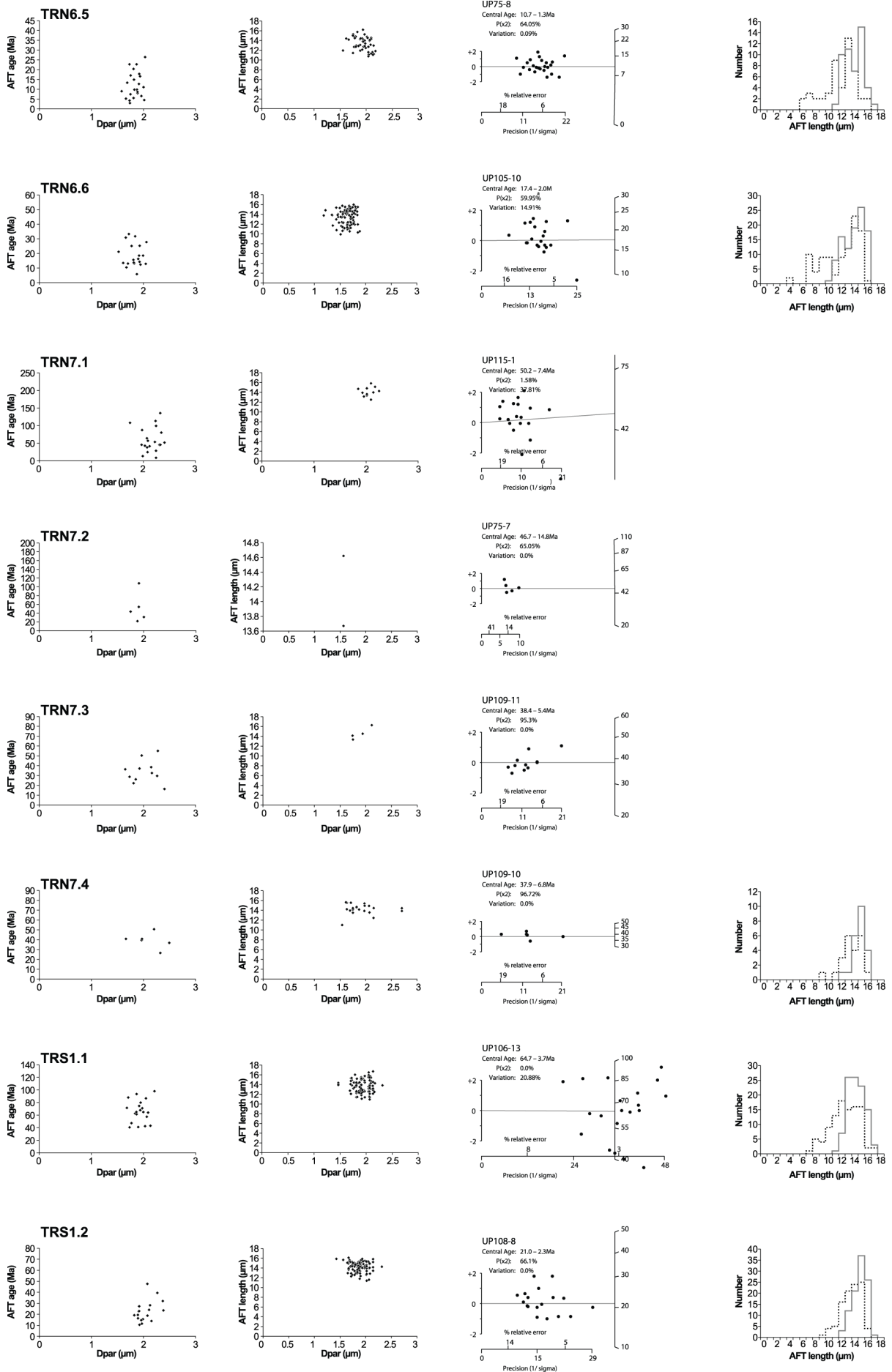
^k Samples with asterisk (*) indicates track lengths measured from heavy ion irradiation slide [Jonckheere et al., 2007] and cross (x) denotes track lengths measured from ²⁵²Cf-irradiation slide [Carlson et al., 1999].

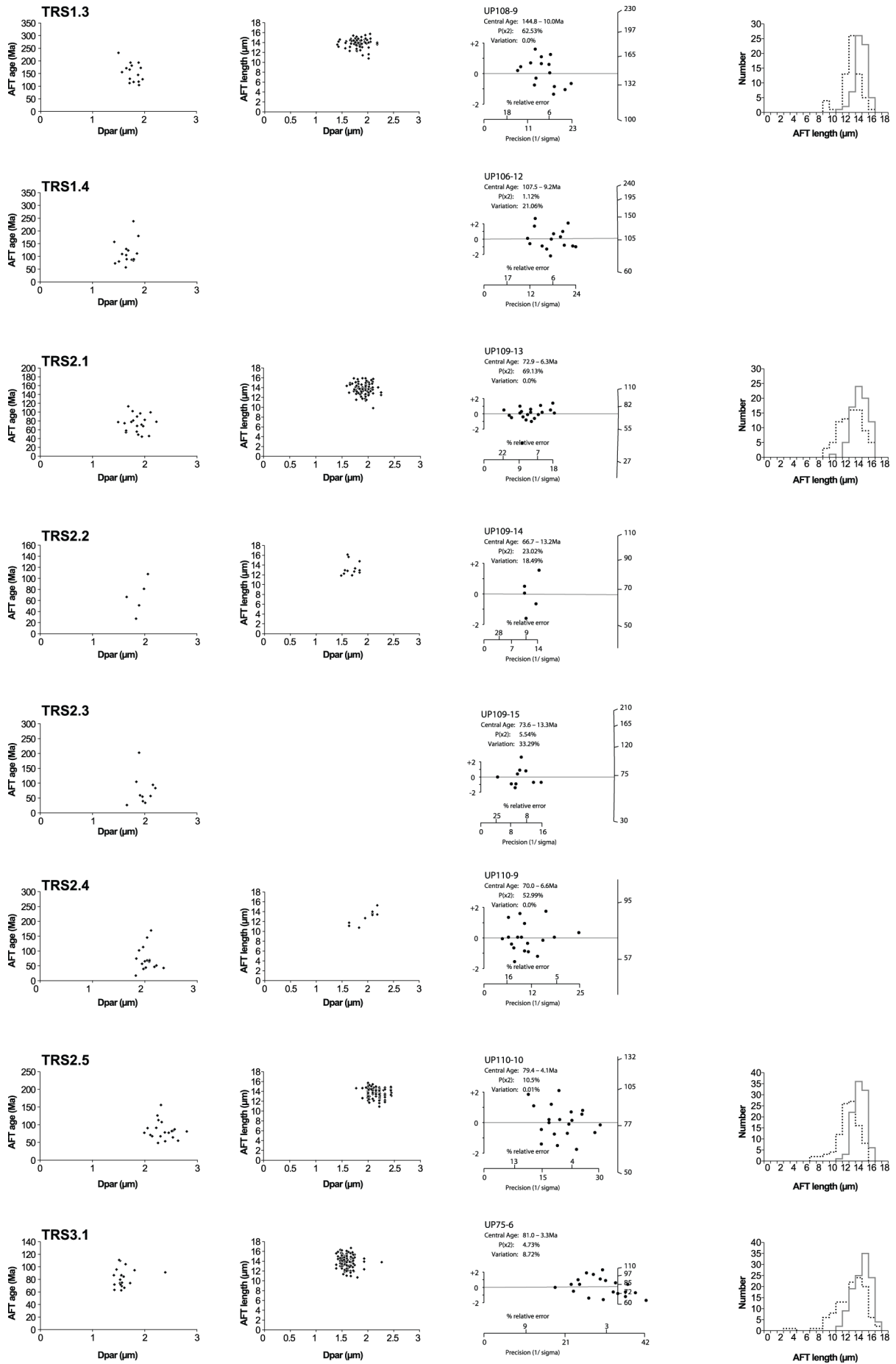
^l Zeta calibration used for apatite: EM1: 357.1 ± 8 (E. Macaulay, unpublished, 2011); EM2: 357.2 ± 8 (E. Macaulay, unpublished, 2011); ES: 369.6 ± 7.6 (E. Sobel, unpublished data, 2003). All lengths were measured by EM. The correction factor [Sobel and Seward, 2010] compared to Durango and FCT apatites [Donelick et al., 1999] were found to be 1.0 for EM and 0.8 for ES.

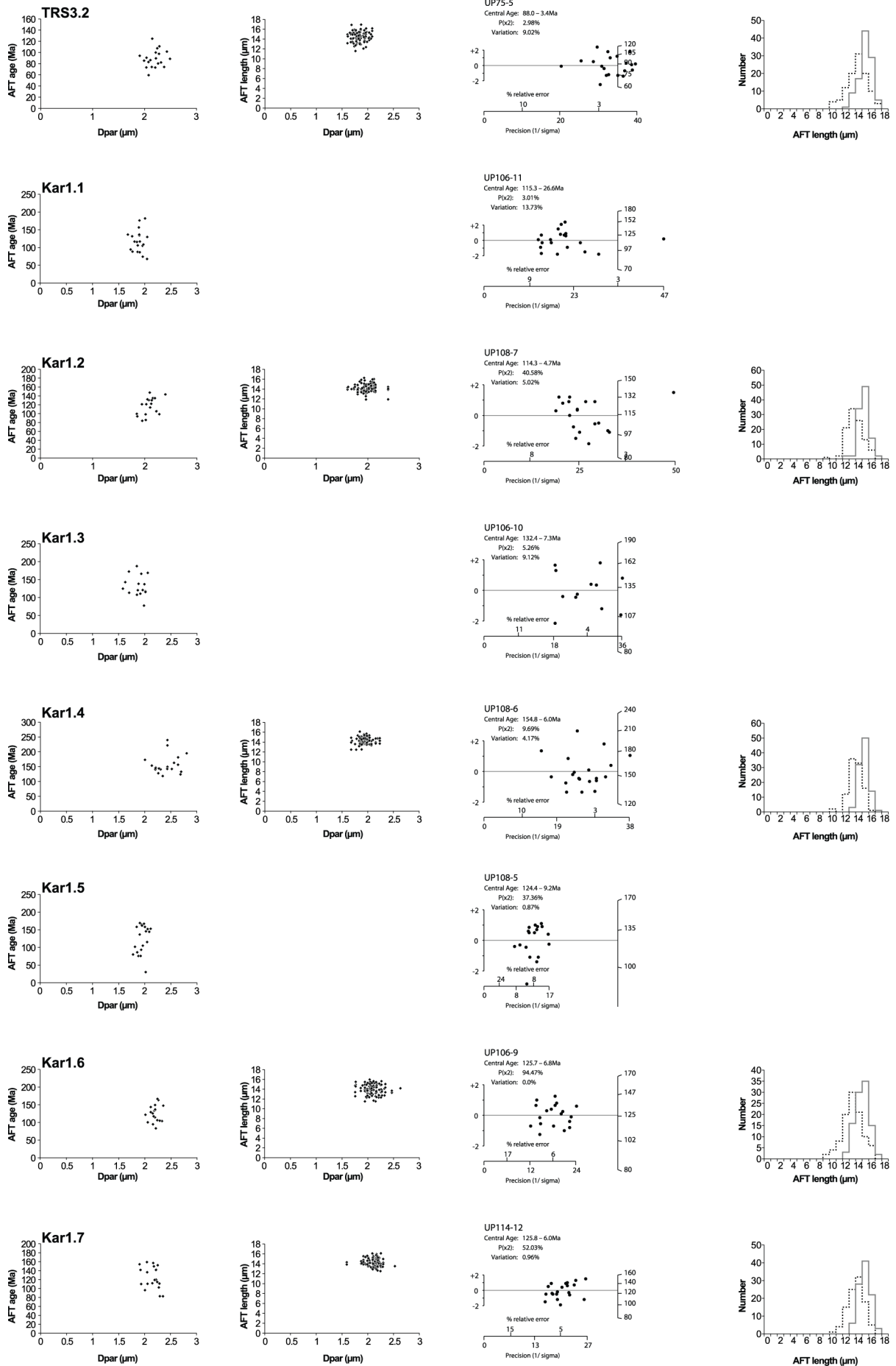


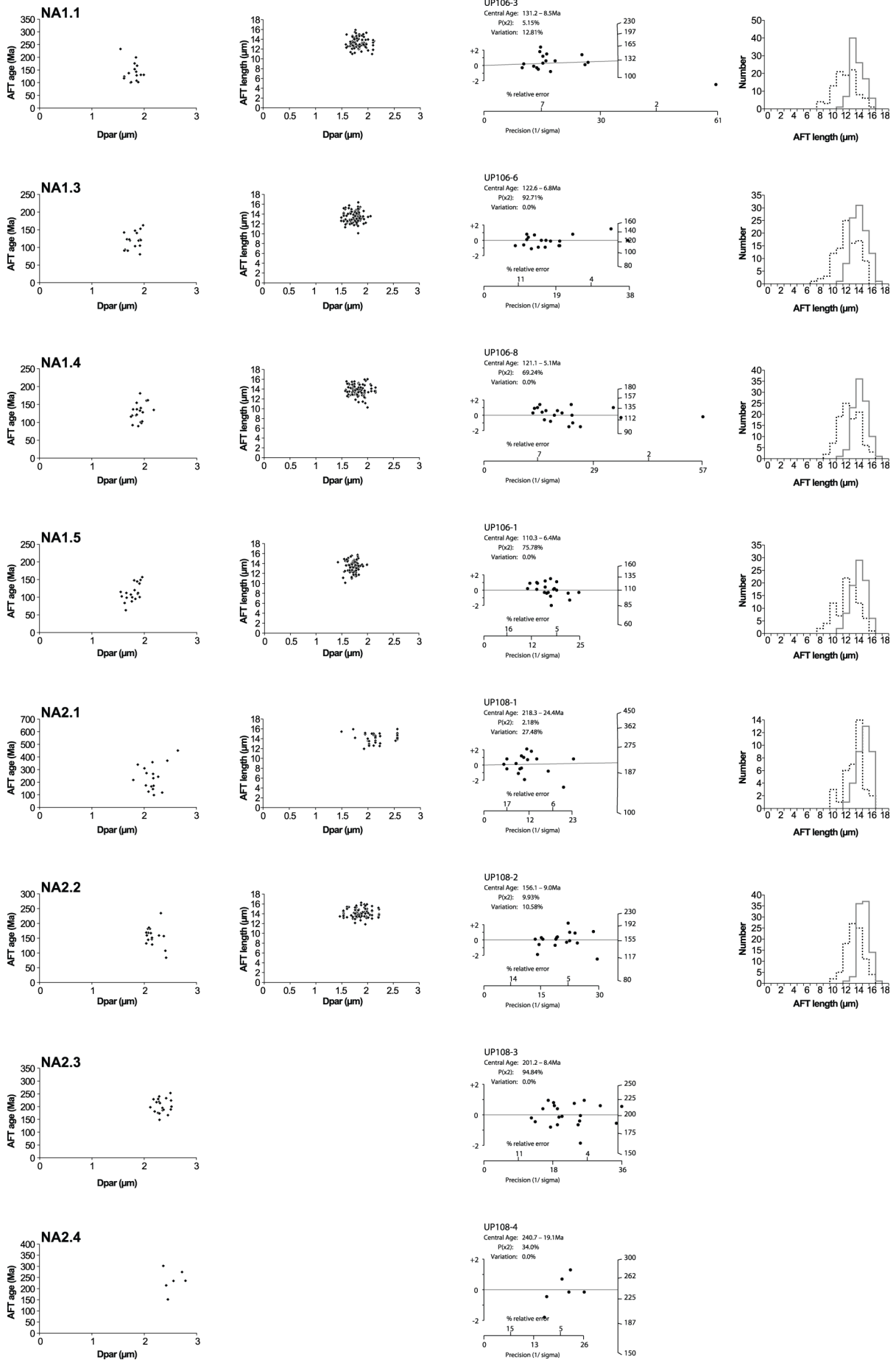


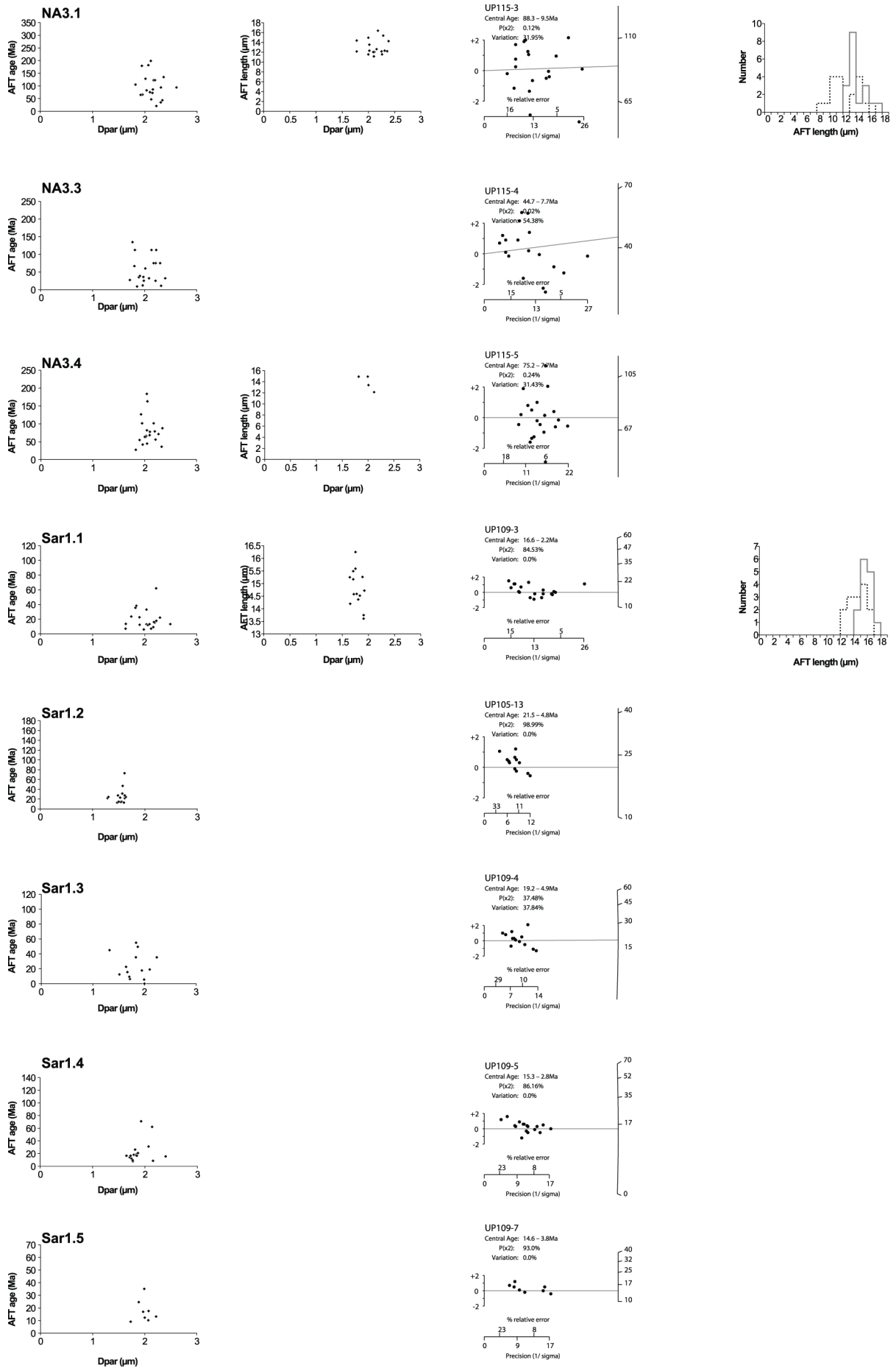


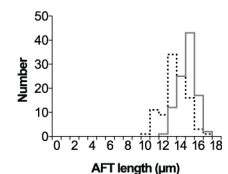
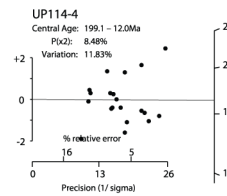
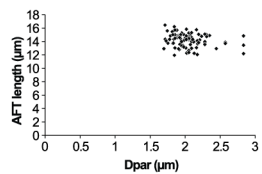
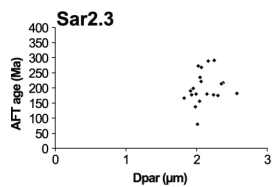
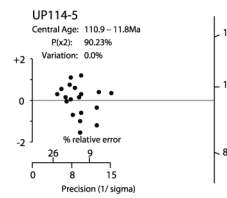
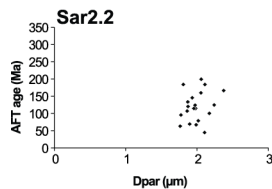
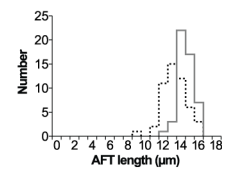
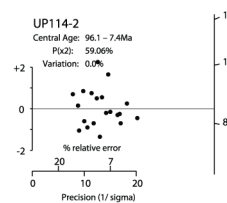
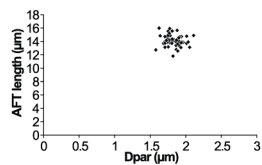
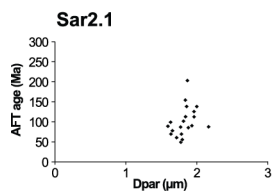
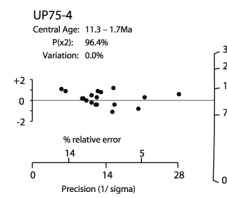
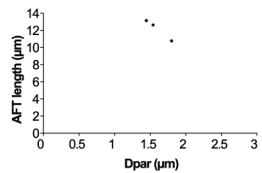
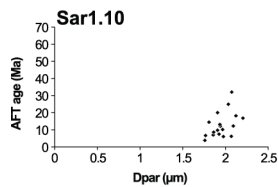
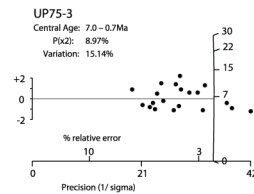
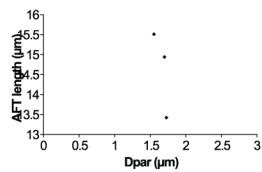
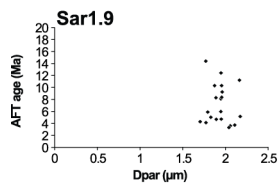
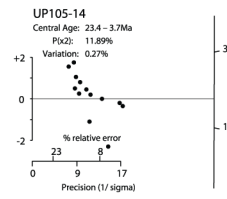
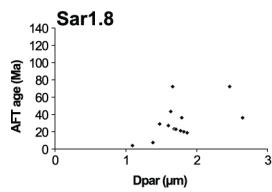
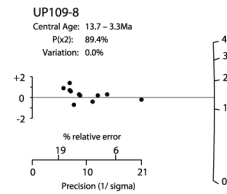
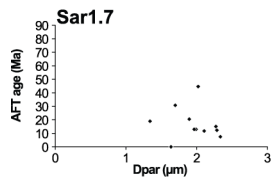
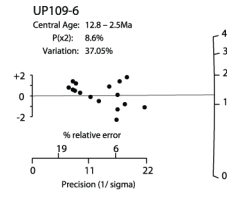
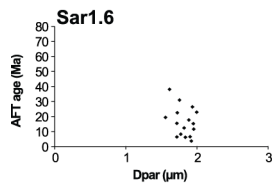












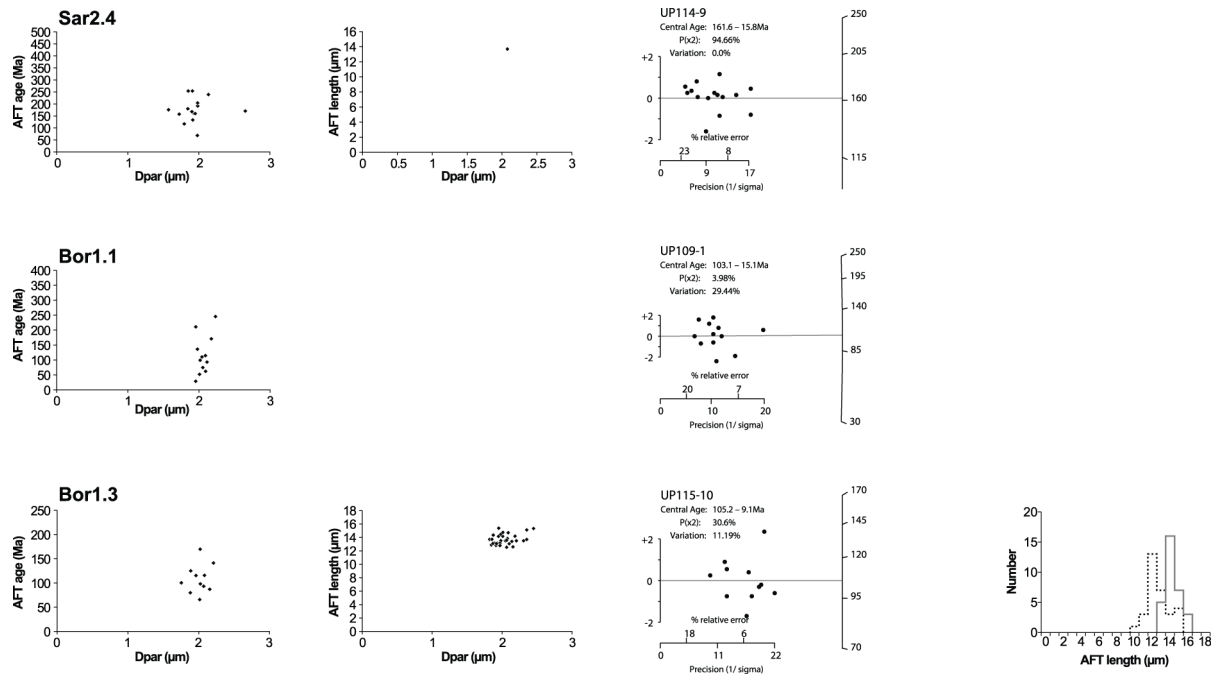


Figure A2.1. Plots of apatite fission track (AFT) data for all samples analysed. From left to right: mean Dpar (μm) against AFT age (Ma) for all counted grains, mean Dpar (μm) against AFT length measurements projected to c-axis (μm), radial plots, and AFT length histograms (solid grey line = histogram for AFT length measurements projected to c-axis; black dashed line = uncorrected AFT length measurements).

Table A2.2. continued

No ^b	Sample	Xls ^c	Age/Lith.	Lat.	Long.	Alt ^d (m)	U ^e	Th ^e	Sm, ppm	He ^f , x10 ⁻⁹ cc	eU ^g , µm	Rs ^h , µm	Term ⁱ	Uncorr		Model error ^k	Ft ^l	Corr age (Ma)	Error	Note
														age ^j (Ma)	Error					
NA3.3(1)	9TS465	1	Pt/granite	42.1291	79.0800	2679	30.0*	3.8*	-	0.11	30.9*	56	2	26.5	0.8	-	0.75	35.3	1.0	
NA3.3(2)	9TS465	1	Pt/granite	42.1291	79.0800	2679	2.5*	5.7*	-	0.10	3.8*	57	2	25.4	1.3	-	0.77	33.1	1.7	
NA3.3(3)	9TS465	1	Pt/granite	42.1291	79.0800	2679	1.7*	5.5*	-	0.12	3.0*	50	1	39.8	1.9	-	0.75	53.3	2-6	Excluded; AFT= 44.7 ± 7.7 Ma
<i>W. Mean</i>																				34.7 0.9
Sar1.2(4)	8TS432	1	P/granite	42.0535	79.0981	3204	4.0*	7.1*	-	0.27	5.7*	51	2	42.8	0.8	-	0.74	58.2	±1	Excluded; AFT= 21.5 ± 4.8 Ma
Sar1.2(6)	8TS432	1	P/granite	42.0535	79.0981	3204	2.4*	5.5*	-	0.08	3.7*	45	1	20.3	2.9	-	0.72	28.3	4.0	Excluded; AFT= 21.5 ± 4.8 Ma
<i>W. Mean</i>																				
Sar1.9(1)	SJTC-1	3	P/granite	42.0426	79.0758	2611	31.1	13.4	362.5	0.23	34.2	52	5	4.3	0.7	-	0.73	5.9	0.4	
Sar1.9(2)	SJTC-1	2	P/granite	42.0426	79.0758	2611	3.6	0.6	57.3	0.20	3.7	56	2	50.7	0.8	-	0.76	67.1	4.2	Excluded; AFT= 6.9 ± 0.7 Ma
Sar1.9(3)	SJTC-1	3	P/granite	42.0426	79.0758	2611	33.5	16.8	423.1	0.28	37.4	48	2	5.2	0.7	-	0.72	7.2	0.4	Excluded; AFT= 6.9 ± 0.7 Ma
<i>W. Mean</i>																				5.9 0.4
Sar1.10(1)	SJTC-2	3	P/granite	42.0695	79.0833	2612	5.6	18.1	215.2	0.17	9.9	57	2	9.8	0.7	-	0.74	13.3	0.8	Excluded; AFT= 11.3 ± 1.7 Ma
Sar1.10(2)	SJTC-2	3	P/granite	42.0695	79.0833	2612	17.1	36.3	332.0	0.22	25.6	54	4	7.6	0.7	-	0.71	10.7	0.7	
Sar1.10(3)	SJTC-2	3	P/granite	42.0695	79.0833	2612	11.0	50.1	347.9	0.31	22.8	48	4	16.3	0.7	-	0.68	24.1	±5	Excluded; AFT= 11.3 ± 1.7 Ma
<i>W. Mean</i>																				10.7 0.7
<i>At Bashi-Borkoldoy-Kaindy-Ipylchek-Kokshaal Ranges (Bor)</i>																				
Bor1.2(2)	8TS428	1	P/granite	42.0796	79.2755	3367	0.3*	1.9*	-	0.06	0.7*	67	1	186.2	13.1	-	0.78	238.8	16-8	Excluded; anomalously old
Bor1.2(3)	8TS428	1	P/granite	42.0796	79.2755	3367	0.3*	3.5*	-	0.04	1.1*	63	0	53.0	3.4	-	0.78	68.2	4.4	
Bor1.2(4)	8TS428	1	P/granite	42.0796	79.2755	3367	17.2*	88.8*	-	2.29	38.1*	68	1	49.9	0.8	-	0.80	62.5	1.0	
<i>W. Mean</i>																				62.8 1.0

^a Sample analysis was similar to that outlined by *Foeken et al.* [2006] for single grained aliquots and *Spiegel et al.*, [2009] for multiple grain aliquots. Grains were placed in platinum tubes and outgassed using a laser.

^b Sample names based on location; described in Chapter 3. Samples are listed in ranges from north to south.

^c Xls is the number of individual crystals in one aliquots; single crystal aliquots were analysed at SUERC and multiple crystal aliquots were analysed at the University of Melbourne.

^d Alt: Altitude of sample taken from SRTM dataset.

^e Uranium and Thorium content in parts per million (ppm); unless marked by asterisk (*) in which case content in nanograms (ng).

^f Helium volume in nano-cubic centimeters (ncc): 10⁹ cubic centimeters.

^g Effective uranium calculated by U + (0.235 x Th) [*Flowers et al.*, 2009]. Values stated as parts per million (ppm); unless marked by asterisk (*) in which case content in nanograms (ng).

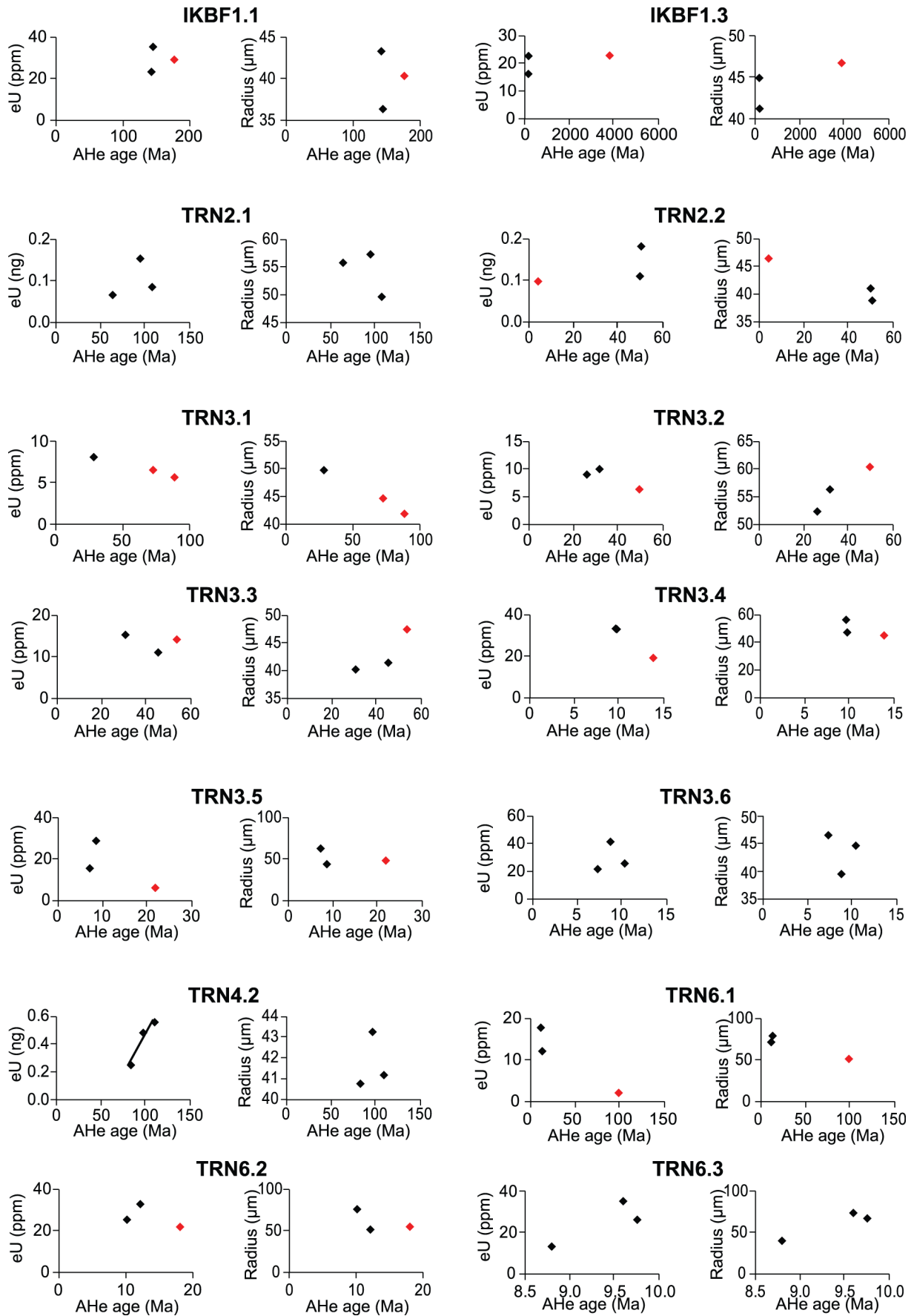
^h Radius of a sphere with the equivalent surface-area-to-volume ratio as cylindrical crystals [*Meesters and Dunai*, 2002].

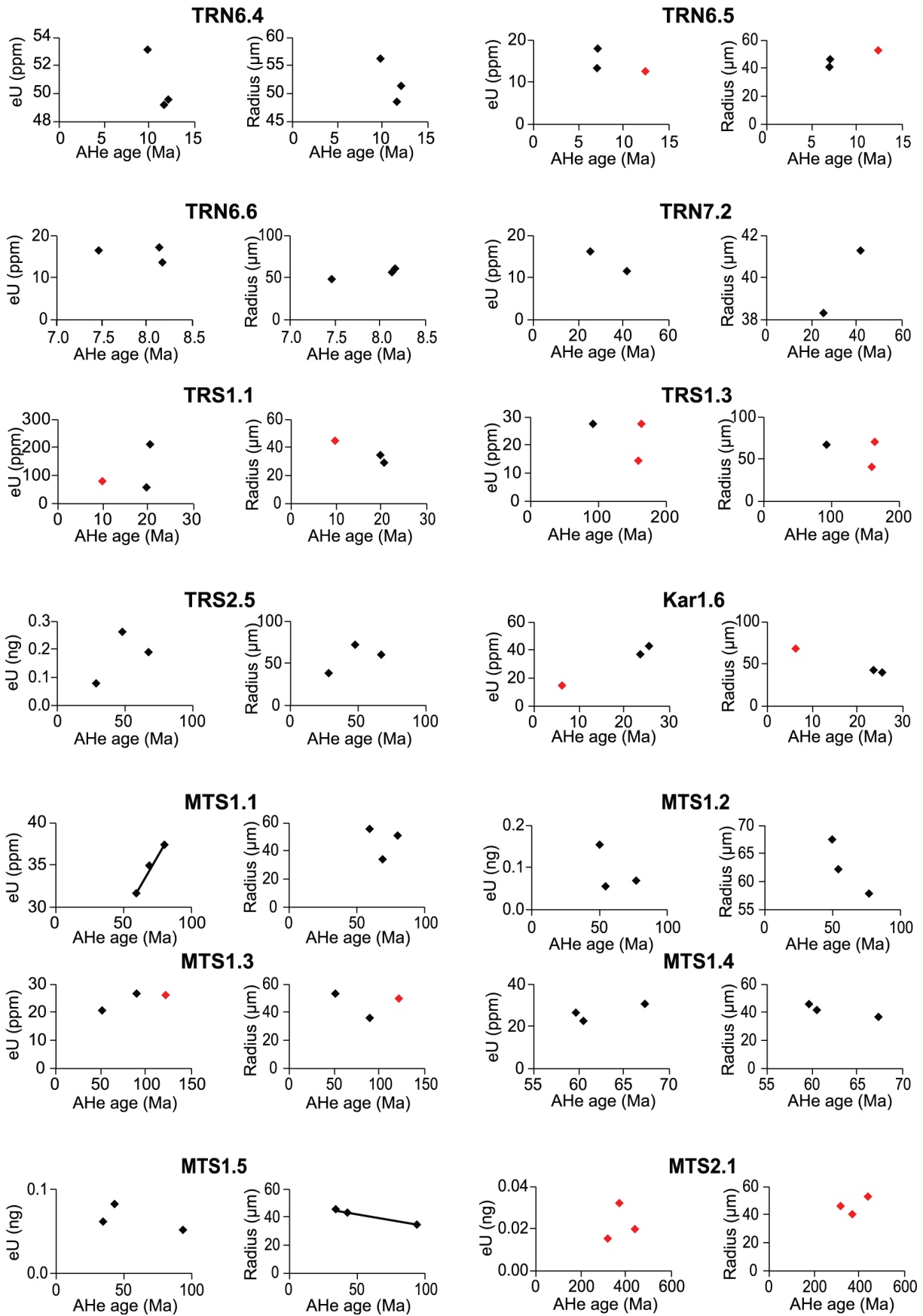
ⁱ The number of complete terminations preserved within an aliquot.

^j Age calculations following *Meesters and Dunai* [2002] for single-grained aliquots and *Farley et al.* [1996] for multiple grained aliquots.

^k Model error used for thermal modelling. Taken to be 10% of uncorrected age or the analytical error, depending on which is higher.

^l α-ejection correction [*Farley et al.*, 1996] calculated using mass-weighted average radii.





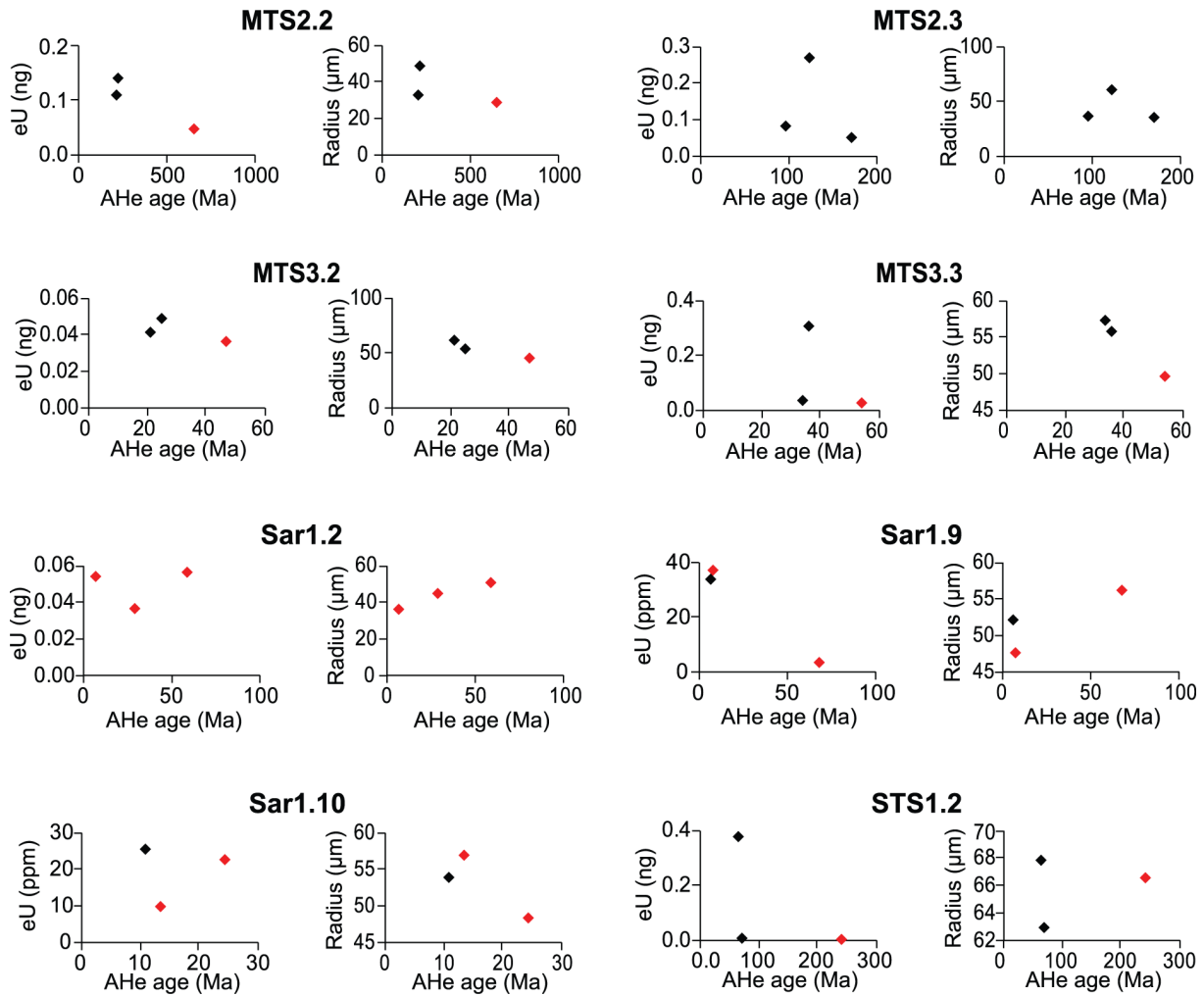


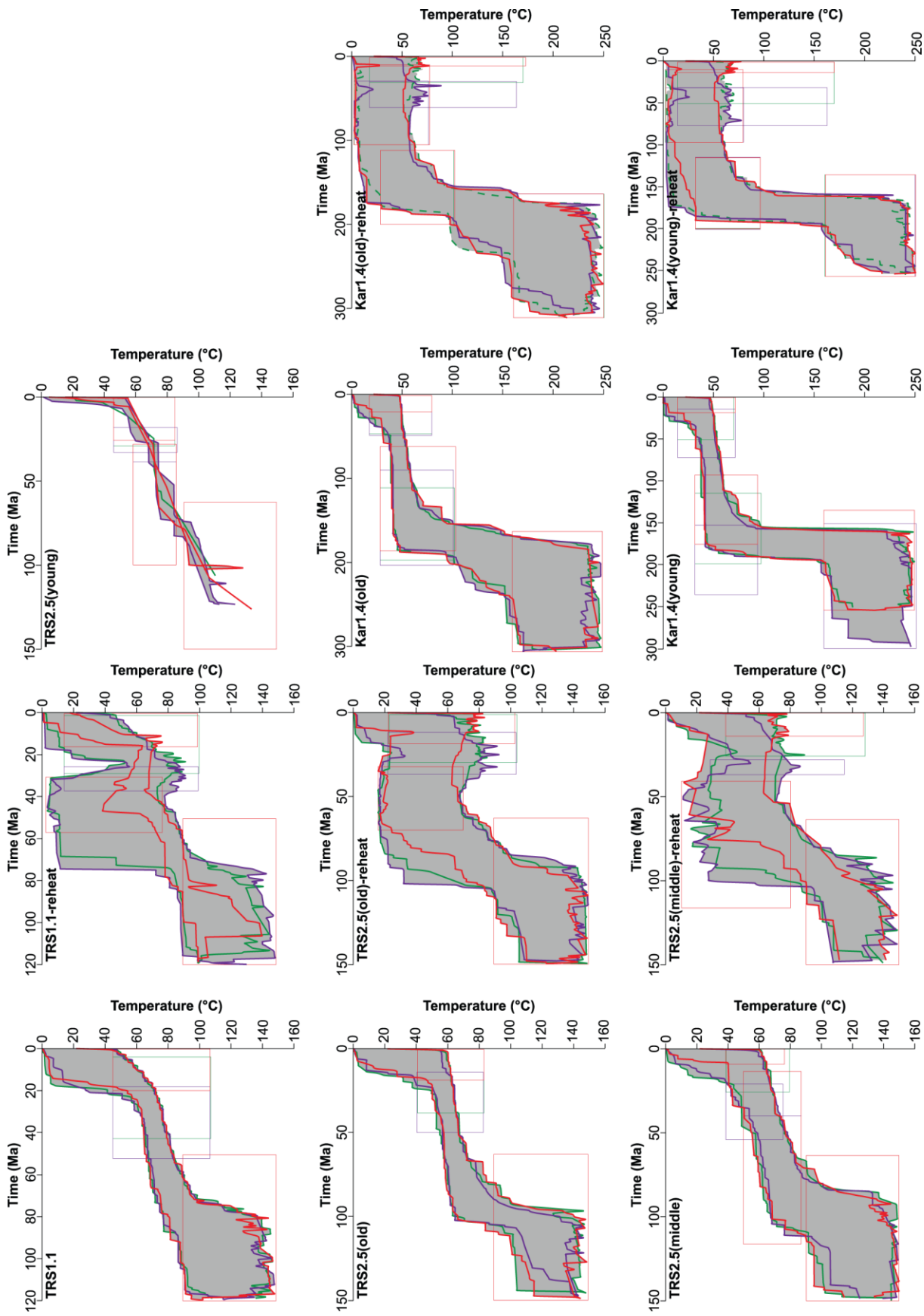
Figure A2.2. Plots of apatite (U-Th)/He (AHe) ages against effective uranium (eU) in ppm or ng and grain radius (μm) for all analysed aliquots. Black points = aliquots used for interpretation; red points = discarded aliquots. Correlations between AHe age and eU or grain radius are shown by straight lines.

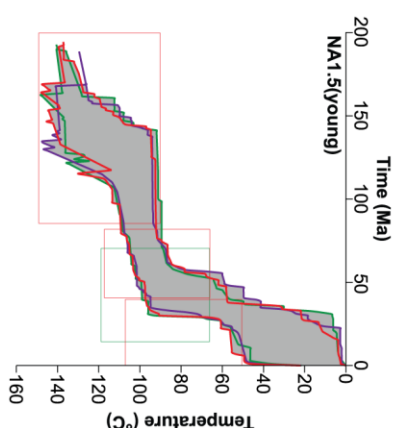
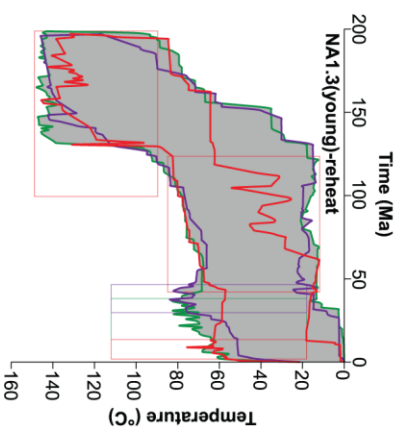
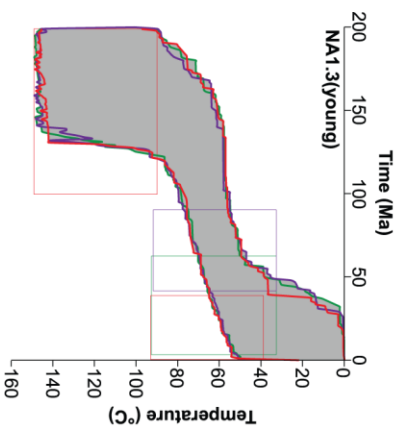
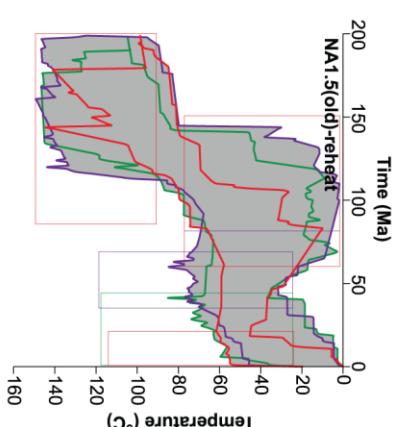
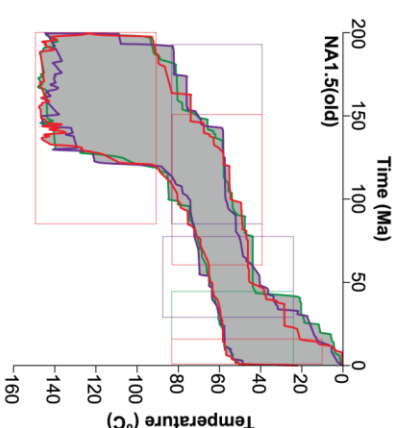
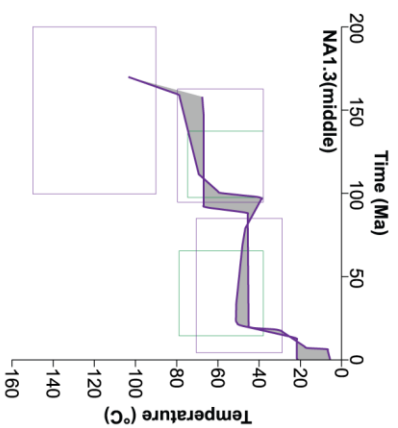
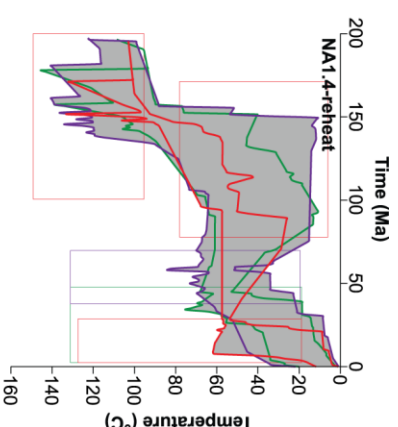
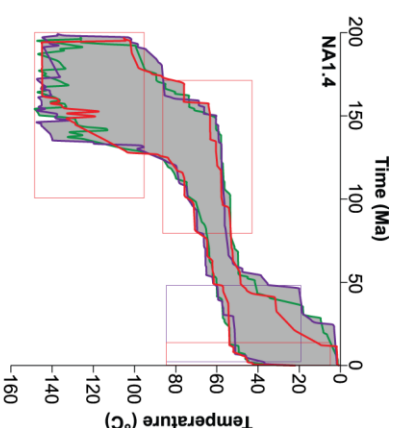
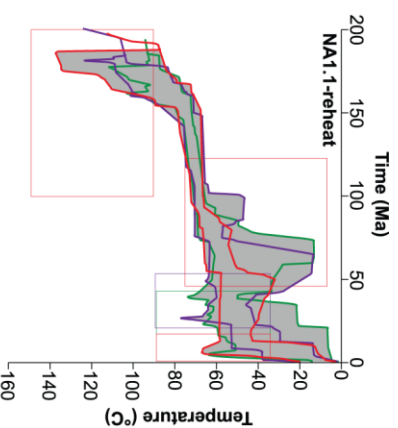
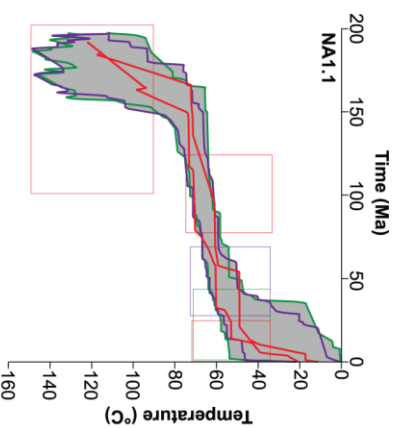
Table A2.3. Zircon (U-Th)/He data^a

No ^b	Sample	Lat.	Long.	Alt., m	U, ppm	Th, ppm	Sm, ppm	Th/U	He, nmol/g	Mass, µg	Uncorrected age, Ma	Uncorrected error, Ma	F _T	eU	Radius, µm	Corrected age, Ma	Corrected error, Ma	Note
SPI(1)*	TS183	41.8735	77.7219	3780	80.2	31.3	0.7	0.39	61.0	4.44	127.7	10.2	0.71	87.5	39	180.7	14.5	Modelled – SPI
SPI(2)*	TS183	41.8735	77.7219	3780	132.9	32.3	3.9	0.24	118.9	5.81	154.8	12.4	0.72	140.4	41	214.6	17.2	Modelled – SPI
SPI(3)*	TS183	41.8735	77.7219	3780	55.0	23.7	1.7	0.43	57.4	9.41	173.2	13.9	0.78	60.4	54	222.0	17.8	Modelled – SPI
<i>W. Mean</i>																202.4	9.4	Grain size-ZHe age positive correlation
Kar1.4(1)	8TS402	41.7349	76.7510	2999	155.4	97.3	1.0	0.63	127.3	6.56	130.9	10.5	0.77	177.8	52	169.8	13.6	Modelled – Kar1.4(young)
Kar1.4(2)	8TS402	41.7349	76.7510	2999	125.7	127.5	0.9	1.01	128.7	4.05	151.3	12.1	0.74	155.1	45	205.4	16.4	Modelled – Kar1.4(old)
Kar1.4(3)	8TS402	41.7349	76.7510	2999	539.2	557.5	10.7	1.03	349.8	6.53	96.0	7.7	0.77	667.6	52	124.6	10.0	Excluded: AFT= 154.9± 6.7 Ma. eU-ZHe age negative correlation
<i>W. Mean</i>																184.3	10.5	
NA2.2(1)	8TS359	41.4986	77.6227	3797	181.2	101.4	1.1	0.56	309.6	6.93	273.2	21.9	0.78	204.6	54	349.3	27.9	Modelled – NA2.2(old)
NA2.2(2)	8TS359	41.4986	77.6227	3797	117.6	77.2	1.1	0.66	110.2	6.01	148.6	11.9	0.75	135.4	46	199.1	15.9	Modelled – NA2.2(young)
NA2.2(3)	8TS359	41.4986	77.6227	3797	153.1	118.3	1.6	0.77	153.7	9.39	155.4	12.4	0.77	180.4	52	201.1	16.1	Modelled – NA2.2(young)
<i>W. Mean</i>																221.2	10.5	Grain size-ZHe age positive correlation
Sar1.6(1)	8TS435	42.0545	79.0912	2857	274.7	151.5	1.3	0.55	180.5	8.42	106.9	8.6	0.80	309.6	60	133.5	10.7	Likely radiation damage – discarded
Sar1.6(2)	8TS435	42.0545	79.0912	2857	765.2	408.6	3.8	0.53	408.8	7.99	87.4	7.0	0.79	859.3	57	110.4	8.8	Likely radiation damage – discarded
Sar1.6(3)	8TS435	42.0545	79.0912	2857	835.6	351.8	2.4	0.42	308.9	3.78	62.1	5.0	0.75	916.6	46	83.1	6.6	Likely radiation damage – discarded
<i>W. Mean</i>																133.5	10.7	eU-ZHe age negative correlation Grain size-ZHe age positive correlation

^a Sample analysis was similar to that outlined by *Shirvell et al.* [2009].

^b Sample names based on location, described in text. Samples are listed in ranges from north to south. Asterisk (*) denotes sample from *Macaulay et al.* [2013].





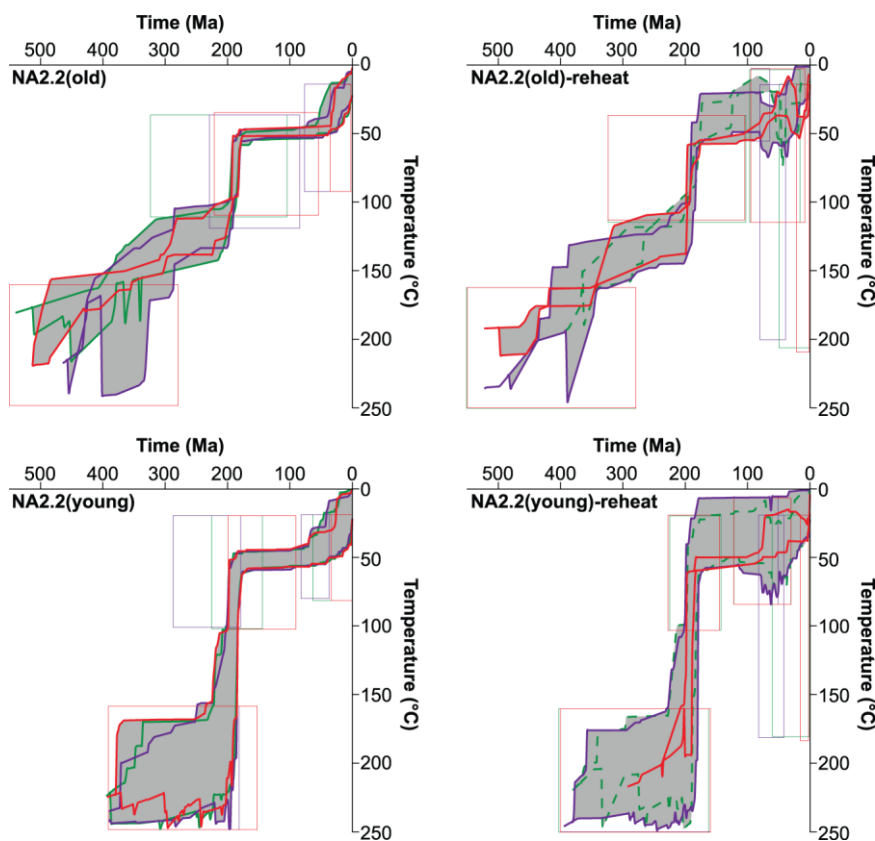
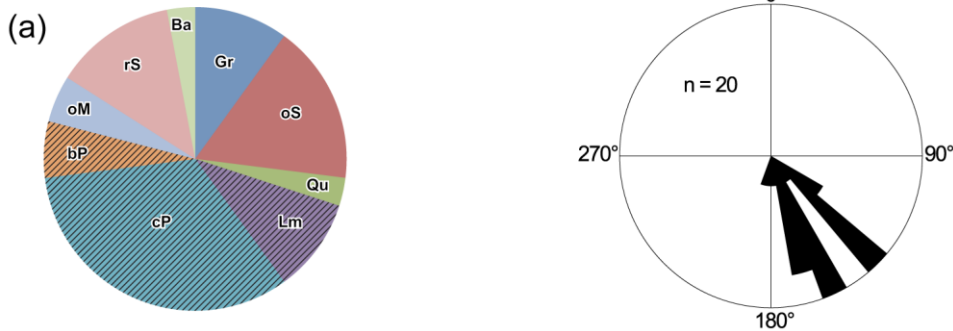
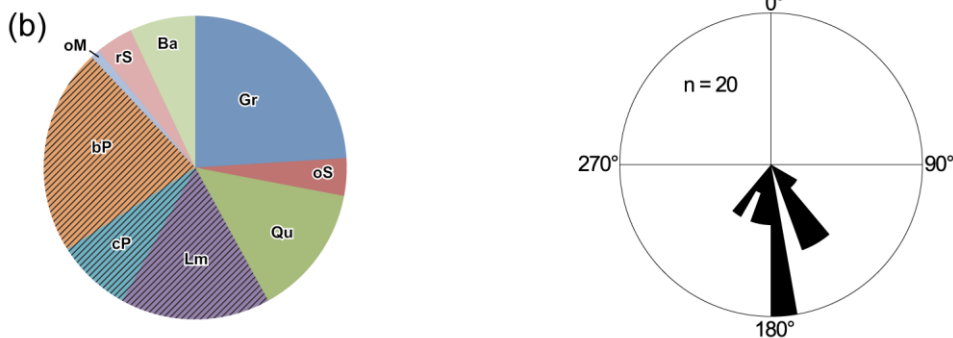


Figure A2.3. Results of all well-constrained thermal models with well-defined inflection points. Summary of input data can be found in Tables S1-3 and the complete AFT track lengths are also included in supplementary material. Thick coloured lines denote envelopes for different model runs. Thinner coloured lines denote constraints input by user. Colours correspond to different model runs. Purple = Median positions – constraints based on inflection point identified during first inverse model runs with single constraint; Green = constraints are slightly older, forcing earlier inflection points; Red = constraints are slightly younger, forcing later inflection points. Note the use of multiple model runs is tests the reliability and reproducibility of inflections points identified during thermal modelling.

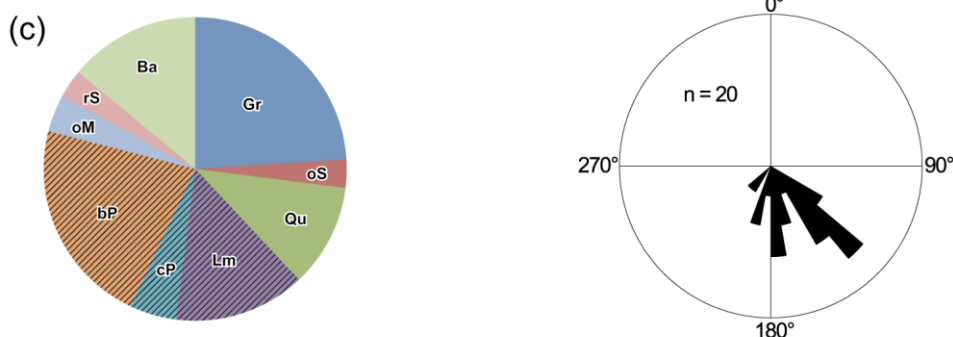
Lower Naryn Formation; map code N1nr1 – Lower Chu unit



Upper Naryn Formation; map code N2nr2 – Upper Chu unit



Upper Naryn Formation; map code N2nr3 – Upper Chu unit



Legend for clast composition

- Gr** Granitic clasts- predominantly sourced from NTS; minor occurrences in MTS and STS
- Ba** Basalt – present in NTS, MTS and STS
- Qu** Quartzite – present in NTS, MTS and STS
- Lm** Limestone/low grade marble – predominantly sourced from MTS sediments
- cP** Chlorite bearing pelite – low grade metamorphism of MTS sediments; possible minor NTS contribution
- bP** Biotite bearing pelite – low grade metamorphism of MTS sediments; possible minor NTS contribution
- oM** Other metamorphics – NTS, MTS or STS?
- oS** Other Paleozoic sediments – NTS, MTS or STS?
- rS** Red clastics – recycled Cenozoic sediment?

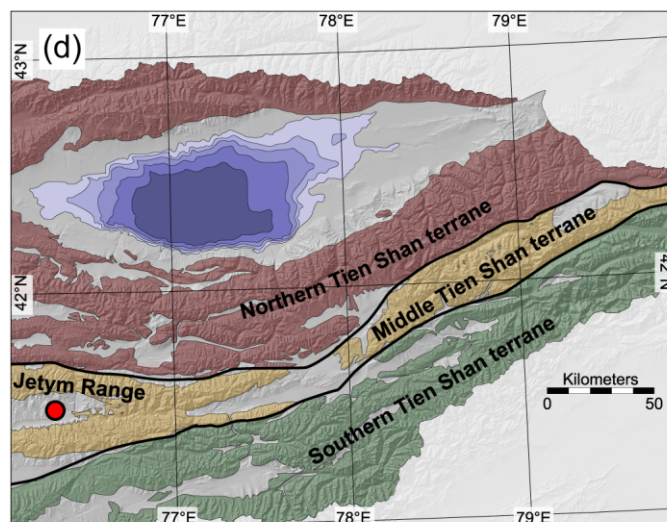


Figure A2.4. (a-f) Conglomerate clast count data and paleocurrent directions from upper Naryn basin that suggest the Chu unit has been sourced from the nearby Jetym Range. Hatching denotes clasts that are abundant in the Middle Tien Shan terrane. From legend: NTS = Northern Tien Shan terrane; MTS = Middle Tien Shan terrane; STS = Southern Tien Shan terrane. Note that the proportion of red clastic sedimentary clasts that are interpreted to represent recycled Cenozoic sediments decreases upsection; this likely corresponds to sediments from the Kokturpak/Suluterek and Shamsi units that were originally deposited above the Jetym Range and later removed by erosion following the onset of deformation and rock uplift. (g) Map of study area showing the three Paleozoic terranes, each of which has a unique rock assemblage.

Appendix 3.

Magnetostratigraphy data (Supplementary material for Chapter 4)

Table A3.1. Sample details

Sample	Latitude	Longitude	No. of cores	Average dip direction	Average dip
IK1	42.42005	78.08577	8	141	36
IK2	42.42196	78.08338	8	174	62
IK3	42.42171	78.08358	8	131	35
IK4	42.44355	78.04549	8	330	47
IK5	42.44635	78.05453	8	354	53
IK6	42.44698	78.05385	8	335	54
CK001	42.29238	78.10874			27
↓	<i>CK section</i>		332	338	
CK310	42.30779	78.08986			37
JO501	42.33809	78.2404			41
↓	<i>JO section</i>		281	355	
JO768	42.35828	78.22502			33

Table A3.2. Properties of normalized average tensors for Chon Kyzylsu and Jeti Oguz sections^a

Site	Part	No. of specimens	k1 ^b	k2 ^b	k3 ^b	Ds ^c	Is1 ^c	Ds2 ^c	Is2 ^c	Ds3 ^c	Is3 ^c
CK	all	98	1.036	0.983	0.981	252.1	5.5	162	1.7	55.1	84.2
CK	4/4	22	1.037	0.983	0.979	251.3	6.1	343.3	18.3	143.6	70.7
CK	3/4	29	1.035	0.986	0.979	250.8	4	160.5	4.8	20.4	83.8
CK	2/4	29	1.035	0.989	0.976	252.9	2.7	156.2	67.9	343.9	21.9
CK	1/4	18	1.045	0.984	0.971	265.3	17.9	5.9	29.7	148.5	54.3
JO	all	60	1.032	0.988	0.979	256.9	14.1	27.8	69	163	15.2
JO	4/4	14	1.033	0.991	0.976	262.7	18.3	11.6	44.4	156.5	39.9
JO	3/4	23	1.049	0.987	0.964	260.8	14.7	93.3	75	351.7	3.1
JO	2/4	11	1.031	1	0.969	253.5	33	48.2	54.3	155.5	12.1
JO	1/4	12	1.02	1.005	0.975	270.1	18	16.6	41.3	162.3	43.2

^a Average tensors shown for all samples and for each quarter of the section (1/4 = basal quarter; 4/4 = upper quarter).

^b Eigenvalues

^c Average eigenvector declination and inclination.

Table A3.3. Fisher and bipolar Watson mean directions of the high temperature magnetization components^a

Location	No. Of specimens	Dg	Ig	Ds	Is	ks	a95s	Mean
IK1	5	350.7	19.7	4.1	52.7	60.7	9.9	Fisher
IK2	6	169.7	-22.8	188.8	-55.5	56.4	9	Fisher
IK3*	4	162.8	14.2	166.1	-35.5	37	15.3	Fisher
IK4	6	265.5	-72.1	182.7	-56.5	125.6	6	Fisher
IK5*	7	36.8	-67.1	148.9	-51.5	9.8	20.3	Fisher
IK6	7	333.7	-63.3	156.3	-62.7	60.8	7.8	Fisher
CK(+)	65	46.5	69.1	6.7	45.8	18.5	4.2	Fisher
CK(-)	48	246.8	-72.7	189	-52.7	20.5	4.7	Fisher
CK	133	52.2	70.9	6.6	48.2	5.7	3.9	Watson
JO(+)	44	28.2	75.7	4.4	40.8	15.8	5.6	Fisher
JO(-)	41	211.2	-81.4	181.6	-47.1	14.2	6.2	Fisher
JO	100	32.6	78.5	4.3	44.7	5.3	4.9	Watson
TM	8	36.2	73.7	2.7	52	47.9	6.2	Watson

^a For the magnetostratigraphic sections (CK and JO), mean directions for normal (+) and inverse polarities are listed separately. TM is the bipolar Watson mean of all sites except those with an asterisk.

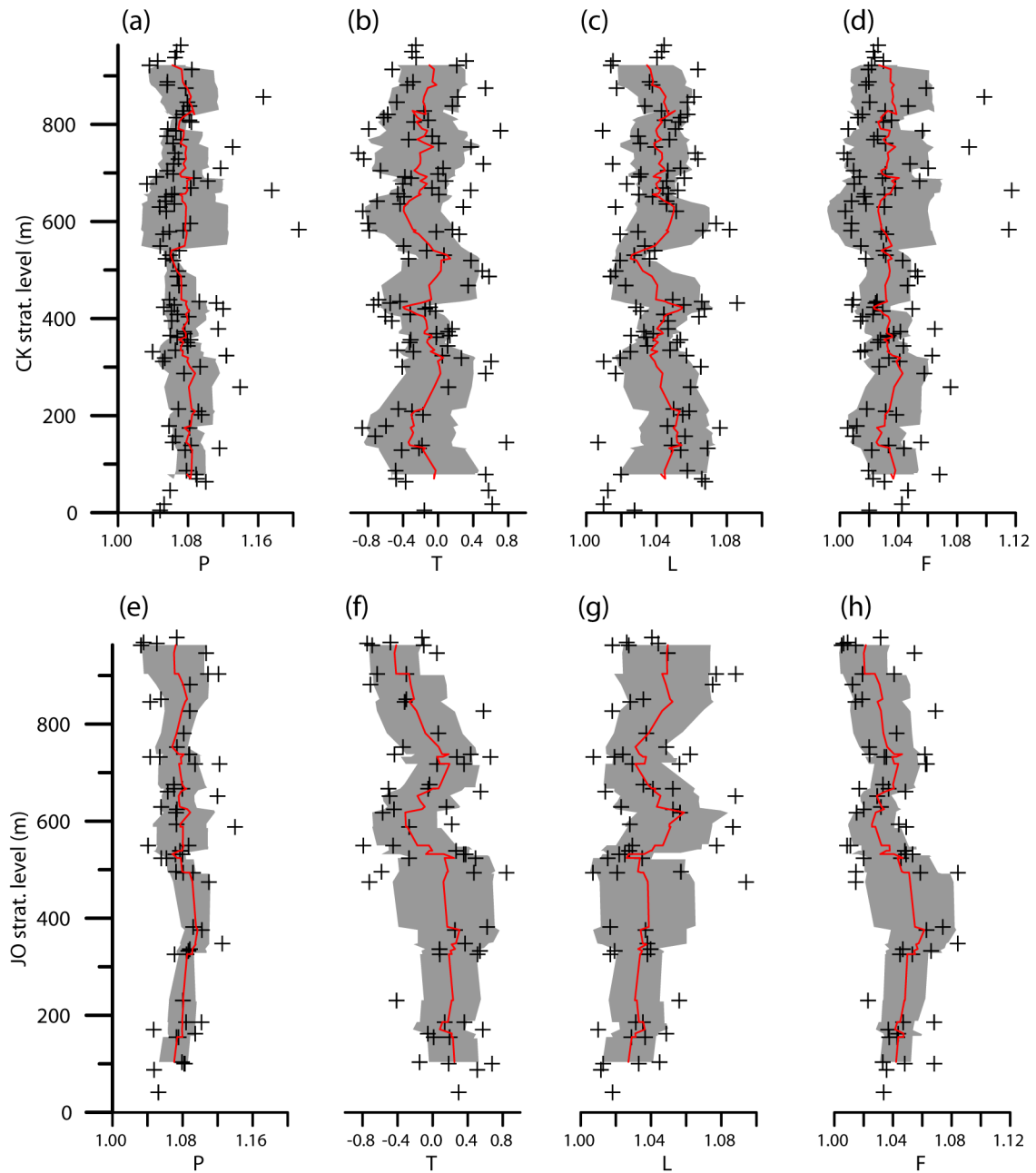


Figure A3.1. Stratigraphic variation of (a,e) degree of anisotropy (P), (b,f) shape parameter (T), (c,g) lineation (L), and (d,h) foliation (F) for the CK (a-d) and JO (e-h) sections as a function of stratigraphy. Red lines are running averages with window width of 9 points. 1σ uncertainties in gray.

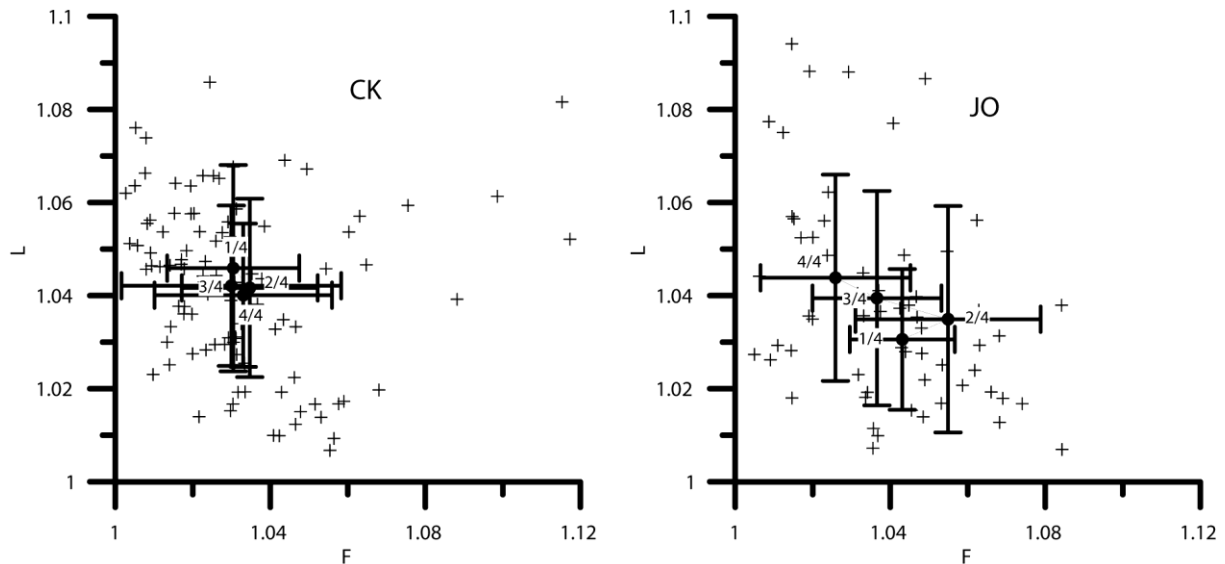


Figure A3.2. Flinn [1962] diagrams for the CK and JO sections. The vertical axis is lineation (L) and the horizontal axis is foliation (F). Filled circles represent averages of each quarter of the section, with 1/4 at the bottom and 4/4 at the top.

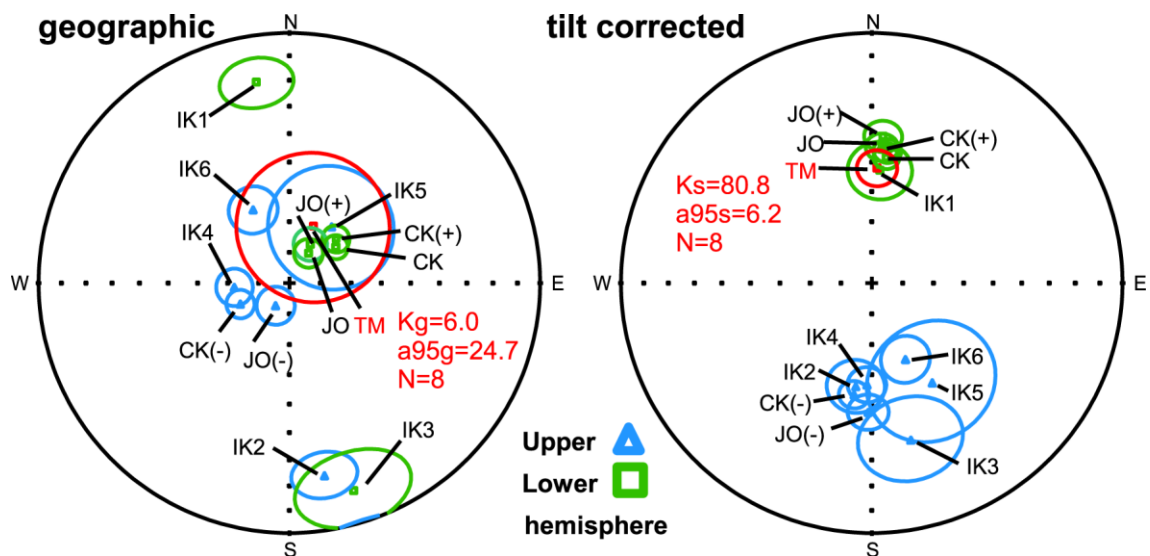


Figure A3.3. Fisher mean directions with a95 confidence ellipses of all sites in geographic and tilt corrected coordinates (data in Table A3.3). Directions from the CK and JO sections were split into normal (+) and reverse (-) polarities. Total mean (TM, shown in red) excludes sites IK3 and IK5.

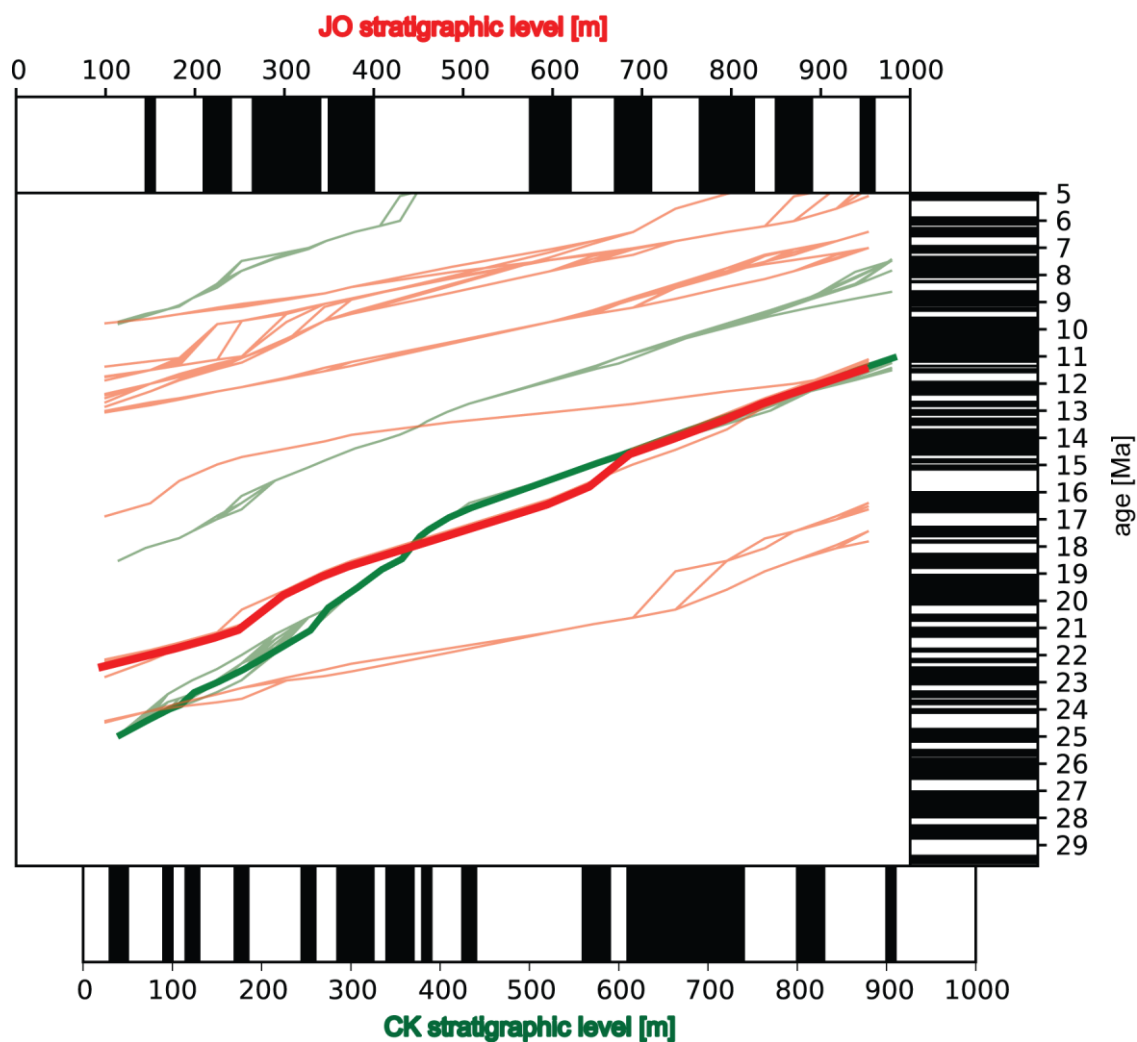


Figure A3.4. Correlations calculated by the Cupydon computer program [Lallier *et al.*, 2013] between the magnetostratigraphy of JO and CK sections and the geomagnetic polarity timescale from Gradstein and Ogg [2004]. The 500 (out of 5000 calculated) least expensive (i.e. best matching) correlations are shown for each section. Two thick lines represent the correlations from each section which are in best agreement regarding the observed change in anhysteretic remanent magnetization (ARM) acquisition in both sections.

JTZ54	66	0.0712	0.0003	0.5467	0.0076	0.0564	0.0009	443.14	442.85	468.15	5.34	443	11
JTZ54	67	0.0680	0.0003	0.5598	0.0080	0.0592	0.0010	424.10	451.42	574.46	26.17	424	11
JTZ54	68	0.0686	0.0003	0.5348	0.0071	0.0575	0.0009	427.41	435.00	511.91	16.51	427	10
JTZ54	69	0.0698	0.0003	0.5409	0.0062	0.0563	0.0009	435.19	439.00	465.79	6.57	435	10
JTZ54	70	0.0641	0.0002	0.5051	0.0066	0.0573	0.0009	400.69	415.18	504.25	20.54	401	10
JTZ54	71	0.0691	0.0003	0.5381	0.0095	0.0560	0.0010	430.79	437.16	451.58	4.60	431	11
JTZ54	72	0.0710	0.0003	0.5489	0.0073	0.0565	0.0009	442.24	444.25	470.11	5.93	442	11
JTZ54	73	0.0678	0.0002	0.5267	0.0062	0.0572	0.0009	422.59	429.62	498.10	15.16	423	10
JTZ54	74	0.0674	0.0003	0.5458	0.0141	0.0570	0.0012	420.41	442.24	491.92	14.54	420	11
JTZ54	75	0.0667	0.0003	0.5396	0.0088	0.0586	0.0010	416.12	438.15	552.64	24.70	416	11
JTZ54	76	0.0663	0.0003	0.5459	0.0151	0.0583	0.0013	414.01	442.33	541.80	23.59	414	12
JTZ54	77	0.2357	0.0009	2.9139	0.0444	0.0904	0.0014	1364.36	1385.53	1433.15	4.80	1433	30
JTZ54	78	0.0706	0.0003	0.6138	0.0087	0.0635	0.0010	439.65	485.98	725.02	39.36	440	11
JTZ54	79	0.0683	0.0003	0.5550	0.0085	0.0592	0.0010	425.72	448.24	574.83	25.94	426	11
JTZ54	80	0.0676	0.0003	0.5439	0.0079	0.0577	0.0009	421.74	440.99	516.49	18.34	422	10
JTZ54	81	0.0654	0.0003	0.5098	0.0101	0.0557	0.0011	408.26	418.31	438.43	6.88	408	11
JTZ54	82	0.0650	0.0003	0.5085	0.0120	0.0556	0.0012	405.90	417.44	434.83	6.65	406	11
JTZ54	83	0.0675	0.0003	0.5619	0.0140	0.0580	0.0012	421.32	452.76	529.76	20.47	421	11
JTZ54	84	0.0680	0.0004	0.5024	0.0149	0.0557	0.0013	424.22	413.29	440.03	3.59	424	12
JTZ54	85	0.0679	0.0003	0.5670	0.0096	0.0606	0.0011	423.19	456.04	625.07	32.30	423	11
JTZ54	86	0.2348	0.0010	3.0931	0.0782	0.0911	0.0015	1359.66	1430.99	1448.07	6.11	1448	33
JTZ54	87	0.0683	0.0004	0.5458	0.0158	0.0620	0.0015	425.85	442.26	672.73	36.70	426	12
JTZ54	88	0.0656	0.0003	0.5393	0.0130	0.0561	0.0012	409.77	437.96	457.12	10.36	410	11
JTZ54	89	0.0653	0.0003	0.5204	0.0084	0.0568	0.0010	407.90	425.41	484.55	15.82	408	10
JTZ54	90	0.0649	0.0003	0.5131	0.0116	0.0548	0.0011	405.36	420.55	403.66	-0.42	405	11
JTZ54	91	0.0656	0.0003	0.5307	0.0117	0.0556	0.0011	409.35	432.24	435.63	6.03	409	11
JTZ54	92	0.0641	0.0003	0.5172	0.0124	0.0590	0.0012	400.21	423.27	565.25	29.20	400	11
JTZ54	93	0.0674	0.0003	0.5182	0.0084	0.0562	0.0010	420.23	423.94	459.09	8.47	420	10
JTZ54	94	0.0687	0.0003	0.5569	0.0093	0.0581	0.0010	428.32	449.51	531.65	19.44	428	11
JTZ54	95	0.0669	0.0003	0.5379	0.0107	0.0575	0.0011	417.15	437.05	510.38	18.27	417	11
JTZ54	96	0.0642	0.0003	0.5113	0.0104	0.0557	0.0011	400.94	419.32	441.63	9.21	401	11
JTZ54	97	0.0683	0.0002	0.5449	0.0078	0.0579	0.0010	425.78	441.68	527.12	19.22	426	10
JTZ54	98	0.0690	0.0003	0.5531	0.0098	0.0557	0.0010	430.01	447.00	439.23	2.10	430	11
JTZ54	99	0.0674	0.0003	0.5241	0.0101	0.0561	0.0011	420.47	427.85	455.93	7.78	420	11
JTZ54	100	0.0670	0.0003	0.5551	0.0107	0.0581	0.0011	418.00	448.35	533.91	21.71	418	11
JTZ54	101	0.0710	0.0003	0.5554	0.0096	0.0566	0.0010	442.18	448.53	474.03	6.72	442	11
JTZ54	102	0.0657	0.0003	0.5194	0.0133	0.0554	0.0012	410.14	424.78	428.40	4.26	410	11
JTZ54	103	0.0695	0.0003	0.5597	0.0108	0.0564	0.0011	433.14	451.31	469.33	7.71	433	11
JTZ54	104	0.0704	0.0003	0.5962	0.0121	0.0597	0.0011	438.32	474.79	590.90	25.82	438	11
JTZ54	105	0.0688	0.0003	0.5427	0.0101	0.0553	0.0010	428.74	440.19	425.58	-0.74	429	11
JTZ54	106	0.0704	0.0003	0.5559	0.0121	0.0568	0.0011	438.69	448.86	484.55	9.47	439	11
JTZ56	1	0.0773	0.0003	0.5635	0.0121	0.0564	0.0011	479.81	453.77	467.36	-2.66	480	19
JTZ56	2	0.0697	0.0003	0.5495	0.0091	0.0557	0.0010	434.05	444.64	440.03	1.36	434	18
JTZ56	3	0.0741	0.0003	0.5563	0.0121	0.0585	0.0011	460.57	449.12	547.04	15.81	461	19
JTZ56	4	0.0765	0.0004	0.5669	0.0137	0.0566	0.0012	475.38	455.98	475.98	0.13	475	19
JTZ56	5	0.0753	0.0004	0.5909	0.0163	0.0564	0.0013	468.01	471.42	468.93	0.20	468	19
JTZ56	6	0.0749	0.0003	0.5589	0.0124	0.0563	0.0011	465.31	450.79	463.83	-0.32	465	19
JTZ56	7	0.0770	0.0003	0.6108	0.0106	0.0568	0.0010	477.89	484.04	485.33	1.53	478	18
JTZ56	8	0.0746	0.0003	0.5804	0.0124	0.0572	0.0011	464.05	464.71	497.33	6.69	464	19
JTZ56	9	0.0628	0.0003	0.4999	0.0102	0.0548	0.0010	392.81	411.62	402.85	2.49	393	18
JTZ56	10	0.0709	0.0003	0.5423	0.0121	0.0575	0.0011	441.70	439.95	510.76	13.52	442	19
JTZ56	11	0.0760	0.0004	0.5653	0.0182	0.0553	0.0014	472.26	454.94	423.97	-11.39	472	20
JTZ56	12	0.0671	0.0003	0.5390	0.0082	0.0566	0.0010	418.36	437.78	474.81	11.89	418	18
JTZ56	13	0.0736	0.0003	0.5717	0.0099	0.0560	0.0010	457.99	459.09	450.38	-1.69	458	18
JTZ56	14	0.0688	0.0003	0.5650	0.0091	0.0563	0.0010	428.86	454.78	464.61	7.69	429	18
JTZ56	15	0.0717	0.0003	0.5416	0.0106	0.0558	0.0010	446.51	439.49	443.62	-0.65	447	18
JTZ56	16	0.0765	0.0003	0.5577	0.0114	0.0556	0.0011	475.08	450.03	437.63	-8.56	475	19
JTZ56	17	0.0956	0.0004	0.8474	0.0155	0.0605	0.0011	588.34	623.24	620.79	5.23	588	19
JTZ56	18	0.0785	0.0005	0.6163	0.0220	0.0570	0.0015	486.86	487.55	489.60	0.56	487	20
JTZ56	19	0.0747	0.0003	0.5867	0.0095	0.0563	0.0010	464.23	468.75	463.04	-0.26	464	18
JTZ56	20	0.0715	0.0003	0.5594	0.0103	0.0562	0.0010	445.31	451.15	458.30	2.84	445	18
JTZ56	21	0.0764	0.0004	0.5674	0.0157	0.0570	0.0013	474.84	456.31	489.60	3.01	475	19
JTZ56	22	0.0744	0.0003	0.5948	0.0130	0.0566	0.0011	462.61	473.91	475.20	2.65	463	19
JTZ56	23	0.0737	0.0004	0.5788	0.0154	0.0561	0.0012	458.41	463.72	457.51	-0.20	458	19
JTZ56	24	0.0720	0.0003	0.5547	0.0132	0.0551	0.0011	448.25	448.09	416.69	-7.58	448	19
JTZ56	25	0.1812	0.0008	1.7691	0.0470	0.0751	0.0014	1073.36	1034.20	1071.18	-0.20	1071	39
JTZ56	26	0.0724	0.0003	0.5606	0.0113	0.0580	0.0011	450.78	451.94	530.89	15.09	451	18
JTZ56	27	0.0784	0.0003	0.6484	0.0106	0.0569	0.0010	486.27	507.51	486.11	-0.03	486	18
JTZ56	28	0.0722	0.0003	0.5703	0.0104	0.0562	0.0010	449.58	458.19	460.67	2.41	450	18
JTZ56	29	0.1752	0.0007	1.7576	0.0355	0.0741	0.0013	1040.75	1029.98	1043.10	0.23	1043	37
JTZ56	30	0.0750	0.0003	0.5526	0.0121	0.0557	0.0011	466.03	446.72	439.23	-6.10	466	19
JTZ56	31	0.2756	0.0010	4.2227	0.0635	0.1037	0.0016	1569.16	1678.44	1692.08	7.26	1692	41
JTZ56	32	0.0746	0.0003	0.5830	0.0112	0.0593	0.0011	463.99	466.37	579.59	19.95	464	18
JTZ56	33	0.0776	0.0005	0.6020	0.0231	0.0571	0.0016	481.48	478.51	495.40	2.81	481	20
JTZ56	34	0.0721	0.0003	0.5318	0.0124	0.0560	0.0012	448.73	433.00	452.76	0.89	449	19
JTZ56	35	0.0741	0.0004	0.5659	0.0156	0.0562	0.0013	461.05	455.35	460.28	-0.17	461	19

JTZ56	36	0.0855	0.0005	0.6770	0.0233	0.0580	0.0015	529.05	524.94	529.01	-0.01	529	20
JTZ56	37	0.0781	0.0005	0.6026	0.0233	0.0575	0.0016	484.65	478.86	509.61	4.90	485	21
JTZ56	38	0.0724	0.0003	0.5906	0.0121	0.0564	0.0011	450.30	471.23	466.97	3.57	450	18
JTZ56	39	0.0836	0.0005	0.6178	0.0222	0.0577	0.0015	517.69	488.45	518.39	0.13	518	21
JTZ56	40	0.0747	0.0003	0.5649	0.0127	0.0562	0.0011	464.41	454.68	460.28	-0.90	464	19
JTZ56	41	0.0717	0.0003	0.5782	0.0112	0.0560	0.0011	446.27	463.27	452.76	1.43	446	18
JTZ56	42	0.0695	0.0003	0.5589	0.0091	0.0556	0.0010	432.90	450.80	437.23	0.99	433	18
JTZ56	43	0.0818	0.0004	0.6399	0.0186	0.0580	0.0013	506.68	502.25	529.01	4.22	507	20
JTZ56	44	0.0695	0.0003	0.5582	0.0112	0.0555	0.0011	432.90	450.36	433.63	0.17	433	18
JTZ56	45	0.0810	0.0004	0.5982	0.0195	0.0559	0.0014	502.15	476.08	448.00	-12.09	502	20
JTZ56	46	0.0811	0.0003	0.6061	0.0128	0.0561	0.0011	502.92	481.07	454.75	-10.59	503	19
JTZ56	47	0.0725	0.0003	0.5703	0.0113	0.0562	0.0011	451.08	458.18	459.09	1.75	451	18
JTZ56	48	0.0737	0.0004	0.5507	0.0154	0.0561	0.0013	458.47	445.46	457.91	-0.12	458	19
JTZ56	49	0.0740	0.0003	0.5603	0.0142	0.0564	0.0012	460.09	451.72	466.19	1.31	460	19
JTZ56	50	0.0749	0.0004	0.5412	0.0179	0.0563	0.0014	465.85	439.22	463.04	-0.61	466	20
JTZ56	51	0.0723	0.0003	0.5594	0.0126	0.0571	0.0012	450.18	451.11	496.55	9.34	450	18
JTZ56	52	0.0717	0.0003	0.5257	0.0143	0.0561	0.0013	446.51	428.97	455.93	2.07	447	19
JTZ56	53	0.0682	0.0003	0.5285	0.0103	0.0553	0.0011	425.48	430.80	425.18	-0.07	425	18
JTZ56	54	0.0763	0.0003	0.5785	0.0145	0.0564	0.0012	474.00	463.48	469.33	-1.00	474	19
JTZ56	55	0.0701	0.0003	0.5575	0.0102	0.0556	0.0010	436.52	449.92	436.83	0.07	437	18
JTZ56	56	0.0781	0.0004	0.6465	0.0205	0.0611	0.0015	484.59	506.29	644.16	24.77	485	20
JTZ56	57	0.0648	0.0003	0.5143	0.0098	0.0552	0.0011	404.57	421.31	421.14	3.94	405	18
JTZ56	58	0.0686	0.0004	0.5072	0.0152	0.0570	0.0014	427.47	416.54	493.08	13.31	427	19
JTZ56	59	0.0775	0.0003	0.5725	0.0134	0.0574	0.0012	481.42	459.62	507.70	5.18	481	19
JTZ56	60	0.3291	0.0012	4.5982	0.0955	0.1071	0.0019	1833.78	1748.94	1750.30	-4.77	1750	45
JTZ56	61	0.0766	0.0004	0.5890	0.0164	0.0567	0.0013	475.62	470.20	479.10	0.73	476	19
JTZ56	62	0.0739	0.0003	0.5440	0.0138	0.0557	0.0012	459.79	441.08	442.03	-4.02	460	19
JTZ56	63	0.0738	0.0003	0.5818	0.0130	0.0560	0.0011	458.89	465.59	453.56	-1.18	459	7
JTZ56	64	0.0700	0.0003	0.5279	0.0135	0.0556	0.0012	435.91	430.42	436.03	0.03	436	7
JTZ56	65	0.0717	0.0003	0.5871	0.0122	0.0572	0.0011	446.33	469.03	497.33	10.25	446	7
JTZ56	66	0.0764	0.0004	0.6624	0.0196	0.0634	0.0014	474.72	516.08	721.68	34.22	475	8
JTZ56	67	0.0793	0.0004	0.6339	0.0196	0.0576	0.0014	491.82	498.53	515.72	4.63	492	8
JTZ56	68	0.0762	0.0004	0.6202	0.0165	0.0588	0.0013	473.10	489.99	557.84	15.19	473	8
JTZ56	69	0.0772	0.0005	0.5883	0.0217	0.0568	0.0015	479.09	469.78	484.94	1.21	479	9
JTZ56	70	0.0778	0.0005	0.5537	0.0221	0.0568	0.0016	482.68	447.42	483.78	0.23	483	9
JTZ56	71	0.0755	0.0003	0.5784	0.0138	0.0569	0.0012	468.91	463.45	488.44	4.00	469	7
JTZ56	72	0.0662	0.0002	0.5412	0.0088	0.0551	0.0010	413.10	439.24	417.09	0.96	413	6
JTZ56	73	0.0744	0.0003	0.5842	0.0144	0.0564	0.0012	462.31	467.16	468.54	1.33	462	7
JTZ56	74	0.0696	0.0003	0.5385	0.0140	0.0557	0.0012	433.99	437.41	441.63	1.73	434	7
JTZ56	75	0.2526	0.0012	3.1932	0.1053	0.0912	0.0017	1451.77	1455.52	1449.95	-0.13	1450	33
JTZ56	76	0.0748	0.0003	0.5815	0.0134	0.0561	0.0011	465.25	465.42	457.91	-1.60	465	7
JTZ56	77	0.0700	0.0005	0.5309	0.0250	0.0570	0.0019	436.10	432.42	490.76	11.14	436	9
JTZ56	78	0.2668	0.0011	3.3913	0.0857	0.0934	0.0017	1524.64	1502.39	1495.81	-1.93	1496	31
JTZ56	79	0.0735	0.0003	0.5653	0.0121	0.0560	0.0011	457.27	454.94	453.95	-0.73	457	7
JTZ56	80	0.0740	0.0003	0.5643	0.0118	0.0561	0.0011	459.91	454.30	455.14	-1.05	460	7
JTZ56	81	0.0689	0.0003	0.5321	0.0151	0.0563	0.0013	429.40	433.21	463.83	7.42	429	7
JTZ56	82	0.0722	0.0003	0.5742	0.0110	0.0561	0.0011	449.34	460.70	454.35	1.10	449	7
JTZ56	83	0.0737	0.0004	0.5744	0.0177	0.0560	0.0013	458.41	460.82	452.76	-1.25	458	8
JTZ56	84	0.0747	0.0003	0.5803	0.0134	0.0564	0.0011	464.17	464.67	467.36	0.68	464	7
JTZ56	85	0.0630	0.0003	0.5000	0.0147	0.0554	0.0013	393.84	411.69	428.40	8.07	394	7
JTZ56	86	0.0708	0.0003	0.5628	0.0130	0.0559	0.0011	441.03	453.33	449.19	1.82	441	7
JTZ56	87	0.0694	0.0004	0.5530	0.0170	0.0555	0.0013	432.48	446.95	432.42	-0.01	432	8
JTZ56	88	0.0771	0.0004	0.5866	0.0185	0.0565	0.0014	478.55	468.67	471.68	-1.46	479	8
JTZ56	89	0.0704	0.0003	0.5882	0.0110	0.0560	0.0010	438.26	469.74	451.18	2.86	438	7
JTZ56	90	0.0729	0.0003	0.5699	0.0144	0.0563	0.0012	453.48	457.95	464.61	2.40	453	7
JTZ56	91	0.0767	0.0003	0.5953	0.0134	0.0566	0.0011	476.34	474.27	476.76	0.09	476	7
JTZ56	92	0.0738	0.0003	0.5753	0.0139	0.0562	0.0012	459.07	461.45	459.09	0.01	459	7
JTZ56	93	0.0671	0.0004	0.5352	0.0172	0.0577	0.0014	418.42	435.23	518.39	19.28	418	8
JTZ56	94	0.0733	0.0003	0.5707	0.0130	0.0562	0.0011	456.19	458.45	459.49	0.72	456	7
JTZ56	95	0.0737	0.0003	0.5787	0.0118	0.0561	0.0011	458.47	463.61	455.14	-0.73	458	7
JTZ56	96	0.0728	0.0003	0.5757	0.0157	0.0560	0.0013	453.00	461.68	453.16	0.03	453	7
JTZ56	97	0.0705	0.0003	0.5475	0.0125	0.0558	0.0011	439.35	443.36	442.82	0.79	439	7
JTZ56	98	0.0718	0.0004	0.5824	0.0183	0.0560	0.0014	447.23	466.00	451.18	0.87	447	8
JTZ56	99	0.0718	0.0003	0.5382	0.0138	0.0548	0.0012	447.11	437.20	402.44	-11.10	447	7
JTZ56	100	0.0690	0.0003	0.5542	0.0119	0.0555	0.0011	429.95	447.76	432.42	0.57	430	7
JTZ56	101	0.0723	0.0003	0.5401	0.0143	0.0556	0.0012	450.00	438.50	436.03	-3.20	450	7
JTZ56	102	0.0762	0.0003	0.5880	0.0149	0.0569	0.0012	473.64	469.62	488.05	2.95	474	7
JTZ56	103	0.0724	0.0004	0.5269	0.0168	0.0538	0.0014	450.66	429.76	361.43	-24.69	451	8
JTZ56	104	0.0726	0.0004	0.5711	0.0222	0.0566	0.0016	451.92	458.72	477.54	5.37	452	9
JTZ56	105	0.0691	0.0003	0.5169	0.0134	0.0557	0.0012	430.67	423.07	442.03	2.57	431	7
JTZ56	106	0.0777	0.0004	0.5978	0.0178	0.0568	0.0013	482.32	475.85	484.55	0.46	482	8
JTZ56	107	0.0722	0.0003	0.5668	0.0151	0.0562	0.0013	449.28	455.94	458.70	2.05	449	7
JTZ56	108	0.0684	0.0004	0.5086	0.0191	0.0528	0.0015	426.45	417.48	321.50	-32.64	426	8
JTZ56	109	0.0730	0.0003	0.5761	0.0138	0.0562	0.0012	454.44	461.96	461.46	1.52	454	7
JTZ56	110	0.0742	0.0003	0.5687	0.0133	0.0549	0.0012	461.35	457.19	408.56	-12.92	461	7
JTZ56	111	0.0671	0.0004	0.5027	0.0203	0.0569	0.0017	418.36	413.54	488.44	14.35	418	8
JTZ56	112	0.0701	0.0004	0.5412	0.0198	0.0570	0.0016	436.82	439.20	491.92	11.20	437	8

JTZ58	1	0.0732	0.0005	0.5621	0.0113	0.0558	0.0010	455.53	452.92	444.02	-2.59	456	10
JTZ58	2	0.0757	0.0005	0.5446	0.0130	0.0565	0.0011	470.47	441.47	470.50	0.01	470	10
JTZ58	3	0.0780	0.0005	0.5766	0.0138	0.0566	0.0011	484.29	462.27	476.76	-1.58	484	10
JTZ58	4	0.0722	0.0005	0.5854	0.0185	0.0609	0.0015	449.28	467.90	636.41	29.40	449	11
JTZ58	5	0.0744	0.0004	0.5712	0.0083	0.0565	0.0008	462.85	458.78	470.50	1.63	463	9
JTZ58	6	0.0781	0.0005	0.5974	0.0100	0.0575	0.0009	484.95	475.57	510.00	4.91	485	10
JTZ58	7	0.0763	0.0005	0.5753	0.0136	0.0578	0.0011	474.24	461.41	522.95	9.31	474	10
JTZ58	8	0.0737	0.0004	0.5503	0.0105	0.0567	0.0009	458.41	445.22	480.27	4.55	458	10
JTZ58	9	0.0738	0.0005	0.5598	0.0132	0.0565	0.0011	458.71	451.37	473.64	3.15	459	10
JTZ58	10	0.0698	0.0004	0.5676	0.0104	0.0584	0.0009	434.77	456.44	545.55	20.31	435	9
JTZ58	11	0.0774	0.0005	0.6277	0.0127	0.0605	0.0010	480.47	494.65	620.79	22.60	480	10
JTZ58	12	0.0682	0.0004	0.5532	0.0097	0.0590	0.0009	425.18	447.08	567.10	25.02	425	9
JTZ58	13	0.0718	0.0004	0.5880	0.0121	0.0602	0.0010	446.93	469.60	612.21	27.00	447	10
JTZ58	14	0.0719	0.0004	0.5417	0.0093	0.0560	0.0009	447.53	439.56	451.18	0.81	448	9
JTZ58	15	0.0770	0.0005	0.5854	0.0116	0.0567	0.0010	478.31	467.94	481.44	0.65	478	10
JTZ58	16	0.0742	0.0005	0.5554	0.0122	0.0567	0.0010	461.47	448.53	478.32	3.52	461	10
JTZ58	17	0.0723	0.0004	0.5718	0.0095	0.0587	0.0009	449.76	459.15	557.10	19.27	450	9
JTZ58	18	0.0701	0.0005	0.5228	0.0148	0.0583	0.0013	436.82	427.04	542.18	19.43	437	10
JTZ58	19	0.0715	0.0004	0.5825	0.0088	0.0591	0.0008	445.07	466.09	570.78	22.03	445	9
JTZ58	20	0.0744	0.0005	0.5698	0.0184	0.0568	0.0014	462.55	457.88	485.33	4.69	463	11
JTZ58	21	0.0754	0.0005	0.5757	0.0125	0.0566	0.0010	468.73	461.69	474.03	1.12	469	10
JTZ58	22	0.0815	0.0007	0.6174	0.0249	0.0576	0.0017	504.95	488.20	513.44	1.65	505	12
JTZ58	23	0.0755	0.0005	0.5792	0.0124	0.0565	0.0010	469.45	463.93	471.68	0.47	469	10
JTZ58	24	0.0738	0.0005	0.5502	0.0137	0.0562	0.0011	458.95	445.15	459.09	0.03	459	10
JTZ58	25	0.0707	0.0004	0.5548	0.0122	0.0600	0.0011	440.13	448.14	602.85	26.99	440	10
JTZ58	26	0.0691	0.0008	0.5315	0.0338	0.0635	0.0029	430.73	432.80	725.69	40.65	431	15
JTZ58	27	0.0717	0.0004	0.5650	0.0086	0.0570	0.0008	446.09	454.77	492.31	9.39	446	9
JTZ58	28	0.0680	0.0004	0.5170	0.0085	0.0567	0.0009	424.16	423.12	479.10	11.47	424	9
JTZ58	29	0.0711	0.0004	0.5699	0.0091	0.0578	0.0009	443.02	457.96	521.81	15.10	443	9
JTZ58	30	0.0735	0.0005	0.5809	0.0155	0.0593	0.0012	457.03	465.04	579.59	21.15	457	10
JTZ58	31	0.0687	0.0005	0.5244	0.0138	0.0582	0.0012	428.56	428.07	537.67	20.29	429	10
JTZ58	32	0.0698	0.0004	0.5288	0.0108	0.0566	0.0010	434.83	431.03	474.03	8.27	435	9
JTZ58	33	0.0665	0.0004	0.5203	0.0103	0.0592	0.0010	414.73	425.38	573.72	27.71	415	9
JTZ58	34	0.0704	0.0004	0.5433	0.0102	0.0570	0.0009	438.75	440.62	492.31	10.88	439	9
JTZ58	35	0.0710	0.0006	0.5178	0.0231	0.0609	0.0020	442.24	423.67	636.06	30.47	442	12
JTZ58	36	0.0750	0.0004	0.5844	0.0112	0.0564	0.0009	466.27	467.30	466.19	-0.02	466	9
JTZ58	37	0.0742	0.0004	0.5685	0.0101	0.0574	0.0009	461.65	457.02	506.93	8.93	462	9
JTZ58	38	0.0710	0.0004	0.5623	0.0087	0.0560	0.0008	442.18	453.00	451.58	2.08	442	9
JTZ58	39	0.0733	0.0004	0.5437	0.0121	0.0561	0.0010	455.77	440.87	457.51	0.38	456	10
JTZ58	40	0.0714	0.0005	0.5193	0.0157	0.0559	0.0013	444.46	424.71	448.40	0.88	444	10
JTZ58	41	0.0697	0.0004	0.5658	0.0112	0.0583	0.0010	434.41	455.31	539.55	19.49	434	9
JTZ58	42	0.0719	0.0004	0.5766	0.0108	0.0565	0.0009	447.59	462.29	470.11	4.79	448	9
JTZ58	43	0.0711	0.0004	0.5297	0.0120	0.0560	0.0011	442.66	431.63	450.38	1.72	443	9
JTZ58	44	0.0770	0.0006	0.6261	0.0204	0.0617	0.0015	477.95	493.66	662.68	27.88	478	11
JTZ58	45	0.0716	0.0005	0.5533	0.0143	0.0569	0.0012	445.79	447.15	486.88	8.44	446	10
JTZ58	46	0.0728	0.0004	0.5545	0.0129	0.0569	0.0011	452.76	447.95	486.88	7.01	453	10
JTZ58	47	0.0705	0.0005	0.5406	0.0197	0.0553	0.0015	439.23	438.80	422.35	-4.00	439	11
JTZ58	48	0.0717	0.0005	0.5275	0.0143	0.0551	0.0012	446.21	430.14	417.50	-6.88	446	10
JTZ58	49	0.0791	0.0005	0.6259	0.0183	0.0615	0.0014	490.87	493.56	657.12	25.30	491	11
JTZ58	50	0.0709	0.0004	0.5729	0.0099	0.0589	0.0009	441.33	459.91	561.55	21.41	441	9
JTZ58	51	0.0766	0.0006	0.6014	0.0221	0.0587	0.0016	475.50	478.09	555.99	14.48	476	11
JTZ58	52	0.0684	0.0004	0.5360	0.0120	0.0584	0.0011	426.63	435.80	544.80	21.69	427	9
JTZ58	53	0.0718	0.0004	0.5540	0.0115	0.0568	0.0010	446.69	447.59	485.33	7.96	447	9
JTZ58	54	0.0680	0.0006	0.5145	0.0205	0.0582	0.0017	423.97	421.48	535.42	20.81	424	11
JTZ58	55	0.0715	0.0004	0.5314	0.0125	0.0561	0.0011	445.25	432.74	456.33	2.43	445	9
JTZ58	56	0.0728	0.0005	0.5240	0.0143	0.0561	0.0012	452.82	427.80	457.12	0.94	453	10
JTZ58	57	0.0758	0.0005	0.5545	0.0157	0.0567	0.0013	471.18	447.94	477.93	1.41	471	10
JTZ58	58	0.0842	0.0005	0.6872	0.0129	0.0604	0.0010	521.26	531.13	617.58	15.60	521	10
JTZ58	59	0.0723	0.0004	0.5236	0.0110	0.0561	0.0010	450.00	427.54	456.72	1.47	450	9
JTZ58	60	0.0765	0.0005	0.5765	0.0147	0.0566	0.0012	475.08	462.19	474.03	-0.22	475	10
JTZ58	61	0.0699	0.0005	0.5481	0.0160	0.0590	0.0013	435.25	443.76	566.73	23.20	435	10
JTZ58	62	0.0719	0.0005	0.5529	0.0163	0.0562	0.0013	447.71	446.88	460.28	2.73	448	10
JTZ58	63	0.0732	0.0004	0.5579	0.0120	0.0576	0.0011	455.11	450.15	514.96	11.62	455	9
JTZ58	64	0.0737	0.0004	0.5471	0.0104	0.0560	0.0010	458.11	443.12	452.76	-1.18	458	9
JTZ58	65	0.0684	0.0004	0.5381	0.0099	0.0568	0.0010	426.51	437.18	485.33	12.12	427	9
JTZ58	66	0.0711	0.0004	0.5494	0.0140	0.0587	0.0012	442.54	444.57	554.87	20.24	443	10
JTZ58	67	0.0720	0.0004	0.5496	0.0137	0.0566	0.0012	448.25	444.73	476.37	5.90	448	10
JTZ58	68	0.0697	0.0004	0.5342	0.0113	0.0570	0.0011	434.23	434.56	489.98	11.38	434	9
JTZ58	69	0.0699	0.0005	0.5352	0.0161	0.0592	0.0014	435.61	435.23	572.99	23.98	436	10
JTZ58	70	0.0701	0.0004	0.5626	0.0097	0.0579	0.0010	436.88	453.22	525.60	16.88	437	9
JTZ58	71	0.0738	0.0004	0.5663	0.0140	0.0575	0.0012	458.83	455.59	511.53	10.30	459	10
JTZ58	72	0.0733	0.0004	0.5732	0.0124	0.0568	0.0011	456.25	460.06	481.83	5.31	456	9
JTZ58	73	0.0727	0.0004	0.5664	0.0139	0.0595	0.0012	452.28	455.71	586.90	22.94	452	10
JTZ58	74	0.0754	0.0005	0.5924	0.0180	0.0581	0.0014	468.55	472.39	533.16	12.12	469	10
JTZ58	75	0.0728	0.0005	0.5695	0.0196	0.0603	0.0016	453.24	457.66	615.07	26.31	453	11
JTZ58	76	0.0766	0.0005	0.5803	0.0204	0.0565	0.0015	475.62	464.63	472.07	-0.75	476	11

JTZ60	1	0.0653	0.0003	0.4643	0.0142	0.0557	0.0014	407.72	387.25	442.03	7.76	408	4
JTZ60	2	0.0679	0.0003	0.5160	0.0113	0.0574	0.0011	423.37	422.47	506.17	16.36	423	4
JTZ60	3	0.0650	0.0003	0.5241	0.0130	0.0616	0.0013	406.14	427.89	659.90	38.45	406	4
JTZ60	4	0.0756	0.0003	0.5860	0.0138	0.0577	0.0012	470.05	468.28	519.91	9.59	470	4
JTZ60	5	0.0744	0.0004	0.5940	0.0166	0.0604	0.0013	462.49	473.44	618.29	25.20	462	4
JTZ60	6	0.0749	0.0003	0.5741	0.0132	0.0582	0.0012	465.85	460.69	535.42	12.99	466	4
JTZ60	7	0.0774	0.0003	0.5984	0.0138	0.0581	0.0012	480.82	476.19	534.29	10.01	481	4
JTZ60	8	0.0690	0.0003	0.5436	0.0093	0.0570	0.0010	429.89	440.80	492.31	12.68	430	3
JTZ60	9	0.0769	0.0003	0.6580	0.0153	0.0632	0.0013	477.35	513.37	715.30	33.27	477	4
JTZ60	10	0.0690	0.0003	0.5523	0.0103	0.0579	0.0011	430.01	446.50	526.36	18.31	430	3
JTZ60	11	0.0699	0.0003	0.5815	0.0123	0.0623	0.0012	435.79	465.44	684.08	36.29	436	4
JTZ60	12	0.0754	0.0003	0.5763	0.0111	0.0582	0.0011	468.61	462.06	535.42	12.48	469	4
JTZ60	13	0.0760	0.0004	0.6690	0.0196	0.0697	0.0016	471.96	520.10	920.12	48.71	472	5
JTZ60	14	0.0714	0.0004	0.6043	0.0183	0.0642	0.0015	444.40	479.93	747.24	40.53	444	4
JTZ60	15	0.0712	0.0003	0.5680	0.0132	0.0572	0.0012	443.38	456.69	499.25	11.19	443	4
JTZ60	16	0.0739	0.0003	0.6187	0.0111	0.0620	0.0011	459.37	489.01	674.45	31.89	459	3
JTZ60	17	0.0762	0.0003	0.6071	0.0139	0.0606	0.0012	473.34	481.71	624.00	24.14	473	4
JTZ60	18	0.0725	0.0003	0.6164	0.0117	0.0607	0.0011	451.44	487.61	628.98	28.23	451	3
JTZ60	19	0.0749	0.0003	0.5838	0.0143	0.0581	0.0012	465.85	466.88	533.53	12.69	466	4
JTZ60	20	0.0740	0.0003	0.5871	0.0126	0.0596	0.0012	459.91	469.02	590.54	22.12	460	4
JTZ60	21	0.0760	0.0003	0.5878	0.0116	0.0571	0.0011	472.08	469.47	495.78	4.78	472	4
JTZ60	22	0.0759	0.0003	0.5743	0.0121	0.0566	0.0011	471.42	460.80	475.20	0.79	471	4
JTZ60	23	0.0713	0.0003	0.5478	0.0135	0.0584	0.0012	443.68	443.57	543.30	18.34	444	4
JTZ60	24	0.0769	0.0005	0.5959	0.0214	0.0600	0.0016	477.71	474.64	605.02	21.04	478	5
JTZ60	25	0.0767	0.0004	0.5750	0.0165	0.0573	0.0013	476.57	461.27	503.10	5.27	477	5
JTZ60	26	0.0799	0.0003	0.6142	0.0131	0.0576	0.0011	495.76	486.18	514.58	3.66	496	4
JTZ60	27	0.0764	0.0005	0.5826	0.0248	0.0588	0.0018	474.66	466.11	559.33	15.14	475	6
JTZ60	28	0.0741	0.0003	0.5743	0.0138	0.0584	0.0012	460.75	460.76	544.43	15.37	461	4
JTZ60	29	0.0727	0.0003	0.5962	0.0114	0.0593	0.0011	452.28	474.79	577.03	21.62	452	5
JTZ60	30	0.0752	0.0003	0.5554	0.0096	0.0570	0.0010	467.23	448.54	492.31	5.09	467	5
JTZ60	31	0.0747	0.0003	0.5505	0.0101	0.0556	0.0010	464.41	445.29	436.83	-6.31	464	5
JTZ60	32	0.0715	0.0003	0.5370	0.0126	0.0569	0.0012	445.19	436.41	488.82	8.93	445	5
JTZ60	33	0.2507	0.0012	2.8312	0.0884	0.0922	0.0017	1442.24	1363.84	1470.68	1.93	1471	29
JTZ60	34	0.0654	0.0003	0.5523	0.0086	0.0613	0.0010	408.20	446.50	650.83	37.28	408	4
JTZ60	35	0.0734	0.0003	0.5362	0.0103	0.0552	0.0010	456.61	435.90	418.71	-9.05	457	5
JTZ60	36	0.0679	0.0003	0.5663	0.0082	0.0592	0.0010	423.37	455.61	573.36	26.16	423	4
JTZ60	37	0.0774	0.0003	0.5840	0.0109	0.0568	0.0010	480.76	467.02	482.61	0.38	481	5
JTZ60	38	0.0698	0.0003	0.5455	0.0073	0.0558	0.0009	434.95	442.05	443.62	1.95	435	4
JTZ60	39	0.0766	0.0003	0.5618	0.0125	0.0574	0.0011	475.74	452.70	507.32	6.23	476	5
JTZ60	40	0.0657	0.0002	0.5048	0.0067	0.0551	0.0009	410.44	414.97	415.47	1.21	410	4
JTZ60	41	0.0720	0.0003	0.5689	0.0088	0.0559	0.0009	447.95	457.28	448.80	0.19	448	4
JTZ60	42	0.0803	0.0004	0.6253	0.0186	0.0586	0.0014	497.61	493.16	551.52	9.77	498	6
JTZ60	43	0.0710	0.0003	0.5346	0.0113	0.0558	0.0011	442.00	434.84	444.82	0.63	442	5
JTZ60	44	0.0707	0.0004	0.5241	0.0175	0.0565	0.0015	440.07	427.90	470.11	6.39	440	6
JTZ60	45	0.0678	0.0003	0.5322	0.0102	0.0567	0.0010	422.59	433.24	480.27	12.01	423	4
JTZ60	46	0.0723	0.0003	0.5788	0.0105	0.0572	0.0010	450.18	463.72	500.02	9.97	450	4
JTZ60	47	0.0722	0.0003	0.5569	0.0112	0.0587	0.0011	449.28	449.50	557.47	19.41	449	5
JTZ60	48	0.0766	0.0003	0.6172	0.0112	0.0574	0.0010	475.50	488.12	505.40	5.92	476	5
JTZ60	49	0.0732	0.0004	0.5174	0.0154	0.0561	0.0013	455.11	423.39	455.54	0.09	455	6
JTZ60	50	0.0733	0.0003	0.5339	0.0119	0.0551	0.0011	456.07	434.37	417.90	-9.13	456	5
JTZ60	51	0.0743	0.0004	0.5571	0.0149	0.0559	0.0012	461.77	449.62	446.81	-3.35	462	5
JTZ60	52	0.0737	0.0003	0.5619	0.0126	0.0570	0.0011	458.11	452.75	491.92	6.87	458	5
JTZ60	53	0.0720	0.0003	0.5523	0.0139	0.0561	0.0012	448.43	446.50	457.12	1.90	448	5
JTZ60	54	0.0694	0.0003	0.5276	0.0094	0.0555	0.0010	432.24	430.18	430.81	-0.33	432	4
JTZ60	55	0.0755	0.0003	0.5705	0.0125	0.0564	0.0011	469.21	458.31	466.97	-0.48	469	5
JTZ60	56	0.0747	0.0003	0.5751	0.0120	0.0566	0.0011	464.47	461.28	476.37	2.50	464	5
JTZ60	57	0.0708	0.0003	0.5634	0.0087	0.0565	0.0010	441.09	453.72	473.64	6.87	441	4
JTZ60	58	0.0783	0.0003	0.6281	0.0116	0.0575	0.0010	485.85	494.91	508.85	4.52	486	5
JTZ60	59	0.0753	0.0003	0.6126	0.0125	0.0563	0.0011	468.13	485.22	462.64	-1.19	468	5
JTZ60	60	0.0821	0.0004	0.6277	0.0138	0.0573	0.0011	508.70	494.69	503.48	-1.04	509	5
JTZ60	61	0.0700	0.0003	0.5636	0.0119	0.0588	0.0011	436.16	453.84	560.81	22.23	436	4
JTZ60	62	0.0769	0.0003	0.5909	0.0111	0.0573	0.0010	477.29	471.45	501.56	4.84	477	5
JTZ60	63	0.0655	0.0003	0.5148	0.0113	0.0584	0.0012	408.75	421.64	545.17	25.02	409	4
JTZ60	64	0.0795	0.0004	0.6273	0.0162	0.0593	0.0013	493.32	494.43	577.76	14.62	493	5
JTZ60	65	0.0710	0.0003	0.5760	0.0156	0.0599	0.0013	441.88	461.89	601.41	26.53	442	5
JTZ60	66	0.0758	0.0003	0.5826	0.0132	0.0582	0.0012	471.24	466.12	536.55	12.17	471	5
JTZ60	67	0.0733	0.0003	0.5395	0.0124	0.0561	0.0011	456.01	438.10	456.33	0.07	456	5
JTZ60	68	0.0750	0.0004	0.5502	0.0178	0.0567	0.0014	466.09	445.15	480.66	3.03	466	6
JTZ60	69	0.0745	0.0003	0.5406	0.0116	0.0555	0.0011	463.09	438.83	433.22	-6.89	463	5
JTZ60	70	0.0750	0.0003	0.5667	0.0125	0.0555	0.0011	466.21	455.85	432.82	-7.71	466	5
JTZ60	71	0.0741	0.0004	0.6009	0.0160	0.0618	0.0014	460.57	477.78	668.58	31.11	461	5
JTZ60	72	0.0763	0.0003	0.5896	0.0143	0.0567	0.0012	474.24	470.62	481.44	1.50	474	5
JTZ60	73	0.0749	0.0004	0.6189	0.0188	0.0607	0.0014	465.43	489.16	629.33	26.04	465	6
JTZ60	74	0.0699	0.0003	0.5787	0.0119	0.0579	0.0011	435.55	463.59	527.49	17.43	436	4
JTZ60	75	0.0741	0.0003	0.5711	0.0113	0.0568	0.0011	460.63	458.71	482.61	4.55	461	4
JTZ60	76	0.0729	0.0003	0.5476	0.0097	0.0558	0.0010	453.54	443.44	446.01	-1.69	454	4

JTZ60	77	0.0715	0.0003	0.5778	0.0087	0.0568	0.0009	445.07	463.01	483.78	8.00	445	4
JTZ60	78	0.0744	0.0003	0.5415	0.0095	0.0556	0.0010	462.67	439.44	434.43	-6.50	463	4
JTZ60	79	0.0699	0.0003	0.5444	0.0083	0.0559	0.0009	435.79	441.32	448.80	2.90	436	4
JTZ60	80	0.0760	0.0003	0.5959	0.0076	0.0567	0.0009	472.02	474.60	479.10	1.48	472	4
JTZ60	81	0.0748	0.0003	0.5371	0.0094	0.0553	0.0010	464.77	436.50	425.58	-9.21	465	4
JTZ60	82	0.2207	0.0008	2.6211	0.0339	0.0860	0.0013	1285.31	1306.58	1337.28	3.89	1337	23
JTZ60	83	0.0799	0.0004	0.5702	0.0126	0.0570	0.0011	495.47	458.14	491.15	-0.88	495	5
JTZ60	84	0.0737	0.0003	0.5747	0.0118	0.0581	0.0011	458.17	461.06	532.03	13.88	458	5
JTZ60	85	0.3857	0.0016	5.9045	0.1368	0.1215	0.0019	2102.86	1961.90	1978.52	-6.28	2103	16
JTZ60	86	0.0722	0.0003	0.5527	0.0106	0.0573	0.0011	449.34	446.73	503.10	10.69	449	4
JTZ60	87	0.0820	0.0004	0.6487	0.0186	0.0622	0.0014	507.99	507.70	680.99	25.40	508	6
JTZ60	88	0.0711	0.0004	0.5005	0.0154	0.0566	0.0014	442.96	412.07	475.20	6.78	443	6
JTZ60	89	0.0643	0.0002	0.5511	0.0071	0.0617	0.0010	401.90	445.73	663.38	39.42	402	4
JTZ60	90	0.0741	0.0003	0.5504	0.0094	0.0558	0.0010	460.93	445.25	444.42	-3.72	461	4
JTZ60	91	0.0705	0.0003	0.5728	0.0114	0.0639	0.0012	439.11	459.79	736.67	40.39	439	4
JTZ60	92	0.0683	0.0003	0.5620	0.0089	0.0592	0.0010	425.60	452.79	574.83	25.96	426	4
JTZ60	93	0.0775	0.0004	0.5492	0.0138	0.0568	0.0012	481.18	444.49	483.00	0.38	481	5
JTZ60	94	0.0696	0.0003	0.5258	0.0112	0.0572	0.0011	433.69	429.04	498.10	12.93	434	4
JTZ60	95	0.0701	0.0003	0.5375	0.0089	0.0565	0.0010	436.58	436.78	471.29	7.36	437	4
JTZ60	96	0.0673	0.0003	0.5524	0.0105	0.0598	0.0011	419.81	446.54	597.79	29.77	420	4
JTZ60	97	0.0733	0.0004	0.5329	0.0170	0.0578	0.0014	456.25	433.75	520.67	12.37	456	6
JTZ60	98	0.0674	0.0003	0.5127	0.0086	0.0558	0.0010	420.17	420.26	444.82	5.54	420	4
JTZ60	99	0.0756	0.0003	0.5629	0.0126	0.0565	0.0011	469.69	453.43	470.90	0.26	470	5
JTZ60	100	0.0765	0.0003	0.5586	0.0119	0.0572	0.0011	475.08	450.63	499.64	4.92	475	5
JTZ60	101	0.0753	0.0004	0.5759	0.0193	0.0596	0.0015	468.07	461.82	587.63	20.35	468	6
JTZ60	102	0.0736	0.0003	0.5191	0.0113	0.0558	0.0011	457.63	424.56	444.02	-3.06	458	5
JTZ60	103	0.0722	0.0003	0.5513	0.0097	0.0558	0.0010	449.64	445.84	442.43	-1.63	450	4
JTZ60	104	0.0686	0.0003	0.5269	0.0120	0.0577	0.0012	427.53	429.74	517.63	17.41	428	5
JTZ60	105	0.0734	0.0003	0.6154	0.0118	0.0652	0.0012	456.85	486.95	779.83	41.42	457	4
JTZ60	106	0.0692	0.0003	0.5078	0.0131	0.0555	0.0012	431.03	416.97	434.03	0.69	431	5
JTZ60	107	0.0702	0.0003	0.5412	0.0096	0.0556	0.0010	437.30	439.20	434.83	-0.57	437	4
JTZ60	108	0.0724	0.0003	0.5802	0.0131	0.0575	0.0012	450.54	464.57	509.61	11.59	451	5
JTZ60	109	0.0685	0.0003	0.5274	0.0099	0.0559	0.0010	427.11	430.10	446.41	4.32	427	4
JTZ60	110	0.0761	0.0003	0.5728	0.0127	0.0581	0.0012	472.98	459.81	532.03	11.10	473	5
JTZ60	111	0.0734	0.0003	0.5643	0.0122	0.0557	0.0011	456.73	454.33	439.63	-3.89	457	5
JTZ60	112	0.0705	0.0003	0.5424	0.0123	0.0549	0.0011	439.23	440.02	408.97	-7.40	439	5
JTZ60	113	0.0753	0.0003	0.5962	0.0129	0.0573	0.0011	468.07	474.81	504.25	7.18	468	5
JTZ60	114	0.0673	0.0003	0.5186	0.0113	0.0577	0.0012	419.81	424.19	518.77	19.08	420	4
JTZ62	1	0.0742	0.0003	0.5557	0.0119	0.0562	0.0011	461.65	448.70	460.67	-0.21	462	6
JTZ62	2	0.0702	0.0003	0.5200	0.0136	0.0549	0.0012	437.06	425.16	407.75	-7.19	437	7
JTZ62	3	0.0759	0.0005	0.5963	0.0222	0.0597	0.0016	471.72	474.88	594.17	20.61	472	8
JTZ62	4	0.0712	0.0003	0.5785	0.0092	0.0560	0.0010	443.62	463.48	451.18	1.67	444	6
JTZ62	5	0.0699	0.0003	0.5478	0.0138	0.0560	0.0012	435.73	443.58	453.95	4.01	436	7
JTZ62	6	0.0738	0.0003	0.5346	0.0104	0.0559	0.0010	458.95	434.84	446.81	-2.72	459	6
JTZ62	7	0.0761	0.0004	0.5849	0.0137	0.0580	0.0012	472.50	467.61	530.52	10.94	473	7
JTZ62	8	0.0671	0.0003	0.5524	0.0095	0.0570	0.0010	418.78	446.56	490.37	14.60	419	6
JTZ62	9	0.0779	0.0003	0.5815	0.0130	0.0570	0.0011	483.52	465.43	489.60	1.24	484	7
JTZ62	10	0.0664	0.0003	0.5556	0.0104	0.0579	0.0011	414.31	448.64	524.09	20.95	414	6
JTZ62	11	0.0718	0.0004	0.5446	0.0149	0.0570	0.0013	447.11	441.42	489.98	8.75	447	7
JTZ62	12	0.0718	0.0004	0.5452	0.0180	0.0556	0.0014	446.75	441.87	435.23	-2.65	447	7
JTZ62	13	0.0734	0.0003	0.5476	0.0107	0.0558	0.0010	456.79	443.44	445.61	-2.51	457	6
JTZ62	14	0.0695	0.0004	0.5166	0.0191	0.0554	0.0016	433.26	422.90	430.01	-0.76	433	8
JTZ62	15	0.3300	0.0015	4.9298	0.1416	0.1086	0.0019	1838.58	1807.37	1776.40	-3.50	1776	31
JTZ62	16	0.0665	0.0003	0.5311	0.0139	0.0577	0.0013	414.79	432.57	516.87	19.75	415	6
JTZ62	17	0.0706	0.0003	0.5008	0.0109	0.0543	0.0011	439.95	412.26	383.51	-14.72	440	6
JTZ62	18	0.0754	0.0003	0.5642	0.0129	0.0559	0.0011	468.85	454.22	446.81	-4.93	469	7
JTZ62	19	0.0782	0.0003	0.6079	0.0139	0.0565	0.0011	485.61	482.20	470.50	-3.21	486	7
JTZ62	20	0.0758	0.0004	0.5992	0.0185	0.0566	0.0014	471.00	476.70	476.37	1.13	471	7
JTZ62	21	0.0792	0.0004	0.6209	0.0192	0.0573	0.0014	491.47	490.44	503.10	2.31	491	8
JTZ62	22	0.0753	0.0003	0.5760	0.0138	0.0561	0.0012	467.77	461.86	457.91	-2.15	468	7
JTZ62	23	0.0780	0.0003	0.6980	0.0140	0.0661	0.0012	484.11	537.57	808.28	40.11	484	6
JTZ62	24	0.0800	0.0004	0.6252	0.0165	0.0577	0.0013	496.00	493.12	518.39	4.32	496	7
JTZ62	25	0.0764	0.0004	0.5974	0.0151	0.0564	0.0012	474.66	475.61	466.58	-1.73	475	7
JTZ62	26	0.0766	0.0004	0.5760	0.0140	0.0558	0.0012	475.86	461.87	445.61	-6.79	476	7
JTZ62	27	0.0688	0.0004	0.5426	0.0185	0.0578	0.0015	428.98	440.11	521.81	17.79	429	7
JTZ62	28	0.0782	0.0005	0.5685	0.0225	0.0572	0.0017	485.13	457.01	497.71	2.53	485	9
JTZ62	29	0.0704	0.0003	0.5652	0.0105	0.0556	0.0010	438.50	454.88	436.83	-0.38	439	6
JTZ62	30	0.0741	0.0003	0.5718	0.0146	0.0569	0.0012	460.57	459.18	489.21	5.85	461	7
JTZ62	31	0.0723	0.0003	0.5829	0.0125	0.0557	0.0011	449.82	466.30	439.23	-2.41	460	6
JTZ62	32	0.0755	0.0003	0.5687	0.0141	0.0568	0.0012	469.21	457.14	483.39	2.93	469	7
JTZ62	33	0.0683	0.0003	0.5739	0.0135	0.0599	0.0013	426.15	460.56	601.41	29.14	426	6
JTZ62	34	0.0746	0.0003	0.5535	0.0131	0.0560	0.0012	463.99	447.31	453.56	-2.30	464	7
JTZ62	35	0.0700	0.0004	0.5731	0.0166	0.0596	0.0014	436.10	459.99	589.08	25.97	436	13
JTZ62	36	0.0760	0.0004	0.5696	0.0150	0.0559	0.0012	472.08	457.77	447.60	-5.47	472	13
JTZ62	37	0.0657	0.0004	0.4907	0.0178	0.0562	0.0016	410.26	405.39	459.88	10.79	410	14
JTZ62	38	0.0674	0.0003	0.5581	0.0094	0.0574	0.0010	420.71	450.27	508.47	17.26	421	12

JTZ62	39	0.0730	0.0003	0.5597	0.0098	0.0564	0.0010	453.90	451.34	469.33	3.29	454	12
JTZ62	40	0.0724	0.0003	0.6287	0.0128	0.0642	0.0012	450.66	495.29	747.90	39.74	451	13
JTZ62	41	0.0673	0.0004	0.5114	0.0154	0.0567	0.0014	419.63	419.40	480.66	12.70	420	13
JTZ62	42	0.0665	0.0004	0.5072	0.0164	0.0550	0.0014	415.03	416.53	413.85	-0.29	415	13
JTZ62	43	0.0653	0.0003	0.5572	0.0090	0.0568	0.0010	407.84	449.68	484.94	15.90	408	12
JTZ62	44	0.0646	0.0003	0.5403	0.0094	0.0568	0.0010	403.24	438.59	484.17	16.71	403	12
JTZ62	45	0.0736	0.0003	0.5757	0.0128	0.0563	0.0011	457.51	461.72	465.79	1.78	458	13
JTZ62	46	0.0699	0.0003	0.5244	0.0094	0.0556	0.0010	435.25	428.05	434.43	-0.19	435	12
JTZ62	47	0.0755	0.0004	0.6061	0.0152	0.0594	0.0012	469.33	481.09	581.42	19.28	469	13
JTZ62	48	0.0645	0.0003	0.5174	0.0088	0.0558	0.0010	402.75	423.40	445.61	9.62	403	12
JTZ62	49	0.0648	0.0003	0.5326	0.0091	0.0569	0.0010	404.45	433.51	487.66	17.06	404	12
JTZ62	50	0.0660	0.0003	0.5290	0.0121	0.0580	0.0012	411.95	431.12	530.52	22.35	412	12
JTZ62	51	0.0720	0.0003	0.5492	0.0127	0.0558	0.0011	448.07	444.46	445.61	-0.55	448	13
JTZ62	52	0.0738	0.0004	0.6030	0.0156	0.0616	0.0013	458.71	479.11	659.90	30.49	459	13
JTZ62	53	0.0698	0.0004	0.5546	0.0215	0.0558	0.0016	435.19	448.01	442.43	1.64	435	14
JTZ62	54	0.0695	0.0004	0.5366	0.0169	0.0556	0.0014	433.38	436.15	434.43	0.24	433	13
JTZ62	55	0.0699	0.0003	0.5463	0.0129	0.0558	0.0011	435.31	442.54	445.22	2.22	435	13
JTZ62	56	0.0671	0.0003	0.5316	0.0154	0.0552	0.0013	418.66	432.89	419.93	0.30	419	13
JTZ62	57	0.0674	0.0003	0.5502	0.0090	0.0553	0.0010	420.29	445.14	422.35	0.49	420	12
JTZ62	58	0.2783	0.0011	3.8280	0.0758	0.1004	0.0016	1582.79	1598.64	1631.51	2.99	1632	35
JTZ62	59	0.0699	0.0003	0.5811	0.0090	0.0559	0.0009	435.73	465.16	449.59	3.08	436	12
JTZ62	60	0.0694	0.0003	0.5718	0.0103	0.0555	0.0010	432.24	459.16	431.22	-0.24	432	12
JTZ62	61	0.0663	0.0003	0.5748	0.0101	0.0586	0.0010	413.77	461.14	551.89	25.03	414	12
JTZ62	62	0.0680	0.0004	0.5380	0.0175	0.0557	0.0014	424.28	437.09	438.83	3.32	424	13
JTZ62	63	0.0682	0.0003	0.5191	0.0102	0.0553	0.0010	425.00	424.53	423.57	-0.34	425	12
JTZ62	64	0.0749	0.0003	0.5885	0.0146	0.0562	0.0012	465.73	469.93	461.07	-1.01	466	13
JTZ62	65	0.0492	0.0003	0.3900	0.0146	0.0590	0.0018	309.61	334.39	565.25	45.23	310	13
JTZ62	66	0.0692	0.0003	0.5725	0.0110	0.0596	0.0011	431.45	459.64	589.08	26.76	431	12
JTZ62	67	0.0718	0.0003	0.5582	0.0116	0.0574	0.0011	446.99	450.38	505.02	11.49	447	12
JTZ62	68	0.0696	0.0003	0.5733	0.0132	0.0572	0.0012	433.50	460.12	498.48	13.04	434	12
JTZ62	69	0.0710	0.0004	0.5871	0.0159	0.0621	0.0014	441.88	469.02	678.59	34.88	442	13
JTZ62	70	0.0695	0.0003	0.5104	0.0121	0.0540	0.0011	432.96	418.70	368.96	-17.35	433	13
JTZ62	71	0.0743	0.0005	0.5786	0.0255	0.0580	0.0018	461.95	463.54	530.89	12.99	462	15
JTZ62	72	0.0705	0.0003	0.5594	0.0131	0.0563	0.0012	439.05	451.14	465.40	5.66	439	13
JTZ62	73	0.0734	0.0003	0.5706	0.0142	0.0563	0.0012	456.37	458.38	465.79	2.02	456	13
JTZ62	74	0.0705	0.0005	0.5481	0.0244	0.0557	0.0018	439.05	443.74	440.43	0.31	439	15
JTZ62	75	0.0725	0.0005	0.5601	0.0229	0.0545	0.0016	451.32	451.59	390.53	-15.57	451	14
JTZ62	76	0.0741	0.0003	0.6001	0.0150	0.0577	0.0012	460.69	477.27	518.39	11.13	461	13
JTZ62	77	0.0632	0.0004	0.5140	0.0200	0.0612	0.0018	394.75	421.10	646.27	38.92	395	14
JTZ62	78	0.0713	0.0004	0.5480	0.0171	0.0559	0.0014	444.04	443.67	449.99	1.32	444	13
JTZ62	79	0.0740	0.0003	0.6038	0.0151	0.0594	0.0013	460.15	479.67	579.96	20.66	460	13
JTZ62	80	0.0736	0.0003	0.5812	0.0147	0.0561	0.0012	457.81	465.22	456.72	-0.24	458	13
JTZ62	81	0.0678	0.0003	0.5251	0.0127	0.0575	0.0012	422.83	428.58	511.53	17.34	423	12
JTZ62	82	0.0670	0.0003	0.5122	0.0123	0.0562	0.0012	418.30	419.89	461.86	9.43	418	12
JTZ62	83	0.0666	0.0003	0.5237	0.0123	0.0571	0.0012	415.70	427.60	496.55	16.28	416	12
JTZ62	84	0.0706	0.0003	0.5630	0.0125	0.0558	0.0011	439.89	453.48	444.02	0.93	440	12
JTZ62	85	0.0730	0.0005	0.5944	0.0241	0.0550	0.0016	453.96	473.65	412.22	-10.13	454	14
JTZ62	86	0.0733	0.0004	0.5600	0.0178	0.0569	0.0014	455.71	451.53	487.27	6.48	456	14
JTZ62	87	0.0897	0.0004	0.7367	0.0201	0.0587	0.0013	553.47	560.50	555.99	0.45	553	14
JTZ62	88	0.0730	0.0004	0.5680	0.0190	0.0569	0.0015	454.44	456.73	488.05	6.89	454	14
JTZ62	89	0.0715	0.0004	0.6038	0.0214	0.0591	0.0016	445.43	479.66	569.31	21.76	445	14
JTZ62	90	0.0725	0.0004	0.5334	0.0150	0.0565	0.0013	451.20	434.04	471.29	4.26	451	13
JTZ62	91	0.2334	0.0013	2.9040	0.1296	0.0844	0.0019	1352.29	1382.94	1302.71	-3.81	1303	42
JTZ62	92	0.0685	0.0003	0.5586	0.0138	0.0558	0.0012	426.87	450.63	442.82	3.60	427	12
JTZ62	93	0.1551	0.0007	1.5077	0.0397	0.0701	0.0014	929.38	933.50	930.70	0.14	929	16
JTZ62	94	0.0788	0.0004	0.6195	0.0175	0.0567	0.0013	489.02	489.53	480.66	-1.74	489	13
JTZ62	95	0.0742	0.0003	0.5865	0.0150	0.0562	0.0012	461.47	468.61	459.49	-0.43	461	13
JTZ62	96	0.0695	0.0005	0.5158	0.0212	0.0562	0.0017	432.96	422.36	460.28	5.93	433	14
JTZ62	97	0.0747	0.0003	0.5855	0.0150	0.0563	0.0012	464.53	468.01	464.61	0.02	465	13
JTZ62	98	0.0699	0.0003	0.5618	0.0137	0.0570	0.0012	435.37	452.70	491.53	11.43	435	12
JTZ62	99	0.0714	0.0003	0.5614	0.0156	0.0559	0.0013	444.28	452.45	448.00	0.83	444	13
JTZ62	100	0.0710	0.0004	0.5387	0.0188	0.0568	0.0015	442.12	437.58	483.78	8.61	442	14
JTZ62	101	0.0716	0.0004	0.5542	0.0173	0.0558	0.0014	445.67	447.74	442.43	-0.73	446	13
JTZ62	102	0.0695	0.0004	0.5330	0.0170	0.0551	0.0014	432.84	433.79	416.69	-3.88	433	13
JTZ62	103	0.0709	0.0005	0.5805	0.0273	0.0606	0.0020	441.76	464.78	625.78	29.41	442	15
JTZ62	104	0.0713	0.0004	0.5689	0.0218	0.0599	0.0017	443.80	457.33	598.16	25.80	444	14
JTZ62	105	0.0694	0.0003	0.5552	0.0155	0.0567	0.0013	432.30	448.40	479.88	9.92	432	13
JTZ62	106	0.0653	0.0004	0.5344	0.0197	0.0605	0.0017	407.66	434.73	620.79	34.33	408	14
JTZ62	107	0.0709	0.0003	0.5535	0.0123	0.0562	0.0012	441.40	447.27	461.07	4.27	441	12
JTZ62	108	0.0695	0.0003	0.5589	0.0139	0.0582	0.0013	433.02	450.79	537.67	19.46	433	12
JTZ62	109	0.0715	0.0003	0.5565	0.0123	0.0579	0.0012	445.07	449.23	527.49	15.63	445	12
JTZ62	110	0.0666	0.0003	0.5061	0.0139	0.0553	0.0013	415.82	415.85	423.97	1.92	416	12
JTZ62	111	0.0604	0.0003	0.5009	0.0135	0.0561	0.0013	377.94	412.33	454.35	16.82	378	13
JTZ62	112	0.0690	0.0004	0.5720	0.0175	0.0615	0.0015	429.95	459.27	657.81	34.64	430	13
JTZ62	113	0.0635	0.0003	0.4880	0.0114	0.0545	0.0012	396.82	403.52	389.71	-1.82	397	12
JTZ62	114	0.0689	0.0004	0.5659	0.0200	0.0606	0.0017	429.77	455.35	625.42	31.28	430	14
JTZ62	115	0.0694	0.0003	0.5395	0.0172	0.0557	0.0018	432.60	438.11	439.23	1.51	433	13

JTZ62	116	0.0744	0.0005	0.6443	0.0246	0.0598	0.0019	462.43	504.95	597.43	22.60	462	14
JTZ62	117	0.0572	0.0004	0.4632	0.0224	0.0577	0.0016	358.57	386.51	519.91	31.03	359	14
JTZ62	118	0.0690	0.0004	0.5334	0.0205	0.0559	0.0019	430.19	434.06	449.99	4.40	430	14
JTZ62	119	0.0678	0.0012	0.5149	0.2342	0.0554	0.0086	423.01	421.75	429.21	1.44	423	24
JTZ62	120	0.0667	0.0003	0.5523	0.0143	0.0597	0.0013	416.49	446.51	591.99	29.65	416	13
JTZ62	121	0.0702	0.0004	0.5468	0.0207	0.0576	0.0017	437.06	442.89	514.58	15.06	437	14
JTZ62	122	0.0706	0.0005	0.5363	0.0515	0.0557	0.0032	439.77	435.98	440.43	0.15	440	15
JTZ64	1	0.0722	0.0005	0.5649	0.0105	0.0578	0.0009	449.22	454.72	520.67	13.72	449	9
JTZ64	2	0.2337	0.0015	2.6864	0.0576	0.0867	0.0012	1353.76	1324.73	1352.95	-0.06	1353	24
JTZ64	3	0.0735	0.0005	0.5639	0.0106	0.0578	0.0009	457.15	454.07	521.81	12.39	457	9
JTZ64	4	0.0737	0.0005	0.5344	0.0109	0.0554	0.0010	458.59	434.70	426.79	-7.45	459	9
JTZ64	5	0.0750	0.0005	0.5444	0.0118	0.0554	0.0010	465.91	441.33	428.00	-8.86	466	9
JTZ64	6	0.0783	0.0005	0.6234	0.0150	0.0570	0.0011	486.15	491.95	489.98	0.78	486	9
JTZ64	7	0.0731	0.0005	0.5807	0.0163	0.0582	0.0013	454.56	464.93	536.92	15.34	455	9
JTZ64	8	0.0713	0.0005	0.5690	0.0154	0.0594	0.0013	444.16	457.34	582.88	23.80	444	9
JTZ64	9	0.0718	0.0004	0.5426	0.0097	0.0561	0.0009	446.75	440.14	457.12	2.27	447	8
JTZ64	10	0.0758	0.0006	0.5539	0.0189	0.0566	0.0015	471.12	447.57	474.81	0.78	471	10
JTZ64	11	0.0619	0.0004	0.4905	0.0115	0.0598	0.0012	386.87	405.25	597.07	35.21	387	8
JTZ64	12	0.0706	0.0005	0.5397	0.0114	0.0566	0.0010	439.47	438.25	476.76	7.82	439	9
JTZ64	13	0.0712	0.0004	0.5496	0.0102	0.0576	0.0009	443.14	444.71	512.67	13.56	443	8
JTZ64	14	0.0757	0.0006	0.5948	0.0182	0.0587	0.0014	470.17	473.91	555.99	15.44	470	10
JTZ64	15	0.0726	0.0005	0.5422	0.0109	0.0565	0.0010	451.56	439.88	470.11	3.95	452	9
JTZ64	16	0.0711	0.0005	0.5767	0.0114	0.0579	0.0010	442.60	462.35	524.84	15.67	443	9
JTZ64	17	0.0716	0.0005	0.5314	0.0109	0.0561	0.0010	446.03	432.73	456.33	2.26	446	9
JTZ64	18	0.0719	0.0005	0.5348	0.0106	0.0549	0.0009	447.47	434.96	409.78	-9.20	447	9
JTZ64	19	0.0723	0.0004	0.5425	0.0087	0.0564	0.0008	449.82	440.06	466.19	3.51	450	8
JTZ64	20	0.0721	0.0005	0.5339	0.0126	0.0566	0.0011	448.80	434.39	475.59	5.63	449	9
JTZ64	21	0.0727	0.0005	0.5467	0.0139	0.0561	0.0011	452.22	442.85	454.35	0.47	452	9
JTZ64	22	0.0677	0.0004	0.4996	0.0088	0.0553	0.0009	422.04	411.42	425.99	0.93	422	8
JTZ64	23	0.0700	0.0004	0.5287	0.0070	0.0550	0.0007	436.04	430.96	411.00	-6.09	436	8
JTZ64	24	0.0715	0.0004	0.5256	0.0086	0.0560	0.0008	445.37	428.91	451.58	1.37	445	8
JTZ64	25	0.0702	0.0004	0.5392	0.0087	0.0560	0.0008	437.18	437.88	452.37	3.36	437	8
JTZ64	26	0.0747	0.0005	0.5879	0.0135	0.0602	0.0011	464.17	469.50	609.69	23.87	464	9
JTZ64	27	0.0741	0.0006	0.5387	0.0166	0.0561	0.0013	460.99	437.58	455.54	-1.20	461	10
JTZ64	28	0.0707	0.0005	0.5530	0.0147	0.0584	0.0012	440.25	446.93	545.17	19.25	440	9
JTZ64	29	0.0810	0.0005	0.6357	0.0117	0.0586	0.0009	502.09	499.62	551.89	9.02	502	9
JTZ64	30	0.0674	0.0004	0.5319	0.0111	0.0601	0.0011	420.35	433.06	605.38	30.56	420	8
JTZ64	31	0.0742	0.0005	0.6094	0.0152	0.0612	0.0012	461.11	483.18	647.67	28.81	461	9
JTZ64	32	0.0764	0.0005	0.5656	0.0128	0.0566	0.0011	474.48	455.17	475.59	0.23	474	9
JTZ64	33	0.0667	0.0004	0.5278	0.0096	0.0571	0.0009	415.94	430.35	496.94	16.30	416	8
JTZ64	34	0.0680	0.0004	0.4908	0.0105	0.0551	0.0010	424.10	405.46	417.50	-1.58	424	8
JTZ64	35	0.0704	0.0006	0.4970	0.0200	0.0558	0.0017	438.44	409.66	442.43	0.90	438	10
JTZ64	36	0.0684	0.0004	0.5295	0.0103	0.0568	0.0010	426.39	431.46	484.55	12.00	426	8
JTZ64	37	0.0693	0.0004	0.5049	0.0093	0.0555	0.0009	431.94	415.04	432.82	0.20	432	8
JTZ64	38	0.0726	0.0005	0.5604	0.0152	0.0574	0.0012	451.50	451.80	508.08	11.14	452	9
JTZ64	39	0.0705	0.0004	0.5177	0.0109	0.0557	0.0010	439.29	423.63	442.03	0.62	439	8
JTZ64	40	0.0728	0.0005	0.5364	0.0145	0.0563	0.0012	453.18	436.03	465.79	2.71	453	9
JTZ64	41	0.0706	0.0004	0.5660	0.0106	0.0588	0.0010	439.95	455.39	560.81	21.55	440	8
JTZ64	42	0.0677	0.0005	0.5130	0.0132	0.0566	0.0012	422.04	420.46	474.42	11.04	422	9
JTZ64	43	0.0729	0.0005	0.5404	0.0107	0.0562	0.0010	453.36	438.68	460.28	1.50	453	8
JTZ64	44	0.0724	0.0005	0.5455	0.0130	0.0572	0.0011	450.42	442.02	500.02	9.92	450	9
JTZ64	45	0.0740	0.0005	0.5757	0.0158	0.0575	0.0012	460.33	461.72	509.23	9.60	460	9
JTZ64	46	0.0724	0.0005	0.5617	0.0131	0.0559	0.0011	450.48	452.63	449.59	-0.20	450	9
JTZ64	47	0.0709	0.0004	0.5568	0.0092	0.0572	0.0009	441.64	449.47	497.71	11.27	442	8
JTZ64	48	0.0672	0.0005	0.4873	0.0149	0.0553	0.0013	419.20	403.04	425.18	1.41	419	9
JTZ64	49	0.0678	0.0004	0.5318	0.0114	0.0556	0.0010	422.59	432.99	436.83	3.26	423	8
JTZ64	50	0.0623	0.0004	0.4814	0.0103	0.0547	0.0010	389.29	399.06	400.80	2.87	389	8
JTZ64	51	0.0702	0.0005	0.5267	0.0145	0.0560	0.0012	437.12	429.59	453.95	3.71	437	9
JTZ64	52	0.0684	0.0004	0.5232	0.0098	0.0561	0.0009	426.39	427.26	457.12	6.72	426	8
JTZ64	53	0.0705	0.0004	0.5243	0.0112	0.0555	0.0010	439.23	428.03	433.63	-1.29	439	8
JTZ64	54	0.0741	0.0007	0.5748	0.0253	0.0581	0.0019	460.75	461.08	535.04	13.89	461	11
JTZ64	55	0.0698	0.0004	0.5335	0.0119	0.0563	0.0010	434.83	434.10	462.25	5.93	435	8
JTZ64	56	0.0708	0.0004	0.5457	0.0114	0.0584	0.0010	441.21	442.16	546.30	19.24	441	8
JTZ64	57	0.0676	0.0004	0.5027	0.0096	0.0554	0.0009	421.56	413.52	427.60	1.41	422	8
JTZ64	58	0.0669	0.0004	0.5233	0.0081	0.0576	0.0008	417.51	427.37	514.58	18.86	418	8
JTZ64	59	0.0700	0.0005	0.5421	0.0150	0.0579	0.0013	436.22	439.83	524.46	16.83	436	9
JTZ64	60	0.0686	0.0004	0.5331	0.0081	0.0553	0.0008	427.66	433.83	425.99	-0.39	428	8
JTZ64	61	0.0775	0.0006	0.6036	0.0221	0.0583	0.0016	481.36	479.52	539.18	10.72	481	10
JTZ64	62	0.0731	0.0005	0.5615	0.0133	0.0570	0.0011	454.62	452.49	490.76	7.36	455	9
JTZ64	63	0.0702	0.0004	0.5117	0.0105	0.0557	0.0010	437.24	419.60	439.23	0.45	437	8
JTZ64	64	0.0711	0.0004	0.5721	0.0123	0.0581	0.0010	443.02	459.38	531.65	16.67	443	8
JTZ64	65	0.0688	0.0004	0.5075	0.0106	0.0555	0.0010	428.98	416.79	434.03	1.16	429	8
JTZ64	66	0.0729	0.0004	0.5448	0.0107	0.0561	0.0010	453.36	441.58	455.93	0.56	453	8
JTZ64	67	0.0676	0.0004	0.5481	0.0113	0.0598	0.0011	421.86	443.72	595.98	29.22	422	8
JTZ64	68	0.0703	0.0004	0.5453	0.0110	0.0573	0.0010	438.08	441.90	501.95	12.72	438	8
JTZ64	69	0.0717	0.0005	0.5344	0.0165	0.0567	0.0013	446.27	434.72	478.71	6.78	446	9

JTZ64	70	0.0689	0.0004	0.5049	0.0095	0.0551	0.0009	429.46	415.00	415.07	-3.47	429	8
JTZ64	71	0.0694	0.0005	0.5106	0.0130	0.0547	0.0011	432.60	418.83	400.80	-7.93	433	9
JTZ64	72	0.0715	0.0004	0.5238	0.0118	0.0558	0.0010	445.01	427.70	442.43	-0.58	445	8
JTZ64	73	0.0710	0.0004	0.5410	0.0114	0.0550	0.0010	442.12	439.10	410.19	-7.78	442	8
JTZ64	74	0.0678	0.0004	0.5488	0.0098	0.0592	0.0010	422.95	444.18	574.09	26.33	423	8
JTZ64	75	0.0728	0.0004	0.5604	0.0122	0.0567	0.0010	453.06	451.80	481.44	5.89	453	8
JTZ64	76	0.0720	0.0005	0.5566	0.0133	0.0571	0.0011	448.07	449.28	494.24	9.34	448	9
JTZ64	77	0.0701	0.0004	0.5331	0.0110	0.0554	0.0010	436.64	433.86	428.00	-2.02	437	8
JTZ64	78	0.0712	0.0004	0.5377	0.0096	0.0566	0.0009	443.20	436.92	475.59	6.81	443	8
JTZ64	79	0.0684	0.0004	0.5095	0.0126	0.0553	0.0011	426.21	418.08	425.18	-0.24	426	8
JTZ64	80	0.0714	0.0005	0.5469	0.0138	0.0562	0.0011	444.83	442.94	459.49	3.19	445	9
JTZ64	81	0.0692	0.0004	0.5322	0.0102	0.0568	0.0010	431.58	433.24	484.94	11.00	432	8
JTZ64	82	0.0718	0.0004	0.5215	0.0117	0.0550	0.0010	446.87	426.17	412.22	-8.41	447	8
JTZ64	83	0.0721	0.0005	0.5696	0.0157	0.0576	0.0012	448.67	457.76	513.44	12.61	449	9
JTZ64	84	0.0694	0.0004	0.5375	0.0094	0.0549	0.0009	432.66	436.75	406.93	-6.32	433	8
JTZ64	85	0.0709	0.0004	0.5407	0.0104	0.0558	0.0009	441.33	438.91	442.43	0.25	441	8
JTZ64	86	0.0680	0.0004	0.5020	0.0114	0.0553	0.0011	423.91	413.03	424.37	0.11	424	8
JTZ64	87	0.0743	0.0004	0.5771	0.0115	0.0564	0.0010	461.89	462.60	469.72	1.67	462	8
JTZ64	88	0.0722	0.0004	0.5639	0.0122	0.0578	0.0011	449.64	454.09	520.67	13.64	450	8
JTZ64	89	0.0708	0.0003	0.5603	0.0084	0.0629	0.0011	440.91	451.73	705.53	37.51	441	7
JTZ64	90	0.0714	0.0004	0.5434	0.0122	0.0557	0.0011	444.34	440.64	439.63	-1.07	444	8
JTZ64	91	0.0720	0.0006	0.5482	0.0212	0.0565	0.0018	448.07	443.84	472.85	5.24	448	10
JTZ64	92	0.0721	0.0004	0.5362	0.0102	0.0571	0.0009	449.04	435.91	493.85	9.08	449	8
JTZ64	93	0.0744	0.0004	0.5638	0.0110	0.0563	0.0010	462.37	454.00	463.04	0.14	462	8
JTZ64	94	0.0712	0.0005	0.5686	0.0166	0.0587	0.0014	443.32	457.11	555.99	20.26	443	9
JTZ64	95	0.0741	0.0005	0.5450	0.0128	0.0563	0.0011	460.99	441.70	465.79	1.03	461	8
JTZ64	96	0.0705	0.0005	0.5208	0.0140	0.0535	0.0012	438.99	425.71	350.48	-25.25	439	9
JTZ64	97	0.0690	0.0005	0.5363	0.0149	0.0575	0.0012	430.07	435.98	510.38	15.74	430	9
JTZ64	98	0.0732	0.0004	0.5656	0.0126	0.0576	0.0011	455.59	455.16	512.67	11.13	456	8
JTZ64	99	0.0672	0.0004	0.5038	0.0134	0.0552	0.0012	419.51	414.24	421.55	0.48	420	8
JTZ64	100	0.0707	0.0004	0.5357	0.0100	0.0562	0.0010	440.07	435.58	459.09	4.14	440	8
JTZ64	101	0.0706	0.0005	0.5422	0.0248	0.0561	0.0018	439.59	439.88	457.91	4.00	440	9
JTZ64	102	0.0738	0.0004	0.6064	0.0115	0.0595	0.0010	459.25	481.26	585.08	21.51	459	8
JTZ64	103	0.0728	0.0004	0.5451	0.0125	0.0560	0.0011	452.88	441.78	453.16	0.06	453	8
JTZ64	104	0.0748	0.0005	0.5583	0.0174	0.0564	0.0013	464.89	450.39	468.93	0.86	465	9
JTZ64	105	0.0661	0.0005	0.5126	0.0126	0.0552	0.0011	412.44	420.22	420.33	1.88	412	9
JTZ64	106	0.0729	0.0003	0.5359	0.0086	0.0560	0.0012	453.66	435.72	452.37	-0.29	454	6
JTZ64	107	0.0718	0.0004	0.5317	0.0134	0.0563	0.0012	446.69	432.91	464.22	3.78	447	8
JTZ64	108	0.0720	0.0004	0.5430	0.0110	0.0569	0.0010	448.13	440.41	487.27	8.03	448	8
JTZ64	109	0.0719	0.0004	0.5255	0.0123	0.0564	0.0011	447.53	428.81	469.72	4.72	448	8
JTZ64	110	0.0692	0.0004	0.5134	0.0117	0.0555	0.0010	431.58	420.70	431.62	0.01	432	8
JTZ64	111	0.0687	0.0005	0.5355	0.0153	0.0554	0.0013	428.20	435.46	428.00	-0.05	428	9
JTZ64	112	0.0724	0.0004	0.5347	0.0092	0.0559	0.0009	450.78	434.89	448.80	-0.44	451	8
JTZ64	113	0.0750	0.0004	0.5476	0.0098	0.0564	0.0010	465.91	443.41	467.76	0.40	466	7
JTZ64	114	0.0745	0.0004	0.6093	0.0118	0.0639	0.0010	462.97	483.11	739.32	37.38	463	8
JTZ64	115	0.0695	0.0005	0.5549	0.0157	0.0572	0.0013	433.02	448.23	497.33	12.93	433	9
JTZ64	116	0.0721	0.0006	0.5296	0.0211	0.0558	0.0016	448.86	431.56	444.82	-0.91	449	10
JTZ64	117	0.0663	0.0004	0.5077	0.0100	0.0545	0.0009	413.83	416.89	389.71	-6.19	414	8
JTZ64	118	0.0755	0.0004	0.6080	0.0115	0.0633	0.0010	469.39	482.32	719.33	34.75	469	8
JTZ64	119	0.0744	0.0004	0.5668	0.0090	0.0557	0.0009	462.67	455.96	441.63	-4.76	463	7
JTZ64	120	0.0681	0.0009	0.5453	0.0380	0.0598	0.0027	424.76	441.92	596.35	28.77	425	14
JTZ64	121	0.0737	0.0005	0.5690	0.0157	0.0576	0.0014	458.65	457.39	513.82	10.74	459	8
JTZ64	122	0.0707	0.0004	0.5247	0.0273	0.0567	0.0024	440.61	428.29	478.32	7.88	441	8
JTZ64	123	0.0653	0.0005	0.5230	0.0170	0.0568	0.0013	407.90	427.12	484.17	15.75	408	9
JTZ64	124	0.0704	0.0004	0.5281	0.0120	0.0558	0.0011	438.44	430.56	443.62	1.17	438	8
JTZ66	1	0.0717	0.0002	0.5582	0.0075	0.0556	0.0009	446.33	450.38	436.03	-2.36	446	9
JTZ66	2	0.0683	0.0002	0.5667	0.0074	0.0596	0.0009	425.60	455.89	589.08	27.75	426	9
JTZ66	3	0.0701	0.0005	0.5898	0.0311	0.0560	0.0020	436.82	470.71	450.38	3.01	437	13
JTZ66	4	0.0727	0.0003	0.5647	0.0100	0.0563	0.0010	452.64	454.57	464.22	2.49	453	9
JTZ66	5	0.0701	0.0003	0.5366	0.0093	0.0552	0.0010	436.76	436.15	419.52	-4.11	437	9
JTZ66	6	0.0692	0.0003	0.5234	0.0139	0.0557	0.0012	431.45	427.45	441.23	2.22	431	10
JTZ66	7	0.0692	0.0003	0.5144	0.0109	0.0546	0.0010	431.39	421.43	397.52	-8.52	431	10
JTZ66	8	0.0677	0.0002	0.5564	0.0085	0.0595	0.0010	422.22	449.19	583.62	27.65	422	9
JTZ66	9	0.0697	0.0003	0.5188	0.0088	0.0549	0.0009	434.23	424.33	407.34	-6.60	434	9
JTZ66	10	0.0718	0.0004	0.5619	0.0176	0.0559	0.0013	446.75	452.73	448.40	0.37	447	11
JTZ66	11	0.0679	0.0003	0.5221	0.0118	0.0555	0.0011	423.31	426.52	430.81	1.74	423	10
JTZ66	12	0.0665	0.0002	0.5213	0.0063	0.0565	0.0009	415.10	425.99	472.46	12.14	415	9
JTZ66	13	0.0628	0.0002	0.5064	0.0080	0.0571	0.0010	392.75	416.02	494.63	20.60	393	9
JTZ66	14	0.0666	0.0002	0.4948	0.0091	0.0549	0.0010	415.76	408.16	409.37	-1.56	416	9
JTZ66	15	0.0665	0.0003	0.5004	0.0104	0.0545	0.0010	415.16	411.95	393.00	-5.64	415	9
JTZ66	16	0.0647	0.0002	0.4737	0.0086	0.0539	0.0010	403.84	393.73	367.29	-9.95	404	9
JTZ66	17	0.0651	0.0002	0.4763	0.0087	0.0541	0.0010	406.26	395.52	376.46	-7.92	406	9
JTZ66	18	0.0620	0.0002	0.4800	0.0081	0.0560	0.0010	387.47	398.04	450.38	13.97	387	9
JTZ66	19	0.0638	0.0002	0.4803	0.0093	0.0539	0.0010	398.57	398.29	367.29	-8.52	399	9
JTZ66	20	0.0637	0.0002	0.4761	0.0095	0.0546	0.0010	398.09	395.39	394.24	-0.98	398	9
JTZ66	21	0.0619	0.0002	0.4727	0.0102	0.0558	0.0011	387.17	393.05	446.01	13.19	387	9

JTZ66	22	0.0649	0.0003	0.4588	0.0127	0.0519	0.0012	405.36	383.39	280.57	-44.48	405	10
JTZ66	23	0.0632	0.0002	0.4948	0.0078	0.0551	0.0009	394.88	408.14	414.25	4.68	395	9
JTZ66	24	0.0652	0.0002	0.4998	0.0105	0.0536	0.0010	406.99	411.55	354.70	-14.74	407	9
JTZ66	25	0.0626	0.0002	0.4577	0.0077	0.0531	0.0009	391.42	382.62	332.22	-17.82	391	9
JTZ66	26	0.0621	0.0002	0.4596	0.0100	0.0537	0.0010	388.32	384.01	358.49	-8.32	388	9
JTZ66	27	0.0540	0.0002	0.4271	0.0075	0.0562	0.0010	339.28	361.14	461.86	26.54	339	8
JTZ66	28	0.0626	0.0003	0.5309	0.0122	0.0599	0.0012	391.48	432.41	599.60	34.71	391	9
JTZ66	29	0.0602	0.0002	0.4392	0.0080	0.0528	0.0009	376.90	369.71	318.92	-18.18	377	9
JTZ66	30	0.0601	0.0002	0.4400	0.0103	0.0533	0.0011	375.99	370.27	341.59	-10.07	376	9
JTZ66	31	0.0594	0.0002	0.4377	0.0076	0.0537	0.0009	372.10	368.63	358.07	-3.92	372	9
JTZ66	32	0.0605	0.0002	0.4493	0.0088	0.0543	0.0010	378.91	376.75	383.51	1.20	379	9
JTZ66	33	0.0574	0.0002	0.4287	0.0107	0.0536	0.0011	359.49	362.25	353.86	-1.59	359	9
JTZ66	34	0.0583	0.0002	0.4255	0.0079	0.0525	0.0009	365.03	359.98	306.38	-19.14	365	9
JTZ66	35	0.0565	0.0002	0.4144	0.0107	0.0529	0.0011	354.18	352.03	323.22	-9.58	354	9
JTZ66	36	0.0560	0.0002	0.4074	0.0087	0.0534	0.0010	351.13	347.03	345.83	-1.53	351	9
JTZ66	37	0.0561	0.0002	0.4237	0.0067	0.0534	0.0009	351.99	358.70	346.68	-1.53	352	8
JTZ66	38	0.0575	0.0002	0.4313	0.0085	0.0537	0.0010	360.46	364.06	356.39	-1.14	360	9
JTZ66	39	0.0555	0.0003	0.4222	0.0117	0.0535	0.0012	348.44	357.62	349.22	0.22	348	9
JTZ66	40	0.0570	0.0002	0.4113	0.0086	0.0519	0.0010	357.05	349.82	280.57	-27.26	357	9
JTZ66	41	0.0572	0.0003	0.3936	0.0139	0.0531	0.0014	358.76	336.96	331.36	-8.27	359	10
JTZ66	42	0.0551	0.0002	0.4015	0.0071	0.0519	0.0009	345.70	342.71	281.45	-22.83	346	8
JTZ66	43	0.0549	0.0002	0.4115	0.0086	0.0527	0.0010	344.60	349.92	314.61	-9.53	345	9
JTZ66	44	0.0551	0.0002	0.4133	0.0093	0.0540	0.0011	345.57	351.24	370.63	6.76	346	9
JTZ66	45	0.0421	0.0002	0.2859	0.0057	0.0484	0.0009	265.65	255.36	118.87	-123.5	266	8
JTZ66	46	0.0418	0.0002	0.2888	0.0062	0.0484	0.0010	263.98	257.63	116.92	-125.8	264	8
JTZ66	47	0.0559	0.0002	0.3909	0.0075	0.0517	0.0010	350.83	335.05	273.49	-28.28	351	8
JTZ66	48	0.0524	0.0002	0.3974	0.0083	0.0530	0.0010	329.42	339.76	327.08	-0.72	329	8
JTZ66	49	0.0557	0.0003	0.3915	0.0128	0.0519	0.0013	349.12	335.43	280.57	-24.43	349	10
JTZ66	50	0.0547	0.0002	0.3950	0.0097	0.0525	0.0011	343.56	338.04	308.12	-11.50	344	9
JTZ66	51	0.0539	0.0002	0.3863	0.0103	0.0516	0.0011	338.60	331.68	267.28	-26.69	339	9
JTZ66	52	0.0543	0.0002	0.3842	0.0078	0.0523	0.0010	341.05	330.11	298.98	-14.07	341	8
JTZ66	53	0.0534	0.0002	0.3867	0.0102	0.0510	0.0011	335.12	331.93	239.47	-39.94	335	9
JTZ66	54	0.0541	0.0002	0.3887	0.0094	0.0509	0.0011	339.83	333.40	236.76	-43.53	340	9
JTZ66	55	0.0535	0.0002	0.4319	0.0118	0.0611	0.0013	335.73	364.55	642.76	47.77	336	9
JTZ66	56	0.0525	0.0002	0.3673	0.0099	0.0512	0.0011	329.61	317.68	248.95	-32.40	330	9
JTZ66	57	0.0529	0.0002	0.3816	0.0100	0.0505	0.0011	332.00	328.18	217.61	-52.56	332	9
JTZ66	58	0.0503	0.0002	0.3573	0.0077	0.0505	0.0010	316.12	310.16	218.07	-44.96	316	8
JTZ66	59	0.0515	0.0002	0.3779	0.0072	0.0518	0.0010	323.97	325.50	277.48	-16.76	324	8
JTZ66	60	0.0503	0.0002	0.3802	0.0081	0.0530	0.0010	316.36	327.16	330.08	4.16	316	8
JTZ66	61	0.0515	0.0002	0.3826	0.0092	0.0520	0.0011	323.48	328.93	286.29	-12.99	323	9
JTZ66	62	0.0487	0.0002	0.3693	0.0069	0.0536	0.0010	306.41	319.14	352.17	12.99	306	8
JTZ66	63	0.0726	0.0004	0.5478	0.0140	0.0565	0.0012	451.92	443.52	471.68	4.19	452	7
JTZ66	64	0.0717	0.0003	0.5642	0.0138	0.0569	0.0012	446.09	454.26	485.72	8.16	446	7
JTZ66	65	0.0722	0.0003	0.5688	0.0114	0.0570	0.0011	449.22	457.26	491.92	8.68	449	6
JTZ66	66	0.0726	0.0003	0.5780	0.0125	0.0572	0.0011	451.74	463.19	497.71	9.24	452	7
JTZ66	67	0.0684	0.0003	0.4954	0.0117	0.0554	0.0012	426.75	408.57	427.19	0.10	427	7
JTZ66	68	0.0705	0.0003	0.5559	0.0092	0.0570	0.0010	439.35	448.85	492.69	10.83	439	6
JTZ66	69	0.0700	0.0003	0.5475	0.0102	0.0564	0.0010	435.91	443.34	468.93	7.04	436	6
JTZ66	70	0.0716	0.0003	0.6196	0.0120	0.0625	0.0011	445.79	489.62	692.29	35.61	446	6
JTZ66	71	0.0734	0.0003	0.5386	0.0116	0.0548	0.0011	456.73	437.49	403.25	-13.26	457	7
JTZ66	72	0.0697	0.0003	0.5556	0.0088	0.0556	0.0009	434.59	448.68	434.43	-0.04	435	6
JTZ66	73	0.0695	0.0003	0.5557	0.0094	0.0573	0.0010	433.38	448.70	503.10	13.86	433	6
JTZ66	74	0.0658	0.0003	0.5093	0.0133	0.0567	0.0013	410.98	417.98	479.49	14.29	411	7
JTZ66	75	0.0746	0.0004	0.5764	0.0152	0.0579	0.0013	463.57	462.14	524.84	11.67	464	7
JTZ66	76	0.0676	0.0003	0.5207	0.0092	0.0567	0.0010	421.80	425.64	479.10	11.96	422	6
JTZ66	77	0.0724	0.0003	0.5517	0.0125	0.0554	0.0011	450.60	446.08	428.80	-5.08	451	7
JTZ66	78	0.0742	0.0003	0.5777	0.0113	0.0572	0.0011	461.35	462.98	500.02	7.73	461	6
JTZ66	79	0.0704	0.0003	0.5504	0.0096	0.0557	0.0010	438.63	445.23	439.23	0.14	439	6
JTZ66	80	0.0665	0.0003	0.5282	0.0110	0.0566	0.0011	414.73	430.59	474.42	12.58	415	6
JTZ66	81	0.0723	0.0003	0.5522	0.0105	0.0555	0.0010	449.70	446.41	431.22	-4.29	450	6
JTZ66	82	0.0688	0.0003	0.5096	0.0119	0.0558	0.0012	428.98	418.15	446.01	3.82	429	6
JTZ66	83	0.0670	0.0003	0.5354	0.0084	0.0566	0.0010	418.18	435.39	475.98	12.14	418	6
JTZ66	84	0.0714	0.0003	0.5618	0.0125	0.0557	0.0011	444.71	452.70	438.83	-1.34	445	6
JTZ66	85	0.0687	0.0004	0.5439	0.0150	0.0583	0.0013	428.08	441.01	541.05	20.88	428	7
JTZ66	86	0.0697	0.0003	0.5450	0.0090	0.0553	0.0010	434.47	441.69	422.35	-2.87	434	6
JTZ66	87	0.0693	0.0003	0.5642	0.0113	0.0570	0.0011	432.18	454.22	492.69	12.28	432	6
JTZ66	88	0.0708	0.0003	0.5391	0.0090	0.0553	0.0010	440.79	437.86	425.99	-3.48	441	6
JTZ66	89	0.0697	0.0003	0.5387	0.0085	0.0562	0.0010	434.05	437.53	460.28	5.70	434	6
JTZ66	90	0.0715	0.0003	0.5471	0.0124	0.0562	0.0011	445.31	443.08	459.09	3.00	445	7
JTZ66	91	0.0685	0.0003	0.5296	0.0106	0.0552	0.0010	426.81	431.54	420.74	-1.44	427	6
JTZ66	92	0.0695	0.0003	0.5419	0.0124	0.0568	0.0011	433.08	439.66	482.22	10.19	433	6
JTZ66	93	0.0688	0.0003	0.5422	0.0104	0.0564	0.0010	429.04	439.89	467.76	8.28	429	6
JTZ66	94	0.0706	0.0003	0.5694	0.0102	0.0566	0.0010	439.59	457.59	474.81	7.42	440	6
JTZ66	95	0.0698	0.0003	0.5630	0.0093	0.0584	0.0010	434.83	453.49	544.80	20.19	435	6
JTZ66	96	0.0679	0.0003	0.5349	0.0106	0.0566	0.0011	423.43	435.02	475.20	10.89	423	6
JTZ66	97	0.0613	0.0003	0.5037	0.0112	0.0580	0.0012	383.77	414.18	528.25	27.35	384	6
JTZ66	98	0.0735	0.0004	0.5699	0.0172	0.0562	0.0013	457.39	457.98	460.67	0.71	457	7

JTZ66	99	0.0688	0.0004	0.5603	0.0206	0.0569	0.0016	429.16	451.69	487.66	12.00	429	8
JTZ66	100	0.0752	0.0003	0.5837	0.0136	0.0561	0.0011	467.35	466.82	457.12	-2.24	467	7
JTZ66	101	0.0718	0.0003	0.5522	0.0107	0.0570	0.0011	447.23	446.42	489.98	8.73	447	6
JTZ66	102	0.0751	0.0003	0.5620	0.0119	0.0560	0.0011	466.63	452.85	452.37	-3.15	467	6
JTZ66	103	0.0702	0.0003	0.5524	0.0082	0.0572	0.0010	437.54	446.57	499.64	12.43	438	6
JTZ66	104	0.0702	0.0005	0.5487	0.0218	0.0561	0.0016	437.06	444.14	457.91	4.55	437	8
JTZ66	105	0.0671	0.0003	0.5110	0.0111	0.0564	0.0011	418.90	419.14	466.97	10.29	419	6
JTZ66	106	0.0691	0.0003	0.5153	0.0107	0.0554	0.0011	430.55	422.01	426.39	-0.98	431	6
JTZ66	107	0.0710	0.0003	0.5291	0.0125	0.0561	0.0012	442.00	431.21	455.54	2.97	442	7
JTZ66	108	0.0692	0.0003	0.5334	0.0111	0.0561	0.0011	431.45	434.04	456.72	5.53	431	6
JTZ66	109	0.0715	0.0003	0.5646	0.0131	0.0563	0.0012	445.31	454.54	465.01	4.24	445	6
JTZ66	110	0.0681	0.0003	0.5246	0.0111	0.0564	0.0011	424.40	428.24	468.93	9.50	424	6
JTZ66	111	0.0690	0.0003	0.5217	0.0124	0.0561	0.0012	429.83	426.27	454.75	5.48	430	6
JTZ66	112	0.0677	0.0003	0.5277	0.0091	0.0569	0.0010	422.47	430.29	488.05	13.44	422	6
JTZ66	113	0.0700	0.0003	0.5324	0.0114	0.0556	0.0011	436.40	433.40	434.43	-0.45	436	6
JTZ66	114	0.0746	0.0003	0.5649	0.0134	0.0562	0.0012	463.63	454.71	458.70	-1.07	464	7
JTZ66	115	0.0705	0.0003	0.5154	0.0096	0.0546	0.0010	439.17	422.07	393.83	-11.51	439	6
JTZ66	116	0.0706	0.0003	0.5248	0.0098	0.0554	0.0010	439.77	428.36	428.80	-2.56	440	6
JTZ66	117	0.0711	0.0003	0.5379	0.0114	0.0556	0.0011	442.96	437.02	437.23	-1.31	443	6
JTZ66	118	0.0694	0.0003	0.5202	0.0120	0.0553	0.0011	432.78	425.28	425.58	-1.69	433	6
JTZ66	119	0.0700	0.0004	0.5599	0.0171	0.0597	0.0014	435.91	451.43	593.81	26.59	436	7
JTZ66	120	0.0655	0.0003	0.5059	0.0094	0.0568	0.0011	409.05	415.66	484.17	15.51	409	6
JTZ66	121	0.0712	0.0003	0.5337	0.0127	0.0567	0.0012	443.32	434.26	477.93	7.24	443	7
JTZ66	122	0.0702	0.0003	0.5381	0.0091	0.0554	0.0010	437.30	437.16	427.19	-2.37	437	6
JTZ66	123	0.0537	0.0002	0.3890	0.0066	0.0528	0.0010	336.95	333.60	320.21	-5.23	337	5
JTZ66	124	0.0544	0.0002	0.4016	0.0075	0.0539	0.0010	341.66	342.79	366.87	6.87	342	5
CKZ-1	1	0.0707	0.0005	0.5482	0.0219	0.0564	0.0007	440.37	443.80	466.97	5.70	440	6
CKZ-1	2	0.0705	0.0005	0.5521	0.0223	0.0563	0.0007	439.35	446.35	463.43	5.20	439	6
CKZ-1	3	0.0715	0.0005	0.5652	0.0227	0.0575	0.0007	445.19	454.88	510.00	12.71	445	6
CKZ-1	4	0.0684	0.0005	0.5524	0.0222	0.0580	0.0007	426.69	446.58	529.76	19.46	427	6
CKZ-1	5	0.0652	0.0004	0.5508	0.0220	0.0610	0.0007	407.17	445.49	638.88	36.27	407	5
CKZ-1	6	0.0702	0.0005	0.5496	0.0220	0.0564	0.0007	437.60	444.72	469.72	6.84	438	6
CKZ-1	7	0.0699	0.0005	0.5516	0.0224	0.0574	0.0008	435.25	446.02	508.47	14.40	435	6
CKZ-1	8	0.0750	0.0005	0.5976	0.0250	0.0608	0.0010	466.45	475.72	631.46	26.13	466	6
CKZ-1	9	0.0652	0.0004	0.5208	0.0210	0.0576	0.0008	407.17	425.65	513.44	20.70	407	5
CKZ-1	10	0.0693	0.0005	0.5418	0.0217	0.0564	0.0007	432.12	439.58	468.15	7.70	432	6
CKZ-1	11	0.0688	0.0005	0.5375	0.0214	0.0563	0.0006	428.74	436.77	464.22	7.64	429	5
CKZ-1	12	0.0685	0.0005	0.5575	0.0223	0.0590	0.0007	427.29	449.92	567.83	24.75	427	6
CKZ-1	13	0.0700	0.0005	0.5441	0.0221	0.0562	0.0008	436.28	441.14	459.09	4.97	436	6
CKZ-1	14	0.0706	0.0005	0.5524	0.0221	0.0567	0.0007	439.59	446.57	478.71	8.17	440	6
CKZ-1	15	0.0741	0.0005	0.5861	0.0239	0.0576	0.0008	460.51	468.37	513.82	10.37	461	6
CKZ-1	16	0.0713	0.0005	0.5556	0.0225	0.0566	0.0008	443.80	448.63	475.20	6.61	444	6
CKZ-1	17	0.0687	0.0005	0.5572	0.0224	0.0586	0.0007	428.26	449.72	552.64	22.51	428	6
CKZ-1	18	0.0704	0.0005	0.5453	0.0219	0.0560	0.0007	438.57	441.93	453.95	3.39	439	6
CKZ-1	19	0.0671	0.0005	0.5278	0.0221	0.0567	0.0010	418.78	430.36	477.93	12.38	419	6
CKZ-1	20	0.0703	0.0005	0.5431	0.0218	0.0563	0.0007	438.08	440.49	462.64	5.31	438	6
CKZ-1	21	0.1517	0.0010	1.4686	0.0583	0.0697	0.0008	910.49	917.53	918.64	0.89	910	11
CKZ-1	22	0.2034	0.0014	2.2635	0.0907	0.0814	0.0010	1193.56	1201.00	1230.64	3.01	1231	19
CKZ-1	23	0.0662	0.0005	0.5157	0.0208	0.0564	0.0007	413.34	422.27	466.58	11.41	413	5
CKZ-1	24	0.0706	0.0005	0.5490	0.0219	0.0565	0.0007	439.83	444.33	470.90	6.60	440	6
CKZ-1	25	0.0759	0.0005	0.5527	0.0225	0.0568	0.0008	471.84	446.76	483.00	2.31	472	6
CKZ-1	26	0.0691	0.0005	0.5324	0.0212	0.0558	0.0006	430.85	433.37	443.22	2.79	431	5
CKZ-1	27	0.0634	0.0004	0.5193	0.0209	0.0592	0.0008	396.45	424.68	572.62	30.77	396	5
CKZ-1	28	0.0674	0.0005	0.5186	0.0209	0.0556	0.0008	420.17	424.22	438.03	4.08	420	6
CKZ-1	29	0.0649	0.0004	0.4994	0.0199	0.0554	0.0007	405.30	411.26	426.79	5.04	405	5
CKZ-1	30	0.0675	0.0005	0.5661	0.0237	0.0607	0.0011	421.08	455.46	627.55	32.90	421	6
CKZ-1	31	0.0705	0.0005	0.5350	0.0212	0.0552	0.0006	438.87	435.12	420.74	-4.31	439	6
CKZ-1	32	0.0693	0.0005	0.5430	0.0215	0.0565	0.0007	431.70	440.38	470.11	8.17	432	6
CKZ-1	33	0.0761	0.0005	0.5931	0.0245	0.0613	0.0010	472.68	472.84	651.18	27.41	473	6
CKZ-1	34	0.0686	0.0005	0.5952	0.0240	0.0625	0.0008	427.72	474.18	692.29	38.22	428	6
CKZ-1	35	0.0676	0.0005	0.5340	0.0216	0.0566	0.0008	421.86	434.43	477.15	11.59	422	6
CKZ-1	36	0.0723	0.0005	0.5929	0.0236	0.0595	0.0007	449.76	472.74	586.53	23.32	450	6
CKZ-1	37	0.0673	0.0004	0.5564	0.0221	0.0600	0.0007	419.87	449.20	602.49	30.31	420	5
CKZ-1	38	0.0715	0.0005	0.5485	0.0218	0.0560	0.0007	445.13	444.03	451.58	1.43	445	6
CKZ-1	39	0.0745	0.0005	0.6368	0.0261	0.0617	0.0010	463.33	500.34	663.38	30.16	463	6
CKZ-1	40	0.0719	0.0005	0.5918	0.0236	0.0598	0.0007	447.47	472.02	597.07	25.06	447	6
CKZ-1	41	0.0699	0.0005	0.5462	0.0220	0.0563	0.0008	435.67	442.50	465.79	6.47	436	6
CKZ-1	42	0.0687	0.0005	0.5375	0.0216	0.0569	0.0008	428.08	436.75	485.72	11.87	428	6
CKZ-1	43	0.0824	0.0005	0.6472	0.0257	0.0570	0.0007	510.55	506.76	491.92	-3.79	511	6
CKZ-1	44	0.0691	0.0005	0.5331	0.0212	0.0561	0.0007	430.55	433.85	455.93	5.57	431	6
CKZ-1	45	0.0707	0.0005	0.5415	0.0219	0.0568	0.0008	440.37	439.41	484.55	9.12	440	6
CKZ-1	46	0.0702	0.0005	0.5445	0.0218	0.0564	0.0007	437.30	441.39	466.58	6.28	437	6
CKZ-1	47	0.0707	0.0005	0.5880	0.0234	0.0605	0.0007	440.55	469.60	620.79	29.03	441	6
CKZ-1	48	0.0722	0.0005	0.5649	0.0223	0.0565	0.0006	449.40	454.72	471.68	4.72	449	6
CKZ-1	49	0.0669	0.0005	0.5674	0.0229	0.0618	0.0009	417.27	456.34	666.50	37.39	417	6
CKZ-1	50	0.0710	0.0005	0.5558	0.0220	0.0571	0.0007	442.18	448.79	496.55	10.95	442	6

CKZ-1	51	0.0717	0.0005	0.6099	0.0246	0.0614	0.0009	446.27	483.51	653.63	31.72	446	6
CKZ-1	52	0.0708	0.0005	0.5467	0.0217	0.0559	0.0007	440.79	442.83	448.80	1.78	441	6
CKZ-1	53	0.0698	0.0005	0.5416	0.0216	0.0560	0.0007	434.95	439.45	450.78	3.51	435	6
CKZ-1	54	0.0675	0.0005	0.5372	0.0217	0.0575	0.0008	421.02	436.55	509.61	17.39	421	6
CKZ-1	55	0.0772	0.0006	0.5487	0.0229	0.0560	0.0010	479.45	444.13	452.37	-5.99	479	7
CKZ-1	56	0.0781	0.0005	0.5589	0.0227	0.0567	0.0008	484.59	450.78	480.27	-0.90	485	6
CKZ-1	57	0.0655	0.0005	0.5286	0.0215	0.0584	0.0009	409.11	430.87	544.05	24.80	409	6
CKZ-1	58	0.2463	0.0017	2.7434	0.1095	0.0880	0.0011	1419.16	1340.29	1381.61	-2.72	1382	21
CKZ-1	59	0.0663	0.0004	0.5512	0.0219	0.0601	0.0007	413.83	445.77	607.18	31.84	414	5
CKZ-1	60	0.0732	0.0005	0.5674	0.0226	0.0566	0.0007	455.11	456.30	475.59	4.31	455	6
CKZ-1	61	0.0710	0.0005	0.5562	0.0228	0.0588	0.0009	442.18	449.08	557.84	20.73	442	6
CKZ-1	62	0.0715	0.0005	0.5503	0.0218	0.0561	0.0007	445.37	445.17	455.14	2.15	445	6
CKZ-1	63	0.0703	0.0005	0.5778	0.0229	0.0600	0.0007	437.78	463.03	604.30	27.55	438	6
CKZ-1	64	0.0723	0.0005	0.6244	0.0252	0.0621	0.0009	449.82	492.58	675.83	33.44	450	6
CKZ-1	65	0.0716	0.0005	0.5530	0.0220	0.0561	0.0007	445.67	446.95	456.72	2.42	446	6
CKZ-1	66	0.0682	0.0005	0.5426	0.0223	0.0575	0.0009	425.18	440.16	509.23	16.51	425	6
CKZ-1	67	0.0723	0.0005	0.5748	0.0229	0.0576	0.0008	450.12	461.14	513.05	12.27	450	6
CKZ-1	68	0.0701	0.0005	0.5546	0.0221	0.0573	0.0007	436.46	447.99	501.18	12.91	436	6
CKZ-1	69	0.0708	0.0005	0.5577	0.0224	0.0567	0.0008	441.09	450.05	479.88	8.08	441	6
CKZ-1	70	0.0765	0.0006	0.5392	0.0225	0.0556	0.0010	475.02	437.90	436.03	-8.94	475	7
CKZ-1	71	0.0699	0.0005	0.5649	0.0227	0.0588	0.0008	435.49	454.71	559.33	22.14	435	6
CKZ-1	72	0.0674	0.0005	0.5756	0.0234	0.0624	0.0009	420.23	461.64	689.21	39.03	420	6
CKZ-1	73	0.0707	0.0005	0.5500	0.0219	0.0560	0.0007	440.25	444.98	452.37	2.68	440	6
CKZ-1	74	0.0740	0.0005	0.5739	0.0227	0.0564	0.0007	460.45	460.50	468.93	1.81	460	6
CKZ-1	75	0.0678	0.0005	0.5505	0.0220	0.0591	0.0008	422.71	445.34	569.31	25.75	423	6
CKZ-1	76	0.0687	0.0005	0.5674	0.0225	0.0596	0.0008	428.14	456.30	589.81	27.41	428	6
CKZ-1	77	0.0683	0.0005	0.5265	0.0212	0.0564	0.0008	426.09	429.51	467.36	8.83	426	6
CKZ-1	78	0.0666	0.0005	0.5346	0.0219	0.0588	0.0009	415.88	434.84	557.84	25.45	416	6
CKZ-1	79	0.0715	0.0005	0.6149	0.0242	0.0627	0.0008	445.13	486.63	698.41	36.27	445	6
CKZ-1	80	0.0641	0.0004	0.5064	0.0199	0.0570	0.0007	400.51	416.03	490.37	18.32	401	5
CKZ-1	81	0.0682	0.0005	0.5521	0.0219	0.0592	0.0007	425.30	446.40	574.09	25.92	425	6
CKZ-1	82	0.0743	0.0005	0.5770	0.0229	0.0567	0.0007	462.25	462.55	480.27	3.75	462	6
CKZ-1	83	0.0720	0.0005	0.5614	0.0223	0.0565	0.0007	447.95	452.46	471.29	4.95	447	6
CKZ-1	84	0.0706	0.0005	0.5487	0.0220	0.0568	0.0008	439.47	444.14	482.61	8.94	439	6
CKZ-1	85	0.0720	0.0005	0.5597	0.0224	0.0566	0.0008	447.89	451.36	474.81	5.67	448	6
CKZ-1	86	0.0706	0.0005	0.5823	0.0232	0.0602	0.0008	439.77	465.94	610.05	27.91	440	6
CKZ-1	87	0.0721	0.0005	0.5691	0.0228	0.0571	0.0008	448.98	457.45	495.40	9.37	449	6
CKZ-1	88	0.0729	0.0005	0.5676	0.0226	0.0563	0.0007	453.72	456.49	463.83	2.18	454	6
CKZ-1	89	0.0685	0.0005	0.5623	0.0221	0.0596	0.0007	427.11	453.02	588.72	27.45	427	6
CKZ-1	90	0.0669	0.0004	0.5329	0.0210	0.0580	0.0007	417.63	433.75	529.76	21.17	418	5
CKZ-1	91	0.0683	0.0005	0.5403	0.0216	0.0575	0.0008	425.72	438.60	511.53	16.77	426	6
CKZ-1	92	0.0703	0.0005	0.5732	0.0226	0.0591	0.0007	437.66	460.10	572.25	23.52	438	6
CKZ-1	93	0.0726	0.0005	0.5528	0.0218	0.0555	0.0007	451.92	446.84	432.02	-4.61	452	6
CKZ-1	94	0.0726	0.0005	0.5613	0.0222	0.0564	0.0007	451.68	452.39	466.97	3.27	452	6
CKZ-1	95	0.0715	0.0005	0.5688	0.0225	0.0575	0.0007	445.37	457.26	512.29	13.06	445	6
CKZ-1	96	0.0698	0.0011	0.5689	0.2509	0.0591	0.0059	434.95	457.32	571.52	23.90	435	13
CKZ-1	97	0.0724	0.0005	0.5706	0.0225	0.0573	0.0007	450.48	458.40	504.63	10.73	450	6
CKZ-1	98	0.0667	0.0005	0.5276	0.0226	0.0574	0.0008	416.30	430.22	505.78	17.69	416	6
CKZ-1	99	0.0716	0.0005	0.5553	0.0228	0.0564	0.0008	445.67	448.46	467.76	4.72	446	6
CKZ-1	100	0.0706	0.0005	0.5972	0.0218	0.0616	0.0007	439.89	475.44	661.64	33.52	440	6
CKZ-1	101	0.0725	0.0004	0.6037	0.0210	0.0606	0.0008	451.20	479.57	626.13	27.94	451	5
CKZ-1	102	0.0696	0.0005	0.5900	0.0237	0.0616	0.0008	433.99	470.89	661.64	34.41	434	6
CKZ-1	103	0.0659	0.0005	0.5556	0.0240	0.0612	0.0008	411.53	448.65	646.27	36.32	412	6
CKZ-1	104	0.0705	0.0005	0.5433	0.0235	0.0561	0.0008	439.05	440.57	454.75	3.45	439	6
CKZ-1	105	0.0719	0.0004	0.5581	0.0219	0.0566	0.0008	447.83	450.26	476.37	5.99	448	5
CKZ-1	106	0.0734	0.0005	0.5693	0.0215	0.0566	0.0007	456.55	457.57	477.15	4.32	457	6
CKZ-1	107	0.0706	0.0005	0.5511	0.0220	0.0565	0.0007	439.77	445.72	473.25	7.07	440	6
CKZ-1	108	0.0686	0.0005	0.5469	0.0225	0.0582	0.0007	427.66	442.95	536.92	20.35	428	6
CKZ-1	109	0.0725	0.0005	0.5651	0.0218	0.0569	0.0007	451.02	454.87	486.88	7.37	451	6
CKZ-1	110	0.0770	0.0005	0.5950	0.0216	0.0595	0.0008	478.31	474.08	584.35	18.15	478	6
CKZ-1	111	0.0713	0.0005	0.5450	0.0224	0.0567	0.0008	443.74	441.70	479.88	7.53	444	6
CKZ-1	112	0.0743	0.0005	0.5750	0.0239	0.0560	0.0009	461.71	461.23	452.37	-2.07	462	6
CKZ-1	113	0.0781	0.0005	0.6600	0.0218	0.0670	0.0008	485.01	514.60	839.02	42.19	485	6
CKZ-1	114	0.0721	0.0005	0.5638	0.0226	0.0568	0.0007	448.73	453.96	482.61	7.02	449	6
CKZ-1	115	0.0688	0.0006	0.5378	0.0265	0.0568	0.0010	428.98	436.97	482.61	11.11	429	7
CKZ-1	116	0.0679	0.0005	0.5769	0.0223	0.0616	0.0008	423.43	462.45	659.90	35.83	423	6
CKZ-1	117	0.0728	0.0005	0.5924	0.0214	0.0592	0.0008	452.94	472.42	574.83	21.20	453	6
CKZ-1	118	0.0719	0.0005	0.6113	0.0227	0.0623	0.0008	447.71	484.39	684.08	34.55	448	6
CKZ-1	119	0.0724	0.0005	0.6020	0.0236	0.0605	0.0008	450.66	478.47	621.15	27.45	451	6
CKZ-1	120	0.0720	0.0005	0.5729	0.0244	0.0577	0.0009	447.95	459.89	516.87	13.33	448	6
CKZ-1	121	0.0721	0.0005	0.5553	0.0237	0.0562	0.0008	449.04	448.44	461.86	2.78	449	6
CKZ-1	122	0.0701	0.0005	0.5468	0.0227	0.0564	0.0008	436.70	442.89	468.93	6.87	437	6
CKZ-1	123	0.0720	0.0005	0.5613	0.0217	0.0566	0.0008	448.19	452.38	474.42	5.53	448	6
CKZ-1	124	0.0720	0.0006	0.5601	0.1217	0.0567	0.0030	447.95	451.58	477.93	6.27	448	7
CKZ-1	125	0.0724	0.0005	0.5752	0.0221	0.0576	0.0007	450.72	461.38	514.96	12.48	451	6
CKZ-1	126	0.0697	0.0005	0.5692	0.0222	0.0594	0.0008	434.53	457.52	582.88	25.45	435	6
CKZ-1	127	0.0809	0.0005	0.5722	0.0229	0.0566	0.0008	501.73	459.43	474.03	-5.84	502	6

CKZ-1 128	0.0698	0.0005	0.5470	0.0223	0.0571	0.0008	434.65	443.04	493.47	11.92	435	6
CKZ-1 129	0.0725	0.0006	0.5526	0.0232	0.0558	0.0009	451.38	446.72	444.42	-1.57	451	7
CKZ-1 130	0.0725	0.0005	0.5787	0.0218	0.0587	0.0008	451.38	463.63	554.13	18.54	451	6
CKZ-1 131	0.0725	0.0005	0.5514	0.0219	0.0556	0.0008	451.26	445.93	435.23	-3.68	451	6
CKZ-1 132	0.0714	0.0005	0.5514	0.0231	0.0564	0.0008	444.64	445.88	466.58	4.70	445	6
CKZ-1 133	0.0740	0.0005	0.5730	0.0219	0.0567	0.0008	460.09	459.97	480.66	4.28	460	6
CKZ-17 1	0.0681	0.0005	0.5622	0.0226	0.0588	0.0009	424.82	452.92	561.18	24.30	425	5
CKZ-17 2	0.0715	0.0005	0.5718	0.0227	0.0572	0.0008	444.95	459.18	497.71	10.60	445	6
CKZ-17 3	0.0716	0.0005	0.5549	0.0220	0.0559	0.0008	445.49	448.19	446.41	0.21	445	6
CKZ-17 4	0.0710	0.0005	0.5566	0.0220	0.0560	0.0008	442.18	449.28	453.95	2.59	442	5
CKZ-17 5	0.0697	0.0004	0.5517	0.0216	0.0571	0.0007	434.11	446.12	495.01	12.30	434	5
CKZ-17 6	0.0696	0.0004	0.5467	0.0217	0.0566	0.0008	433.81	442.84	475.98	8.86	434	5
CKZ-17 7	0.0696	0.0007	0.5810	0.0295	0.0601	0.0020	433.93	465.13	607.90	28.62	434	8
CKZ-17 8	0.0710	0.0005	0.5619	0.0226	0.0574	0.0009	442.06	452.73	505.40	12.53	442	6
CKZ-17 9	0.0689	0.0005	0.5252	0.0218	0.0562	0.0011	429.22	428.59	461.46	6.99	429	6
CKZ-17 10	0.0716	0.0005	0.5665	0.0228	0.0579	0.0009	445.73	455.72	525.60	15.20	446	6
CKZ-17 11	0.0737	0.0005	0.6011	0.0248	0.0592	0.0011	458.59	477.96	575.56	20.32	459	6
CKZ-17 12	0.0728	0.0006	0.5544	0.0241	0.0549	0.0012	453.12	447.86	406.52	-11.46	453	7
CKZ-17 13	0.0719	0.0005	0.6257	0.0248	0.0623	0.0009	447.65	493.39	683.74	34.53	448	6
CKZ-17 14	0.0769	0.0005	0.5917	0.0237	0.0562	0.0009	477.83	471.97	461.86	-3.46	478	6
CKZ-17 15	0.0676	0.0005	0.5675	0.0229	0.0610	0.0010	421.86	456.38	637.82	33.86	422	5
CKZ-17 16	0.0697	0.0004	0.5254	0.0208	0.0551	0.0008	434.05	428.75	415.47	-4.47	434	5
CKZ-17 17	0.0704	0.0005	0.5251	0.0215	0.0555	0.0010	438.44	428.58	432.02	-1.49	438	6
CKZ-17 18	0.0735	0.0005	0.5615	0.0225	0.0562	0.0009	457.33	452.52	458.30	0.21	457	6
CKZ-17 19	0.0726	0.0005	0.5684	0.0236	0.0567	0.0011	451.80	456.95	478.71	5.62	452	6
CKZ-17 20	0.0735	0.0005	0.5896	0.0237	0.0585	0.0009	457.45	470.64	546.67	16.32	457	6
CKZ-17 21	0.0702	0.0007	0.5674	0.0293	0.0603	0.0021	437.42	456.31	613.28	28.68	437	8
CKZ-17 22	0.0686	0.0005	0.5633	0.0224	0.0590	0.0009	427.66	453.67	566.73	24.54	428	5
CKZ-17 23	0.0799	0.0005	0.6202	0.0252	0.0566	0.0010	495.41	489.95	475.20	-4.25	495	6
CKZ-17 24	0.0721	0.0005	0.5431	0.0218	0.0550	0.0009	448.73	440.49	411.00	-9.18	449	6
CKZ-17 25	0.0763	0.0005	0.6631	0.0274	0.0638	0.0012	473.76	516.52	734.67	35.51	474	6
CKZ-17 26	0.0628	0.0006	0.4629	0.0227	0.0547	0.0017	392.57	386.28	398.34	1.45	393	7
CKZ-17 27	0.0761	0.0005	0.6600	0.0273	0.0640	0.0012	472.50	514.63	740.64	36.20	473	6
CKZ-17 28	0.0743	0.0005	0.5677	0.0226	0.0555	0.0009	462.13	456.55	432.02	-6.97	462	6
CKZ-17 29	0.0686	0.0005	0.5935	0.0236	0.0620	0.0009	427.41	473.07	673.42	36.53	427	5
CKZ-17 30	0.0703	0.0005	0.5460	0.0220	0.0559	0.0009	438.08	442.34	448.40	2.30	438	6
CKZ-17 31	0.0738	0.0005	0.6164	0.0243	0.0592	0.0009	459.25	487.58	574.46	20.06	459	6
CKZ-17 32	0.0683	0.0005	0.5194	0.0207	0.0569	0.0009	426.03	424.72	487.66	12.64	426	5
CKZ-17 33	0.0720	0.0005	0.5576	0.0219	0.0557	0.0008	447.89	449.96	441.23	-1.51	448	6
CKZ-17 34	0.0741	0.0005	0.5659	0.0223	0.0559	0.0008	460.57	455.38	448.00	-2.81	461	6
CKZ-17 35	0.0720	0.0005	0.5469	0.0216	0.0563	0.0008	448.37	442.96	463.43	3.25	448	6
CKZ-17 36	0.0768	0.0006	0.5684	0.0253	0.0551	0.0014	476.75	456.99	417.09	-14.30	477	7
CKZ-17 37	0.0722	0.0005	0.5347	0.0221	0.0550	0.0011	449.28	434.92	412.22	-8.99	449	6
CKZ-17 38	0.0749	0.0005	0.5700	0.0232	0.0561	0.0010	465.61	458.00	456.33	-2.03	466	6
CKZ-17 39	0.0748	0.0005	0.5784	0.0230	0.0564	0.0009	464.95	463.43	467.76	0.60	465	6
CKZ-17 40	0.0713	0.0004	0.5537	0.0215	0.0560	0.0007	443.80	447.42	451.97	1.81	444	5
CKZ-17 41	0.0733	0.0005	0.5585	0.0220	0.0560	0.0008	455.77	450.54	451.58	-0.93	456	6
CKZ-17 42	0.0717	0.0005	0.5565	0.0230	0.0565	0.0011	446.27	449.23	471.68	5.39	446	6
CKZ-17 43	0.0712	0.0005	0.6192	0.0243	0.0625	0.0009	443.32	489.36	690.92	35.84	443	6
CKZ-17 44	0.0731	0.0005	0.5631	0.0220	0.0560	0.0008	454.69	453.52	452.37	-0.51	455	6
CKZ-17 45	0.0667	0.0005	0.5233	0.0213	0.0568	0.0010	416.36	427.32	482.61	13.73	416	6
CKZ-17 46	0.0718	0.0005	0.5314	0.0211	0.0546	0.0009	447.11	432.74	393.83	-13.53	447	6
CKZ-17 47	0.0743	0.0005	0.5904	0.0242	0.0586	0.0011	461.95	471.12	551.89	16.30	462	6
CKZ-17 48	0.0741	0.0005	0.5662	0.0227	0.0566	0.0009	460.81	455.52	476.76	3.35	461	6
CKZ-17 49	0.0735	0.0005	0.6253	0.0251	0.0625	0.0011	457.21	493.18	690.58	33.79	457	6
CKZ-17 50	0.0731	0.0005	0.5573	0.0228	0.0569	0.0010	454.93	449.76	487.66	6.71	455	6
CKZ-17 51	0.0631	0.0007	0.4878	0.0275	0.0576	0.0024	394.27	403.44	513.82	23.27	394	8
CKZ-17 52	0.0743	0.0005	0.5981	0.0236	0.0588	0.0009	462.13	476.04	558.96	17.32	462	6
CKZ-17 53	0.0735	0.0005	0.5690	0.0231	0.0570	0.0010	457.03	457.37	493.08	7.31	457	6
CKZ-17 54	0.0750	0.0005	0.5730	0.0226	0.0565	0.0009	466.15	459.93	473.25	1.50	466	6
CKZ-17 55	0.0731	0.0005	0.6260	0.0256	0.0629	0.0012	454.99	493.58	705.53	35.51	455	6
CKZ-17 56	0.0773	0.0005	0.5992	0.0241	0.0583	0.0010	479.81	476.75	540.68	11.26	480	6
CKZ-17 57	0.0714	0.0005	0.5477	0.0225	0.0567	0.0011	444.28	443.46	478.71	7.19	444	6
CKZ-17 58	0.0709	0.0005	0.5458	0.0213	0.0556	0.0008	441.82	442.23	434.43	-1.70	442	5
CKZ-17 59	0.0703	0.0005	0.5410	0.0212	0.0559	0.0008	437.84	439.11	449.99	2.70	438	5
CKZ-17 60	0.0728	0.0005	0.5678	0.0226	0.0582	0.0010	453.12	456.61	537.30	15.67	453	6
CKZ-17 61	0.0728	0.0005	0.5731	0.0229	0.0580	0.0010	453.18	460.03	529.76	14.46	453	6
CKZ-17 62	0.0685	0.0004	0.5484	0.0215	0.0578	0.0009	427.11	443.92	521.81	18.15	427	5
CKZ-17 63	0.0728	0.0005	0.5404	0.0228	0.0555	0.0012	453.06	438.66	430.41	-5.26	453	6
CKZ-17 64	0.0731	0.0005	0.5544	0.0218	0.0558	0.0009	454.93	447.86	442.82	-2.73	455	6
CKZ-17 65	0.0683	0.0005	0.5104	0.0203	0.0548	0.0009	426.09	418.74	404.89	-5.24	426	5
CKZ-17 66	0.0713	0.0005	0.5630	0.0218	0.0568	0.0009	444.16	453.44	483.00	8.04	444	6
CKZ-17 67	0.0721	0.0005	0.5946	0.0220	0.0598	0.0009	448.92	473.83	597.43	24.86	449	6
CKZ-17 68	0.0739	0.0005	0.5617	0.0331	0.0563	0.0013	459.55	452.66	465.79	1.34	460	5
CKZ-17 69	0.0708	0.0005	0.5888	0.0563	0.0598	0.0019	440.85	470.12	594.90	25.89	441	6
CKZ-17 70	0.0732	0.0005	0.5639	0.0327	0.0562	0.0014	455.17	454.07	459.09	0.86	455	6

CKZ-17	71	0.0709	0.0005	0.5771	0.0235	0.0590	0.0010	441.27	462.60	565.62	21.98	441	6
CKZ-17	72	0.0716	0.0005	0.5352	0.0224	0.0557	0.0009	445.79	435.27	438.43	-1.68	446	6
CKZ-17	73	0.0720	0.0005	0.5330	0.0224	0.0554	0.0009	448.01	433.79	426.39	-5.07	448	5
CKZ-17	74	0.0698	0.0005	0.5625	0.0217	0.0595	0.0010	434.71	453.12	586.17	25.84	435	6
CKZ-17	75	0.0732	0.0005	0.5951	0.0213	0.0593	0.0010	455.29	474.13	576.66	21.05	455	6
CKZ-17	76	0.0717	0.0006	0.5931	0.0245	0.0610	0.0014	446.21	472.83	638.88	30.16	446	7
CKZ-17	77	0.0689	0.0005	0.5569	0.0237	0.0583	0.0010	429.22	449.49	539.18	20.39	429	6
CKZ-17	78	0.0727	0.0005	0.5578	0.0234	0.0556	0.0010	452.52	450.12	435.23	-3.97	453	6
CKZ-17	79	0.0714	0.0005	0.5509	0.0219	0.0575	0.0009	444.28	445.55	511.91	13.21	444	5
CKZ-17	80	0.0688	0.0005	0.5532	0.0218	0.0584	0.0009	428.62	447.06	543.30	21.11	429	6
CKZ-17	81	0.0739	0.0005	0.5624	0.0271	0.0566	0.0014	459.31	453.08	475.98	3.50	459	6
CKZ-17	82	0.0730	0.0008	0.6414	0.0952	0.0638	0.0046	454.26	503.18	733.68	38.08	454	9
CKZ-17	83	0.0709	0.0005	0.5390	0.0223	0.0558	0.0010	441.58	437.78	442.82	0.28	442	6
CKZ-17	84	0.0734	0.0005	0.5814	0.0253	0.0572	0.0010	456.73	465.33	500.41	8.73	457	6
CKZ-17	85	0.0756	0.0006	0.6080	0.0264	0.0598	0.0015	469.87	482.32	595.26	21.07	470	7
CKZ-17	86	0.0752	0.0006	0.5795	0.0587	0.0576	0.0024	467.53	464.13	514.20	9.08	468	7
CKZ-17	87	0.0725	0.0004	0.5768	0.0248	0.0586	0.0012	451.38	462.42	551.15	18.10	451	5
CKZ-17	88	0.0731	0.0005	0.5564	0.0422	0.0567	0.0020	454.75	449.18	478.32	4.93	455	6
CKZ-17	89	0.0716	0.0006	0.5492	0.0691	0.0559	0.0027	445.91	444.47	447.60	0.38	446	7
CKZ-17	90	0.0712	0.0005	0.5534	0.0224	0.0559	0.0010	443.08	447.22	449.59	1.45	443	6
CKZ-17	91	0.0707	0.0005	0.5350	0.0216	0.0565	0.0009	440.13	435.15	473.64	7.07	440	6
CKZ-17	92	0.0748	0.0005	0.5649	0.0216	0.0565	0.0009	465.19	454.68	471.29	1.29	465	6
9TS511	1	0.0719	0.0006	0.5431	0.0238	0.0558	0.0012	447.35	440.46	445.22	-0.48	447	7
9TS511	2	0.0664	0.0005	0.5056	0.0222	0.0559	0.0012	414.25	415.49	447.21	7.37	414	6
9TS511	3	0.0698	0.0004	0.5478	0.0218	0.0570	0.0008	434.77	443.55	491.15	11.48	435	5
9TS511	4	0.0706	0.0005	0.5591	0.0223	0.0568	0.0008	439.71	450.96	484.94	9.33	440	5
9TS511	5	0.0673	0.0005	0.4943	0.0214	0.0550	0.0012	419.81	407.81	412.63	-1.74	420	6
9TS511	6	0.0707	0.0005	0.5620	0.0225	0.0586	0.0008	440.61	452.80	551.15	20.06	441	5
9TS511	7	0.0706	0.0005	0.5372	0.0217	0.0556	0.0008	439.77	436.58	435.63	-0.95	440	6
9TS511	8	0.0730	0.0005	0.5718	0.0233	0.0573	0.0009	454.02	459.20	503.87	9.89	454	6
9TS511	9	0.0739	0.0005	0.5798	0.0231	0.0562	0.0008	459.37	464.31	461.07	0.37	459	6
9TS511	10	0.0694	0.0005	0.5511	0.0227	0.0575	0.0010	432.30	445.69	510.38	15.30	432	6
9TS511	11	0.2201	0.0015	2.6132	0.1059	0.0883	0.0013	1282.19	1304.36	1389.89	7.75	1390	27
9TS511	12	0.0697	0.0004	0.5536	0.0221	0.0575	0.0008	434.17	447.32	509.61	14.80	434	5
9TS511	13	0.0677	0.0005	0.5280	0.0219	0.0572	0.0010	422.47	430.51	498.87	15.32	422	6
9TS511	14	0.0710	0.0005	0.5651	0.0225	0.0573	0.0008	442.18	454.82	503.10	12.11	442	5
9TS511	15	0.0754	0.0005	0.5810	0.0238	0.0572	0.0009	468.55	465.09	500.41	6.37	469	6
9TS511	16	0.0744	0.0006	0.5453	0.0240	0.0552	0.0013	462.67	441.92	420.33	-10.07	463	7
9TS511	17	0.0724	0.0005	0.5616	0.0242	0.0567	0.0012	450.78	452.57	480.27	6.14	451	6
9TS511	18	0.0737	0.0005	0.5772	0.0234	0.0578	0.0009	458.29	462.65	523.71	12.49	458	6
9TS511	19	0.0724	0.0005	0.5524	0.0225	0.0567	0.0009	450.84	446.56	478.71	5.82	451	6
9TS511	20	0.0741	0.0005	0.5534	0.0228	0.0565	0.0010	460.51	447.23	470.50	2.12	461	6
9TS511	21	0.0697	0.0005	0.5326	0.0220	0.0564	0.0010	434.05	433.53	466.58	6.97	434	6
9TS511	22	0.0726	0.0005	0.5581	0.0233	0.0560	0.0010	451.62	450.30	451.97	0.08	452	6
9TS511	23	0.0727	0.0005	0.5945	0.0237	0.0602	0.0008	452.40	473.75	611.13	25.97	452	6
9TS511	24	0.0730	0.0005	0.5899	0.0234	0.0590	0.0008	454.02	470.77	568.57	20.15	454	6
9TS511	25	0.0715	0.0004	0.5601	0.0220	0.0568	0.0007	445.37	451.59	483.78	7.94	445	5
9TS511	26	0.0741	0.0005	0.6047	0.0252	0.0595	0.0011	460.81	480.19	586.17	21.39	461	6
9TS511	27	0.0685	0.0005	0.5163	0.0216	0.0557	0.0010	427.35	422.68	438.83	2.62	427	6
9TS511	28	0.0731	0.0005	0.5821	0.0230	0.0574	0.0008	454.81	465.81	505.78	10.08	455	6
9TS511	29	0.0717	0.0005	0.5468	0.0219	0.0560	0.0008	446.51	442.89	453.95	1.64	447	6
9TS511	30	0.0734	0.0005	0.5615	0.0226	0.0569	0.0009	456.31	452.50	485.72	6.06	456	6
9TS511	31	0.0736	0.0006	0.5953	0.0260	0.0601	0.0013	457.93	474.27	605.74	24.40	458	7
9TS511	32	0.0723	0.0005	0.5455	0.0218	0.0562	0.0008	449.70	442.04	461.07	2.47	450	6
9TS511	33	0.0699	0.0005	0.5340	0.0213	0.0562	0.0008	435.25	434.48	458.30	5.03	435	5
9TS511	34	0.0709	0.0005	0.5510	0.0218	0.0563	0.0008	441.27	445.65	462.64	4.62	441	5
9TS511	35	0.0732	0.0005	0.6409	0.0255	0.0631	0.0009	455.47	502.84	711.94	36.02	455	6
9TS511	36	0.0708	0.0005	0.5594	0.0221	0.0569	0.0008	441.03	451.14	488.82	9.78	441	5
9TS511	37	0.0656	0.0005	0.5072	0.0213	0.0567	0.0011	409.59	416.57	481.44	14.92	410	6
9TS511	38	0.0679	0.0005	0.5313	0.0214	0.0567	0.0009	423.55	432.70	480.66	11.88	424	5
9TS511	39	0.0727	0.0005	0.5583	0.0228	0.0566	0.0010	452.10	450.43	475.98	5.02	452	6
9TS511	40	0.0726	0.0005	0.5715	0.0230	0.0588	0.0009	451.86	458.96	558.22	19.05	452	6
9TS511	41	0.0687	0.0004	0.5314	0.0212	0.0563	0.0008	428.38	432.76	463.83	7.64	428	5
9TS511	42	0.0704	0.0005	0.5061	0.0217	0.0538	0.0011	438.75	415.81	361.85	-21.25	439	6
9TS511	43	0.0693	0.0004	0.6003	0.0237	0.0620	0.0008	432.06	477.43	673.42	35.84	432	5
9TS511	44	0.0700	0.0005	0.5481	0.0218	0.0569	0.0008	436.40	443.74	489.21	10.80	436	5
9TS511	45	0.0709	0.0005	0.5458	0.0215	0.0557	0.0008	441.70	442.22	441.23	-0.11	442	5
9TS511	46	0.0708	0.0005	0.5362	0.0214	0.0564	0.0008	440.79	435.91	466.19	5.45	441	6
9TS511	47	0.0739	0.0005	0.5637	0.0229	0.0561	0.0009	459.43	453.94	457.12	-0.51	459	6
9TS511	48	0.0677	0.0004	0.5395	0.0212	0.0580	0.0008	421.98	438.09	527.87	20.06	422	5
9TS511	49	0.0695	0.0005	0.5454	0.0216	0.0569	0.0008	433.08	441.97	486.50	10.98	433	5
9TS511	50	0.0691	0.0004	0.5962	0.0234	0.0622	0.0008	430.79	474.84	679.27	36.58	431	5
9TS511	51	0.0674	0.0004	0.5044	0.0201	0.0552	0.0008	420.65	414.68	421.14	0.12	421	5
9TS511	52	0.0702	0.0005	0.5442	0.0220	0.0572	0.0009	437.30	441.17	499.25	12.41	437	6
9TS511	53	0.0656	0.0005	0.4825	0.0215	0.0550	0.0013	409.29	399.78	413.04	0.91	409	6
9TS511	54	0.0766	0.0005	0.6630	0.0267	0.0641	0.0010	475.62	516.42	743.61	36.04	476	6

9TS511	55	0.0693	0.0005	0.5436	0.0221	0.0580	0.0010	432.06	440.80	530.52	18.56	432	6
9TS511	56	0.0751	0.0005	0.5594	0.0228	0.0560	0.0009	466.81	451.15	450.38	-3.65	467	6
9TS511	57	0.0736	0.0005	0.5786	0.0232	0.0568	0.0009	457.87	463.56	484.17	5.43	458	6
9TS511	58	0.0705	0.0005	0.5487	0.0218	0.0558	0.0008	439.05	444.14	445.22	1.39	439	6
9TS511	59	0.0734	0.0005	0.5810	0.0235	0.0576	0.0009	456.37	465.13	513.82	11.18	456	6
9TS511	60	0.0746	0.0005	0.5674	0.0230	0.0565	0.0009	464.05	456.31	470.90	1.45	464	6
9TS511	61	0.0727	0.0005	0.5526	0.0231	0.0563	0.0011	452.22	446.70	464.61	2.67	452	6
9TS511	62	0.0691	0.0005	0.5285	0.0210	0.0570	0.0008	430.43	430.83	491.15	12.36	430	5
9TS511	63	0.0704	0.0005	0.5486	0.0220	0.0573	0.0009	438.69	444.10	503.48	12.87	439	6
9TS511	64	0.0669	0.0004	0.4964	0.0198	0.0550	0.0008	417.33	409.28	413.44	-0.94	417	5
9TS511	65	0.0729	0.0005	0.5773	0.0232	0.0583	0.0009	453.30	462.71	539.55	15.99	453	6
9TS511	66	0.1374	0.0009	1.4613	0.0585	0.0779	0.0012	829.94	914.52	1144.32	27.47	830	10
9TS511	67	0.0733	0.0005	0.5536	0.0222	0.0562	0.0009	456.19	447.36	459.88	0.80	456	6
9TS511	68	0.0727	0.0005	0.5361	0.0216	0.0551	0.0009	452.10	435.88	415.07	-8.92	452	6
9TS511	69	0.0725	0.0005	0.5565	0.0223	0.0564	0.0009	451.02	449.26	466.97	3.42	451	6
9TS511	70	0.0722	0.0005	0.5420	0.0219	0.0557	0.0009	449.40	439.72	441.63	-1.76	449	6
9TS511	71	0.0701	0.0005	0.5368	0.0217	0.0567	0.0010	436.46	436.33	480.66	9.20	436	6
9TS511	72	0.0747	0.0005	0.5985	0.0236	0.0581	0.0008	464.65	476.29	533.53	12.91	465	6
9TS511	73	0.0722	0.0005	0.5716	0.0227	0.0580	0.0009	449.46	459.07	529.38	15.10	449	6
9TS511	74	0.0730	0.0005	0.5613	0.0220	0.0560	0.0008	454.14	452.39	453.95	-0.04	454	6
9TS511	75	0.0629	0.0005	0.4856	0.0209	0.0563	0.0012	392.93	401.89	463.83	15.28	393	6
9TS511	76	0.0710	0.0006	0.5501	0.0239	0.0578	0.0013	442.12	445.06	520.29	15.02	442	7
9TS511	77	0.0676	0.0005	0.5251	0.0213	0.0570	0.0010	421.92	428.57	493.08	14.43	422	6
9TS511	78	0.0721	0.0005	0.5614	0.0220	0.0562	0.0008	448.67	452.44	459.88	2.44	449	5
9TS511	79	0.0763	0.0005	0.5819	0.0234	0.0568	0.0009	473.94	465.67	482.22	1.72	474	6
9TS511	80	0.0705	0.0005	0.5552	0.0218	0.0571	0.0008	439.41	448.40	494.63	11.16	439	5
9TS511	81	0.0677	0.0005	0.5206	0.0209	0.0551	0.0009	422.22	425.57	415.47	-1.63	422	5
9TS511	82	0.0732	0.0005	0.6103	0.0244	0.0619	0.0010	455.35	483.77	669.96	32.03	455	6
9TS511	83	0.0742	0.0007	0.5722	0.0297	0.0589	0.0021	461.47	459.46	561.55	17.82	461	9
9TS511	84	0.0737	0.0005	0.5555	0.0222	0.0557	0.0009	458.35	448.58	440.83	-3.97	458	6
9TS511	85	0.0699	0.0006	0.5902	0.0368	0.0612	0.0018	435.25	471.02	644.87	32.51	435	7
9TS511	86	0.0766	0.0005	0.5736	0.0308	0.0557	0.0012	475.56	460.33	442.03	-7.59	476	6
9TS511	87	0.0719	0.0005	0.5399	0.0234	0.0558	0.0009	447.41	438.34	443.62	-0.85	447	6
9TS511	88	0.0666	0.0005	0.5092	0.0231	0.0553	0.0009	415.58	417.90	425.99	2.44	416	6
9TS511	89	0.0708	0.0005	0.5252	0.0221	0.0547	0.0010	441.09	428.61	401.62	-9.83	441	6
9TS511	90	0.0745	0.0004	0.5755	0.0200	0.0568	0.0008	463.21	461.56	484.55	4.40	463	5
9TS511	91	0.0726	0.0005	0.5933	0.0218	0.0602	0.0011	451.86	472.95	610.41	25.97	452	6
9TS511	92	0.0704	0.0005	0.5244	0.0231	0.0555	0.0009	438.32	428.10	432.82	-1.27	438	6
9TS511	93	0.0721	0.0046	0.5404	0.4532	0.0558	0.0119	448.92	438.67	442.82	-1.38	449	55
9TS511	94	0.0741	0.0006	0.5602	0.0263	0.0558	0.0016	460.69	451.68	444.42	-3.66	461	7
9TS511	95	0.0702	0.0005	0.5365	0.0222	0.0553	0.0010	437.18	436.13	423.16	-3.31	437	6
9TS511	96	0.0707	0.0005	0.5477	0.0228	0.0564	0.0012	440.49	443.47	468.54	5.99	440	6
9TS511	97	0.0748	0.0005	0.5656	0.0273	0.0561	0.0012	465.01	455.14	455.93	-1.99	465	6
9TS511	98	0.0707	0.0005	0.5534	0.0215	0.0598	0.0008	440.19	447.23	596.71	26.23	440	5
9TS511	99	0.0648	0.0006	0.5010	0.0241	0.0573	0.0012	404.63	412.35	502.71	19.51	405	7
9TS511	100	0.0725	0.0018	0.5405	0.0895	0.0552	0.0070	451.14	438.72	420.74	-7.23	451	22
9TS511	101	0.0691	0.0011	0.5142	0.1291	0.0554	0.0061	430.43	421.25	429.61	-0.19	430	13
9TS511	102	0.0719	0.0005	0.5421	0.0218	0.0559	0.0010	447.65	439.81	446.81	-0.19	448	6
11TS02	1	0.0709	0.0005	0.5305	0.0218	0.0547	0.0007	441.52	432.11	401.62	-9.93	442	6
11TS02	2	0.0687	0.0005	0.5955	0.0250	0.0695	0.0011	428.56	474.34	912.43	53.03	429	6
11TS02	3	0.0705	0.0005	0.5530	0.0227	0.0565	0.0007	439.17	446.93	470.50	6.66	439	6
11TS02	4	0.0702	0.0005	0.5300	0.0217	0.0547	0.0007	437.54	431.80	399.98	-9.39	438	6
11TS02	5	0.0706	0.0005	0.5399	0.0222	0.0558	0.0007	439.71	438.33	442.43	0.61	440	6
11TS02	6	0.0735	0.0006	0.5329	0.0236	0.0582	0.0012	457.39	433.73	538.05	14.99	457	7
11TS02	7	0.0712	0.0005	0.5560	0.0225	0.0566	0.0006	443.26	448.92	474.81	6.64	443	6
11TS02	8	0.0747	0.0006	0.5473	0.0234	0.0586	0.0010	464.53	443.23	550.78	15.66	465	7
11TS02	9	0.0739	0.0005	0.5587	0.0234	0.0607	0.0009	459.79	450.65	629.33	26.94	460	6
11TS02	10	0.0797	0.0006	0.5758	0.0240	0.0573	0.0008	494.51	461.74	502.33	1.56	495	7
11TS02	11	0.0712	0.0005	0.5459	0.0223	0.0559	0.0007	443.20	442.31	449.19	1.33	443	6
11TS02	12	0.0724	0.0005	0.5543	0.0228	0.0561	0.0007	450.48	447.82	455.54	1.11	450	6
11TS02	13	0.0806	0.0006	0.5757	0.0248	0.0569	0.0010	499.58	461.69	488.44	-2.28	500	7
11TS02	14	0.0714	0.0006	0.6173	0.0264	0.0639	0.0011	444.28	488.16	737.99	39.80	444	7
11TS02	15	0.0720	0.0005	0.5561	0.0233	0.0566	0.0009	448.43	449.00	474.81	5.55	448	6
11TS02	16	0.0665	0.0005	0.5400	0.0220	0.0595	0.0007	415.28	438.44	585.08	29.02	415	6
11TS02	17	0.0692	0.0005	0.5492	0.0226	0.0575	0.0008	431.39	444.45	508.85	15.22	431	6
11TS02	18	0.0739	0.0005	0.6130	0.0250	0.0600	0.0007	459.67	485.43	603.57	23.84	460	6
11TS02	19	0.0725	0.0005	0.6011	0.0243	0.0602	0.0007	451.44	477.93	610.41	26.04	451	6
11TS02	20	0.0671	0.0005	0.5180	0.0224	0.0573	0.0011	418.54	423.79	503.10	16.81	419	6
11TS02	21	0.0712	0.0005	0.5788	0.0237	0.0589	0.0008	443.08	463.66	564.14	21.46	443	6
11TS02	22	0.0749	0.0005	0.5864	0.0238	0.0571	0.0007	465.49	468.57	496.17	6.18	465	6
11TS02	23	0.0681	0.0005	0.5275	0.0214	0.0562	0.0007	424.52	430.12	459.49	7.61	425	6
11TS02	24	0.0697	0.0005	0.5397	0.0223	0.0563	0.0008	434.05	438.21	462.25	6.10	434	6
11TS02	25	0.0714	0.0007	0.5609	0.0273	0.0617	0.0018	444.64	452.13	662.34	32.87	445	8
11TS02	26	0.0693	0.0005	0.5560	0.0233	0.0588	0.0009	432.12	448.91	559.70	22.79	432	6
11TS02	27	0.0800	0.0006	0.6104	0.0258	0.0584	0.0010	496.12	483.79	544.43	8.87	496	7
11TS02	28	0.0746	0.0006	0.5762	0.0241	0.0565	0.0009	463.51	462.04	470.90	1.57	464	7

11TS02	29	0.0720	0.0006	0.5674	0.0242	0.0564	0.0010	448.19	456.31	469.72	4.58	448	7
11TS02	30	0.0750	0.0005	0.5759	0.0232	0.0555	0.0006	466.15	461.85	432.02	-7.90	466	6
11TS02	31	0.0827	0.0006	0.5842	0.0247	0.0568	0.0009	512.40	467.17	483.39	-6.00	512	7
11TS02	32	0.0733	0.0005	0.5637	0.0229	0.0562	0.0007	456.07	453.93	461.07	1.08	456	6
11TS02	33	0.0809	0.0006	0.5709	0.0237	0.0559	0.0008	501.61	458.58	449.59	-11.57	502	7
11TS02	34	0.0724	0.0005	0.5595	0.0231	0.0566	0.0008	450.66	451.22	475.59	5.24	451	6
11TS02	35	0.0727	0.0005	0.5718	0.0232	0.0569	0.0007	452.46	459.15	489.21	7.51	452	6
11TS02	36	0.0796	0.0006	0.5662	0.0234	0.0575	0.0008	493.44	455.58	509.23	3.10	493	7
11TS02	37	0.0763	0.0008	0.5557	0.0285	0.0570	0.0019	473.70	448.72	492.31	3.78	474	9
11TS02	38	0.0697	0.0005	0.5368	0.0217	0.0560	0.0006	434.59	436.30	451.58	3.76	435	6
11TS02	39	0.0704	0.0005	0.5433	0.0219	0.0561	0.0006	438.44	440.62	455.93	3.84	438	6
11TS02	40	0.0804	0.0006	0.5917	0.0248	0.0590	0.0009	498.57	471.92	568.20	12.25	499	7
11TS02	41	0.0813	0.0006	0.5749	0.0243	0.0571	0.0010	504.00	461.19	494.63	-1.89	504	7
11TS02	42	0.0761	0.0006	0.5711	0.0239	0.0559	0.0009	473.04	458.70	449.19	-5.31	473	7
11TS02	43	0.0748	0.0005	0.5674	0.0235	0.0564	0.0008	464.71	456.33	468.93	0.90	465	6
11TS02	44	0.0730	0.0005	0.5562	0.0226	0.0551	0.0007	454.44	449.04	417.50	-8.85	454	6
11TS02	45	0.0684	0.0005	0.5281	0.0215	0.0565	0.0007	426.33	430.57	472.07	9.69	426	6
11TS02	46	0.0821	0.0006	0.5950	0.0247	0.0582	0.0009	508.70	474.07	535.42	4.99	509	7
11TS02	47	0.0751	0.0005	0.5739	0.0236	0.0563	0.0008	467.05	460.52	465.79	-0.27	467	6
11TS02	48	0.0731	0.0005	0.5572	0.0225	0.0553	0.0006	454.93	449.71	422.76	-7.61	455	6
11TS02	49	0.0693	0.0005	0.5899	0.0244	0.0624	0.0009	432.12	470.81	686.48	37.05	432	6
11TS02	50	0.0796	0.0006	0.6959	0.0293	0.0712	0.0012	493.79	536.36	962.87	48.72	494	7
11TS02	51	0.0761	0.0005	0.5785	0.0237	0.0576	0.0008	472.74	463.48	513.82	7.99	473	6
11TS02	52	0.0788	0.0006	0.6008	0.0246	0.0588	0.0008	489.08	477.72	560.81	12.79	489	7
11TS02	53	0.0727	0.0005	0.5589	0.0229	0.0559	0.0007	452.58	450.82	449.99	-0.58	453	6
11TS02	54	0.0731	0.0005	0.5721	0.0232	0.0568	0.0007	454.99	459.35	483.39	5.88	455	6
11TS02	55	0.0760	0.0006	0.5258	0.0219	0.0559	0.0009	472.02	429.01	447.60	-5.46	472	7
11TS02	56	0.0740	0.0005	0.5738	0.0232	0.0564	0.0007	460.15	460.44	467.36	1.54	460	6
11TS02	57	0.0742	0.0005	0.5777	0.0233	0.0567	0.0007	461.47	462.98	480.27	3.92	461	6
11TS02	58	0.0756	0.0006	0.5831	0.0241	0.0569	0.0008	469.93	466.47	486.11	3.33	470	7
11TS02	59	0.0685	0.0005	0.5166	0.0210	0.0558	0.0007	427.11	422.88	444.02	3.81	427	6
11TS02	60	0.0762	0.0005	0.6062	0.0244	0.0576	0.0007	473.40	481.19	514.58	8.00	473	6
11TS02	61	0.0760	0.0005	0.5834	0.0239	0.0571	0.0008	472.44	466.67	496.17	4.78	472	6
11TS02	62	0.0726	0.0005	0.5584	0.0228	0.0556	0.0007	451.68	450.47	436.83	-3.40	452	6
11TS02	63	0.0757	0.0006	0.5269	0.0222	0.0561	0.0009	470.64	429.78	455.54	-3.32	471	7
11TS02	64	0.0766	0.0007	0.5571	0.0255	0.0588	0.0014	475.74	449.63	559.70	15.00	476	8
11TS02	65	0.0732	0.0005	0.5609	0.0228	0.0558	0.0007	455.65	452.13	444.02	-2.62	456	6
11TS02	66	0.0773	0.0006	0.5687	0.0234	0.0556	0.0008	479.87	457.17	437.23	-9.75	480	7
11TS02	67	0.0744	0.0005	0.5740	0.0234	0.0563	0.0008	462.43	460.58	463.04	0.13	462	6
11TS02	68	0.0803	0.0007	0.7089	0.0320	0.0736	0.0017	497.67	544.10	1029.42	51.65	498	8
11TS02	69	0.0843	0.0006	0.5886	0.0247	0.0570	0.0009	521.56	470.00	493.08	-5.78	522	7
11TS02	70	0.0725	0.0005	0.5717	0.0231	0.0573	0.0007	450.96	459.12	501.56	10.09	451	6
11TS02	71	0.0729	0.0005	0.5553	0.0224	0.0558	0.0007	453.66	448.47	445.22	-1.90	454	6
11TS02	72	0.0763	0.0006	0.6232	0.0268	0.0669	0.0013	474.18	491.88	835.91	43.27	474	7
11TS02	73	0.0766	0.0006	0.5311	0.0227	0.0558	0.0010	476.04	432.55	445.22	-6.92	476	7
11TS02	74	0.0744	0.0005	0.5776	0.0236	0.0560	0.0008	462.73	462.93	453.56	-2.02	463	6
11TS02	75	0.0751	0.0006	0.5318	0.0234	0.0566	0.0012	466.75	433.00	476.76	2.10	467	7
11TS02	76	0.0795	0.0006	0.6084	0.0253	0.0584	0.0009	493.38	482.55	544.05	9.31	493	7
11TS02	77	0.0695	0.0005	0.5308	0.0214	0.0556	0.0007	433.08	432.36	436.03	0.68	433	6
11TS02	78	0.0742	0.0005	0.5691	0.0230	0.0560	0.0007	461.23	457.40	453.95	-1.60	461	6
11TS02	79	0.0743	0.0005	0.5730	0.0231	0.0564	0.0007	461.71	459.92	469.72	1.71	462	6
11TS02	80	0.0717	0.0005	0.5537	0.0226	0.0558	0.0008	446.33	447.40	442.43	-0.88	446	6
11TS02	81	0.0802	0.0006	0.5768	0.0238	0.0568	0.0008	497.26	462.39	484.55	-2.62	497	7
11TS02	82	0.0823	0.0006	0.5796	0.0239	0.0577	0.0009	509.72	464.21	516.87	1.38	510	7
11TS02	83	0.0754	0.0006	0.6518	0.0276	0.0710	0.0013	468.85	509.56	958.28	51.07	469	7
11TS02	84	0.0725	0.0005	0.5437	0.0222	0.0556	0.0008	451.02	440.88	436.83	-3.25	451	6
11TS02	85	0.0744	0.0005	0.5525	0.0226	0.0559	0.0008	462.43	446.66	447.21	-3.40	462	6
11TS02	86	0.0811	0.0006	0.5657	0.0237	0.0570	0.0009	502.69	455.20	490.76	-2.43	503	7
11TS02	87	0.0720	0.0005	0.5565	0.0226	0.0560	0.0008	448.37	449.23	451.18	0.62	448	6
11TS02	88	0.0753	0.0006	0.5259	0.0218	0.0564	0.0009	468.19	429.07	468.15	-0.01	468	7
11TS02	89	0.0721	0.0005	0.5529	0.0222	0.0560	0.0007	449.04	446.90	452.76	0.82	449	6
11TS02	90	0.0807	0.0006	0.5630	0.0230	0.0564	0.0008	500.24	453.48	466.58	-7.21	500	7
11TS02	91	0.0775	0.0006	0.5531	0.0227	0.0550	0.0008	481.30	446.99	413.44	-16.41	481	7
11TS02	92	0.0751	0.0006	0.5255	0.0219	0.0575	0.0009	466.87	428.83	508.85	8.25	467	7
11TS02	93	0.0528	0.0006	0.3796	0.0227	0.0533	0.0008	331.75	326.72	342.44	3.12	332	7
11TS02	94	0.0728	0.0006	0.5565	0.0219	0.0555	0.0009	452.76	449.27	433.22	-4.51	453	7
11TS02	95	0.0744	0.0004	0.5662	0.0158	0.0620	0.0009	462.43	455.53	673.76	31.37	462	5
11TS02	96	0.0719	0.0005	0.5527	0.0223	0.0559	0.0006	447.47	446.76	449.19	0.38	447	6
11TS02	97	0.0711	0.0006	0.5459	0.0261	0.0559	0.0016	442.60	442.31	447.60	1.12	443	8
11TS02	98	0.0707	0.0005	0.5472	0.0226	0.0564	0.0008	440.07	443.19	469.33	6.23	440	6
11TS02	99	0.0805	0.0005	0.5578	0.0220	0.0561	0.0007	499.05	450.11	454.75	-9.74	499	6
11TS02	100	0.0802	0.0006	0.5602	0.0231	0.0568	0.0009	497.44	451.65	485.33	-2.49	497	7
11TS02	101	0.0725	0.0006	0.5795	0.0228	0.0580	0.0008	451.20	464.17	531.27	15.07	451	7
11TS02	102	0.0770	0.0006	0.5699	0.0231	0.0567	0.0009	478.07	457.95	481.05	0.62	478	7
11TS02	103	0.0725	0.0005	0.5549	0.0233	0.0561	0.0007	451.32	448.22	455.54	0.93	451	6
11TS02	104	0.0734	0.0006	0.5761	0.0232	0.0570	0.0008	456.49	461.94	491.53	7.13	456	7
11TS02	105	0.0735	0.0005	0.5675	0.0223	0.0561	0.0007	457.45	456.37	455.93	-0.33	457	6

11TS02 106	0.0735	0.0005	0.5668	0.0234	0.0561	0.0008	456.91	455.92	457.12	0.05	457	6
11TS02 107	0.0785	0.0005	0.5442	0.0229	0.0570	0.0007	487.40	441.22	490.37	0.61	487	6
11TS02 108	0.0767	0.0007	0.5617	0.0252	0.0598	0.0015	476.16	452.60	594.53	19.91	476	8
11TS02 109	0.0741	0.0006	0.5719	0.0540	0.0563	0.0020	460.81	459.21	464.22	0.73	461	7
11TS02 110	0.0797	0.0005	0.5727	0.0233	0.0558	0.0008	494.21	459.77	445.22	-11.01	494	6
11TS02 111	0.0742	0.0006	0.5686	0.0235	0.0561	0.0008	461.17	457.12	454.75	-1.41	461	7
11TS02 112	0.0812	0.0005	0.5594	0.0233	0.0566	0.0008	503.52	451.15	475.20	-5.96	475	25
11TS02 113	0.0697	0.0006	0.5259	0.0235	0.0560	0.0008	434.23	429.09	450.78	3.67	434	7
11TS02 114	0.0822	0.0007	0.5709	0.0247	0.0570	0.0009	509.12	458.61	492.31	-3.42	492	26
11TS02 115	0.0753	0.0006	0.5886	0.0225	0.0574	0.0012	468.19	469.98	507.70	7.78	468	7
11TS02 116	0.0744	0.0005	0.5800	0.0237	0.0569	0.0007	462.49	464.47	488.05	5.24	462	6
11TS02 117	0.0819	0.0006	0.5847	0.0223	0.0573	0.0010	507.16	467.49	503.87	-0.65	507	7
11TS02 118	0.0758	0.0005	0.5894	0.0236	0.0568	0.0008	471.06	470.47	484.94	2.86	471	6
11TS02 119	0.0832	0.0006	0.5839	0.0242	0.0567	0.0009	515.37	466.94	478.71	-7.66	515	7
11TS02 120	0.0747	0.0006	0.5825	0.0241	0.0562	0.0008	464.29	466.07	461.07	-0.70	464	7
11TS02 121	0.0823	0.0006	0.5759	0.0245	0.0570	0.0010	509.78	461.83	492.69	-3.47	510	8
11TS02 122	0.0734	0.0005	0.5544	0.0238	0.0547	0.0008	456.49	447.84	399.16	-14.36	456	6
11TS02 123	0.0725	0.0006	0.5616	0.0237	0.0562	0.0009	451.26	452.57	458.70	1.62	451	7

Table A4.2. Compilation of zircon U-Pb ages from basement lithologies in eastern Kyrgyzstan

Sample	Latitude	Longitude	Age ^a	±2σ	Reference
<i>U-Pb analysis</i>					
3030	41.7904	78.1769	997		Baev [1989]
3030/1	41.7904	78.1769	773		Baev [1989]
4029	41.9878	78.4192	426		Baev [1989]
4087	41.9923	78.4960	820		Baev [1989]
4092	41.9841	78.4988	687		Baev [1989]
4345	41.8814	78.4562	361		Baev [1989]
4417/1	42.0686	78.3021	454		Baev [1989]
4528	41.7917	78.1227	573		Baev [1989]
5106	41.9383	78.4745	990		Baev [1989]
80-87	42.4319	79.2249	240		Apayarov [2002; 2009; 2010]
2236	41.7391	79.1418	774		Kiselev [1993; 1999]
1093	42.3660	80.0807	422		Esmintsev [1989]
1-1	42.3426	80.1924	303		Esmintsev [1989]
1211-1	42.4246	80.1134	398		Esmintsev [1989]
1211-2	42.4246	80.1134	388		Esmintsev [1989]
1211-3	42.4246	80.1134	329		Esmintsev [1989]
1211-4	42.4246	80.1134	394		Esmintsev [1989]
13042	42.4221	80.0316	372		Esmintsev [1989]
13502	42.4438	80.0514	240		Esmintsev [1989]
13571	42.4187	80.1277	372		Esmintsev [1989]
13573	42.6040	80.0028	431		Esmintsev [1989]
1432-3	42.4585	80.1292	398		Esmintsev [1989]
1432-4	42.4585	80.1292	409		Esmintsev [1989]
1433-1	42.4281	80.1256	818		Esmintsev [1989]
1433-2	42.4281	80.1256	543		Esmintsev [1989]
1433-3	42.4281	80.1256	578		Esmintsev [1989]
1433-4	42.4281	80.1256	888		Esmintsev [1989]
277	42.4838	80.0903	441		Esmintsev [1989]
66-v	42.7202	76.3339	345		Ges [person com.]
1273	42.3638	79.0471	601		Grischenko [1985]
1305	42.3671	79.0532	661		Grischenko [1985]
1565-1	42.0250	79.0552	309		Grischenko [1985]
1959	42.2976	79.0617	701		Grischenko [1985]
273	42.5422	79.2874	369		Grischenko [1985]
4202	42.5435	79.0413	438		Grischenko [1985]
4253	42.5218	79.1223	333		Grischenko [1985]
528	42.1052	79.0691	728		Grischenko [1985]
535	42.5425	79.0499	403		Grischenko [1985]
6155	42.3503	78.9208	398		Grischenko [1985]
6261	42.0582	79.0860	262		Grischenko [1985]
6262	42.0643	79.0835	265		Grischenko [1985]
7321	42.5093	79.1326	386		Grischenko [1985]
7354	42.5222	79.1415	359		Grischenko [1985]
48-84	41.7399	77.0378	328		Kiselev [1993; 1999]
210a	41.4962	76.5088	580		Kiselev [1993]
210b	41.4962	76.5088	576		Kiselev [1993]
26-82	41.7563	77.0211	592		Kiselev [1993]
3259	41.5221	77.1080	452		Kiselev [1993]
49-84	41.7617	77.0355	773		Kiselev [1993]
6-81	41.7152	77.6504	980		Kiselev [1993]
7-81	41.7271	77.6395	892		Kiselev [1993]
9-81a	41.5194	77.1134	823		Kiselev [1993]
9-81b	41.5194	77.1134	824		Kiselev [1993]
1959a	42.2976	79.0617	579		Kiselev [1993; 1999]
1959b	42.2976	79.0617	561		Kiselev [1993; 1999]

3453	42.2021	79.0533	2578	<i>Kiselev</i> [1993; 1999]
3453X	42.2021	79.0533	2607	<i>Kiselev</i> [1993; 1999]
39-83-1	42.2022	79.0482	1844	<i>Kiselev</i> [1993; 1999]
39-83-2	42.2022	79.0482	1904	<i>Kiselev</i> [1993; 1999]
110-89	42.6861	75.9243	465	<i>Kiselev</i> [1993]
15-82	42.2737	75.6979	899	<i>Kiselev</i> [1993]
16-82	42.2697	75.6895	782	<i>Kiselev</i> [1993]
35-83	42.2664	76.0105	837	<i>Kiselev</i> [1993]
76-87	42.1759	76.3388	557	<i>Kiselev</i> [1993]
95-88	42.6867	75.9270	741	<i>Kiselev</i> [1993]
96-88	42.6856	75.9220	507	<i>Kiselev</i> [1993]
101-89	42.2252	76.3282	550	<i>Kiselev</i> [1999]
105-89	42.7594	77.9967	1806	<i>Kiselev</i> [1999]
107-89	42.7562	77.8430	457	<i>Kiselev</i> [1999]
145-90	42.6508	75.4757	364	<i>Kiselev</i> [1999]
145-90-1	42.6508	75.4757	344	<i>Kiselev</i> [1999]
146-90	42.7310	75.7136	86	<i>Kiselev</i> [1999]
148-90	42.7641	76.0534	703	<i>Kiselev</i> [1999]
148-90-A	42.7641	76.0534	490	<i>Kiselev</i> [1999]
159-91	42.7315	75.6493	129	<i>Kiselev</i> [1999]
162-91	42.0981	77.3750	337	<i>Kiselev</i> [1999]
1-80	41.9022	74.9899	383	<i>Kiselev</i> [1999]
18-82	42.0886	77.3693	442	<i>Kiselev</i> [1999]
1G	42.2554	75.8075	307	<i>Kiselev</i> [1999]
2000-2	42.0106	75.7184	313	<i>Kiselev</i> [1999]
2000-3	42.0039	75.7248	380	<i>Kiselev</i> [1999]
2043	42.3730	76.0495	148	<i>Kiselev</i> [1999]
2044	42.4070	75.9932	273	<i>Kiselev</i> [1999]
20-82-1	42.1263	77.9612	341	<i>Kiselev</i> [1999]
36-83	42.4557	79.4013	490	<i>Kiselev</i> [1999]
400	42.6690	76.1980	298	<i>Kiselev</i> [1999]
41-83	41.9701	77.6381	455	<i>Kiselev</i> [1999]
53-85	41.7954	78.1473	225	<i>Kiselev</i> [1999]
66-?	42.7202	76.3339	405	<i>Kiselev</i> [1999]
77-87	42.4567	79.4016	437	<i>Kiselev</i> [1999]
77-87*	42.4567	79.4016	146	<i>Kiselev</i> [1999]
77-87-4	42.4567	79.4016	518	<i>Kiselev</i> [1999]
803	41.8762	76.0940	431	<i>Kiselev</i> [1999]
96	41.7985	76.4933	412	<i>Kiselev</i> [1999]
CK-1-80	41.8985	75.0361	515	<i>Kiselev</i> [1999]
G-06/1	42.7514	77.8367	263	<i>Kiselev</i> [1999]
G-06/2	42.7514	77.8367	218	<i>Kiselev</i> [1999]
G-90-107	42.2358	76.3288	415	<i>Kiselev</i> [1999]
0445	41.7925	76.3314	212	<i>Mikolaichuk</i> [1994]
2138	41.9136	75.9270	374	<i>Mikolaichuk</i> [1994]
340	41.9082	75.8262	333	<i>Mikolaichuk</i> [1994]
5068	41.8977	75.7823	275	<i>Mikolaichuk</i> [1994]
546	41.8538	75.9426	403	<i>Mikolaichuk</i> [1994]
564	41.8770	75.8988	325	<i>Mikolaichuk</i> [1994]
679	41.9338	75.8273	1082	<i>Mikolaichuk</i> [1994]
8039	41.9822	75.8477	471	<i>Mikolaichuk</i> [1994]
8039	41.9822	75.8477	582	<i>Mikolaichuk</i> [1994]
9021	41.7792	76.4235	396	<i>Mikolaichuk</i> [1994]
9047	41.7742	76.4364	404	<i>Mikolaichuk</i> [1994]
10346	42.7955	76.1630	391	<i>Morozov</i> [1993]
7803	42.6974	76.2435	391	<i>Morozov</i> [1993]
10342	42.7252	76.2122	191	<i>Morozov</i> [1993]
10344	42.7734	76.2304	317	<i>Morozov</i> [1993]
10345	42.7777	76.1989	203	<i>Morozov</i> [1993]
10346	42.7955	76.1630	391	<i>Morozov</i> [1993]
10402	42.7254	76.2282	183	<i>Morozov</i> [1993]
10403	42.7270	76.2407	301	<i>Morozov</i> [1993]
109-89	42.7837	76.1197	307	<i>Morozov</i> [1993]
144-90	42.7038	75.6657	468	<i>Morozov</i> [1993]
144a-90	42.7038	75.6657	448	<i>Morozov</i> [1993]
144b-90	42.7038	75.6657	896	<i>Morozov</i> [1993]
170	42.7390	75.6903	391	<i>Morozov</i> [1993]
2034	42.8826	76.1469	868	<i>Morozov</i> [1993]
3356	42.7558	75.7861	444	<i>Morozov</i> [1993]
3357	42.8238	75.8249	321	<i>Morozov</i> [1993]
3363	42.7444	75.7316	437	<i>Morozov</i> [1993]
3364	42.7423	75.7382	352	<i>Morozov</i> [1993]
3500	42.8255	76.0430	271	<i>Morozov</i> [1993]
3503	42.6605	75.5105	158	<i>Morozov</i> [1993]
3504	42.8048	76.0296	436	<i>Morozov</i> [1993]
3505	42.8015	76.0335	316	<i>Morozov</i> [1993]
748	42.9292	75.8590	811	<i>Morozov</i> [1993]

7814	42.6748	76.1952	361	<i>Morozov</i> [1993]
8012	42.6968	76.2337	138	<i>Morozov</i> [1993]
988	42.7882	76.1037	432	<i>Morozov</i> [1993]
10010	42.1161	77.7582	479	<i>Rubtsov</i> [1984]
10148	41.8401	77.3846	426	<i>Rubtsov</i> [1984]
10166-1	41.8469	77.3990	0	<i>Rubtsov</i> [1984]
10214	41.8731	77.0608	300	<i>Rubtsov</i> [1984]
10214-1	41.8715	77.0578	414	<i>Rubtsov</i> [1984]
10233	42.0597	77.3958	361	<i>Rubtsov</i> [1984]
10234	42.0879	77.3703	403	<i>Rubtsov</i> [1984]
10235	42.0861	77.3715	389	<i>Rubtsov</i> [1984]
10470	42.1207	77.4532	381	<i>Rubtsov</i> [1984]
10534	41.9949	77.6169	496	<i>Rubtsov</i> [1984]
10535	42.2072	78.1916	420	<i>Rubtsov</i> [1984]
10538	41.7053	77.6517	713	<i>Rubtsov</i> [1984]
10560	41.7005	77.6046	982	<i>Rubtsov</i> [1984]
10616	41.8082	77.9492	521	<i>Rubtsov</i> [1984]
10626	41.9039	77.6455	424	<i>Rubtsov</i> [1984]
10635	41.8229	77.5895	478	<i>Rubtsov</i> [1984]
10655	41.8182	77.6033	455	<i>Rubtsov</i> [1984]
10663	41.7861	77.5419	426	<i>Rubtsov</i> [1984]
10740	42.0793	77.2879	264	<i>Rubtsov</i> [1984]
10901	41.6630	77.0145	454	<i>Rubtsov</i> [1984]
10935	41.9213	77.8685	328	<i>Rubtsov</i> [1984]
10965	41.9497	77.8944	228	<i>Rubtsov</i> [1984]
11149	42.1176	77.9638	473	<i>Rubtsov</i> [1984]
2080	42.1050	77.7262	387	<i>Rubtsov</i> [1984]
301	41.7103	77.0188	405	<i>Rubtsov</i> [1984]
2022/1	42.2195	74.8652	399	<i>Rubtsov</i> [1999]
2052	42.2616	74.8420	394	<i>Rubtsov</i> [1999]
2121	42.5520	74.8953	406	<i>Rubtsov</i> [1999]
2124	42.5299	74.8714	341	<i>Rubtsov</i> [1999]
2128	42.5591	74.9249	292	<i>Rubtsov</i> [1999]
1042	42.3668	75.8165	237	<i>Rubtsov</i> [1999]
1068	42.3548	75.8367	267	<i>Rubtsov</i> [1999]
1090	42.4300	75.8494	224	<i>Rubtsov</i> [1999]
1287	42.1321	75.9320	466	<i>Semenov</i> [1987]
157	42.1006	75.7589	467	<i>Semenov</i> [1987]
160-91	42.2306	76.2620	278	<i>Semenov</i> [1987]
5434	42.2120	76.3190	460	<i>Semenov</i> [1987]
5435	42.2149	76.3341	562	<i>Semenov</i> [1987]
7125	41.9970	76.9384	538	<i>Semenov</i> [1987]
7126	42.0270	76.9175	499	<i>Semenov</i> [1987]
7130	42.0479	76.9167	465	<i>Semenov</i> [1987]
7132	42.2257	76.3280	509	<i>Semenov</i> [1987]
7331	41.8322	76.8478	424	<i>Semenov</i> [1987]
7332	41.8355	76.8707	446	<i>Semenov</i> [1987]
7333	41.8209	76.8612	432	<i>Semenov</i> [1987]
7376	41.9049	76.8283	447	<i>Semenov</i> [1987]
7377	41.8989	76.8386	443	<i>Semenov</i> [1987]
7378	41.8686	76.8329	435	<i>Semenov</i> [1987]
7408	42.0219	76.4276	409	<i>Semenov</i> [1987]
7409	42.0316	76.4195	379	<i>Semenov</i> [1987]
7410	42.0288	76.3651	365	<i>Semenov</i> [1987]
74-87-1	42.2546	76.1984	371	<i>Semenov</i> [1987]
74-87-2	42.2546	76.1984	361	<i>Semenov</i> [1987]
7557	41.9960	76.9116	525	<i>Semenov</i> [1987]
7558	42.0007	76.9228	489	<i>Semenov</i> [1987]
F34-87	42.2274	76.2580	518	<i>Semenov</i> [1987]
I	42.0980	76.3439	394	<i>Semenov</i> [1987]
II	42.1982	76.3457	457	<i>Semenov</i> [1987]
III	42.0383	76.2815	465	<i>Semenov</i> [1987]
V	42.1565	76.3332	372	<i>Semenov</i> [1987]
VI	42.0324	76.3144	440	<i>Semenov</i> [1987]
VII	42.0254	76.3546	399	<i>Semenov</i> [1987]
VIII	42.2067	76.3394	324	<i>Semenov</i> [1987]
XXXVII	41.9854	76.7508	421	<i>Semenov</i> [1987]
1233	42.5393	79.3054	350	<i>Severinov</i> [1990]
1629	42.4346	79.2843	273	<i>Severinov</i> [1990]
270	42.5309	79.2903	465	<i>Severinov</i> [1990]
4104	42.4686	79.3694	209	<i>Severinov</i> [1990]
7167	42.4388	79.2852	260	<i>Severinov</i> [1990]
145	42.6555	75.4808	766	<i>Zakharov</i> [1986]
2037	42.7831	76.1241	432	<i>Zakharov</i> [1986]
2040	42.7465	76.0487	379	<i>Zakharov</i> [1986]
518-?	42.8074	76.0297	540	<i>Zakharov</i> [1986]
10944	41.8896	77.8617	200	<i>Zamaletdinov</i> [1994]

20460	42.3591	78.3887	291		Zamaletdinov [1994]
20530	42.3529	78.4710	451		Zamaletdinov [1994]
20530a	42.3529	78.4710	437		Zamaletdinov [1994]
20540	42.3606	78.4693	346		Zamaletdinov [1994]
20560	42.3723	78.5262	449		Zamaletdinov [1994]
20561	42.3741	78.5250	437		Zamaletdinov [1994]
2064	42.2108	74.9110	294		Zamaletdinov [1994]
20640	42.3997	78.5039	409		Zamaletdinov [1994]
20660	42.3748	78.4597	346		Zamaletdinov [1994]
20750	42.2506	78.4907	483		Zamaletdinov [1994]
20830	42.8554	77.2263	400		Zamaletdinov [1994]
20840	42.8213	77.1639	434		Zamaletdinov [1994]
20850	42.8226	77.2315	436		Zamaletdinov [1994]
20860	42.8183	77.2726	397		Zamaletdinov [1994]
20861	42.8183	77.2742	386		Zamaletdinov [1994]
21390	42.4451	78.6417	412		Zamaletdinov [1994]
21580	42.2445	78.5405	444		Zamaletdinov [1994]
21590	42.2593	78.5398	451		Zamaletdinov [1994]
21750	42.3817	79.1113	578		Zamaletdinov [1994]
21790	42.3428	78.7137	410		Zamaletdinov [1994]
31070-A	42.2840	75.8784	845		Zamaletdinov [1994]
31070-B	42.2840	75.8784	733		Zamaletdinov [1994]
31101-A	42.3048	75.8875	938		Zamaletdinov [1994]
31101-B	42.3048	75.8875	974		Zamaletdinov [1994]
31110	42.3070	75.8932	800		Zamaletdinov [1994]
5433-1	42.2448	76.3539	714		Zamaletdinov [1994]
5433-2	42.2448	76.3539	699		Zamaletdinov [1994]
87629	42.8256	77.2819	335		Zamaletdinov [1994]
G-81-44	42.2592	75.6971	822		Zamaletdinov [1994]
<i>SHRIMP analysis</i>					
NT-8	41.7384	75.4165	293	1	Alekseev et al. [2009]
KG33	42.7137	75.6170	1263	10	Kröner et al. [2012]
KG33	42.7137	75.6170	503	8	Kröner et al. [2012]
KG-16	42.0581	75.6814	441	6	Kröner et al. [2013]
KG49	42.7289	75.6914	451.9	4.6	Kröner et al. [2012]
Ki-679	41.9330	75.8265	1186	6	Kröner et al. [2013]
KG44	42.7208	75.8317	448.9	5.6	Kröner et al. [2012]
KG-54	42.2724	75.8543	1168	12	Kröner et al. [2013]
KG-54	42.2724	75.8543	1615	18	Kröner et al. [2013]
KG-55	42.2765	75.8544	1151	13	Kröner et al. [2013]
KG-132	41.9208	75.8659	1373	5	Kröner et al. [2013]
KG-15	42.2969	75.8758	451	5	Kröner et al. [2013]
IK-02	42.3096	75.8776	292.4	4.5	Glorie et al. [2010]
KG-13	42.3028	75.8819	461	4	Kröner et al. [2013]
KG1	42.6928	75.8819	844	9	Kröner et al. [2012]
KG2	42.6925	75.8837	810	4.2	Kröner et al. [2012]
KG-14	42.3056	75.8847	1153	4	Kröner et al. [2013]
KG11	42.6851	75.8898	810	10	Kröner et al. [2012]
KG43	42.6899	75.8986	814	5	Kröner et al. [2012]
KG36	42.7714	75.9644	799	6	Kröner et al. [2012]
KG37	42.8034	76.0258	471.9	3.5	Kröner et al. [2012]
KG38	42.8034	76.0258	472	3.1	Kröner et al. [2012]
012-2	40.9967	76.0669	284	1	Seltmann et al. [2011]
KG42	42.8497	76.0675	320.9	4.1	Kröner et al. [2012]
KG47	42.8624	76.0908	531.2	3.7	Kröner et al. [2012]
KG46	42.8723	76.1109	778	6	Kröner et al. [2012]
KG46	42.8723	76.1109	581	4	Kröner et al. [2012]
KG39	42.8865	76.1272	540.8	3.1	Kröner et al. [2012]
KG3	42.8819	76.1347	562	7	Kröner et al. [2012]
KG5	42.8819	76.1347	834	8	Kröner et al. [2012]
340002	42.2972	76.1461	292	1	Seltmann et al. [2011]
KG-51	42.2207	76.1980	1085	11	Kröner et al. [2013]
KG-52	42.1777	76.2512	1045	7	Kröner et al. [2013]
KG-53	42.1777	76.2512	1101	5	Kröner et al. [2013]
KG-135	41.6679	76.4477	1101	13	Kröner et al. [2013]
280701	40.8911	76.5458	278.9	2.7	Konopelko et al. [2007]
280001	40.8981	76.6042	281.4	2.2	Konopelko et al. [2007]
413100_1	41.6822	76.6288	466	10	Konopelko et al. [2008]
KG-139	41.7957	76.6348	1139	15	Kröner et al. [2013]
412600	41.7149	76.6744	435	3.4	Konopelko et al. [2008]
412200	41.7008	76.7176	437	3.2	Konopelko et al. [2008]
320000	42.8597	76.9347	414	7	Seltmann et al. [2011]
217001	41.4647	77.4411	303	3	Seltmann et al. [2011]
KG-127	41.6763	77.7256	1365	6	Kröner et al. [2013]
206801	41.7756	78.6772	279	8	Konopelko et al. [2007]
209202	41.6614	78.7958	296.7	4.2	Konopelko et al. [2007]
215701	41.7756	78.9297	292	3	Seltmann et al. [2011]

416000	42.0600	79.0860	291	5	<i>Konopelko et al. [2009]</i>
416705	42.0443	79.0983	294	5	<i>Konopelko et al. [2009]</i>
416506	41.9950	79.1244	299	4	<i>Konopelko et al. [2009]</i>
416801	42.0333	79.1333	295	4	<i>Konopelko et al. [2009]</i>
416803	42.0985	79.2802	289	6	<i>Konopelko et al. [2009]</i>
<i>LA-ICP-MS analysis</i>					
AI-97	41.8436	74.9011	502.7	9.2	<i>De Grave et al. [2011]</i>
AI-98	41.8850	75.0181	498.3	5.8	<i>De Grave et al. [2011]</i>
AI-100	41.9281	75.0375	453.6	7.2	<i>De Grave et al. [2011]</i>
AI-92	42.0842	75.0781	263.1	3.9	<i>De Grave et al. [2011]</i>
KYR-19	41.7378	75.1894	291	3.9	<i>De Grave et al. [2011]</i>
AI-75	40.8275	75.5564	286	4	<i>Glorie et al. [2011]</i>
AI-77	40.8273	75.5565	282	3	<i>Glorie et al. [2011]</i>
AI-62	40.9833	75.5995	788	26	<i>Glorie et al. [2011]</i>
AI-62	40.9833	75.5995	1004	31	<i>Glorie et al. [2011]</i>
AI-62	40.9833	75.5995	1174	32	<i>Glorie et al. [2011]</i>
AI-62	40.9833	75.5995	2441	110	<i>Glorie et al. [2011]</i>
AI-73	41.0572	75.6515	410	4	<i>Glorie et al. [2011]</i>
AI-71	41.0535	75.6528	417	5	<i>Glorie et al. [2011]</i>
AI-71	41.0535	75.6528	457	12	<i>Glorie et al. [2011]</i>
IK-06	41.8805	75.7198	515.5	7.1	<i>Glorie et al. [2011]</i>
AI-79	40.8088	76.2628	283	4	<i>Glorie et al. [2010]</i>
AI-82	40.9857	76.6052	286	4	<i>Glorie et al. [2011]</i>
AI-60	41.3011	76.7371	282	6	<i>Glorie et al. [2011]</i>
AI-60	41.3011	76.7371	428	11	<i>Glorie et al. [2011]</i>
AI-60	41.3011	76.7371	504	28	<i>Glorie et al. [2011]</i>
AI-31	41.7367	78.0664	842	16	<i>Glorie et al. [2011]</i>
AI-31	41.7367	78.0664	2057	55	<i>Glorie et al. [2011]</i>
AI-29	41.7147	78.1636	806	20	<i>Glorie et al. [2011]</i>
AI-29	41.7147	78.1636	1866	42	<i>Glorie et al. [2011]</i>
AI-29	41.7147	78.1636	2324	35	<i>Glorie et al. [2011]</i>
AI-15	42.1111	79.0686	831	6	<i>Glorie et al. [2011]</i>
AI-13	42.0643	79.0872	302	6	<i>Glorie et al. [2011]</i>
AI-13	42.0643	79.0872	438	13	<i>Glorie et al. [2011]</i>
AI-12	42.0633	79.0887	295	15	<i>Glorie et al. [2011]</i>
AI-12	42.0633	79.0887	221	19	<i>Glorie et al. [2011]</i>
AI-11	42.0420	79.1027	288	10	<i>Glorie et al. [2011]</i>
AI-20	42.1998	79.1161	1087	290	<i>Glorie et al. [2011]</i>
AI-20	42.1998	79.1161	2270	90	<i>Glorie et al. [2011]</i>
AI-16	42.0198	79.1404	307	4	<i>Glorie et al. [2011]</i>

^a Stated ages for U-Pb analysis are the ²⁰⁶U/²³⁸U age for ages <1000 Ma and ²⁰⁷U/²⁰⁶U for ages >1000 Ma.

